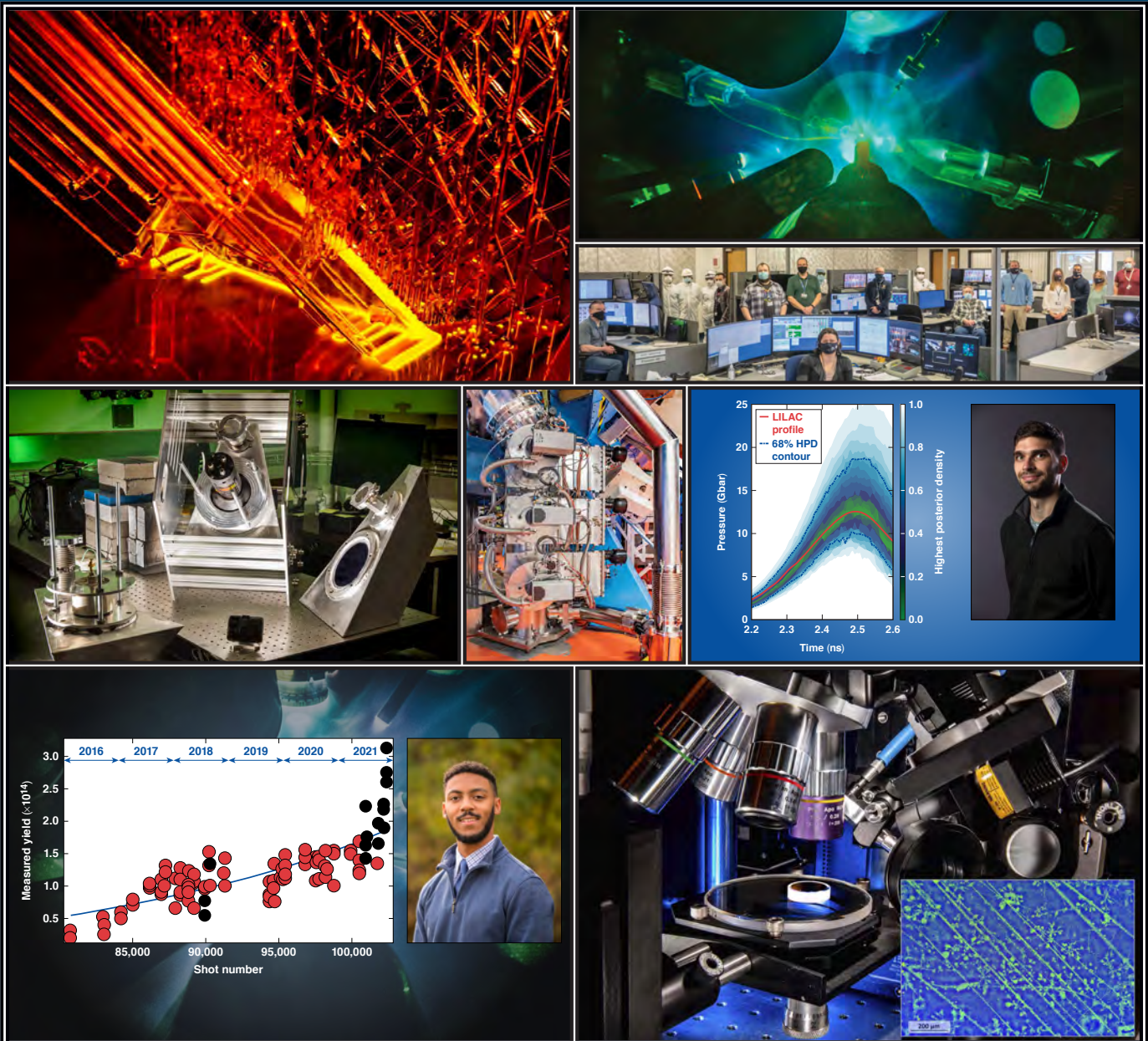


LLE 2021 Annual Report

October 2020 – September 2021



About the Cover:

Top left: LLE has deployed 3-D printing techniques to produce a variety of target components to support the large Omega User Community. Shown here is the 3-D–printed vibration absorber attached to the printer support structure. The vibration absorber can protect future fill-tube cryogenic targets from vibrations caused when the protective shroud is quickly retracted to expose the target to laser beams.

Top right: Shot number 100,000 is a historic marker of the productivity and longevity of the 60-beam OMEGA Laser System. The OMEGA shot counter has cycled the “state machine” through all shot types from laser system shots to diagnostic timing test shots to target physics shots. The OMEGA 100,000th shot marks the 33,374th target shot, which means that more than 33% of the total were for target physics. This milestone shot was conducted during a high-energy-density (HED) campaign (CyLDRT-21A) led by Los Alamos National Laboratory. Shown is the shot image and a group photo of the operations team.

Middle left: LLE’s expertise in fusion research and instrumentation is well recognized by the community including industry. Shown here is the LLE neutronic lab that provided testing and calibration of neutron detector prototypes developed by NK Labs for muon catalyzed fusion experiments. This work was supported by ARPA-E (DOE’s Advanced Research Project Agency–Energy).

Middle center: LLE completed the multiyear OMEGA cryogenic pump isolation project (shown in the picture). The new system has reduced the vibrations imparted to the OMEGA target chamber by a factor of 30 compared to the old system. In addition,

This report was prepared as an account of work conducted by the Laboratory for Laser Energetics and sponsored by New York State Energy Research and Development Authority, the University of Rochester, the U.S. Department of Energy, and other agencies. Neither the above-named sponsors nor any of their employees makes any warranty, expressed or implied, or assumes any legal liability or responsibility for the accuracy, completeness, or usefulness of any information, apparatus, product, or process disclosed, or represents that its use would not infringe privately owned rights. Reference herein to any specific commercial product, process, or service by trade name, mark, manufacturer, or otherwise, does not necessarily constitute or imply its endorsement, recommendation, or favoring by the United States Government or any agency thereof or any other sponsor. Results reported in the LLE Review should not be taken as necessarily final results as they represent active research. The views and opinions of authors expressed herein do not necessarily state or reflect those of any of the above sponsoring entities.

The work described in this volume includes current research at the Laboratory for Laser Energetics, which is supported by New York State Energy Research and Development Authority, the University of Rochester, the U.S. Department of Energy Office of Inertial Confinement Fusion under Cooperative Agreement No. DE-NA0003856, and other agencies.

tion, the new system has noticeably damped the vibration from the pumps transmitted to the rest of the facility.

Middle right: LLE Horton graduate student John J. Ruby (Ph.D. 2021) was awarded the prestigious Lawrence Fellowship from Lawrence Livermore National Laboratory. During his graduate research at LLE, Ruby built models of the physical system and combined them with Bayesian inference techniques to extract information from integrated HED physics experimental measurements to self-consistently inform the underlying physical models (sample case is shown here).

Bottom left: LLE Horton graduate student Connor Williams developed a novel laser-fusion target design with a temporally shaped laser pulse to achieve record fusion yield for direct-drive cryogenic DT implosions on OMEGA. His initial design yielded 220 trillion fusion reactions—a new facility record for fusion yield on 17 June 2021. Follow-on experiments also designed by Connor with the most-optimized target specifications surpassed the 300 trillion fusion reaction in November 2021.

Bottom right: LLE developed an in-house UV fluorescence microscope that captures the images in the inset showing a dielectric material monolayer and a network of absorbing defect structures formed inside the layer. Such absorbing structures are believed to lower the laser-induced–damage performance of optical components used in high-power laser systems. Understanding the defects’ distributions and how to control them is critical for developing optical components that exhibit higher resistance to laser damage and, ultimately, increase the power output of such systems.

For questions or comments, Laboratory for Laser Energetics,
250 East River Road, Rochester, NY 14623-1299, (585) 275-5286.
www.lle.rochester.edu

Prepared for
U.S. Department of Energy
Albuquerque Service Center
DOE/NA/3856-1688

Distribution Category
October 2020–September 2021

Printed in the United States of America
Available from

National Technical Information Services
U.S. Department of Commerce
5285 Port Royal Road
Springfield, VA 22161
www.ntis.gov

LLE 2021 Annual Report

October 2020 – September 2021



Inertial Fusion Program and
National Laser Users' Facility Program

Contents

Executive Summary	ix
LLE REVIEW 165 (OCTOBER–DECEMBER 2020)	
INERTIAL CONFINEMENT FUSION	
High-Yield Polar-Direct-Drive Fusion Neutron Sources at the National Ignition Facility	1
Unabsorbed Light Beamlets for Diagnosing Coronal Density Profiles and Absorption Nonuniformity in Direct-Drive Implosions on OMEGA	5
Mitigation of Mode-One Asymmetry in Laser-Direct-Drive Inertial Confinement Fusion Implosions	8
High-Energy-Density–Physics Measurements in Implosions Using Bayesian Inference.....	11
Ionization State and Dielectric Constant in Cold Rarefied Hydrocarbon (CH) Plasmas of Inertial Confinement Fusion	13
PLASMA AND ULTRAFAST PHYSICS	
Cross-Beam Energy Transfer Saturation by Ion Heating	16
Thresholds of Absolute Two-Plasmon–Decay and Stimulated Raman Scattering Instabilities Driven by Multiple Broadband Lasers	19
Temporal Reflection and Refraction of Optical Pulses Inside a Dispersive Medium: An Analytical Approach	22
HIGH-ENERGY-DENSITY PHYSICS	
Equation of State, Sound Speed, and Reshock of Shock-Compressed Fluid Carbon Dioxide	26
Carbon-Doped Sulfur Hydrides as a Room-Temperature Superconductor at 270 GPa	29
Unraveling the Intrinsic Atomic Physics Behind X-Ray Absorption Line Shifts in Warm Dense Silicon Plasmas.....	32
DIAGNOSTIC SCIENCE AND DETECTORS	
A Transmitted-Beam Diagnostic for the Wavelength-Tunable UV Drive Beam on OMEGA	35
Reconstructing Three-Dimensional Asymmetries in Laser-Direct-Drive Implosions on OMEGA ...	39

Application of an Energy-Dependent Instrument Response Function to the Analysis of Neutron Time-of-Flight Data from Cryogenic DT Experiments.....	42
The Scattered-Light Time-History Diagnostic Suite at the National Ignition Facility	46
LASER TECHNOLOGY AND DEVELOPMENT	
Characterization of Partially Deuterated KDP Crystals Using Two-Wavelength Phase-Matching Angles	49
High-Efficiency, Fifth-Harmonic Generation of a Joule-Level Neodymium Laser in a Large-Aperture Ammonium Dihydrogen Phosphate Crystal.....	52
Dynamics of Electronic Excitations Involved in Laser-Induced Damage in HfO ₂ and SiO ₂ Films...	57
LASER FACILITY	
FY21 Q1 Laser Facility Report	60
Project RemotePI: COVID-19 Mitigation-Compliant Operations on OMEGA and OMEGA EP	62
LLE REVIEW 166 (JANUARY–MARCH 2021)	
INERTIAL CONFINEMENT FUSION	
LLE and General Atomics: A Partnership for the Future.....	67
A Proposal for Pentagonal Prism Spherical Hohlraum Experiments on OMEGA	76
Impact of Areal-Density Asymmetries on the Loss of Confinement and Ignition Threshold in Inertial Confinement Fusion Capsules	81
PLASMA AND ULTRAFAST PHYSICS	
Microcoulomb (0.7±0.4/0.2-μC) Laser-Plasma Accelerator on OMEGA EP.....	83
Cross-Beam Energy Transfer Saturation by Ion-Trapping–Induced Detuning.....	86
Magnetically Collimated Relativistic Charge-Neutral Electron–Positron Beams from High-Power Lasers	90
Enhancing Positron Production Using Front-Surface Target Structures	93
Optical Thomson Scattering.....	95
HIGH-ENERGY-DENSITY PHYSICS	
Melting of Magnesium Oxide to 2 TPa Using Double-Shock Compression	101
Metastability of Liquid Water Freezing into Ice VII Under Dynamic Compression	104
DIAGNOSTIC SCIENCE AND DETECTORS	
Measurement of Chromatic Aberrations Using Phase Retrieval.....	107

LASER TECHNOLOGY AND DEVELOPMENT

A Highly Efficient, 10-J Output Signal Amplifier for Ultra-Intense All-OPCPA Systems.....	111
Broadband Sum-Frequency Generation of Spectrally Incoherent Pulses.....	114

PULSED-POWER SYSTEMS

Generation of Strong Magnetic Fields for Magnetized Plasma Experiments on a 1-MA Pulsed-Power Machine	117
--	-----

LASER FACILITY

FY21 Q2 Laser Facility Report	121
-------------------------------------	-----

LLE REVIEW 167 (APRIL–JUNE 2021)**INERTIAL CONFINEMENT FUSION**

Direct Evidence of Fuel–Ablator Mix from Monochromatic Time-Gated Radiography in OMEGA Cryogenic Implosions.....	123
Measuring Magnetic-Flux Suppression in High-Power Laser–Plasma Interactions.....	127
Observed Suppression of Self-Generated Magnetic Fields in a Laser-Driven Cylindrical Implosion.....	131
Inverse Ray Tracing on Icosahedral Tetrahedron Grids for Nonlinear Laser–Plasma Interactions Coupled to 3-D Radiation Hydrodynamics	134
Experimentally Inferred Fusion-Yield Dependencies of OMEGA Inertial Confinement Fusion Implosions	137
Density Evolution After Shock Release from Laser-Driven Polystyrene Targets in Inertial Confinement Fusion.....	141
Experimental Characterization of Hot-Electron Emission and Shock Dynamics in the Context of the Shock-Ignition Approach to Inertial Confinement Fusion	144

PLASMA AND ULTRAFAST PHYSICS

Experimental Observations of Laser-Driven Tin Ejecta Microjet Interactions.....	147
Optical Shock-Enhanced Self-Photon Acceleration.....	150
Nonlinear Thomson Scattering of Spatiotemporally Shaped Laser Pulses.....	153
Kinetic Simulation Study of Magnetized Collisionless Shock Formation on a Terawatt Laser System.....	155
Relativistically Transparent Magnetic Filaments: Scaling Laws, Initial Results, and Prospects for Strong-Field Quantum Electrodynamics Studies	159

HIGH-ENERGY-DENSITY PHYSICS

Ramp-Compressed Sodium at 480 GPa: A Dense Plasma Electride	162
On the Liquid–Liquid Phase Transition in Dense Hydrogen	166

DIAGNOSTIC SCIENCE AND DETECTORS

Impact of Electrode Geometry on the Efficiency of Metal–Semiconductor–Metal AlGaN Ultraviolet Photodiodes.....	170
Impact of Boundary Sharpness on Temporal Reflection in Dispersive Media	173
Time-Domain Fabry–Perot Resonators Formed Inside a Dispersive Medium	175

LASER TECHNOLOGY AND DEVELOPMENT

MTW-OPAL: A Technology Development Platform for Ultra-Intense All-OPCPA Systems	177
Alignment Tolerance Analysis for Divided-Pulse Nonlinear Compression.....	180

USERS REPORT

Eddy Killing from Global Satellite Observations	182
The 12th Omega Laser Facility Users Group Workshop	184

LASER FACILITY REPORT

FY21 Q3 Laser Facility Report	187
-------------------------------------	-----

LLE REVIEW 168 (JULY–SEPTEMBER 2021)**INERTIAL CONFINEMENT FUSION**

Computational and Experimental Evidence of Species Separation in CH Shock Release	189
Nonuniform Absorption and Scattered Light in Direct-Drive Implosions Driven by Polarization Smoothing.....	192
Feasibility Study of Diagnosing In-Flight Shell Thickness for Laser-Direct-Drive DT Cryogenic Implosions on OMEGA	195
Shock-Ignition Laser–Plasma Interactions in Ignition-Scale Plasmas.....	200
Hot-Electron Preheat and Mitigation in Polar-Direct-Drive Experiments at the National Ignition Facility	205
Thermal Decoupling of Deuterium and Tritium During the Inertial Confinement Fusion Shock-Convergence Phase	208
Enhanced Laser–Energy Coupling with Small-Spot Distributed Phase Plates (SG5-650) in OMEGA DT Cryogenic Target Implosions	210
The Benefits of Spin Polarization for Fusion Propulsion.....	213

PLASMA AND ULTRAFAST PHYSICS

Scaling of Turbulent Viscosity and Resistivity: Extracting a Scale-Dependent Turbulent Magnetic Prandtl Number.....	216
First Demonstration of a Triton Beam Using Target Normal Sheath Acceleration.....	218
Spatiotemporal Control of Laser Intensity Through Cross-Phase Modulation.....	220

HIGH-ENERGY-DENSITY PHYSICS

Improved Equation-of-State Table of Deuterium for High-Energy-Density Applications	223
--	-----

DIAGNOSTIC SCIENCE AND DETECTORS

An X-Ray Penumbra Imager for Measurements of Electron-Temperature Profiles in Inertial Confinement Fusion Implosions on OMEGA.....	226
--	-----

LASER TECHNOLOGY AND DEVELOPMENT

Advanced Laser Development and Plasma-Physics Studies on the Multi-Terawatt Laser	229
Analytic Phase Solutions of Three-Wave Interactions.....	237
Overcoming Gas-Ionization Limitations with Divided-Pulse Nonlinear Compression. II. Experimental Demonstration.....	240

MATERIALS SCIENCE

Electric-Field Enhancement Caused by Subwavelength-Sized Particles Located on the Surface of Multilayer Dielectric Mirrors.....	243
---	-----

TARGET ENGINEERING AND RESEARCH

Central Density and Low-Mode Perturbation Control of Inertial Confinement Fusion Dynamic Shell Targets	245
High Yields in Direct-Drive Inertial Confinement Fusion Using Thin-Ice DT Liner Targets	248

EDUCATION AND OUTREACH

LLE's Summer High School Research Program.....	251
--	-----

LASER FACILITY REPORT

FY21 Q4 Laser Facility Report	253
-------------------------------------	-----

NATIONAL LASER USERS' FACILITY AND EXTERNAL USERS' PROGRAMS YEAR-END REPORTS

National Laser Users' Facility and External Users' Programs	255
FY21 National Laser Users' Facility Program	259
FY21 Laboratory Basic Science Program	295

FY21 LaserNetUS Program 323

FY21 Lawrence Livermore National Laboratory Experimental Programs
at the Omega Laser Facility 328

FY21 Los Alamos National Laboratory Experimental Campaigns at the Omega Laser Facility 363

FY21 Sandia National Laboratories Progress Report on Omega Laser Facility Experiments 379

FY21 Naval Research Laboratory Report on Omega Laser Facility Experiments 382

PUBLICATIONS AND CONFERENCE PRESENTATIONS

Publications and Conference Presentations 383

APPENDIX A: EXECUTIVE SUMMARY TABLES

Table I: FY21 Horton Fellowship Program Graduate Students 406

Table II: LLE Ph.D. Theses for 2021 410

Executive Summary

C. Deeney

Director, Laboratory for Laser Energetics

The Laboratory for Laser Energetics (LLE) is funded primarily by the U.S. Department of Energy (DOE) National Nuclear Security Administration's (NNSA's) Office of Experimental Sciences Inertial Confinement Fusion (ICF) Program through a five-year Cooperative Agreement. The fiscal year ending September 2021 (FY21) comprised the third year of LLE work under DOE/NNSA Cooperative Agreement No. DE-NA0003856. The New York State Energy Research Development Authority (NYSERDA) and other federal agencies including the DOE Office of Science (Fusion Energy Sciences), Advanced Research Projects Agency–Energy (ARPA-E), and the National Science Foundation (NSF) also sponsor work at the Laboratory.

In all cases, high-quality science and technology advances were delivered while maximizing impact to our sponsors. This annual report summarizes work conducted at LLE during FY21 and includes research on the ICF and High-Energy-Density (HED) science campaigns; laser, optical materials and advanced technology development; operation of the Omega Laser Facility for the ICF and HED campaigns, the National Laser Users' Facility (NLUF), the Laboratory Basic Science (LBS) Program, and other external users including the newly established LaserNetUS supported by the DOE Office of Fusion Energy Sciences (FES); and programs focusing on the education of high school, undergraduate, and graduate students. Most of this work has been submitted to and accepted by scientific journals and is also therefore covered in the 128 peer reviewed journal papers in 2021.

Inertial Confinement Fusion Research

ICF is one of the principal missions of the Laboratory. ICF research supports the NNSA goal of achieving fusion ignition and determining what capabilities are needed to achieve ignition and then be ready for future capabilities to achieve 100-MJ fusion outputs. The NNSA program uses the Omega Laser Facility, the National Ignition Facility (NIF), and the full experimental, theoretical, computational and engineering resources of the Laboratory. By taking advantage of remote operations throughout FY21, the Omega Laser Facility (comprised of the 60-beam OMEGA UV laser and the four-beam, high-energy petawatt OMEGA EP laser) performed 2098 individual target experiments. The ICF and HED campaigns accounted for 67% of the facility shots.

LLE is the lead laboratory worldwide for the laser-direct-drive approach to fusion ignition with research focused on cryogenic DT implosions on the 60-beam OMEGA laser and on laser–plasma interaction physics of importance to all laser-driven ignition concepts at both the Omega and the NIF facilities. LLE has also developed, tested, and constructed a number of diagnostics currently being used at both the Omega Laser Facility and on the NIF. During the past year, progress in the ICF Program continued in three principal areas: (1) ICF cryogenic DT implosion experiments on OMEGA and focused physics experiments in support of ICF on OMEGA, OMEGA EP, and the NIF; (2) design efforts aimed at improving direct-drive implosion performance and the development of advanced ignition concepts such as magnetized implosions; and (3) the development of diagnostics for experiments on the NIF, OMEGA, and OMEGA EP Laser Systems. This annual report includes the summaries published in the LLE Review (Quarterly Reports) on LLE research performed during FY21 in these areas. Twenty-seven of the summaries highlighted in the report concern research on various aspects of ICF by LLE scientists and external Omega users including:

- polar-direct-drive (PDD) exploding-pusher experiments on the NIF;
- unabsorbed light measurements on OMEGA using the gated optical imagers;

- mode-one drive asymmetries in OMEGA implosions due to beam mispointing;
- the Bayesian inference technique to infer hot-spot plasma conditions and uncertainties;
- density functional theory to calculate more-accurate values for the ionization state and index of refraction in the partially ionized material that is released after shock breakout;
- progress enabled by the collaboration between LLE and General Atomics;
- pentagonal prism hohlraums as a test bed for high-symmetry ICF experiments;
- the impact of 3-D ρR asymmetries on the generalized Lawson criterion;
- hydrodynamic modeling to infer the degree of fuel–shell mixing near stagnation;
- extended-magnetohydrodynamic models that include both nonlocal suppression of Biermann battery field generation and radiation transport;
- the suppression of self-generated magnetic fields in a cylindrical implosion;
- the comparison of the laser model *IFRIIT* to direct-drive implosion experiments;
- scaling laws for higher adiabat fusion yields on OMEGA;
- a comparison of shock release in radiation-hydrodynamic models to laser-driven CH shell data;
- hot-electron source characterization and shock dynamics relevant to shock ignition;
- a comparison of plasma-jet interactions at 11.7 and 116 GPa;
- a demonstration of species separation during CH shock release;
- a correlation of scattered-light nonuniformity with polarization smoothing on OMEGA;
- quantification of shell decompression from the imprint-seeded Rayleigh–Taylor instability;
- a demonstration that the dominant instability in NIF-scale ablation plasmas relevant for shock ignition is convective stimulated Raman scattering (SRS);
- a demonstration of SRS and preheat mitigation using mid-Z layers in an ablator;
- a description of thermal decoupling in deuterium and tritium in OMEGA and NIF implosions;
- a demonstration of increased energy coupling using the SG-650 distributed phase plates;
- a proposal of using spin-polarized fuels for fusion-based spacecraft propulsion systems;
- a demonstration that electron-temperature profile measurements are in good agreement with *HYADES* predictions;

- a demonstration of increasing convergence ratio in simulations of dynamic in-flight shell formation using an extended series of picket pulses; and
- performance predictions of a new cryogenic DT target design using thin-ice DT liners.

Plasma and Ultrafast Science

Theoretical and experimental plasma physics and ultrafast science including the generation of more powerful, efficient, and compact radiation sources (high-energy photons and directed particle beams) for use as advanced probes underlies much of the ICF and HED mission science supported by NNSA, LLE, and the National Laboratories. In addition, understanding the interaction of intense laser fields with plasmas can significantly enhance ICF designs and experiments. Fifteen of the summaries highlighted in this report concern research on various aspects of plasma physics and ultrafast science by researchers at LLE including:

- measurements of cross-beam energy transfer (CBET) saturation;
- calculations of absolute thresholds for SRS and two-plasmon–decay instabilities;
- the development of an analytic approach to the reflection and transmission of light at a temporal boundary inside of a dispersive medium;
- a description of a laser-plasma accelerator with an electron charge exceeding 700 nC and conversion efficiencies up to 11%;
- the nonlinear saturation of CBET using vector particle-in-cell (VPIC) simulations;
- the collimation of a relativistic charge neutral electron–positron beam using the MIFEDS (magneto-inertial fusion electrical discharge system);
- the use of Thomson scattering to measure plasma conditions and distribution functions;
- a description of magnetized plasma experiments on the Zebra pulsed-power machine;
- the use of shaped space–time and transverse intensity profiles to drive optical shocks for self-photon acceleration;
- a description of nonlinear Thomson scattering with ponderomotive control;
- a simulation of the kinetics of magnetized collisionless shock formation;
- analytical scaling laws for the radiative properties of magnetic filaments;
- deriving a scale-dependent turbulent magnetic Prandtl number using magnetohydrodynamic simulations;
- a demonstration of triton beam production using target normal sheath acceleration; and
- cross-phase modulation to produce “flying-focus” spatiotemporally shaped pulses.

High-Energy-Density Physics

High-energy-density physics (HEDP) is the study of matter at extreme conditions. Understanding HED conditions, often defined as an energy density (in pressure units) in excess of 1 Mbar (at high temperature), is foundational for ICF ignition and national nuclear security (weapons physics) in a broad range of temperatures. These conditions are also ubiquitous in the universe and lead to basic science experiments at the Omega Laser Facility that include the study of star formation and stellar interiors, primordial

magnetic fields and reconnection, giant planets and exoplanets (including those in the solar system), supernovae explosions, and unique chemistry. LLE has a leading role in the national HEDP Program with the work carried out (often, in collaboration with scientists from the national laboratories) by LLE scientists and graduate students. This report presents eight summaries of the work by LLE including:

- equation-of-state measurements of CO₂ up to 800 GPa;
- using density functional theory (DFT) to determine stable high-pressure carbonaceous sulfur hydride compounds and their critical temperature for superconductivity;
- a novel free-energy DFT-based methodology for calculating x-ray absorption in warm dense plasmas;
- equation-of-state measurements of CO₂ up to 800 GPa;
- the metastability of the liquid-to-ice VII phase transition;
- the observation of the *hP4* phase of sodium at 480 GPa;
- large-scale *ab initio* molecular-dynamics simulations to understand the subcritical character of the insulator–metal transition in warm dense liquid hydrogen; and
- an improved first-principles equation of state for deuterium.

Diagnostic Development

Better science/understanding comes from better measurements. Therefore, advanced diagnostic research and development is a core mission at LLE. The work is part of the general education mission at LLE and is often part of the thesis work of both internal and external graduate students (and a popular topic at the annual Omega Laser Users Group workshops). As a national priority, diagnostic development is managed by the National Diagnostics Working Group that includes experts from all of the national laboratories, LLE, and a number of academic institutions. There are five research summaries on diagnostics work in this Report including:

- a transmitted beam diagnostic for diagnosing the time-resolved power spectrum of the wavelength-tunable TOP9 beam on OMEGA;
- a technique for reconstructing the hot-spot velocity, apparent ion temperature, and areal density in ICF implosions using neutron spectroscopy;
- a forward-fitting technique for analyzing neutron time-of-flight spectra;
- a description of the new scattered-light time-history diagnostic (SLTD) on the NIF; and
- a new generation of fast UV photodiodes using Al_xGa_{1-x}N substrates.

Laser System Science

Safe, efficient, and effective operation of the Omega Laser Facility requires a dedicated team of scientists and engineers that can solve the various challenges presented by the operation of ultrahigh-power laser systems at their performance limits. This Report contains a summary of research on the optical characterization of OMEGA laser beams at target chamber center using the updated full-beam in-tank diagnostic (FBIT). FBIT is capable of accurate measurements of the beam-to-beam focal-spot variation in target-plane fluence. This year the dynamic range of the focal-spot diagnostic was increased tenfold, improving the ability to answer longstanding questions of on-target uniformity. An additional capability, implemented in FY21, allows FBIT

to capture the wavefront of the pulsed UV beams at chamber center. Data sets will be acquired on many of the OMEGA beams with this new capability in FY22.

Laser Technology and Development

Laser technology and development (LTD) is a primary technical mission for LLE (along with ICF/HED science, education/training, and facility operations). The generation of a 100-J broadband 3ω laser to confirm computational predictions of laser-plasma instability mitigation is highly anticipated by NNSA as broadband and is likely to be a key part of the technical design for the construction of a high-yield (nominally 100-MJ) facility in the 2040–2050 time frame. LLE is also developing technology for the generation of ultra-intense lasers (tens to 100 PW) using the Multi-Terawatt (MTW) Laser System and submitted an RI-1 proposal to NSF at the end of FY21 to provide resources to solve the remaining technical questions and design an EP-OPAL (OMEGA EP optical parametric amplifier line) Laser System. LLE will be resubmitting a modified proposal to NSF in 2022. EP-OPAL will be a laser both to advance fundamental science and to create new diagnostics and platforms for NNSA stewardship research. There are 12 research summaries spanning laser technology and development in this Report including:

- developing a novel two-wavelength phase-matching technique for measuring the deuteration level of partially deuterated KPD crystals;
- achieving high-efficiency fifth-harmonic generation in large-aperture ADP crystals;
- developing a method for laser wavefront phase retrieval in the presence of chromatic aberrations;
- demonstrating high-efficiency (37%) optical parametric chirped-pulse amplification on the MTW Laser System using large-aperture DKDP crystals;
- developing a novel sum-frequency generation technique for broadband frequency conversion;
- developing a frequency-domain transfer-matrix approach to solving temporal reflection and refraction with finite rise time;
- calculating a temporal analog of a Fabry–Perot resonator;
- demonstrating first light on the MTW-OPAL (MTW optical parametric amplifier line) Laser System;
- deriving an analytical model for angular alignment tolerance in divided-pulse nonlinear compression;
- the design and capabilities of the MTW laser at LLE;
- analytic phase solutions for three-wave interactions showing the signal beam has a pump-beam intensity-dependent phase profile; and
- an experimental demonstration of divided-pulse nonlinear compression.

Optical Materials Science

A strong materials science effort underpins laser facility operations/engineering and the laser development and technology efforts at LLE. The work involves materials research and characterization, optical surface preparation (polishing, etching, figuring and cleaning) and optical surface laser-damage evaluation. This report includes the following two summaries of materials science research at LLE:

- laser-induced–damage testing of silica and hafnia monolayers; and
- electric-field enhancement simulations that show particles as small as $1/4$ the laser wavelength can induce field strengths exceeding coating design parameters.

Omega Laser Facility Operations

Under the facility governance plan, experimental time at the Omega Laser Facility is allocated to four NNSA-supported programs: ICF, HED, NLUF, and LBS. FY22 will be the final year under these programs; beginning in FY23 the allocation will be determined by the combined HED Council per guidance from the NNSA Office of Experimental Science. During FY21, the Omega Laser Facility conducted 1221 target shots on OMEGA and 877 target shots on OMEGA EP, with a total of 2098 target shots (see Fig. 1 for the fractional use by the various programs including shot time that is purchased by outside users). OMEGA investigators rated the overall experimental effectiveness of the facility at 93.9% while OMEGA EP was rated at 94.2%. The ICF and HED Programs conducted 67% of the NNSA-supported facility shots in FY21. Nearly half of these experiments were conducted by scientists from Lawrence Livermore National Laboratory (LLNL), Los Alamos National Laboratory (LANL), Sandia National Laboratories, and the Naval Research Laboratory. About 5% of the facility shots were used to maintain operational effectiveness. The NLUF and LBS programs described below conducted 33% of the NNSA target shots. The facility also delivered 181 shots (~9% of the total) for external users who purchased the shot time. Overall, externally led investigators used 57% of the facility time.

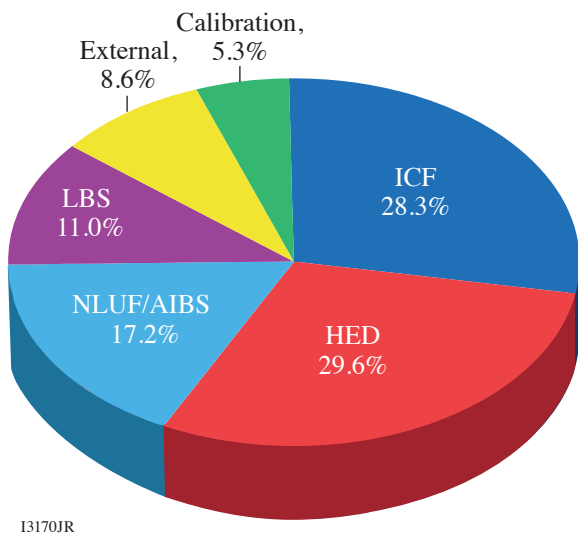


Figure 1
Fractional breakdown of FY21 shots at the Omega Laser Facility by NNSA supported programs.

The remote PI system was available to users on both laser facilities throughout FY21. Neither the effectiveness nor the availability of the facilities was compromised by remote PI operations. This Report includes quarterly summaries of the facility operations and a detailed summary of the Remote PI development and implementation.

Fundamental Science and External Users' Programs

The NNSA-supported Fundamental Science Program at the Omega Laser Facility is allocated target shot days, with individual campaigns selected through a well-defined open-call and peer-reviewed process. The Fundamental Science program has two components: (1) the NLUF Program (biennial call) makes shot time awards for the Omega Laser Facility to principal investigators (PI's) at U.S. academic institutions and commercial companies [note: a special one-time Academic and Industrial Basic Science (AIBS) Program was created to provide shot opportunities in FY20–FY21 with beam time from the unassigned NLUF allocation]; and (2) the LBS Program (annual call) makes shot time awards for basic science experiments conducted by NNSA (including LLE) and Office of Science laboratories.

Education and graduate student training is an important aspect of the NLUF and the DOE Office of Fusion Energy sponsored LaserNetUS programs (shot time is purchased for the LaserNetUS projects). Graduate student education and training at the Omega Laser Facility is also possible through collaborations between the national laboratories and academic partners and LLE. There were 66 graduate students from 20 universities involved in external user-led research programs at the Omega Laser Facility (see Table I in **National Laser Users' Facility and External Users' Programs**, p. 256).

FY21 was the second year of a two-year period of performance for eleven NLUF grant projects and ten AIBS beam-time awards with Omega shot allocations (see Table I in the **FY21 National Laser Users' Facility Program**, p. 259). PI's performed 360 target shots during 17 NLUF/AIBS campaigns, accounting for 17% of the overall Omega Laser Facility shots.

In FY21, 22 LBS projects were allocated 23 shot days for experiments at the Omega Laser Facility along with five LBS shot days that were postponed in FY20 due to COVID-19 restrictions. The initial COVID guidance caused Omega to suspend operations for two months to adjust to a new operational model. Scientists from LLNL, LANL, LLE, and Lawrence Berkeley National Laboratory conducted ~230 target shots (11% of the total) for 21 LBS projects (see Table I in the **FY21 Laboratory Basic Science Program**, p. 295).

During FY21, LLE issued a solicitation for LBS proposals for shot time in FY22. Twenty-seven proposals were submitted, requesting 36 shot days, more than double the NNSA allocation for the LBS program. After review, 15 proposals were selected and allocated 15.5 shot days for experiments at the Omega Laser Facility (see Table II in the **FY21 Laboratory Basic Science Program**, p. 297).

Through a coordinated call for proposals and an independent Proposal Review Panel (PRP) process, the FES-funded LaserNetUS network makes available a variety of ultrafast, high-peak-power and high-energy petawatt-class lasers (including the OMEGA EP laser) to users who do not have routine access to ultrahigh-intensity lasers. During FY21, six LaserNetUS Cycle-3 proposals along with one LaserNetUS Cycle-2 project were awarded nine shot days on OMEGA EP for experiments in FY21 and FY22 (see Table I in the **FY21 LaserNetUS Program**, p. 323). Scientists from LLNL, General Atomics, and the University of California, San Diego conducted 29 target shots over four shot days in FY21 for three LaserNetUS projects.

Since FY21, the newly established Center for Matter at Atomic Pressures (CMAP) hosted at the University of Rochester and funded by the National Science Foundation (NSF) has been using the Omega Laser Facility for experiments to explore "matter under the uncharted, extreme conditions at which most of the known mass in the universe resides." CMAP is the first NSF Physics Frontier Center in the field of HED science. Members of the CMAP team from UR, Massachusetts Institute of Technology (MIT), Princeton University, the Universities of California at Berkeley and Davis, the University of Buffalo, and LLNL conducted 66 target shots on OMEGA and OMEGA EP in FY21.

Omega Laser Facility Users Group

LLE hosted the 12th meeting of the Omega Laser Facility Users Group (OLUG) on 27–30 April 2021. The three-day virtual meeting smashed the attendance record that had been previously space limited for in-person meetings at LLE with registered attendees including 217 students and scientists from 40 institutions around the world. The enhanced international participation was reflected in the poster session where three of the six best poster prizes in the graduate student and post-doctoral categories were won by international participants. The highlight of the meeting (at least for the LLE management) was the identification and discussion of Findings & Recommendations (F&R's) to enhance Omega Laser Facility capabilities and experimental preparations/operations. The 29 F&R's include expanded ten-inch manipulator (TIM) access to active shock breakout (ASBO)/streaked optical pyrometer (SOP) and the addition of an optical Thomson-scattering diagnostic on OMEGA EP, improved navigation on the Diagnostics Usage page on the LLE website, the addition of a time-resolved x-ray history diagnostic for high-neutron-yield environments, a third VISAR (velocity interferometer system for any reflector) leg, and opposing UV beams on OMEGA EP. Professor M. Koepke (University of W. Virginia), the outgoing OLUG chair, welcomed the new chair J. A. Frenje (MIT) and co-chair P. Valdivia (Johns Hopkins University) for two-year terms. This Report contains a summary of the FY21 OLUG workshop. Additional information on past OLUG workshops and the FY21 workshop (e.g., the agenda) are available on the LLE website at Omega Laser Facility Users Group 2021 Workshop – Laboratory for Laser Energetics (rochester.edu).

Education

As noted above, education/training is a primary technical mission for LLE. LLE is the only place where students can be trained at scale for careers in National Security related to the science of Stockpile Stewardship. The education programs at the Laboratory include a high school program that exposes students to a professional environment where they work alongside scientists and

engineers for a summer; undergraduate programs where students work part-time with scientists and engineers often throughout an academic year (or longer) to understand how classroom education is applied to real world problems; graduate education where students are immersed in the science of HED physics to earn MS and Ph.D. degrees; and a new high school program for under-represented minority students and their teachers in the local Rochester area. This report provides a summary of these activities in FY21, including:

1. Summer High School Research Program

Since 1989, LLE has held an annual Summer High School Research Program for Rochester-area high school students who have just completed their junior year. The eight-week program provides an exceptional opportunity for highly motivated students to experience scientific research in a professional environment. Eight students participated in the virtual 2021 program (see **LLE's Summer High School Research Program**, p. 251). To date, 399 from 55 high schools have participated in the program, including 137 female students. Thirty-nine students have become Scholars in the prestigious Regeneron Science Talent Search based on the research projects they carried out at LLE. To date, 105 students from this program have obtained doctorate degrees.

2. Broad Exposure to Science and Technology Student and Teacher Research Program

During the summer of FY21, LLE ran a pilot program for the research and education initiative called BEST (Broad Exposure to Science and Technology). Started during FY20 by T. J. Kessler, the LLE Diversity Manager, the goal of this initiative is to involve underrepresented high school students and their teachers from the Rochester City School District (RCSD) in various aspects of science and technology that support laser science and applications research at LLE. The summer 2021 pilot program included two RCSD high school science and technology teachers and four high school students of color. Ten LLE scientists, engineers, and technicians inspired and guided the students and their teachers, encouraging them to explore the next generation of STEM-related jobs and careers. The RCSD teachers gained knowledge and experience that enhanced the science and technology curricula going into the 2021–2022 school year. In addition, both the teachers and students acted as BEST ambassadors to encourage participation in the FY22 summer BEST program. Both an RCSD teacher and student participated in a visit by the director of the National Science Foundation to UR/LLE during the spring of 2022.

3. Undergraduate Student Program

LLE provides unique work–study opportunities for undergraduate research and co-op internships by involving undergraduate students and community college students in its research activities. These students come from the University of Rochester, the Rochester Institute of Technology, the State University of New York (SUNY) at Geneseo, Cornell University, Monroe Community College, and other institutions. LLE scientists also host and mentor students participating in the Research Experience for Undergraduate Program funded by NSF, and from 2022 the new Plasma and Fusion Undergraduate Research Opportunity Program funded by FES. During FY21, LLE employed 32 undergraduate and nineteen co-op students. LLE also funded 21 undergraduate students and six faculty advisors from SUNY Geneseo (one of the long-standing academic partners at LLE) and Houghton College to conduct research in physics and engineering and training students in the area of nuclear and plasma diagnostics.

4. Graduate Student Programs

Graduate students use the Omega Laser Facility as well as other LLE facilities to conduct ICF and HEDP research to earn advanced degrees. These students make significant contributions to LLE research output (e.g., they write a large fraction of the manuscripts published annually by LLE). Thirty-five University of Rochester faculty members (across eight academic departments) hold secondary appointments with LLE, increasing the breadth of leadership in science and technology. Eighteen scientists and engineers at LLE hold secondary faculty appointments with the University in five different academic departments. The large number of faculty and LLE staff enable the Laboratory to pull together a new high-energy-density science curriculum and educate a large number of graduate students. Approximately 90 UR graduate students were involved in research at LLE in FY21. LLE directly sponsored 63 Ph.D. students via the NNSA-supported University of Rochester Frank Horton Fellowship Program (see Table I in the **Appendix**, p. 406). Their research includes theoretical and experimental plasma physics and fusion science, HED physics, x-ray and atomic physics, nuclear physics, material properties under extreme pressure, astrophysics, ultrafast optoelectronics, high-power laser development and applications, nonlinear optics, optical materials and optical fabrication technology, and target fabrication.

In FY21, LLE directly funded graduate/undergraduate research with academic partners including the University of Delaware, the MIT Plasma Science and Fusion Center, the University of Michigan, the University of Nebraska-Lincoln, the University of Nevada at Reno, Stony Brook University, Imperial College London, and Oxford University. These programs involved two undergraduate students, 21 graduate students, four postdoctoral researchers, eight scientists and research staff, and eight faculty members.

In addition, the Omega Laser Facility and LLE significantly facilitated the education and training of more than 250 graduate students and postdoctoral researchers in the HEDP and ICF science areas from other universities through their participation in NLUF, LBS, LaserNetUS, and collaborations with LLE and the DOE national laboratories. Sixty-six graduate students (including 16 mentioned above) from 20 universities (see Table I in the **National Laser Users' Facility and External Users' Programs**, p. 256) were involved in these external user-led research programs with experiments conducted at the Omega Laser Facility in FY21.

Fifteen graduate students, including ten from the University of Rochester and eight from other academic institutions have successfully completed their thesis research and obtained Ph.D. degrees in calendar year 2021. Table II (**Appendix**, p. 410) lists their name, university, and current employer. Six of them (40% of the total), including five from UR, joined one of the DOE NNSA laboratories, five stayed within academia, and four work in the private sector.

High-Yield Polar-Direct-Drive Fusion Neutron Sources at the National Ignition Facility

R. S. Craxton,¹ C. B. Yeaman,² G. E. Kemp,² Z. B. Walters,² H. D. Whitley,² P. W. McKenty,¹ E. M. Garcia,¹ Y. Yang,¹
and B. E. Blue²

¹Laboratory for Laser Energetics, University of Rochester

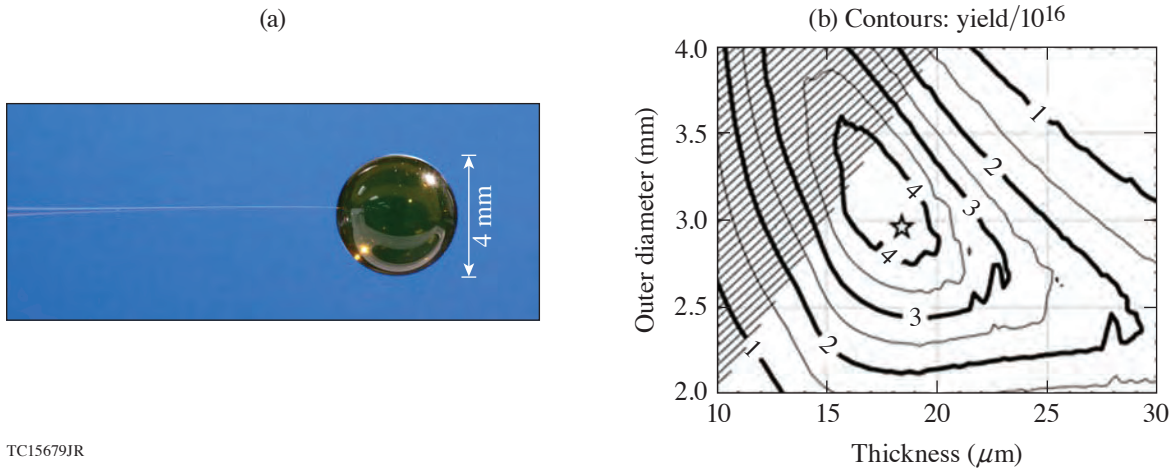
²Lawrence Livermore National Laboratory

Direct-drive implosions at the National Ignition Facility (NIF) that produce high neutron yields from DT-filled targets are of substantial current interest as high-fluence fusion neutron sources. These sources are routinely used for neutron radiation effects experiments in support of programs at the national laboratories. This summary describes the development of these sources, focusing on the target designs and the high-yield experimental results that have been obtained to date.

The targets used for these experiments, typically thin shells of glow-discharge-polymer plastic (CH)¹ filled with DT gas, are sometimes known as “exploding pushers”² because they resemble the targets that have consistently been used since the earliest implosions³ to maximize neutron yield. The earliest targets were irradiated with short pulses of IR laser light that deposited energy largely into energetic electrons. These electrons passed back and forth through the shell, depositing their energy throughout the shell. The shell exploded, causing its inner portion to compress the fuel. Later experiments using UV laser light, including the current experiments, differ in that the shell is ablatively accelerated by the laser, but the shell still decompresses (explodes) as it moves inward, producing high ion temperatures through shock convergence but precluding the high densities needed for ignition. Cryogenic designs, in contrast, provide a path to ignition and gain, but the most convenient source on the NIF of high neutron fluxes is the exploding pusher.

A typical target is shown in Fig. 1(a): a 4-mm-diam, $\sim 25\text{-}\mu\text{m}$ -thick CH shell, filled with 8 atm of DT. Experiments have typically used diameters ranging from 3 mm to 5 mm, depending on the laser energy. The design of an experiment at a given laser energy entails a number of considerations, particularly the 1-D design to optimize the yield and the pointing design to optimize implosion uniformity. The 1-D designs were done using *HYDRA*.⁴ Figure 1(b) summarizes the results of thousands of 1-D runs in the form of a contour plot of yield as a function of the shell diameter and thickness for a laser energy of 585 kJ. The optimum design calls for a diameter of 3 mm and a thickness of 18 μm , the parameters of the shot known as “Little Guy.” Targets that are too thin or have a diameter that is too small are fully imploded before all of the laser energy can be delivered. Targets in the upper-right quadrant are too massive to be accelerated sufficiently with the available laser energy. The hatched region represents targets that are too thin to reliably hold the 8-atm pressure.

The pointing designs were done using the 2-D hydrodynamics code *SAGE*, which includes a 3-D ray-tracing capability.⁵ The need for beam pointing optimization arises because the NIF beams (grouped into 48 quads) are located in four rings in each hemisphere at angles ranging between 23.5° and 50° from the vertical axis. Most of the beams must be repointed toward the equator in order to provide close-to-uniform drive at all angles on the surface of the target, a concept known as polar direct drive.⁶ The problem is complex because the best-focus phase-plate spot profiles, chosen to meet the requirements of indirect-drive designs, are different in size and shape for each ring of beams. The beams also need to be defocused so that their focal spots better match the target diameter, especially for the larger targets. It was shown in Ref. 7 that reasonable implosion uniformity can be achieved using the indirect-drive phase plates by a combination of appropriate repointings and beam-defocus distances.

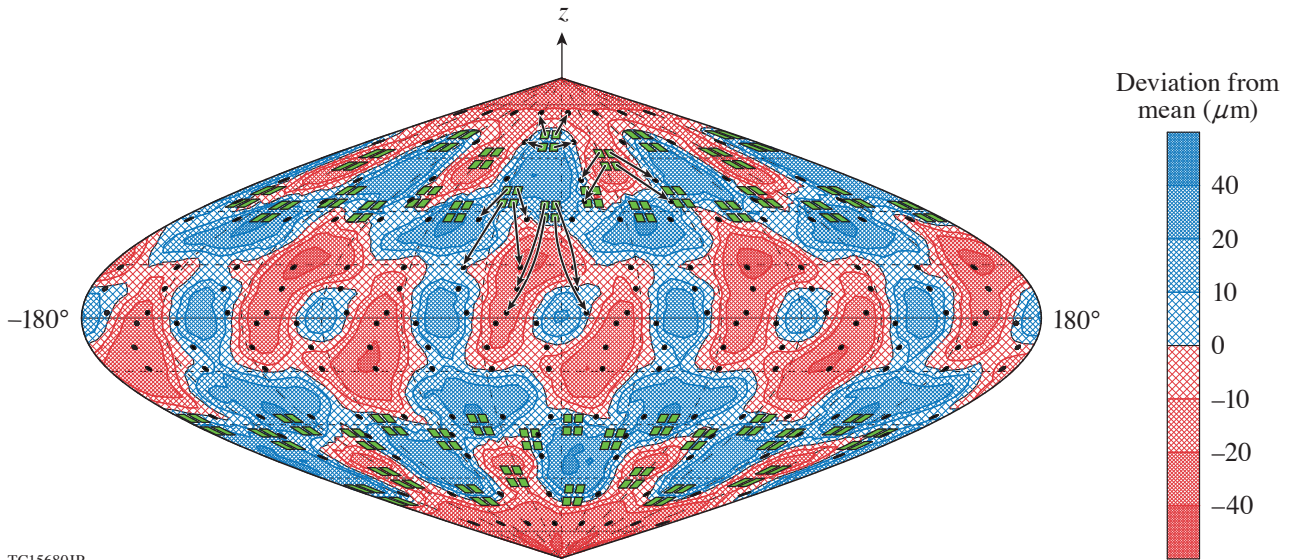


TC15679JR

Figure 1

(a) A typical 4-mm-diam plastic target supported by a glass microcapillary fill-tube stalk. (b) Contour plot of neutron yield as a function of target thickness and diameter, based on a large number of 1-D simulations using the code *HYDRA*. This scan was done for a laser pulse delivering 585 kJ; the optimum parameter combination, indicated by the star, was used for the “Little Guy” shot.

Combining its 2-D hydrodynamics with its 3-D ray trace, *SAGE* is able to predict the 3-D implosion uniformity pattern over the target surface. Figure 2 is a contour plot of the deviation from the mean of the center-of-mass radius of the imploding shell, with red indicating overdriven and blue underdriven. The plot also shows the locations of the 192 beam ports (green squares) and their aim points (black circles) on the target surface. The rms deviation is just 20.5 μm after the shell has imploded 923 μm, corresponding to a 2.22% nonuniformity in the distance traveled, or equivalently in the average velocity. This is made up of a quadrature sum of 1.23% in the θ direction and 1.85% in the azimuthal (ϕ) direction, illustrating the importance of spreading the beams appropriately in the azimuthal direction.



TC15680JR

Figure 2

Contour plot, relative to the spherical coordinate angles (θ, ϕ), of the deviation from the mean of the center-of-mass radius of a 4-mm-diam plastic target after implosion through 923 μm, predicted using the code *SAGE*. The plot shows that the average velocity variation over the sphere is 2.22% rms, the quadrature sum of 1.23% in the θ direction and 1.85% in the ϕ direction. The green squares indicate the 192 NIF beams, the black circles their aim points, and the arrows the beam repointings in θ and ϕ .

Experimental results for the neutron yield are shown in Fig. 3. Neutron images viewing in the polar and equatorial directions are given in Figs. 3(a) and 3(b), respectively, for Little Guy. The images are approximately round, indicating very acceptable uniformity. Figure 3(c) gives a compilation of the yields obtained on a large number of shots, including direct-drive shots using 3-mm- and 4-mm-diam CH shells and some (at lower energy) using ~ 2 -mm-diam SiO_2 shells. The highest yields come from indirect-drive cryogenic targets close to the nominal 1.8-MJ NIF energy. However, the direct-drive targets provide significantly higher neutron fluxes: test objects can be placed much closer to the source because of the decrease in debris load from the much smaller target vaporized mass.⁸ In addition, the direct-drive targets are non-cryogenic and therefore much simpler to field.

Basic parameters and yield results are given in Table I for the three particularly noteworthy shots highlighted in Fig. 3. Little Guy, a 3-mm target, produced 4.81×10^{15} neutrons at an energy of 585 kJ that was low enough to incur no damage to NIF optics. “Orange,” an optimized 4-mm target driven by 1.1 MJ, produced 1.11×10^{16} neutrons with an efficiency (fusion energy divided by incident laser energy) of 2.85%, the yield scaling with energy from OMEGA experiments according to the predictions of

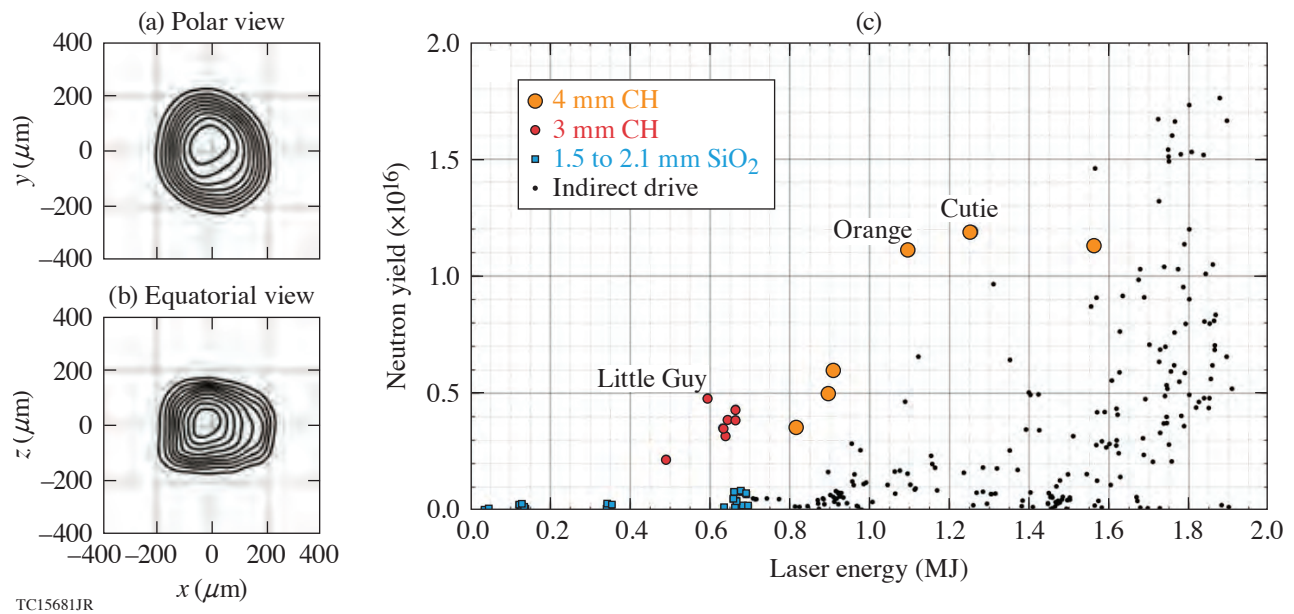


Figure 3

[(a),(b)] Experimental time-integrated neutron images at $10\text{-}\mu\text{m}$ resolution of the 3-mm Little Guy target, with contours in units of 10% of the peak intensity. (c) Yield from a variety of NIF neutron sources (through October 2020) as a function of target energy. Details of the three labeled shots are given in Table I.

Table I: Selected parameters of three NIF shots of particular interest. Each target is filled with 8 atm of DT ($\sim 64\%$ D).

		Little Guy	Orange	Cutie
	NIF shot	N190707-001	N190227-001	N191027-003
Capsule	Outer radius (μm)	1480	1971	1978
	Thickness (μm)	18.4	25	22.7
Laser	Laser energy (kJ)	585	1097	1256
	Peak power (TW)	328	390	425
Results	Yield (#DT neutrons)	4.81×10^{15}	1.11×10^{16}	1.19×10^{16}
	Fusion conversion efficiency G_L	2.28%	2.85%	2.67%
	Ion temperature (keV)	11.14	8.94	10.22

Ref. 7. “Cutie,” a little thinner than Orange and irradiated with a higher peak power, was somewhat overdriven and produced a slightly higher yield with lower efficiency. All three targets produced high ion temperatures of ~ 10 keV, measured by four neutron time-of-flight detectors with different viewing angles.⁹ Further information on this work can be found in Ref. 10. Work on the modeling of these targets is in progress and will be reported elsewhere.

This platform is being routinely used for neutron effects experiments. Further work on platform development is focused on optimizing designs that deliver the full NIF energy to larger targets subject to the maximum power constraints of the NIF.

This material is based upon work supported by the Department of Energy National Nuclear Security Administration under Award Number DE-NA0003856, the U.S. Department of Energy by Lawrence Livermore National Laboratory under Contract DE-AC52-07NA27344, the University of Rochester, and the New York State Energy Research and Development Authority. H. D. Whitley was supported by the PECASE award.

1. A. Nikroo *et al.*, *Fusion Sci. Technol.* **41**, 214 (2002).
2. M. D. Rosen and J. H. Nuckolls, *Phys. Fluids* **22**, 1393 (1979).
3. G. Charatis *et al.*, in *Plasma Physics and Controlled Nuclear Fusion Research 1974* (IAEA, Vienna, 1975), Vol. II, pp. 317–335.
4. M. M. Marinak *et al.*, *Phys. Plasmas* **8**, 2275 (2001).
5. R. S. Craxton and R. L. McCrory, *J. Appl. Phys.* **56**, 108 (1984).
6. S. Skupsky *et al.*, *Phys. Plasmas* **11**, 2763 (2004).
7. A. M. Cok, R. S. Craxton, and P. W. McKenty, *Phys. Plasmas* **15**, 082705 (2008).
8. N. D. Masters *et al.*, *J. Phys.: Conf. Ser.* **717**, 012108 (2016).
9. V. Yu. Glebov *et al.*, *Rev. Sci. Instrum.* **81**, 10D325 (2010).
10. C. B. Yeamans *et al.*, *Nucl. Fusion* **61**, 046031 (2021).

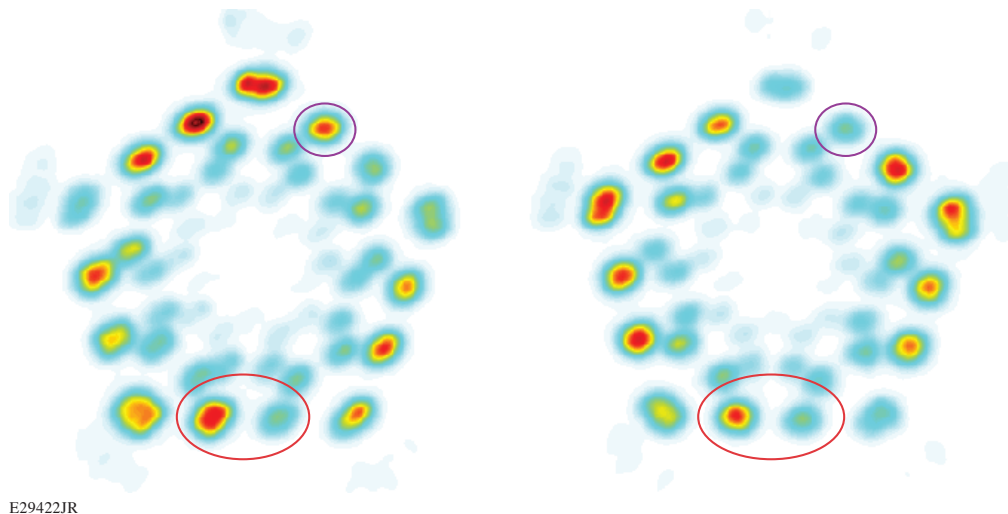
Unabsorbed Light Beamlets for Diagnosing Coronal Density Profiles and Absorption Nonuniformity in Direct-Drive Implosions on OMEGA

D. H. Edgell, A. M. Hansen, J. Katz, D. Turnbull, and D. H. Froula

Laboratory for Laser Energetics, University of Rochester

Laser-direct-drive implosions require spherically symmetric compression to avoid low-mode asymmetries and hydrodynamic instabilities.^{1,2} Absorption efficiency is known to be severely degraded by cross-beam energy transfer (CBET),^{3,4} and scattered-light observations with the diagnostic described in this summary have revealed significant asymmetry during OMEGA implosions. The most-direct diagnostic for laser absorption is the light scattered from the implosion. Isolating the unabsorbed light from each individual OMEGA beam using the 3ω gated optical imager (GOI) diagnostic⁵ has facilitated our understanding of the effect that CBET and other physics have on absorption.

The imaged scattered light appears as a pattern of distinct spots, each corresponding to a single beam (Fig. 1). Each spot can be thought of as the end of a “beamlet”—a small component of the beam originating from a specific point in the beam’s far-field spatial profile and following a path through the plasma determined by refraction. The intensity of the beamlet varies along its path due to absorption and CBET until it exits the plasma and ultimately reaches the diagnostic. An important component of the 3ω GOI is a Wollaston prism that splits the collected light into orthogonal polarization components, resulting in two separate beamlet spot images at every camera exposure time.



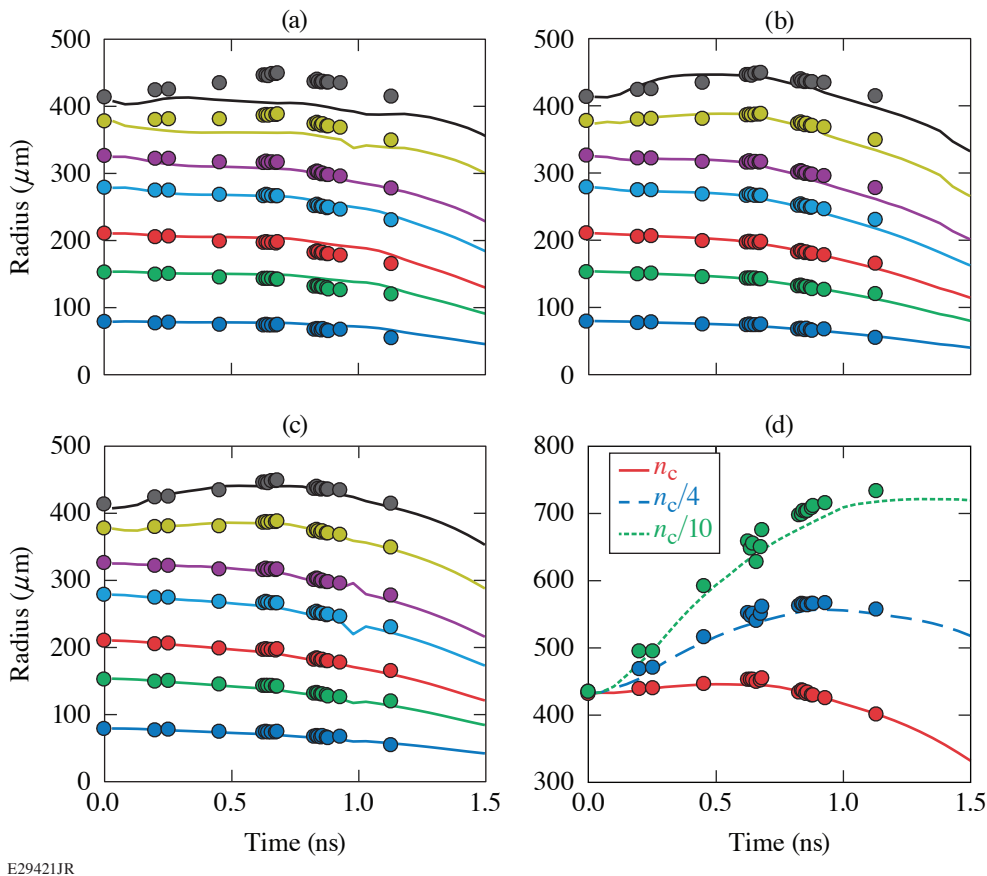
E29422JR

Figure 1

3ω GOI beamlet images collected during an OMEGA implosion for two orthogonal polarizations. The magenta circles highlight a beamlet that is strongly polarized. The red ovals highlight two beamlets that are in the same angular group but clearly have much different intensities.

In a symmetric implosion, all beamlets collected from beams at the same angular distance from the diagnostic should have traveled equivalent paths. With polarization smoothing, each beamlet in the group will have identical CBET and absorption along their paths. All spots in the group are expected to have similar intensities and be equally split between the two orthogonal polarization sub-images. Diagnostic images show that neither of these assumptions is true (Fig. 1). Nonuniformities in the scattered light from an implosion suggest that corresponding nonuniformities may occur in the laser absorption that could severely impact implosion performance. The nonuniformity is believed to be a result of the effect of CBET on the polarization smoothing method used by OMEGA.⁶

The positions of the beamlet spots in the images are determined by the refraction of each beamlet through the plasma and can be used as a density profile diagnostic. In Figs. 2(a)–2(c), the measured beamlet radii are compared to predictions using ray tracing through density profiles calculated by the *LILAC* code using three different physics models. The outer spot positions are most sensitive to the model used. The flux-limited no-CBET⁷ model does not predict spot locations for the outer beam groups similar to those measured [Fig. 2(a)]. The Goncharov nonlocal electron transport model⁸ is better at predicting the actual spot positions [Fig. 2(b)], and the match is further improved [Fig. 2(c)] when a CBET model is included. Least-square fitting of the density profile was performed to find the best fit to the measured spot positions and to gain further insight into the accuracy of the density profile modeling. The best fits suggest that even the Goncharov/CBET model underpredicts the plasma density farther out in the corona [Fig. 2(d)].



E29421JR

Figure 2

A comparison between the measured beamlet radii (circles, each beam group in a different color) and the predictions using ray tracing through the coronal plasma density profiles (curves) predicted using different physics models: (a) flux-limited ($f = 0.06$) electron heat transport, no CBET; (b) Goncharov nonlocal electron heat transport, no CBET; and (c) Goncharov nonlocal electron heat transport with CBET. (d) Predictions using the same model as in (c) for the time-varying positions of the plasma critical density (n_c) radius, along with the $n_c/4$ and $n_c/10$ surfaces (curves). The circles show the surface radii given by a best fit to the actual measured spot positions.

The 3ω GOI diagnostic was used in conjunction with the wavelength-tunable TOP9 laser⁹ to measure the effect of wavelength detuning on CBET.¹⁰ TOP9 appears in the 3ω GOI image as an additional spot. The intensity of the TOP9 beamlet depends strongly on CBET with the other beams. Shifting the TOP9 wavelength with respect to the OMEGA beams alters the magnitude (and even the direction) of energy exchange between TOP9 and the other OMEGA beams. Figure 3(a) shows the predicted TOP9 beamlet intensity versus the wavelength detuning (solid red curve). The measured TOP9 beamlet intensity [Fig. 3(a), magenta circles] supports these predicted trends in general but not in all of the specific details. Since polarization smoothing was used on TOP9, the beamlet polarization was predicted to always be at 45° , but the measurements show significant polarization variation [Fig. 3(b)]. Like the implosion nonuniformity discussed above, these discrepancies may be due to the polarization smoothing method used on OMEGA.

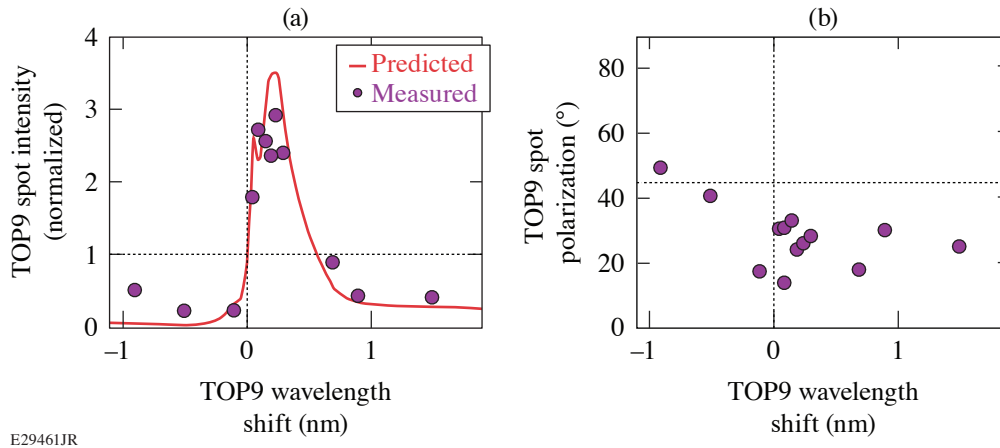


Figure 3

(a) Intensity of the TOP9 beamlet and (b) polarization of the TOP9 beamlet versus the wavelength shift of the TOP9 beam with respect to the 60 OMEGA beams. Predicted intensity was normalized to the intensity when $\Delta\lambda = 0$ and the uncalibrated measured intensity is arbitrarily scaled to match the predicted range.

This material is based upon work supported by the Department of Energy National Nuclear Security Administration under Award Number DE-NA0003856, the University of Rochester, and the New York State Energy Research and Development Authority.

1. S. E. Bodner *et al.*, *Phys. Plasmas* **5**, 1901 (1998).
2. S. Skupsky and R. S. Craxton, *Phys. Plasmas* **6**, 2157 (1999).
3. W. L. Kruer *et al.*, *Phys. Plasmas* **3**, 382 (1996).
4. C. J. Randall, J. J. Thomson, and K. G. Estabrook, *Phys. Rev. Lett.* **43**, 924 (1979).
5. D. H. Edgell *et al.*, *Rev. Sci. Instrum.* **89**, 10E101 (2018).
6. D. H. Edgell *et al.*, "Low-Mode Asymmetry due to Polarization Smoothing in OMEGA Implosions," to be submitted to *Physical Review Letters*.
7. R. C. Malone, R. L. McCrory, and R. L. Morse, *Phys. Rev. Lett.* **34**, 721 (1975).
8. V. N. Goncharov *et al.*, *Phys. Plasmas* **15**, 056310 (2008).
9. B. E. Kruschwitz *et al.*, *Proc. SPIE* **10898**, 1089804 (2019).
10. D. H. Edgell *et al.*, *Phys. Plasmas* **24**, 062706 (2017).

Mitigation of Mode-One Asymmetry in Laser-Direct-Drive Inertial Confinement Fusion Implosions

O. M. Mannion,¹ I. V. Igumenshchev,¹ K. S. Anderson,¹ R. Betti,¹ E. M. Campbell,¹ D. Cao,¹ C. J. Forrest,¹ M. Gatu Johnson,² V. Yu. Glebov,¹ V. N. Goncharov,¹ V. Gopalaswamy,¹ S. T. Ivancic,¹ D. W. Jacobs-Perkins,¹ A. Kalb,¹ J. P. Knauer,¹ J. Kwiatkowski,¹ A. Lees,¹ F. J. Marshall,¹ M. Michalko,¹ Z. L. Mohamed,¹ D. Patel,¹ H. G. Rinderknecht,¹ R. C. Shah,¹ C. Stoeckl,¹ W. Theobald,¹ K. M. Woo,¹ and S. P. Regan¹

¹Laboratory for Laser Energetics, University of Rochester

²Plasma Science and Fusion Center, Massachusetts Institute of Technology

Mode-one ($\ell = 1$) asymmetries have been identified as one of the most detrimental to inertial confinement fusion implosion performance¹ and have been observed in laser-indirect-drive implosions at the National Ignition Facility.² Mode-one asymmetries can be described as those asymmetries that cause the initial radial implosion velocity of the shell to have the form $v_r(\theta) = v_0 - \Delta v \cos(\theta)$, where v_0 is the average implosion velocity, Δv is the variation in the implosion velocity, and θ is the angle between the mode-one direction and a direction on the target. As the target implodes, this asymmetry causes the formation of a jet within the hot spot.¹ This jet undergoes a Helmholtz instability, which results in the formation of vortices within the hot spot and an asymmetric fuel areal density around the hot spot. The asymmetric fuel distribution leads to poor confinement of the hot spot, while the motion within the hot spot represents residual kinetic energy not used to heat and compress the target.¹ The poor confinement and residual kinetic energy present in the target result in a severe reduction in the fusion yield of the implosion.

To diagnose mode-one asymmetries in laser-direct-drive (LDD) implosions performed on the OMEGA laser, 3-D nuclear and x-ray diagnostics have been developed.³⁻⁵ Neutron time-of-flight (nTOF) and charged-particle spectrometers are used to measure the neutron energy spectrum emitted from the target from which the fusion yield, hot-spot velocity, apparent ion temperature, and fuel areal density are inferred. X-ray imaging diagnostics are used to measure the x-ray self-emission from the hot spot and to infer the size and shape of the hot spot. These diagnostics have been fielded strategically around the OMEGA target chamber to provide a set of 3-D measurements of the hot spot and fuel conditions near peak compression. Using measurements from these diagnostics, the magnitude and direction of mode-one asymmetries are determined.

Measurements made with these detectors have revealed that large mode-one drive asymmetries can be introduced when laser-alignment errors exist. For the experiments described below, defects in the targets used for laser alignment result in the OMEGA Laser System having abnormally large laser-alignment errors. In particular, the aluminum oxide coating on the target used during the laser-alignment process had unintentional coating defects, which caused gross mispointing of the laser beams to be introduced. Furthermore, the Au spheres used during the laser-pointing procedure for these experiments had unintentional nonuniform Au coatings as a result of target fabrication issues. The nonuniform Au coating resulted in weak x-ray signals being generated by specific beams. The weak signals led to large uncertainties in identifying the position of these beams and resulted in large beam-pointing errors being introduced during the beam-pointing procedure. The compounding errors in the alignment of the laser system during these experiments resulted in a large laser mode-one asymmetry being present.

Figure 1(a) shows the laser illumination perturbation on target for shot 94712. The laser illumination on target was determined from a hard sphere calculation, which determines the overlap intensity of all 60 beams on the initial target radius, accounting for the laser beam pointing, laser beam energy, and target offset. The laser beam pointing was determined during the beam-alignment procedure prior to the shot, the laser beam energy was measured using a calorimeter, and the target offset was measured by both

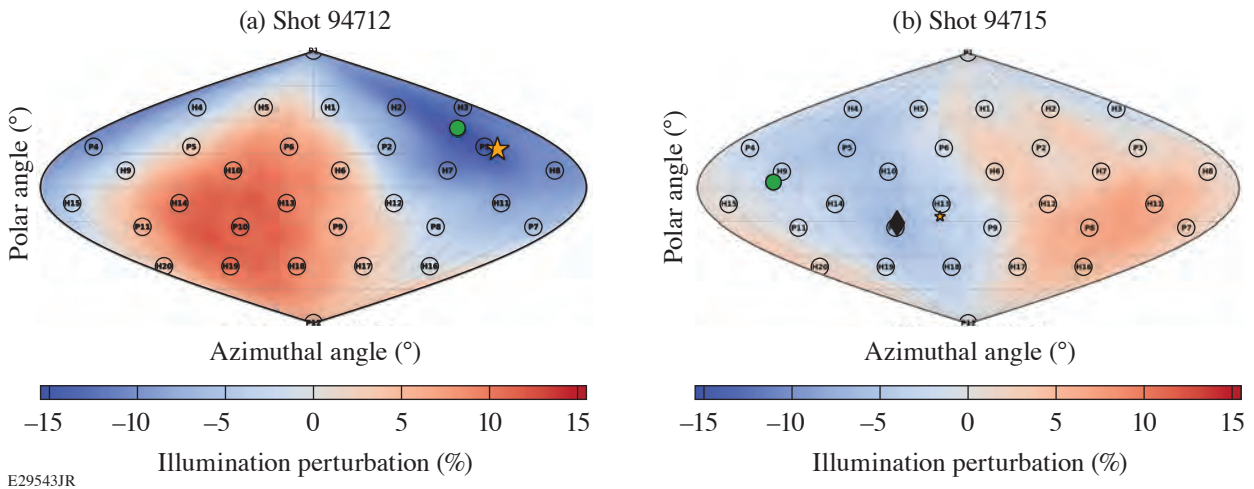


Figure 1

A sinusoidal projection of the OMEGA target chamber showing the illumination perturbation from the mean for (a) shot 94712 and (b) shot 94715 determined from a hard sphere calculation that used the measured laser beam pointing, energy, and target offset. The direction of the measured hot-spot velocity is shown as the orange star and had a magnitude of 146 km/s for shot 94712 and 27 km/s for shot 94715. The laser mode-one illumination asymmetry σ_{rms} amplitude was 7.3% for shot 94712 and 4.3% for shot 94715; the directions are shown as the green circles. The target offset correction for shot 94715 was 43 μm and is shown as the black diamond.

a high-speed video camera and an x-ray pinhole camera. For this experiment, the target offset was $<5 \mu\text{m}$ and nonuniformities in the individual laser beam energies did not contribute significantly to the on-target illumination nonuniformity, which was dominated by the beam-pointing errors. The calculated on-target illumination nonuniformity shows a large mode-one drive asymmetry present with a total peak to valley variation of 27.3% across the target and a mode-one illumination asymmetry σ_{rms} amplitude of 7.3% in the direction $\theta = 51^\circ$ and $\phi = 122^\circ$.

This initial drive asymmetry in the laser resulted in a strong mode-one being present in the experiment, which was observed in both the nuclear and x-ray diagnostics. A hot-spot velocity of $146 \pm 12 \text{ km/s}$ was inferred from the nTOF's in the direction $\theta = 64 \pm 7^\circ$ and $\phi = 133 \pm 4^\circ$. The apparent ion temperature asymmetry was $1.8 \pm 0.5 \text{ keV}$ as measured from the nTOF detectors and the areal-density asymmetry was $104 \pm 18 \text{ mg/cm}^2$ as measured by the nTOF and magnetic recoil spectrometer detectors. The direction of the hot-spot velocity, apparent ion temperature asymmetry, and areal-density asymmetry were all aligned with the initial mode-one drive asymmetry identified in the laser. Furthermore, the mode-one asymmetry was observed in the x-ray self-emission images shown in Fig. 2.

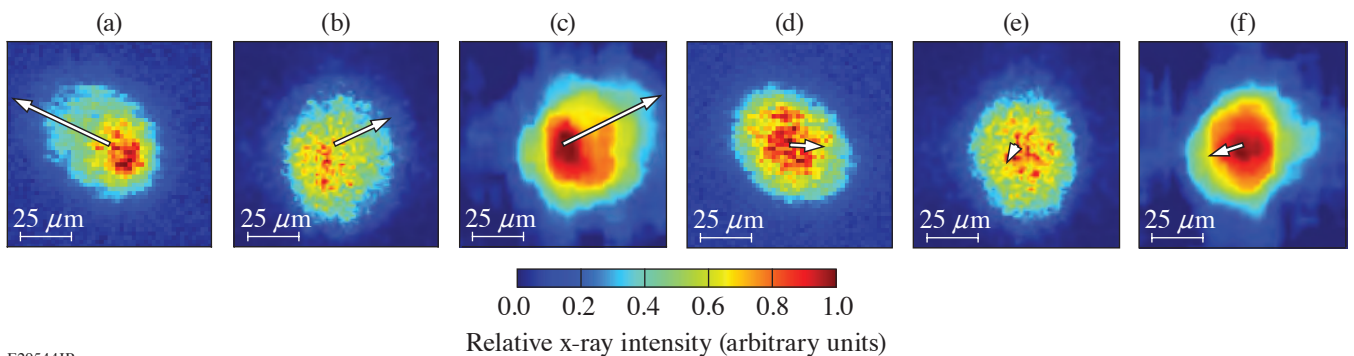


Figure 2

X-ray self-emission images measured for [(a)–(c)] shot 94712 and [(d)–(f)] shot 94715. The [(a) and (d)] single-line-of-sight time-resolved x-ray imager and [(b) and (e)] KBframed images are time resolved and averaged over a 40- and 15-ps time window around peak neutron production, respectively. The [(c) and (f)] gated monochromatic x-ray image is time integrated. The projection of the measured hot-spot velocity onto the detector plane is indicated by the white arrow. The magnitude of the projection is indicated by the length of the arrow. The elongation observed in the x-ray images from shot 94712 has been eliminated by applying the offset correction on shot 94715.

With the mode-one asymmetry characterized on shot 94712, we used a mitigation strategy that employed an intentional target offset to compensate for the observed asymmetry. When a target offset is present in an experiment, it results in a geometric redistribution of the beam overlap intensity on the target and can be used to mitigate mode-one drive asymmetries present in the laser. To determine the appropriate target offset required to mitigate a given mode-one observed on shot 94712, the measured hot-spot velocity was used. The hot-spot velocity \vec{u}_{hs} is assumed to have a linear relationship with the target offset \vec{o} and is given by

$$\vec{u}_{\text{hs}} = \alpha \vec{o} = \alpha(\vec{r} + \vec{c}), \quad (1)$$

where α is the offset-to-velocity conversion in km/s/ μm , and the total offset is assumed to be the sum of the measured offset \vec{r} from the high-speed video camera and some unknown effective target offset \vec{c} . The unknown effective target offset is the component of the hot-spot velocity generated from an assumed static mode-one present in the laser.

These calculations were performed using the results from the experiments discussed above, and the target was positioned to the calculated location to eliminate the mode-one asymmetry. The offset-to-velocity conversion for these experiments was found to be 4.1 ± 0.2 km/s/ μm . The unknown effective target offset was determined to be $\vec{c} = \langle -26, 33, 17 \rangle \mu\text{m}$. This corresponds to a total target offset of $45 \mu\text{m}$ in the direction $\theta = 112^\circ$ and $\phi = 308^\circ$. For shot 94715, the target was positioned at $\vec{r} = \langle 28, -35, -19 \rangle \mu\text{m}$, which was within a few microns away from the requested location of $\langle 26, -33, -17 \rangle \mu\text{m}$. With the target positioned to this location, the asymmetry present in the previous experiments was greatly mitigated. In particular, the hot-spot velocity was reduced to 27 ± 11 km/s in the direction $\theta = 109 \pm 35^\circ$ and $\phi = 341 \pm 26^\circ$ and is shown in Fig. 1(b). The apparent ion-temperature asymmetry was greatly reduced to 0.5 ± 0.5 keV and the areal-density asymmetry was reduced to 37 ± 12 mg/cm². Finally, the hot-spot x-ray self-emission images were found to be significantly more symmetric with the mode-one mitigation and are shown in Fig. 2.

To understand how this target-offset correction was able to mitigate the mode-one asymmetry, it is instructive to analyze the hard sphere illumination nonuniformity for shot 94715. Figure 1(b) shows that when the target correction was applied, the on-target illumination uniformity was improved by a factor of 2 as compared to shot 94712. In particular, the total peak-to-valley variation around the target was reduced to 14%. This technique therefore is a viable mitigation strategy for LDD implosions that have large mode-one drive asymmetries.

This material is based upon work supported by the Department of Energy National Nuclear Security Administration under Award Number DE-NA0003856, the University of Rochester, and the New York State Energy Research and Development Authority.

1. B. K. Spears *et al.*, Phys. Plasmas **21**, 042702 (2014).
2. H. G. Rinderknecht *et al.*, Phys. Rev. Lett. **124**, 145002 (2020).
3. O. M. Mannion *et al.*, Nucl. Instrum. Methods Phys. Res. A **964**, 163774 (2020).
4. F. J. Marshall *et al.*, Rev. Sci. Instrum. **88**, 093702 (2017).
5. W. Theobald *et al.*, Rev. Sci. Instrum. **89**, 10G117 (2018).

High-Energy-Density–Physics Measurements in Implosions Using Bayesian Inference

J. J. Ruby,^{1,2} J. A. Gaffney,³ J. R. Rygg,^{1,2,4} Y. Ping,³ and G. W. Collins^{1,2,4}

¹Department of Physics and Astronomy, University of Rochester

²Laboratory for Laser Energetics, University of Rochester

³Lawrence Livermore National Laboratory

⁴Department of Mechanical Engineering, University of Rochester

Convergent high-energy-density experimental platforms are used to study matter under some of the most extreme conditions that can be produced on Earth, comparable to the interior of stars. There are many challenges in using these systems for fundamental measurements currently being addressed by new analysis methods, such as the combination of a reduced-physics model and Bayesian inference,^{1,2} allowing for a self-consistent inference of physical quantities with a robust error analysis. These methods in combination with simple [as compared to inertial confinement fusion (ICF)] implosion platforms, which can be modified to show sensitivity to different physical mechanisms of interest, can be used to study the physical properties of matter under extreme conditions and analysis.

One example of simplified implosion designs includes shock-dominated systems, such as thin-shelled, gas-filled targets sometimes known as “exploding pushers” and solid-sphere targets, while another includes thick-shelled, gas-filled implosions that create a compressive hot spot much like modern ICF experiments but at lower convergence ratios for high stability. These systems are able to access different regimes where different physical mechanisms are most relevant.

This work discusses these different regimes and gives a detailed example of an experimental design of a thick-shelled implosion informed by Bayesian inference. A reduced-physics model informed by many of the previously published hot-spot models in literature^{3,4} is constrained by a suite of synthetic measurements generated from a *LILAC* simulation using Bayesian inference. (*LILAC* is a radiation-hydrodynamics code.)

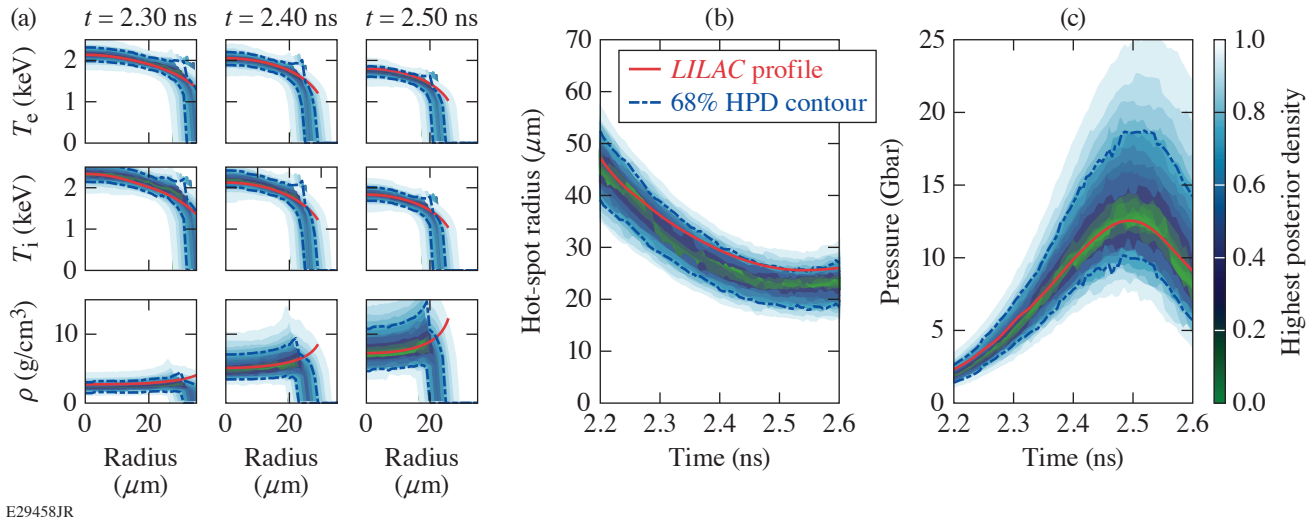
The reduced model parameterizes the hot spot in terms of the time history of the total internal energy and the trajectory of the outer edge of the hot spot (in this case defined by the fuel–shell interface) while assuming an isobaric hot spot. This parameterization is used in combination with boundary conditions for the temperature profiles, an ideal gas equation of state, and a Spitzer-like conductivity of the form

$$\kappa = \kappa_0 \left(\frac{\rho}{\rho_0} \right)^a \left(\frac{T}{T_0} \right)^b, \quad (1)$$

where κ is the thermal conductivity, κ_0 is a constant factor, ρ is the mass density, T is the temperature, and both a and b are constant exponents that define the conductivity response to temperature and density. Using this conductivity along with conservation relations and the equation of state results in a radial temperature profile that depends on the quantity $(1 + b - a)^{-1}$, meaning that the details of the temperature profile provide information on the thermal conductivity of the hot-spot plasma.

Three key details determine the efficacy of this process: (1) The full-physics model being used (in this case *LILAC*) is able to reasonably represent the experimental system; (2) the reduced-physics model accurately represents quantities of interest from the full-physics model; and (3) the reduced-physics model can be constrained by the available measurements. The (synthetic) measurements used in this work include x-ray framing camera measurements, x-ray temporal histories in different spectral channels, the neutron temporal history, and the neutron spectrum.

Figure 1 shows the inferred profiles informed by all of the above measurements compared to the underlying truth from *LILAC*, showing that the thermodynamic conditions within the hot spot can be reconstructed using readily available measurements, assuming that a 1-D model is appropriate to describe the system, i.e., the system is sufficiently stable that asymmetries are not a significant perturbation on the conditions.



E29458JR

Figure 1

The inferred profiles for (a) the radial distribution of electron temperature, ion temperature, and mass density at three different times around peak emission; (b) the temporal history of the hot-spot radius; and (c) the temporal history of the hot-spot pressure. The color map shows the highest posterior density intervals for the inferred profiles, essentially producing credible intervals where the dashed blue line represents the 68.7% credible interval. The solid red curve shows the profile from the underlying *LILAC* simulation used to generate the synthetic diagnostics. In all cases the profiles are in excellent agreement with the underlying simulation with the exception of the edges of the hot spot where the radius is underpredicted by about 10% at later times, likely due to the fact that there is very little emission coming from the edge of the hot spot and therefore little information about its location. HPD: highest posterior density.

This material is based upon work supported by the Department of Energy National Nuclear Security Administration under Award Number DE-NA0003856, the U.S. Department of Energy, Office of Science, Office of Fusion Energy Sciences under Award No. DE-SC001926, the University of Rochester, and the New York State Energy Research and Development Authority. Y. P. acknowledges support from the DOE OFES Early Career Program and the LLNL LDRD Program.

1. J. J. Ruby *et al.*, Phys. Rev. E **102**, 053210 (2020).
2. J. J. Ruby *et al.*, Phys. Rev. Lett. **125**, 215001 (2020).
3. R. Betti *et al.*, Phys. Plasmas **9**, 2277 (2002).
4. P. T. Springer *et al.*, Nucl. Fusion **59**, 032009 (2019).

Ionization State and Dielectric Constant in Cold Rarefied Hydrocarbon (CH) Plasmas of Inertial Confinement Fusion

A. Shvydky, A. V. Maximov, V. V. Karasiev, D. Haberberger, S. X. Hu, and V. N. Goncharov

Laboratory for Laser Energetics, University of Rochester

Inertial confinement fusion (ICF) has been an active field of research for more than 50 years because of its application as a future energy source. In laser-driven ICF, a cryogenically cooled, thin spherical shell of deuterium–tritium (DT) fuel is imploded and compressed by material ablation to form a high-density confinement around a central core where the conditions for thermonuclear ignition can be created. During the implosion, the ablation pressure launches multiple shocks through the DT shell and accelerates it inward. Later, the buildup of pressure in the compressing vapor region decelerates the shell and, at stagnation, creates the conditions in the central core closest to ignition. The pressure buildup and the temperature and density in the core at stagnation are strongly affected by the amount of material that is released from the shell into the vapor region during the implosion.

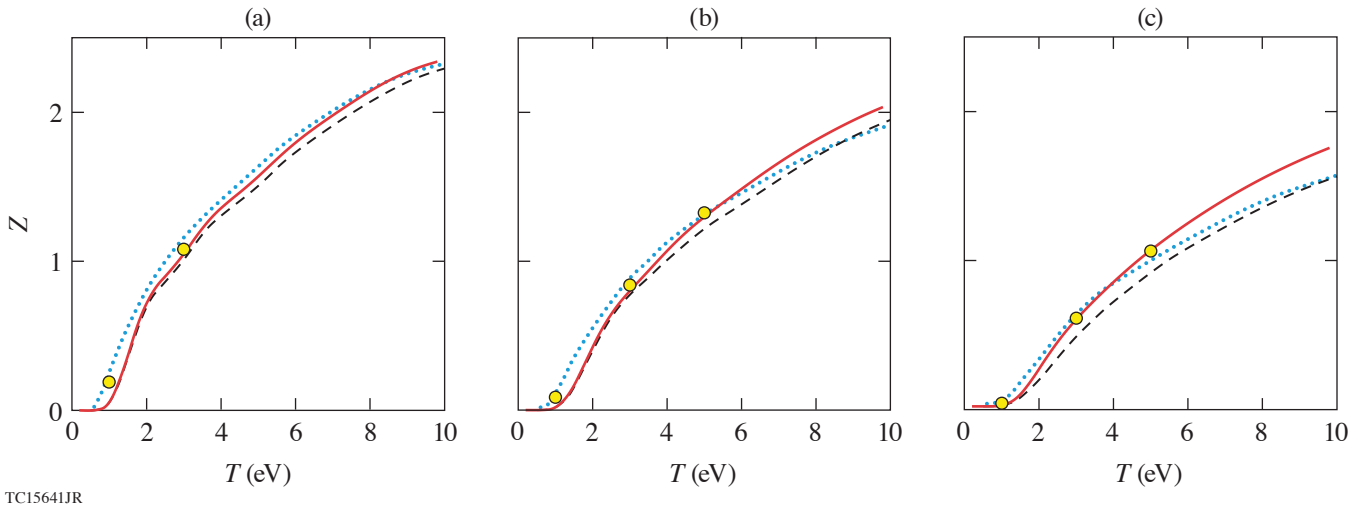
It is very challenging to measure the material released from the inner surface of the shell in the imploding capsule. However, in a planar geometry, one can access similar conditions with a CH foil and probe it using optical interferometry.¹ This technique was used for the first time in recent experiments² to diagnose the low-density part of the rarefaction wave formed when the shock driven by two OMEGA EP laser beams breaks out of a CH foil. The optical interferometry produces images in the focal plane that are proportional to the optical path (phase) that is accumulated by the wavefront of the probe laser propagating through the region of interest. The images are analyzed to obtain spatial profiles of the index of refraction. In low-density and low-temperature conditions, such as in the shock-release material, the plasma is partially ionized and the index of refraction is expected to have contributions from bound and free electrons and to depend on densities of atoms and free electrons which are connected to each other by the ionization state Z . Therefore, the index of refraction and Z are required to deduce the free-electron (plasma) density profiles from the interferograms.

The index of refraction at low densities and temperatures of shock-release material at a specific frequency of the laser probe is not generally expected to be available. While there are many studies of the optical properties of CH at solid or few times solid density,³ no experimental data are available for rarefied CH gas at 10^{-5} to 10^{-2} g/cm³ and few-eV temperatures. Recently *ab initio* simulations have become popular, are now accessible for calculating optical properties of arbitrary materials, and can be used to obtain the index of refraction at a desired laser frequency and thermodynamic conditions, i.e., mass density ρ and temperature T . The ionization state Z for CH material as a function of ρ and T is traditionally available via numerous Z tables used in ICF radiation-hydrodynamic codes. The simulations and analysis of the shock-release experiments² used the astrophysical opacity tables (AOT's) and collisional radiative equilibrium (CRE) tables, which predict different Z 's for the release conditions, and plasma index of refraction, which has no atomic contribution. These shortcomings motivated the present investigation.

In this summary we calculate the ionization state Z and the dielectric constant (which we use to obtain the index of refraction) as a function of density and temperature under conditions relevant to shock release. The conditions span several orders of magnitude in density $\rho = 10^{-5}$ to 10^{-2} g/cm³ at a few-eV temperatures. We develop an algorithmically transparent, easy-to-follow method for calculating Z [which we call the Saha–Fermi–Debye–Hückel (SFDH) method] based on the free-energy minimization approach,⁴ with free energy containing nonideal terms accounting for binary collisions and Coulomb interactions. We also obtain Z using *ab initio* calculations based on the Mermin–Kohn–Sham density functional theory (DFT) and test it against the semi-analytical method. After verifying the DFT-calculated ionization state against the semi-analytical method, we use the electron population

states obtained with the DFT and Kubo–Greenwood formulation to calculate the dielectric constant. Using the combined approach outlined above, we found that (a) Z calculated with the developed method and DFT agrees well with each other and is in reasonable agreement with that from CRE and AOT tables; (b) DFT-calculated atomic polarizabilities were within 20% of the reference data; and (c) a fit to the DFT-calculated dielectric constant contains an extra term due to atomic polarizabilities (i.e., contributions from bound states of electrons in atoms) that dominate the dielectric constant at low temperatures and Z . Based on these calculations, we revisited the shock-release experiments² and found more-accurate electron density profiles that, however, have not changed the main conclusions of Ref. 2.

Figure 1 shows the average ionization state Z as a function of temperature T for three mass densities ρ . The ionization state in Fig. 1 was obtained using four different sources: AOT tables, CRE tables, results of our SFDH method, and *ab initio* calculations. The *ab initio* calculations of Z used Kohn–Sham DFT and were performed using the Vienna *ab initio* simulation package (VASP) with the Perdew–Burke–Ernzerhof exchange–correlation (XC) functional. The DFT method calculates the electron states and their populations for each thermodynamic condition. Optical properties at each thermodynamic condition, which are used in the following sections, were calculated using the Kubo–Greenwood formulation⁵ implemented in the KGEC@*Quantum Espresso*⁶ package with the strongly constrained and appropriately normed XC functional.



TC15641JR

Figure 1

Average ionization state Z as a function of temperature from four different models: AOT (dashed black curves), CRE (dotted blue curves), our SFDH method (solid red curves), and the DFT calculations (yellow circles) for three mass densities: (a) 10^{-4} g/cm³, (b) 10^{-3} g/cm³, and (c) 10^{-2} g/cm³.

As one can see from Fig. 1, the *ab initio* calculations (yellow circles) are in very good agreement with the calculations using the SFDH method (solid red curves) at 3- and 5-eV temperatures, while Z from AOT (dashed black curves) and CRE (dotted blue curves) are up to 20% off. At lower temperatures (1 eV), the DFT method predicts noticeably higher Z than SFDH. The discrepancy is caused by the self-interaction error inherent in the DFT local and semi-local approximations for the XC energy.⁷ The electron self-interaction decreases the ionization energy of H and to a lesser degree C atoms and leads to an artificial increase in Z , which is more apparent for temperatures much smaller than the ionization energies.

Figure 2 shows the dependence of the dielectric constant of CH on the temperature for two densities at the OMEGA EP laser probe wavelength of $\lambda = 263$ nm. Analysis of the index of refraction of CH at 1-, 3-, and 5-eV temperatures and 0.01- and 0.001-g/cm³ densities leads to the following approximate formula for the real part of the dielectric constant (dashed red curves in Fig. 2):

$$\epsilon_{\text{DFT}} = 1 + 4\pi(1.7 \text{ \AA}^3 \cdot n_i - 4.9 \text{ \AA}^3 \cdot n_e), \quad (1)$$

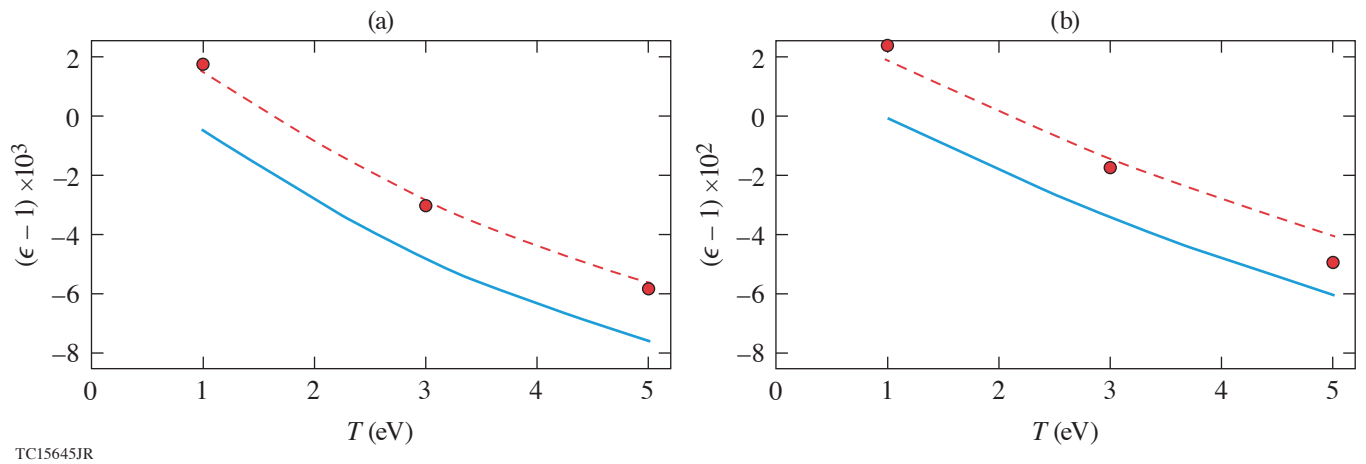


Figure 2

The real part of the dielectric permittivity in CH as a function of temperature from DFT calculations (red circles), from Eq. (1) (dashed red curves), and from Eq. (2) (solid blue curves) for mass densities of (a) 10^{-3} g/cm³ and (b) 10^{-2} g/cm³.

where $n_e = Z n_i$ is the electron density in \AA^{-3} and n_i is the ion density in \AA^{-3} , $n_i = \rho \langle A \rangle$, where $\langle A \rangle = 6.5$ amu is the average ion mass for 50% C – 50% H. The dielectric constant from Eq. (1) should be compared to the dielectric constant (solid blue curves in Fig. 2)

$$\epsilon_p = 1 - 4\pi \cdot 4.9 \text{\AA}^3 \cdot n_e \quad (2)$$

that was previously used in the analysis of the shock-release experiments.² The formula in Eq. (2) is the high-frequency plasma dielectric constant $\epsilon_p = 1 - n_e/n_c$ (referred to below as the plasma dielectric constant),⁸ where n_c is the critical density and $n_c = 1/(4\pi \times 4.9) \text{\AA}^{-3}$ for $\lambda = 263$ nm. The fit of Eq. (1) to the DFT-calculated dielectric constant contains a term $\sim n_i$, which is the contribution from atomic polarizabilities (i.e., the contribution from bound states of electrons in atoms) and is not present in the plasma dielectric constant [Eq. (2)].

The index of refraction calculated with the DFT method, $n_{\text{DFT}} = \sqrt{\epsilon_{\text{DFT}}}$, was used to revisit the interferometry data from the shock-release experiments.² Electron densities were found to be up to 40% higher and the position of the rarefaction wave up to 20 μm further than reported in Ref. 2. It is important to note that for a laser drive of lower intensity than in Ref. 2, the plasma index of refraction is not valid and the DFT index of refraction must be used in the analysis of the shock-release experiments.

This material is based upon work supported by the Department of Energy National Nuclear Security Administration under Award Number DE-NA0003856, the University of Rochester, and the New York State Energy Research and Development Authority.

1. A. Howard *et al.*, Rev. Sci. Instrum. **89**, 10B107 (2018).
2. D. Haberberger *et al.*, Phys. Rev. Lett. **123**, 235001 (2019).
3. W. Theobald *et al.*, Phys. Plasmas **13**, 122702 (2006).
4. D. G. Hummer and D. Mihalas, Astrophys. J. **331**, 794 (1988).
5. R. Kubo, J. Phys. Soc. Jpn. **12**, 570 (1957); D. A. Greenwood, Proc. Phys. Soc. Lond. **71**, 585 (1958).
6. L. Calderín, V. V. Karasiev, and S. B. Trickey, Comput. Phys. Commun. **221**, 118 (2017); V. V. Karasiev, T. Sjoström, and S. B. Trickey, Comput. Phys. Commun. **185**, 3240 (2014).
7. J. P. Perdew and A. Zunger, Phys. Rev. B **23**, 5048 (1981).
8. J. D. Jackson, *Classical Electrodynamics*, 3rd ed. (Wiley, New York, 1999).

Cross-Beam Energy Transfer Saturation by Ion Heating

A. M. Hansen,^{1,2} K. L. Nguyen,^{1,2} D. Turnbull,¹ B. J. Albright,³ R. K. Follett,¹ R. Huff,¹ J. Katz,¹ D. Mastrosimone,¹
A. L. Milder,¹ L. Yin,³ J. P. Palastro,¹ and D. H. Froula^{1,2}

¹Laboratory for Laser Energetics, University of Rochester

²Department of Mechanical Engineering, University of Rochester

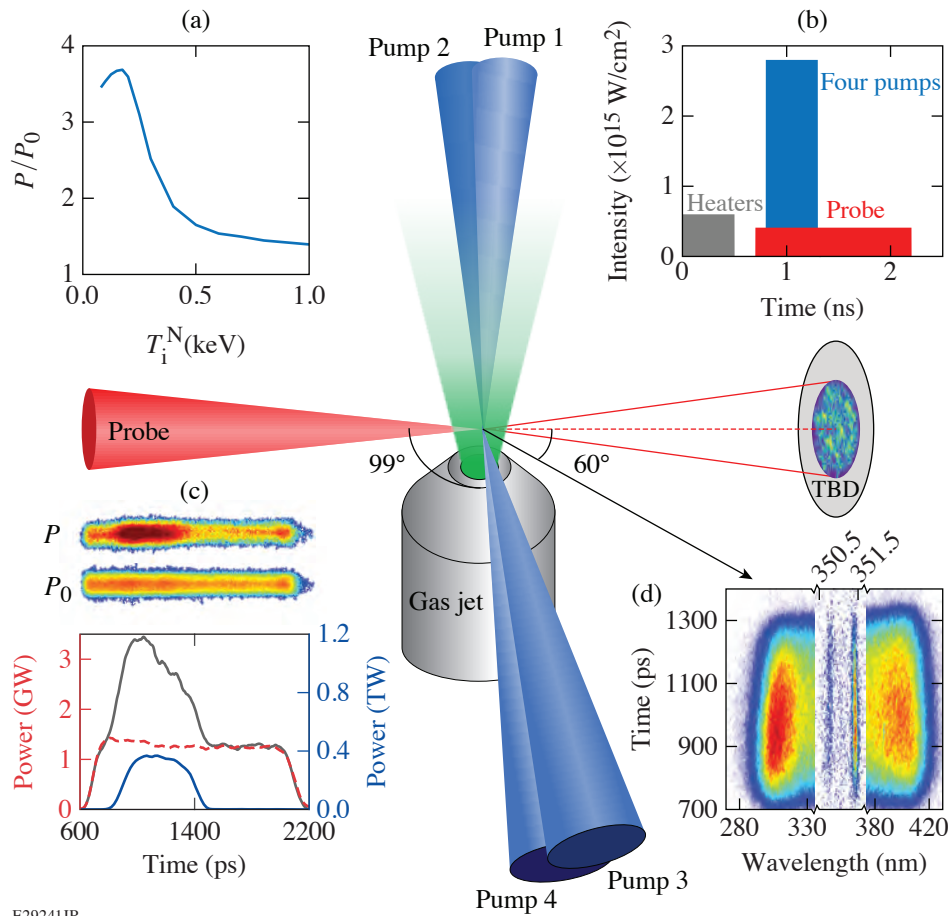
³Los Alamos National Laboratory

Cross-beam energy transfer (CBET) saturation by ion heating was measured in a gas-jet plasma characterized using Thomson scattering. A wavelength-tunable UV probe laser beam interacted with four intense UV pump beams to drive large-amplitude ion-acoustic waves. For the highest-intensity interactions, the power transferred to the probe laser dropped, demonstrating ion-acoustic-wave saturation. Over this time, the ion temperature was measured to increase by a factor of 7 during the 500-ps interaction. Particle-in-cell simulations show ion trapping and subsequent ion heating consistent with measurements. Linear kinetic CBET models were found to agree well with the observed energy transfer when the measured plasma conditions were used.

In laser-driven inertial confinement fusion (ICF), high-intensity lasers are used to drive capsules that reach pressure and temperature conditions required for nuclear fusion.¹ This requires multiple overlapping laser beams to propagate through plasmas surrounding the fusion capsule. The plasma mediates energy transfer between the laser beams, which can disrupt the energy coupling and/or cause irradiation nonuniformity.^{2,3} To account for this CBET, linear models have been implemented in the hydrodynamic codes used to simulate ICF experiments.^{4,5} The ability to predict this transfer of energy is critical to the success of all laser-driven ICF concepts.

The experiment was performed on the OMEGA laser-plasma interaction platform. Figure 1 illustrates the experimental configuration that consisted of a gas-jet system that produced a gas plume, which was heated by nine 500-ps-long UV beams. The target gas was a mixture of 45% nitrogen and 55% hydrogen to approximately reproduce the ion-acoustic wave damping from typical ICF experiments. The probe beam used the tunable OMEGA port 9 (TOP9) laser, which was wavelength tunable over ~ 3 nm around the pump beams' wavelength of 351.11 nm. The resonant wavelength of the probe beam (351.40 nm) was used for all experiments and was determined by maximizing the energy transfer while scanning its wavelength. The four CBET pump beams used half-wave plates to align their linear polarizations to the probe beam's polarization and had single-beam averaged intensities of $\sim 7 \times 10^{14}$ W/cm². The power in the probe beam was measured before and after the CBET interaction using the transmitted beam diagnostic (TBD). The time-resolved plasma conditions were measured using the streaked Thomson-scattering system.

Shots were performed for a range of incident probe-beam intensities, and time-resolved measurements of the plasma conditions and outgoing probe intensity were made. Figure 2 shows the amplification of the probe beam due to CBET at four initial probe intensities. Although the ion-acoustic wave (IAW) amplitudes are expected to increase with increasing probe intensity, linear CBET theory predicts a constant P/P_0 (pump depletion was negligible in the experiment by design). The fact that the power ratio P/P_0 decreases with increasing probe intensity with minimal pump depletion suggests nonlinear saturation. Furthermore, every probe-beam intensity greater than 0.1×10^{14} W/cm² exhibits a strong time-dependent reduction in amplification. For the three highest initial probe-beam intensities, the amplification started high (~ 1000 ps) but decreased over time before plateauing toward the end of the pump pulse (~ 1300 ps).



E29241JR

Figure 1

(a) The ratio of the output power (P) to the incident power (P_0) of the probe beam was calculated using a linear kinetic CBET model for the conditions of these experiments over a range of nitrogen ion temperatures. (b) The laser intensity, pulse shapes, and beam timings for each of the beam groups. (c) TBD data showing the input- (dashed red curve) and output- (solid black curve) probe and pump (solid blue curve) powers. (d) Time-resolved Thomson-scattering data showing the electron plasma wave and ion-acoustic wave spectra of a pump beam with minimal ion heating.

The plasma conditions measured using Thomson scattering revealed ion heating due to CBET in the high-intensity probe-beam shots ($I_0 > 0.1 \times 10^{14}$ W/cm 2). Kinetic linear theory predictions of CBET were in excellent agreement with the measured energy transfer when these increased ion temperatures were considered. As the ions were heated, the IAW dispersion evolved along a new branch with increased frequency at the wave number determined by the beam crossing angle. Because the driving frequency was fixed, the driven IAW was no longer at a resonant frequency, which increased the wave damping and saturated CBET.

Simulations of the high-intensity CBET interaction using the code VPIC were performed and found to qualitatively reproduce the measured energy transfer and ion heating. These simulations showed that at high probe-beam intensities, the large driven IAW's trapped and accelerated ions to the wave's phase velocity. The trapped ions were then detrapped through ion-ion collisions on short time scales (~ 10 ps), which resulted in bulk ion heating on ~ 100 -ps time scales.

Although significant nonlinear CBET physics is occurring at the high probe-beam intensities, it is interesting that the linear CBET theory reproduces the measured results when accounting for the instantaneous plasma conditions. The plasma conditions are affected by CBET, however, suggesting that feedback from laser-plasma instabilities on hydrodynamics must be accounted for in modeling to accurately predict the energy transfer.⁵

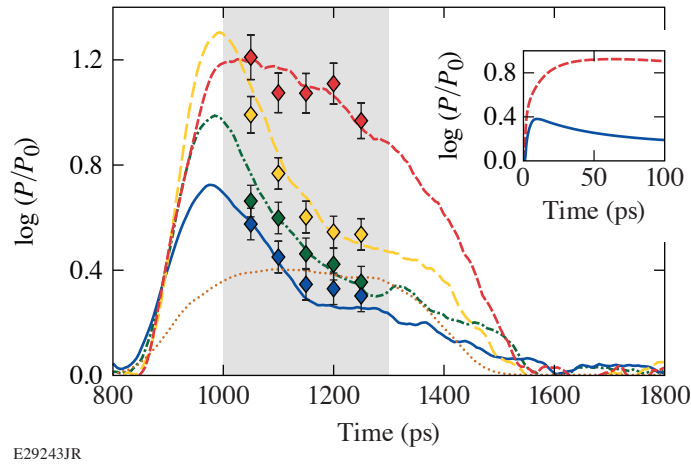


Figure 2

The power transferred into the probe beam for four different initial probe-beam intensities [0.1×10^{14} W/cm² (dashed red curve), 0.9×10^{14} W/cm² (dashed yellow curve), 2.0×10^{14} W/cm² (dashed-dotted green curve), 4.1×10^{14} W/cm² (solid blue curve)], and the corresponding calculated power transfer using linear kinetic theory for the measured plasma conditions (diamonds). The pulse shape of the pump beams is overlaid for reference (dotted orange curve). The inset shows VPIC simulated probe beam amplification corresponding to the lowest (dashed red curve) and highest (solid blue curve) experiment probe intensities.

This material is based upon work supported by the Department of Energy National Nuclear Security Administration under Award Number DE-NA0003856, the University of Rochester, and the New York State Energy Research and Development Authority.

1. R. Betti and O. A. Hurricane, *Nat. Phys.* **12**, 435 (2016).
2. V. N. Goncharov *et al.*, *Phys. Plasmas* **15**, 056310 (2008).
3. D. J. Strozzi *et al.*, *Phys. Rev. Lett.* **118**, 025002 (2017).
4. P. Michel *et al.*, *Phys. Rev. Lett.* **102**, 025004 (2009).
5. P. Michel *et al.*, *Phys. Rev. Lett.* **109**, 195004 (2012).

Thresholds of Absolute Two-Plasmon–Decay and Stimulated Raman Scattering Instabilities Driven by Multiple Broadband Lasers

R. K. Follett,¹ J. G. Shaw,¹ J. F. Myatt,² H. Wen,¹ D. H. Froula,¹ and J. P. Palastro¹

¹Laboratory for Laser Energetics, University of Rochester

²Department of Electrical and Computer Engineering, University of Alberta

In direct-drive inertial confinement fusion (ICF), a millimeter-scale spherical capsule is illuminated by symmetrically oriented laser beams.¹ The lasers ablate the outer layer of the capsule, which generates pressure to implode the fuel. In addition to depositing thermal energy in the ablator, the lasers can resonantly drive various laser–plasma instabilities that can degrade the quality of the implosion. Large-amplitude electron plasma waves (EPW’s) are particularly problematic because they accelerate electrons to suprathermal energies, which can prematurely heat the fuel and impede compression of the capsule. The primary instabilities that generate EPW’s in ICF experiments are stimulated Raman scattering (SRS) and two-plasmon decay (TPD).²

It has been known since the 1970s that broadband lasers can be used to suppress parametric instabilities,^{3,4} but all of the large-scale lasers used in ICF experiments use neodymium glass amplifiers and have very little native bandwidth (<0.1%). There have been a number of studies on parametric instability suppression using excimer gas lasers that have sufficient native bandwidth (~0.1%) to suppress slowly growing instabilities, like filamentation, but not enough to suppress TPD and SRS.⁵ Experiments have demonstrated the use of stimulated rotational Raman scattering to significantly increase the bandwidth of both solid-state and gas lasers.^{6,7} Another potential path toward high-energy broadband lasers is through the use of optical parametric amplifiers, where a high-energy narrowband laser is used to pump a broadband seed beam. This technique has demonstrated ~70% conversion efficiency to a seed beam with ~5% relative bandwidth at 1053 nm (Ref. 8).

These laser-technology developments have led to a resurgence of interest in using broadband lasers to suppress parametric instabilities in ICF experiments.^{9,10} The majority of existing numerical studies considered only one or a few beams in 1-D or 2-D. In actual ICF experiments, many overlapping laser beams are focused onto the target surface. Although the single-beam intensities are typically low, overlapping beams can drive the same plasma waves, resulting in instability even when the intensities of the individual beams are below the single-beam thresholds.^{11,12} To assess the viability of using bandwidth to suppress parametric instabilities in ICF experiments, the existing results need to be extended to realistic multibeam geometries.

This summary presents a numerical study of the bandwidth required to suppress absolute TPD and SRS under conditions relevant to direct-drive ICF. Multibeam absolute instability thresholds are obtained for SRS (backscatter and sidescatter) and TPD using 3-D simulations with realistic ICF drive-beam configurations including phase plates and polarization smoothing. Bandwidth is found to be more effective at mitigating multibeam absolute TPD and SRS backscatter than the corresponding single-beam instabilities. The effectiveness of bandwidth at mitigating multibeam absolute SRS sidescatter is found to be similar to the single-beam instability. Despite having the largest fractional increase in threshold relative to the monochromatic case, absolute SRS backscatter has the lowest absolute instability threshold for ignition-relevant plasma conditions over the range of bandwidths considered. Studies of the sensitivity to beam geometry and spectral dispersion suggest that the main results presented here are applicable to a broad range of potential ICF driver geometries.

Figure 1 shows the absolute TPD and SRS thresholds near $n_c/4$ as a function of laser bandwidth for $L_n = 200 \mu\text{m}$, $T_e = 2 \text{ keV}$ [Fig. 1(a)] and $L_n = 400 \mu\text{m}$, $T_e = 4 \text{ keV}$ [Fig. 1(b)]. The thresholds are normalized to the zero-bandwidth thresholds to highlight

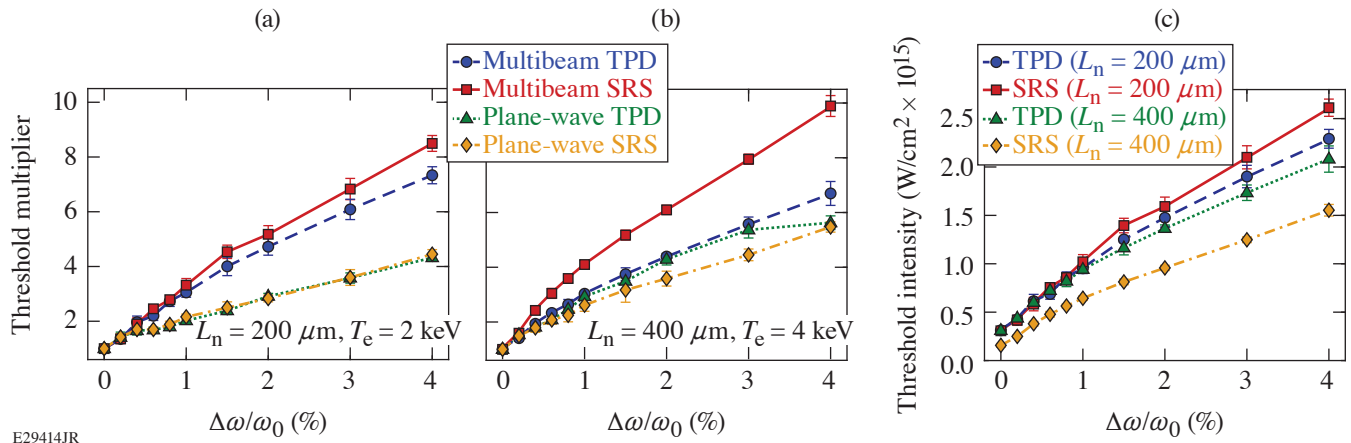


Figure 1

Absolute instability thresholds as a function of the laser normalized to the monochromatic threshold for (a) $L_n = 200 \mu\text{m}$, $T_e = 2 \text{ keV}$ and (b) $L_n = 400 \mu\text{m}$, $T_e = 4 \text{ keV}$. The various curves correspond to multibeam TPD (blue circles), multibeam SRS (red squares), single-beam TPD (green triangles), and single-beam SRS (yellow diamonds). (c) The multibeam thresholds from (a),(b) in W/cm^2 for TPD (blue circles) and SRS (red squares) at $L_n = 200 \mu\text{m}$ and TPD (green triangles) and SRS (yellow diamonds) at $L_n = 400 \mu\text{m}$.

the relative effectiveness of bandwidth mitigation. The error bars correspond to the standard deviation from an ensemble of four threshold calculations with random realizations of polarization, speckle pattern, and spectral phase.

The thresholds for a single plane-wave drive beam are plotted in Figs. 1(a) and 1(b) to show the relative effectiveness of using bandwidth to mitigate single-beam and multibeam instabilities. Intuitively we might expect that the impact of bandwidth on the instability thresholds is independent of the multibeam coupling. If that were the case, the plane-wave and multibeam curves for a given instability would be the same, and only the monochromatic multibeam thresholds and the broadband single-beam thresholds would be needed to calculate the broadband multibeam thresholds. However, the single-beam threshold multipliers are always less than the corresponding multibeam threshold multipliers. This suggests that in addition to increasing the single-beam instability thresholds, broadband lasers reduce the effectiveness of multibeam coupling.

Figure 1(c) shows the multibeam threshold curves from Figs. 1(a) and 1(b) in terms of the absolute overlapped laser intensity (W/cm^2). For the $L_n = 200\text{-}\mu\text{m}$ case, the TPD and SRS thresholds are similar at all laser bandwidths. Despite having the largest fractional increase in threshold for a given bandwidth, multibeam SRS with $L_n = 400 \mu\text{m}$ always has the lowest absolute threshold because of its low monochromatic threshold.

This material is based upon work supported by the Department of Energy National Nuclear Security Administration under Award Number DE-NA0003856, ARPA-E BETHE grant number DE-FOA-0002212, the University of Rochester, and the New York State Energy Research and Development Authority.

1. J. Nuckolls *et al.*, *Nature* **239**, 139 (1972).
2. W. L. Kruer, *The Physics of Laser Plasma Interactions*, *Frontiers in Physics*, Vol. 73, edited by D. Pines (Addison-Wesley, Redwood City, CA, 1988).
3. J. J. Thomson and J. I. Karush, *Phys. Fluids* **17**, 1608 (1974).
4. G. Laval *et al.*, *Phys. Fluids* **20**, 2049 (1977).
5. T. A. Peyser *et al.*, *Phys. Fluids B* **3**, 1479 (1991).
6. D. Eimerl, D. Milam, and J. Yu, *Phys. Rev. Lett.* **70**, 2738 (1993).
7. J. Weaver *et al.*, *Appl. Opt.* **56**, 8618 (2017).
8. C. Dorrer, E. M. Hill, and J. D. Zuegel, *Opt. Express* **28**, 451 (2020).

9. J. W. Bates *et al.*, Phys. Rev. E **97**, 061202(R) (2018).
10. R. K. Follett *et al.*, Phys. Plasmas **26**, 062111 (2019).
11. D. F. DuBois, B. Bezzerides, and H. A. Rose, Phys. Fluids B **4**, 241 (1992).
12. C. Stoeckl *et al.*, Phys. Rev. Lett. **90**, 235002 (2003).

Temporal Reflection and Refraction of Optical Pulses Inside a Dispersive Medium: An Analytic Approach

J. Zhang,¹ W. R. Donaldson,^{2,3} and G. P. Agrawal^{1,2}

¹The Institute of Optics, University of Rochester

²Laboratory for Laser Energetics, University of Rochester

³Department of Electrical and Computer Engineering, University of Rochester

Reflection of electromagnetic waves at a temporal boundary has attracted considerable attention in several contexts over the last 20 years.¹ Most of these studies have focused on a nondispersive medium and ignored the frequency dependence of the refractive index on each side of the temporal boundary. The dispersive effects were included in a 2015 study² that considered the reflection and refraction of optical pulses at a moving boundary.

We develop an analytic approach for reflection of light at a temporal boundary inside a dispersive medium and derive frequency-dependent expressions for the reflection and transmission coefficients. Using the analytic results, we study the temporal reflection of an optical pulse and show that our results agree fully with a numerical approach used earlier. Our approach provides approximate analytic expressions for the electric fields of the reflected and transmitted pulses; where the width of transmitted pulse is modified, the reflected pulse is a mirrored version of the incident pulse. When a part of the incident spectrum lies in the region of total internal reflection, both the reflected and transmitted pulses are considerably distorted.

We consider propagation of optical pulses inside a dispersive medium (such as an optical fiber) with the propagation constant $\beta(\omega)$. We assume that the pulse's spectrum is relatively narrow (quasi-monochromatic approximation), and we can expand $\beta(\omega)$ around a reference frequency in a Taylor series as

$$\beta(\omega) = \beta_0 + \beta_1(\omega - \omega_0) + \frac{1}{2}\beta_2(\omega - \omega_0)^2, \quad (1)$$

where ω_0 is a reference frequency close to the central frequency of the pulse and we neglected the third- and higher-order dispersive terms. We assume that the pulse is approaching a temporal boundary moving at the speed v_B . The refractive index changes across this boundary by a constant amount Δn and the propagation constant after the boundary becomes

$$\beta_t(\omega) = \beta_0 + \beta_B + \beta_1(\omega - \omega_0) + \frac{1}{2}\beta_2(\omega - \omega_0)^2, \quad (2)$$

where $\beta_B = (\omega_0/c)\Delta n$.

The evolution of the pulse across the temporal boundary is governed by the following Eq. (2) satisfied by the slowly varying envelope $A(z,t)$ of the pulse:

$$\frac{\partial A}{\partial z} + \Delta\beta_1 \frac{\partial A}{\partial t} + i \frac{\beta_2}{2} \frac{\partial^2 A}{\partial t^2} = i\beta_B H(t - T_B)A, \quad (3)$$

where we work in a frame in which the temporal boundary appears stationary, i.e., $t = t' - z/v_B$, where t' is the time in the laboratory frame; $\Delta\beta_1 = \beta_1 - 1/v_B$ is the relative group delay of the pulse in this time frame. In Eq. (3), $H(t - T_B)$, is the heaviside step

function taking the value 1, when $t > T_B$, and 0, when $t < T_B$. Given the initial pulse shape $A(0,t)$, numerical solutions of Eq. (3) show that the pulse splits into two parts moving at different speeds because of the spectral shifts induced at the boundary.²

Our objective is to solve Eq. (3) analytically. The numerical solutions of Eq. (3) indicate that any input pulse is partially reflected and partially transmitted at the temporal boundary such that the two parts have spectra shifted from that of the input pulses. We expect the same to occur for a plane wave. In other words, a plane wave at the frequency $\omega_0 + \Delta\omega$ is also reflected and transmitted at the boundary with different frequency shifts such that the slowly varying amplitude takes the form:

$$A = \begin{cases} e^{i(\beta'z - \Delta\omega t)} + Re^{i(\beta'_r z - \Delta\omega_r t)}, & t < T_B \\ Te^{i(\beta'_t z - \Delta\omega_t t)}, & t > T_B \end{cases}, \quad (4)$$

where R and T are the reflection and transmission coefficients that depend on $\Delta\omega$. Here $\Delta\omega$ is the frequency shift of the input plane wave from the reference frequency ω_0 , and $\Delta\omega_r$ and $\Delta\omega_t$ are frequency shifts of the reflected and transmitted plane waves, respectively. These frequency shifts depend on $\Delta\omega$.

We note that Eq. (4) does not violate causality because it is based on plane waves and the time variable $t = t' - z/v_B$ is defined in a moving frame with t' representing the real time. Causality requires only that the wave packets, representing the reflecting and transmitted parts of the incident pulse, form only after the pulse has arrived at the temporal boundary located at $z_B = T_B/\Delta\beta_1$. As discussed later, this is indeed the case.

We find the frequency shifts $\Delta\omega_r$ and $\Delta\omega_t$ by substituting the solution in Eq. (4) into Eq. (3) for $z < z_B$ and $z > z_B$. This yields the following relations:

$$\begin{cases} \beta'(\Delta\omega) = \Delta\beta_1 \Delta\omega + \frac{\beta_2}{2} \Delta\omega^2 \\ \beta'_r(\Delta\omega_r) = \Delta\beta_1 \Delta\omega_r + \frac{\beta_2}{2} \Delta\omega_r^2 \\ \beta'_t(\Delta\omega_t) = \beta_B + \Delta\beta_1 \Delta\omega_t + \frac{\beta_2}{2} \Delta\omega_t^2 \end{cases}. \quad (5)$$

These are the dispersion relation in the moving frame. From Eq. (3), $A(z,t)$ should be continuous for all values of z . This happens when the three propagation constants are equal, i.e.,

$$\beta' = \beta'_r = \beta'_t. \quad (6)$$

As discussed in Ref. 2, these conditions result from the conservation of momentum in the moving frame. Combining Eqs. (5) and (6), we find two quadratic equations whose solutions determine $\Delta\omega_r$ and $\Delta\omega_t$ for a given $\Delta\omega$. The solution for $\Delta\omega_r$ is

$$\Delta\omega_r = -\frac{2\Delta\beta_1}{\beta_2} \Delta\omega. \quad (7)$$

The solution for $\Delta\omega_t$ is a more complicated and is given by²

$$\Delta\omega_t = -\frac{\Delta\beta_1}{\beta_2} + \frac{1}{\beta_2} \sqrt{(\Delta\beta_1 + \beta_2 \Delta\omega)^2 - 2\beta_2 \beta_B}. \quad (8)$$

To find the reflection and transmission coefficients, R and T , we make use of the temporal boundary conditions at $t = T_B$. Specifically, we demand that both A and $\partial A/\partial t$ are continuous across the time boundary for any z . This requirement results in the following two equations:

$$\begin{aligned} e^{i(\beta'_z - \Delta\omega T_B)} + R e^{i(\beta'_r z - \Delta\omega_r T_B)} &= T e^{i(\beta'_t z - \Delta\omega_t T_B)}, \\ -i\Delta\omega e^{i(\beta'_z - \Delta\omega T_B)} - i\Delta\omega_r R e^{i(\beta'_r z - \Delta\omega_r T_B)} &= -i\Delta\omega_t T e^{i(\beta'_t z - \Delta\omega_t T_B)}. \end{aligned} \quad (9)$$

Using $\beta' = \beta'_r = \beta'_t$ from Eq. (6), we obtain the following analytic expressions for R and T :

$$\begin{cases} R(\Delta\omega) = \frac{\Delta\omega_t - \Delta\omega}{\Delta\omega_r - \omega_t} e^{i(\Delta\omega_r - \Delta\omega)T_B} \\ T(\Delta\omega) = \frac{\Delta\omega_r - \Delta\omega}{\Delta\omega_r - \omega_t} e^{i(\Delta\omega_t - \Delta\omega)T_B} \end{cases}. \quad (10)$$

These expressions contain a linear phase shift that depends on the boundary's location T_B . This phase shift is not important and can be removed by choosing $T_B = 0$; however, R and T can still be complex quantities. Figure 1 shows how their moduli and phases vary as a function of the physically measured frequency shift $\Delta\nu = (\Delta\omega/2\pi)$ using the notation $R = |R|e^{i\phi(R)}$ and $T = |T|e^{i\phi(T)}$. The parameters used in Fig. 1 are appropriate for an optical fiber acting as a dispersive medium² and have values $\Delta\beta_1 = 0.1$ ps/m, $\beta_2 = 5$ ps²/km, and $\beta_B = 0.5$ m⁻¹.

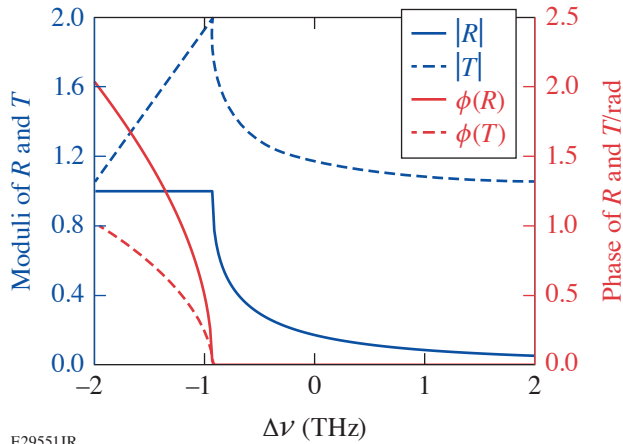


Figure 1

Frequency dependence of the reflection and transmission coefficients for $\Delta\beta_1 = 0.1$ ps/m, $\beta_2 = 5$ ps²/km, and $\beta_B = 0.5$ m⁻¹. The solid blue curve represents the modulus of reflected wave and the solid red curve is the phase of the reflected wave. Likewise, the dashed blue curve is the modulus of the transmitted wave and the dashed red curve is the phase of the transmitted wave.

The most-striking feature in Fig. 1 occurs near $\Delta\nu_c = \sqrt{2\beta_2\beta_B} - \Delta\beta_1/2\pi\beta_2 = -0.93$ THz. When $\Delta\nu > \Delta\nu_c$, both R and T are real quantities; when $\Delta\nu < \Delta\nu_c$, they become complex. The reason for this change is related to the form of Eqs. (7) and (8). While $\Delta\omega_r$ is always real, $\Delta\omega_t$ can be complex depending on the sign of the discriminant in Eq. (8). The condition for this to occur is given by $(\Delta\beta_1 + \beta_2\Delta\omega)^2 < 2\beta_2\beta_B$. In this situation, $\Delta\omega_t$ becomes complex and the transmitted wave becomes evanescent. It can be shown that $|R| = 1$ holds for $\Delta\omega < \Delta\omega_c$. This is the temporal analog of total internal reflection discussed in Ref. 2. We call $\Delta\nu_c$ the critical frequency.

The preceding discussion applies to each specific frequency component of a pulse. We can use it to study how an incident pulse gets reflected and transmitted at the temporal boundary. Consider an incident pulse with the slowly varying amplitude

$$A(z = 0, t) = A_{\text{in}}(t). \quad (11)$$

We can decompose it into plane waves of different frequencies using the Fourier transform:

$$\tilde{A}(\Delta\omega) = \int A_{\text{in}}(t) e^{i\Delta\omega t} dt. \quad (12)$$

The evolution of each plane-wave component is governed by Eq. (4). The total field can be calculated by integrating over the input pulse's spectrum to obtain:

If $t < T_B$,

$$\begin{aligned} A(z, t) = & \frac{1}{2\pi} \int \tilde{A}(\Delta\omega) e^{i[\beta'(\Delta\omega)z - \Delta\omega t]} d\Delta\omega \\ & + \frac{1}{2\pi} \int \tilde{A}(\Delta\omega) R(\Delta\omega) e^{i[\beta'_r(\Delta\omega)z - \Delta\omega_r t]} d\Delta\omega. \end{aligned} \quad (13)$$

If $t > T_B$,

$$A(z, t) = \frac{1}{2\pi} \int \tilde{A}(\Delta\omega) T(\Delta\omega) e^{i[\beta'_t(\Delta\omega)z - \Delta\omega_t t]} d\Delta\omega. \quad (14)$$

This being our main result, it can be used to find the shapes and spectra of the reflected and transmitted parts of any input pulse.

This material is based upon work supported by the Department of Energy National Nuclear Security Administration under Award Number DE-NA0003856, the University of Rochester, and the New York State Energy Research and Development Authority.

1. J. T. Mendonça and P. K. Shukla, *Phys. Scr.* **65**, 160 (2002).
2. B. W. Plansinis, W. R. Donaldson, and G. P. Agrawal, *Phys. Rev. Lett.* **115**, 183901 (2015).

Equation of State, Sound Speed, and Reshock of Shock-Compressed Fluid Carbon Dioxide

L. E. Crandall,^{1,2} J. R. Rygg,^{1,2,3} D. K. Spaulding,⁴ M. F. Huff,^{1,2} M. C. Marshall,⁵ D. N. Polsin,¹ R. Jeanloz,⁶ T. R. Boehly,¹ M. Zaghoo,¹ B. J. Henderson,^{1,2} S. Brygoo,⁷ P. M. Celliers,⁵ J. H. Eggert,⁵ D. E. Fratanduono,⁵ A. Lazicki,⁵ M. Millot,⁵ and G. W. Collins,^{1,2,3}

¹Laboratory for Laser Energetics, University of Rochester

²Department of Mechanical Engineering, University of Rochester

³Department of Physics and Astronomy, University of Rochester

⁴University of California, Davis

⁵Lawrence Livermore National Laboratory

⁶University of California, Berkeley

⁷Commissariat à l'énergie atomique et aux énergies alternatives, France

Mechanical equation-of-state data of initially liquid and solid CO₂ shock compressed to terapascal conditions are reported. Diamond–sapphire anvil cells were used to vary the initial density and state of CO₂ samples, which were then further compressed with laser-driven shock waves, resulting in a data set from which precise derivative quantities including Grüneisen parameter and sound speed are determined. Reshock states were measured to 800 GPa and map the same pressure–density conditions as the single shock using different thermodynamic paths. The compressibility data reported here do not support current density-functional-theory (DFT) calculations but are better represented by tabular equation-of-state models.

The covalent double bonds that bind the atoms in a CO₂ molecule at ambient conditions are among the strongest of chemical bonds, but at pressures reaching tens of GPa, the compression energy becomes comparable to this bonding energy (hundreds of kJ/mol) and the previously stable molecule exhibits complex chemical behavior.^{1,2} Laser-heated diamond-anvil cell experiments have characterized the solid phase diagram of CO₂ up to 120 GPa, which exhibits five molecular crystalline polymorphic phases before transforming into both crystalline and amorphous polymeric phases.^{1–7}

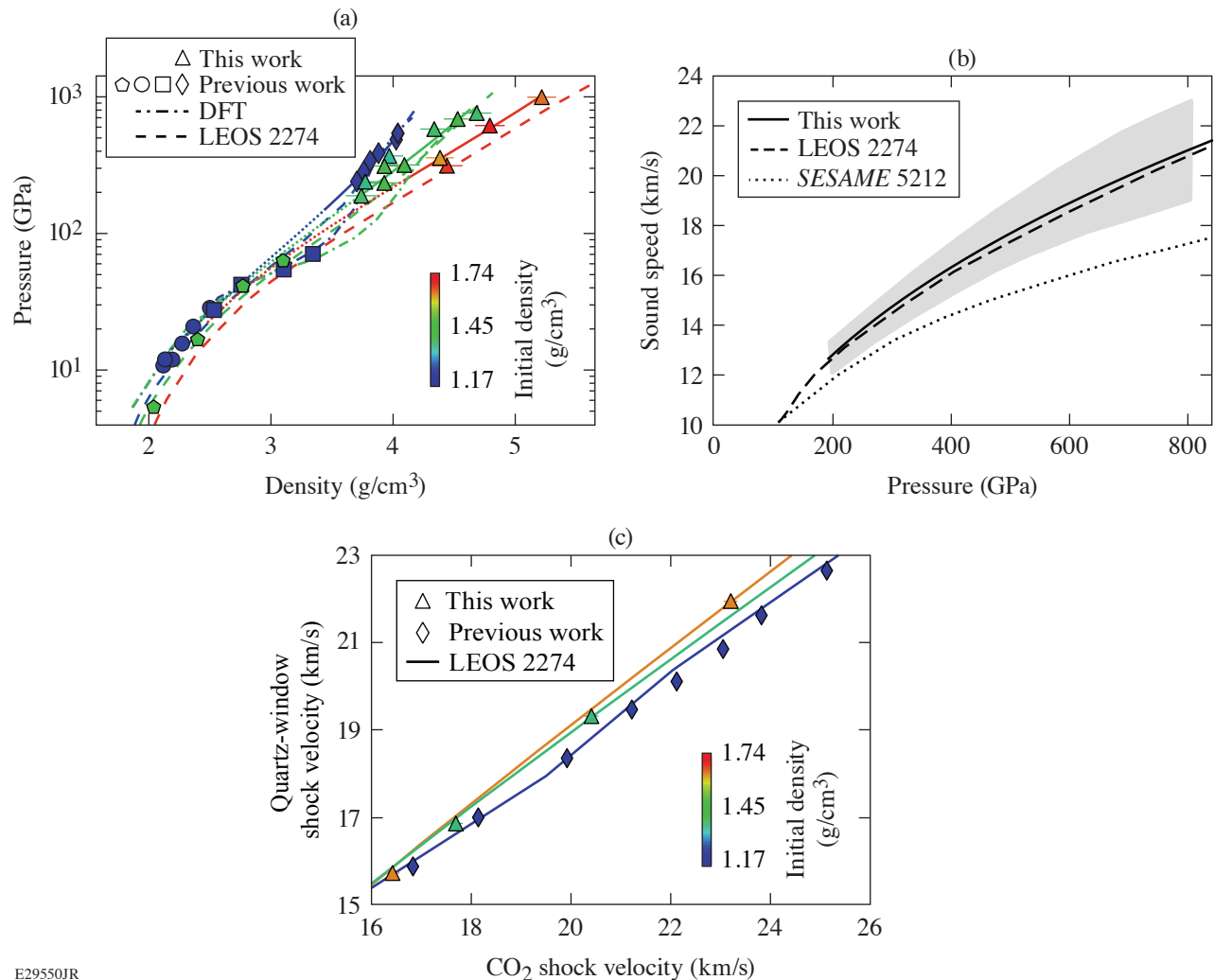
The fluid phase diagram of CO₂ has been experimentally explored to 1 TPa (Refs. 8–14) and is proposed to exhibit similar chemical complexity to the solid phase diagram.¹⁵ When shock compressed, molecular liquid CO₂ (Fluid I) is stable up to 40 GPa, above which it transforms into an insulating 3- and 4-coordinated polymeric fluid (Fluid II).^{12,15} Above 100 GPa, CO₂ transitions into the Fluid-III phase and begins to ionize.¹⁴ The present work is a study of the Fluid-III phase of CO₂.

The pressure, density, temperature, and reflectivity of shocked CO₂ have been measured to 1 TPa and 93,000 K in Ref. 14. Experimental evidence indicates that CO₂ at the highest pressures and temperatures studied is in a complex bonded state as opposed to the previously predicted¹³ fully atomic C, O fluid. This work reports further details of the study presented in Ref. 14, and it additionally reports the experimentally determined Grüneisen parameter and isentropic sound speed of shocked CO₂ and the mechanical behavior of CO₂ under reshock.

The pressure and density results from these experiments are plotted in Fig. 1(a) (triangles); the present measurements support LEOS¹⁶ over current DFT¹⁷ calculations in the high-pressure fluid regime. Variation in initial density was leveraged to measure multiple Hugoniot curves, from which derivative quantities were probed using a difference method.¹⁸ The theoretical Grüneisen parameter is systematically higher than the experimental result, but all curves tend to the ideal gas limit of 2/3. The Eulerian

sound speed, plotted in Fig. 1(b), can be directly calculated from the measured Hugoniot and Grüneisen parameter.¹⁹ LEOS 2274 (Ref. 16) shows excellent agreement with our experimental data. This is expected given the good agreement between LEOS 2274 (Ref. 16) and our Hugoniot data. The present work measured four reshock states in CO₂ and shows strong agreement with LEOS, as shown in Fig. 1(c).

To summarize, this work provides additional details on recently published¹⁴ equation-of-state measurements of shock-compressed CO₂ to 1 TPa and 93,000 K from varying initial densities and presents new information on the Grüneisen parameter, sound speed, and reshock behavior of high-pressure shocked CO₂. We find that the compressibility, Grüneisen parameter, and sound speed of shocked CO₂ are well represented by LEOS;¹⁶ this work does not support the extreme curvature in compressibility



E29550JR

Figure 1

(a) Log pressure versus density for shocked CO₂: OMEGA data (triangles), Sandia Z data¹³ (diamonds), and gas-gum data (pentagons),⁸ circles,¹⁰ and squares¹². LEOS¹⁶ (dashed curves) and density functional theory (DFT)¹⁷ (dashed-dotted curves) are also calculated. Solid curves are fits to the OMEGA and Z data; dotted curves extrapolate this fit to lower pressure. The initial density of all data points and curves is given by the color bar. (b) Sound speed of shocked CO₂. This work (solid curve) calculates the sound speed from the measured Hugoniot and Grüneisen parameter. LEOS¹⁶ (dashed curve) shows excellent agreement with these results, while *SESAME* (dotted curve) underpredicts the sound speed. (c) Shock velocity in the quartz window versus shock velocity in the CO₂ sample on either side of their respective interfaces. A reshock is launched back into the CO₂ sample when the shock traverses into the higher-impedance quartz window. These OMEGA data are represented by triangles and the Sandia Z data by diamonds. Solid lines are LEOS curves based on the modeled reshock intersecting with the experimental quartz Hugoniot.^{20,21}

modeled by DFT.¹⁷ Notably, lower-pressure gas-gun data support DFT over LEOS. This complexity in the compressibility behavior of shocked CO₂ warrants further study since there is currently a gap between 71 and 189 GPa where no data exist to constrain theory. We report four reshock states of CO₂ and discuss the effect of the Grüneisen parameter on the reshock curve. This work provides significant new benchmarks for theoretical calculations of fluids in the warm-dense-matter regime.

This material is based upon work supported by the Department of Energy National Nuclear Security Administration under Award Number DE-NA0003856, the University of Rochester, the New York State Energy Research and Development Authority, NNSA support to the University of California, Berkeley, and NSF 19-528 Physics Frontier Centers, Award Number 2020249, Center for Matter at Atomic Pressures. This work was performed under the auspices of the U.S. Department of Energy by Lawrence Livermore National Laboratory under Contract DE-AC52-07NA27344 and was supported by the LLNL-LDRD Program under Project No. 12-SI-007.

1. F. Datchi and G. Weck, *Z. Kristallogr.* **229**, 135 (2014).
2. C.-S. Yoo, *Phys. Chem. Chem. Phys.* **15**, 7949 (2013).
3. K. D. Litasov, A. F. Goncharov, and R. J. Hemley, *Earth Planet. Sci. Lett.* **309**, 318 (2011).
4. K. F. Dziubek *et al.*, *Nat. Commun.* **9**, 3148 (2018).
5. V. M. Giordano *et al.*, *J. Chem. Phys.* **133**, 144501 (2010).
6. V. M. Giordano, F. Datchi, and A. Dewaele, *J. Chem. Phys.* **125**, 054504 (2006).
7. H. Shimizu, T. Kitagawa, and S. Sasaki, *Phys. Rev. B* **47**, 11,567 (1993).
8. V. N. Zubarev and G. S. Telegin, *Sov. Phys.-Dokl.* **7**, 34 (1962).
9. Zubarev and Telegin⁸ report two different initial densities for their solid CO₂: 1.45 and 1.54 g/cm³. Cited in Schott¹⁰ are “verbal inquires and replies conveyed through C. L. Mader and A. N. Dremin, ca. 1983” that confirm that 1.54 g/cm³ is a misprint, and the initial density of the data published by Zubarev and Telegin is 1.45 g/cm³.
10. G. L. Schott, *High Press. Res.* **6**, 187 (1991).
11. Each measurement of the shock velocity in Ref. 8 is the average of 4 to 12 independent measurements with a 1% to 2% deviation from the mean. Reference 10 similarly presents duplicate measurements of transit times but does not indicate uncertainty. No rigorous systematic uncertainty analysis associated with the data in Refs. 8 and 10 was reported.
12. W. J. Nellis *et al.*, *J. Chem. Phys.* **95**, 5268 (1991).
13. S. Root *et al.*, *Phys. Rev. B* **87**, 224102 (2013).
14. L. Crandall *et al.*, *Phys. Rev. Lett.* **125**, 165701 (2020).
15. B. Boates, A. M. Teweldeberhan, and S. A. Bonev, *Proc. Natl. Acad. Sci.* **109**, 14808 (2012).
16. C. J. Wu *et al.*, *J. Chem. Phys.* **151**, 224505 (2019).
17. B. Boates *et al.*, *J. Chem. Phys.* **134**, 064504 (2011).
18. D. G. Hicks *et al.*, *Phys. Rev. Lett.* **97**, 025502 (2006).
19. R. G. McQueen, S. P. Marsh, and J. N. Fritz, *J. Geophys. Res.* **72**, 4999 (1967).
20. M. P. Desjarlais, M. D. Knudson, and K. R. Cochran, *J. Appl. Phys.* **122**, 035903 (2017).
21. S. Brygoo *et al.*, *J. Appl. Phys.* **118**, 195901 (2015).

Carbon-Doped Sulfur Hydrides as a Room-Temperature Superconductor at 270 GPa

S. X. Hu,^{1,2} R. Paul,^{1,2} V. V. Karasiev,¹ and R. P. Dias^{2,3}

¹Laboratory for Laser Energetics, University of Rochester

²Department of Mechanical Engineering, University of Rochester

³Department of Physics and Astronomy, University of Rochester

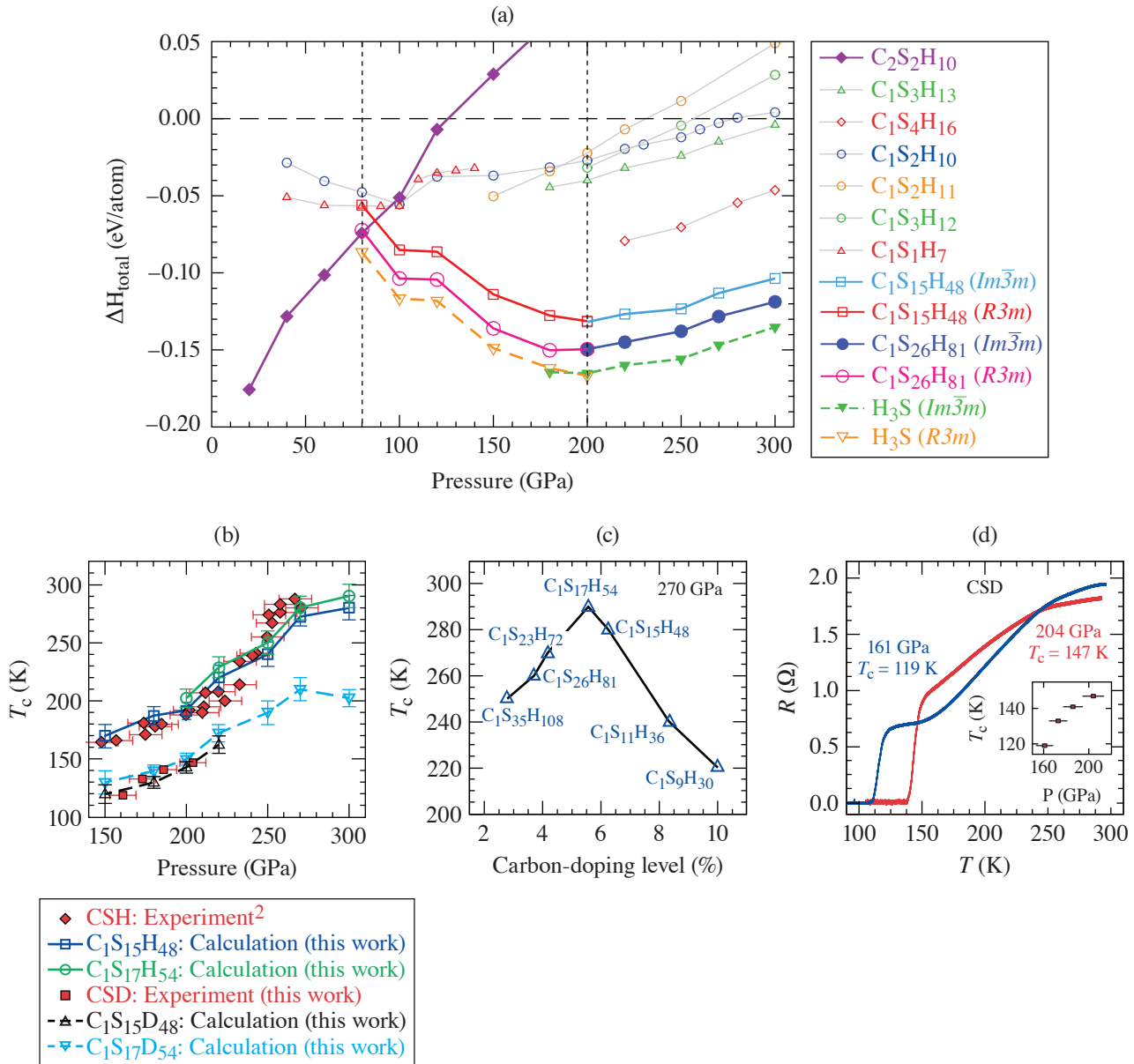
Superconductivity is the property of the complete absence of electrical resistance at temperatures below a critical transition temperature (T_c). For conventional superconductors, the electron–phonon coupling mediates the formation of a Cooper pair of electrons with opposite spins, as described in the Bardeen–Cooper–Schrieffer (BCS) theory. However, the highest transition temperature attained by any conventional superconductors so far is $T_c = 39$ K in MgB₂. In the past five years, exciting high- T_c superconducting materials have been discovered. In particular, the first experimental synthesis of H₃S gave an unprecedentedly high $T_c = 203$ K at a pressure of $P \approx 150$ GPa (Ref. 1). Most recently, a room-temperature superconductor has been experimentally realized in a carbonaceous sulfur hydride (CSH) system,² which demonstrated $T_c = 287.7 \pm 1.2$ K at 267 ± 10 GPa. This experimental finding has excited the condensed-matter and high-pressure physics communities to understand this “puzzling” ternary CSH system since recent studies^{3,4} prior to the experiment² did not predict room-temperature T_c behavior.

We used the evolutionary structure searching code USPEX combined with the density-functional-theory code VASP to determine the possible stoichiometry and stable crystal structures, in a wide pressure range from 20 to 300 GPa, for various combinations of C_{*i*}S_{*j*}H_{*k*} using the electronic formation enthalpy ΔH (eV/atom) < 0 as the criterion. These results showed a general trend: CSH compounds composed of one CH₄ “guest” molecule and integer numbers of H₃S “host” molecules tend to have lower formation enthalpy. This energetics observation prompted us to look into the binary components of C_{*i*}H_{*k*}, S_{*j*}H_{*k*}, and C_{*i*}S_{*j*}. These binary searches resulted in the following conclusion: the basic unit of H₃S in its *Im-3m* cubic structure gives the lowest formation enthalpy of $\Delta H_{\text{H}_3\text{S}} \approx -0.125$ eV/atom among all such binary compounds. From a thermodynamic stability point of view, these results unambiguously suggest that a higher H₃S concentration in a ternary CSH compound should drive the system to lower formation enthalpy (more stable). This led us to explore the energetics and stability of carbon doping in H₃S systems.

To examine the formation enthalpy of carbon-doped H₃S systems, we varied the ratio of carbon to sulfur in a “supercell” composed of an integral number of H₃S units in its *R3m* or *Im-3m* structure, i.e., taking systems like C₁S₁₅H₄₈ and C₁S₁₇H₅₄ as examples. We then calculated the total formation enthalpy (including the zero point energy of ions: ΔE_{ZPE}) for these energetically optimized CSH compounds in the pressure range of 80 to 300 GPa. The H₃S system has the lowest formation enthalpy for all the structures examined in this pressure range. Carbon-doped sulfur hydrides, varying from C₁S₃₅H₁₀₈ to C₁S₁₉H₃₀, are energetically second to the pure H₃S system within an ~50-meV difference of ΔH_{total} . Nevertheless, these carbon-doped sulfur hydrides are both thermodynamically and dynamically stable since they all have $\Delta H_{\text{total}} < 0$ and no imaginary components in their phonon spectra. At low pressures (< 80 GPa), the CSH system takes the most-stable stoichiometry of C₂S₂H₁₀, composed of one C₂H₆ (ethane) molecule linked by hydrogen bonding with two H₂S molecules in *P*₁ symmetry.

To examine if these identified carbon-doped sulfur hydrides exhibit any high-temperature superconductivity, we employed the Allen–Dynes–McMillian equation implemented in the density functional theory code *Quantum Espresso* to estimate the T_c for compounds varying from C₁S₉H₃₀ to C₁S₃₅H₁₀₈ in the pressure range of 150 to 300 GPa, with the virtual crystal approximation. The T_c results from these calculations for C₁S₁₅H₄₈ and C₁S₁₇H₅₄, as shown in Fig. 1(b) as a function of pressure, showed good

agreement with experiment and a room-temperature $T_c = 280 \pm 10$ K at ~ 270 GPa. Figure 1(c) plots the estimated maximum T_c variation as a function of carbon-doping level, corresponding to the stable CSH compounds ranging from $C_1S_9H_{30}$ to $C_1S_{35}H_{108}$ at 270 GPa. A peak of $T_c \sim 290$ K appears at an *optimal* carbon-doping level of $\sim 5.56\%$ (corresponding to $C_1S_{17}H_{54}$). In the CSH experiment² there was no intentional control of the carbon-doping level. Therefore, the experimentally synthesized CSH samples



TC15678JR

Figure 1

(a) The Convex Hull Analysis of CSH compounds: the total formation enthalpy versus pressure for different CSH compounds in the pressure range of 20 to 300 GPa. (b) The calculated superconducting transition temperature T_c versus pressure for compounds $C_1S_{15}H_{48}/C_1S_{17}H_{54}$ and $C_1S_{15}D_{48}/C_1S_{17}D_{54}$ compared to both the CSH experiment² and the new CSD (carbon sulfur deuterium) experiment. (c) The maximum T_c as a function of carbon doping level in different CSH compounds at the same pressure of 270 GPa. (d) The measured temperature-dependent electrical resistance of carbonaceous sulfur deuteride at high pressures, showing the superconducting transitions as high as 147 K at 204 GPa, the highest pressure measured in this experimental run. Inset: The pressure dependence of the T_c as determined by the sharp drop in electrical resistance, showing the increase in T_c with pressure.

in the diamond-anvil cell might contain around 5%–6% carbon doping that should dominantly contribute to the measured zero resistance. The new CSD experimental results in Fig. 1(d) show good agreement between CSD experiments and calculations for $C_1S_{15}H_{48}$ and $C_1S_{17}D_{54}$, and demonstrate a pronounced shift of T_c from an isotopic substitution. The substitution of deuterium lowers T_c , indicating phonon-assisted superconductivity. This is a result of carbon doping contributing more to the higher-frequency phonon mode due to its strong covalent bonding to hydrogen atoms. This leads to a significant enhancement of the logarithmic averaged phonon frequency, changing from $\omega_{ln} \sim 1010$ K at 200 GPa to $\omega_{ln} \sim 1550$ K at 270 GPa, with the transition temperature T_c being saturated at above ~ 270 GPa. For $C_1S_{17}D_{54}$, the logarithmic averaged phonon frequency ω_{ln} is overall lower than that of $C_1S_{17}H_{54}$ at the same pressure due to the heavier deuterium mass. This suggests that the synthesized carbonaceous sulfur hydride superconducts via an electron–phonon mechanism consistent with the BCS theory of conventional superconductors.

This material is based upon work supported by the Department of Energy National Nuclear Security Administration under Award Number DE-NA0003856, the University of Rochester, and the New York State Energy Research and Development Authority. This work is partially supported by U.S. National Science Foundation PHY Grant No. 1802964 for S. X. Hu and V. V. Karasiev. R. P. Dias acknowledges NSF Grant No. DMR-1809649 and the DOE Stockpile Stewardship Academic Alliance Program, Grant No. DE-NA0003898.

1. A. P. Drozdov *et al.*, *Nature* **525**, 73 (2015).
2. E. Snider *et al.*, *Nature* **586**, 373 (2020).
3. W. Cui *et al.*, *Phys. Rev. B* **101**, 134504 (2020).
4. Y. Sun *et al.*, *Phys. Rev. B* **101**, 174102 (2020).

Unraveling the Intrinsic Atomic Physics Behind X-Ray Absorption Line Shifts in Warm Dense Silicon Plasmas

V. V. Karasiev and S. X. Hu

Laboratory for Laser Energetics, University of Rochester

Accurate knowledge of radiative properties of matter in a wide range of material densities across different temperature regimes is of growing importance in many areas of research such as planetary science, astrophysics, and inertial confinement fusion (ICF).^{1–4} Our current incomplete understanding of atomic physics in dense plasmas has been demonstrated by the measurements (in Refs. 5–7) of the ionization potential depression (IPD) in warm/hot dense aluminum plasmas, which have called into question the traditional continuum-lowering plasma physics models such as Ecker–Kröll⁸ and Stewart–Pyatt.⁹

In this work, we develop a novel methodology based on *all-electron* density functional theory (DFT) for calculating the optical properties of warm dense plasmas of mid- Z materials in a broad range of x-ray photon energies (up to $h\nu \sim 10$ keV). To demonstrate its applicability, we have used this novel method to systematically calculate the x-ray absorption of dense silicon plasmas for a wide range of densities and temperatures ($\rho = 0.5$ to 500 g/cm³ and $T = 5 \times 10^3$ to 10^7 K). Based on these data, a first-principles opacity table (FPOT) of silicon has been built for ICF and high-energy-density physics applications. These *ab initio* results revealed interesting trends of density/temperature-induced red-to-blue shifts of K-edge and $1s \rightarrow 2p$ absorption lines along both the isotherm and isochore. These absorption-line shifts provide a ubiquitous measure of the competition between screening of deep bound electrons and screening of outer-shell electrons due to the warm-dense-plasma environment. Our data indicate that one can use the absorption ratio of $1s \rightarrow 2p$ to K edge for characterizing thermodynamic conditions of warm dense plasmas through x-ray spectroscopy measurements coupled with DFT calculations.

These shifts for the $T = 500$ -kK isotherm are summarized in Fig. 1(a) for different silicon densities [solid red and dashed curves (circles) labeled “DFT (this work)”], where the solid and dashed horizontal lines refer to the K edge and $1s \rightarrow 2p$ locations for silicon at ambient density 2.33 g/cm³ and $T = 500$ kK. It is clearly seen that both absorption lines have the similar trend of red-to-blue shift as ρ increases. This behavior underlines the competition between electron screening and ion–ion interaction effects on the deeply bound electrons and the outer-shell electrons. Figure 1(b) shows results for the $\rho = 35$ -g/cm³ isochore [solid red and dashed curves (circles) labeled “DFT (this work)”]. Along this thermodynamic path, the deeply bounded $1s$ states move down as temperature increases as a consequence of the decreased screening by upper-bound electrons (due to thermal-induced ionization). As a result, the K edge shifts upward overall, except for an ~ 40 -eV red shift at temperatures between 125 kK and 250 kK, shown in Fig. 1(b); meanwhile, the $1s \rightarrow 2p$ absorption line exhibits a monotonic blue shift. To further understand these interesting features, we examine the widely used continuum-lowering models. These plasma-physics models predict the IPD for a given plasma condition (density, temperature, and an ion charge state \bar{Z}) with respect to an isolated ion. Figure 1(a) indicates that the atomic models of Stewart–Payatt,⁹ corrected Stewart–Payatt,¹⁰ modified ion sphere,¹¹ and Crowley¹² fail to predict the K-edge red shift, providing only a qualitatively correct trend for the blue shift occurring at $\rho > 50$ g/cm³.

Finally, we plot the ratio of the $1s \rightarrow 2p$ absorption to the K-edge absorption coefficients in Figs. 1(c) and 1(d), as the function of thermodynamic conditions varies. Figure 1(c) shows this ratio peaks at $\rho \sim 5$ to 7 g/cm³ for $T = 500$ kK, then decreases to zero as the density increases. For the constant density shown in Fig. 1(d), the ratio monotonically increases as plasma temperature increases. Guided by such DFT calculations, one can measure this absorption ratio to infer the density and temperature in experiments.

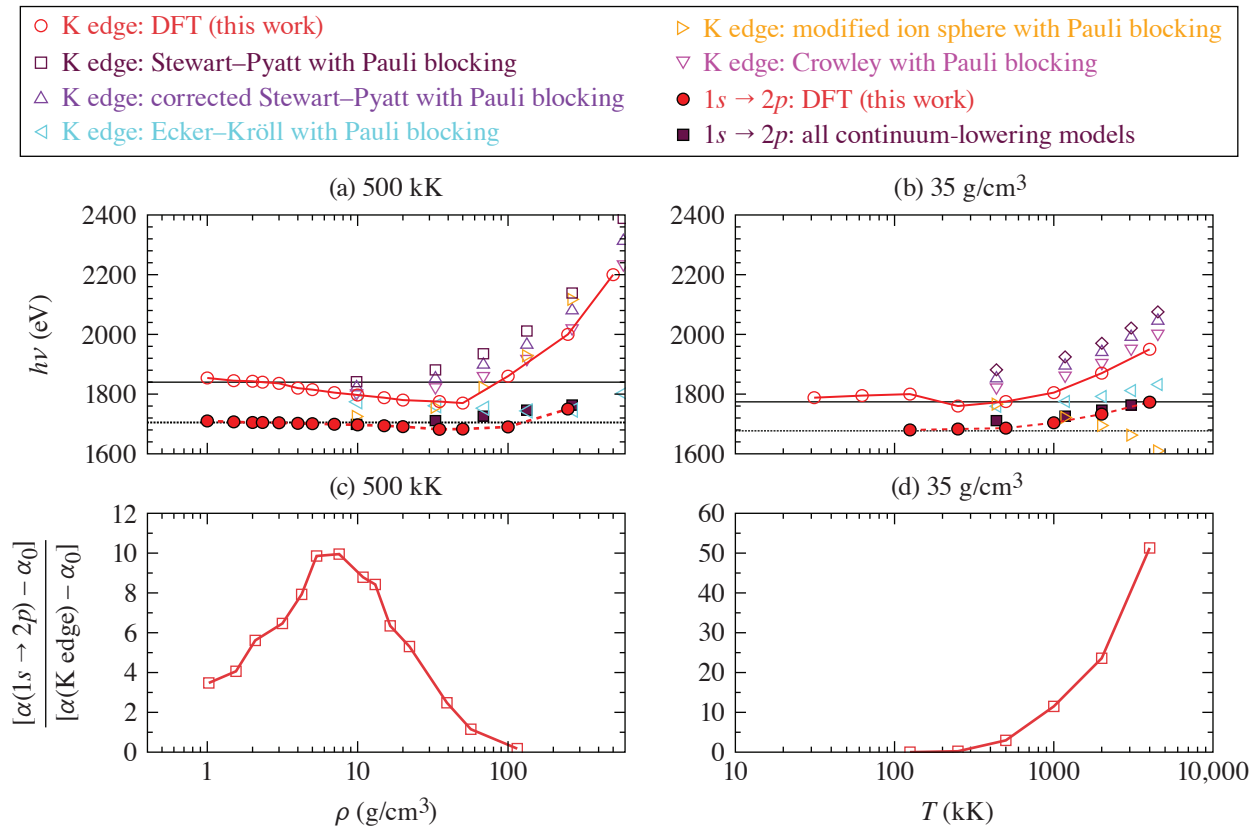
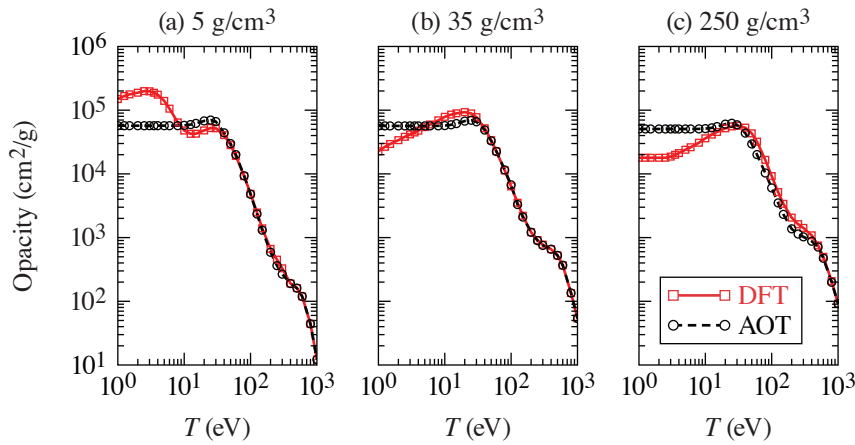


Figure 1

(a) Pressure-induced effect on the K-edge and $1s \rightarrow 2p$ absorption lines in silicon plasmas along the $T = 500$ -kK isotherm; (b) temperature-induced effect on the K-edge and $1s \rightarrow 2p$ absorption line location in silicon plasmas along $\rho = 35.0$ -g/cm³ isochores; (c) the ratio of absorption coefficients between α (K–L) and α (K-edge) with subtracted L-tail background absorption α_0 along $T = 500$ -kK isotherm; (d) similar to (c) for the $\rho = 35.0$ -g/cm³ isochores.

The total opacities from our DFT and astrophysical opacity table (AOT) calculations are further compared in Fig. 2. The total/gray Rosseland mean opacity K_R of Si is shown as a function of temperature for three representative cases: $\rho = 5, 35,$ and 250 g/cm³. Both DFT and AOT total opacities agree well for temperatures above a few tens of eV; however, the AOT model significantly underestimates the total opacity for $\rho = 5$ at temperatures below 10 eV. This finding is similar to the comparison between DFT and AOT for CH plasmas.¹³ For densities $\rho = 35$ and 250 g/cm³ at low temperatures (near 10 eV and below), the AOT total opacities are higher than the reference DFT values.

In conclusion, a novel free-energy DFT-based methodology has been developed that enables us to perform first-principles calculations of x-ray absorption in warm dense mid-/high- Z plasmas for a wide range of photon energies and plasma conditions. Applying the developed method to warm dense silicon plasmas, we revealed interesting red-to-blue shifts of K-edge and K–L absorption, which are explained by the competition between the free-electron screening of the K-shell core electrons and the screening of outer L-shell and M-shell electrons. Observing the fact that the relative magnitude of the K–L and K-edge absorption strongly depend on plasma environment, we propose using the ratio of $1s \rightarrow 2p$ absorption to the K-edge absorption to characterize the thermodynamic properties of dense plasmas through the x-ray spectroscopy technique. Novel methodology developed in this work was applied for systematic calculations of absorption and mean grouped opacity of silicon plasmas in a wide range of thermodynamic conditions. The resulting FPOT data were compared with the widely used AOT model. We found significant quantitative and qualitative discrepancies.



TC15624JR

Figure 2

Total Rosseland mean opacity of silicon at $\rho = 5, 35,$ and 250 g/cm^3 as a function of temperature as predicted by our first-principles DFT calculations and AOT model.

This material is based upon work supported by the Department of Energy National Nuclear Security Administration under Award Number DE-NA0003856, U.S. National Science Foundation PHY Grant No. 1802964, the University of Rochester, and the New York State Energy Research and Development Authority.

1. J. J. Fortney and N. Nettelmann, *Space Sci. Rev.* **152**, 423 (2010).
2. C. A. Iglesias, F. J. Rogers, and D. Saumon, *Astrophys. J. Lett.* **569**, L111 (2002).
3. S. X. Hu *et al.*, *Phys. Rev. E* **90**, 033111 (2014).
4. S. X. Hu *et al.*, *Phys. Plasmas* **22**, 056304 (2015).
5. O. Ciricosta *et al.*, *Phys. Rev. Lett.* **109**, 065002 (2012).
6. S. M. Vinko *et al.*, *Nature* **482**, 59 (2012).
7. D. J. Hoarty *et al.*, *Phys. Rev. Lett.* **110**, 265003 (2013).
8. G. Ecker and W. Kröll, *Phys. Fluids* **6**, 62 (1963).
9. J. C. Stewart and K. D. Pyatt, Jr., *Astrophys. J.* **144**, 1203 (1966).
10. B. J. B. Crowley, *High Energy Density Phys.* **13**, 84 (2014).
11. D. Liberman and J. Albritton, *J. Quant. Spectrosc. Radiat. Transf.* **51**, 197 (1994).
12. B. J. B. Crowley, *Phys. Rev. A* **41**, 2179 (1990).
13. S. X. Hu *et al.*, *Phys. Rev. B* **96**, 144203 (2017).

A Transmitted-Beam Diagnostic for the Wavelength-Tunable UV Drive Beam on OMEGA

J. Katz, D. Turnbull, B. E. Kruschwitz, A. L. Rigatti, R. Rinefierd, and D. H. Froula

Laboratory for Laser Energetics, University of Rochester

Understanding how light propagates through plasma is of great importance in many fields of physical science. In the absence of a critically dense surface, the majority of light incident into a plasma will pass through with little perturbation. Yet, much can be learned about the plasma by studying the properties of light that transmits through it. Measuring the power, spectrum, and spatial profile of transmitted light provides a means to investigate a number of key laser–plasma interactions (LPI’s) such as filamentation, laser absorption, and cross-beam energy transfer (CBET). Figure 1 shows a new experimental platform developed on the OMEGA laser to explore these processes.¹ A wavelength-tunable (350- to 353-nm) UV drive beam (TOP9) has been added to OMEGA’s 61st beamline in port P9 (Ref. 2) and a transmitted-beam diagnostic (P9TBD), located in the opposing port P4, characterizes the properties of the TOP9 beam after it propagates through the plasma. Together, these capabilities support a range of experiments designed to validate and constrain plasma-physics models and CBET mitigation strategies.

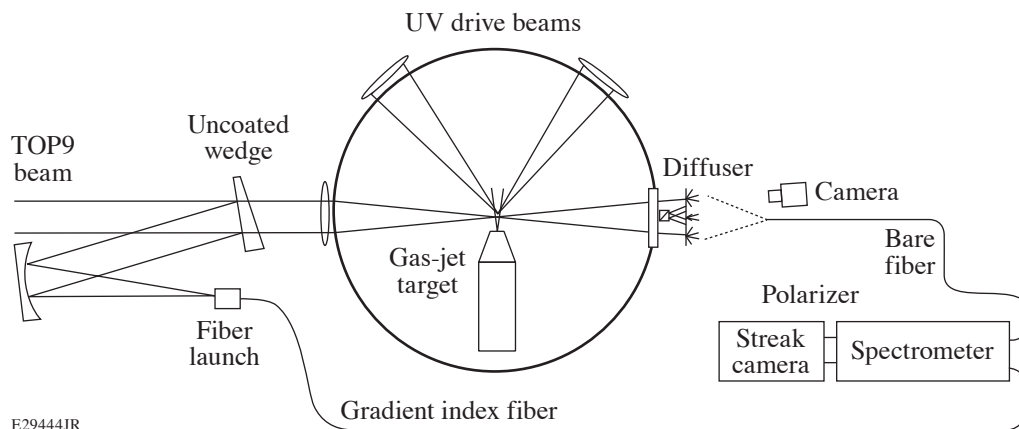


Figure 1

A charge-coupled–device (CCD) camera and fiber-coupled streaked spectrometer measure the energy, power, and near-field fluence of TOP9 after it transmits through an underdense plasma. The initial spectral power of the beam is also measured.

The P9TBD measures the energy, fluence, power, and spectrum of the TOP9 beam after it propagates through an underdense plasma. After passing through focus at target chamber center (TCC), the TOP9 beam expands and is projected on a semi-transparent diffuser. A fraction of the incident light transmits through the diffuser and forward scatters off the rear surface, generating an object that can be imaged. Internal scattering in the bulk of the 500- μm -thick diffuser limits the spatial resolution to 800- μm FWHM. Because the plasma and laser focus at TCC are small (~ 1 mm) and the diffuser is far away (1.9 m), a given position on the diffuser corresponds to the angle at which the light left the plasma. The vacuum window and diffuser have a 450-mm optical clear aperture that represents an $f/4.2$ angular field of view (Fig. 2). This allows one to observe plasma-induced refraction and filamentation^{3,4} of the TOP9 beam beyond its native $f/6.7$ cone. A serviceable debris shield protects the thicker and more costly

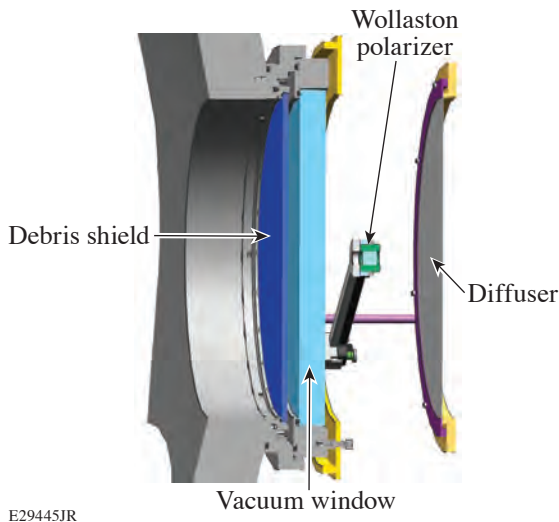


Figure 2

A cross-section view of the P4 port assembly. A 480-mm-diam debris shield protects the vacuum window and can be swapped prior to critical experiments to ensure nominal transmission through the optics. A Wollaston polarizer placed in front of the diffuser samples a 20-mm sub-aperture of the transmitted beam.

vacuum window from damage and particulate accumulation. The debris shield can be replaced prior to P9TBD experiments to restore nominal optical transmission. A Wollaston polarizer can be installed to measure the polarization of the central 20-mm subsection of the transmitted beam.

A CCD camera and imaging lens assembly is used to measure the time-integrated spatial profile of the transmitted beam (Fig. 3). The spectrally resolved power of the transmitted beam is measured using a fiber-coupled streaked spectrometer. A flat, cleaved optical fiber pointed at the center of the diffuser couples a spatially averaged sample of the incident light. The effective field of view at the diffuser plane is determined by the angular acceptance of the fiber optic. To improve sampling uniformity across the entire diffuser area, the fiber is positioned with a 3.5-m standoff distance, limiting the range of angles coupled to 0° to 3.8° . This also maintains the roll-off in sensitivity due to area foreshortening, which scales with $\cos^4(\theta)$, to a less-than-1% effect. The total power coupled into the fiber is given by $\Phi_{\text{fiber}} = \Phi_{\text{in}} \sin^2(\theta_{\text{max}}) A_f * T/A_d$, where Φ_{in} is the power incident on the diffuser, T is the diffuser transmission (0.1), A_f is the area of the fiber core (430- μm -diam core), and A_d is the diffuser area.

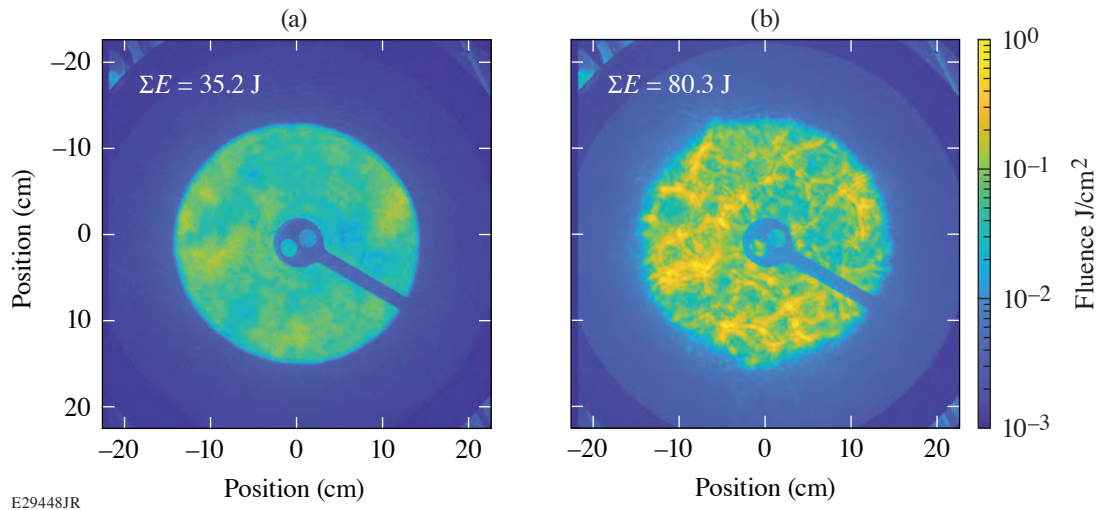


Figure 3

(a) The spatial profile of the TOP9 beam is imaged after terminating on a semi-transparent diffuser. The P9TBD instruments are photometrically calibrated to the laser system calorimetry by taking a blow-through shot with no plasma present at TCC. (b) The TOP9 beam refracted as it propagated through a preformed, underdense plasma. The spatial resolution of the recorded image corresponds to the angular distribution of energy that left TCC. In this experiment, LPI's produced high-frequency variations in the transmitted beam's intensity.

Together, this results in a coupling efficiency of $\sim 4 \times 10^{-10}$. This approach is lossy compared to an image relay but avoids issues with the high numerical apertures required to demagnify a large object onto a small fiber core.

The initial power and spectrum of the TOP9 beam are measured prior to entering the target chamber using a full-aperture, uncoated wedged optic located in front of the final focusing lens. The pickoff beam is focused into a dual-diffuser-based fiber launcher and is routed to the streaked spectrometer. Samples of both the input and transmitted beam are recorded simultaneously on the same streaked image using a custom-built multichannel fiber input head. The standard spectrometer entrance slit assembly is replaced with a V-groove array that positions up to 20 individual fibers in discrete locations offset horizontally along the axis of dispersion.

The P9TBD uses a 1.0-m-focal-length Czerny–Turner spectrograph (McPherson, 2061) and a 4320-grooves/mm grating that produces a linear dispersion of 8.0 mm/nm at the streak camera photocathode. A mask attached to the front of the V-groove array positions a series of laser-cut, vertical slits in front of each fiber face, allowing optimization of slit width for each channel. A typical streaked image, shown in Fig. 4, demonstrates P9TBD’s ability to directly observe CBET, in this case from an OMEGA drive beam to the TOP9 beam. The temporal resolution of the streaked image is approximately 100-ps FWHM limited by contributions from optical path length differences from TCC to the fiber input, modal dispersion in the fiber transport, pulse-front tilt in the spectrometer, and streak camera temporal resolution.

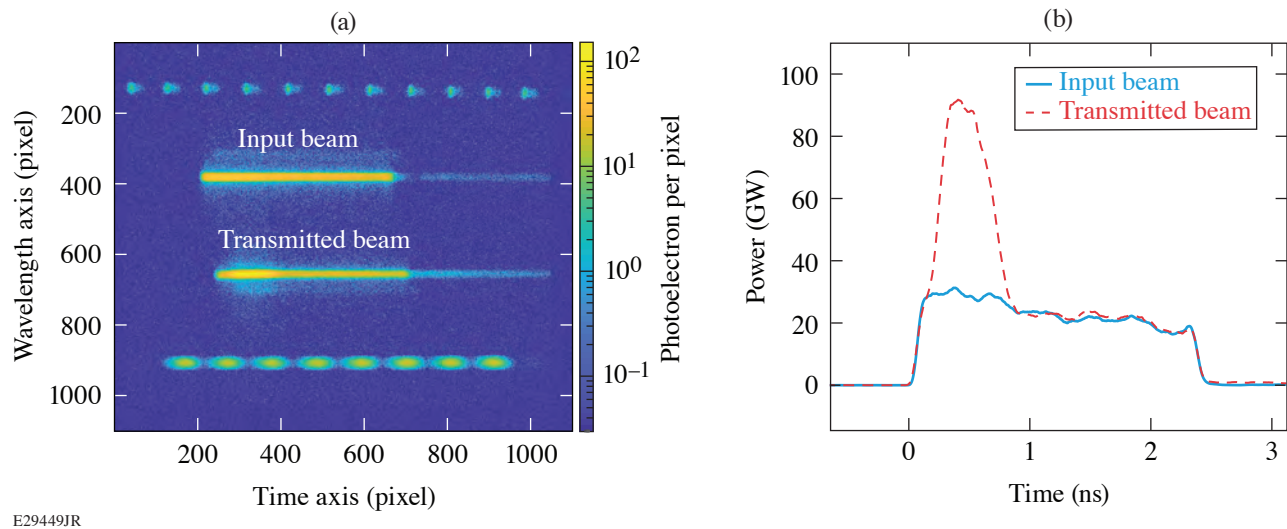


Figure 4

(a) An example of the raw data produced by the streaked spectrometer. For this shot, both channels used 500- μm slits to maximize measurement of the dynamic range. At peak power, a 100-ps time bin contains approximately 40,000 photoelectrons. (b) Cross-beam energy transfer can be measured directly by comparing the input and transmitted power of the TOP9 beam. In this experiment, a 500-ps, 0.4-TW OMEGA beam interacted with the TOP9 beam in a preformed plasma, producing 27 J of energy transfer.

The P9TBD instruments are cross-calibrated, in absolute terms, to the OMEGA EP Laser System’s calorimetry by taking a full-energy shot with no plasma present at TCC [Fig. 3(a)]. This generates a calibration factor relating the total energy that leaves TCC to the total ADU’s in the CCD and streaked image. Fluence and power can then be determined from the image magnification and sweep rate.

Understanding and managing LPI processes are necessary to produce deterministic and reliable plasmas. The next generation of fusion class lasers will likely make use of broadband ($\Delta\omega > 1\%$) or multicolor drive beams to mitigate CBET. TOP9 and P9TBD provide experimental access to this parameter space and a means to validate advanced LPI models. Terminating the transmitted beam onto a semi-transparent diffuser enables an imaging CCD camera and fiber-coupled streaked spectrometer to characterize its spatial profile, polarization, power, and spectrum.

This material is based upon work supported by the Department of Energy National Nuclear Security Administration under Award Number DE-NA0003856, the University of Rochester, and the New York State Energy Research and Development Authority.

1. D. Turnbull *et al.*, Nat. Phys. **16**, 181 (2020).
2. B. E. Kruschwitz *et al.*, Proc. SPIE **10898**, 1089804 (2019).
3. D. H. Froula *et al.*, Phys. Rev. Lett. **98**, 085001 (2007).
4. A. M. Hansen *et al.*, Phys. Plasmas **26**, 103110 (2019).

Reconstructing Three-Dimensional Asymmetries in Laser-Direct-Drive Implosions on OMEGA

O. M. Mannion,¹ K. W. Woo,¹ A. J. Crilly,² C. J. Forrest,¹ J. A. Frenje,³ M. Gatu Johnson,³ V. Yu. Glebov,¹ J. P. Knauer,¹ Z. L. Mohamed,¹ M. H. Romanofsky,¹ C. Stoeckl,¹ W. Theobald,¹ and S. P. Regan¹

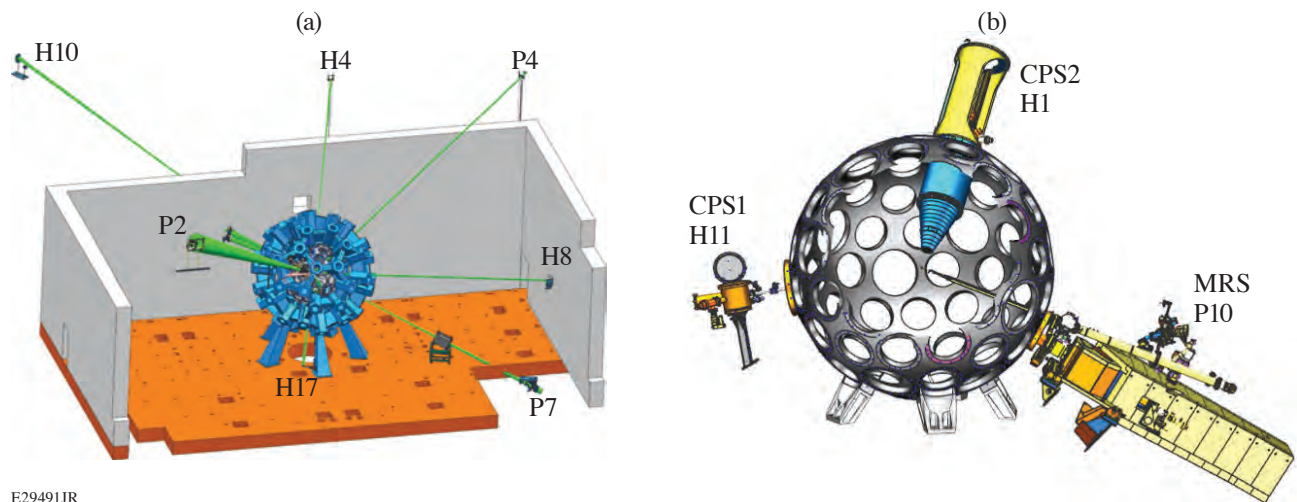
¹Laboratory for Laser Energetics, University of Rochester

²Centre for Inertial Fusion Studies, Imperial College, UK

³Plasma Science and Fusion Center, Massachusetts Institute of Technology

Neutron spectroscopy is a key diagnostic tool in inertial confinement fusion experiments. The primary fusion neutron energy spectrum is used to infer the fusion yield, hot-spot apparent ion temperature, and hot-spot velocity, while the scattered neutron energy spectrum is used to infer the areal density of the compressed DT fuel. These measurements are key to understanding and identifying sources of 3-D asymmetries and the effect that these asymmetries have on target performance.

Over the past decade, a suite of neutron spectrometers have been fielded to measure the neutron energy spectrum emitted in laser-direct-drive implosions on the OMEGA laser. The detectors have been strategically positioned around the OMEGA target chamber such that each detector provides unique data that can be used to reconstruct the 3-D conditions of the compressed target. The current detector suite on OMEGA consists of neutron time-of-flight (nTOF)¹ detectors positioned along seven different lines of sight (LOS's),² a magnetic recoil spectrometer (MRS),³ and two charged-particle spectrometers (CPS's).⁴ The configuration of the nTOF and charged-particle spectrometers around the OMEGA target chamber is shown in Fig. 1. Measurements of the neutron energy spectrum are made using the nTOF and MRS detectors, while measurements of the knock-on deuteron spectrum are made with the CPS detectors.



E29491JR

Figure 1
The lines of sight along which (a) nTOF detectors and (b) charged-particle spectrometers are fielded on OMEGA.

The neutron spectrometers on OMEGA measure either the fusion yield, apparent ion temperature, hot-spot velocity, or the areal density along a particular direction of the target. To make use of these individual LOS measurements, 3-D reconstruction algorithms have been developed⁵ that combine the individual measurements into a holistic 3-D view of the hot spot and dense fuel conditions. In this work, models for the hot-spot velocity, apparent ion temperature,⁶ and areal density⁷ are used to fit the measured values along each LOS. Once the optimal parameters are found in each model, the results can be used to gain a greater understanding of the implosion symmetry.

The reconstruction algorithms that have been developed were applied to OMEGA shot 94660. This shot was known to have a large mode-one drive asymmetry due to anomalous laser beam-pointing errors.⁸ This experiment is therefore a good candidate for testing these reconstruction algorithms since the asymmetries in the hot spot and DT fuel are exacerbated, in a known direction, and can be resolved with the current measurement uncertainties. Three-dimensional radiation-hydrodynamic simulations predict that experiments with large mode-one drive asymmetries will have large hot-spot flow velocities (>100 km/s) in the direction of the mode-one drive asymmetry.⁸ Additionally, simulations predict that a large apparent ion temperature (>1.0 -keV) asymmetry and areal-density asymmetry will be present and aligned with the hot-spot velocity and mode-one direction.⁸⁻¹⁰ Therefore, we can use these experimental results to check if the reconstruction techniques are consistent with the expectation from radiation-hydrodynamic simulations.

The hot-spot velocity reconstruction for this experiment had a magnitude of 155 ± 11 km/s. The direction of the velocity was $\theta = 74 \pm 6^\circ$ and $\phi = 139 \pm 5^\circ$ in the OMEGA coordinate system. This direction was nearly aligned with the direction of the known mode-one drive asymmetry,⁸ $(\theta, \phi) = (51^\circ, 122^\circ)$. The mode-one drive-asymmetry direction was determined using a hard sphere laser illumination calculation using the measured beam pointing, target offset, and laser energies on the experiment.⁶

The apparent ion temperature reconstruction was performed for this shot, and the velocity variances and covariances were determined. The square root of the reconstructed velocity covariance matrix elements were large (>100 km/s), indicating large residual motion within the hot spot. The magnitude of these values is consistent with those found in highly perturbed radiation-hydrodynamic simulations.¹¹ The principle eigenvector of the flow velocity's covariance matrix is along the direction $(\theta, \phi) = (53^\circ, 135^\circ)$ and represents the direction of maximum flow-velocity variance. This direction is consistent with the direction of the hot-spot velocity reconstruction. The apparent ion temperature reconstruction is shown in Fig. 2.

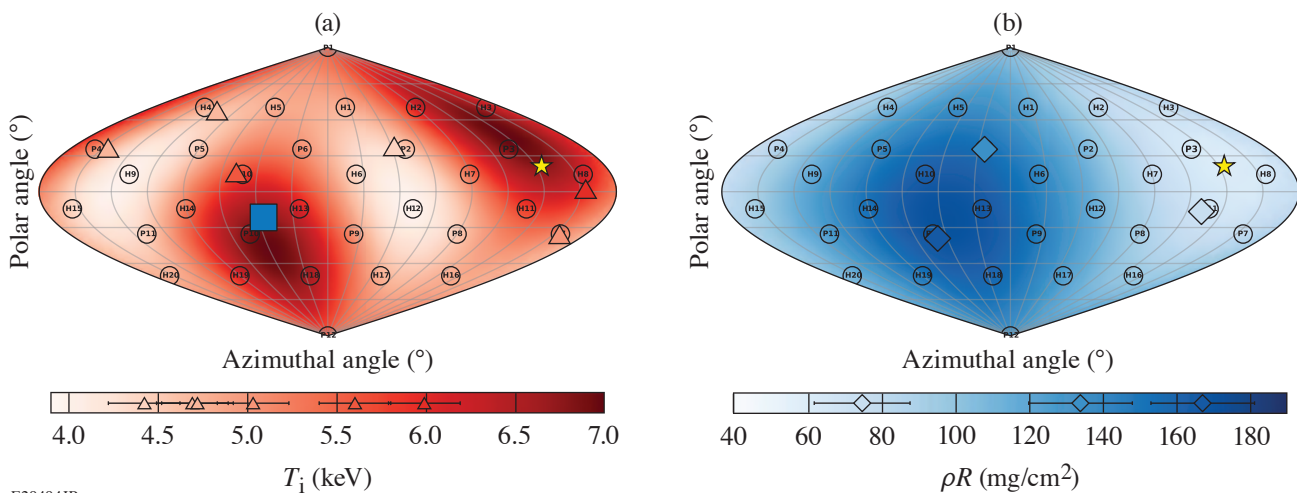


Figure 2

(a) A sinusoidal projection of the OMEGA target chamber's coordinate system showing the reconstructed hot-spot velocity direction (yellow star), the antipodal direction of the hot-spot velocity (blue square), the measured DT apparent ion temperatures (triangles), and the apparent ion temperature reconstruction (red color map) for shot 94660. (b) A sinusoidal projection of the OMEGA target chamber's coordinate system showing the reconstructed hot-spot velocity direction (yellow star), measured areal densities (diamonds), and areal-density reconstruction (blue color map) for shot 94660.

The areal-density reconstruction has been performed for shot 94660 and the average areal density and areal-density variation were determined. Due to the limitations of the current detector suite, a mode-one areal-density model was used, and the direction of the asymmetry was assumed to be along the direction of the hot-spot velocity. From the reconstruction, the average 4π areal density was inferred to be $\rho R_0 = 115 \pm 9$ mg/cm², while the variation in the areal density was found to be $\Delta\rho R = 54 \pm 12$ mg/cm². The areal-density reconstruction is shown in Fig. 2, where we see that the areal-density measurements are consistent with the apparent ion temperature and hot-spot velocity data.

The techniques described in this work can now be used to diagnose low-mode asymmetries in laser-direct-drive implosions on OMEGA. Future work will focus on extending these reconstructions by incorporating more measurements. In particular, recent theoretical work¹¹ has demonstrated that if the DD apparent ion temperature measurements are included in the apparent ion temperature reconstruction, the thermal ion temperature can be inferred. A more-general areal-density reconstruction will be developed so that the direction of the areal-density asymmetry need not be assumed along the direction of the hot-spot velocity. This will require the inclusion of more areal-density measurements. Additional areal-density measurements can be obtained from measurements of the knock-on deuteron spectrum measured by the CPS detectors already fielded on OMEGA (see Fig. 1) but will require that a more-advanced analysis of the knock-on deuteron spectrum be developed that can be used at an areal density >100 mg/cm².

This material is based upon work supported by the Department of Energy National Nuclear Security Administration under Award Number DE-NA0003856, the University of Rochester, and the New York State Energy Research and Development Authority.

1. R. A. Lerche *et al.*, Appl. Phys. Lett. **31**, 645 (1977).
2. O. M. Mannion *et al.*, Nucl. Instrum. Methods Phys. Res. A **964**, 163774 (2020).
3. D. T. Casey *et al.*, Rev. Sci. Instrum. **84**, 043506 (2013).
4. D. G. Hicks, "Charged Particle Spectroscopy: A New Window on Inertial Confinement Fusion," Ph.D. thesis, Massachusetts Institute of Technology, 1999.
5. O. M. Mannion *et al.*, Rev. Sci. Instrum. **92**, 033529 (2021).
6. K. M. Woo *et al.*, Phys. Plasmas **25**, 102710 (2018).
7. A. J. Crilly *et al.*, Phys. Plasmas **28**, 022710 (2021).
8. O. M. Mannion *et al.*, Phys. Plasmas **28**, 042701 (2021).
9. B. K. Spears *et al.*, Phys. Plasmas **21**, 042702 (2014).
10. K. M. Woo *et al.*, Phys. Plasmas **25**, 052704 (2018).
11. K. M. Woo *et al.*, Phys. Plasmas **27**, 062702 (2020).

Application of an Energy-Dependent Instrument Response Function to the Analysis of Neutron Time-of-Flight Data from Cryogenic DT Experiments

Z. L. Mohamed, O. M. Mannion, J. P. Knauer, C. J. Forrest, V. Yu. Glebov, and C. Stoeckl

Laboratory for Laser Energetics, University of Rochester

Neutron time-of-flight (nTOF) detectors are used to diagnose the conditions present in inertial confinement fusion (ICF) and basic laboratory physics experiments performed on an ICF platform. As detailed in Ref. 1, the instrument response function (IRF) of these detectors is constructed by the convolution of two components: an x-ray IRF and a neutron interaction response. The shape of the neutron interaction response varies with incident neutron energy, changing the shape of the total IRF. Analyses of nTOF data that span a broad range of energies must account for this energy dependence in order to accurately infer plasma parameters and nuclear properties in ICF experiments. This method is applied to synthetic data resembling symmetric cryogenic DT implosions to examine the effect of the energy-dependent IRF on the inferred areal density. Results of forward fits that infer ion temperatures and areal densities from nTOF data collected during cryogenic DT experiments on OMEGA are also discussed.

Areal density is a quantity that is used to diagnose the compressive performance of cryogenic DT ICF experiments. With the recent development of a second xylene nTOF line of sight (LOS) on OMEGA that uses the same detector design as an existing OMEGA nTOF,²⁻⁴ an additional measurement of backscatter areal density is now available, enabling the study of implosion symmetry via variations in nTOF areal density.

Analysis of the nTOF data is conducted via forward fit. The standard forward-fit model⁵ can be written as

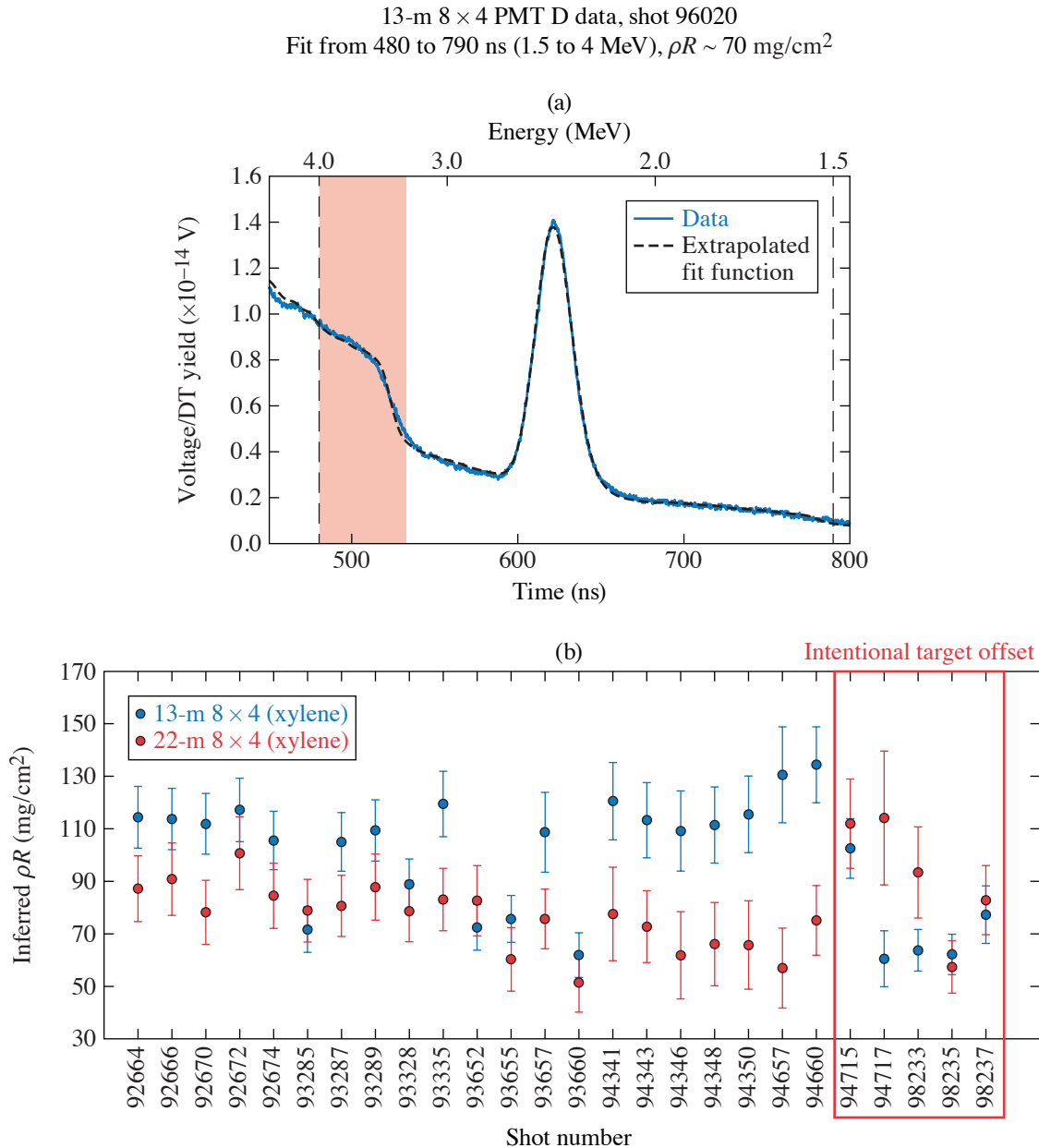
$$V(t) = \left\{ 50 \Omega \times k \times s(E) \times a(E) \times \frac{dN}{dE_{4\pi}} \frac{dE}{dt} \right\} \otimes \text{IRF}(E, t) + B(t), \quad (1)$$

where $V(t)$ represents the fit to the nTOF data in units of volts, k represents a charge calibration constant in units of nC/neutron, 50Ω represents digitizer impedance, $s(E)$ represents detector sensitivity as calculated by MCNP⁶ (a Monte Carlo code) simulations of the xylene detector, $a(E)$ represents beamline attenuation of neutrons as calculated using MCNP simulations of the detector and the LOS from the center of the OMEGA target chamber,⁴ $dN/dE_{4\pi}$ represents the total neutron spectrum exiting the ICF target into 4π , dE/dt represents the relativistic Jacobian, IRF represents the total instrument response function, \otimes represents convolution, and B is a background model. For these detectors, the background is represented by an exponential decay function and is mainly associated with the scattering of DT neutrons on structures near the detector's LOS. For cryogenic DT implosions, the energy spectrum $dN/dE_{4\pi}$ contains contributions from the DD primary, TT, and n(D,p)2n reactions as well as the neutrons that scatter elastically on D and T within either the hot spot or the cold fuel shell (i.e., nD and nT elastic single scatters). Since areal densities on OMEGA are relatively low ($<350 \text{ mg/cm}^2$), a spectrum for multiple scatters is not currently included in this model.

The model spectra for nD and nT elastic single scatters are built such that

$$\frac{dN}{dE_{nT+nD}} = \rho L \times Y_{DT} \times \frac{\int_{3.3 \text{ MeV}}^{4 \text{ MeV}} \left[f_T \frac{d\sigma_{nT}}{dE} + f_D \frac{d\sigma_{nD}}{dE} \right] dE}{f_T m_T + f_D m_D}. \quad (2)$$

Note that the use of this equation assumes a point source of neutrons and uses the elastic scattering cross sections for DT neutrons on D and T. The model for the $n(D,p)2n$ spectrum comes from the cross sections inferred in Ref. 7. This spectrum also scales with areal density and is calculated similarly to Eq. (2), but using the $n(D,2n)p$ cross section in Ref. 7. In this model, it is assumed that the nT and nD elastic single scatters and the $n(D,2n)p$ components represent the same areal density. An example of the total fit is shown in Fig. 1.



E29437JR

Figure 1

(a) Example of a forward fit to experimental nTOF data for the 13-m xylene detector. The blue curve represents the data while the black curve represents the fit. The vertical dashed lines indicate the range of the fit (1.5 to 4 MeV). The red shaded area represents the region in which nT and nD single-scatter components of the fit are integrated to calculate a backscatter areal density (3.5 to 4 MeV). (b) Areal densities for several shots as inferred by the forward fit outlined in this work. The 22-m LOS generally infers about 20 mg/cm² lower than the 13-m LOS. With imposed target offsets based on the measured flow velocities, the direction of the asymmetry can be reversed or the asymmetry can be minimized.

Recent developments in the analysis of nTOF data at the Omega Laser Facility include the analysis of a larger range of energies (1.5 to 4 MeV). Analysis over this wide range of energies allows one to more accurately determine the background, which affects the inferred spectra of nD and nT single elastic scatters. Because this analysis spans a wide range of energies, it is most accurate to use an energy-dependent IRF as detailed in Ref. 1. The final fit has six parameters. Four parameters are related to the neutron energy spectrum: DD ion temperature, DD mean energy, DD yield, and areal density. The background is modeled as an exponential decay. The remaining two parameters in the forward fit are the magnitude and time decay constant for the background. The final inferred areal density is calculated by inverting Eq. (2), where the integrated energy spectra are the best-fit spectra for the elastically scattered nD and nT neutrons. Note that this analysis focuses on the backscattered nT neutrons by integrating over 3.3 to 4 MeV.

This analysis has been benchmarked using synthetic data that represent symmetric, isobaric implosions. The neutron energy spectra were generated using an ice block model in *IRIS3D*.⁸ Synthetic nTOF data were then generated using Eq. (1) along with these energy spectra. The data set involved here represents isobaric 2-keV implosions with areal densities from 50 to 250 mg/cm². The forward fits to the synthetic data were carried out using the method that was previously detailed, which is also applied to experimental data.

The forward-fit analysis with an energy-dependent IRF recovers the ρL calculated directly from the *IRIS3D* energy spectra almost exactly. If either the 2.45-MeV or 3.5-MeV monoenergetic IRF is used, $\sim 2\%$ – 3% inaccuracy is introduced. This is a relatively small inaccuracy with the current analysis, which spans 1.5 to 4 MeV, because the only sharp features within this region are the DD signal (2.45 MeV) and the nT edge (3.5 MeV), which are relatively close in energy. For these detectors, the difference in the width of the IRF's is relatively small between 2.45 and 3.5 MeV (~ 0.7 -ns difference in FWHM). The inaccuracy introduced with the use of a monoenergetic IRF is expected to grow substantially if the range of the fit is extended to 9 MeV, although the exact magnitude of the effect has not yet been predicted because a more-advanced energy spectrum model and a different method of determining the background will likely be required to reach this goal.

The forward fit described above is designed to be applicable for approximately symmetric implosions; however, asymmetric implosions can be more complicated. Since the n(D,p)2n spectrum is known to be forward-peaked while this analysis focuses on the elastically backscattered nD and nT neutrons, these spectra may not scale by the same areal densities as this analysis assumes. It is assumed that the differences between the realistic asymmetric spectrum and the modeled symmetric spectrum will go into the “background” component of the fit. It is for this reason that the background is not fixed. Changes in the background (i.e., background from environmental scattering + any asymmetric contributions) have been observed in experimental data.

The current analysis using the fit for background parameters along with the symmetric nD and nT elastic scatter and n(D,2n)p models has been applied to cryogenic data dating back to early 2019 (when the second nTOF LOS came online on OMEGA). With the standard beam-pointing procedure and no imposed target offset, the 22-m LOS, which views part of the lower hemisphere of the target, sees an average of 20 mg/cm² lower areal densities than the 13-m LOS, which views part of the upper hemisphere of the target. Variations in these inferred nTOF areal densities are consistent with measured variations in ion temperature.⁹ As shown in Fig. 1, this trend has been reversed with intentionally imposed target offsets based on measured flow velocities. In other instances, strategic target offsets based on flow velocity^{9,10} have been used to minimize the areal-density asymmetry. The ability to minimize or reverse the direction of the areal-density asymmetry indicates that the areal-density measurement responds as expected when a mode-one perturbation is minimized or reversed in direction. These instances of minimized differences in areal densities along the two LOS correspond to shots with minimal ion temperature asymmetries as well as flow velocities.¹⁰

Future work will include further benchmarking of this analysis with asymmetric synthetic data. This will test the current handling of the background as well as the scaling of the different components [i.e., nT elastic scatters versus nD elastic scatters versus n(D,2n)p, which originate from different parts of the shell] and should additionally reveal any sensitivities of the current analysis to the exact shape of the nT, nD, and n(D,2n)p spectra under asymmetric conditions.

This material is based upon work supported by the Department of Energy National Nuclear Security Administration under Award Number DE-NA0003856, the University of Rochester, and the New York State Energy Research and Development Authority.

1. Z. L. Mohamed *et al.*, *J. Appl. Phys.* **128**, 214501 (2020).
2. C. Stoeckl *et al.*, *Rev. Sci. Instrum.* **81**, 10D302 (2010).
3. V. Yu. Glebov *et al.*, *Rev. Sci. Instrum.* **85**, 11E102 (2014).
4. C. J. Forrest *et al.*, *Nucl. Instrum. Methods Phys. Res. A* **888**, 169 (2018).
5. R. Hatarik *et al.*, *J. Appl. Phys.* **118**, 184502 (2015).
6. X-5 Monte Carlo Team, Los Alamos National Laboratory, Los Alamos, NM, Report LA-UR-03-1987 (2008).
7. C. J. Forrest *et al.*, *Phys. Rev. C* **100**, 034001 (2019).
8. F. Weilacher, P. B. Radha, and C. Forrest, *Phys. Plasmas* **25**, 042704 (2018).
9. O. M. Mannion *et al.*, *Rev. Sci. Instrum.* **92**, 033529 (2021).
10. O. M. Mannion *et al.*, *Nucl. Instrum. Methods Phys. Res. A* **964**, 163774 (2020).

The Scattered-Light Time-History Diagnostic Suite at the National Ignition Facility

M. J. Rosenberg,¹ J. E. Hernandez,² N. Butler,² T. Filkins,¹ R. E. Bahr,¹ R. K. Jungquist,¹ M. Bedzyk,¹ G. Swadling,² J. S. Ross,² P. Michel,² N. Lemos,² J. Eichmiller,² R. Sommers,² P. Nyholm,² R. Boni,¹ J. A. Marozas,¹ R. S. Craxton,¹ P. W. McKenty,¹ A. Sharma,¹ P. B. Radha,¹ D. H. Froula,¹ P. Datte,² M. Gorman,² J. D. Moody,² J. M. Heinmiller,³ J. Fornes,³ P. Hillyard,³ and S. P. Regan¹

¹Laboratory for Laser Energetics, University of Rochester

²Lawrence Livermore National Laboratory

³Nevada National Security Site

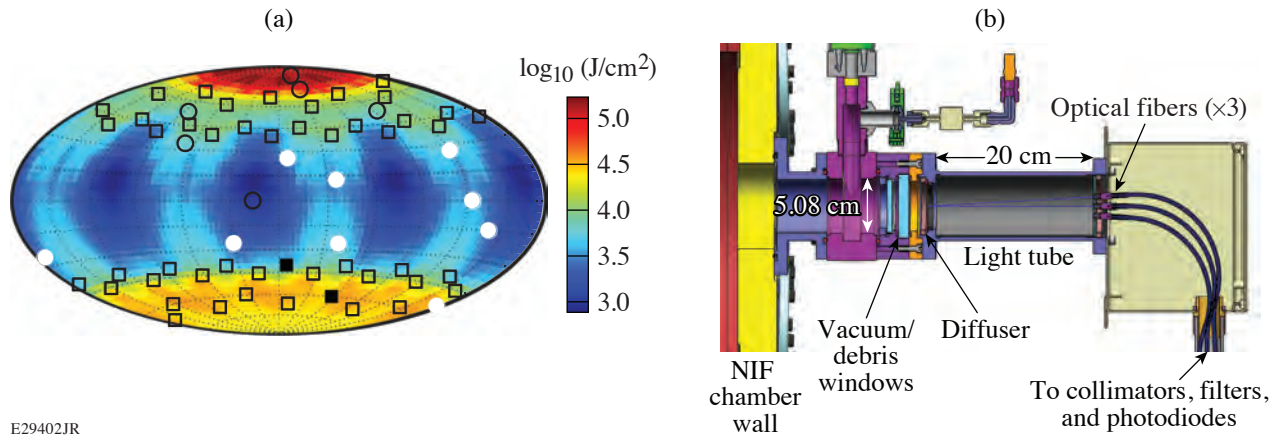
Measurements of scattered light are important diagnostics of laser energy coupling and laser-plasma instabilities (LPI's) such as stimulated Brillouin scattering (SBS), stimulated Raman scattering (SRS), or two-plasmon decay (TPD) in inertial confinement fusion (ICF) experiments. At the National Ignition Facility (NIF), scattered-light diagnostics were originally implemented only at limited beam-port (or "quad," collections of four beams) locations, and extrapolation to total scattered light is predicated on assumptions of predominantly backscattered light and symmetry in polar and azimuthal angles, which may not be valid. For polar-direct-drive (PDD) experiments in particular, the existing diagnostics are not adequate to capture the variation in scattered light.

These considerations motivate additional scattered-light measurements between beam ports to infer the total scattered-light distribution. Therefore, the scattered light time-history diagnostic (SLTD) has been developed to measure the time-resolved scattered light in three different wavelength bands—350 to 352 nm (SBS), 430 to 760 nm (SRS), and 695 to 745 nm ($\omega/2$, corresponding to SRS- or TPD-related scattered light at the quarter-critical density)—at 15 locations around the NIF target chamber outside the NIF beam-port envelope.

Figure 1(a) shows the simulated distribution of SBS scattered light in an example PDD implosion, the locations of NIF beam ports, and the locations of the SLTD suite. Figure 1(b) shows a schematic of the instrument. Light enters the SLTD through a set of vacuum and debris windows and is incident on an optical diffuser after being apertured down to a diameter of 5.08 cm. The 250- μm -thick diffuser, which is located around 590 cm from target chamber center, disperses the light forward in a near-Lambertian distribution with a transmission around 0.2. Three optical fibers positioned 20 cm from the diffuser, with a numerical aperture of 0.22 and a 400- μm core diameter, capture the light from the entire surface of the diffuser. The light is contained within a light tube coated black on the interior to minimize multiple reflections.

The light is transported through 2 m of fiber and relayed by a collimator through a set of bandpass filters that differentiate the three channels. The SRS channel is additionally filtered by a flattening filter with a wavelength-dependent transmission (0.1 at 532 nm) that compensates for the wavelength-dependent transmission of the diffuser and sensitivity of the photodiode. Neutral-density (ND) filters are also used to control light fluence on the photodiodes and are individually calibrated. The collimation system was designed so that the projected beam underfills the 10-mm-diam active area of the photodiodes. Filter and collimator transmissions were measured at the appropriate wavelengths and used in the overall photometric calculations.

Hamamatsu R1328U-52 and R1328U-53 fast photodiodes, with 60-ps rise and 90-ps fall times, detect the light over the wavelength bands of interest. Photodiode sensitivity ranges from ~ 65 mA/W at 351 nm for the SBS channel to ~ 4 mA/W at 730 nm for the SRS and $\omega/2$ channels and are calibrated individually. Current from the photodiodes is carried by coaxial cables (LMR400 or



E29402JR

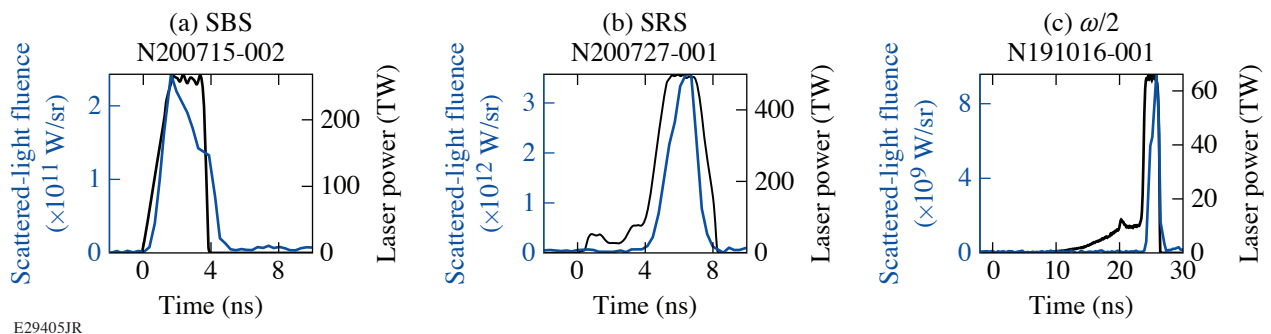
Figure 1

(a) Simulated distribution of SBS scattered light for a PDD experiment overlaid with the NIF laser quad port map (squares). Existing full-aperture backscatter stations are located in two quads (solid black squares), while SLTD's (circles) are being implemented. Out of an eventual 15 SLTD's, a total of six (black circles) have been implemented to date. (b) SLTD optical components include an optical diffuser and optical fibers at the back of a light tube assembly that relay the light to filtered photodiodes.

LMR600) over a distance of 35 to 65 m to a Tektronix MSO58LP 1-GHz digitizer with 12-bit resolution. The digitizer response determines the temporal resolution of the SLTD. The SLTD was designed to achieve measurement accuracy of better than $\pm 15\%$, temporal resolution of 1.5 ns, and a signal-to-noise ratio >100 .

The integrated throughput of the SLTD optical components, including the vacuum and debris windows, diffuser, light tube, and optical fibers, was calibrated at 532 nm using a 200-mJ, 5-ns pulsed source. The throughput was measured to be $5.93 \pm 0.41 \times 10^{-7}$ at 532 nm. Calibration of other SLTD components, including the filters, collimators, and photodiodes, was conducted individually using wavelength-tunable continuous sources between 300 and 800 nm. The total sensitivity of each channel, in terms of volts measured on the oscilloscope per watt incident on SLTD, before accounting for ND filters, is approximately 6.7×10^{-7} V/W (SBS), 6.7×10^{-8} V/W (SRS), and 1.8×10^{-7} V/W ($\omega/2$).

The first six SLTD units, positioned between polar angles of $\theta = 7^\circ$ and 90° , have collected data on a variety of NIF shots. A collection of sample data from the unit at $\theta = 18^\circ$ is shown in Fig. 2, including SBS signal from PDD shot N200715-002, SRS signal from indirect-drive shot N200727-001, and $\omega/2$ signal from x-ray diffraction shot N191016-001. The data demonstrate that requirements on temporal resolution and dynamic range or signal-to-noise ratio are satisfied.



E29405JR

Figure 2

SLTD data obtained at $\theta = 18^\circ$ on different NIF experiments in the (a) SBS, (b) SRS, and (c) $\omega/2$ channels. The SLTD trace (blue curve) is overlaid with the total laser power (black curve).

On a given shot, SLTD data can be used to map out the angular dependence of the scattered-light distribution with an uncertainty in each measurement of $\pm 9\%$. The measurements can be used to evaluate the relative angular distribution in radiation-hydrodynamic calculations of ICF implosions. A comparison of shot N200715-002 SBS data to *SAGE* calculations of unabsorbed light shows qualitative agreement in the relative angular variation, with a peak near $\theta = 40^\circ$ and less unabsorbed light near the pole and equator, although with some quantitative differences in the trends.

In summary, the NIF SLTD suite is being implemented to diagnose time-resolved scattered light in three wavelength bands—SBS, SRS, and $\omega/2$. Six units have collected data, validating the diagnostic performance. Nine additional units will be installed. The SLTD suite will constrain models of laser energy coupling and LPI in direct-drive and indirect-drive ICF experiments.

This material is based upon work supported by the Department of Energy National Nuclear Security Administration under Award Number DE-NA0003856, the University of Rochester, and the New York State Energy Research and Development Authority.

Characterization of Partially Deuterated KDP Crystals Using Two-Wavelength Phase-Matching Angles

C. Dorrer, I. A. Begishev, S.-W. Bahk, and J. Bromage

Laboratory for Laser Energetics, University of Rochester

Large-aperture partially deuterated KDP crystals enable high-energy broadband parametric amplifiers pumped by frequency-converted, high-energy nanosecond Nd:glass lasers, opening the way for the generation of optical pulses with energy of hundreds of joules and bandwidth supporting sub-20-fs pulses.^{1–5} The optimal noncollinear angle between signal and pump beams for broadband gain depends on the deuteration level. This optimization is practically difficult because of uncertainties in the deuteration level of grown DKDP crystals, as well as in the models used to calculate the wavelength-dependent and deuteration-dependent optical indices that are required for phase-matching calculations.

We present the concept and application of a novel two-wavelength phase-matching technique that precisely determines the deuteration level of a DKDP crystal consistent with known index models. The determined deuteration level and model are the much-needed combination required for performance modeling and experimental optimization of an optical parametric amplifier (OPA). By experimentally determining the deuteration level of a crystal consistent with a specific index model, the described technique allows for more-accurate performance simulations as well as better identification of optimal phase-matching conditions for experimental implementation.

Determining a deuteration level consistent with a specific index model relies on the measurements of phase-matching angles at two different wavelengths [Fig. 1(a)]. Combined monochromatic sources at λ_1 and λ_2 are used as the OPA seed to facilitate the measurement of the gain as a function of phase-matching angle and allow one to directly determine the crystal's deuteration

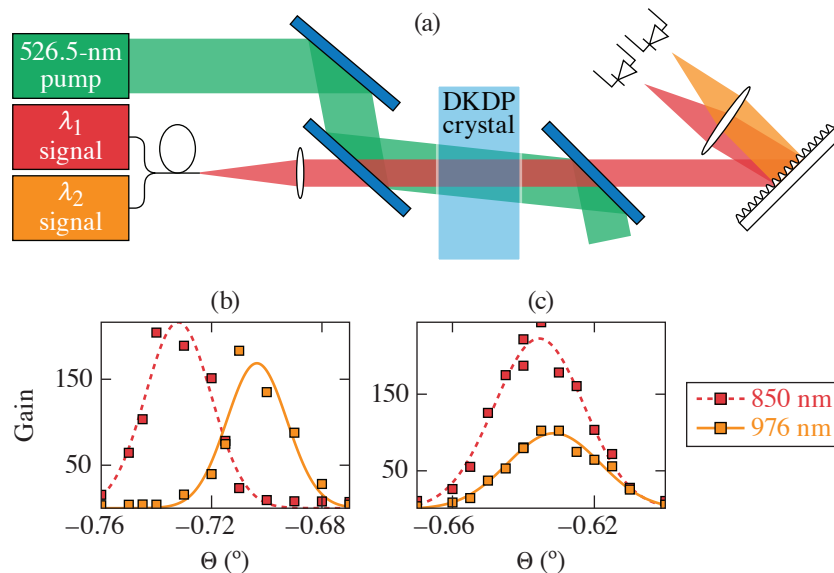


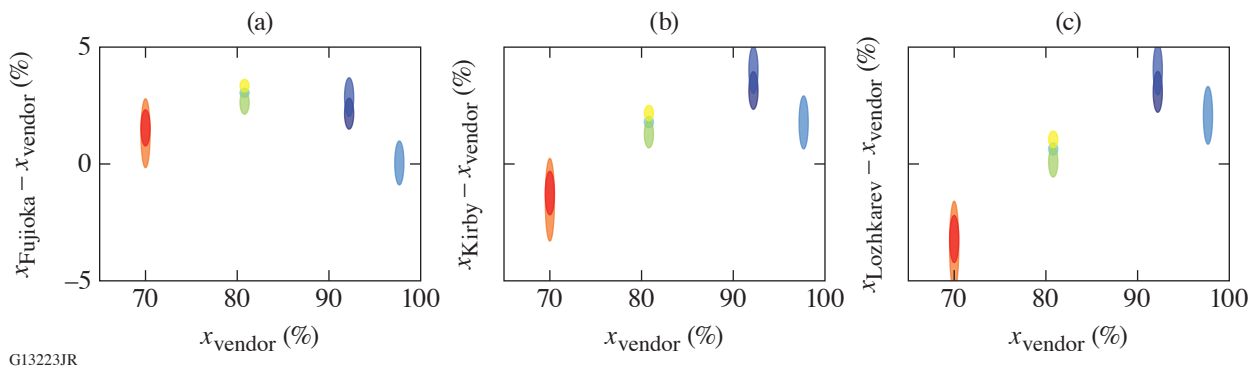
Figure 1

(a) Layout of the experimental setup. [(b),(c)] Measured gain versus rotation-stage angle for one crystal at $\alpha = 0.49^\circ$ and $\alpha = 0.61^\circ$, respectively. The data at each wavelength (squares) are fitted by a Gaussian function (solid and dashed curves).

G13014JR

level. Indeed, simulations and analysis of the phase-matching conditions for a noncollinear OPA show that there is a one-to-one relation between the difference $\theta_1 - \theta_2$ in phase-matching angles and the deuteration level x for a given noncollinear angle and index model. Examples of measured small-signal gain curves at two wavelengths as a function of the crystal angle relative to normal incidence are shown in Fig. 1(b). For each wavelength, the optimal angle for phase matching is determined by fitting the data with a Gaussian function. The deuteration level consistent with the measured angle difference and a specific index model is then determined, as well as a confidence interval obtained from the fitting routines. The ordinary and extraordinary indices of DKDP are determined as a function of wavelength and deuteration level using interpolation or extrapolation of indices calculated from Sellmeier equations. These equations originate either from the Kirby model for non-deuterated KDP and 96% DKDP,⁶ the combination of the Kirby model for 96% DKDP with the Zernike model for KDP (used for studies of broadband phase-matching in DKDP by Webb *et al.*⁷ and then applied to broadband parametric amplification by Lozhkarev *et al.*⁸), or the Fujioka model for DKDP at various deuteration levels.⁹

Four DKDP crystals with a nominal deuteration level ranging from 70% to 98% have been characterized. For each crystal, a noncollinear angle was calculated using the nominal deuteration level and Fujioka index model to phase-match the two cw wavelengths at the same crystal angle. The actual difference in phase-matching angle $\theta_1 - \theta_2$ measured during a first campaign was used to determine the deuteration level that is consistent with the data for each index model [see, for example, Fig. 1(b)]. For some crystals, an updated noncollinear angle was calculated from the determined deuteration level for $\theta_1 - \theta_2 = 0$ and used for a second measurement campaign [see, for example, Fig. 1(c)]. Figure 2 presents the difference between the determined deuteration levels x_{Fujioka} , x_{Kirby} , and $x_{\text{Lozhkarev}}$ and the deuteration level x_{vendor} determined by the crystal's vendor from pycnometer measurements performed on the solution during crystal growth. The length of each marker in the vertical direction indicates the 95% confidence interval on the deuteration level determined during each campaign, which is 1.4% on average. The results show excellent consistency between campaigns. Whereas different models yield different deuteration levels from the same measured data, the calculated gain properties for a specific model and the corresponding deuteration level are in excellent agreement between models. This experimental technique has supported the development of broadband gain models and the determination of optimal phase-matching conditions for high-energy amplification on the MTW-OPAL Laser System, an optical parametric amplifier line (OPAL) pumped by the Multi-Terawatt (MTW) laser at the Laboratory for Laser Energetics.⁵



G13223JR

Figure 2

Determined deuteration level for the four crystals over eight campaigns using the index model from (a) Fujioka, (b) Kirby, and (c) Lozhkarev.

This material is based upon work supported by the Department of Energy National Nuclear Security Administration under Award Number DE-NA0003856, the University of Rochester, and the New York State Energy Research and Development Authority.

1. I. N. Ross *et al.*, *Opt. Commun.* **144**, 125 (1997).
2. N. F. Andreev *et al.*, *J. Exp. Theor. Phys. Lett.* **79**, 144 (2004).
3. O. V. Chekhlov *et al.*, *Opt. Lett.* **31**, 3665 (2006).
4. V. V. Lozhkarev *et al.*, *Laser Phys. Lett.* **4**, 421 (2007).

5. J. Bromage *et al.*, High Power Laser Sci. Eng. **7**, e4 (2019).
6. K. W. Kirby and L. G. DeShazer, J. Opt. Soc. Am. B **4**, 1072 (1987).
7. M. S. Webb, D. Eimerl, and S. P. Velsko, J. Opt. Soc. Am. B **9**, 1118 (1992).
8. V. V. Lozhkarev *et al.*, Laser Phys. **15**, 1319 (2005).
9. K. Fujioka *et al.*, J. Appl. Phys. **117**, 093103 (2015); **119**, 249902(E) (2016).

High-Efficiency, Fifth-Harmonic Generation of a Joule-Level Neodymium Laser in a Large-Aperture Ammonium Dihydrogen Phosphate Crystal

I. A. Begishev,¹ G. Brent,¹ S. Carey,¹ R. Chapman,¹ I. A. Kulagin,² M. H. Romanofsky,¹ M. J. Shoup III,¹ J. D. Zuegel,¹ and J. Bromage¹

¹Laboratory for Laser Energetics, University of Rochester

²Independent researcher

High-energy deep UV sources are required for high-density plasma diagnostics. The fifth-harmonic generation (5HG) of large-aperture neodymium lasers in ammonium dihydrogen phosphate (ADP) can significantly increase UV energies due to the availability of large ADP crystals. Noncritical phase matching in ADP for ($\omega + 4\omega$) was achieved by cooling a 65- × 65-mm crystal in a two-chamber cryostat to 200 K. The cryostat used helium as the thermally conductive medium between the crystal and the internal crystal chamber, which was surrounded by the high-vacuum external chamber with a liquid nitrogen reservoir. A temperature variation of 0.2 K across the crystal aperture was obtained. The total conversion efficiency from the fundamental to the fifth harmonic at 211 nm was 26%.

The higher harmonic provides better penetration of the plasma. An estimated 5ω beam energy of 10 J requires a large-aperture laser and, accordingly, large crystals. Recently we demonstrated a record 5HG efficiency of 30%, producing 335 mJ at 211 nm in a 12- × 12- mm beam, using a cesium lithium borate (CLBO) crystal.¹ CLBO has high second-order nonlinearity, can be grown in a relatively large size, and is phase matched at room temperature. Although a CLBO boule could be grown up to 146 × 132 × 118 mm (Ref. 2), practically, the size of a finished optic does not exceed 5 cm. Furthermore, the extremely hygroscopic property of CLBO crystals requires that they be at high temperatures (~120°C). Finally, the cost of manufacturing large CLBO crystals is prohibitive for many applications. ADP crystals, which can be easily grown to much larger sizes, are an alternative way of generating a high-energy beam at 211 nm.

Potassium dihydrogen phosphate (KDP) and ADP crystals are popular nonlinear crystals because of their good nonlinear properties, wide range of transmission, and large sizes. For cascade 5HG, however, they have a significant limitation: phase-matching conditions for sum-frequency generation are not met at room temperature. Noncritical phase-matching conditions could be reached by cooling crystals to -140°C (KDP) and -70°C (ADP). This is not trivial, especially for large-aperture crystals, because a definite temperature must be strictly stabilized and maintained across the entire crystal. Any holder that keeps a crystal in a vacuum chamber and maintains the crystal temperature through thermally conductive contacts provides some temperature gradient across the crystal. The most effective way to stabilize an entire crystal at low temperature is a two-chamber cryostat.³ In our two-chamber cryostat, shown in Fig. 1(a), the tank with liquid nitrogen is connected to the internal chamber through the solid copper (upper) and the hollow stainless-steel (lower) cylinders. The lower hollow cylinder has two 50-W flexible Kapton insulated heaters mounted on the outside surfaces to stabilize the internal chamber temperature. The internal chamber contains the crystal holder with minimized contacts with the crystal to improve the cooling uniformity from the 1 atm of helium that surrounds the crystal. Helium, the main thermal agent between the internal chamber and the crystal, was chosen because of its high (compared with other gases) thermal conductivity. Three silicon diode cryostat temperature sensors are located on two outside points of the internal chamber and on one side of the crystal inside the internal chamber. Two 120-mm-diam, 10-mm-thick fused-silica windows are located on opposite sides of the internal chamber coaxially to the crystal to pass input and output beams.

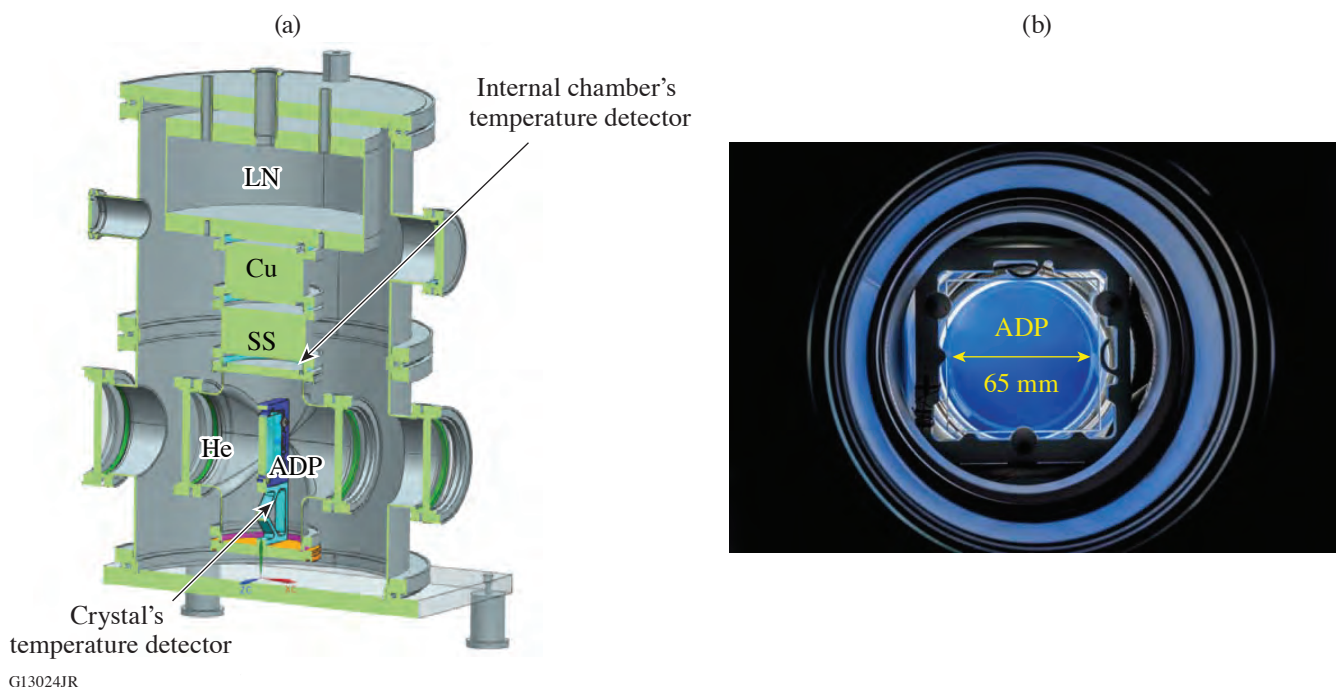


Figure 1

(a) The cross section of the two-chamber cryostat with the liquid nitrogen tank (LN), the copper cylinder (Cu), the stainless-steel cylinder (SS), and the internal chamber filled with helium (He) with an ADP crystal inside; (b) a photo of an ADP crystal inside the two-chamber cryostat through two input windows.

“Cold flow” goes down from the liquid nitrogen tank to the internal chamber; it then reaches the crystal through the helium. As soon as the temperature of the crystal reaches a chosen set point temperature, the heaters begin working to maintain that temperature through a temperature-stabilization loop with 0.01°C resolution controlled by a proportional integral derivative feedback loop. The feedback continually adjusts the output power to the heaters in order to keep the chosen temperature constant. The system has high thermal mass and reaches the target 200 K temperature in about 36 h.

The internal chamber is installed into the external chamber, which is pumped down to a vacuum of better than 5×10^{-7} Torr. The external chamber also has input and output windows, so the two-chamber cryostat has a total of four windows. The two input windows have sol-gel antireflection (AR) coatings at 266 nm (4ω), while the output windows are coated at 211 nm (5ω). The ADP crystal ($65 \times 65 \times 10$ mm, type I, $\theta = 90^{\circ}$, $\phi = 45^{\circ}$) has AR coatings at 1ω and 4ω on the input face and an uncoated output face.

A special heavy-duty rotation stage was designed and fabricated to carry this large, heavy two-chamber cryostat and rotate it within an angular range of 5° with microradian accuracy. As a result, phase matching could be tuned by both crystal temperature and angle.

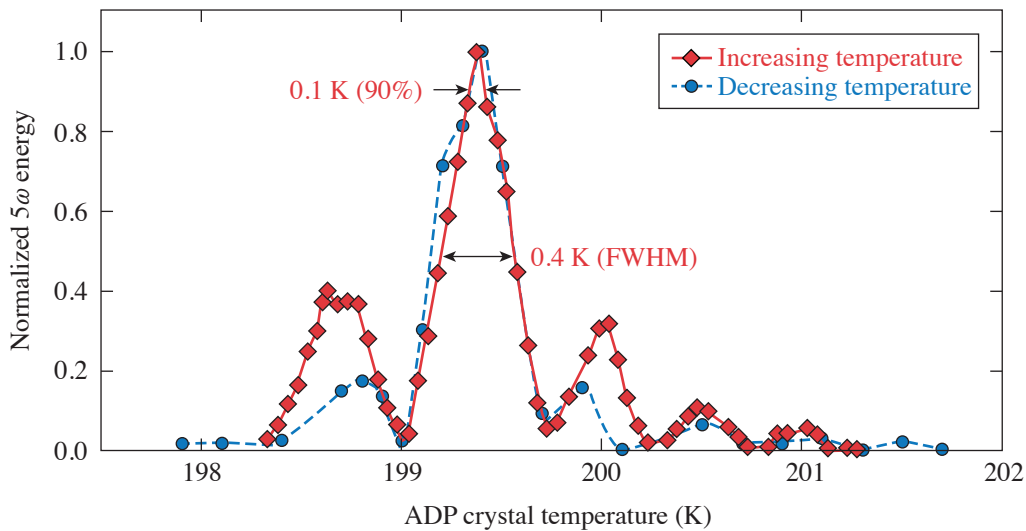
The thermal model was developed based on COMSOL Multiphysics[®] and was able to predict the lowest-reachable temperature of 170 K and the cooling time to reach that temperature.

There are two possible frequency-conversion schemes to optimize 5HG in a cascade of three nonlinear crystals, remembering that no type-II phase matching for 4HG (fourth-harmonic generation) and 5HG exists in KDP and ADP: $o_1o_1 \rightarrow e_2:o_2o_2 \rightarrow e_4:o_1o_4 \rightarrow e_5$ and $o_1e_1 \rightarrow e_2:o_2o_2 \rightarrow e_4:o_1o_4 \rightarrow e_5$, where o and e are ordinary and extraordinary waves in crystals. In the first case, we must detune sum-harmonic generation (SHG) down from the maximum by adjusting the length of the first crystal, while two

other processes (4HG and 5HG) should be maximized. In the second case, the required energy distribution between orthogonal polarizations could be set by rotating the input beam polarization. Here the energy distribution is adjustable for any given input energy, making the second case preferable.

The angle α between input-beam polarization and the horizontal plane was tuned by a half- λ wave plate in front of the first crystal. It changes the balance of energy between the ordinary and extraordinary axes in the first type-II doubler and preserves some fraction of the fundamental frequency beam through the first two crystals for the interaction in the last crystal. The first frequency doubler was a deuterated potassium dihydrogen phosphate (DKDP) crystal ($30 \times 30 \times 27$ mm), which was chosen instead of KDP to decrease linear absorption at the fundamental frequency. It was cut in a type-II configuration to convert $1\omega \rightarrow 2\omega$. A second frequency doubler, a type-I KDP crystal ($30 \times 30 \times 15.5$ mm), was used to convert $2\omega \rightarrow 4\omega$. The final crystal, made of ADP, was located at the image plane of a Nd:YLF laser⁴ that was optimized to produce a flattopped, square-beam profile with a square pulse (1053 nm, 12×12 mm, from 1 ns to 2.8 ns, ≤ 1.5 J, 5 Hz, 0.1 Hz, or a single shot). A fused-silica prism separates the harmonic beams in space. The input and output beam energies were measured using identical cross-calibrated pyroelectric energy meters.

We reached 5HG at -73°C (200 K). The temperature acceptance of 5HG in ADP at a fixed crystal angle was measured (see Fig. 2). Each point was taken without temperature stabilization at a given temperature: 5ω energy was measured while the temperature of the ADP crystal was slowly drifting. “Red” data were taken while the crystal temperature was increasing, and “blue” data were taken while crystal temperature was decreasing. Note that the red curve was shifted down by 0.07 K to match the blue curve. This difference likely comes from the temperature gradient without stabilization and system lag because of the thermal mass.



E28202JR

Figure 2
Fifth-harmonic energy temperature (T) acceptance at a fixed position angle of the ADP crystal.

An important point here is that the temperature acceptance is only 0.4 K (FWHM). To keep the system close to the maximum (>90%) of 5HG efficiency, an ADP crystal must be temperature stabilized with an accuracy better than 0.1 K. Figure 3 shows beam profiles of the input beam at the fundamental frequency (a) before the first crystals and (b) fifth-harmonic beam after the cryostat. Compared to the relatively uniform 1ω beam, the 5ω beam is slightly more spatially varied. Some residual radial nonuniformity of the 5ω beam was caused by a small phase mismatch inside the ADP crystal and corresponds to a temperature gradient over the ADP crystal. Overall conversion efficiency could be better with improved temperature uniformity of the ADP crystal.

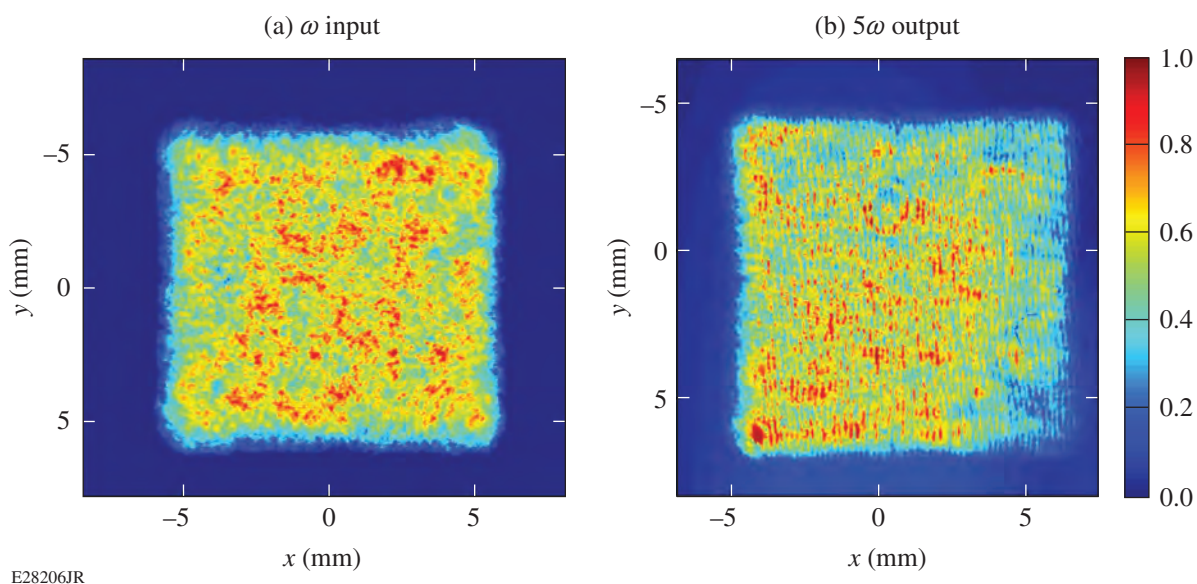


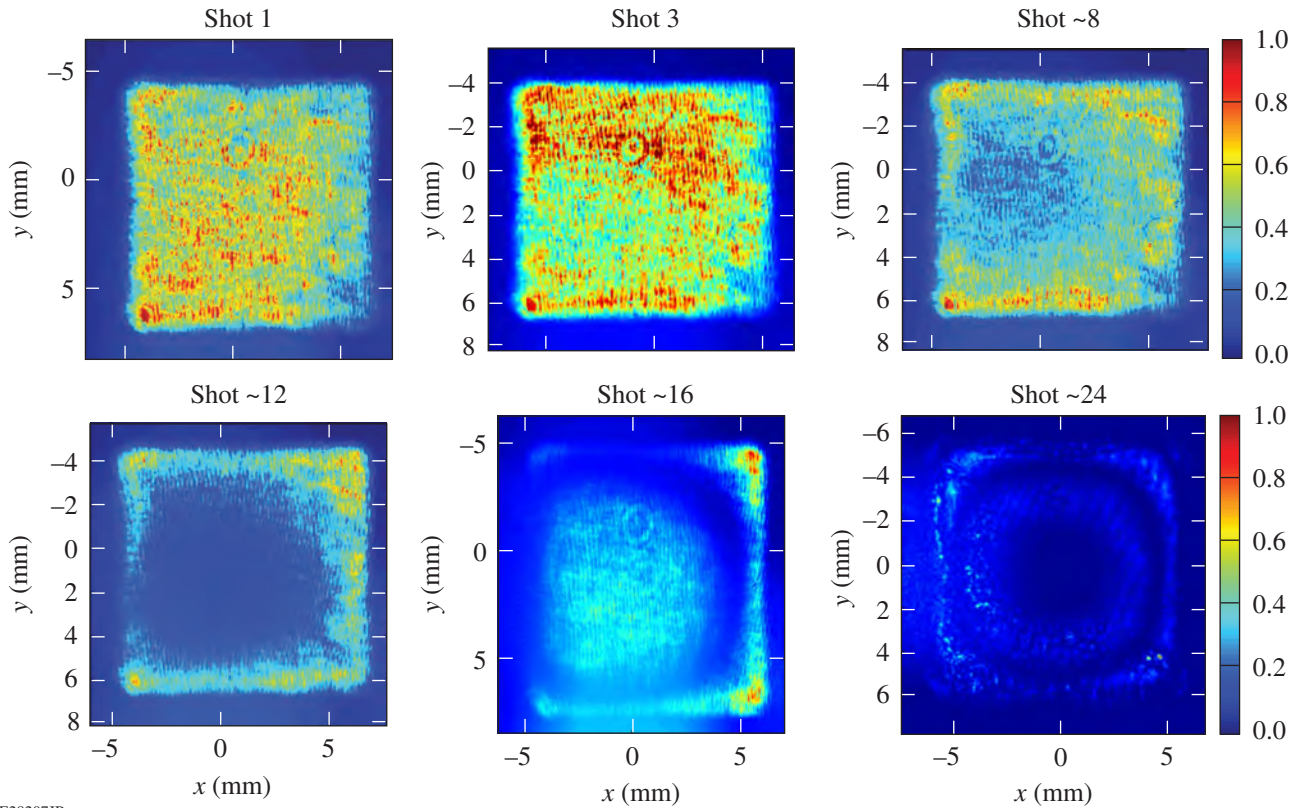
Figure 3

Input beam image (a) at the fundamental frequency on the front of the cascade of crystals and fifth-harmonic output beam image (b) after the cryostat.

Because the ADP crystal is isolated in a helium atmosphere with very low direct conductivity to the chamber, even a small amount of energy absorption from the interaction laser beams cannot be rapidly dissipated. As a result, the ADP and other crystals in a gas cryostat work well in a single-shot regime (about one shot per minute) but cannot work at a high repetition rate because of phase mismatch caused by laser heating. Figure 4 shows the sequence of fifth-harmonic output beam images behind the cryostat taken after a various number of shots running at a 5-Hz repetition rate. Even a small amount of absorbed laser energy inside a crystal after the first shot makes the crystal warmer in the center and disturbs the temperature distribution, resulting in a spatially varying phase mismatch that grows as a series of radial rings. The 5ω beam almost disappears after 24 shots. This effect is negligible provided there is sufficient time for the crystal to thermalize. A one-minute interval between shots is enough to maintain the required temperature distribution of 0.1 K over the crystal aperture.

The angular acceptance of 5HG at a given temperature of the ADP crystal was measured as 8 mrad external (FWHM). After careful optimization, the 5HG efficiency became as high as 26% at a 0.1-Hz repetition rate with a 2.4-ns pulse and an input intensity of 0.3 GW/cm^2 . This efficiency describes the portion of the input 1ω energy that has been transformed into the fifth harmonic and is available at the output of the cascade of crystals for use in any application, and includes linear and nonlinear loss mechanisms.

The energy balance is the ratio of the total energy of all beams after the cryostat to the 1ω energy at the input of the first crystal of the cascade. Therefore, it represents a fraction of energy transmitted from input to output through all three crystals and the cryostat. The initial balance is just 62% at very low input beam intensity and corresponds to passive losses, mostly coming from linear absorption and Fresnel reflections. It also demonstrates that the total conversion efficiency of 5HG could be increased by, for example, better AR coatings and crystalline windows. At high input beam intensity the total energy transmitted through the system and the energy balance drop due to significant nonlinear losses, which dramatically limits 5ω conversion efficiency. The energy balance at peak 5HG efficiency was 48%, with the additional losses coming mainly from two-photon absorption (TPA). We measured TPA at 211 nm in air (13.5 m) and in the longer (15-mm) ADP crystal cut at the x plane using the 5ω beam from the above-described setup. The TPA coefficient of ADP at 211 nm was measured as $(1.2 \pm 0.2) \text{ cm/GW}$. Due to a relatively small dynamic range of the input energy, that measurement is not very accurate. The difference in TPA's of ADP along different crystal axes is within the error of the measurement. We also measured TPA in the air ($0.0008 \pm 0.0002 \text{ cm/GW}$) and in fused silica ($0.5 \pm 0.1 \text{ cm/GW}$) at 211 nm and in ADP at 263 nm ($0.25 \pm 0.1 \text{ cm/GW}$).



E28207JR

Figure 4
Fifth-harmonic output beam images after the cryostat taken after a various number of shots running at a 5-Hz repetition rate.

The authors thank S. Yang, P. Datte, and S. Patankar at Lawrence Livermore National Laboratory for the support and helpful discussions. This material is based upon work supported by the Department of Energy National Nuclear Security Administration under Award Number DE-NA0003856, the University of Rochester, and the New York State Energy Research and Development Authority.

1. I. A. Begishev *et al.*, *Opt. Lett.* **43**, 2462 (2018).
2. X. Yuan *et al.*, *J. Cryst. Growth* **293**, 97 (2006).
3. I. A. Begishev *et al.*, *J. Appl. Spectrosc.* **51**, 1218 (1989).
4. V. Bagnoud *et al.*, *Appl. Opt.* **44**, 282 (2005).

Dynamics of Electronic Excitations Involved in Laser-Induced Damage in HfO₂ and SiO₂ Films

K. R. P. Kafka, B. N. Hoffman, A. A. Kozlov, and S. G. Demos

Laboratory for Laser Energetics, University of Rochester

Progress toward the development of thin-film-based optical components to meet the increasing demand for higher peak or average-power short-pulse laser systems requires improvements in their resistance to laser-induced damage. Understanding the dynamics of electron excitations associated with the initiation of laser-induced damage and the role of defects is of fundamental interest. The presence of native defects in a thin film is largely dependent on the manufacturing process.¹ Recent work has demonstrated that different defect species are responsible for damage initiation depending on the laser pulse length.² This suggests that the excitation and relaxation parameters of the precursor defects are directly expressed by the fluence where these defects can initiate damage for a given set of laser parameters. Pump-probe time-resolved experiments are a standard method being used to study the dynamics of electronic excitations. Such damage-testing experiments previously performed have provided important information (such as the relaxation time of the conduction band electrons and the presence of a delayed return to pre-exposure conditions).³

The present work aims to reveal information on the dynamics of the electronic excitation at the onset of damage initiation in plasma ion-assisted deposition silica and hafnia monolayers. The experiments employ a pump-probe damage-testing configuration using 1053-nm, 0.6-ps laser pulses. Special attention was given to the determination of damage-initiation conditions, which are defined by any observable material modification using differential-interference contrast (DIC) microscopy. In each set of data, the pump pulse intensity/fluence is kept constant and below that of the single-pulse laser-induced-damage threshold (LIDT₁), while the temporally delayed probe pulse fluence is independently adjusted to the onset of damage initiation. By analyzing the probe beam's damage threshold (LIDT_{probe}) as a function of delay, combined with detailed study of the resulting morphology, we aim to characterize the relaxation dynamics of defects that are involved in the damage process.

The measured LIDT_{probe} values (markers) are shown in Fig. 1 for both hafnia and silica samples for the indicated pump fluence levels. The LIDT_{probe} values increase with increasing delay toward the respective LIDT₁ values (horizontal lines). This behavior provides insight into the dynamics of the relaxation of electronic excitations associated with the damage initiation process that are activated by the pump pulse. The experimental results in hafnia show that the effective relaxation time of the pump-induced excitation depends on the pump fluence. For the lowest pump fluence, the LIDT_{probe} returns to the single-pulse value by a 100-ps delay, while for the highest pump fluence, the LIDT_{probe} value does not fully return within the 1-ns delay range of this experiment.

The morphology of the damage sites was studied using DIC and SEM microscopies. DIC microscopy images (not shown) demonstrate that when the pump and probe fluences are held constant, the density (severity) of damage significantly decreases as the delay increases for both materials. SEM analysis reveals that all damage sites of both materials (generated at damage threshold conditions) are composed of nanoscale pits, including sites formed by a single pulse. Characteristic images are shown in Fig. 2 for the case of silica. The SEM image of damage formed by a single pulse with fluence at LIDT₁ [Fig. 2(a)] demonstrates a nanopit damage density >10⁸ cm⁻².

The series of SEM images at different delay times shown in Fig. 2 indicates that the morphology of the silica damage sites changes with pump-probe delay time, with their size being the most-characteristic attribute of this effect. There are two general types of pits, which for simplicity we will refer to as "smaller" (having a diameter <100 nm) and "larger" (having a diameter

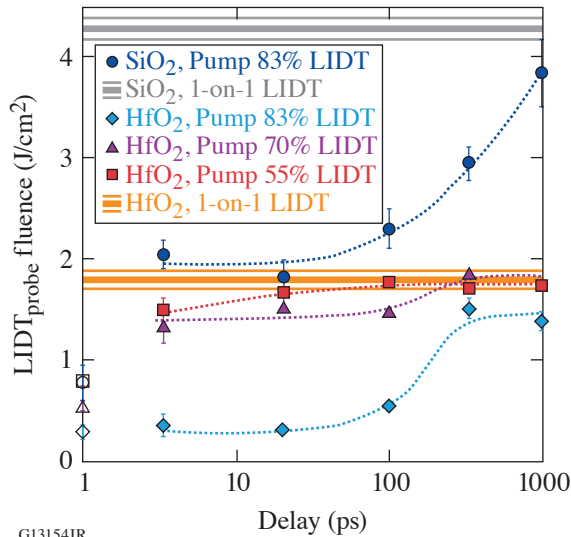


Figure 1
Double-pulse damage thresholds as a function of delay for indicated pump fluences. Horizontal lines indicate the one-pulse LIDT and uncertainty values for hafnia (orange lines) and silica (gray lines). Open markers represent the theoretical minimum value. Dotted lines are drawn to guide the eye.

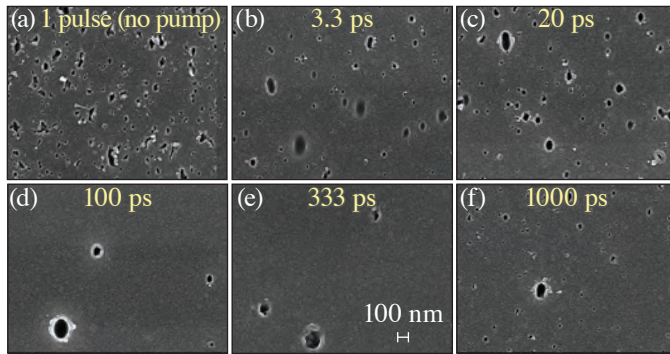


Figure 2
SEM images of damage sites on SiO₂ tested in vacuum at near-threshold fluences and indicated delay times. Fluences: (a) $\phi_{\text{pump}} = 0$, $\phi_{\text{probe}} = 4.5 \text{ J/cm}^2$, [(b)–(f)] $\phi_{\text{pump}} = 83\% \text{ LIDT}_1$ with ϕ_{probe} values as follows: (b) 2.2 J/cm^2 , (c) 2.0 J/cm^2 , (d) 2.5 J/cm^2 , (e) 3.2 J/cm^2 , and (f) 3.8 J/cm^2 .

>100 nm). Damage with a single pulse exclusively contains the smaller pits at very high damage density. These smaller pits are also observed for short delay times (3.3 ps and 20 ps) and reappear at 1000 ps, when the LIDT_{probe} has returned to single-pulse damage behavior. In contrast, the larger pits were generated with much lower damage density and observed at all tested double-pulse delays (>3 ps) but not under single-pulse damage. Therefore, both types of pits were observed to coexist only at delays of 3.3 ps, 20 ps, and 1000 ps, as manifested in Fig. 2. SEM analysis of hafnia damage sites also shows the nanopit morphology but lacks any evidence suggesting a change in the damage morphologies as a function of the delay time.

Previous observations demonstrated that damage in silica/hafnia multilayer dielectric coatings is initiated by two different mechanisms as a function of the pulse duration, where the change in mechanism occurs at about 2.5 ps (Ref. 2). It was suggested that this may arise from defect populations having different properties, either physical (such as size) or stoichiometric/electronic. Following this line of reasoning, we postulate that the morphology behavior observed for silica in this work is due to two types of defects that have different relaxation times. This hypothesis requires further investigation that is outside the scope of this work.

Finally, it must be noted that the SEM images clearly show that damage initiates at distinct locations, even though some adjacent pits do merge together. Due to this high areal density of nanopits at damage initiation conditions with a single pulse, of the order of 10^8 cm^{-2} , it is not surprising that damage appears to be uniform at lower magnifications for subpicosecond laser pulses, giving rise to the widely adopted assumption that damage is “intrinsic.” This perception becomes dominant in optical components employing multilayer dielectric coatings, when damage initiates below the top layer of the multilayer coating.

In conclusion, the results indicate that the relaxation time of electronic excitations associated with laser-induced–damage initiation depends on the pump fluence and extends up to about 1 ns. Furthermore, the damage morphology near $LIDT_1$ in all cases was observed to be a collection of nanopits. The results for silica show two different types of nanopit morphologies, arguably suggesting two types of defects, that manifest on different time scales: (1) <100 ps and (2) >3 ps, while observations for hafnia were unable to distinguish multiple morphologies. Future work identifying these defect structures could potentially enable subsequent material optimization for damage performance with subpicosecond lasers.

This material is based upon work supported by the Department of Energy National Nuclear Security Administration under Award Number DE-NA0003856, the University of Rochester, and the New York State Energy Research and Development Authority.

1. M. Chorel *et al.*, *Opt. Express* **27**, 16,922 (2019).
2. A. A. Kozlov *et al.*, *Sci. Rep.* **9**, 607 (2019).
3. D. N. Nguyen *et al.*, *Appl. Phys. Lett.* **97**, 191909 (2010); **98**, 079902(E) (2011).

FY21 Q1 Laser Facility Report

J. Puth, M. Labuzeta, D. Canning, and R. T. Janezic

Laboratory for Laser Energetics, University of Rochester

During the first quarter of FY21, the Omega Laser Facility conducted 326 target shots on OMEGA and 210 target shots on OMEGA EP for a total of 536 target shots (see Tables I and II). OMEGA averaged 10.9 target shots per operating day, averaging 92.7% Availability and 90.8% Experimental Effectiveness. OMEGA EP averaged 8.1 target shots per operating day averaging 92.7% Availability and 92.4 Experimental Effectiveness.

Table I: OMEGA Laser System target shot summary for Q1 FY21.

Program	Laboratory	Planned Number of Target Shots	Actual Number of Target Shots
ICF	LLE	71.5	71
	LANL	11	9
	LLNL	16.5	18
ICF Subtotal		99	98
HED	LLE	22	19
	LANL	11	11
	LLNL	33	31
	SNL	11	10
HED Subtotal		77	71
LBS	LLE	22	22
	LLNL	11	12
LBS Subtotal		33	34
AIBS		33	35
ARPA-E		22	24
NLUF		44	39
Calibration	LLE	11	25
Grand Total		319	326

Table II: OMEGA EP Laser System target shot summary for Q1 FY21.

Program	Laboratory	Planned Number of Target Shots	Actual Number of Target Shots
ICF	LLE	14	16
	LLNL	7	8
	NRL	7	11
ICF Subtotal		28	35
HED	LLE	28	35
	LANL	7	6
	LLNL	21	29
	SNL	7	10
HED Subtotal		63	80
LBS	LLE	14	20
	LLNL	7	7
LBS Subtotal		21	27
AIBS		14	15
Marvel		14	24
NLUF		17.5	19
Calibration	LLE	0	10
Grand Total		157.5	210

During this period, the OMEGA target chamber's vacuum pumps were reconfigured for improved vibration isolation to achieve better target stability. This upgrade will be particularly important for campaigns where target offsets are undesirable but reduces the probability of vibrations causing target damage for all users. The newly commissioned IR optical transmission inspection system (IR OTIS) is being employed to characterize components in the beamline path. Measurements have resulted in a better understanding of the small variations in polarization at the beamline splits and are helping operations determine strategies to mitigate. In the future, this diagnostic will be used regularly to identify damage issues for maintenance on the OMEGA Beamline System.

Project RemotePI: COVID-19 Mitigation-Compliant Operations on OMEGA and OMEGA EP

G. Pien, S. F. B. Morse, B. E. Kruschwitz, and T. J. Kessler

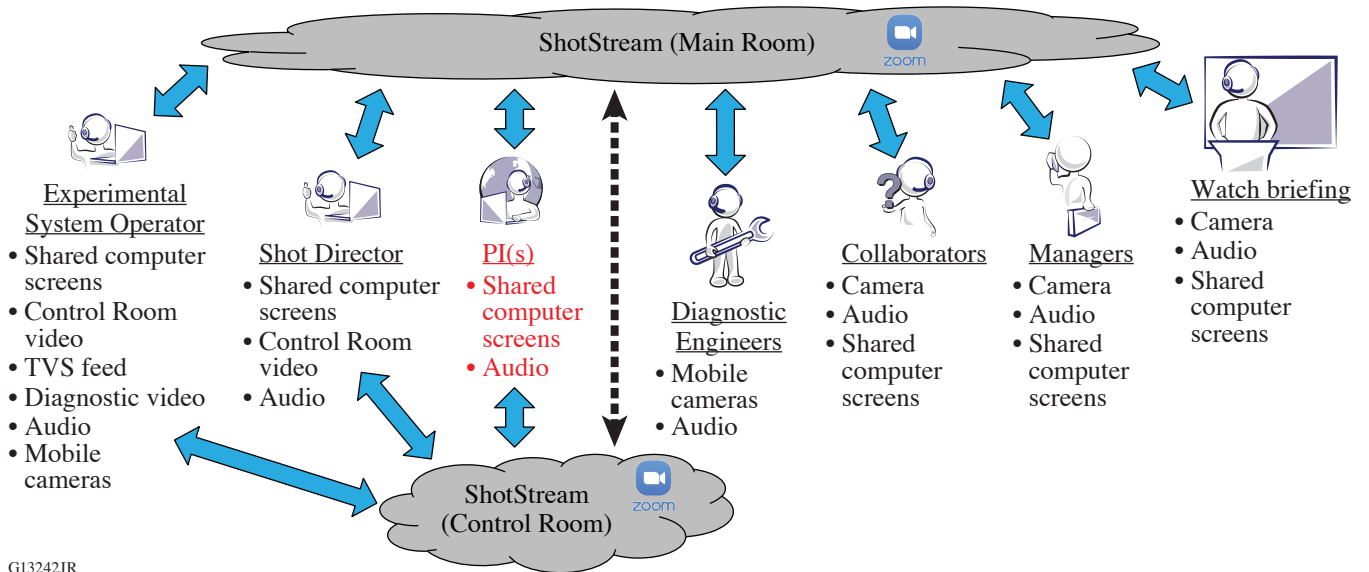
Laboratory for Laser Energetics, University of Rochester

The COVID-19 pandemic presented an unprecedented challenge to our highly productive experimental facility. While the Omega Laser Facility was in standby mode for “NY State on PAUSE,” our operations team evaluated and modified the Omega operating processes to deliver “normal” operational throughput with most scientists and some support staff working remotely. Since the Omega user base is located around the globe, the experiment-planning process was already conducted largely via online, e-mail, and video conferencing methods; therefore, little change to that was necessary. However, shot-day operations required extensive changes. Shot-day transactions between the Principal Investigators (PI’s) and the operations crew had been done in person only, requiring the PI’s to be on-site. New travel restrictions meant this was seldom possible. Additionally, new occupancy restrictions to support social distancing limited the number of personnel on-site.

To address these new constraints, the remotePI protocol was implemented. The primary objective was to facilitate PI-to-Operations shot-day transactions while complying with COVID-19 mitigation rules (social distancing and travel limitations) by implementing a minimal set of changes to our existing processes—changes that were implementable on a very short development cycle, easy to learn, and used only existing and available equipment, particularly for the off-site participants. We achieved these goals while supporting efficient operations—meeting or exceeding “usual” Omega levels of effectiveness, availability, and flexibility.

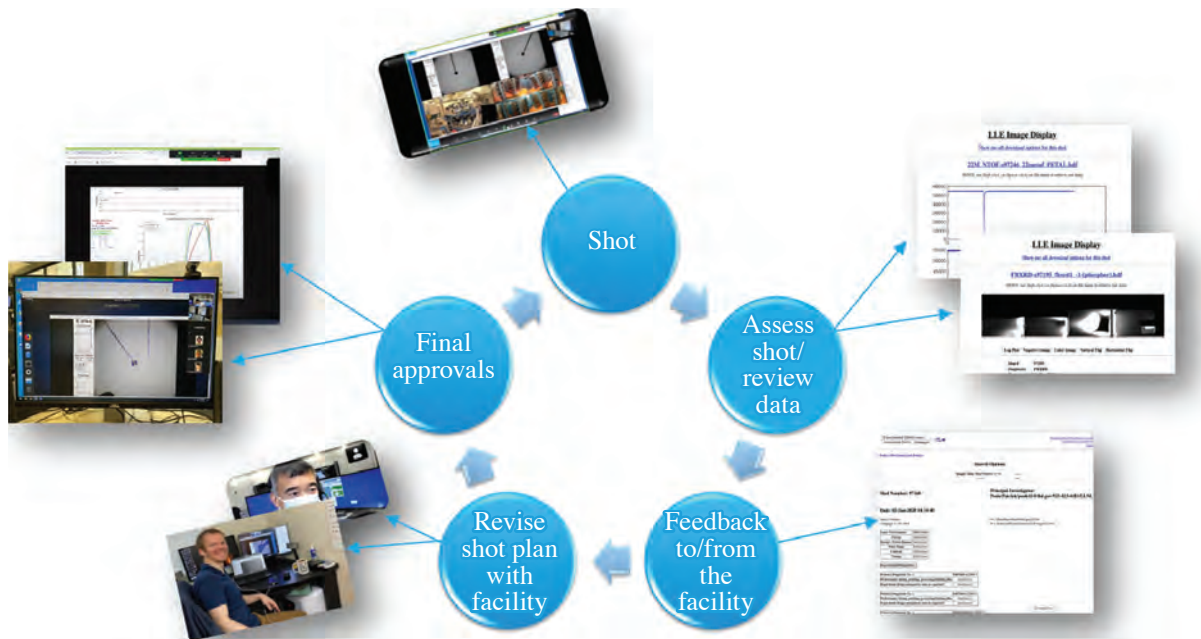
Each OMEGA 60 or OMEGA EP shot cycle is governed by a series of transactions between the PI and the facility. The remotePI system eliminates PI location dependence by creating a virtual venue for these transactions using an intuitive platform and commonly available equipment. The centerpiece of remotePI is an all-day Zoom meeting for each facility, which we dubbed “ShotStream.” ShotStream connects the PI to the facility, as well as to collaborators and technical staff. Each day there is one ShotStream opened for each facility, comprising two virtual rooms: one “main room” used as a collaboration space for PI’s and another area (the “control room”) used exclusively for communication between the PI and the operations crew (see Fig. 1). A simple rule set is implemented to allow concise communication between the PI and Operations crew.

ShotStream provides a venue for all the shot-day transactions between the PI and the facility (see Fig. 2). The audio channel from one of the ShotStream rooms is connected directly to a facility intercom channel, allowing the PI to communicate directly with any of the on-site staff. Screen sharing and video feeds allow the PI to receive important information such as target images, pulse-shape predictions, and shot configuration database changes. Also available on the Zoom are direct video from key diagnostics, such as VISAR/ASBO (velocity interferometer system for any reflector/active shock breakout) cameras, and real-time video of any piece of equipment can also be piped into ShotStream. Final approvals prior to the shot are conducted on ShotStream. Additionally, the PI conducts the pre-watch briefings to the Operations crew on ShotStream. The PI observes Control Room operations during the shot on ShotStream and can participate whenever appropriate. Regardless of their actual location in the world, ShotStream puts the PI into our Control Rooms during the shot. Data from each shot are posted online for the PI to review. Electronic data [e.g., charge-coupled device, image plate, or oscilloscope readouts] have been traditionally available online, but



G13242JR

Figure 1
ShotStream virtual facility conceptual layout. The virtual main room is used by all participants as a collaboration area, for crew briefings, etc. The virtual control room is used for direct communication between the PI and shot crew.



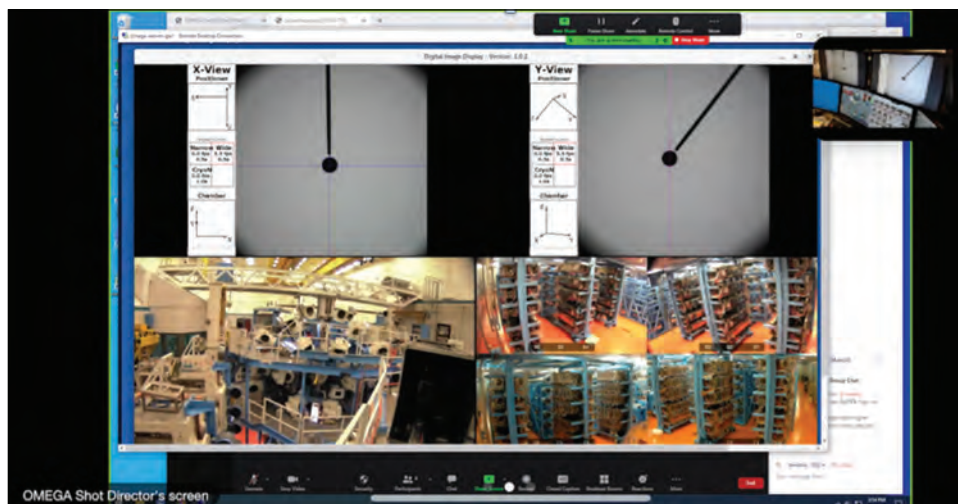
G13271JR

Figure 2
All of the shot-day transactions between the PI and the facility are supported by the remotePI process.

film data usually had been handled in person. Film data are now scanned and posted to the LLE website shortly after each shot. The post-shot feedback paper forms have been replaced with similar online forms for quick and precise feedback to the facility.

Additionally, mobile cameras can be deployed to the field and broadcast on ShotStream to allow on-demand video/audio communications between remote participants (PI's or technical staff) and on-site operators. This supports precise instrument setup and troubleshooting even when the system experts are not on-site.

Today, PI's as well as many support staff and managers use the remotePI system to participate in shot operations on OMEGA 60 and OMEGA EP on a daily basis while complying with the strict social distancing requirements that are essential to COVID-19 mitigation. While the modifications to the system to implement remotePI are modest in scope and now operate with little overhead cost, the software and hardware updates needed to initially deploy the system required participation by many of our support staff, most of whom were working remotely themselves. Key to the success of remotePI, only commonly available equipment (a PC or mobile device with an internet connection) is needed for a PI to fully participate in shot operations. A typical ShotStream user view is shown in Fig. 3.



G13270JR

Figure 3
Typical ShotStream view shown on a mobile device.

Since resumption of shot operations in June 2020, all OMEGA 60 and OMEGA EP shots have used the remotePI system. Changing to the remotePI protocol does not appear to have adversely affected the availability or effectiveness of our facility. During our first seven months of operations, the effectiveness and availability results on both OMEGA 60 and OMEGA EP are comparable to those of the seven months leading up to the pandemic. After-action reports from PI's have been largely complimentary. Comparison of performance in legacy operations mode (9/1/19–3/22/20) and remote PI operations mode (6/3/20–12/14/20) are shown in Tables I and II. Because of the numerous benefits brought to the facility by remotePI and demonstrated over the past year, including enhanced scheduling flexibility and more efficient use of support resources, LLE plans to continue to make remotePI available in our operational toolkit even after the constraints of the Covid-19 pandemic are lifted.

Table I: Comparison of OMEGA 60 performance pre-/post-COVID-19.

Date Range	Number of Shots	Average Availability	Average Effectiveness
9/1/19 to 3/22/20	648	93.9%	94.9%
6/3/20 to 12/14/20	658	91.1%	94.5%

Table II: Comparison of OMEGA EP performance pre-/post-COVID-19.

Date Range	Number of Shots	Average Availability	Average Effectiveness
9/1/19 to 3/22/20	503	96.7%	95.7%
6/3/20 to 12/14/20	516	93.9%	95.4%

LLE and General Atomics: A Partnership for the Future

T. W. Overton

General Atomics

The Three-Decade Relationship has been a High-Impact Influence on Inertial Fusion Research

For a collaboration that is often measured in microns, it is a bit ironic that the Laboratory for Laser Energetics (LLE) and General Atomics (GA) are more than 2500 miles apart. LLE was established in 1970 as a center for the investigation of the interaction between matter and intense laser radiation (Fig. 1). The development of a series of high-powered, neodymium-glass laser systems at LLE (DELTA, ZETA, and the 24-beam OMEGA) eventually led to the 60-beam OMEGA Laser System. The 60-beam OMEGA laser has been operational since 1995 and is one of the primary research tools for inertial confinement fusion (ICF) and high-energy-density (HED) physics research in the U.S.



U2735JR

Figure 1
Exterior of the Laboratory for Laser Energetics at the University of Rochester.

OMEGA is maintained and operated by LLE for the Department of Energy's (DOE's) National Nuclear Security Administration (NNSA). OMEGA can focus up to 30,000 J of 351-nm laser energy onto a target that measures less than 1 mm diam in approximately one billionth of a second. In addition to the 60-beam OMEGA, the 4-beam OMEGA EP laser has also been a main research tool for the community since 2008.

OMEGA EP consists of four beamlines similar to those at the National Ignition Facility (NIF). Two of those beams can be compressed for short-pulse, petawatt-class operation. Both of these facilities allow scientists to explore physics conditions at extremely high pressures and temperatures—including fusion, the process that powers the Sun. Approximately 60% of all experiments conducted at the Omega Laser Facility are led by researchers from outside LLE.

Since 1991, nearly all of the LLE target capsules, which hold the material that is compressed by high-powered laser pulses, have been manufactured by GA in San Diego. Dr. Mike Campbell, the director of LLE, is frank about the close interdependence

of LLE and GA. “LLE is the main facility for direct-drive fusion research, where the laser directly impinges on the fusion capsule. So, in addition to the laser and diagnostics that make up the facility, you need to have targets to shoot. All those capsules are made for us at General Atomics, and the progress that we can make in the fusion program is directly dependent on the characteristics of the targets that GA delivers.”

“It’s been a three-decade, high-impact relationship,” said Mike Farrell, vice president of inertial fusion at GA. “Whether it’s been engineered systems, targets, diagnostic instrumentation, or other activities in support of the science that researchers are conducting at LLE, GA’s contributions to enabling the physics research performed at LLE have been a constant and significant enabling factor.”

GA’s involvement in fusion research reaches back to its founding in the 1950s. Although its global operations now extend into technologies as diverse as aerospace and biotech, fusion remains a core focus of its research and development activities (Fig. 2). For decades, GA has worked with DOE and its predecessor agency, the Atomic Energy Commission, on a wide variety of fusion energy initiatives. Many GA employees have worked at DOE laboratories and facilities like LLE—including Dr. Campbell, who headed up GA’s target fabrication operations from 2000 to 2007.



U2736JR

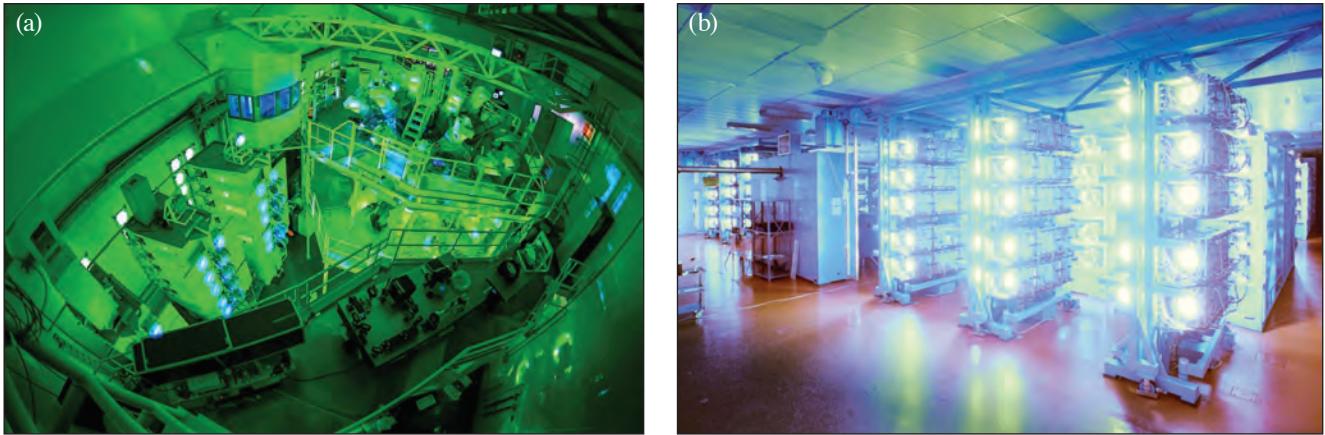
Figure 2
The General Atomics campus in San Diego
(photo Ronalyn Conception/GA).

Target Development

The LLE–GA collaboration began in the early 1990s, when DOE awarded GA the contract to fabricate targets for the U.S. ICF program, which supports much of the research at LLE (Fig. 3). One of the first major projects to emerge from LLE’s work with GA was an upgraded Cryogenic Target Handling System. Direct-drive fusion targets on OMEGA need to be filled with fusion fuel, which is a mixture of the hydrogen isotopes deuterium and tritium (DT). In order to increase the amount of fuel each target can hold and to start with the highest density, the DT fuel is frozen at cryogenic temperatures. These tiny capsules are then placed into the target chamber.

Dr. David Harding, group leader for target fabrication at LLE, joined the team during development of the new system in 1995. “On the old system, the researchers would fill the targets with a very small amount of tritium at room temperature so that the capsule wouldn’t burst, and put it into the cryostat at 19 K to create a very rudimentary DT ice layer,” he explained.

This was sufficient for early experiments in the late 1980s, but researchers wanted to shoot targets with significantly more fuel. The goal of the new system was to load very thick (up to $\sim 100\text{-}\mu\text{m}$) DT layers into very thin-walled (less than $5\text{-}\mu\text{m}$) polymer capsules (Fig. 4). The experiments also required that the ice wall be uniformly thick with a smooth surface. As might be expected, creating targets with these attributes was a significant challenge.



U2737JR

Figure 3
The (a) Target Bay and (b) Laser Bay at LLE during a laser shot.



U2738JR

Figure 4
One of the cryogenic targets used on OMEGA, fabricated by GA.

“The capsules are filled with fuel by diffusion, which is placing the capsules under more 1000 atm of pressure in a vessel filled with the fuel gas, so that it diffuses across the thin capsule walls,” Dr. Harding said. “After you’ve pressurized the capsule, you have to freeze the fuel to keep it from bursting once the target is removed from the pressure vessel.”

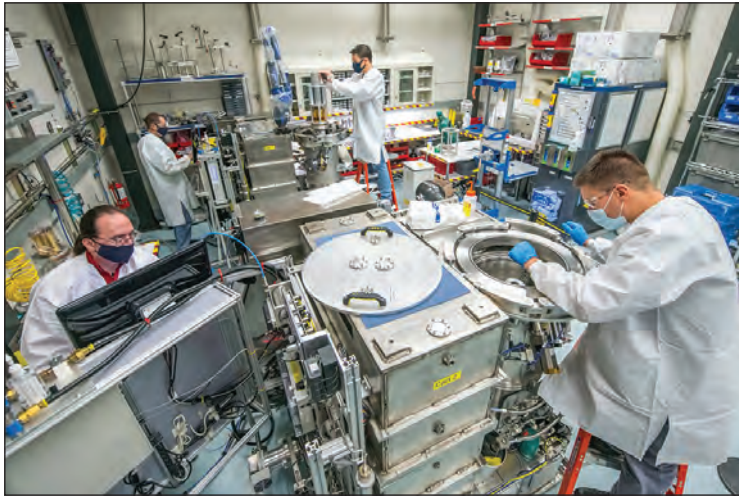
The challenge was doing this in a way that the capsules could be filled, frozen, placed into the target chamber, and shot before the ice thawed and the capsules burst. “The job was to design a cryostat with a pressure vessel inside it, so you could ramp the pressure up, cool the targets, and do it in a very controlled manner,” Dr. Harding said.

On top of that, the targets still needed to get to the chamber where they could be shot by the lasers. The team designed a smaller, mobile cryostat that would take the target from the larger cryostat and place it into the target chamber. To maintain the cryogenic temperatures, the target would be covered by a copper shroud during transport.

That might sound simple, but the process needed to operate in an extremely precise manner. The target had to be placed within $5\ \mu\text{m}$ of the center of the target chamber, and the cryogenic protective shroud had to be retracted very rapidly, less than $100\ \mu\text{s}$ prior to the shot.

The challenging demands of this system led to some initial difficulties in development. GA and LLE began working together on the process in 1995, and GA designed all the major components with assistance from LLE. The parts were then shipped to Rochester and assembled, integrated, and tested by LLE staff. “It was a complete collaboration between LLE scientists and engineers and GA’s personnel,” Dr. Harding said. “It was a great success, especially given that it was completed in such a short time.”

The first target using the new system was shot on 14 July 2000—just five years after the project began. The new system was a major improvement over the old one on the 24-beam OMEGA laser. It was able to process and shoot four targets per day in exactly the conditions the researchers needed (Fig. 5). “There were no compromises on the physics quality of the targets,” Dr. Harding said.



U2739JR

Figure 5

Operators from LLE’s Cryogenic and Tritium Facility are shown performing routine maintenance and performance checks on moving cryostat transport carts (MCTC’s) in the Cart Maintenance Room. Steven Verbridge and Chad Fella (foreground) are preparing to raise the moving cryostat (MC) from MCTC#2 in order to perform service. Sean Adams and Michael Coffey (background) are employing a coordinate measuring machine on an (elevated) MC on MCTC#7 to verify proper alignment of the removable shroud. Operators are wearing disposable jackets and gloves given the trace tritium surface contamination on internal equipment.

The system was so successful that elements of the tritium-handling approach were used to inform the design of the cryogenic target system on the NIF at Lawrence Livermore National Laboratory (LLNL), which GA also developed. LLE shared its experiences with the new system with GA, which incorporated it into the work on the NIF. “Many of the features in our cryogenic system fed directly into the NIF system,” Dr. Harding said.

Another innovation that flowed from the LLE–GA partnership related to the composition of the polymer target capsules. Researchers at LLNL first demonstrated a process for making the polymer shells known as glow-discharge polymerization (GDP). However, LLNL had little interest in pursuing the process at the time. LLE staff asked GA to improve and develop the technology for use on OMEGA. “We used the targets and told GA how they performed and what changes they needed to make,” Dr. Harding said. “They used results from OMEGA implosions to further define the target specifications. That technology is now the baseline target fabrication methodology.”

Working together, GA and LLE scientists have continued to refine methods for producing the polymer capsules and making them much smoother and free from defects. This is important because any defect or imperfection in the capsule serves as a “noise” source from which hydrodynamic instabilities can grow and adversely affect the quality of the implosion experiments. At LLE’s request, GA developed a technique for producing polystyrene shells using a solvent-based microencapsulation method, resulting in capsules that are significantly smoother than GDP targets (Fig. 6). “GA was able to control the uniformity and thickness of the shells and make them many, many orders of magnitude smoother than the GDP targets,” Dr. Harding said.

Diagnostics

Another key element of LLE’s work are the diagnostic systems that record data from the laser shots. After all, the experiments are of little use unless scientists are able to analyze exactly what happened. Here too, LLE and GA have worked together

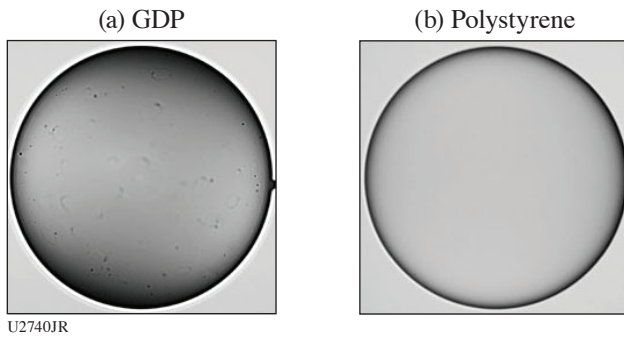


Figure 6

The improvement in smoothness between (a) 1-mm-diam GDP shells and (b) polystyrene shells, both made by GA for experiments on OMEGA. The shell wall is 0.01 mm thick. The notable difference is the absence of features on the surface of the polystyrene shell, which is important for high-performing implosions.

to bring significant innovations to the field. “In these implosion experiments, we need to know the shape of the central hot-spot plasma formed in a laser-direct-drive implosion,” said Dr. Sean Regan, LLE’s Experimental Division Director. “To do that, we need some very specialized instrumentation.”

The ideal implosion is spherically symmetric. “We don’t get that,” Dr. Regan said, “because we don’t position the target accurately enough, or the laser is stronger on one side than the other, or some other factor. So, we need to understand the causal relationships between the implosion inputs and the outputs.”

Several years ago, through the National Diagnostics Working Group, LLE joined a productive collaboration between GA, LLNL, Sandia National Laboratories (SNL), and Kentech Instruments that involved the development of a single-line-of-sight (SLOS) camera that can capture multiple images with a shutter speed of about 25 ps (Fig. 7). GA has delivered two versions of the SLOS instrument so far. The SLOS-CBI (crystal backlighter imager) was delivered to LLNL in 2017 and is in use on the NIF. The SLOS-TRXI (time-resolved x-ray imager) was delivered to LLE and is now operating as part of OMEGA (Fig. 8).



U2741JR

Figure 7

Terry Hilsabeck and Kyle Engelhorn of General Atomics with the SLOS-TRXI instrument during assembly (photo: Eugene Kowaluk).

SLOS-TRXI is a primary diagnostic for the DT cryogenic implosion campaigns on OMEGA (Fig. 8). It images the hot-spot plasma emission with 25-ps temporal resolution and 10- μm spatial resolution using a pinhole camera and a time-dilation tube. To put that speed in perspective, 25 ps is the time it takes a beam of light to travel almost half of an inch. As impressive as this is, the researchers at the Omega Laser Facility are not satisfied with the status quo. “Because the hot spot is about 40 μm ,” Dr. Regan said, “a 10- μm resolution doesn’t give you a very crisp image. We want to do better. We also want to diagnose the low-mode structure of the hot-spot plasma.”



U2742JR

Figure 8
The SLOS-TRIXI instrument
being installed on OMEGA.

The team is currently designing what might be termed “SLOS-TRIXI 2.0” that will add a third line of sight to the instrument, allowing for a full 3-D low-mode reconstruction of the hot-spot plasma. Under this same collaboration, a hot-spot x-ray imager with 20-ps temporal resolution and 5- μm spatial resolution is being developed for OMEGA. This imager will allow scientists to determine the overall shape of the hot spot and how it deviates from a perfectly spherical shape. This can also be compared to data from the other OMEGA diagnostics.

“Using nuclear spectroscopy measurements recorded along three quasi-orthogonal diagnostic lines of sight, we can infer the hot-spot flow velocity,” Dr. Regan said. “If there’s a significant flow in the hot spot caused by an asymmetric implosion, it will doppler-shift the DT fusion neutron spectrum, and you’ll see the mean energy of the spectrum shifted up or down. Combining the hot-spot flow measurements with the SLOS-TRIXI x-ray images of the hot spot allows us to model the structure of the hot spot. This will ultimately help us understand how the hot-spot formation is affected by multidimensional effects on the implosion.”

The working group is drawing on lessons learned from SLOS-TRIXI to develop the third line-of-sight instrument. LLE is responsible for project oversight and design and the x-ray pinhole camera, while GA is developing the drift tube. SNL, LLNL, Kentech, and Sydor Technologies are developing other elements. A conceptual design has been developed, and discussions about the construction have recently started. “It’s a fantastic collaboration between LLE, GA, the national labs, and these other innovative and highly talented private firms,” Dr. Regan said.

National Laser Users’ Facility

Another key element of the collaboration has occurred through the DOE’s National Laser Users’ Facility (NLUF) program, which provides beam-time access at the Omega Laser Facility for scientists in both academia and private industry to conduct basic research and train graduate students. These experiments explore a wide range of HED science topic areas such as plasma physics, laboratory astrophysics, high-pressure materials, magnetized HED plasmas, nuclear science, and novel diagnostic development. NLUF is part of the Joint Program in High-Energy-Density Laboratory Plasmas, which is sponsored jointly by the NNSA Office of Research, Development, Test, and Evaluation and the DOE Office of Fusion Energy Sciences.

DOE funds the operation of NLUF, making it possible for researchers, including students, to conduct experiments without a direct facility charge. In addition, DOE provides research funds directly to these users for experiments. To broaden the science scope and grow the user community, NLUF will become a facility access program starting in 2022 with no restrictions on the source of the research funds users may have.

“The benefits of the NLUF Program are really tremendous,” said Dr. Mingsheng Wei, an alumna of NLUF and GA who now serves as the NLUF Manager at LLE. “NLUF has compiled a strong record of excellence in HED and frontier science research

and trained over 200 Ph.D. graduate students and postdoctoral researchers.” More than 60 graduate students from 18 institutions (excluding UR) are currently conducting thesis research using OMEGA, primarily through the NLUF.

GA fabricates a wide variety of targets and components and performs metrology and target assembly to support over 350 shots at the Omega Laser Facility each year for NLUF users. “There are a lot of specialized targets and materials that we aren’t able to make in our lab because we don’t have the machinery or the expertise here,” said Dr. Carolyn Kuranz, associate professor of nuclear engineering and radiological sciences at the University of Michigan. “We depend on GA for that. For example, there are hydrodynamic instability experiments that we wouldn’t be able to do or characterize without those targets and materials. And we’ve been able to do some really cool and exciting work because of it.”

After earning her Ph.D., Dr. Wei worked as a project scientist performing HED physics research at the University of California San Diego (UCSD) including NLUF-supported research on OMEGA. She joined GA in 2010, where she continued her research in HED physics, leading several NLUF projects with experiments on OMEGA and supporting target development, before moving to LLE in 2018. Kuranz also participated in the NLUF Program and now supervises graduate students doing their own research through it.

Professor Farhat Beg at UCSD has been involved in the NLUF for more than ten years. The UCSD campus is directly across the street from GA’s main campus in the Torrey Pines neighborhood of San Diego. “NLUF makes it possible for us to do state-of-the-art science that we simply cannot do on any other facility,” Prof. Beg said. “The program has given us an outstanding platform and opportunities for our students and post-docs to carry out top-quality work on OMEGA. GA has been instrumental in providing us with the complex targets we need to do this.”

A 2016 article¹ in *Nature Physics* co-authored by Dr. Wei and Prof. Beg serves as one example of what the NLUF has helped achieve. A team of researchers from UCSD, GA, LLE, LLNL, and several other institutions (Fig. 9) conducted a series of experiments on OMEGA using copper-doped plastic shell targets from GA to demonstrate a significant improvement in energy coupling of high-intensity, laser-produced relativistic electrons in integrated cone-in-shell fast-ignition experiments. The lead graduate student on the project, Leonard C. Jarrott from UCSD, is now a staff scientist at LLNL.



U2743JR

Figure 9

This NLUF-supported team of scientists from UCSD, GA, LLE, and LLNL demonstrated a significant improvement in energy coupling of high-intensity, laser-produced relativistic electrons in integrated cone-in-shell fast-ignition experiments on OMEGA. Front row (left to right): Chris McGuffey (UCSD), Chad Mileham (LLE), and Wolfgang Theobald (LLE); middle row: Farhat Beg (UCSD), Gennady Giksel (then at LLE, currently with University of Michigan), and Mingsheng Wei (then at General Atomics, currently with LLE); back row: Leonard Charlie Jarrott (then a graduate student at UCSD, currently a Staff Scientist at LLNL), Toshinori Yabuuchi (then at UCSD, currently at SACLA, Japan), Richard Stephens (then at GA, currently retired), and Hiroshi Sawada (then at UCSD, currently at University of Nevada, Reno). (Photo: Farhat Beg.)

Professor Beg praised the record of the NLUF in preparing students for careers in HED physics and particularly the work at DOE national labs. He noted that most of his graduate students have gone on to work at LLNL, LLE, and GA. One of his former post-doc researchers, Dr. Christine Krauland, did her doctoral work at LLE with NLUF funding while at the University

of Michigan, and now works in GA's Inertial Fusion Division studying an alternative ICF scheme called "shock ignition," also under an award from NLUF (Fig. 10). "I have only good things to say about NLUF and LLE," Dr. Krauland said. "It's a critical talent pipeline for the ICF labs and the HED community as a whole."



U2744JR

Figure 10
Dr. Christine Krauland (photo: Christine Krauland).

Dr. Johan Frenje, assistant head of the High Energy Density Physics Division at MIT's Plasma Science and Fusion Center, had similar praise for the NLUF program. "It's everything for us," he said of the opportunity to work on OMEGA through the collaboration with GA. Frenje has guided about 15 to 20 doctoral students through the program in the 20 years he's been at MIT. "Of those," he said, "80% to 90% have gone on to work at the national labs."

"GA's participation in the NLUF Program is absolutely essential," Dr. Frenje said. "There's no question that we can't do this otherwise. We rely on GA to help us push the boundaries of science. Our requirements for targets have gotten tougher and tougher, but GA has delivered."

"We are equal partners, and it is a very collaborative process," Prof. Beg said of GA. "They provide opportunities for us to do really challenging science. They work to make the targets we need and have devoted substantial R&D money to make these projects possible."

Dr. Wei found that her experience working at GA to design targets for experiments on OMEGA gave her additional perspective on what the program has accomplished: "Working on the target side, it was really rewarding being able to bridge the gap between the physics and design and the actual experiments."

Toward the Future

"We do 10 to 15 experiments a day," Dr. Campbell said, "and maybe 3 or 4 cryogenic experiments. I'd like to do a hundred a day. That means we have to learn how to fabricate targets much more rapidly, and higher quality, and that's a real challenge. To be more relevant to NNSA and others, we need more-complicated targets made from multiple layers—multi-shell rather than single shell. That's something that GA is working on."

"Target design offers the greatest level of flexibility of all of the experimental parameters available to academic and laboratory researchers and physicists," M. Farrell said. "Enabling today's experiments while advancing the state of the art in targets for future designs is a passion for the engineers and scientists at GA. Transitioning from a "single shot" to "repetition-rated shot" capability is a grand challenge the GA and LLE collaboration is looking forward to taking on."

As much as the collaboration has accomplished, Dr. Campbell believes there is still much more to be done, given sufficient support. “I think the country does not devote enough R&D toward target fabrication,” he said, “and I would like to see that grow. We have these three active facilities: Omega, the NIF, and the Z Machine at Sandia. We need to not only supply the targets for the ongoing programs, but also supply the targets for the future. That’s critical to maintaining U.S. leadership in this field and ensuring we can reap the benefits of all this effort.”

1. L. C. Jarrott *et al.*, Nat. Phys. **12**, 499 (2016).

A Proposal for Pentagonal Prism Spherical Hohlräum Experiments on OMEGA

W. Y. Wang and R. S. Craxton

Laboratory for Laser Energetics, University of Rochester

An important requirement for achieving ignition and gain through inertial confinement fusion is obtaining high levels of drive uniformity on a spherical capsule.¹⁻³ In the indirect-drive approach,² the fuel capsule is placed inside a case, known as a hohlraum, which is made of a high-Z material (typically gold) and converts the laser energy into an x-ray radiation field that provides a smooth drive on the capsule surface. On the National Ignition Facility (NIF),⁴ the laser beams enter through two laser entrance holes (LEH's) on the axis of a cylindrical hohlraum.² For future laser systems, however, spherical hohlraums have attracted recent interest as a means of achieving better uniformity.⁵⁻⁷ The work presented here explores the use of a spherical hohlraum, known as a pentagonal prism (PEPR) hohlraum, that will allow spherical hohlraums to be tested before future large-scale laser systems are constructed. The PEPR hohlraum has seven LEH's and is well suited to the OMEGA geometry. Proposed experiments on OMEGA are predicted to produce highly uniform compressions of the capsule.

The first spherical hohlraum to be proposed was the tetrahedral hohlraum,⁸⁻¹⁰ shown in Fig. 1(a), with four LEH's located at the vertices of a tetrahedron. Tetrahedral hohlraum experiments were performed on OMEGA, producing highly uniform capsule compressions^{11,12} consistent with the radiation drive on the capsule having less than 1% nonuniformity. Recently, octahedral hohlraums [Fig. 1(b)] were proposed as a more-uniform alternative to cylindrical and tetrahedral hohlraums, with flux nonuniformity as low as 0.1% (Refs. 5-7). The octahedral hohlraum has six LEH's corresponding to the centers of the faces of a cube or the vertices of an octahedron.

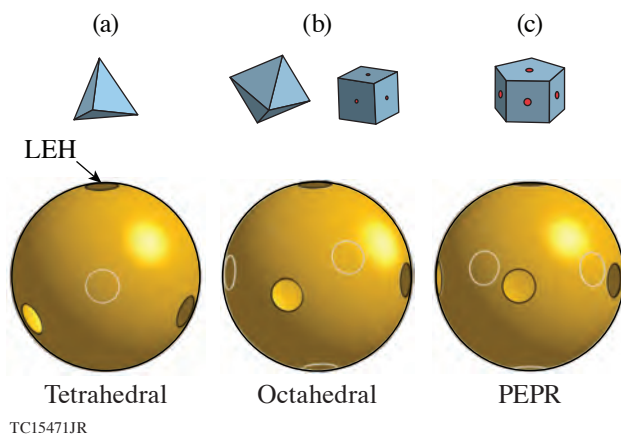


Figure 1

(a) Tetrahedral, (b) octahedral, and (c) pentagonal prism (PEPR) hohlraums. Laser entrance holes on the far side of the hohlraums are shown in outline.

Although the 60-beam OMEGA laser is geometrically unsuitable for driving octahedral hohlraums (as is also true of the NIF), the PEPR hohlraum [Fig. 1(c)] is well matched to the symmetry of the OMEGA target chamber, whose beam configuration has fivefold symmetry about the vertical axis. The LEH's of the PEPR hohlraum are based on the faces of a pentagonal prism, with five LEH's around the equator and one on each pole. This configuration was first suggested by Farmer *et al.*¹³

The PEPR hohlraum design presented here has dimensions taken from Ref. 10: the hohlraum diameter is $2800\ \mu\text{m}$, the capsule diameter is $550\ \mu\text{m}$, and the LEH diameter is $700\ \mu\text{m}$. Five beams enter each of the two polar LEH's and ten beams enter each of the equatorial LEH's. Figure 2(a) shows which beams enter each LEH. The angle of incidence θ_i relative to the LEH normal ranges from 21.4° (for beams passing through the polar LEH's) to 69.7° . For comparison, θ_i ranges from 23.2° to 58.8° for the OMEGA tetrahedral hohlraum¹⁰ and from 21.2° to 52.4° for the NIF. The ray paths of the beams passing through the polar LEH's are shown in Fig. 2(b). They are focused inside the hohlraum to maximize the clearance from the capsule, as was done for the earlier tetrahedral hohlraum experiments on OMEGA. There are problems associated with the use of small angles of incidence on large systems such as the NIF, including laser–plasma instabilities along the large propagation distances and absorption in the hohlraum plasma. The proposed octahedral hohlraum avoids low values of θ_i because all beams enter in the optimal range of 50° to 60° .

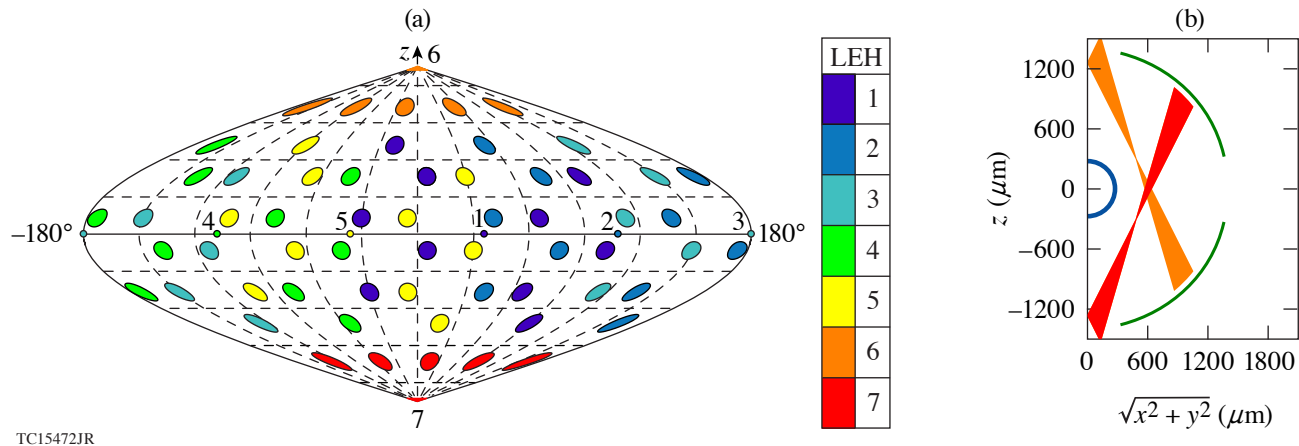


Figure 2

(a) LEH assignments used in *LORE* simulations for a PEPR hohlraum on OMEGA. Colors of beam ports represent LEH assignments. The small colored circles indicate the LEH locations. (b) Ray paths of beams entering through the LEH's (6 and 7) on the z axis. These beams are focused inside the hohlraum to maximize the clearance from the capsule.

The PEPR hohlraum is analyzed using a new view-factor code *LORE*,¹⁴ which follows the physics model used in the code *BUTTERCUP*.⁹ *LORE* traces beam paths starting from the target chamber port. Each beam is divided into multiple rays, each traveling through the best-focus point of the beam. *LORE* finds the intersection of each ray with the hohlraum wall and includes an *ad hoc* model of how much energy is deposited at that point and how much is reflected to the next intersection point. Typically, all the energy is deposited at the first intersection since the hohlraum wall is strongly absorbing. Figure 3(a) shows contours of deposited energy. One can see 60 distinct laser spots, spread fairly uniformly over the hohlraum wall. As recognized in Ref. 9, this is desirable for capsule uniformity. The beam spots are all clear of the LEH's.

After tracing all the beams, *LORE* determines a spatially independent background radiation temperature T_r by assuming a Planckian radiation field in the hohlraum. T_r is calculated by balancing the power entering the radiation field (the absorbed laser power multiplied by the laser-to-radiation conversion efficiency) with the power lost to the hohlraum wall, the capsule, and the LEH's. Of particular importance is the loss to the wall, equal to $\sigma T_r^4(1-\alpha_w)A_w$, where σ is the Stefan–Boltzmann constant, α_w is the wall albedo, and A_w is the wall area. Early in time, the albedo is low and most of the radiation incident on the wall goes into heating the wall. Later in time, the heated wall re-radiates most of its incident energy into the hohlraum and the albedo approaches unity.

Next, *LORE* calculates the emitted radiation flux at every point on the wall as the sum of the re-radiated portion of the incoming radiation ($\alpha_w \sigma T_r^4$) and the portion of the absorbed laser flux that is converted to radiation. The emitted radiation flux I_e is parametrized in terms of the effective radiation temperature T_e , defined at each point on the wall such that ($I_e = \sigma T_e^4$).

To determine the radiation uniformity on the capsule, *LORE* scans over multiple points on the capsule. For each point, *LORE* integrates the radiation flux I_e over all viewing directions. These integrals typically involve scanning over 60,000 points on the capsule and, for each point, looking along $\sim 100,000$ directions. A contour plot of the flux variations on the capsule is given in Fig. 3(b) for an albedo α_w of 0.85. The nonuniformity level is very low at 0.6% rms.

Figure 3(b) shows that, while the variations in drive on the capsule are very small, the strongest drive occurs at the poles. This is because at late times (high albedos) the heated hohlraum wall provides the dominant contribution to the drive. As a result of the two LEH's on the poles being spaced farther from other LEH's than the five equatorial LEH's, the poles of the capsule receive more drive. Conversely, at early times (low albedos), the laser-heated spots provide the dominant contribution to the drive. As a result of these spots being more "clumped" around the equator than the poles [Fig. 3(a)], the equatorial region of the capsule receives slightly more drive (but the nonuniformity is still small at 1.1% rms).

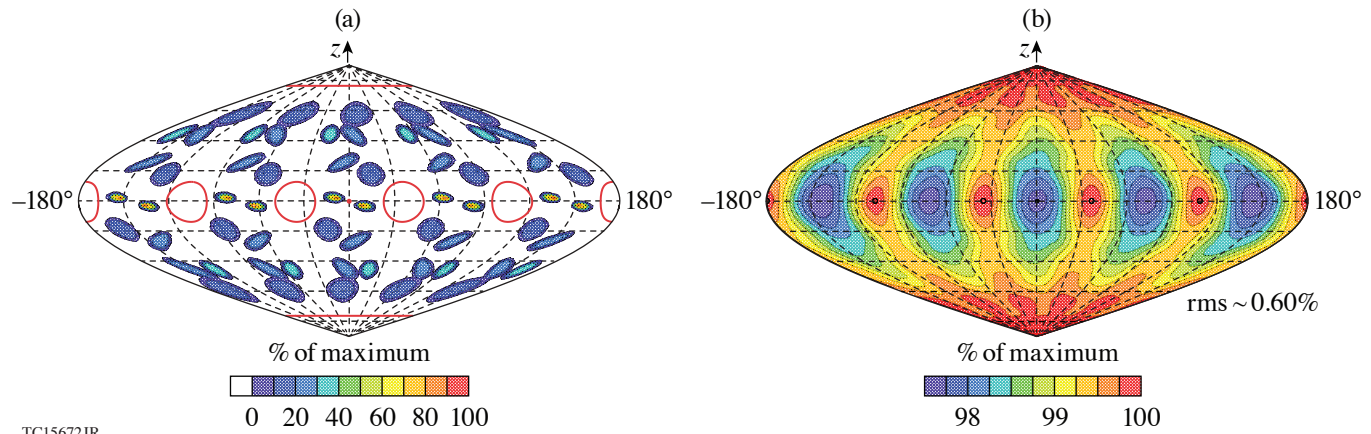


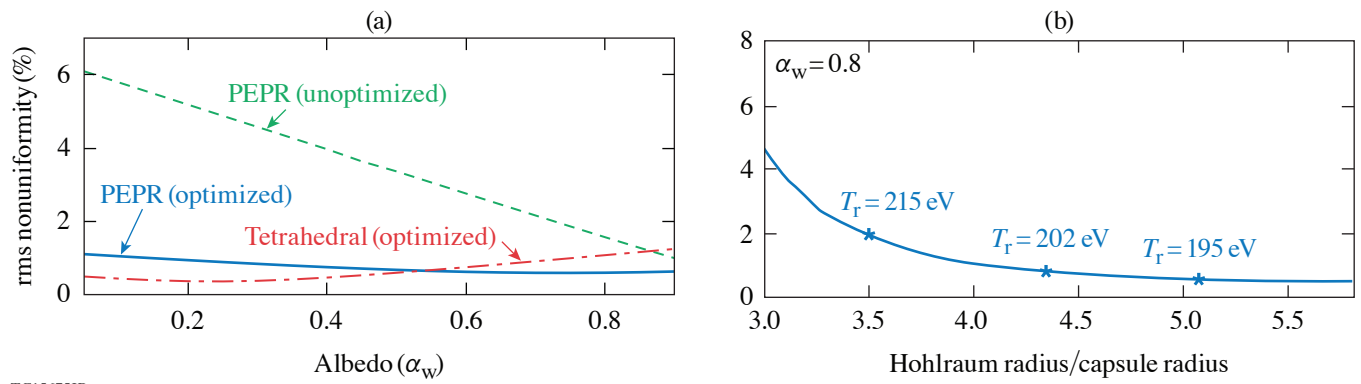
Figure 3

(a) Contour plot of deposited laser energy per unit area on the wall of the PEPR hohlraum. The LEH's are indicated in red. (b) Contour plot of radiation flux variations on the capsule for an albedo of 0.85.

The design was optimized to provide good uniformity at all albedos, i.e., good time-dependent uniformity. This was accomplished by adjusting the aim points of the beams within their LEH's to shift the laser-heated spots closer to the poles. Figure 4(a) shows the dependence of the nonuniformity on albedo for the optimized case, varying from 1.1% at low albedo to 0.6% at high albedo. To achieve this level of time-dependent uniformity requires that both contributions to the drive (laser spots and wall) produce good uniformity since they each dominate at a different time. This is hard to accomplish with cylindrical hohlraums, for which "beam phasing" (different pulse shapes in different sets of beams²) is typically required to provide the best balance between the two contributions. While this can produce a low time-averaged nonuniformity, time-dependent nonuniformity can limit the attainable fuel convergence. In the PEPR hohlraum, as in tetrahedral and octahedral hohlraums, all beams can be given the same laser temporal pulse shape.

Figure 4(a) includes, for comparison, an unoptimized PEPR hohlraum design, in which all beams are aimed through the centers of the LEH's. The 6% nonuniformity at low albedo results from the beam spots clumping closer to the equator than shown in Fig. 3(a). The nonuniformity declines at higher albedo as the wall contribution increases. Also shown in Fig. 4(a) is a prediction for optimized tetrahedral hohlraums with the same dimensions. At values of albedo below 0.5, the tetrahedral hohlraum provides better uniformity than the optimized PEPR hohlraum because the locations of deposited laser energy on the tetrahedral hohlraum are more evenly spread out. At albedos greater than 0.5, however, the nonuniformity is lower for the PEPR hohlraum.

A critical role in hohlraum design is played by the case-to-capsule ratio, i.e., the hohlraum radius divided by the capsule radius. It has long been recognized that a large ratio provides better uniformity at the expense of a lower radiation temperature.² This



TC15675JR

Figure 4

(a) The rms nonuniformity on the capsule for optimized and unoptimized PEPR hohlraums and an optimized tetrahedral hohlraum as a function of albedo. (b) The rms nonuniformity as a function of the ratio of hohlraum radius to capsule radius for the optimized PEPR hohlraum (with the capsule and LEH radii held fixed), illustrating the tradeoff between uniformity and radiation temperature. The albedo here is 0.8.

tradeoff is shown in Fig. 4(b) for the PEPR hohlraum, where the hohlraum radius is varied with the capsule and LEH radii held fixed. The point at a ratio of 5.09 corresponds to the design used in this article, with $T_r = 195$ eV. This can be increased to 215 eV at a ratio of 3.5 at the expense of a greater nonuniformity of 2%. These values of T_r are limited by the 18-TW laser power assumed here (approximately the peak power used for the OMEGA tetrahedral hohlraum experiments). A NIF-scale PEPR design predicts $T_r = 293$ eV at a ratio of 3.5 with a nonuniformity of 1.23% (Ref. 14).

An ignition-scale laser system irradiating an octahedral hohlraum would have lower nonuniformity than a PEPR hohlraum for a given case-to-capsule ratio because of the better geometrical symmetry. It would also benefit from more-favorable beam paths because of the elimination of small angles of incidence. While not a candidate for an ignition system, the PEPR hohlraum has the advantage that it can be used on an existing facility, offering a platform for the performance of a variety of experiments. It can be used to demonstrate high-quality spherical implosions using minimal tuning compared with the NIF. Beam phasing is not required: all beams use the same temporal pulse shape. The ratio of hohlraum-to-capsule radius may be adjusted to explore the trade-off between capsule uniformity and background radiation temperature. In addition, the anticipated ease with which near-symmetric implosions can be generated offers a platform for the examination of hot-spot physics and the development of improved diagnostics.

While the PEPR hohlraum promises to drive implosions that are substantially symmetric and 1-D, the geometry is inherently 3-D, requiring 3-D simulations for detailed hohlraum design. Many years ago, the difficulty of carrying out 3-D simulations may have favored the selection of cylindrical hohlraums, which, in spite of their uniformity issues, are well suited to 2-D modeling. The PEPR platform on OMEGA can provide a useful test bed for 3-D modeling.

Further information on this work can be found in Ref. 14.

This material is based upon work supported by the Department of Energy National Nuclear Security Administration under Award Number DE-NA0003856, the University of Rochester, and the New York State Energy Research and Development Authority.

1. J. Nuckolls *et al.*, *Nature* **239**, 139 (1972).
2. J. D. Lindl, *Phys. Plasmas* **2**, 3933 (1995).
3. R. S. Craxton *et al.*, *Phys. Plasmas* **22**, 110501 (2015).
4. C. A. Haynam *et al.*, *Appl. Opt.* **46**, 3276 (2007).
5. K. Lan *et al.*, *Phys. Plasmas* **21**, 052704 (2014).

6. K. Lan and W. Zheng, *Phys. Plasmas* **21**, 090704 (2014).
7. K. Lan *et al.*, *Phys. Plasmas* **21**, 010704 (2014).
8. D. W. Phillion and S. M. Pollaine, *Phys. Plasmas* **1**, 2963 (1994).
9. J. D. Schnittman and R. S. Craxton, *Phys. Plasmas* **3**, 3786 (1996).
10. J. D. Schnittman and R. S. Craxton, *Phys. Plasmas* **7**, 2964 (2000).
11. J. M. Wallace *et al.*, *Phys. Rev. Lett.* **82**, 3807 (1999).
12. G. R. Bennett *et al.*, *Phys. Plasmas* **7**, 2594 (2000).
13. W. A. Farmer *et al.*, *Phys. Plasmas* **26**, 032701 (2019).
14. W. Y. Wang and R. S. Craxton, *Phys. Plasmas* **28**, 062703 (2021).

Impact of Areal-Density Asymmetries on the Loss of Confinement and Ignition Threshold in Inertial Confinement Fusion Capsules

K. M. Woo and R. Betti

Laboratory for Laser Energetics, University of Rochester

In inertial confinement fusion implosion experiments, variations in the shell areal density ρR reduce the shell's inertia to confine the core pressure. Distorted capsules with large areal-density modulations decompress faster than uniform capsules in the disassembly phase. In this summary, a simple 3-D analytic hot-spot model is derived to include the effects of low-mode areal-density modulations in the ignition criterion. The generalized 3-D ignition criterion for low modes is shown to depend on both the harmonic mean and the arithmetic mean of the areal density. The “thin spots” in the shell are shown to dominate the loss of confinement as reflected by the harmonic mean definition of areal densities.

Effects of low-mode asymmetries on confinement can be described by a highly idealized ignition model. In this analysis, the 3-D hot-spot energetics in the disassembly phase are studied by a simple form of the 3-D hot-spot energy equation [Eq. (9) in Ref. 1]

$$\frac{d}{dt} \ln(PV^\gamma) = P/S_f. \quad (1)$$

Here $S_f \equiv 24 T_i^2 / (\langle \sigma v \rangle_{DT} E_\alpha)$ is approximated with a constant, valid for DT fusion reactivities $\langle \sigma v \rangle_{DT}$ within the ion-temperature range $6 < T_i < 20$ keV; $S_f \simeq 7.24$ atm s is the minimum ignition threshold;^{2,3} $\gamma = 5/3$ is the ratio of specific heat for an ideal gas; and $E_\alpha = 3.5$ MeV is the DT fusion alpha particle's initial kinetic energy; heat conduction loss and radiation loss are neglected. The time evolution of the hot-spot volume V is approximated by a second-order expansion of V in time t after the capsule is compressed to the minimum volume. Hereafter, quantities with the subscript “s” are evaluated at the stagnation time t_s , which is the moment of the minimum hot-spot volume. For igniting capsules, the hot-spot pressure P grows rapidly as the rate of alpha heating exceeds the rate of PdV work in the disassembly phase. As a result, the generalized 3-D ignition threshold is obtained, $\chi_{3-D} \equiv P_s \tau_c / S_f \rightarrow 1$ as the hot-spot pressure grows to infinity in Eq. (1). The confinement time $\tau_c = (V_s / \ddot{V}_s)^{1/2}$ is given by the second time derivative of the hot-spot volume V_s . The impact of areal-density asymmetries on the loss of confinement is hidden in the second time derivative of the hot-spot volume. It can be shown that the confinement time depends on the harmonic mean (HM) definition of areal densities:

$$\tau_c \approx \sqrt{\frac{V_s}{P_s A_s} \langle \rho R \rangle_{HM}}, \quad (2)$$

where A_s is the hot-spot surface area at stagnation. In the harmonic mean definition, the areal densities of thinner regions are weighted more than that of thicker regions. As a result, in the presence of low modes, the hot spot disassembles faster, leading to a shorter confinement time τ_c with respect to 1-D since $\langle \rho R \rangle_{HM} < \rho R_{1-D}$. The harmonic mean is the only way to account for “thin spots” (areas of ultralow areal density) in the shell that dominate the loss of confinement. If localized, thin spots do not significantly contribute to the arithmetic mean of the areal density. Measuring only the arithmetic mean would overestimate the confinement and therefore the Lawson parameter in the presence of severe asymmetries, leading to areas of ultralow areal density.

As shown in Fig. 1(a), the no- α Lawson criterion $\chi_{no-\alpha}^{3-D} = P_s \tau_c / S_f$ is shown to capture the onset of ignition for low modes $\ell = 1$ to 2 when $\chi_{no-\alpha}^{3-D} \approx 1$. The confinement time τ_c is calculated from the curvature of the temporal hot-spot volume at stagnation as the hot spot is compressed to the minimum volume. The yield amplification is shown to be well approximated by the fitting

formula $Y_{\text{amp}}^{3\text{-D}} \approx (1 - \chi_{\text{no}\alpha}^{3\text{-D}}/0.96)^{-1.14}$. In Fig. 1(b), the harmonic mean ρR of mode $\ell = 1$ is shown to degrade faster with the ion-temperature ratio $T_{\text{min}}/T_{\text{max}}$ than that of the arithmetic-mean ρR . This result implies that the 1-D values of areal densities can be inferred from the measured ion-temperature measurement asymmetry. Consequently, the degradation of the 3-D Lawson criterion $\chi_{\text{no}\alpha}^{3\text{-D}}$ for $\ell = 1$ asymmetries can be assessed as a unique function of the ion-temperature measurement asymmetry.

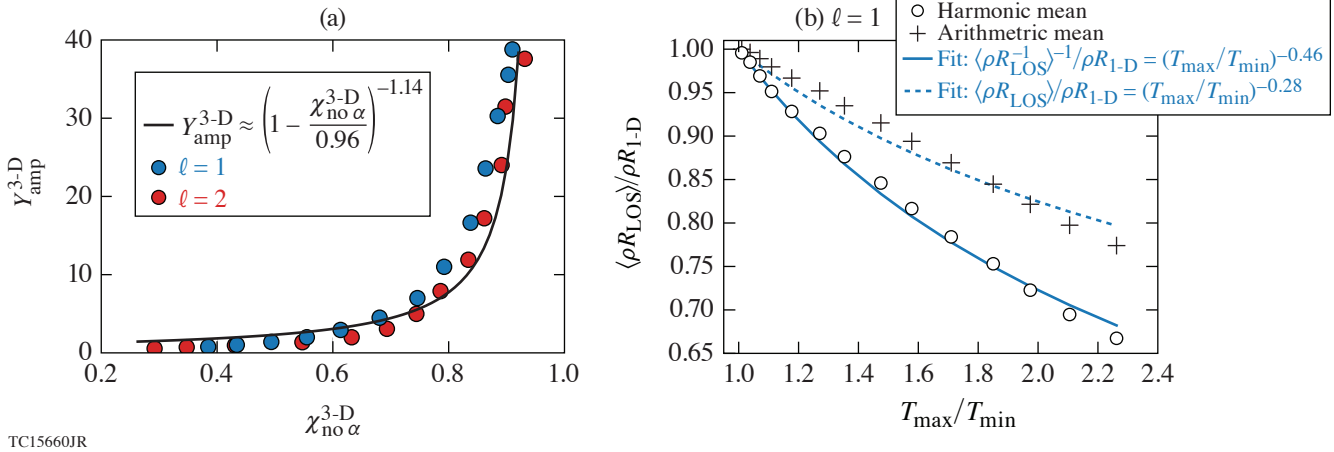


Figure 1

(a) Yield amplification as a function of the no- α Lawson criterion $\chi_{\text{no}\alpha}^{3\text{-D}}$ using the confinement time τ_c defined by the second time derivative of the hot-spot volume at the time when the capsule is compressed to the minimum volume. (b) The degradation of harmonic-mean and arithmetic-mean areal densities against the ion-temperature measurement asymmetry.

This material is based upon work supported by the Department of Energy National Nuclear Security Administration under Award Number DE-NA0003856, the University of Rochester, and the New York State Energy Research and Development Authority.

1. K. M. Woo *et al.*, Phys. Plasmas **25**, 052704 (2018).
2. R. Betti *et al.*, Phys. Rev. Lett. **114**, 255003 (2015).
3. C. D. Zhou and R. Betti, Phys. Plasmas **15**, 102707 (2008); **16**, 079905(E) (2009).

Microcoulomb ($0.7 \pm 0.4/0.2$ - μC) Laser-Plasma Accelerator on OMEGA EP

J. L. Shaw,¹ M. A. Romo-Gonzalez,^{1,2} N. Lemos,³ P. M. King,^{3,4} G. Bruhaug,¹ K. Miller,⁵ C. Dorrer,¹ B. E. Kruschwitz,¹ L. J. Waxer,¹ G. J. Williams,³ M. V. Ambat,¹ M. M. McKie,¹ M. D. Sinclair,⁵ W. B. Mori,⁵ C. Joshi,⁵ H. Chen,³ J. P. Palastro,¹ F. Albert,³ and D. H. Froula¹

¹Laboratory for Laser Energetics, University of Rochester

²California State University Stanislaus

³Lawrence Livermore National Laboratory

⁴University of Texas at Austin

⁵University of California Los Angeles

Laser-plasma accelerators (LPA's) driven by short-pulse, kilojoule-class lasers provide a path to producing compact sources of high-charge, high-energy electron beams for conversion into x-ray and positron sources. Here, we report on the first LPA driven by a short-pulse, kJ-class laser (OMEGA EP) connected to a multikilojoule high-energy-density science (HEDS) driver (OMEGA).

Experiments were performed on the OMEGA EP Laser System.¹ The laser was run with a central wavelength λ of 1054 nm at best compression (pulse duration of 700 ± 100 fs). To improve the quality of the focal spot and increase the Rayleigh length, the focusing geometry of the short-pulse laser beams was converted from its nominal $f/2$ geometry by using spatially filtered apodizers² located at the injection plane before amplification in the Nd:glass beamline to control the beam diameter and generate an $f/5$, $f/6$, $f/8$, or $f/10$ geometry. At focus, the R_{80} spot size of the laser (i.e., radius that contains 80% of the total energy) was between 11.5 and 19.9 μm . The apodized laser energy varied from 10 to 115 J, which produced on-target peak normalized vector potentials [$\alpha_0 \cong 8.6 \times 10^{-10} \sqrt{I_0(\text{W}/\text{cm}^2)} \lambda(\mu\text{m})$], where I_0 is the vacuum intensity, between 1.8 and 6.7. The apodized laser pulse was focused 500 μm inside a Mach 5 gas jet with nozzle diameters varying between 2 and 10 mm as shown in Fig. 1(c). The gas was 100% He, and the resultant plasma densities in the plateau ranged from 1.5×10^{18} to $4.5 \times 10^{19} \text{ cm}^{-3}$, depending on nozzle diameter and backing pressure.

Figure 2(a) shows that the total charge in the electron beams scales approximately linearly with a_0 . The data shown are for a 6-mm-diam nozzle operating at a plasma density of $5 \times 10^{18} \text{ cm}^{-3}$, but plasma densities of 1, 2, and $3 \times 10^{19} \text{ cm}^{-3}$ showed the same trend. This trend was also seen for 4-mm-diam nozzles operating at $1 \times 10^{19} \text{ cm}^{-3}$ and 10-mm-diam nozzles at densities of 0.2, 0.5, 1, and $3.5 \times 10^{19} \text{ cm}^{-3}$. The charge in the electron beams was calculated using the method described in Ref. 3.

Figure 2(b) shows that the charge in the electron beam scales approximately linearly with plasma density until a density of $1 \times 10^{19} \text{ cm}^{-3}$. The two data sets shown each have a different a_0 value; the rate of increase of charge with plasma density is steeper for the higher a_0 value. The highest-charge electron beam measured in this experiment, which had a charge of $707 \pm 429/224 \text{ nC}$, was produced at an a_0 of 6.6 and a plasma density of $7.5 \times 10^{18} \text{ cm}^{-3}$. Using an electron energy of 17.9 MeV, which is the weighted average electron energy of the representative electron spectrum from this experiment [Fig. 1(d)], this charge corresponds to a conversion efficiency from laser energy to electron energy of 11%. The details of this calculation can be found in Ref. 3. Of that total energy, 30%, 50%, and 90% is contained in electrons with energies below 18.5 MeV, 25.6 MeV, and 85.1 MeV, respectively. Figure 2(c) shows that when the charge scaling was extended to higher plasma densities, the maximum charge produced plateaus with density. A similar trend was seen for data taken on a 6-mm-diam nozzle for both a_0 values of 5 and 6.

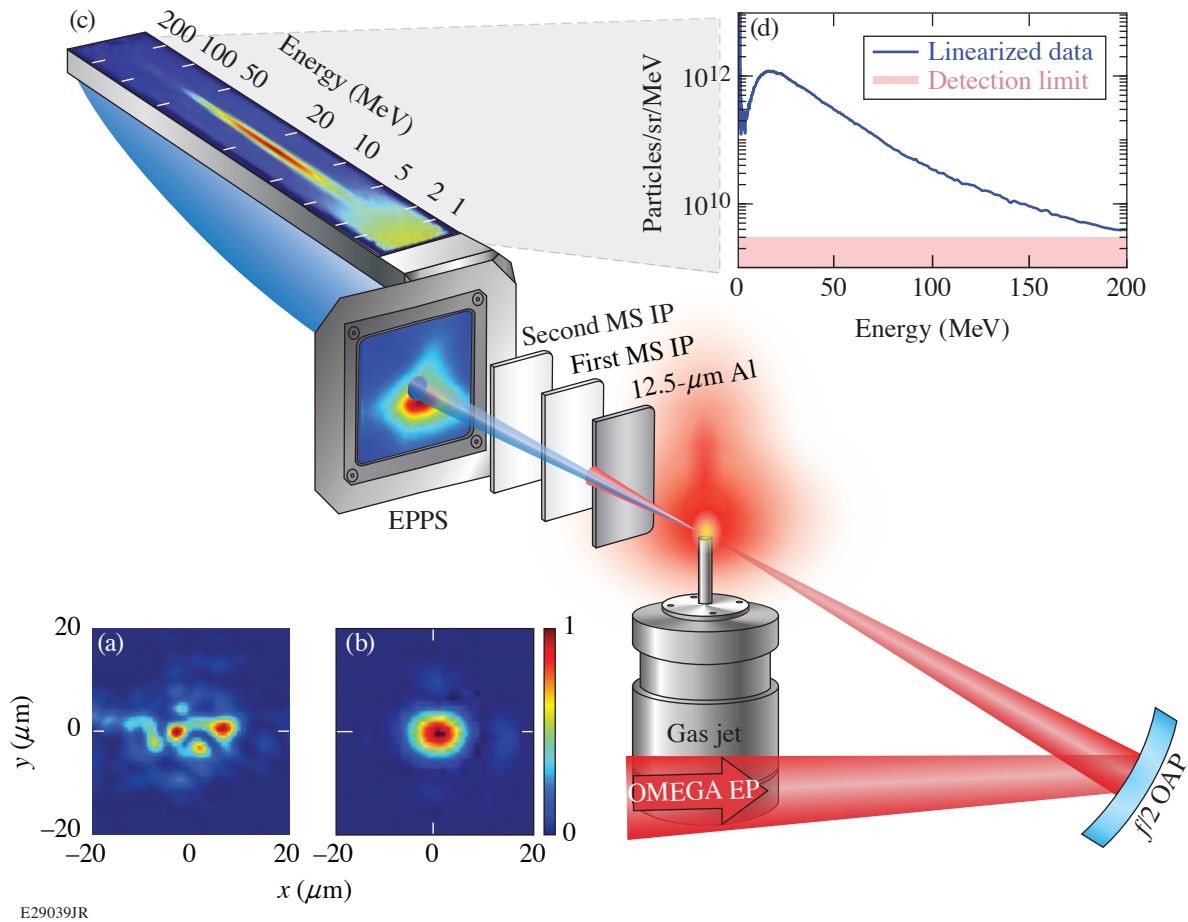


Figure 1 [(a),(b)] Examples of a target spot at the focal plane for the standard $f/2$ focus and the $f/6$ apodized focus, respectively. The peak fluence per energy for (a) and (b) is 7.9 and $11.8 \times 10^5 \text{ cm}^{-2}$, respectively. (c) Relative layout of the laser, target, and diagnostics. (d) Electron spectrum from an $a_0 = 5.1$ laser shot propagating through a plasma density of $5.4 \times 10^{18} \text{ cm}^{-3}$ generated by a 6-mm-diam nozzle. The shaded region marks the detection limit of the electron–positron–proton spectrometer (EPPS). OAP: off-axis parabola.

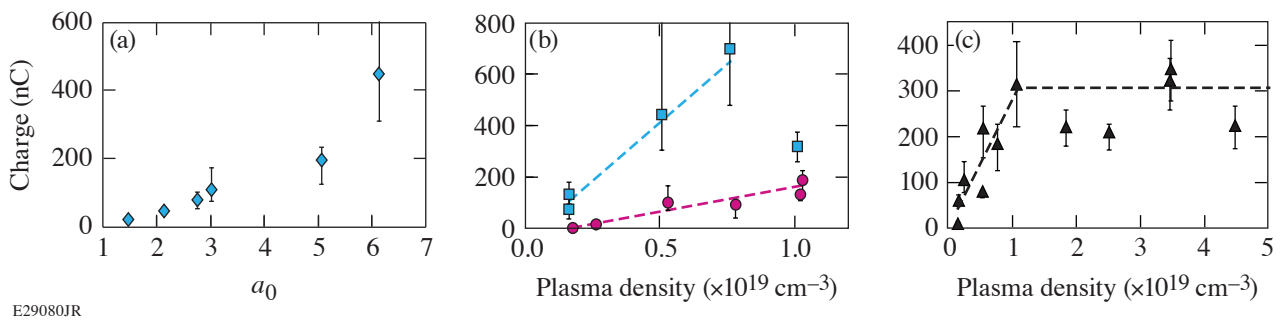


Figure 2 (a) Electron-beam charge versus a_0 for a 6-mm-diam nozzle operating at a plasma density of $5 \times 10^{18} \text{ cm}^{-3}$. Electron-beam charge as a function of plasma density (b) up to $\sim 1 \times 10^{19} \text{ cm}^{-3}$ for $a_0 \sim 3$ (magenta circles) and $a_0 \sim 6$ (blue squares) for a 6-mm-diam nozzle and (c) over the entire sampled plasma density range for $a_0 \sim 5$ and a 10-mm-diam nozzle. The dashed lines are added to guide the eye.

A microcoulomb-class, high-conversion-efficiency laser-plasma accelerator was demonstrated, providing the first laser-plasma accelerator driven by a short-pulse, kJ-class laser (OMEGA EP) connected to a multi-kJ HEDS driver (OMEGA). The produced electron beams have maximum energies that exceed 200 MeV, divergences as low as 32 mrad, record-setting charges that exceed 700 nC, and laser-to-electron conversion efficiencies up to 11%. The total charge in the electron beam is found to scale with both a_0 and plasma density. Based on these empirical scalings, higher-charge electron beams may be possible using laser systems that can deliver a_0 values larger than the maximum a_0 of 6.7 produced in this configuration while still maintaining longer f numbers and near-Gaussian, single-moded laser spots on target.

This material is based upon work supported by the U.S. Department of Energy under Awards # DE-SC0017950, DE-SC0016253, DE-SC0021057, and DE-SC0010064, the National Science Foundation under Award # PHY-1705224, the Department of Energy National Nuclear Security Administration under Award Number DE-NA0003856 and DE-NA0003873, the University of Rochester, and the New York State Energy Research and Development Authority.

1. D. D. Meyerhofer *et al.*, J. Phys.: Conf. Ser. **244**, 032010 (2010).
2. C. Dorrer and J. D. Zuegel, J. Opt. Soc. Am. B **24**, 1268 (2007).
3. J. L. Shaw *et al.*, Sci. Rep. **11**, 7498 (2021).

Cross-Beam Energy Transfer Saturation by Ion-Trapping-Induced Detuning

K. L. Nguyen,^{1,2,3} L. Yin,³ B. J. Albright,³ A. M. Hansen,^{1,2} D. H. Froula,¹ D. Turnbull,¹ R. K. Follett,¹ and J. P. Palastro¹

¹Laboratory for Laser Energetics, University of Rochester

²Department of Physics and Astronomy, University of Rochester

³Los Alamos National Laboratory

The performance of direct-drive inertial confinement fusion (ICF) implosions relies critically on the coupling of laser energy to the target plasma. Cross-beam energy transfer (CBET), the resonant exchange of energy between intersecting laser beams mediated by ponderomotively driven ion-acoustic waves (IAW's), inhibits this coupling by scattering light into unwanted directions. The variety of beam intersection angles and varying plasma conditions in an implosion results in IAW's with a range of phase velocities. Here, we show that CBET saturates through a resonance detuning that depends on the IAW phase velocity and that results from trapping-induced modifications to the ion distribution functions. For smaller phase velocities, the modifications to the distribution functions can rapidly thermalize in the presence of mid-Z ions, leading to a blue shift in the resonant frequency. For larger phase velocities, the modifications can persist, leading to a red shift in the resonant frequency. Ultimately, these results may reveal pathways toward CBET mitigation and inform reduced models for radiation-hydrodynamic codes to improve their predictive capability.

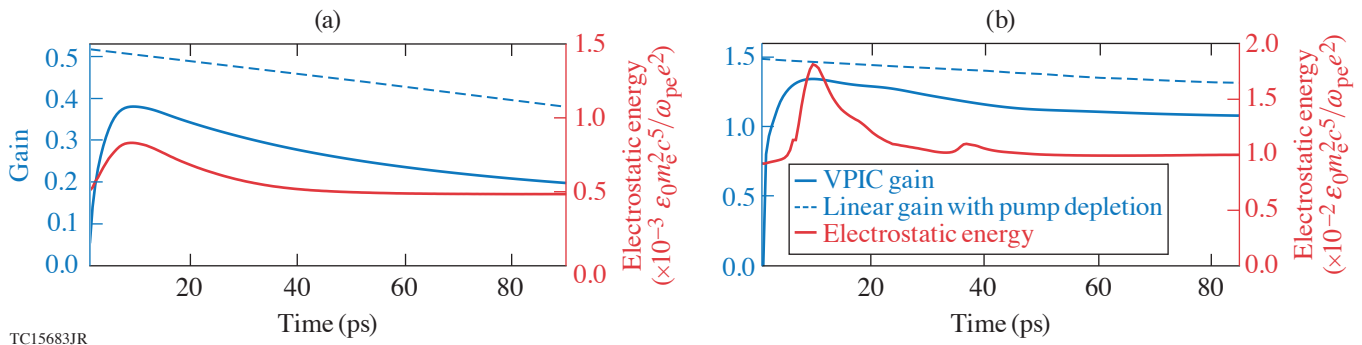
Laser-driven ICF experiments are subject to numerous nonlinear couplings between the electromagnetic waves and plasma waves. Among these couplings, CBET, the resonant exchange of energy between intersecting laser pulses mediated by ponderomotively driven IAW's, has emerged as particularly troublesome.¹ CBET inhibits the performance of both direct- and indirect-drive implosions by scattering light into unwanted directions.²⁻⁴ In direct drive, this reduces the coupling of laser energy to the capsule, while in indirect drive, it can spoil the symmetry of the x-ray illumination. Both approaches have achieved some success in mitigating CBET by using independent wavelength shifts on the beams to detune the interaction.⁵⁻⁸ More-extensive mitigation, however, requires pulses with a much larger bandwidth⁹—a technology in active development at LLE and the Naval Research Laboratory.¹⁰⁻¹²

Comprehensive, predictive models of CBET can guide both ongoing and future mitigation strategies and help define the expanded ICF design space that these strategies afford. Current integrated models of ICF implosions, using radiation-hydrodynamic simulations, typically implement simple linear models of CBET due to the computational expense associated with more-complete models. While more-sophisticated models have been developed,¹³⁻¹⁶ common approximations include ray optics (i.e., speckle and diffractive effects are ignored) and a steady-state plasma response, while neglecting nonlinear processes.¹⁷ This is in spite of a mounting body of work pointing to the importance of processes such as ion trapping, stochastic heating, two-ion decay, nonlinear sound waves, and IAW breakup.¹⁸⁻²³ Perhaps the most-convincing indication comes from a number of experiments that have observed nonlinear saturation.²⁴⁻²⁶ The most recent of these experiments, performed on the OMEGA laser, demonstrated that, at high intensities, a drop in the power transferred from a pump to seed pulse was accompanied by an $\sim 7\times$ increase in the ion temperature.²⁶

Motivated by this observation, this work provides a detailed description of the underlying physics responsible for CBET saturation for conditions relevant to these experiments. Specifically, we show that depending on the phase velocity of the IAW (v_p), CBET can saturate through two types of resonance detuning, both of which result from trapping-induced modifications to the ion distribution function. For “small” IAW phase velocities, the modifications to the distribution function rapidly thermalize in the presence of mid-Z ions, blue shifting the resonant IAW frequency. For “large” IAW phase velocities, the modifications to the

distribution function persist for a longer time and red shift the resonant frequency. These results, obtained using the collisional particle-in-cell code VPIC,²⁷ avoid many of the pitfalls associated with the reduced models used in radiation-hydrodynamic codes and provide insight into the evolution and feedback of CBET with the coronal plasma.

Figure 1 demonstrates that, in both the small and large v_p cases, CBET evolves through three stages: an initial linear stage (<5 ps), an early saturation stage (~ 5 to 20 ps), and a final late-time saturation stage (>20 ps). During each of these stages, the gain, i.e., $G = \ln(P^{\text{out}}/P^{\text{in}})$, where P^{in} and P^{out} are the probe input and output powers, tracks the electrostatic energy. The initial stage corresponds to transient growth of the IAW as the interaction attempts to evolve toward a linear, steady state.



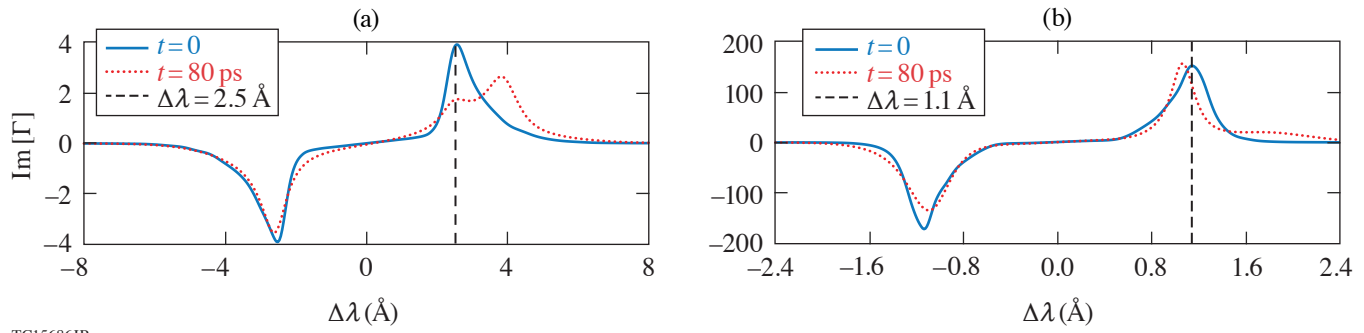
TC15683JR

Figure 1 Evolution of the CBET gain and electrostatic energy for the (a) “small” and (b) “large” phase velocity cases. The CBET gain generally tracks the electrostatic energy. Due to an interplay of IAW transverse breakup and reduced Landau damping from ion trapping, the gain saturates at a value lower than the linear, steady-state gain.

Before this state can be reached, however, the interaction becomes nonlinear and the IAW undergoes transverse breakup.²⁸ The IAW initially exhibits coherent phase fronts, but after 20 ps, the fronts have broken up into smaller transverse structures. Due to its observed correlation with ion trapping, the breakup likely results from the trapped particle modulational instability (TPMI).^{28–31} In the TPMI, the nonlinear frequency shift from ion trapping with inhomogeneity in the IAW amplitude creates variations in the phase velocity across the phase fronts. If a section of the phase front advances or retards by more than $\sim \pi/2$ with respect to adjacent sections, the front breaks. At this point, the wave amplitude crashes and the energy is transferred to the ions. The local dissipation of the wave prevents additional trapping and changes to the phase velocity. In fact, the rapid drop in electrostatic energy after ~ 10 ps results from initially trapped ions carrying away the energy of the now-broken IAW.

The rapid decay of the electrostatic energy (Fig. 1) is followed by a slow drop in the gain and marks the beginning of the late-time saturation stage. During this stage, the small and large v_p interactions exhibit strikingly different behaviors. Foremost, the gain drops substantially for small v_p and only modestly for large v_p . While both trends have their origin in ion-trapping–induced detuning, the cause of this detuning depends on the role of each ion species in collisional energy transfer and thermalization.

After ~ 50 ps, the plasma conditions and gain evolve slowly enough that CBET occurs in a quasi-steady state (Fig. 1). In this quasi-steady state, the kinetic coupling coefficient $\text{Im}[\Gamma]$, calculated using the electron and ion distribution function and averaged over the interaction region, provides the response and resonant behavior of the plasma. For small v_p , the thermalization of the H and N ions causes a gradual blue shift in the resonant IAW frequency [Fig. 2(a)]. With the fixed wavelength shift of the probe beam, the gradual blue shift in resonant frequency causes the gain to drop. In addition, the increased damping from the modified distribution function has broadened the resonance peak and lowered its maximum. For large v_p all of the collision rates are generally lower than in the small- v_p case because of the larger phase velocity. This allows the trapping-induced modifications to the distribution function to persist for a much longer time. Consistent with the trapped ion frequency shift,^{32,33} these modifications cause a red shift in the resonant frequency [Fig. 2(b)].



TC15686JR

Figure 2

The $\text{Im}[\Gamma]$, which determines the gain in the steady-state approximation, calculated using the electron- and ion-velocity distribution functions from VPIC at $t = 0$ and 80 ps. Initially, the IAW is driven on resonance for both the (a) small- (ν_p) and (b) large- ν_p cases (intersection of the dashed black lines and the peak of the solid curve). Later, (a) the increase in ion temperatures and flow blueshift the peak in the small- ν_p case, while (b) the persistent tails of the distribution function due to trapping redshift the peak in the large- ν_p case. Both detunings cause the gain to drop.

This material is based upon work supported by the Department of Energy National Nuclear Security Administration under Award Number DE-NA0003856, the University of Rochester, and the New York State Energy Research and Development Authority. LANL work was performed under the auspices of the U.S. Department of Energy by the Triad National Security, LLC Los Alamos National Laboratory, and was supported by the LANL Directed Research and Development (LDRD) program and the LANL Office of Experimental Science Inertial Confinement Fusion program. VPIC simulations were run on the LANL Institutional Computing Clusters.

1. C. J. Randall, J. R. Albritton, and J. J. Thomson, *Phys. Fluids* **24**, 1474 (1981).
2. W. Seka *et al.*, *Phys. Rev. Lett.* **89**, 175002 (2002).
3. I. V. Igumenshchev *et al.*, *Phys. Plasmas* **17**, 122708 (2010).
4. A. L. Kritcher *et al.*, *Phys. Rev. E* **98**, 053206 (2018).
5. P. Michel *et al.*, *Phys. Rev. Lett.* **102**, 025004 (2009).
6. S. H. Glenzer *et al.*, *Science* **327**, 1228 (2010).
7. J. D. Moody *et al.*, *Nat. Phys.* **8**, 344 (2012).
8. J. A. Marozas *et al.*, *Phys. Rev. Lett.* **120**, 085001 (2018).
9. J. W. Bates *et al.*, *Phys. Rev. E* **97**, 061202(R) (2018).
10. C. Dorrer, *J. Opt. Soc. Am. B* **38**, 792 (2021).
11. J. Weaver *et al.*, *Appl. Opt.* **56**, 8618 (2017).
12. R. H. Lehmburg *et al.*, *Phys. Rev. A* **102**, 063530 (2020).
13. R. K. Follett *et al.*, *Phys. Rev. E* **98**, 043202 (2018).
14. A. Colaitis *et al.*, *Phys. Plasmas* **26**, 032301 (2019).
15. A. Colaitis *et al.*, *Phys. Plasmas* **26**, 072706 (2019).
16. A. Debayle *et al.*, *Phys. Plasmas* **26**, 092705 (2019).
17. A. Debayle *et al.*, *Phys. Plasmas* **25**, 052702 (2018).
18. E. A. Williams *et al.*, *Phys. Plasmas* **11**, 231 (2004).
19. P. Michel *et al.*, *Phys. Rev. Lett.* **109**, 195004 (2012).
20. P. Michel *et al.*, *Phys. Plasmas* **20**, 056308 (2013).
21. T. Chapman *et al.*, *Phys. Rev. Lett.* **119**, 055002 (2017).
22. S. Hüller *et al.*, *Phys. Plasmas* **27**, 022703 (2020).
23. L. Yin *et al.*, *Phys. Plasmas* **26**, 082708 (2019).
24. R. K. Kirkwood *et al.*, *Phys. Rev. Lett.* **89**, 215003 (2002).
25. D. Turnbull *et al.*, *Plasma Phys. Control. Fusion* **60**, 054017 (2018).

26. A. M. Hansen *et al.*, Phys. Rev. Lett. **126**, 075002 (2021).
27. K. J. Bowers *et al.*, Phys. Plasmas **15**, 055703 (2008).
28. L. Yin *et al.*, Phys. Rev. Lett. **99**, 265004 (2007).
29. W. L. Kruer, J. M. Dawson, and R. N. Sudan, Phys. Rev. Lett. **23**, 838 (1969).
30. R. L. Dewar, W. L. Kruer, and W. M. Manheimer, Phys. Rev. Lett. **28**, 215 (1972).
31. S. Brunner and E. J. Valeo, Phys. Rev. Lett. **93**, 145003 (2004).
32. G. J. Morales and T. M. O'Neil, Phys. Rev. Lett. **28**, 417 (1972); 709(E) (1972).
33. R. L. Berger *et al.*, Phys. Plasmas **20**, 032107 (2013).

Magnetically Collimated Relativistic Charge-Neutral Electron–Positron Beams from High-Power Lasers

J. L. Peebles,¹ G. Fiksel,² M. R. Edwards,³ J. von der Linden,³ L. Willingale,² D. Mastro Simone,¹ and H. Chen³

¹Laboratory for Laser Energetics, University of Rochester

²G erard Mourou Center for Ultrafast Optical Science, University of Michigan

³Lawrence Livermore National Laboratory

Relativistic electron–positron pair plasmas are important objects for study in fundamental plasma physics; they have unique properties resulting from mass symmetry and are used to explain observations of multiple astrophysical phenomena, such as gamma-ray bursts, black holes, and active galactic nuclei.^{1–7} The creation of dense, relativistic pair plasmas in the laboratory has remained elusive due to the short positron lifetime and difficulty in producing plasmas of high-enough density.⁸ To create a useful pair plasma for laboratory astrophysics, three conditions must be satisfied: (1) high-energy (MeV) particles must be confined longer than the plasma time scale of interest; (2) the plasma dimensions must be significantly greater than the Debye length; and (3) the plasma must be charge neutral. To date, there are limited experiments that produce high-temperature pair plasmas and high-flux pair jets required to simulate astrophysical phenomena.^{9,10}

One method to generate energetic positron–electron pairs relevant to laboratory astrophysics experiments is to use ultrashort high-intensity lasers. Previous experiments have produced jets of positrons and electrons with MeV energies in a small volume (<3 mm³), with particle densities of about 10¹⁵ cm^{–3} and 10¹³ cm^{–3} at the source for electrons and positrons, respectively.^{11,12} These positrons are generated through the Bethe–Heitler process, whereby bremsstrahlung γ rays from high-energy electrons decay into electrons and positrons. So far, of the three plasma conditions, the confinement condition (2) has been achieved experimentally using an imposed magnetic field,¹² and the neutrality condition (3) has been achieved in another experiment using a very thick, high-Z target to generate equal numbers of electrons and positrons with >5-MeV energy.¹³ No previous experiment has produced a high-temperature, neutral pair-plasma beam; many experiments have produced jets with electron density exceeding the positron density by severalfold but have not confined or collimated them for long periods.

Magnetic focusing has provided a promising path toward satisfying the conditions of charge neutrality and MeV confinement. Indeed, previous experiments demonstrated the use of an externally imposed magnetic field to collimate electrons and positrons for measurement.^{14,15} These experiments measured nearly 70 \times as many positrons on magnetized shots as unmagnetized shots due to collimation by the magnetic field. Ratios of electrons to positrons ranged from 10 to 3 for various shots during the experiment, but did not reach charge neutrality. This improvement suggests that externally imposed magnetic fields have great potential to collimate fully neutral pair plasmas. Here we report the measurement of a neutral, collimated electron–positron beam by utilizing recent upgrades to the pulsed-power system known as MIFEDS (magneto-inertial fusion electrical discharge system).¹⁶ This represents a significant step toward generating charge-neutral electron–positron pair-plasma jets in the laboratory.

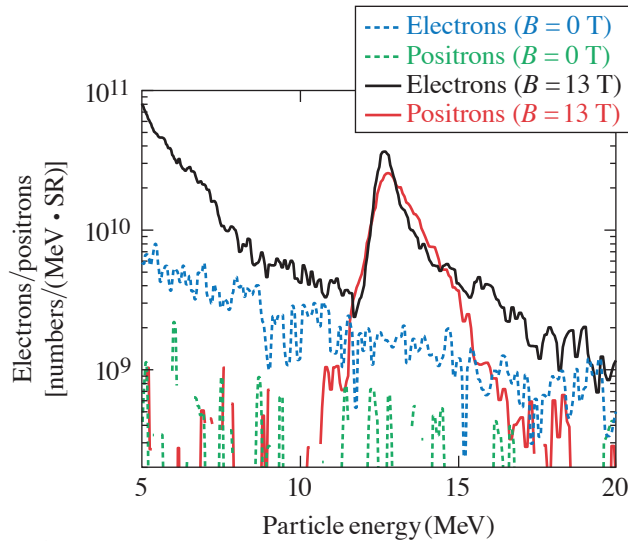
Five magnetized shots and one unmagnetized reference shot were carried out in the experiment on the OMEGA EP laser, which used 10-ps pulses with $\lambda = 1054$ -nm light, focused on a 500- μ m-diam, 20- μ m-thick gold disk. The laser energy was 900 \pm 20 J (intensity = 9 \times 10¹⁸ W/cm²). It should be noted, however, that MIFEDS-related debris and copper deposition on laser optics caused an estimated loss of energy and intensity of 15% to 20% after the first magnetized shot, leading to on-target energies in the range of 770 \pm 40 J with an intensity of 7 \pm 1 \times 10¹⁸ W/cm². At these conditions, the positron yield can be estimated from Myatt *et al.*¹⁷ Assuming a laser energy of about 800 J and a laser-to-electron conversion efficiency of 30%,¹⁸ the expected positron yield is about

7.5×10^{10} in total, with a density of approximately 3×10^{10} positrons/sr since without collimation, the positrons diverge with an angle of 1 to 2 sr (Ref. 16). The combination of positron number and divergence results in a measurement that is barely above the detection threshold of the spectrometer.

In order to magnetize shots, field-generating coils were set up in a magnetic mirror configuration with wire loops 14 mm apart with an inner diameter of 10 mm. These produced a field of up to 13 T at the ends of the mirror and 5 T in the center near the source. For two of the five shots, the MIFEDS charge voltage was tuned to examine a lower field of approximately 4 T and 9 T at the center and edges, respectively. The energy distributions of electrons and positrons were measured with an electron–positron–proton spectrometer (EPPS), which was placed along the primary magnetic-field axis. The magnetic field axis and spectrometer collection region were aligned perpendicular to the laser and target axis.

Initial particle-tracing simulations, carried out with the multiphysics code COMSOL, show that when the field is imposed, particles with energy less than 2.5 MeV are completely confined radially. For higher-energy particles, those with a small initial pitch angle relative to the mirror field axis will be well focused and collimated by the magnetic field due to slight deflections. Particles of roughly 13 MeV from a point source 8 mm away from the coil would be collimated, given the coil radius and peak magnetic-field profile used on the experiment. For particles with energy higher or lower than this optimum energy, particles will be overfocused prior to reaching the spectrometer or not focused at all.

These simulation predictions were borne out in the experiment, which consisted of five magnetized shots (three at high field and two at low field) and one unmagnetized reference shot. In the no-field case, almost no positrons were measured above noise level (as expected) and electrons followed a single temperature spectrum across all energies of interest. When the field was applied, positrons of equal energy and number to the electrons were measured. The positron signal peaked at 13 MeV (Fig. 1), which matches the estimated best focus from the initial simulations. Two shots were also performed using a weaker, 9-T field, which decreased the peak energy of focused particles to 10 MeV, while still maintaining an even ratio between positrons and electrons. These collimated beams of pair particles were maintained over the 50-cm distance between the experiment and the spectrometer.



E29500JR

Figure 1

Electron and positron spectra measured using the field axis EPPS. With no field (dotted curves), only electrons characterized by a single slope temperature were measured along this direction. When the 13-T collimating field was applied, nearly identical quantities of electrons and positrons peaked at around 13-MeV energy were measured.

While these measurements of charge-neutral, focused electron–positron beams represent a step forward toward a true pair plasma, the densities are still insufficient for many astrophysics purposes. To effectively create scaled astrophysical shocks within the pair plasma, densities of at least 10^{13} cm^{-3} and energies of over 10 MeV are required. While our jet contains energies of 13 MeV and is collimated over a long distance ($>50 \text{ cm}$), the density is considerably lower—roughly $2 \times 10^8 \text{ cm}^{-3}$ based on the assumption that the particles are accelerated throughout the laser pulse. To increase density toward meeting the confined pair-plasma goals, future work will concentrate on increasing the density of the pair-plasma beam. Thicker gold or microstructured targets can be used in

the future (similar to those used in other pair-plasma-generating experiments¹⁴), which will substantially increase the conversion to positrons. Further upgrades to MIFEDS will also be applied in order to increase the energy range for confined or collimated particles.

This material is based upon work supported by the Department of Energy National Nuclear Security Administration under Award Number DE-NA0003856, the University of Rochester, and the New York State Energy Research and Development Authority. This work was also performed under the auspices of the U.S. Department of Energy by Lawrence Livermore National Laboratory under Contract DE-AC52-07NA27344 and was supported by the LDRD Program under Project No. 20-LW-021.

1. E. Fermi, Phys. Rev. **75**, 1169 (1949).
2. A. R. Bell, Mon. Not. R. Astron. Soc. **182**, 147 (1978).
3. R. D. Blandford and J. P. Ostriker, Astrophys. J. **221**, L29 (1978).
4. P. Mészáros, Annu. Rev. Astron. Astrophys. **40**, 137 (2002).
5. J. F. C. Wardle *et al.*, Nature **395**, 457 (1998).
6. A. Spitkovsky, Astrophys. J. Lett. **673**, L39 (2007).
7. G. Weidenspointer *et al.*, Nature **451**, 159 (2008).
8. V. Tsytovich and C. B. Wharton, Comments Plasma Phys. Control. Fusion **4**, 91 (1978).
9. A. Bret, L. Gremillet, and M. E. Dieckmann, Phys. Plasmas **17**, 120501 (2010).
10. C. M. Surko and R. G. Greaves, Phys. Plasmas **11**, 2333 (2004).
11. H. Chen *et al.*, Phys. Rev. Lett. **105**, 015003 (2010).
12. H. Chen *et al.*, High Energy Density Phys. **7**, 225 (2011).
13. G. Sarri *et al.*, Nat. Commun. **6**, 6747 (2015).
14. H. Chen *et al.*, Phys. Plasmas **21**, 040703 (2014).
15. D. H. Barnak *et al.*, Bull. Am. Phys. Soc. **59**, BAPS.2014.DPPTO6.13 (2014).
16. G. Fiksel *et al.*, Rev. Sci. Instrum. **86**, 016105 (2015).
17. J. Myatt *et al.*, Phys. Rev. E **79**, 066409 (2009).
18. P. M. Nilson *et al.*, Phys. Rev. Lett. **105**, 235001 (2010).

Enhancing Positron Production Using Front-Surface Target Structures

S. Jiang,¹ A. Link,¹ D. Canning,² J. A. Fooks,³ P. A. Kempler,⁴ S. Kerr,¹ J. Kim,⁵
M. Krieger,² N. S. Lewis,⁴ R. Wallace,¹ G. J. Williams,¹ S. Yalamanchili,⁴ and H. Chen¹

¹Lawrence Livermore National Laboratory

²Laboratory for Laser Energetics, University of Rochester

³General Atomics

⁴California Institute of Technology

⁵Center for Energy Research, University of California San Diego

Electron–positron pair plasmas generated by laser–solid interactions offer a wide range of potential applications in different fields, including astrophysics, material science, biology, etc. We report a target design that produced a substantial gain in relativistic electron–positron pair production using high-intensity lasers and targets with large-scale microstructures on their surface. Compared to an unstructured target, a selected Si microwire array target yielded a near-100% increase in the laser-to-positron conversion efficiency and produced a 10-MeV increase in the average emitted positron energy under nominally the same experimental conditions.

The experiment was performed on the OMEGA EP Laser System. A schematic diagram of the experimental setup is shown in Fig. 1(a). The target was irradiated using a short-pulse laser with a wavelength of $1.053\ \mu\text{m}$, an energy of 500 J, and a pulse length of approximately 700 fs. The peak intensity was estimated to be $4.5 \times 10^{20}\ \text{W}/\text{cm}^2$. Figures 1(b) and 1(c) show scanning electron microscope (SEM) images of two different target structures used in the experiment. Structure 1 was optimized through particle-in-cell (PIC) simulations of the hot-electron temperature prior to the experiment. For comparison, structure 2 showed detrimental effects on electron energies in simulations. The structures were made of Si microwires and were embedded in a thin plastic layer and then glued to a 1-mm-thick Au backing layer. The high-energy electrons generated and guided by the surface structures transport through the thick Au layer and induce pair production. The positron and electron spectra were measured by a spectrometer on the back side of the target along the laser direction (which was also the target normal direction).

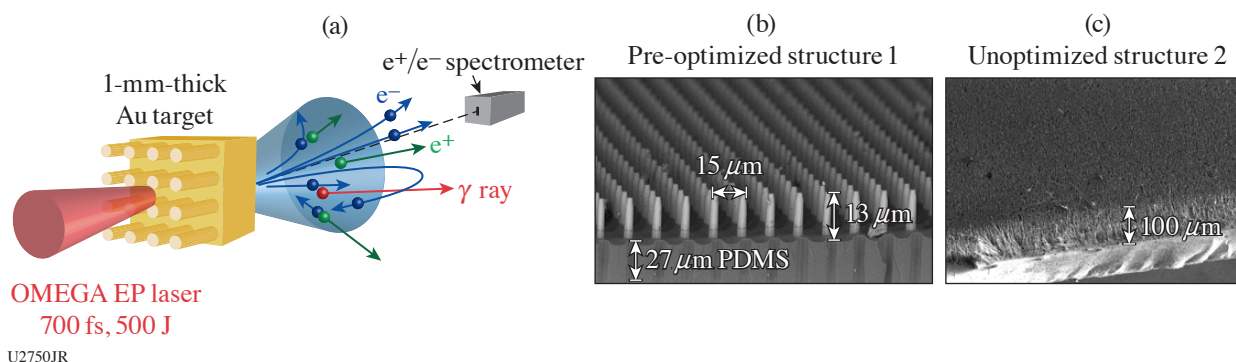


Figure 1

(a) Schematic diagram of the experimental setup; (b) SEM image of the pre-optimized target structure 1; (c) SEM image of the unoptimized structure 2. PDMS: polydimethylsiloxane.

The measured spectra for both types of structured targets as well as a flat unstructured target are shown in Fig. 2. Target structure 1 generated about 50% more positrons than the regular flat target, and its laser-to-positron conversion efficiency increased by $\sim 97\%$. The spectrum peak also shifted from ~ 50 MeV for the flat target to ~ 60 MeV for structure 1. Structure 2 showed fewer as well as much lower energy positrons, in accordance with expectations since the length and spacing of the microwires encumber the laser focusing. The electron spectrum from structure 2 also showed the same trend, in agreement with the positron measurements. The electron spectra from the flat unstructured target and from structure 1 were mutually similar, however, with both having an electron temperature of about 21 MeV.

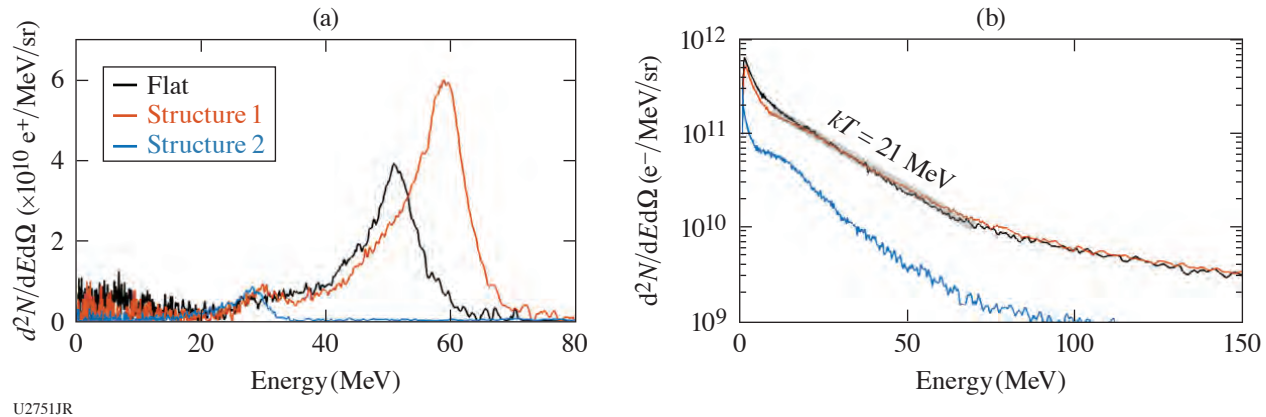


Figure 2 Experimentally measured spectra for (a) positrons and (b) electrons. Different colors indicate the results from different targets under the same laser conditions.

We have performed multiple simulations to model the entire process and explain the observed phenomena. We adopted a two-stage approach since the laser–plasma interaction was modeled with a 2-D Cartesian PIC simulation and the electron transport and pair production process was modeled with a 2-D cylindrical simulation. The simulations successfully reproduced the experimental results. Compared to a flat target, structure 1 generated more high-energy (tens to hundreds of eV) electrons. Two acceleration mechanisms are responsible for these electrons, including the loop-injected direct acceleration,¹ which is associated with any targets having moderate scale-length pre-plasma, and the structure-guided direct laser acceleration, which occurs only with the structured target.² We have also found strong Weibel instabilities near the critical-density surface for both target types, which largely widens the electron divergence, explaining why the electron spectra measured at 0° look similar for both the flat and the structure 1 target. The energy of positrons is largely determined by the sheath field on the back side of the target. The simulations suggested that the integrated sheath voltage for structure 1 is about 10 MV higher than for the flat target, which is consistent with the measured energy difference between their positron peaks.

In summary, front-surface target structures have been shown experimentally to substantially enhance the positron yield and energy. The follow-up simulations explain the entire process of how the laser–plasma interaction that is manipulated by the target structure affects the yield and energy of positrons. The agreement between the simulated and experimental spectra indicates the possibility of further target optimization using two-stage PIC simulations.

We thank the OMEGA EP team for laser operation and technical support. This work was performed under the auspices of the U.S. DOE by LLNL under Contract DEAC5207NA27344, and funded by LDRD (#17ERD010). The fabrication of Si microwire arrays was supported through the Office of Science of the U.S. Department of Energy under Award No. DE- SC0004993. Additional support for this work was provided by the Lockheed Martin Corporation (Award 4103810021). We thank the staff at the Kavli Nanoscience Institute at Caltech for their technical assistance with fabrication.

1. A. G. Krygier, D. W. Schumacher, and R. R. Freeman, *Phys. Plasmas* **21**, 023112 (2014).
2. S. Jiang *et al.*, *Phys. Rev. Lett.* **116**, 085002 (2016).

Optical Thomson Scattering

D. H. Froula, J. P. Palaastro, and R. K. Follett

Laboratory for Laser Energetics, University of Rochester

Introduction

Thomson scattering provides a direct observation of electron motion in a plasma by encoding their velocities on the frequency spectrum of the scattered light. By propagating a beam of photons (ω_0, \mathbf{k}_0) through a plasma and isolating the Thomson-scattering volume collected into a spectrometer (Fig. 1), a spatially resolved measurement of the plasma conditions can be determined from the scattered frequency spectrum (ω_s, \mathbf{k}_s) (Ref. 1). The scattered-power spectrum observed by the detector is given by

$$\frac{dP_s}{d\omega_s} = \frac{P_i r_0^2 L d\Omega}{2\pi} \left(1 + \frac{2\omega}{\omega_0}\right) n_e S(\mathbf{k}, \omega), \quad (1)$$

where $r_0^2 = 7.95 \times 10^{-26}$ cm is the classical electron radius, L is the length of the scattering volume along the probe beam, $\mathbf{k} = \mathbf{k}_s - \mathbf{k}_0$, $\omega = \omega_s - \omega_0$, $d\Omega$ is the solid angle of the collected scattered photons, and P_i is the average incident laser power. The density fluctuations of the plasma around its average density dictate the primary shape of the scattered spectrum through the dynamic structure factor. For a collisionless plasma with no magnetic fields affecting the motion of the particles, the dynamic structure factor is

$$S(\mathbf{k}, \omega) = \frac{2\pi}{k} \left| 1 - \frac{\chi_e}{\varepsilon} \right|^2 f_e\left(\frac{\omega}{k}\right) + \sum_j \frac{2\pi}{k} \frac{Z_j^2 n_j}{n_e} \left| \frac{\chi_e}{\varepsilon} \right|^2 f_j\left(\frac{\omega}{k}\right), \quad (2)$$

where f_e and f_j are the normalized 1-D electron and ion-velocity distribution functions, respectively, projected along the scattering vector (\mathbf{k}), Z_j is the average charge of the j th ion species, $n_e = \sum_j n_j Z_j$, and n_j is the density of j th ion species. The longitudinal dielectric function is

$$\varepsilon = 1 + \chi_e + \sum_j \chi_j, \quad (3)$$

where the kinetic plasma susceptibilities are given by

$$\chi_e(\mathbf{k}, \omega) = \frac{4\pi e^2 n_e}{m_e k^2} \int_{-\infty}^{\infty} d\mathbf{v} \frac{\mathbf{k} \cdot \partial f_e / \partial \mathbf{v}}{\omega - \mathbf{k} \cdot \mathbf{v}}, \quad (4)$$

$$\chi_j(\mathbf{k}, \omega) = \frac{4\pi Z_j^2 e^2 n_j}{m_j k^2} \int_{-\infty}^{\infty} d\mathbf{v} \frac{\mathbf{k} \cdot \partial f_j / \partial \mathbf{v}}{\omega - \mathbf{k} \cdot \mathbf{v}}, \quad (5)$$

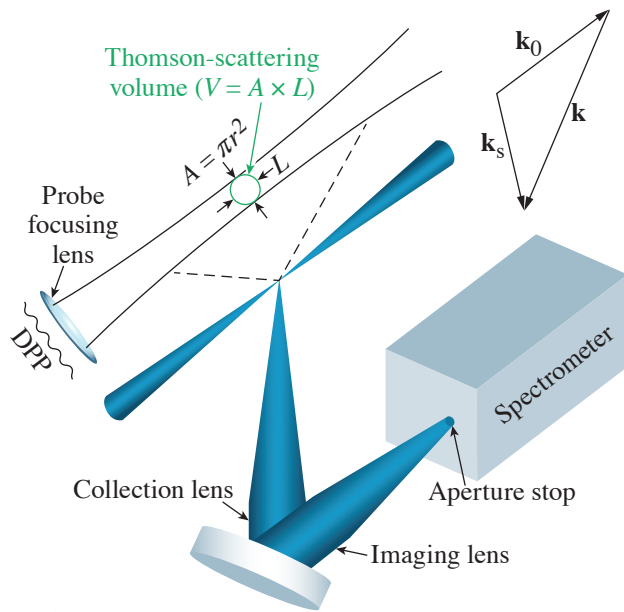


Figure 1

A typical Thomson-scattering system is shown where the probe laser beam propagates through a distributed phase plate (DPP) before being focused to an area (A) at the Thomson-scattering volume. An aperture stop is imaged into the plasma to define the Thomson-scattering volume along the propagation of the probe beam (L).

E29539JR

The scattering spectrum can be used to measure the electron distribution function, which is most evident in the high-frequency noncollective Thomson-scattering regime. Here the collective motion of the electrons is heavily damped and the power scattered at a particular frequency is proportional to the number of electrons with a velocity that Doppler shifts the frequency of the probe laser to the measured frequency [Fig. 2(a)]. In this strong damping regime, where the scattering parameter $\alpha \equiv 1/k\lambda_{De} \ll 1$ ($\lambda_{De}^2 = \kappa T_e / 4\pi e^2 n_e$ is the electron Debye length), Eq. (1) is reduced to light that is scattered from an ensemble of uncorrelated electrons,

$$\frac{dP_s}{d\omega_s} = \frac{P_1 r_0^2 L d\Omega}{2\pi} \left(1 + \frac{2\omega}{\omega_0}\right) n_e f_e(\omega/k). \quad (6)$$

From here it is evident that the noncollective spectrum provides a direct measurement of the electron distribution function, but in practice, the small scattering cross section of the electron and the small number of electrons at high velocities lead to low signal-to-noise, typically limiting this technique to measuring electrons in the bulk of the distribution function.

It is also possible to measure the electron distribution function in the regime where the high-frequency scattering spectrum is governed by the collective electron motion introduced by weaker damping of the density fluctuations.^{2,3} In this collective regime, the thermal particle motion drives a rich spectrum of fluctuations, which when probed, can present themselves in the scattering spectrum as peaks shifted around the incident frequency of the laser (Fig. 2). As charged particles propagate through the plasma, they leave electrostatic fluctuations in their wake. The amplitude of each fluctuation is determined by the balance of its damping rate with the rate at which it is driven by the plasma particles. The high-frequency electron plasma wave fluctuations start to play an important role in the scattering spectrum when $\alpha \sim 2$, but when the fluctuations are more weakly damped ($\alpha \geq 2$), the resonant features have separated clearly from the noncollective scattering spectrum [Fig. 2(a)]. For the low-frequency fluctuations [Fig. 2(b)], there are similar regimes, but related to the ion motion. The transition between the collective and noncollective regime in a collisionless plasma is governed by the ion Landau damping, and the collective low-frequency regimes occur for the scattering parameter $\alpha > (ZT_e/3T_i - 1)^{-1/2}$. For $ZT_e/3T_i < 3$, the fluctuations are heavily damped by the ions.

The frequency of these resonant peaks can be found approximately by solving the dispersion relation ($\varepsilon = 0$) for the natural modes of the plasma by finding the real parts of the roots of the dielectric function [Eq. (3)], which is where one can see the power of collective Thomson scattering in determining the plasma conditions. Assuming Maxwellian electron distribution functions and weakly

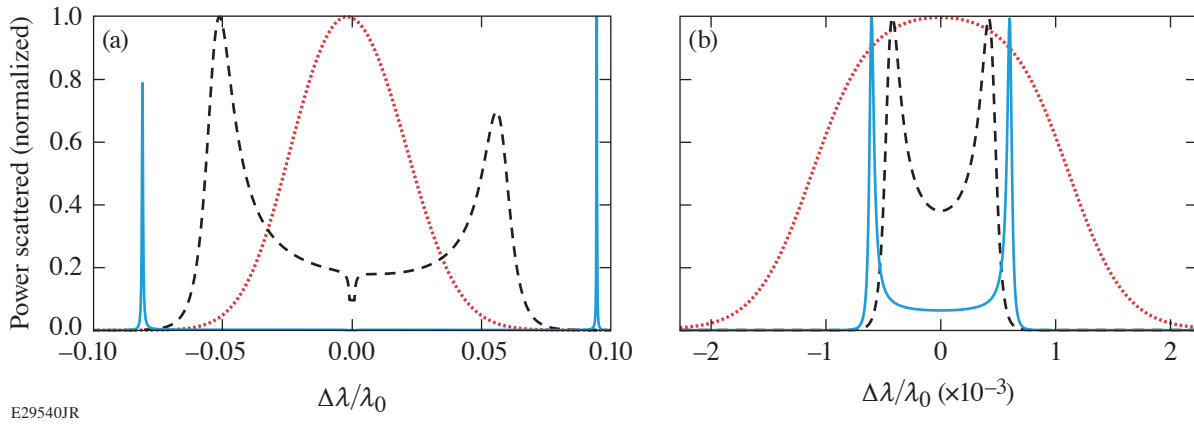


Figure 2

(a) High-frequency spectrum calculated from Eq. (1) in the heavily damped noncollective regime, $\alpha = 0.25$ (red dotted curve); mildly damped collective regime, $\alpha = 2.0$ (black dashed curve); and weakly damped collective regime, $\alpha = 4.0$ (blue solid curve). The temperature was maintained at $T_e = 100$ eV and the density was scaled $n_e = 1 \times 10^{17}$ cm $^{-3}$ (red), $n_e = 6 \times 10^{18}$ cm $^{-3}$ (black), $n_e = 2.5 \times 10^{19}$ cm $^{-3}$ (blue). The low-frequency spectrum calculated from Eq. (1) in the heavily damped noncollective regime, $ZT_e/T_i = 0.5$ (red); mildly damped collective regime $ZT_e/T_i = 3.5$ (black); and weakly damped collective regime $ZT_e/T_i = 10$ (blue). The scattering parameters $\alpha = 2$ and $T_e/T_i = 10$ were held constant. For all calculations, the angle between incident and scattered light was held constant ($\theta = 90^\circ$).

damped fluctuations, the real part of the dispersion relation for the ion-acoustic waves simplifies to $\omega_{\text{iaw}} \simeq k \sqrt{[(Z\kappa T_e + 3\kappa T_i)/m_i]}$, in the low-frequency spectrum, and the real part of the high-frequency part of the dispersion relation, corresponding to the electron plasma waves simplifies to $\omega_{\text{epw}}^2 = \omega_{\text{pe}}^2 + 3\kappa T_e k^2 / m_e$, where $\omega_{\text{pe}}^2 = 4\pi n_e e^2 / m_e$ is the electron plasma frequency. Thomson-scattered light from these collective electron motions generates constructive interference at the detector plane, and the frequency of this interference can be directly related to the plasma conditions through the plasma dispersion relations; note that measuring the difference between the frequency of the laser and the peak features in the spectrum ($\omega = \omega_s - \omega_0 = \Delta\omega$) is a measure of the plasma conditions through the associated dispersion relations ($\Delta\omega/\omega_0 \approx \Delta\lambda/\lambda_0$).

Collective Thomson scattering is a powerful diagnostic regime used to overcome background radiation because of the need to resolve only the frequencies of the spectral peaks. This is in contrast with the noncollective regime, where the shape of the scattering spectrum is used to infer the plasma conditions, therefore challenging one to understand the background radiation spectrum and the wavelength sensitivity of the diagnostic. In practice, modern collective Thomson-scattering systems can resolve the complete spectrum, providing detailed measurements of the electron distribution functions,⁴ electron temperatures, ion temperatures,^{5,6} plasma flow velocities, and electron densities.^{7,8}

Laser Beam Propagation

The small Thomson-scattering cross section is one of the most-challenging aspects of Thomson scattering. Integrating Eq. (1) over frequency provides the total power scattered, $P_s/P_i \simeq (8\pi/3)n_e r_0^2 L d\Omega \sim 10^{-12}$ for typical parameters ($n_e = 10^{19}$ cm $^{-3}$, $L = 50$ μm , $d\Omega = 10^{-4}$). To overcome this small cross section, lasers are used to deliver sufficient power to the Thomson-scattering volume, but the laser power must be balanced against laser-plasma instabilities that can prevent the laser beam from reaching the Thomson-scattering volume. One of the most-limiting instabilities is ponderomotively driven self-focusing. For a laser beam with a Gaussian spatial profile, the self-focusing power threshold is $P_c = 3 \times 10^7 [T_e(\text{keV})/n_e/n_c]$, where $n_c = m_e \omega_0^2 / 4\pi e^2$ is the critical density for the probe laser.

By limiting the power of the laser to the critical power for self-focusing, the maximum power scattered is given by

$$P_s^{\text{max}}(\text{W}) \simeq 4 \times 10^{-29} \omega_0^2 T_e (\text{eV}) L (\text{cm}) d\Omega. \quad (7)$$

To demonstrate how restrictive this condition is on the parameter space accessible by Thomson scattering, the signal-to-noise can be calculated by assuming Poisson statistics, $S/N \approx \sqrt{P_s^{\max} \Delta t / \hbar \omega_0}$, where \hbar is Planck's constant.⁹ For typical conditions ($T_e = 100$ eV, $L = 10^{-2}$ cm, $d\Omega = 10^{-4}$, $\omega_0 = 3.8 \times 10^{15}$ 1/s), spread evenly over 100 resolution units in an ideal system suggests $S/N \sim 10$. From here, it is evident that Thomson scattering requires high electron temperatures, long integration times (Δt), large Thomson-scattering volumes along the axis of the probe beam (L), or large solid angle collection optics ($d\Omega$) to increase the signal-to-noise, but each of these parameters has significant constraints within the experimental design.

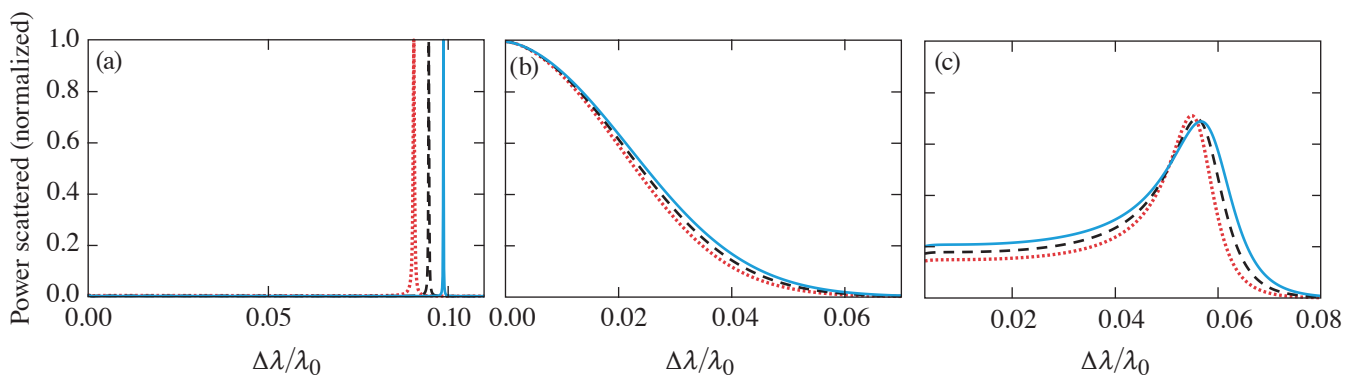
Intuitively one would expect higher laser powers or higher densities to improve the signal-to-noise, but once the laser power has reached the critical power for self-focusing, the beam will not propagate well to the Thomson-scattering volume. Increasing the density does not help because the increased signal that results from the higher density is directly compensated by the need to reduce the laser power to remain below the critical power for self-focusing. One way to overcome self-focusing, typically at the cost of increasing the Thomson-scattering volume, is to use a DPP.¹⁰ A DPP introduces spatial phase modulation across the laser beam prior to the focusing lens. This phase increases the diameter of the laser spot by distributing the laser power into many speckles, which increases the self-focusing threshold by a factor of ~ 100 (Ref. 9).

Thomson Scattering from a Maxwellian Plasma

Figure 2 shows the high-frequency and low-frequency parts of the Thomson-scattering spectrum calculated using Eq. (1) assuming Maxwellian ion and electron distribution functions. To measure these spectra, a typical Thomson-scattering instrument uses two spectrometers to independently resolve the high-frequency and low-frequency regimes.^{11,12} The high-frequency spectrum requires lower dispersion to spread the $\Delta\lambda/\lambda_0 \sim 0.1$ spectrum over a detector with approximately 200 resolution units. This can be achieved with a 1/3-m spectrometer with a 150-grooves/mm grating. Resolving the low-frequency spectrum requires a high-dispersion system that can resolve the separation between the ion-acoustic peaks $\Delta\lambda/\lambda_0 \sim 10^{-3}$ over at least 20 resolution units. This can be achieved with a 1-m spectrometer with a 2400-grooves/mm grating. Often the spectrometers are coupled to optical streak cameras to measure the evolution of the plasma conditions. In these systems, the temporal resolution is determined by the pulse-front tilt introduced by the spectrometers, which is typically of the order of 100 ps (Ref. 13). By trading unrealized spectral resolution for improved time resolution, the temporal resolution can be optimized to the Heisenberg limit.^{14,15}

1. High-Frequency Fluctuations—Electron Plasma Waves

Figure 3 shows the sensitivity of the high-frequency spectrum to the plasma conditions in three different scattering regimes. In the weakly damped regime, the scattering features are very narrow and the sensitivity of the frequency of their peaks provides an accurate measure of the electron density. In this regime, the width of these features is typically dominated by instrument



E29541JR

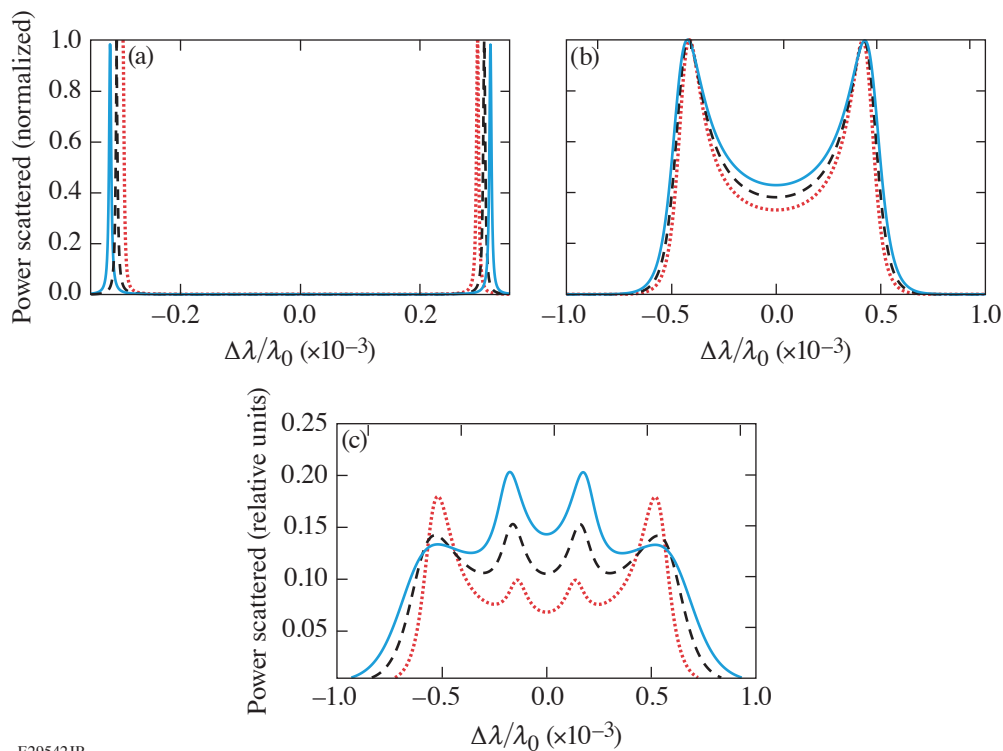
Figure 3

The sensitivity of the spectrum shown in Fig. 2 to (a) the electron density in the weakly damped regime and electron temperature in (b) the strongly damped regime and (c) the mildly damped regime. The parameters were varied around the central value (black) by +10% (blue) and -10% (red).

broadening and density gradients within the Thomson-scattering volume.¹⁶ By reducing the scattering parameter such that the waves are mildly damped, their width can be increased significantly beyond typical broadening due to gradients and the shape becomes an accurate measurement of the electron temperature, while the peak location remains a measure of the electron density. Further increasing the damping results in a noncollective spectrum where the shape of the scattering spectrum represents the electron distribution function.

2. Low-Frequency Fluctuations—Ion-Acoustic Waves

Figure 4(a) shows the sensitivity of the low-frequency spectrum in the collective regime to the product ZT_e . In this weakly damped regime, the scattering features are very narrow and the sensitivity of their peak location in frequency provides an accurate measure of ZT_e , provided $ZT_e \gg 3T_i$. When this condition is not met, it is convenient to work in the mildly collective regime, where the shape of the ion-acoustic peaks can be resolved, providing a measure of the ion temperature [Fig. 4(b)]. Another technique that is often used to measure the ion temperature in low- Z plasmas is to introduce a small fraction of higher- Z atoms.^{5,6} When the ratio of atomic number to the average ionization (A/Z) is sufficiently different between the two species, additional low-frequency modes are resolvable in the scattering spectrum [Fig. 4(c)].¹⁷ From the relative amplitudes of these two modes, an accurate measure of the ion temperature can be obtained.^{8,18}



E29542JR

Figure 4

Low-frequency spectrum (a) for a single species nitrogen plasma, where $ZT_e = 630$ eV (red), $ZT_e = 700$ eV (black), and $ZT_e = 770$ eV (blue), where $T_i = 20$ eV. (b) In the mildly damped regime, the width of the ion feature can be used to measure the ion temperature: $T_i = 18$ eV (red), $T_i = 20$ eV (black), $T_i = 22$ eV (blue), and $ZT_e = 700$ eV. (c) Introducing 5% nitrogen ($Z = 7$) to a hydrogen ($Z = 1$) plasma provides two low-frequency modes, and their relative amplitudes provide an accurate measure of the ion temperature: $T_e/T_i = 5$ (red), $T_e/T_i = 3.3$ (black), $T_e/T_i = 2.5$ (blue); and $T_e = 100$ eV was held constant. For all calculations, $\alpha = 2$.

This material is based upon work supported by the Department of Energy National Nuclear Security Administration under Award Number DE-NA0003856, the University of Rochester, and the New York State Energy Research and Development Authority. The support of DOE does not constitute an endorsement by DOE of the views expressed in this paper.

1. D. H. Froula *et al.*, *Plasma Scattering of Electromagnetic Radiation: Theory and Measurement Techniques*, 2nd ed. (Academic Press, Amsterdam, 2011).
2. A. L. Milder *et al.*, *Phys. Rev. Lett.* **124**, 025001 (2020).
3. A. Milder *et al.*, *Phys. Rev. Lett.* **127**, 015001 (2021).
4. A. Milder *et al.*, *Phys. Plasmas* **28**, 082102 (2021).
5. S. H. Glenzer *et al.*, *Phys. Rev. Lett.* **77**, 1496 (1996).
6. D. H. Froula *et al.*, *Phys. Plasmas* **9**, 4709 (2002).
7. J. S. Ross *et al.*, *Rev. Sci. Instrum.* **81**, 10D523 (2010).
8. D. H. Froula *et al.*, *Rev. Sci. Instrum.* **77**, 10E522 (2006).
9. A. M. Hansen *et al.*, *Phys. Plasmas* **26**, 103110 (2019).
10. T. J. Kessler *et al.*, *Proc. SPIE* **1870**, 95 (1993).
11. J. S. Ross *et al.*, *J. Instrum.* **6**, P08004 (2011).
12. J. Katz *et al.*, *Rev. Sci. Instrum.* **83**, 10E349 (2012).
13. A. Visco *et al.*, *Rev. Sci. Instrum.* **79**, 10F545 (2008).
14. J. Katz *et al.*, “A High Throughput, Pulse-Front-Tilt–Compensated Streaked Spectrometer for Picosecond Optical Thomson Scattering,” presented at the 22nd Topical Conference on High Temperature Plasma Diagnostics, San Diego, CA, 16–19 April 2018.
15. A. S. Davies *et al.*, *Phys. Rev. Lett.* **122**, 155001 (2019).
16. R. K. Follett *et al.*, *Rev. Sci. Instrum.* **87**, 11E401 (2016).
17. E. A. Williams *et al.*, *Phys. Plasmas* **2**, 129 (1995).
18. D. H. Froula *et al.*, *Phys. Plasmas* **13**, 052704 (2006).

Melting of Magnesium Oxide to 2 TPa Using Double-Shock Compression

L. E. Hansen,^{1,2} D. E. Fratanduono,³ S. Zhang,¹ D. G. Hicks,⁴ T. Suer,^{1,5} Z. K. Sprowal,^{1,2} M. F. Huff,^{1,2} X. Gong,^{1,6}
B. J. Henderson,^{1,2} D. N. Polsin,^{1,6} M. Zaghou,¹ S. X. Hu,^{1,6} G. W. Collins,^{1,2,6} and J. R. Rygg^{1,2,6}

¹Laboratory for Laser Energetics, University of Rochester

²Department of Physics and Astronomy, University of Rochester

³Lawrence Livermore National Laboratory

⁴Optical Sciences Centre, Swinburne University of Technology, Australia

⁵Department of Earth and Planetary Sciences, Harvard University

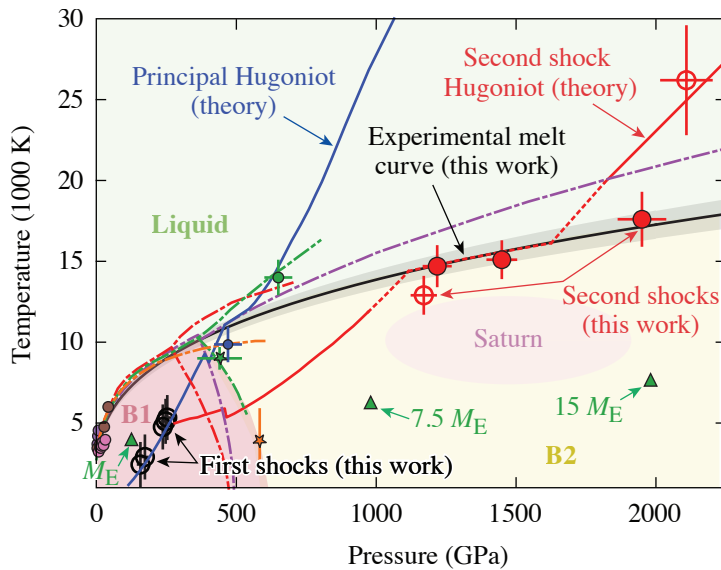
⁶Department of Mechanical Engineering, University of Rochester

Magnesium oxide (MgO, periclase) is an end-member of the (Mg, Fe)O magnesiowustite mineral, a major constituent of the Earth's lower mantle.^{1,2} It is likely present in the deep interiors of gas giants such as Jupiter and Saturn and in rocky extra-solar planets known as super-Earths.^{3,4} As an abundant component in planets, the physical properties of MgO can influence planetary structure and evolution. The B2 phase (CsCl type) of MgO is expected to be abundant in the mantles of super-Earths and in the rocky cores of gas giants due to the dissociation of MgSiO₃-perovskite.⁴ The melting of MgO could therefore be an important driver of thermal and chemical exchange in the mantles and the core–mantle boundary regions of these planets.^{5,6} Quantifying the melting behavior of MgO to the high pressures and temperatures of planetary interiors is therefore relevant to investigating a number of topical issues in planetary science.

The melt curve of MgO has been studied up to 40 GPa using laser- and resistance-heated diamond-anvil cells,^{7–10} and up to 550 GPa on the principal Hugoniot with decaying-shock experiments.^{11,12} Single shock waves can be used to study melting of a material to the pressure at which the principal Hugoniot crosses the melt curve; however, different experimental techniques are necessary to probe melting at higher pressures. In this work, we apply the double-shock self-impedance-matching technique^{13,14} to measure the melt curve of MgO to 2 TPa—the highest pressure to which any material's melt curve has been studied experimentally.

These experiments were performed on the OMEGA EP Laser System.¹⁵ The targets consisted of a 20- μ m-thick CH polystyrene ablator, a 50- μ m-thick quartz pusher, and a 100- or 200- μ m-thick single-crystal $\langle 100 \rangle$ MgO sample. All pieces were laterally 3-mm squares. The target components were held together with 1 to 3 μ m of low-viscosity epoxy. The quartz pusher produced steady shocks in the MgO sample and served as a temperature/reflectivity reference.^{16,17} Two successive shock waves were launched into the sample with a dual laser pulse through ablation of the CH. The first shock was produced with 400 J in a single laser beam with a 6- or 4-ns flattop pulse (0.067 TW or 0.1 TW); the second shock was produced with a net 1500 to 6400 J in one to three beams with a 2-ns flattop pulse (0.75 to 3.2 TW). Distributed phase plates were used to create a spatially uniform irradiance profile with a 95% encircled energy spot diameter of 1100 μ m. The time-resolved diagnostics included a streaked optical pyrometer (SOP)¹⁸ and a dual-channel line-imaging VISAR (velocity interferometer system for any reflector).¹⁹

The measured first (black open circles) and second (red open and solid circles) shock pressure and temperature results are plotted in Fig. 1. At a phase boundary, a material's Hugoniot is often marked by a plateau or reversal in temperature with increasing pressure as thermal energy contributes to a phase transition.^{20,21} This behavior has been observed in shock experiments on diamond,²² SiO₂ (Ref. 17), and the principal Hugoniot of MgO.^{11,12} Results of the second shock show a temperature increase of only 3000 K from 1.2 to 2 TPa; above this pressure, temperature rises rapidly. The three central second-shock data points (solid



E29670JR

Figure 1

The phase diagram of MgO. Black open circles represent the first-shock B1 states in the present work. Red open and solid circles are the second-shock states; both pressure and temperature are measured. The three central second-shock states (solid red circles) are interpreted to be on the melting curve of MgO due to a lack of heating across a large increase in pressure. Melting data from previous experiments are plotted with small solid circles (pink,⁷ purple,⁹ brown,¹⁰ green,¹¹ and blue¹²) and B1–B2 transition data are plotted with ×'s (green,¹¹ and orange²³). Dotted–dashed curves are previously predicted phase boundaries (green,¹³ red,²⁴ orange,²⁵ and purple²⁶). The solid blue curve is a prediction for the principal Hugoniot,^{26–28} and the solid red curve (interpolated with dashed red) is a prediction for the second shock Hugoniot.^{26–29} The core–mantle boundary conditions are plotted for Saturn³⁰ and 1-, 7.5-, and 15-Earth-mass (M_E) super-Earths.³¹ The solid black curve is the Simon–Glatzel fit [Eq. (1)] to the melting data in this work and lower-pressure anvil cell melt data,^{8,10} with gray shading representing the uncertainty in the fit parameters.

red circles) are interpreted to lie on the melt curve of MgO because they demonstrate a lack of heating across a large increase in shock pressure, which is attributed to the latent heat of MgO melting. These experiments did not determine the structure of solid MgO, and no structural data exist at these pressures. It is assumed that the MgO melts from B2 in these experiments because no other solid phases are predicted above the B1–B2 transition.

To capture the shape of the high-pressure melt curve, we performed a fit to our data by combining select lower-pressure anvil cell melting data^{8,10} with a Simon–Glatzel equation of the form

$$T_m[K] = 3098 \left[\frac{P_m(\text{GPa})}{a} + 1 \right]^{1/b}, \quad (1)$$

where T_m and P_m are the temperature and pressure of the melt curve and 3098 K is the melting temperature of MgO at atmospheric pressure.⁸ This empirical relation has been used to describe the melting behavior of other oxides including SiO₂ (Ref. 15) and MgSiO₃ (Ref. 32). The best-fit parameters are given by $a = 9.15$ (2.23) GPa and $b = 3.14$ (0.19) with a covariance of -0.39 , determined from a nonlinear least squares analysis. A previously published melting curve of MgO (Ref. 15) based on extrapolation of anvil-cell and decaying-shock melting data^{8,9,11} overestimates the melting temperature at 1950 GPa by 27%. This simple fit was chosen based on the discrepancy in the melting temperature of MgO on the principal Hugoniot.

The melt curve in Eq. (1) is plotted in Fig. 1 (solid black) and shows strong agreement with recent density functional theory²⁶ (dashed–dotted purple curve) up to 650 GPa before the curves diverge. Reference 20 overestimates the measured melting temperature at 1950 GPa by 17%. The highest-pressure second-shock equation-of-state point in this work is in the liquid regime of the 173-GPa secondary Hugoniot of MgO and shows general agreement with first-principles equation-of-state simulations of secondary Hugoniots from similar initial shock conditions;^{27–29} the slope of the secondary Hugoniot defined by the two highest-pressure second-shock points in this work does appear steeper than theoretical predictions. The discrepancy between experiment and theory on the melt curve could originate from the complex elastic and plastic responses of MgO during the shock/re-shock and phase transformation processes, which have not been considered in the first-principles calculations. This calls for larger-scale nonequilibrium simulations and crystallographic diagnostics to better understand problems as such. The low-pressure second-shock data in this work demonstrate that the double-shock technique is a valuable method for probing the behavior of MgO in the solid phase at the temperatures and pressures directly relevant to the core–mantle boundary of gas giants similar in size and composition to Saturn³⁰ and super-Earths in the 7.5- to 15-Earth-mass range.³¹

In summary, laser-driven double-shock compression is a valuable method for probing the behavior of MgO in the solid phase at extreme conditions. The present work uses this technique to extend the melting curve of MgO up to 2 TPa and 20,000 K, the highest pressures and temperatures to which any material's melt curve has been probed experimentally. These measurements allowed us to explore the state of the deep interiors of Saturn-sized gas giants and super-Earths. This technique can be used to further quantify the melting behavior of other planetary materials to further investigate the diversity of planetary structures. Additionally, the technique presented in this work will lead to new advances in probing phase transitions of transparent materials up to TPa pressures and significantly advance warm dense matter physics.

This material is based upon work supported by the Department of Energy National Nuclear Security Administration under Award Number DE-NA0003856, the University of Rochester, and the New York State Energy Research and Development Authority.

1. W. F. McDonough and S.-s. Sun, *Chem. Geol.* **120**, 223 (1995).
2. J.-Fu. Lin *et al.*, *Proc. Natl. Acad. Sci.* **100**, 4405 (2003).
3. S. Seager *et al.*, *Astrophys. J.* **669**, 1279 (2007).
4. K. Umemoto, R. M. Wentzcovitch, and P. B. Allen, *Science* **311**, 983 (2006).
5. L. Stixrude, *Phil. Trans. R. Soc. A* **372**, 20130076 (2014).
6. W. B. Tonks and H. J. Melosh, *J. Geophys. Res.* **98**, 5319 (1993).
7. A. Zerr and R. Boehler, *Nature* **371**, 506 (1994).
8. L. S. Dubrovinsky and S. K. Saxena, *Phys. Chem. Minerals* **24**, 547 (1997).
9. L. Zhang and Y. Fei, *Geophys. Res. Lett.* **35**, L13302 (2008).
10. Z. Du and K. K. M. Lee, *Geophys. Res. Lett.* **41**, 8061 (2014).
11. R. S. McWilliams *et al.*, *Science* **338**, 1330 (2012).
12. R. M. Bolis *et al.*, *Geophys. Res. Lett.* **43**, 9475 (2016).
13. M. Guarguaglini *et al.*, *Phys. Plasmas* **26**, 042704 (2019).
14. M. Guarguaglini *et al.*, *Nat. Commun.* **12**, 840 (2021).
15. D. D. Meyerhofer *et al.*, *J. Phys.: Conf. Ser.* **244**, 032010 (2010).
16. S. Brygoo *et al.*, *J. Appl. Phys.* **118**, 195901 (2015).
17. D. G. Hicks *et al.*, *Phys. Rev. Lett.* **97**, 025502 (2006).
18. J. E. Miller *et al.*, *Rev. Sci. Instrum.* **78**, 034903 (2007).
19. P. M. Celliers *et al.*, *Rev. Sci. Instrum.* **75**, 4916 (2004).
20. S. B. Kormer, *Sov. Phys.-Usp.* **11**, 229 (1968).
21. G. A. Lyzenga, T. J. Ahrens, and A. C. Mitchell, *J. Geophys. Res.* **88**, 2431 (1983).
22. J. H. Eggert *et al.*, *Nat. Phys.* **6**, 40 (2010).
23. F. Coppari *et al.*, *Nat. Geosci.* **6**, 926 (2013).
24. S. Root *et al.*, *Phys. Rev. Lett.* **115**, 198501 (2015).
25. N. de Koker and L. Stixrude, *Geophys. J. Int.* **178**, 162 (2009); **183**, 478(E) (2010).
26. F. Soubiran and B. Militzer, *Phys. Rev. Lett.* **125**, 175701 (2020).
27. F. Soubiran *et al.*, *J. Chem. Phys.* **151**, 214104 (2019).
28. The principal and the second-shock Hugoniot at 20,000 K or higher are calculated by using the first-principles equation-of-state (FPEOS) database published in Refs. 27 and 29 for MgO. The initial conditions for the second shocks are estimated following the approach of S. Zhang, R. Paul, M. A. Morales, F. Malone, and S. X. Hu, in preparation. See the supplemental material for details.
29. B. Militzer *et al.*, *Phys. Rev. E* **103**, 013203 (2021).
30. F. González-Cataldo, H. F. Wilson, and B. Militzer, *Astrophys. J.* **787**, 79 (2014).
31. F. W. Wagner *et al.*, *Astron. Astrophys.* **541**, A103 (2012).
32. D. E. Fratanduono *et al.*, *Phys. Rev. B* **97**, 214105 (2018).

Metastability of Liquid Water Freezing into Ice VII Under Dynamic Compression

M. C. Marshall,^{1,2} M. Millot,² D. E. Fratanduono,² D. M. Sterbentz,^{2,3} P. C. Myint,² J. L. Belof,² Y.-J. Kim,²
F. Coppari,² S. J. Ali,² J. H. Eggert,² R. F. Smith,² and J. M. McNaney²

¹Laboratory for Laser Energetics, University of Rochester

²Lawrence Livermore National Laboratory

³University of California Davis

Dynamic compression is often used to create the nonequilibrium conditions needed to study metastability and kinetic effects in materials as they undergo phase transitions.^{1,2} In particular, the pressure-induced phase transformation of liquid water solidifying into ice VII has been the focus of many experimental and theoretical works.^{3–9} Under rapid submillisecond compression, the liquid phase can persist metastably well into pressure–temperature conditions where ice VII is the stable phase.^{3–5} Previous experimental studies found that liquid water can remain metastable to at least 7 GPa— ~ 5 GPa higher than expected based on the equilibrium phase diagram—before homogeneously freezing into ice VII when quasi-isentropically (ramp) compressed over hundreds of nanoseconds.^{3–5} This work ramp compresses liquid water over the highest compression rates to date (up to ~ 3 GPa/ns) to further investigate its metastability limit.

Water was ramp compressed into the ice VII phase in experiments at the Omega Laser Facility.^{10,11} The liquid–ice VII phase transition in a thin water layer, sandwiched between a baseplate and a sapphire or quartz window, was diagnosed using a velocity interferometer system for any reflector (VISAR).¹² Since ice VII is $\sim 5\%$ more dense than liquid water at the phase transition conditions, the volume of the thin water layer abruptly decreases during the phase transition (~ 1 -ns duration), which alleviates pressure on the water/window interface despite the continuously increasing pressure drive.^{3–5} The VISAR records a corresponding dip in the water/window interface velocity, which we interpret as the liquid freezing into ice VII (Fig. 1).

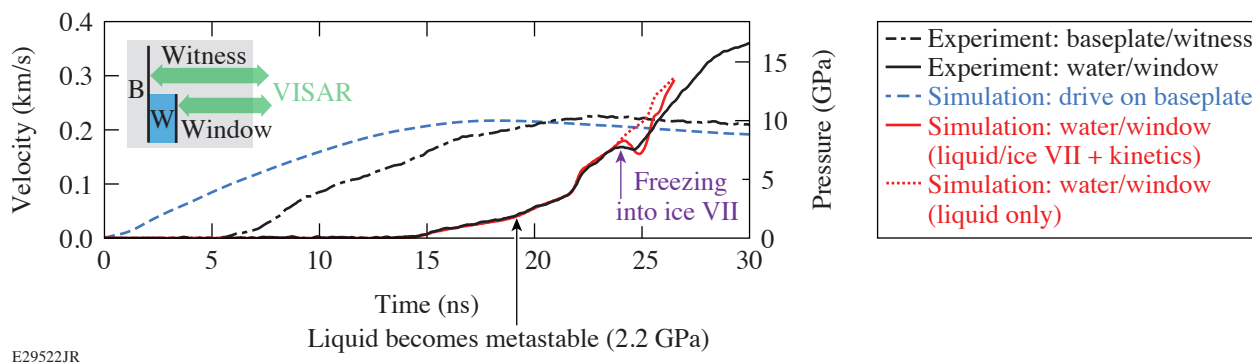


Figure 1

Interface velocities and corresponding pressures (applicable to all curves) from experiment shot 29419 and the post-shot simulations. An inset of the target components relevant to the experimental measurements and simulations is shown, where “B” is the sapphire baseplate, “W” is the water, “Witness” is the sapphire witness, and “Window” is the sapphire window. The VISAR probes a reflective Al coating at the baseplate/witness and water/window interfaces to measure their velocities. A dip in the water/window interface pressure, resulting from the liquid water freezing into the $\sim 5\%$ -more-dense ice VII phase, is observed near 24 ns and 7.5 GPa in the experiment and simulation using the liquid/ice VII equation of state and classical nucleation theory–based kinetics model.

Water was compressed at rates spanning from 0.2 to 3 GPa/ns over 15 experiments, where the loading rate was varied by changing the laser intensity, the baseplate thickness, and the window material (e.g., the lower impedance of quartz compared to sapphire leads to shallower ramp compression profiles) (Fig. 2). We find that the liquid–ice VII freezing pressure, defined as the pressure in the liquid at the peak velocity before the dip, for water compressed on the principal isentrope increases with compression rate to at least ~ 8 GPa [Fig. 2(a)]. We observed freezing at pressures as high as ~ 9 GPa; however, additional heating of < 8 K above the principal isentrope cannot be ruled out, which could further raise the freezing pressure.⁴ These results indicate that liquid water can exist to at least $\sim 3.5\times$ higher pressure than the onset of metastability (2.2 GPa) (Ref. 9) and that the metastability limit is at least $\sim 11\%$ higher than previously reported.^{3–5} Agreement between data at 0.1 to 0.3 GPa/ns in Fig. 2(a) from this work (Omega), Dolan *et al.* (Z),³ and Nissen *et al.* (Thor)⁴ (all room temperature), obtained using different target component materials, suggests that ice VII is nucleated homogeneously in the bulk and not heterogeneously at the various window or baseplate surfaces.

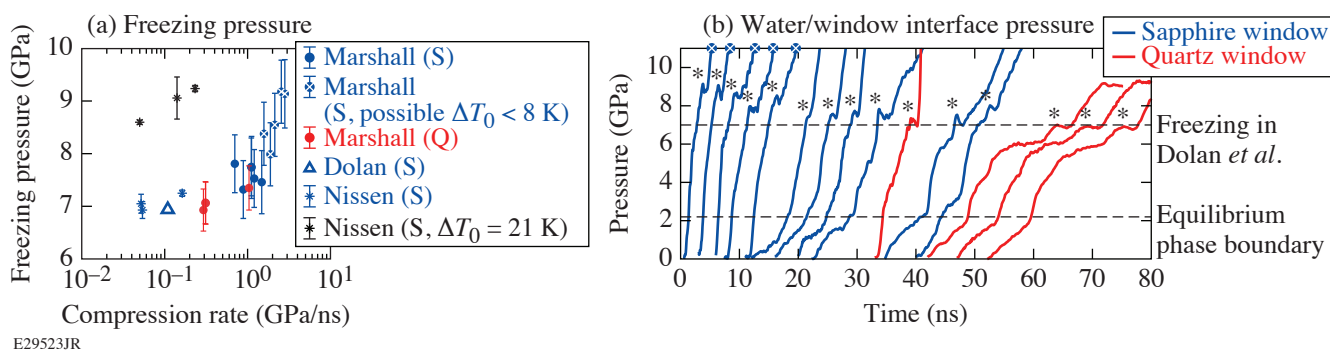


Figure 2

(a) Liquid–ice VII freezing pressure versus compression rate [(defined from 2.2 GPa ([onset of metastability]) to the freezing pressure)] and (b) pressure histories of the water/window interface for all shots ordered by decreasing compression rate and shifted in time for clarity. In the legend of (a), S and Q denote sapphire and quartz windows, respectively, and ΔT_0 is the initial temperature increase above the principal isentrope. Asterisks in (b) mark the pressure relaxation interpreted as freezing.

Our experimental results can be reproduced in hydrodynamic simulations (*ARES*) using a kinetics model (*SAMSA*)¹³ that, remarkably at these extreme conditions, is fundamentally based on classical nucleation theory (CNT).⁸ The baseplate/water/window portions of the target were simulated using a pressure input on the front baseplate surface that were determined from the shot-specific sapphire “witness” measurements adjacent to the water layer. The same pressure relaxation at the water/window interface observed in the experiment is also observed in the simulation using the CNT-based kinetics model⁸ and a multiphase equation of state (EOS) for the liquid and ice VII phases¹⁴ (Fig. 1). This pressure relaxation is concurrent with the onset and completion of freezing in the simulations. The “null case” of no phase transition, represented by using only the liquid EOS, does not show the dip in the water/window interface pressure, suggesting that the dip observed in the experiment is indeed the result of freezing and not wave reverberations within the target.

The experiments reported here are at the frontier of using experimental ultrafast science to explore metastability and kinetics associated with phase transitions. It is remarkable that recent theoretical and numerical advances provide a detailed understanding of the observed phenomena, while relying on the fundamentally simple picture of homogeneous nucleation using CNT. This could have implications for our general understanding of phase transformations at extreme conditions.

This material is based upon work supported by the Department of Energy National Nuclear Security Administration under Award Number DE-NA0003856, the University of Rochester, and the New York State Energy Research and Development Authority. This work was performed under the auspices of the U.S. Department of Energy by Lawrence Livermore National Laboratory under Contract No. DE-AC52-07NA27344.

1. R. F. Smith *et al.*, Phys. Rev. Lett. **101**, 065701 (2008).
2. S. J. Tracy, S. J. Turneaure, and T. S. Duffy, Sci. Adv. **6**, eabb3913 (2020).
3. D. H. Dolan *et al.*, Nat. Phys. **3**, 339 (2007).
4. E. J. Nissen and D. H. Dolan, J. Appl. Phys. **126**, 015903 (2019).
5. M. Bastea *et al.*, Phys. Rev. B **75**, 172104 (2007).
6. A. E. Gleason *et al.*, Phys. Rev. Lett. **119**, 025701 (2017).
7. P. C. Myint *et al.*, Phys. Rev. Lett. **121**, 155701 (2018).
8. D. M. Sterbentz *et al.*, J. Chem. Phys. **151**, 164501 (2019).
9. P. C. Myint and J. L. Belof, J. Phys.: Condens. Matter **30**, 233002 (2018).
10. T. R. Boehly *et al.*, Opt. Commun. **133**, 495 (1997).
11. D. D. Meyerhofer *et al.*, J. Phys.: Conf. Ser. **244**, 032010 (2010).
12. P. M. Celliers *et al.*, Rev. Sci. Instrum. **75**, 4916 (2004).
13. P. C. Myint *et al.*, AIP Adv. **10**, 125111 (2020).
14. P. C. Myint, L. X. Benedict, and J. L. Belof, J. Chem. Phys. **147**, 084505 (2017).

Measurement of Chromatic Aberrations Using Phase Retrieval

M. D. Bergkoetter,^{1,2} B. E. Kruschwitz,^{1,3} S.-W. Bahk,³ and J. R. Fienup¹

¹The Institute of Optics, University of Rochester

²NASA Goddard Space Flight Center

³Laboratory for Laser Energetics, University of Rochester

Phase retrieval is a computational method for estimating the phase of an electromagnetic field based on measurements of the intensity in one or more planes. For wavefront-sensing applications, the phase of interest is in the pupil plane of an optical system, and typically the aperture and image-plane intensity from a point source [the point-spread function (PSF)] are known.¹ The iterative process of retrieving the phase involves forming an initial estimate of the wavefront in the pupil plane, simulating a propagation of that field to the image plane (which typically involves a Fourier transform), and comparing the resulting intensity distribution with the measured intensity via an error metric. The wavefront estimate is then modified to improve agreement in the image plane.

Among the various applications of this general approach is the improvement of diagnostic tools for the OMEGA EP laser. In this case, phase retrieval complements measurements provided by a conventional Shack–Hartmann wavefront sensor (SHWFS) with an estimate of non-common-path error and differential piston between regions of the segmented beam.² A proposed way to improve this system is to also estimate chromatic aberrations in the system. These can arise in a chirped-pulse–amplification laser such as OMEGA EP in the form of (1) residual angular dispersion from the pulse stretcher and compressor and (2) axial dispersion (longitudinal chromatic aberration) due to transmissive elements, both of which can lead to a significant reduction in the focused intensity.

We use a modal approach to modeling chromatic effects. Angular dispersion is modeled as a wavefront tilt that varies linearly with wavelength and longitudinal chromatic aberration as a defocus that varies linearly with wavelength. By forcing the spectrally varying components of the wavefronts to fit this model, we can mitigate uniqueness problems that would arise if they were allowed to vary independently. In our model, we assume that (1) there is an initial estimate of the monochromatic wavefront W_0 measured by a SHWFS and (2) there is also a non-common-path error between the SHWFS and the focusing optics, which must be estimated in terms of a monochromatic wavefront W_M , in addition to the chromatic aberrations $(\lambda - \lambda_r) W_c$, relative to a reference wavelength λ_r , so that

$$W(\xi, \eta) = W_0(\xi, \eta) + W_M(\xi, \eta) + (\lambda - \lambda_r) W_c(\xi, \eta), \quad (1)$$

where $W_M(\xi, \eta) \equiv \sum_{n=0}^N a_n Z_n(\xi, \eta)$ and $W_c(\xi, \eta) \equiv \sum_{n=0}^N c_n Z_n(\xi, \eta)$.

Having mentioned above “differential piston between regions of the segmented beam,”² this model does not capture the segment-to-segment errors that can exist from a tiled grating. The a_n and c_n coefficients would usually vary from segment to segment (including piston tip and tilt).

In Eq. (1), ξ and η are pupil-plane coordinates, λ is the wavelength of a single spectral component, and Z_n is the n th Zernike polynomial. The phase-retrieval algorithm jointly estimates the unknown monochromatic wavefront along with the chromatic

aberrations in terms of the sets of coefficients a_n and c_n , respectively. The exit pupil amplitude is assumed to be a known aperture with transmittance $P(\xi, \eta)$, and each spectral component is given a scalar amplitude weight, based on the known power spectrum. Each spectral component is propagated from the pupil plane to the image plane separately, and the total PSF in the image plane is the incoherent sum of the spectral components. The error metric is the normalized sum-squared difference between the simulated and measured PSF's.

As a simple test case, we simulated PSF's with angular dispersion of 1.2 waves peak-to-valley (p-v) of tip/tilt and axial dispersion of 1 wave of defocus, both across an 8-nm bandwidth. Besides the global minimum, three local minima also appear, where one or both of the signs of the dispersion parameters are reversed. When a known defocus is added, two of the local minima disappear and the error metric appears as in Fig. 1(a).

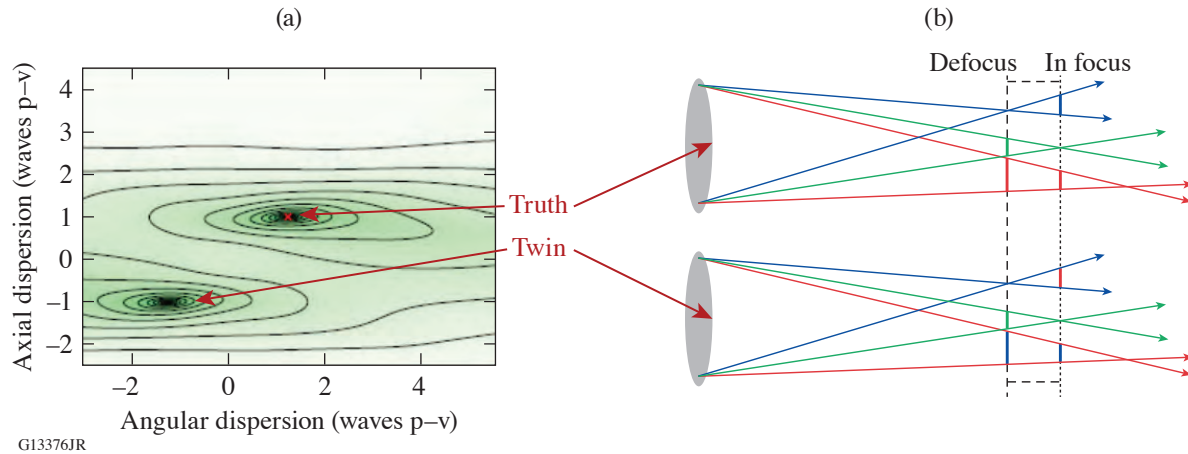


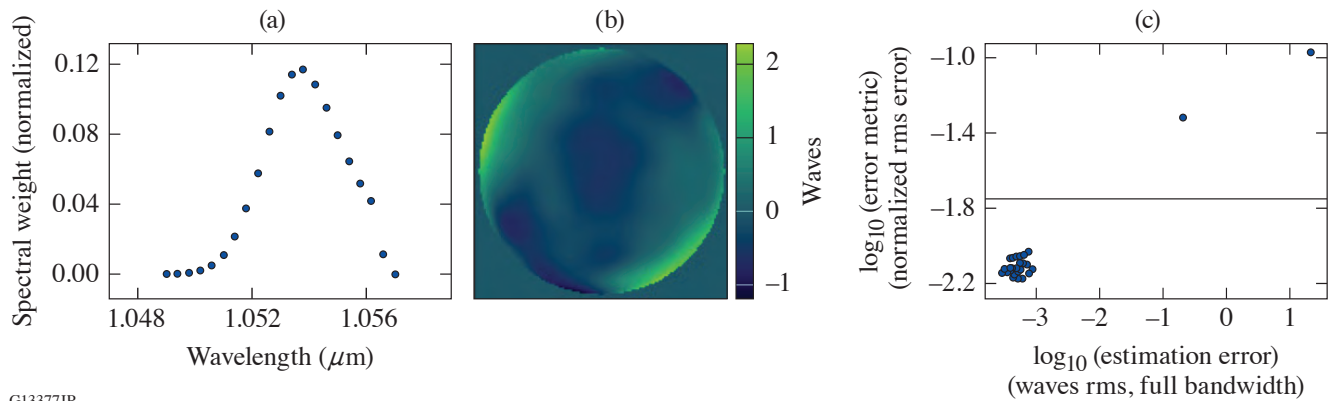
Figure 1

The twin image problem is illustrated. (a) Error metric as a function of the two dispersion variables, with a known defocus included. The global minimum (correct values) is in the center of the plot at coordinates (1.2, 1). (b) Illustration of how defocus does not eliminate the joint axial-angular twin.

We can explain the appearance of these minima and their relation with defocus by analogy to the well-known twin image problem in monochromatic phase retrieval, which arises because the absolute value of the Fourier transform of any complex signal $f(u)$ is the same as that of its complex conjugate flipped about the origin $f^*(-u)$. Defocus cannot eliminate the joint axial-angular twin, when the signs of both the angular and axial dispersion are reversed simultaneously. This effect can be visualized with the ray trace in Fig. 1(b), which shows axial dispersion causing each spectral component to focus at a different horizontal position and angular dispersion causing the focal points to spread vertically.

However, the PSF produced by the twin is subtly different due to the scaling effect of the wave number $2\pi/\lambda$ in the complex exponential and any asymmetry in the spectrum. If this results in a significantly higher error metric for the twin than the true solution, a sufficient strategy for avoiding this minimum is to check the error metric against a threshold value after the optimizer converges; if it is too high, reverse the signs of the dispersion coefficients and perform another round of local nonlinear optimization to confirm whether that minimizes the error metric.

To test this strategy, the algorithm was run through a series of trials with a variety of simulated true reference wavefronts and various starting guesses for the dispersion parameters. In all cases, the true chromatic aberrations were 1.2 waves p-v of angular dispersion and 1 wave p-v of axial dispersion across an 8-nm bandwidth (or equivalently stated as 0.15 waves/nm and 0.125 waves/nm, respectively). The spectral weights for intensity were representative of measured spectra in fully amplified shots on OMEGA EP [shown in Fig. 2(a)]. Each of the randomized true reference wavefronts was the sum of a known part W_0 with a magnitude 0.4 waves rms and an unknown part W_M [simulating non-common-path error, an example of which is shown in Fig. 2(b)] that had to be retrieved and had a magnitude of 0.11 waves rms. Known defocus in the amount of 1.5 waves was also added.



G13377JR

Figure 2

Monte Carlo simulation results: (a) Intensity spectrum used in Monte Carlo simulations; (b) representative example of random monochromatic wavefront aberration (defocus removed); and (c) resulting phase-retrieval error metric versus error of the reconstruction, where the error is computed over the full bandwidth. Successful cases in (c) have a low estimation error, and failed cases are identifiable by a large error metric in the PSF fit. Cases above the vertical line are considered failed cases.

Both the unknown part of the monochromatic reference wavefront and the dispersion terms were retrieved. A bootstrapping process was used in which the monochromatic reference wavefront was optimized alone while the dispersion terms were left at zero. Once that converged, a second stage was carried out, allowing both the monochromatic and dispersion terms to vary. In combination with the twin phase check described earlier, this strategy was successful in all but two of the 1600 tested cases. In the failed cases, the normalized root-mean-squared error between the estimated and true PSF's was about $10\times$ greater than the error metric for successful cases, as shown by the outliers in Fig. 2(c). Therefore, if one of these failures occurs in practice, it can be recognized by the large residual error metric and recovered from by performing another optimization run from a different random starting point.

To test the proposed chromatic aberration retrieval algorithm in a real-world scenario, we applied the method to a small-scale laboratory setup. This test bed was previously built to generate and measure chromatic aberrations with a method that utilizes a 2-D grating to simultaneously disperse spectral components and provide focus diversity.³ For consistency with Ref. 3, we represent angular and axial dispersion in terms of pulse-front delay (PFD), and radial group delay (RGD), respectively.

The conceptual layout of the experimental setup is shown in Fig. 3(a). A Superlum SLD-52 superluminescent light-emitting diode (SLED) served as a broadband light source, having a bandwidth of approximately 100 nm and spectral distribution of intensity shown in Fig. 3(b). Given the large bandwidth of the source, significant chromatic dispersion can be introduced with a pair of lenses (L1 and L2), which together provided $\gamma = 10.0$ fs of RGD. A fused-silica wedge (W) with a 1° apex angle imparted $\beta = 2.5$ fs of PFD. Images of the PSF were captured by a camera, which was translated along the optical axis to provide focus diversity.

The focal sweep was performed first with a Semrock narrowband filter (F) with a FWHM bandwidth of less than 7.2 nm and a central wavelength of $1.03 \mu\text{m}$ to provide images that were effectively monochromatic; in the second sweep the narrowband filter was replaced by a neutral-density filter. From the spectrally filtered images, we measured the monochromatic contribution to the wavefront without the risk of confounding effects from dispersion. The nonfiltered set of PSF images exhibited a very subtle blurring effect due to dispersion and the increased bandwidth. Because these effects are subtle, the dominant monochromatic wavefront was first estimated in terms of Zernike coefficients; then the dispersion was retrieved in terms of tip, tilt, and focus coefficients that vary linearly with wavelength. Lastly, all of the variables were jointly optimized to produce the final estimate.

The final pupil wavefront estimate, shown in Fig. 3(c), differed by only 16.9-nm rms from the monochromatic result. The final dispersion estimate consisted of 4.68 fs of PFD and 9.13 fs of RGD, which differ by 6.4% and 8.7% from the expected values of

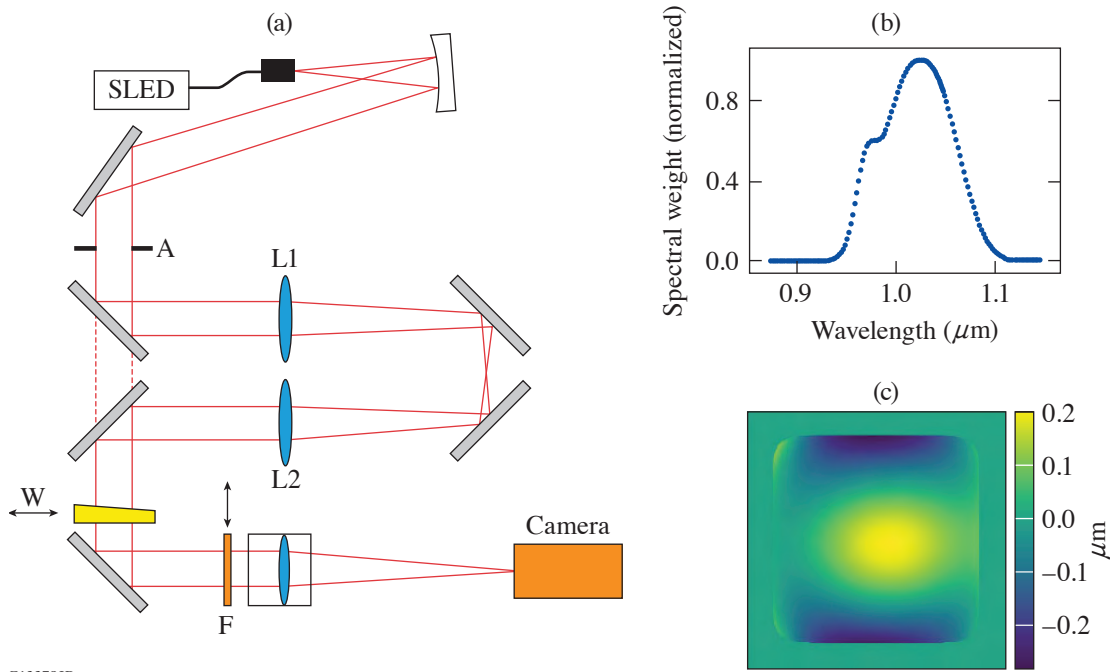


Figure 3

Laboratory experiment setup and results: (a) Experimental system layout (reprinted from Ref. 3); (b) intensity spectrum of the SLED; and (c) final wavefront estimate (full bandwidth). A: apodizer.

5.0 fs and 10.0 fs, respectively. Compared to the results in Ref. 3, where the PFD estimate was within 0.5 fs of expectations and the RGD within 0.1 fs, these results for PFD are similar, while the RGD is less accurate.

In summary, we have developed a simulation model and optimization process for the joint estimation of linear chromatic aberrations in addition to monochromatic aberrations using a measured broadband PSF together with a known aperture, spectrum, and initial wavefront estimate. We found a bootstrapping strategy that first estimated the monochromatic wavefront correction followed by optimization of the chromatic parameters to be highly successful. A test of this approach in a laboratory experiment produced encouraging results.

This material is based upon work supported by the Department of Energy National Nuclear Security Administration under Award Number DE-NA0003856, the University of Rochester, and the New York State Energy Research and Development Authority.

1. J. R. Fienup, *Appl. Opt.* **21**, 2758 (1982).
2. B. E. Kruschwitz *et al.*, *Opt. Express* **20**, 20,874 (2012).
3. S.-W. Bahk, C. Dorrer, and J. Bromage, *Opt. Express* **26**, 8767 (2018)

A Highly Efficient, 10-J Output Signal Amplifier for Ultra-Intense All-OPCPA Systems

I. A. Begishev, S.-W. Bahk, C. Dorrer, C. Feng, M. J. Guardalben, C. Jeon, C. Mileham, R. G. Roides, M. Spilatro, B. Webb, D. Weiner, J. D. Zuegel, and J. Bromage

Laboratory for Laser Energetics, University of Rochester

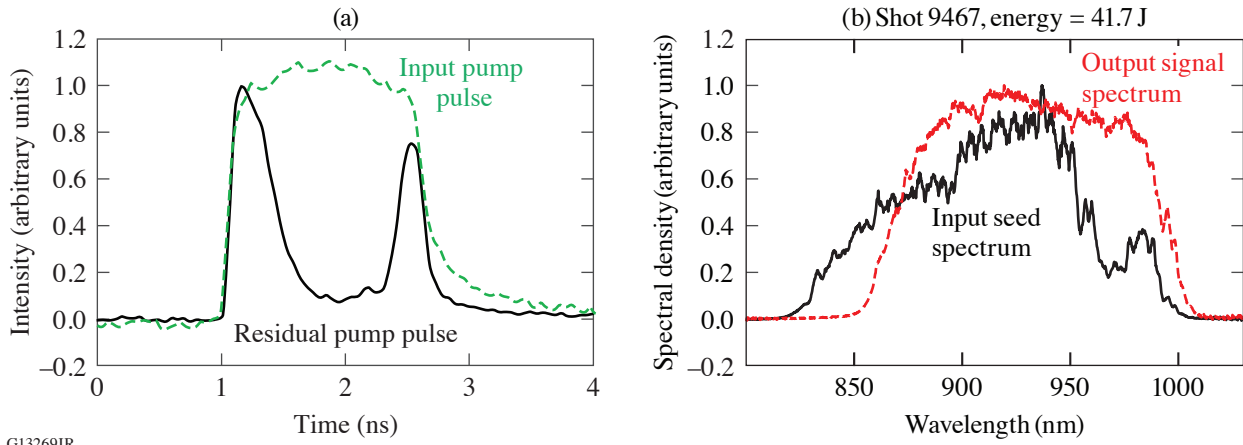
The highest-energy beams and the shortest pulses are always in the mainstream of laser science and engineering to create peta- and exawatt lasers.¹ Optical parametric chirped-pulse–amplification (OPCPA) systems, pumped by high-energy Nd:glass lasers, have the potential to produce ultra-intense pulses ($>10^{23}$ W/cm²). Existing large-scale glass lasers could be used to pump a large all-OPCPA system.² While front-end OPCPA stages are mainly focused on spectral, temporal, and phase characteristics of beams, the final OPCPA stages additionally need to be energy efficient. We report on the performance of the final high-efficiency amplifier in an OPCPA system based on large-aperture (63×63 -mm²), partially deuterated potassium dihydrogen phosphate (DKDP) crystals.

The experiment was performed on the Multi-Terawatt (MTW) Laser System, which is a hybrid OPCPA and Nd:glass laser. For all-OPCPA,² the MTW laser was switched to a narrowband mode at 1053 nm with energy up to 60 J and pulse-length variation from 1.2 to 1.6 ns. This radiation was converted to 526 nm using second-harmonic generation with an efficiency of 70%. The “green” beam at 526 nm travels by way of two large-scale periscopes into the next room through a series of vacuum spatial filters to maintain high beam quality. Finally, this 45-mm \times 45-mm beam pumps a 48-mm or 52-mm-long DKDP crystal on the final stage synchronously with the seed beam. The chirped seed beam ($\tau = 1.5$ ns, $E = 240$ mJ, $\Delta\lambda$ from 830 to 1010 nm) was created using a sequence of four lower-energy amplifiers seeded by a white-light continuum. The 11.8-J output signal was compressed to 19 fs.

The maximum pump-to-signal conversion efficiency of 37% was achieved with a 52-mm-long DKDP crystal (deuteration level of 70%) and 40 J of pump energy at 527 nm due to the flattop super-Gaussian pump beam profile and flat-in-time pulse. The seed and the pump were precisely synchronized in time. The shape of the 1.6-ns pump pulse was precompensated in the front end to reach a top-flat shape on the final amplifier. The input pump pulse and the residual pump pulse are shown in Fig. 1(a). The resulting hole in the residual pulse corresponds to the place where the seed pulse is located. It also demonstrates how deeply the pump pulse is depleted.

A deep saturation regime in the 52-mm-long crystal smooths output intensity modulation of the seed beam. Figure 1(b) shows a much better output signal spectrum at higher pump energies, even with a moderate quality of the initial seed spectrum. Figure 2 shows saturation of amplification with much better quality of the signal beam (d) than the seed beam (a) and deep depletion of the residual beam at 2ω (b) compared to the pump beam (c).

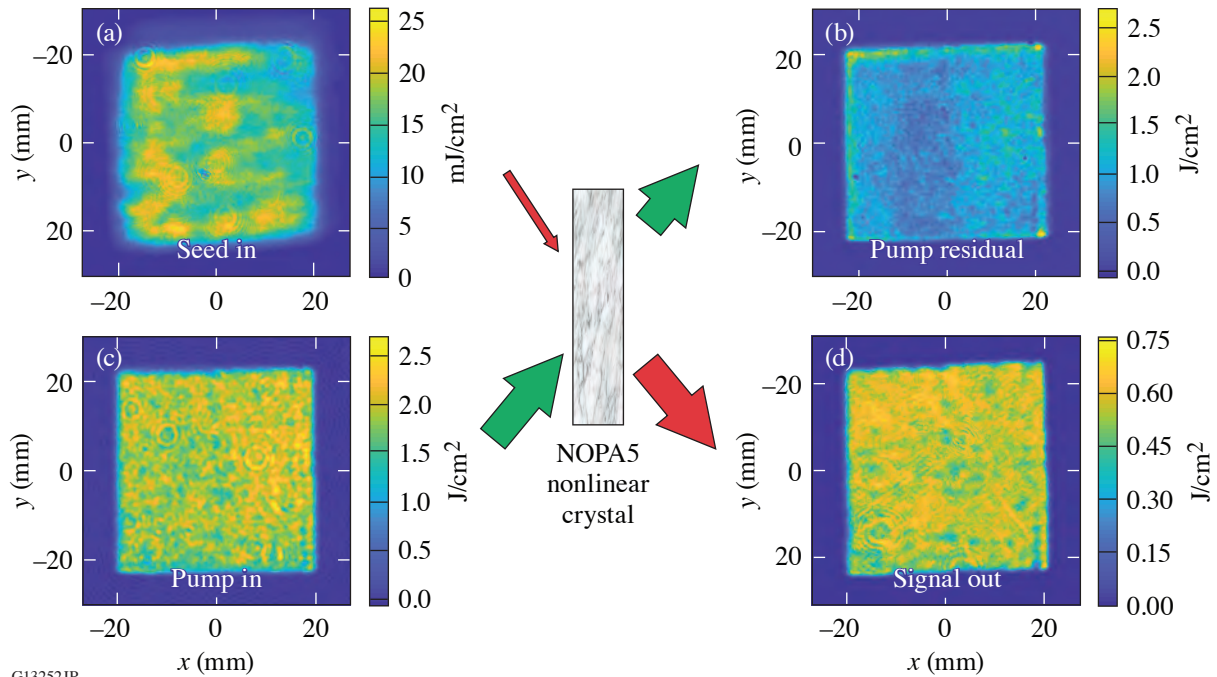
The maximum conversion efficiency from the pump beam into a signal of 37% (Fig. 3) was achieved with the 52-mm-long DKDP crystal (70% deuteration level) and pulse duration of 1.2 ns (FWHM).



G13269JR

Figure 1

(a) An oscilloscope with the input pump pulse and output residual pump pulse, both at 526 nm; (b) spectrum of the input seed beam (black curves) and the output signal beam (red curves) at the maximum pump beam energy.



G13252JR

Figure 2

Images of typical interaction beams in the 52-mm-long DKDP: (a) the input seed beam, (b) the residual pump beam at 2ω , (c) the input pump beam, and (d) the output signal beam. NOPA: noncollinear optical parametric amplifier.

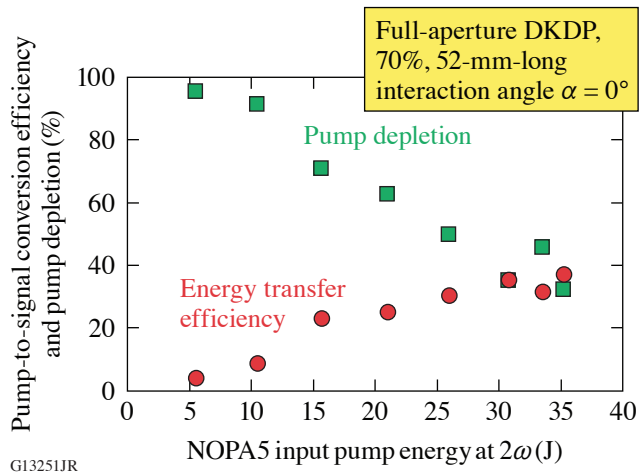


Figure 3
Maximum pump-to-signal conversion efficiency and depletion of the pump energy for the 1.2-ns pump pulse.

This material is based upon work supported by the Department of Energy National Nuclear Security Administration under Award Number DE-NA0003856, the University of Rochester, and the New York State Energy Research and Development Authority.

1. C. N. Danson *et al.*, High Power Laser Sci. Eng. **7**, e54 (2019).
2. J. Bromage *et al.*, High Power Laser Sci. Eng. **7**, e4 (2019).

Broadband Sum-Frequency Generation of Spectrally Incoherent Pulses

C. Dorrer, M. Spilatro, S. Herman, T. Borger, and E. M. Hill

Laboratory for Laser Energetics, University of Rochester

High-energy nanosecond solid-state laser systems operating in the near infrared require frequency conversion to improve the efficiency of laser-matter interaction. This is generally done with a sequence of two nonlinear crystals, one for frequency doubling from 1ω (1053 nm) to 2ω (526.5 nm) and one for mixing of the resulting 2ω with the remaining 1ω to generate 3ω pulses (351 nm) (Ref. 1). The spectral acceptance of the tripling stage can be increased using two crystals or angular dispersion at 1ω (Refs. 2 and 3), but neither scheme allows for efficient operation beyond ~ 1 THz with incoherent nanosecond pulses. Simulations show that spectrally incoherent broadband pulses can mitigate the detrimental laser-plasma instabilities and on-target beam imprint, therefore increasing the coupling efficiency of energy into the target.⁴

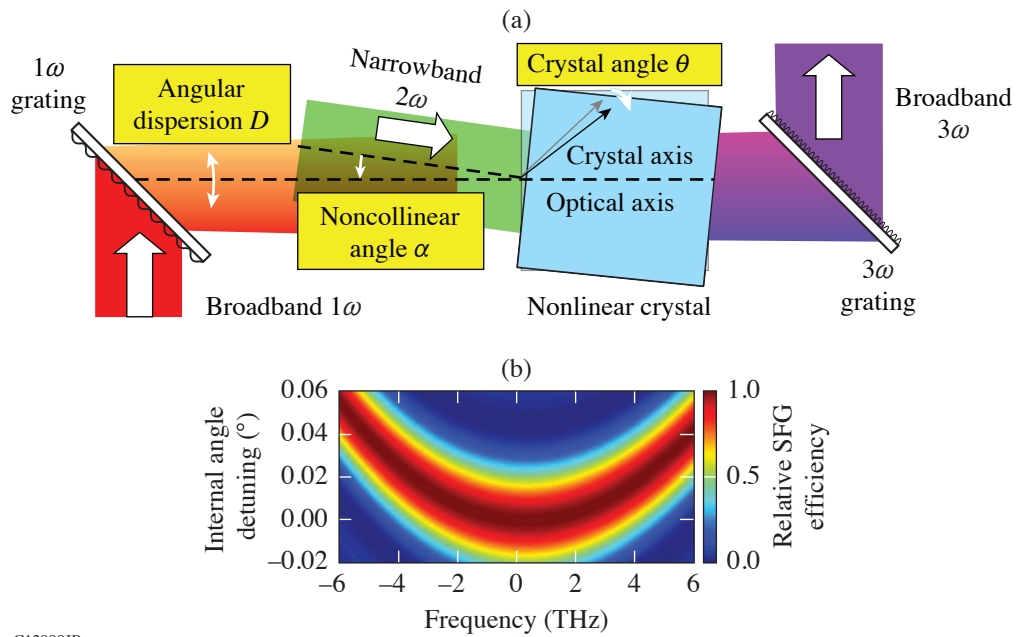
A novel sum-frequency generation (SFG) scheme based on a noncollinear interaction between a 1ω broadband angularly dispersed pulse and a narrowband 2ω pulse allows for efficient frequency conversion into broadband 3ω pulses. Experimental results are in excellent agreement with simulations, demonstrating the generation of spectrally incoherent 3ω pulses with bandwidths larger than 10 THz in a relatively thick 1-cm KDP crystal. This scheme can be implemented with commercially available large-aperture diffraction gratings and nonlinear crystals to support a new generation of high-energy laser facilities delivering spectrally incoherent pulses.

The wave-vector mismatch for SFG of a broadband angularly dispersed pulse (frequency $\omega + \Omega$, angular dispersion D) with a narrowband pulse (frequency 2ω) in a noncollinear geometry [Fig. 1(a)] along the wave vector at ω is

$$\Delta k(\Omega, \alpha, D, \theta) = k_o(\omega + \Omega)\cos(D\Omega) + k_o(2\omega)\cos(\alpha) - k_e(3\omega + \Omega, \theta)\cos[\beta(\Omega, \alpha, D, \theta)], \quad (1)$$

where α is the internal noncollinear angle between the 1ω and 2ω beams, θ is the frequency-dependent angle between the crystal axis and the wave vector at $3\omega + \Omega$, and β is the frequency-dependent angle between 1ω and $3\omega + \Omega$ beams. There is a continuum of combinations of the three degrees of freedom (D , α , and θ) that cancels the phase mismatch and its frequency derivative at $\Omega = 0$, therefore yielding broadband SFG. For example, operation with $\alpha = 1.7^\circ$ and $\Delta = -0.59$ mrad/nm ($\Delta = -2\pi cD/\lambda^2$) in a Type-I KDP crystal allows for the conversion of ~ 10 THz of bandwidth from 1053 nm to 351 nm in a 1-cm crystal, i.e., $10\times$ larger than in a collinear scheme [Fig. 1(b)]. Crystal-angle detuning allows for SFG of frequency components symmetrically located relative to 1ω , e.g., the signal and idler resulting from parametric amplification of a 1ω signal close to spectral degeneracy with a pump at 2ω (Ref. 5).

The SFG demonstration follows the principle described in Fig. 1(a). A collinear optical parametric amplifier (OPA) seeded with either a monochromatic tunable signal or a spectrally incoherent signal originating from an amplified spontaneous emission source at wavelengths below 1053 nm is pumped by a 1.5-ns pulse at 526.5 nm, leading to a combined signal and idler symmetric relative to 1053 nm (Ref. 5). The OPA 1ω output is spectrally dispersed by an 802.5-l/mm transmission grating at Littrow, which is re-imaged onto a 1-cm KDP crystal, itself re-imaged onto a 2305-l/mm transmission grating that compensates for the 3ω angular dispersion resulting from the 1ω angular dispersion and noncollinear SFG geometry. The OPA 2ω pump is separately re-imaged to the SFG crystal. For the fixed 1ω angular dispersion D , the noncollinear angle α is optimized for frequency conversion of a

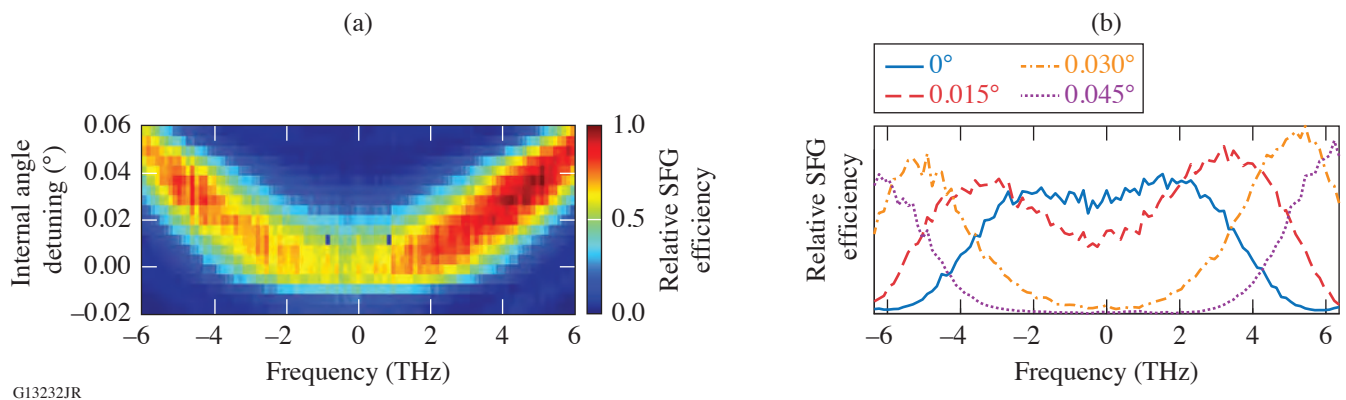


G12999JR

Figure 1 (a) Sum-frequency generation of a broadband angularly dispersed 1ω pulse with a narrowband 2ω pulse in a noncollinear geometry; (b) relative SFG efficiency for $\alpha = 1.7^\circ$ and $\Delta = -0.59$ mrad/nm versus crystal angle detuning.

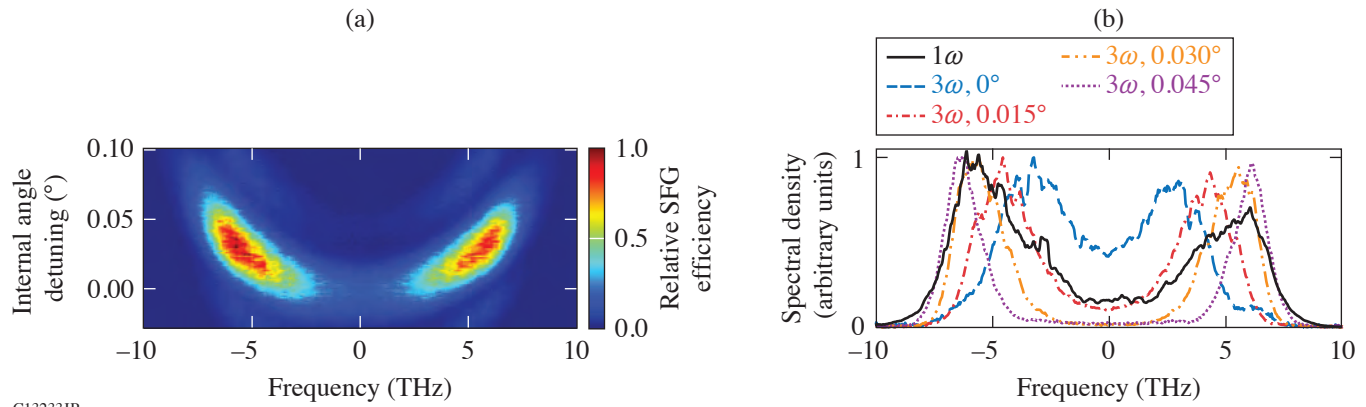
monochromatic signal at 1030 nm and the corresponding idler at 1077 nm at the same crystal angle, therefore ensuring symmetric phase matching relative to 1053 nm.

The spectral acceptance measured with a monochromatic tunable 1ω OPA seed shows that noncritical SFG is obtained at one specific crystal angle, while detuning matches the SFG to a pair of signal and idler beams at opposite frequencies relative to 1ω [Figs. 2(a) and 2(b)], in excellent agreement with the simulations [Fig. 1(b)]. Broadband spectrally incoherent light at 1ω is obtained by seeding the OPA with an amplified spontaneous emission pulse covering ~ 10 nm at 1030 nm. With the combined signal and idler, SFG-crystal tuning allows for the generation of more than 10 THz of bandwidth either centered at 351 nm or in two symmetric side lobes, depending on the crystal angle (Fig. 3).



G13232JR

Figure 2 Spectral acceptance characterization of a 1-cm KDP crystal with a tunable monochromatic 1ω signal: relative SFG energy versus (a) frequency relative to 3ω and crystal angle and (b) lineouts at four crystal angles.



G13233JR

Figure 3

Spectral density of a generated broadband spectrally incoherent pulse at 3ω (a) as a function of crystal angle and (b) for four crystal angles. In (b), the spectral density of the 1ω input to the SFG stage is plotted with a black line.

This material is based upon work supported by the Department of Energy National Nuclear Security Administration under Award Number DE-NA0003856, the University of Rochester, and the New York State Energy Research and Development Authority.

1. R. S. Craxton, IEEE J. Quantum Electron. **QE-17**, 1771 (1981).
2. A. Babushkin *et al.*, Opt. Lett. **23**, 927 (1998).
3. M. D. Skeldon *et al.*, IEEE J. Quantum Electron. **28**, 1389 (1992).
4. R. K. Follett *et al.*, Phys. Plasmas **26**, 062111 (2019).
5. C. Dorrer, E. M. Hill, and J. D. Zuegel, Opt. Express **28**, 451 (2020).

Generation of Strong Magnetic Fields for Magnetized Plasma Experiments on a 1-MA Pulsed-Power Machine

V. V. Ivanov,¹ A. V. Maximov,^{2,3} R. Betti,^{2,3,4} L. S. Leal,^{2,4} J. D. Moody,⁵ K. J. Swanson,¹ and N. A. Huerta¹

¹Department of Physics, University of Nevada, Reno

²Laboratory for Laser Energetics, University of Rochester

³Department of Mechanical Engineering, University of Rochester

⁴Department of Physics & Astronomy, University of Rochester

⁵Lawrence Livermore National Laboratory

Introduction

The development of techniques for the generation of strong magnetic fields provides an opportunity to investigate plasmas in megagauss (MG) fields. Strong magnetic fields change basic properties of hot and dense plasma. Studies of magnetized plasmas are relevant to basic and applied plasma physics, controlled fusion research, and astrophysics. Astrophysical magnetic fields can reach a value of 10^9 MG in magnetars¹ and a value of 1 to 100 MG in white dwarf plasma.² High magnetic fields also provide an increased neutron yield in inertial confinement fusion.³ A 30- to 40-MG magnetic field plays a key role in the magnetized liner inertial fusion (MagLIF) approach to fusion.⁴ Magnetic fields change the dynamics of plasma expansion,^{5–7} the development of plasma instabilities, and parametric effects. Laser–plasma interactions in external magnetic fields display unusual plasma expansion such as the generation of disk-like plasma in a 2- to 3-MG transverse magnetic field.⁷ Narrow plasma jets are generated in the longitudinal magnetic field.^{5,6} Astrophysical magnetized plasmas can be scaled to laboratory plasmas.⁵ Megaampere-class pulsed-power machines routinely generate MG magnetic fields.

Plasma in an Azimuthal Magnetic Field

Unusual dynamics of plasma expansion in the azimuthal 1- to 3-MG magnetic field of a rod load were observed in Ref. 7. Here, the results of an additional series of shots are presented. Figure 1(a) shows a scheme of the laser–plasma interaction (LPI) experiment with a laser pulse focused on the surface of the Al rod load 0.9 mm in diameter. A current in the load generates an azimuthal magnetic field. The laser intensity in the focal spot is 3 to 5×10^{15} W/cm². Without the laser pulse, a strong magnetic field contains plasma that arises on the surface of the load. After the laser shot, side-on laser-imaging diagnostics show the formation of two plasma jets on the front and rear sides of the load. The shadowgrams in Figs. 1(b) and 1(c) present jets of laser-produced plasma at 6 ns after the laser pulse. The magnetic field on the surface of the rod is $B = 1.3$ MG. One plasma jet propagated out from the focal spot; the second smaller jet was seen on the rear side of the rod load. Diagnostics with a tilted probe [Fig. 1(c)] explain the front and rear jets as parts of a plasma disk around the load. Plasma propagated along the magnetic field and formed a thin disk around the load with ring structures in it.

The radial size of the disk is longer and the plasma density is higher in the front half-disk, so the disk is not symmetric. Plasma expansion is observed during >10 ns after the laser pulse. The electron plasma density in the rings is 6 to 8×10^{18} cm⁻³. The formation of the disk happens only in the presence of the strong azimuthal B field. Two-frame shadowgrams and interferograms show that the disk expands radially with a velocity of ~ 250 km/s. The electron temperature of the plasma is measured from the x-ray Al K-shell spectra to be about 400 eV in the area of interaction. Plasma disks were observed in LPI with Al, Cu, and Ti rod loads.

Two-dimensional cylindrical magnetohydrodynamic (MHD) simulations of the plasma in the strong transverse magnetic field were performed in Ref. 8. The simulations with the current in the rod that resulted in a magnetic field of 3 MG on the rod

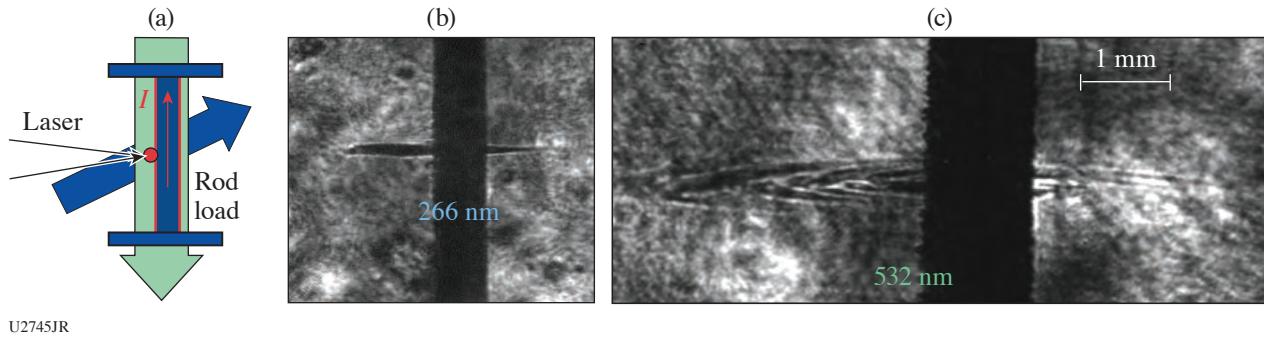


Figure 1
 (a) Experimental setup; [(b),(c)] side-on shadowgrams of a plasma disk [with a tilted probe beam in (c)].

showed the formation of the density wave localized in the axial direction and moving in the radial direction. The propagation of the density wave continues after the end of the laser pulse. The azimuthal magnetic field strongly changes in time in the region of the density wave due to magnetic-field generation by crossing density and temperature gradients. The change in the azimuthal magnetic field due to the density wave is comparable to the magnitude of the azimuthal field generated by the current in the rod. The magnetic β parameter at 1 to 2 ns after the laser pulse is about 1 and decreases after the pulse. The thermal pressure is responsible for the motion of the plasma. When plasma moves in the radial direction away from the rod, the thermal pressure decreases and the magnetic pressure has the main role in the plasma expansion. The density of the plasma in the MHD simulations is shown in Fig. 2 and is in agreement with the side-on shadowgrams in Fig. 1(b).

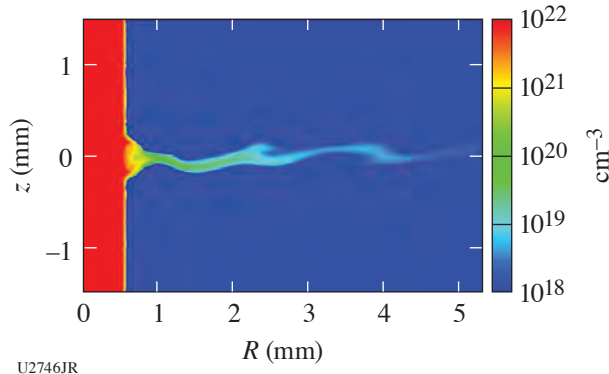


Figure 2
 Density of ablated plasma in the external magnetic field of 3 MG at 4 ns after the end of the laser pulse.

Plasma in the Longitudinal Magnetic Field

Plasma takes the shape of a jet in the longitudinal magnetic field of 0.1 to 0.2 MG (Ref. 5). A 1-MA pulsed-power machine allows for the investigation of plasma jets in higher magnetic fields.⁶ Plasma in the B field of the coil was produced by the Leopard laser operated with a 0.4-ps pulse. Intensity of the laser beam in the focal spot was 2 to 6×10^{18} W/cm². The laser target was placed at 1 mm from the copper coil 2.5 to 3 mm in internal diameter. The axial B field at this point was 0.5 to 0.7 MG, depending on the timing relative to the current pulse. A Si laser target was used to avoid the influence of eddy currents. The size of the target was 2×2 mm² and 10 μ m thick. The interferogram and shadowgram in Fig. 3 illustrate the collimation of plasma and the formation of the long plasma jet on the front side and the shorter rear jet in the B field of 0.7 MG. A plasma plume begins focusing at ~ 1 mm from the target and forms a narrow jet. The velocity of propagation of the jet tip calculated is ~ 200 km/s. Laboratory plasma jets of this type can be scaled to the astrophysical jets.⁵ In MHD simulations, plasma expands, forming a jet, and the magnetic field in the plasma is much weaker than the external magnetic field. At the same time, the magnetic field at plasma edges increases and becomes larger than the external field that results in collimation due to magnetic pressure. While the magnetic field is compressed at the edges of the jet, it is much smaller inside the jet forming the magnetic-field envelope. This

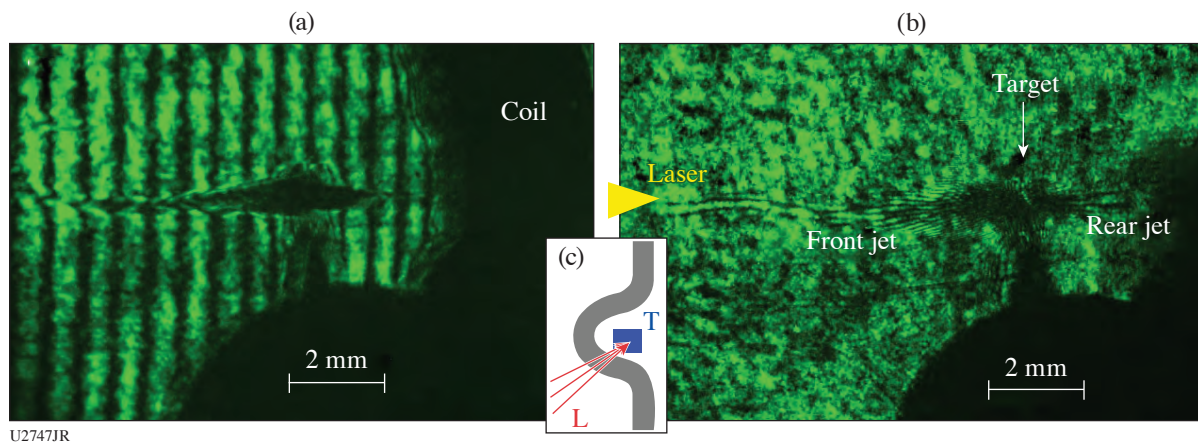


Figure 3

(a) Interferogram and (b) shadowgram of the Si target during the current and the magnetic field in the coil load at 7 ns after the laser pulse; (c) a schematic of the laser beam (L) and target (T) near the coil load.

envelope maintains the collimated jet during all its evolution. Later the diffusion of the magnetic field into the envelope makes the field inside the envelope close to the field on its edge. A plasma jet in a magnetic field depends on the magnetic β parameter being small. Figure 4 shows the expansion of the jet tip in simulations (the dashed line), and the tip positions in experiment and simulations are in a good agreement.

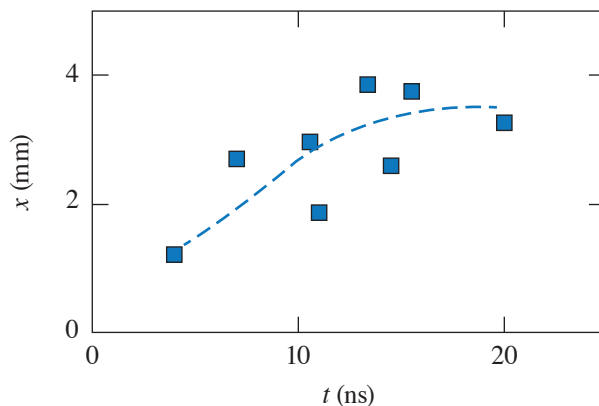


Figure 4

Positions of the jet tips (squares). MHD simulation (dashed curve).

Two-Plasmon Decay in the MG Magnetic Field

Two-plasmon decay (TPD) plays an important role in LPI. TPD occurs near one quarter of the plasma critical density n_c for the laser frequency ω_0 , and the resulting two Langmuir waves (plasmons) have “blue” and “red” spectral shifts compared to the $\omega_0/2$ frequency. Wave conversion involving these two plasmons generates new light waves with frequencies around $\omega_0/2$. Wave conversion involving TPD plasmons can also generate light with frequency around $3/2\omega_0$, which easily leaves the plasma and makes a robust diagnostic. The strong magnetic field produces a shift proportional to the square of the electron Larmor frequency $\omega_e \sim (\omega_{ce})^2/\omega_0$ in addition to the thermal shifts of the “red” and “blue” spectral components.⁹ The narrowband Nd:glass laser used in the TPD experiments generated pulses at 1053 nm with $\Delta\lambda_0 \sim 10$ pm and an energy of 6 J at 2 ns. Al and Ni rod loads 1 mm in diameter were used to generate the magnetic field of 2 to 3 MG in the surface plasma. A laser pulse was focused on the rod surface with an intensity of 1 to 3×10^{14} W/cm². An intensified charge-coupled-device (ICCD) camera was used to record the $3/2\omega_0$ emission.

Figure 5(a) presents $3/2\omega_0$ spectra from the Al rod load. The strong 2- to 3-nm widening and 2- to 4-nm shift of “red” and “blue” $3/2\omega_0$ spectral components were observed. Both red and blue $3/2\omega_0$ components are clearly seen but the blue component is weaker. The $3/2\omega_0$ emission was not seen in Ni and Cu loads. $3/2\omega_0$ emission can be observed only if TPD instability develops, and the TPD threshold is inversely proportional to the density scale length. The strong $3/2\omega_0$ emission in Fig. 5(a) is an indication of extended plasma with a gradual density profile, and the absence of $3/2\omega_0$ emission is an indication of more-localized plasma with a steep density profile.

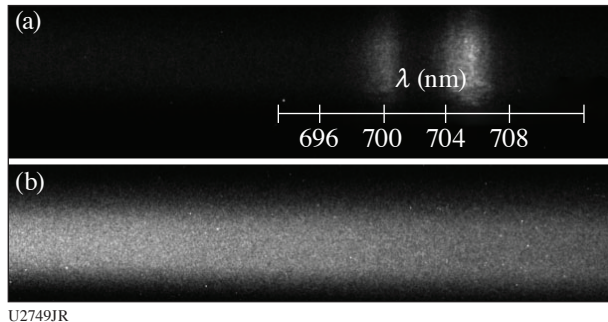


Figure 5
(a) Spectra of $3/2\omega_0$ harmonics from the Al rod load recorded by an ICCD camera with a 3-ns gate; (b) spectrum from the Ni load.

Conclusion

In this work, it was shown that the 1-MA pulsed-power machine provides a robust platform for experiments with plasma in MG magnetic fields. The dynamics of expansion of the laser-produced plasma in the strong transverse and longitudinal magnetic fields were studied with the rod and coil loads. The expanding plasma takes the shape of a thin plasma disk in the azimuthal field of the rod load. Plasma is confined in the vertical direction by the 2- to 3-MG magnetic fields. In the longitudinal magnetic field, laser-produced plasma generates narrow 3- to 4-mm jets with a density of 10^{19} to 10^{20} cm^{-3} . The TPD parametric instability generates wide and shifted “red” and “blue” components of $3/2\omega_0$ emission in the 2- to 2.7-MG field. Finally, pulsed-power technology provides a capability for the investigation of plasmas and laser–matter interaction in 1- to 4-MG magnetic fields at the university-scale machine.

This material is based upon work supported by the National Science Foundation (NSF) award PHY-1903355 through the NSF–DOE Partnership in Basic Plasma Science and Engineering and by the DOE NNSA under Award DE-NA0003991.

1. D. M. Palmer *et al.*, *Nature* **434**, 1107 (2005).
2. S. Jordan *et al.*, *Astron. Astrophys.* **462**, 1097 (2007).
3. P. Y. Chang *et al.*, *Phys. Rev. Lett.* **107**, 035006 (2011).
4. A. B. Sefkow *et al.*, *Phys. Plasmas* **21**, 072711 (2014).
5. B. Albertazzi *et al.*, *Science* **346**, 325 (2014).
6. V. V. Ivanov *et al.*, *Phys. Plasmas* **26**, 062707 (2019).
7. V. V. Ivanov *et al.*, *Plasma Phys. Control. Fusion* **59**, 085008 (2017).
8. L. S. Leal *et al.*, *Phys. Plasmas* **27**, 022116 (2020).
9. N. G. Basov *et al.*, *JETP* **65**, 954 (1987).

FY21 Q2 Laser Facility Report

J. Puth, M. Labuzeta, D. Canning, and R. T. Janezic

Laboratory for Laser Energetics, University of Rochester

During the second quarter of FY21, the Omega Facility conducted 295 target shots on OMEGA and 202 target shots on OMEGA EP for a total of 497 target shots (see Tables I and II). OMEGA averaged 10.2 target shots per operating day, averaging 91.5% Availability and 97.8% Experimental Effectiveness. OMEGA EP averaged 7.8 target shots per operating day, averaging 88.4% Availability and 94.1% Experimental Effectiveness.

Table I: OMEGA Laser System target shot summary for Q2 FY21.

Program	Laboratory	Planned Number of Target Shots	Actual Number of Target Shots
ICF	LLE	60.5	61
	LANL	22	24
	LLNL	11	14
ICF Subtotal		93.5	99
HED	LANL	33	34
	LLNL	27.5	31
HED Subtotal		60.5	65
LBS	LLE	22	23
	LLNL	11	9
LBS Subtotal		33	32
AIBS		27.5	21
NLUF		55	51
Calibration	LLE	0	27
Grand Total		269.5	295

Table II: OMEGA EP Laser System target shot summary for Q2 FY21.

Program	Laboratory	Planned Number of Target Shots	Actual Number of Target Shots
ICF	LLE	28	40
	LLNL	7	7
ICF Subtotal		35	47
HED	LLE	7	8
	LANL	14	19
	LLNL	14	14
HED Subtotal		35	41
LBS	LLE	21	31
	LLNL	35	42
LBS Subtotal		56	73
LNet		7	6
NLUF		24.5	23
Calibration	LLE	0	12
Grand Total		157.5	202

For OMEGA and OMEGA EP shot planning efforts, the Experimental Proposal and Shot Request Form (SRF) systems were upgraded. The SRF now requires an association to the Proposal template during creation and uses this information to determine the date of the SRF. With this upgrade all SRF’s can follow schedule changes with a single update.

The OMEGA Stage-F Alignment Sensor Package upgrade project has now completed 30 of 60 beamline systems. The cameras are being replaced with higher-resolution digital charge-coupled–device (CCD) equipment.

The OMEGA EP beam apodization system that ensures that the gaps between gratings in the pulse compressors do not see damaging laser fluence (known as the “gapodizers”) had position sensors relocated for enhanced system safety. Two optics replacements have occurred of interest to the PI community: The OMEGA EP lower compressor deformable mirror was replaced due to laser damage accumulated over years of operation, and the OMEGA EP “backlighter” beam’s off-axis parabola (OAP) focusing optic was replaced with a reworked OAP.

Direct Evidence of Fuel–Ablator Mix from Monochromatic Time-Gated Radiography in OMEGA Cryogenic Implosions

T. J. B. Collins, C. Stoeckl, R. Epstein, W. A. Bittle, C. J. Forrest, V. Yu. Glebov, V. N. Goncharov, D. R. Harding, S. X. Hu, D. W. Jacobs-Perkins, T. Z. Kosc, J. A. Marozas, C. Mileham, F. J. Marshall, S. F. B. Morse, P. B. Radha, S. P. Regan, B. Rice, T. C. Sangster, M. J. Shoup III, W. T. Shmayda, C. Sorce, W. Theobald, and M. D. Wittman

Laboratory for Laser Energetics, University of Rochester

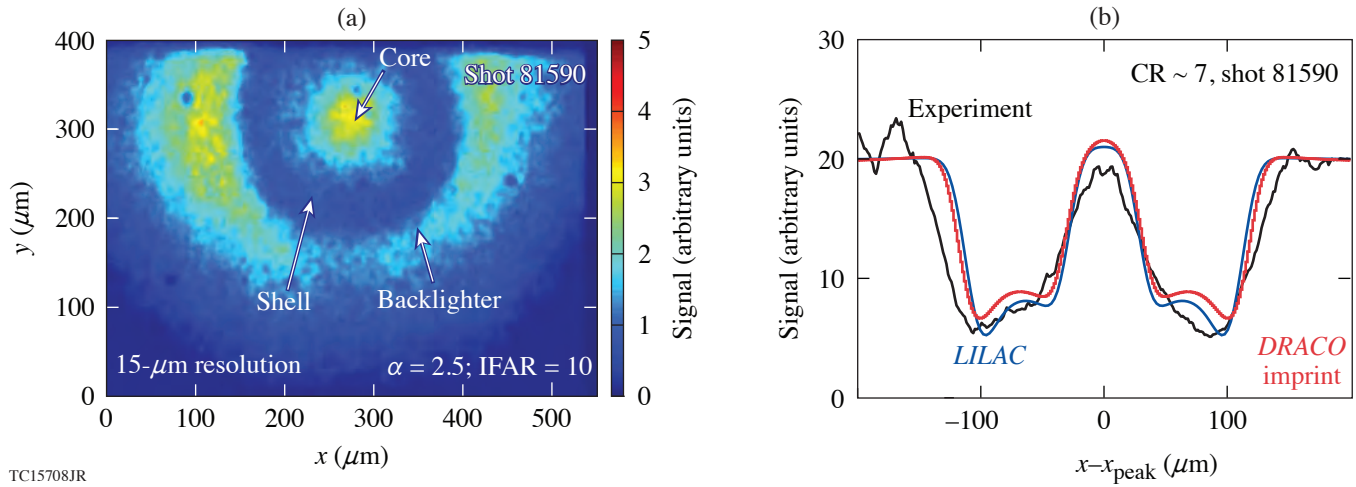
In direct-drive inertial confinement fusion,¹ a shell is imploded via direct laser-light illumination. The shell is composed of an inner layer of fuel (typically equimolar deuterium and tritium, which maximizes yield) and a thinner outer “ablator” layer of non-fuel material (e.g., a CH polymer). The implosion of a two-layer shell filled with gaseous fuel is used to briefly assemble a “hot spot” of sufficiently high temperature (4 or more keV) and density for D–T fusion reactions to occur. The fusion neutron yield depends on the hot-spot conditions and the confinement time, the latter depending on the areal density of the shell and ablator at stagnation. Various phenomena can reduce the shell areal density, such as heating of the shell by suprathermal electrons generated in the corona surrounding the imploding target; shock dynamics, which must be carefully engineered due to the increase in entropy generated by mistimed shocks; absorption of coronal radiation by the shell, which places an additional constraint on the choice of ablator material; and mixing of the ablator and shell fuel material due to hydrodynamic instabilities, particularly the Rayleigh–Taylor instability (RTI).

In this summary we infer the degree of fuel–shell mixing using 2-D radiation-hydrodynamic modeling of two OMEGA cryogenic implosions. The properties of the two implosions in question are shown in Table I (with 1-D simulated data calculated using the radiation hydrocode *LILAC*²). Direct evidence that this is due to Rayleigh–Taylor fuel–ablator mixing in these two implosions was previously obtained using a Si He α backlighter driven by an \sim 20-ps short pulse generated by OMEGA EP.³ The shadow cast by the shell shortly before stagnation, as diagnosed using backlit radiographs, shows a softening near the limb, which is evidence of an ablator–fuel mix region for a low-adiabat implosion ($\alpha \sim 1.9$, in-flight aspect ratio IFAR = 14) but not for a moderate adiabat implosion ($\alpha \sim 2.5$, IFAR = 10). We consider various possible causes of fuel–shell mix, using the radiation-hydrodynamic code *DRACO*, and find good agreement between experimental and simulated radiographs when imprint is modeled and for a particular ablator thickness that lies within the range of possible thicknesses as determined by pre-shot target metrology. Modeling with *DRACO*⁴ includes multigroup radiative transport, nonlocal electron heat transport, scattering due to cross-beam energy transfer,⁵ and first-principles⁶ equation of state and opacity models, and is post-processed with *Spect3D*⁷ to generate synthetic x-ray images for direct comparison

Table I: Simulated and experimental properties of the moderate- and low-adiabat shots 81590 and 82717, respectively. The ratio of the pressure to the Fermi pressure at zero temperature is given by α ; IFAR is the in-flight aspect ratio, the ratio of the initial shell radius to the thickness at a convergence of 1.5; T_i is the neutron-weighted ion temperature; ρR is the neutron-weighted areal density of the shell; $\rho R/\text{clean}$ is the ratio of measured to 1-D simulated areal density; and YOC is the ratio of experimental to 1-D yield.

Shot	<i>LILAC</i> (1-D)						Experiment		
	α	IFAR	v_{imp} (km/s)	ρR (mg/cm ²)	$T_{i,LILAC}$ (keV)	Y_{LILAC} (10 ¹³)	$\rho R/\text{clean}$	$T_{i,\text{exp}}$ (keV)	YOC
81590	2.5	10	240	250	2.2	1.4	78%	2.7	19%
82717	1.9	14	280	246	2.4	2.6	41%	2.4	8%

with experimental framing-camera images. Furthermore, because lineouts from synthetic radiographs of 1-D and 2-D simulations show good agreement for the moderate adiabat shot 81590 (see Fig. 1), we focus below on the lower-adiabat shot 82717. In the possible sources of mix described below, we begin with those found to be the less significant, concluding with the most significant, imprint.



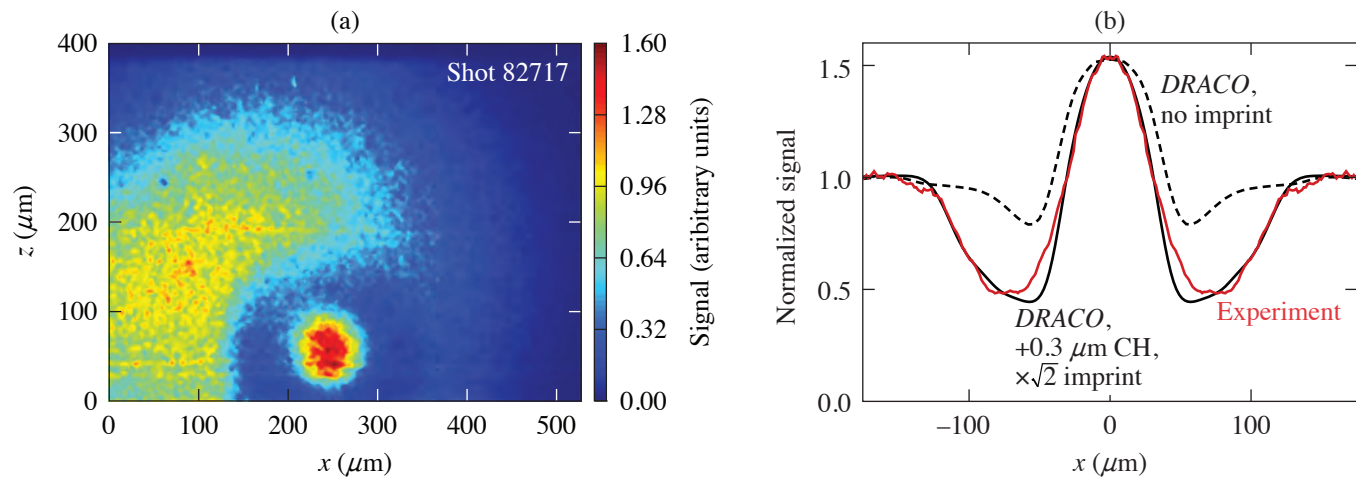
TC15708JR

Figure 1

The (a) experimental radiograph for shot 81590 and (b) radiographic lineouts for the experiment (black curve), *LILAC* (blue curve), and *DRACO* (red curve), plotted as functions of the horizontal coordinate measured relative to the position of the peak core emission (x_{peak}). CR: convergence ratio.

Long-Wavelength Modes

The imploding shell is unstable to Rayleigh–Taylor and Richtmyer–Meshkov instabilities, which can be seeded by target and laser nonuniformities and imperfections. We modeled the effects of long-wavelength laser drive nonuniformities, including beam-to-beam power imbalance, and beam pointing error. Long-wavelength mode growth can also be seeded by nonuniformity in the inner edge of the DT ice, the greatest amplitudes of which occur for Legendre modes with modal index less than 10. The impact of these was found to be negligible in the fuel–ablator mix used for both shots, although perturbations with Legendre-mode indices 1 and 2 have a visible effect on the shape of the core emission and may be responsible for the slight elongation of the hot spot [Fig. 2(a)].



TC15717JR

Figure 2

(a) The experimental radiograph for shot 82717 shows a hot central core (red) surrounded by a dark ring of shell absorption, further surrounded by the off-center backlighter emission. (b) Radiographic lineouts of shot 82717 for the experiment (red curve), symmetrized about $x = 0$, where x is the horizontal position in the image plane; a simulation without imprint (dashed black curve); and a *DRACO* simulation with imprint and an additional 0.3 μm of initial ablator thickness.

Kinetic Effects and Concentration Diffusion

Another mechanism investigated as a means of transporting carbon deep into the imploding shell is concentration diffusion. One of many kinetic effects that have received attention in recent years,⁸ concentration diffusion is expected to occur wherever a concentration gradient exists in a multispecies plasma.⁹ The flux in this case is given by Fick's law and is proportional to the concentration gradient. A second-order accurate ion concentration diffusion model was implemented in *DRACO* to investigate this effect. At the fuel–shell interface the concentration gradient scale length is small, being comparable to the mean-free path for the cold shell material. Due to the low temperatures and high densities, the concentration flux remains small throughout the implosion, increasing only upon complete ablation of the CH ablator, which occurs late in time. Once the CH is ablated, the temperature quickly rises and the density drops, causing the diffusion coefficient to rise; however, the region where the concentration gradient is large has also ablated. Therefore, concentration diffusion is able to flux material within the corona but not within the shell.

Classical Instability Growth at the Fuel–Ablator Interface

One natural source of mix to consider is perturbation growth at the fuel–ablator interface seeded by perturbations on that surface. Unlike at the ablation surface, growth of modes here due to the RTI is not diminished by ablation, so no high-mode ablative cutoff exists. Beta decay from tritium decay in permeation-filled–target cases causes localized damage at the inner shell surface, potentially seeding the perturbation growth. This may play a role in the known relationship between target age and performance.¹⁰ In addition, the surface roughness of the polystyrene ablator shell may seed perturbation growth. A simulation of shot 82717 was performed with a piecewise power-law function approximating the measured polystyrene power spectrum and was repeated with the spectrum multiplied by various multiples. For the nominal case, the effects of the perturbation are small and have a negligible impact on the shell mass density. For the enhanced simulation, the impact is more significant on the shell mass density, but there is still minimal material mixing due to perturbation growth.

Laser Imprint

For the lower-adiabat shot, 82717, the radiograph lineout from a 1-D simulation fails to match either the radial extent (width) or depth of the shadow cast by the shell. *DRACO* simulations were performed with the expected level of laser imprint, as well as for enhanced levels in which the imprint spectrum was multiplied by factors of $\sqrt{2}$ and 2. These simulations were able to reproduce the depth of the shell shadow but not the width, the closest agreement in the shell depth being found for the $\sqrt{2}$ simulation. Because 3-D perturbations are known to grow more quickly than 2-D perturbations, the need for an enhanced imprint spectrum in a 2-D simulation is expected.¹¹

The discrepancy in the depth of the shell shadow has a ready explanation in the markedly greater bound–free absorption of the CH compared to the free–free absorption of the DT fuel. A survey of simulations with the same shell mass but different initial ablator thickness shows that an ablator thickness of $0.3\ \mu\text{m}$ has a marked impact on the thickness of the shell shadow. A radiographic lineout from a simulation using an ablator thickness of $11.5\ \mu\text{m}$ and incorporating enhanced imprint shows a close agreement with the experimental data (Fig. 2). It should be noted that the impact of ablator thickness on the shadow width and imprint on the shadow depth are independent; increasing the degree of imprint fails to increase the thickness of the shadow, and increasing the ablator thickness alone cannot reproduce the depth of the shadow without making it far too wide. The important result of this study is that the experimental radiograph is only reproduced by enhanced imprint (not unexpected) combined with an ablator that lies within the measured range of $10.9\ \mu\text{m}$ to $11.5\ \mu\text{m}$ but lies at the upper limit of the range of uncertainty of the measurement. The latter observation allows two possible inferences: (a) The actual ablator thickness was within the measurement error, or (b) the ablator thickness was actually smaller but the simulated ablation rate exceeded the experimental rate, a possibility suggested by previous warm-target implosions.¹² This suggests value in developing and investing in higher-precision target metrology.

In conclusion, two OMEGA cryogenic implosions were backlit by OMEGA EP, obtaining radiographs of the hot-spot and stagnation fuel–shell assembly close to peak convergence. The implosions were designed to lie on either side of the stability threshold, and both simulations and experimental data bear this out. Modeling of the moderate-adiabat implosion agrees well with experiment, as expected. Modeling of the low-adiabat implosion agrees when an enhanced level of imprint is modeled, and only when a sufficiently thick ablator (within measurement error) is assumed.

This material is based upon work supported by the Department of Energy National Nuclear Security Administration under Award Number DE-NA0003856, the University of Rochester, and the New York State Energy Research and Development Authority.

1. R. S. Craxton *et al.*, *Phys. Plasmas* **22**, 110501 (2015).
2. J. Delettrez *et al.*, *Phys. Rev. A* **36**, 3926 (1987).
3. R. Epstein *et al.*, *High Energy Density Phys.* **23**, 167 (2017); C. Stoeckl *et al.*, *Phys. Plasmas* **24**, 056304 (2017).
4. P. B. Radha *et al.*, *Phys. Plasmas* **23**, 056305 (2016); I. V. Igumenshchev *et al.*, *Phys. Plasmas* **17**, 122708 (2010).
5. C. J. Randall, J. J. Thomson, and K. G. Estabrook, *Phys. Rev. Lett.* **43**, 924 (1979).
6. J. J. MacFarlane *et al.*, *High Energy Density Phys.* **3**, 181 (2007).
7. S. X. Hu *et al.*, *Phys. Rev. B* **84**, 224109 (2011); S. X. Hu *et al.*, *Phys. Rev. E* **92**, 043104 (2015); S. X. Hu *et al.*, *Phys. Rev. E* **90**, 033111 (2014); S. X. Hu *et al.*, *Phys. Plasmas* **25**, 056306 (2018).
8. P. Amendt *et al.*, *Phys. Plasmas* **18**, 056308 (2011).
9. R. B. Bird, W. E. Stewart, and E. N. Lightfoot, *Transport Phenomena*, Revised 2nd ed. (John Wiley & Sons, Inc., New York, 2007).
10. E. M. Campbell *et al.*, *Phil. Trans. R. Soc. A* **379**, 20200011 (2020); A. Lees *et al.*, *Phys. Rev. Lett.* **127**, 105001 (2021).
11. M. M. Marinak *et al.*, *Phys. Rev. Lett.* **80**, 4426 (1998); R. Yan *et al.*, *Phys. Plasmas* **23**, 022701 (2016).
12. D. T. Michel *et al.*, *High Power Laser Sci. Eng.* **3**, e19 (2015).

Measuring Magnetic-Flux Suppression in High-Power Laser–Plasma Interactions

P. T. Campbell,¹ C. A. Walsh,² B. K. Russell,¹ J. P. Chittenden,³ A. Crilly,³ G. Fiksel,¹ L. Gao,⁴ I. V. Igumenshchev,⁵
P. M. Nilson,⁵ A. G. R. Thomas,¹ K. Krushelnick,¹ and L. Willingale¹

¹G rard Mourou Center for Ultrafast Optical Science, University of Michigan

²Lawrence Livermore National Laboratory

³Blackett Laboratory, Imperial College, London

⁴Princeton Plasma Physics Laboratory

⁵Laboratory for Laser Energetics, University of Rochester

In high-power-laser-produced plasmas, strong magnetic fields can be spontaneously generated by a number of mechanisms, although the primary source is the Biermann battery effect caused by nonparallel temperature and density gradients ($\partial B/\partial t \propto \nabla T_e \times \nabla n_e$). A detailed understanding of self-generated magnetic fields is critical to laser-fusion research because strong fields can influence thermal energy transport and potentially impact the evolution of hydrodynamic instabilities. Laser-driven magnetic fields also enable laboratory investigations of magnetized astrophysical phenomena, especially magnetic reconnection.

The extended-magnetohydrodynamics (extended-MHD) framework has been developed to describe transport of energy and magnetic fields in high-energy-density (HED) plasmas.¹ Predictive modeling used in concert with experimental observations is often essential for developing and interpreting both laser-fusion and laboratory astrophysics experiments. Although relatively simple in the broader context of HED experiments, a single laser spot interacting with a foil target can provide a powerful platform for validating extended-MHD modeling.

Using proton deflectometry to make high spatial and temporal resolution measurements of magnetic-field generation driven by moderate laser intensities ($I_L = 10^{14}$ to 10^{15} W/cm²), recent experiments demonstrated that simulations of laser–foil interactions must incorporate key physical processes such as Biermann battery field generation and Nernst advection.^{2,3} By varying the target material the influence of atomic or radiation physics on transport and field dynamics can be explored. Incorporating radiation transport into extended-MHD simulations reproduced recent experimental observations of two distinct regions of magnetic-field generation around radiation-driven double ablation fronts in mid-*Z* targets.⁴

In that work, however, it was found that extended-MHD simulations overestimated the generated magnetic flux. It is anticipated that nonlocal effects not captured by the extended-MHD framework can suppress the rate of Biermann battery field generation in regions where the electron mean free path (λ_{ei}) approaches (or exceeds) the local temperature-gradient length scale ($l_T = |T_e/\nabla T_e|$). Using empirical fits to kinetic simulations, Sherlock and Bissell⁵ developed a scaling for the suppression of classical Biermann battery generation rates as a function of the ratio λ_{ei}/l_T .

In this summary, experimental observations of magnetic flux are used to help validate extended-MHD simulations that include the new scaling for nonlocal suppression of Biermann battery field generation, as well as radiation transport. Experimental data are drawn from two campaigns performed with the OMEGA EP laser. Magnetic-field generation was driven by either one⁴ ($I_L = 2.2 \times 10^{14}$ W/cm²) or two overlapped³ ($I_L = 4.4 \times 10^{14}$ W/cm²) UV laser pulses interacting with thin foil targets. The foil material was varied between 50- μ m-thick plastic (CH), 25- μ m copper, 25- μ m aluminum, or 50- μ m aluminum coated with either 1 μ m of copper (Cu + Al) or gold (Au + Al). Self-generated magnetic fields were imaged by protons in a point-projection geometry.

In both experiments a high-intensity laser pulse was used to produce a proton probe via the target normal sheath acceleration mechanism. A 1-D polar-coordinates field reconstruction technique was developed to extract quantitative path-integrated magnetic-field information from radial lineouts through the proton images.^{4,6}

Experimental measurements were compared to extended-MHD simulations performed using the Gorgon code,¹ which was updated with the option to include the new scaling for suppression of magnetic-field generation due to kinetic effects (referred to throughout as “Biermann suppression”). The results for CH foil targets are summarized in Fig. 1. Proton images show the evolution of magnetic-field structures using the higher laser intensity ($2I_0$, overlapped pulses) in Fig. 1(a). Corresponding reconstructed magnetic-field profiles are plotted in Fig. 1(b). Figure 1(c) compares the evolution of the azimuthal magnetic flux from the experiment and extended-MHD simulations for both laser intensities. Simulations without Biermann suppression greatly overestimate the magnetic flux ($>5\times$). Agreement is significantly improved by including Biermann suppression, indicating that this effect is likely influencing the field dynamics. In the simulations, the suppression results in a $3\times$ to $4\times$ reduction in the predicted magnetic flux.

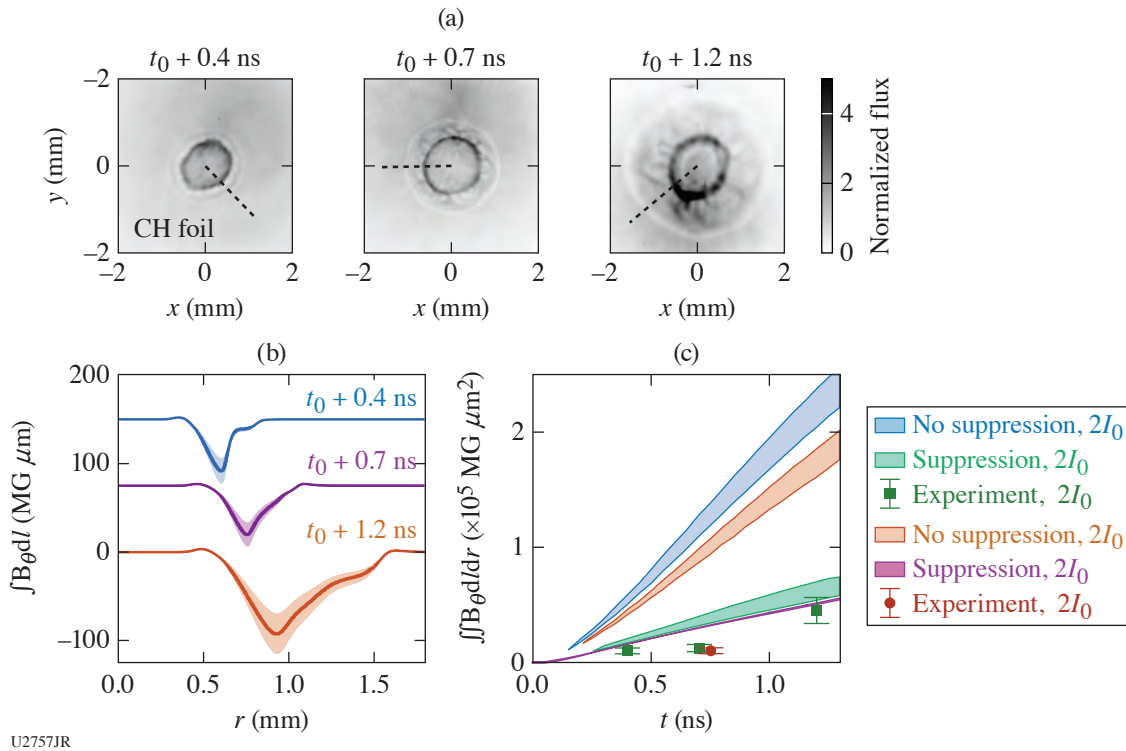
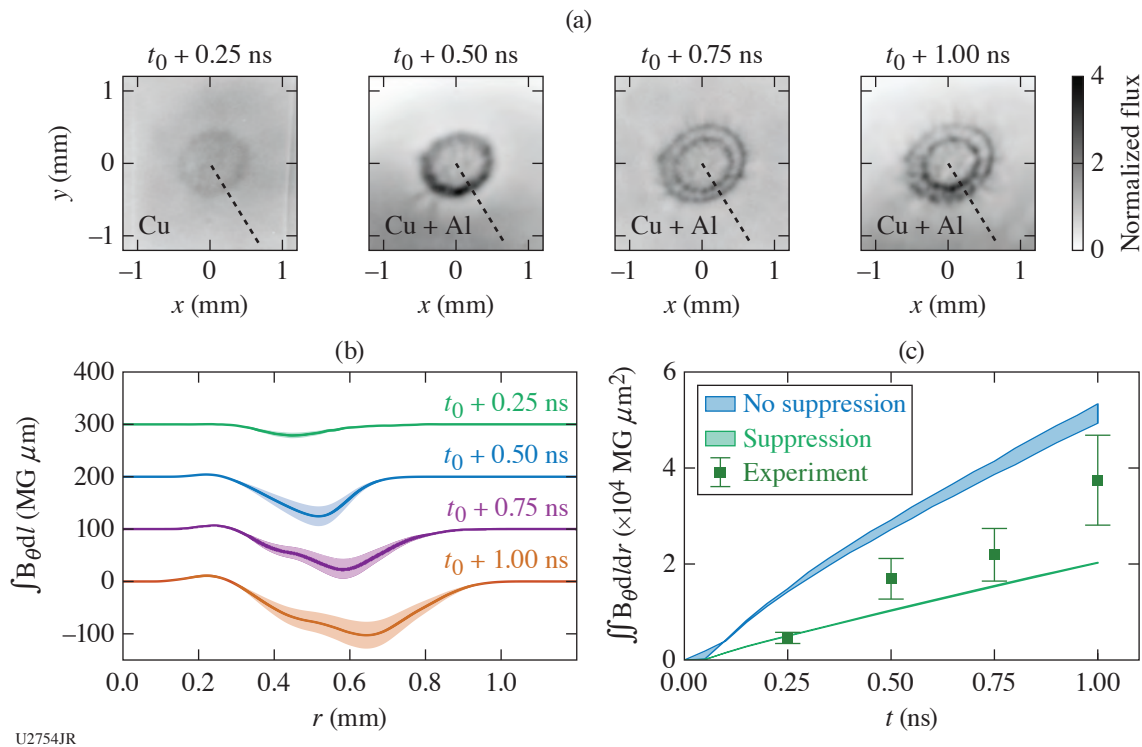


Figure 1

Comparison of experimental and simulation results for CH foils. (a) Proton images of fields driven by the higher, overlapped laser intensity ($2I_0$) taken at 0.4 ns, 0.7 ns, and 1.2 ns. Radial lineout locations are indicated by dashed lines. (b) Reconstructed magnetic-field profiles (offset vertically for clarity). (c) Magnetic-flux predictions from simulations both without and with Biermann suppression for each laser intensity are compared to experimental measurements. Upper and lower bounds on the simulation results are produced by tuning the laser energy to approximate the influence of energy-coupling efficiency (corresponding to $\sim 90\%$ and $\sim 70\%$ coupling, respectively).

Figure 2 summarizes the results for Cu foil targets with the lower laser intensity. As with CH targets, the simulations without suppression overestimate the flux, although the discrepancy is not as large. For Cu targets, however, the Biermann suppression model reduces the predicted flux below experimental observations. Overall, the simulation and experimental results suggest that nonlocal suppression effects are more significant for low- Z targets. Without Biermann suppression, simulations with Cu targets predict lower magnetic flux than the CH results, likely due to additional radiative losses at higher Z , reducing temperature gradients. In contrast, the experimental measurement of the magnetic flux increases when the target changes from CH to Cu. The same



U2754JR

Figure 2

Comparison of experimental and simulation results for Cu foils. (a) Proton images at 0.25 ns, 0.5 ns, 0.75 ns, and 1.0 ns. Lineout locations are indicated by dashed lines. The target for $t_0 + 0.25$ ns was a 25- μm -thick Cu foil, and the other probing times use a Cu + Al layered target. (b) Reconstructed magnetic-field profiles. (c) Magnetic-flux predictions from simulations both without and with Biermann suppression are compared.

qualitative trend is also seen in the simulations including Biermann suppression, where the copper targets are less kinetic, due to both lower temperature gradients from radiative losses and shorter mean free paths for higher- Z plasmas.

In conclusion, quantitative measurements of magnetic flux enable detailed comparisons between experiments and extended-MHD simulations, demonstrating the need to account for suppression of Biermann battery generation due to nonlocal effects. Even with the Biermann suppression, the simulations with CH targets overestimate magnetic-flux generation. For Cu, however, while some suppression is necessary, the implementation of the suppression scaling decreases the predicted flux below experimental observations. The effects of radiation-hydrodynamics and the equation of state likely influence the details of simulations but are beyond the scope of this work. In future experiments, additional diagnostics, such as Thomson scattering and interferometry, can help constrain plasma parameters to further validate and improve extended-MHD models. Combined with the magnetic-field analysis presented in this work, measurements of the temperature and density profiles can elucidate the dynamic interplay between energy transport and field generation in HED plasmas.

This material is based upon work supported by the Department of Energy, National Nuclear Security Administration under Award Numbers DE-NA0003606, DE-NA0003764, and DE-AC52-07NA27344. P. T. Campbell is supported by the U.S. Department of Energy Fusion Energy Sciences Postdoctoral Research Program administered by the Oak Ridge Institute for Science and Education (ORISE) for DOE. ORISE is managed by Oak Ridge Associated Universities (ORAU) under DOE contract number DE-SC0014664. B. K. Russell acknowledges support from National Science Foundation Award Number 1751462.

1. C. A. Walsh *et al.*, Phys. Plasmas **27**, 022103 (2020).
2. L. Willingale *et al.*, Phys. Rev. Lett. **105**, 095001 (2010).

3. L. Gao *et al.*, Phys. Rev. Lett. **109**, 115001 (2012).
4. P. T. Campbell *et al.*, Phys. Rev. Lett. **125**, 145001 (2020).
5. M. Sherlock and J. J. Bissell, Phys. Rev. Lett. **124**, 055001 (2020).
6. P. T. Campbell *et al.*, “Measuring Magnetic Flux Suppression in High-Power Laser-Plasma Interactions,” Physics Archive, <https://arxiv.org/abs/2107.12864> (2021).

Observed Suppression of Self-Generated Magnetic Fields in a Laser-Driven Cylindrical Implosion

P. V. Heuer,¹ L. S. Leal,¹ J. R. Davies,¹ E. C. Hansen,¹ D. H. Barnak,¹ J. L. Peebles,¹ and A. Birkel²

¹Laboratory for Laser Energetics, University of Rochester

²Plasma Science and Fusion Center, Massachusetts Institute of Technology

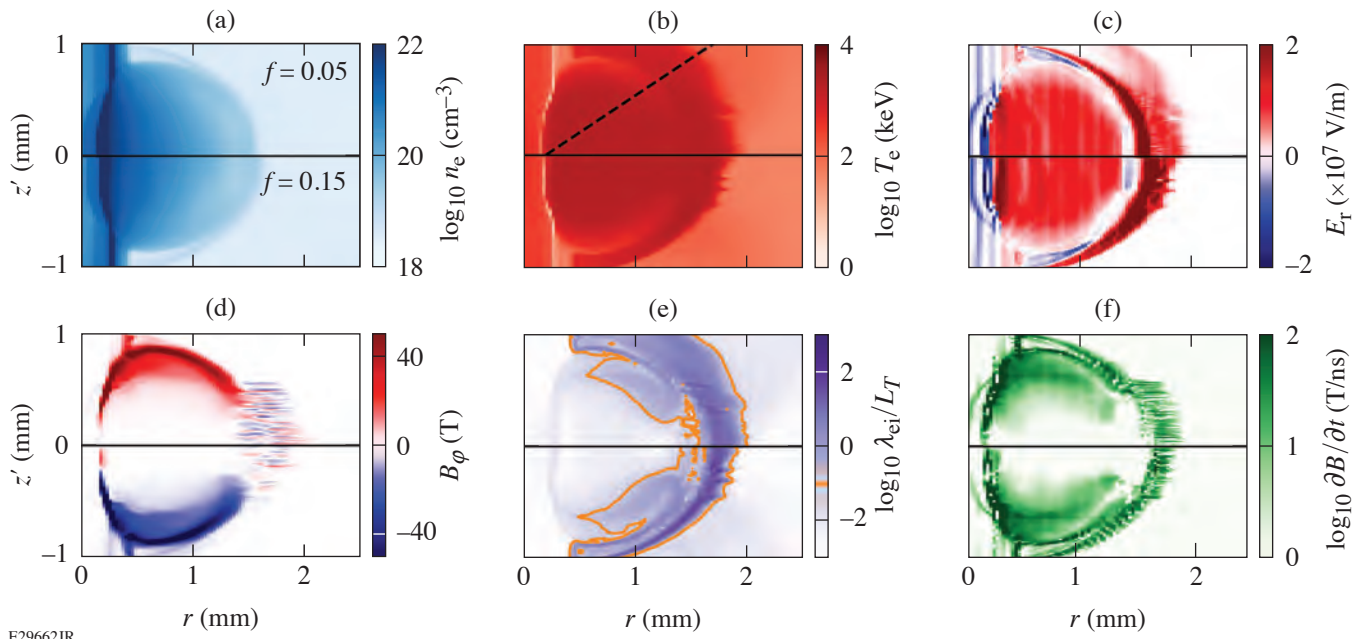
The spontaneous generation of magnetic fields in plasmas is responsible for the creation of astrophysical magnetic fields from the primordial universe to stellar environments. Self-generated magnetic fields are also key features of many laboratory experiments on subjects ranging from laboratory astrophysics to inertial confinement fusion. Once generated, these fields can substantially alter particle and energy transport in the plasma, fundamentally modifying the plasma dynamics. Accurate computational modeling of magnetic-field self-generation is therefore crucial to correctly simulating these systems.

Many systems of interest require large simulation volumes and/or resolutions that are only computationally tractable using magnetohydrodynamics (MHD). However, recent theoretical articles^{1,2} comparing MHD and Vlasov–Fokker–Planck (VFP) kinetic simulations have predicted that kinetic (nonlocal) effects neglected in MHD could lead to a substantial overestimate of self-generated magnetic fields in MHD simulations. This discrepancy could result in substantial errors in MHD simulations that include regions of low collisionality (where kinetic effects are non-negligible). This is particularly (but not exclusively) significant for laboratory experiments with laser-produced plasmas, which self-generate magnetic fields within the relatively low-density ablated plasma.

Results from a cylindrical implosion experiment on the OMEGA Laser System recently provided the first experimental evidence directly demonstrating the suppression of self-generated magnetic fields relative to MHD simulations in an inertial confinement fusion experiment. This measurement is made using oblique proton radiography, which allows axially resolved measurements of self-generated azimuthal magnetic fields that are undetectable at normal incidence. Comparisons to synthetic radiographs generated using simulated fields show that the observed field is a factor of $\sim 0.4\times$ smaller than predicted by MHD. Simulation results also indicate that nonlocal effects are likely responsible for this discrepancy.

The experiment utilizes a platform³ initially developed for studying laser-driven magnetized liner inertial fusion (MagLIF)⁴ on the OMEGA Laser System. The target is a gas-filled (11 atm D_2) parylene-N cylinder (CH, 20 μm thick, outer diameter of 580 μm) imploded using 40 beams (1.5-ns square pulse length, 16-kJ total energy) with an overlapped intensity of 10^{14} W/cm². Prior to compression, an axial beam (180 J) blows down a thin window on the end of the cylinder and preheats the D_2 gas. A set of external coils driven by MIFEDS (magneto-inertial fusion electrical discharge system)⁵ provides an axial magnetic field ($B_z = 9$ T) for one shot but is inactive for a second unmagnetized shot. Proton radiography⁶ is used to diagnose the self-generated magnetic fields.

The multiphysics radiation-hydrodynamics code *HYDRA*⁷ is used to perform two 3-D simulations of the unmagnetized experiment with different flux limiters ($f = 0.15$ and $f = 0.05$) and one simulation of the magnetized experiment ($f = 0.15$). Varying the flux limiter tests the extent to which it affects the Biermann battery mechanism by modifying the electron temperature gradients.² The unmagnetized simulation results (Fig. 1) show a coronal plasma expanding away from the axis as the cylinder implodes. Steep density and temperature gradients are present within the ablated plasma and the cylinder. The dominant electromagnetic field components are a radial electric field $E_r \sim 10^7$ V/m and an azimuthal magnetic field $B_\phi \sim 50$ T. The orientation of this mag-



E29662JR

Figure 1

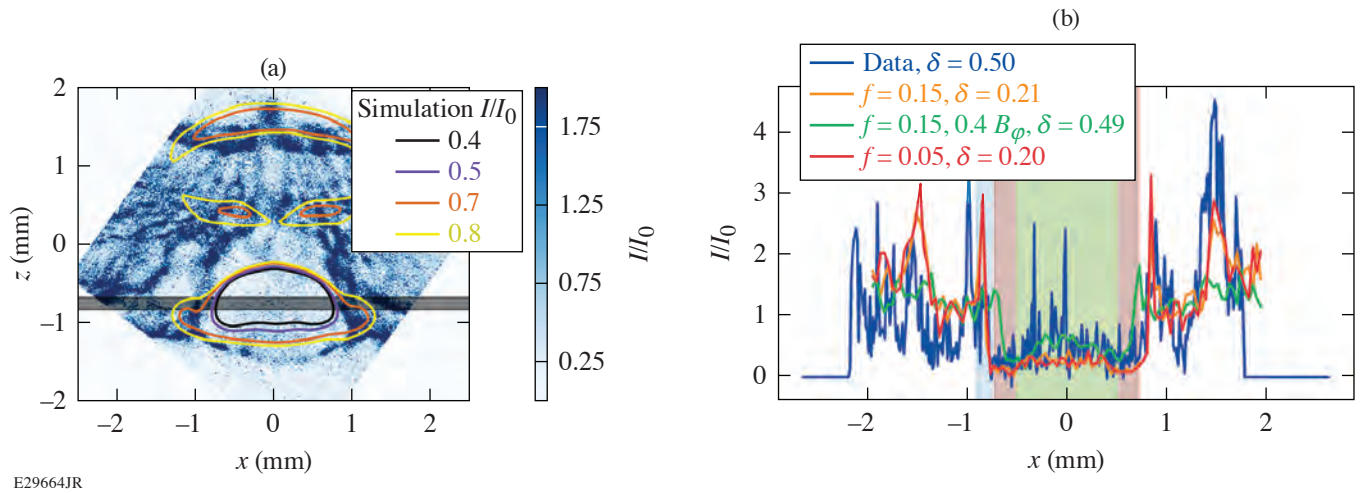
HYDRA outputs of the (a) electron density, (b) electron temperature, (c) radial electric field, (d) azimuthal magnetic field, (e) nonlocality parameter λ_{ei}/L_T , and (f) MHD Biermann battery source term at $t = 0.9$ ns. The top and bottom halves of each plot show the $f = 0.05$ and $f = 0.15$ unmagnetized simulations, respectively. An orange contour in (e) marks the region $\lambda_{ei}/L_T > 0.1$, where nonlocal effects are expected to be significant.

netic field is consistent with it being generated by the Biermann battery mechanism due to nonparallel temperature and pressure gradients in the coronal plasma. The magnetized simulation is comparable, but it also includes a compressed axial magnetic field at the center of the cylinder. The self-generated magnetic field is found to be insensitive to the choice of flux limiter.

To determine the possible impact of nonlocal effect on thermal transport, the nonlocality parameter λ_{ei}/L_T is calculated from the HYDRA results, where $L_T = T_e/\nabla T_e$ is the gradient length scale of the electron temperature T_e and λ_{ei} is the electron ion mean free path; and $16\pi\epsilon_0^2 T_e^2 / Z n_e e^4 \log\Lambda$, and where ϵ_0 is the permittivity of free space, n_e is the electron density, and e is the fundamental charge. The mean ion charge is $Z = 4$ and the Coulomb logarithm is $\log\Lambda = 8$. Significant nonlocal effects are expected when $\lambda_{ei}/L_T > 0.1$ (Ref. 8). The MHD Biermann battery source term, $\partial B/\partial t = \nabla T_e \times \nabla n_e / en_e$ is also calculated. Comparing these quantities [Figs. 1(e) and 1(f)] shows that substantial Biermann growth is predicted within the region of the ablated plasma where nonlocal effects are expected to be significant.

The primary feature observed in the experimental proton radiographs is a bell-shaped region of depleted proton flux [Fig. 2(a)], from which 15-MeV protons have been deflected in z by at least 0.1 rad (since a corresponding peak is not visible on the radiograph). This deflection is in the nonlinear regime,^{6,9} so a linear inversion to recover the integrated field is not possible. However, as an order-of-magnitude estimate and assuming a length scale of ~ 1 mm, an electric field of $E \sim 10^9$ V/m or magnetic field of $B \sim 50$ T is required to reproduce the observed deflection. Comparing these values to those predicted by the MHD simulation ($E_r \sim 10^7$ V/m, $B_\phi \sim 50$ T) indicates that the azimuthal magnetic field must be responsible.

To directly compare HYDRA simulations to experimental results, synthetic proton radiographs are generated using an open-source particle-tracing algorithm that was developed for the PlasmaPy project as part of this work.¹⁰ Direct comparisons show that the synthetic radiographs reproduce the bell feature observed in the experimental radiographs [Fig. 2(a)]. To make a quantitative comparison, a horizontal lineout is taken through the center of the bell region [averaging in z over the shaded region in Fig. 2(a)]. The normalized intensity lineout comparisons in Fig. 2(b) show that the bell-shaped depression in the synthetic radiographs is



E29664JR

Figure 2

(a) A synthetic radiograph created using the fields from the unmagnetized $f = 0.15$ simulation (contours) qualitatively reproduces the bell-shaped depression observed in the 15-MeV proton radiograph from the unmagnetized experiment (image). (b) Lineouts through the gray-shaded region in (a), normalized to their mean. The $f = 0.05$ and $f = 0.15$ simulations are identical, but both overpredict the measured depletion [$\delta = \text{mean}(I/I_0)$ averaged over the shaded region in (b)] by a factor of ~ 2 . Reducing the simulated B_ϕ by a factor of ~ 0.4 reproduces the depletion of the experimental radiograph.

twice as deep as measured in the unmagnetized experiment. This result implies that the azimuthal magnetic field measured in the experiments is significantly weaker than predicted by the MHD simulation. Similar comparisons with different flux limiters as well as the magnetized shot support the same conclusion.

We hypothesize that this discrepancy is the direct effect of a non-Maxwellian distribution on the Biermann battery source term. The measured reduction in the self-generated magnetic field is consistent with previously published work comparing Biermann battery growth in MHD and VFP simulations.¹ This measurement constitutes experimental evidence for the previous theoretical prediction that nonlocal effects result in the overprediction of self-generated fields in MHD simulations.

This material is based upon work supported by the Department of Energy, National Nuclear Security Administration under Award Number DE-NA0003856, the University of Rochester, and the New York State Energy Research and Development Authority.

1. M. Sherlock and J. J. Bissell, *Phys. Rev. Lett.* **124**, 055001 (2020).
2. C. P. Ridgers *et al.*, *Phil. Trans. R. Soc. A* **379**, 20200017 (2021).
3. J. R. Davies *et al.*, *Phys. Plasmas* **24**, 062701 (2017).
4. S. A. Slutz *et al.*, *Phys. Plasmas* **17**, 056303 (2010).
5. G. Fiksel *et al.*, *Rev. Sci. Instrum.* **86**, 016105 (2015).
6. N. L. Kugland *et al.*, *Rev. Sci. Instrum.* **83**, 101301 (2012).
7. M. M. Marinak *et al.*, *Phys. Plasmas* **8**, 2275 (2001).
8. A. R. Bell, R. G. Evans, and D. J. Nicholas, *Phys. Rev. Lett.* **46**, 243 (1981).
9. A. F. A. Bott *et al.*, *J. Plasma Phys.* **83**, 905830614 (2017).
10. PlasmaPy Community *et al.*, PlasmaPy (Version 0.6.0), Zenodo, Accessed 14 March 2021, <http://doi.org/10.5281/zenodo.4602818>.

Inverse Ray Tracing on Icosahedral Tetrahedron Grids for Nonlinear Laser-Plasma Interactions Coupled to 3-D Radiation Hydrodynamics

A. Colaitis,¹ I. V. Igumenshchev,² J. Mathiaud,¹ and V. N. Goncharov²

¹Université de Bordeaux, Centre Lasers Intenses et Applications, France

²Laboratory for Laser Energetics, University of Rochester

Three major avenues to inertial confinement fusion (ICF) are currently being explored worldwide:¹ laser direct drive (LDD), laser (x-ray) indirect drive (LID), and magnetic drive using pulsed power. These approaches have in common the use of laser beams and face challenges related to laser-plasma instabilities (LPI's). LPI's are nonlinear microscopic processes that couple plasma eigenmodes (electron or ion plasma waves) to the laser beams or scattered light or each other.² In the case of LDD and LID, the main LPI's at play are cross-beam energy transfer (CBET), stimulated Raman scattering (SRS), stimulated Brillouin scattering (SBS), and two-plasmon decay (TPD). Their consequences for large-scale plasma hydrodynamics are often important, leading to significant loss of laser/target coupling, introducing asymmetries in target compression, and generating suprathermal-electron populations.³

While LPI's have a paramount influence in ICF, they are also difficult to model in radiation-hydrodynamic (RH) codes that describe the plasma motion at fluid scales. This relates to an incompatibility of dimensions between the typical plasma size (~mm) and driver duration (~ns) compared to the scales required to resolve the kinetic processes at play in LPI's (~nm and ~fs). These six-orders-of-magnitude differences in time and space prevent direct numerical calculations of LPI's in 3-D geometries at fluid scales. As such, they are often computed at reduced scales, for short periods of time, in a reduced number of dimensions, and/or for a limited number of laser beams. For these reasons, models for laser propagation in hydrodynamic codes have long been limited to the linear process of collisional absorption. This is usually modeled in the geometrical optics (GO) framework for computing laser trajectories,⁴ which offers adequate performance at fluid scales, even in 3-D geometries.

Given the importance of LPI's in ICF, significant efforts have been made in the last 10 to 15 years to include reduced LPI models in fluid codes, mainly based on GO models for numerical efficiency. These reduced models must address two main questions: (1) how to compute laser intensities or fields in the GO framework, key properties for LPI's, and (2) how to account for the microscopic processes. The first issue stems from the infinitely thin property of GO rays, which prevents a straightforward definition of ray intensity. The GO framework also breaks down at laser caustics, which are prominent in LDD. The second issue relates to the formulation of theoretical models that reproduce microscopic physics from macroscopic quantities. Such models have been notably proposed for CBET by considering the laser wave as locally plane and homogeneous⁵ and are used across a variety of codes. Significant technical difficulties arise, however, in coupling these models with the intensity calculation methods of GO. Usually, such details are handled with the introduction of free numerical parameters in CBET models, thereby allowing one to tune results of calculations to match experimental data. In this summary, we aim to propose a fluid-scale laser model, *IFRIIT*, which consistently follows the GO framework to compute laser fields and eliminates such free parameters. In addition, we present the coupling of *IFRIIT* to the *ASTER*⁶ RH code for the specific spherical geometries of LDD. Calculations presented here were conducted in the framework of the OMEGA Laser System configuration and diagnostics.⁷

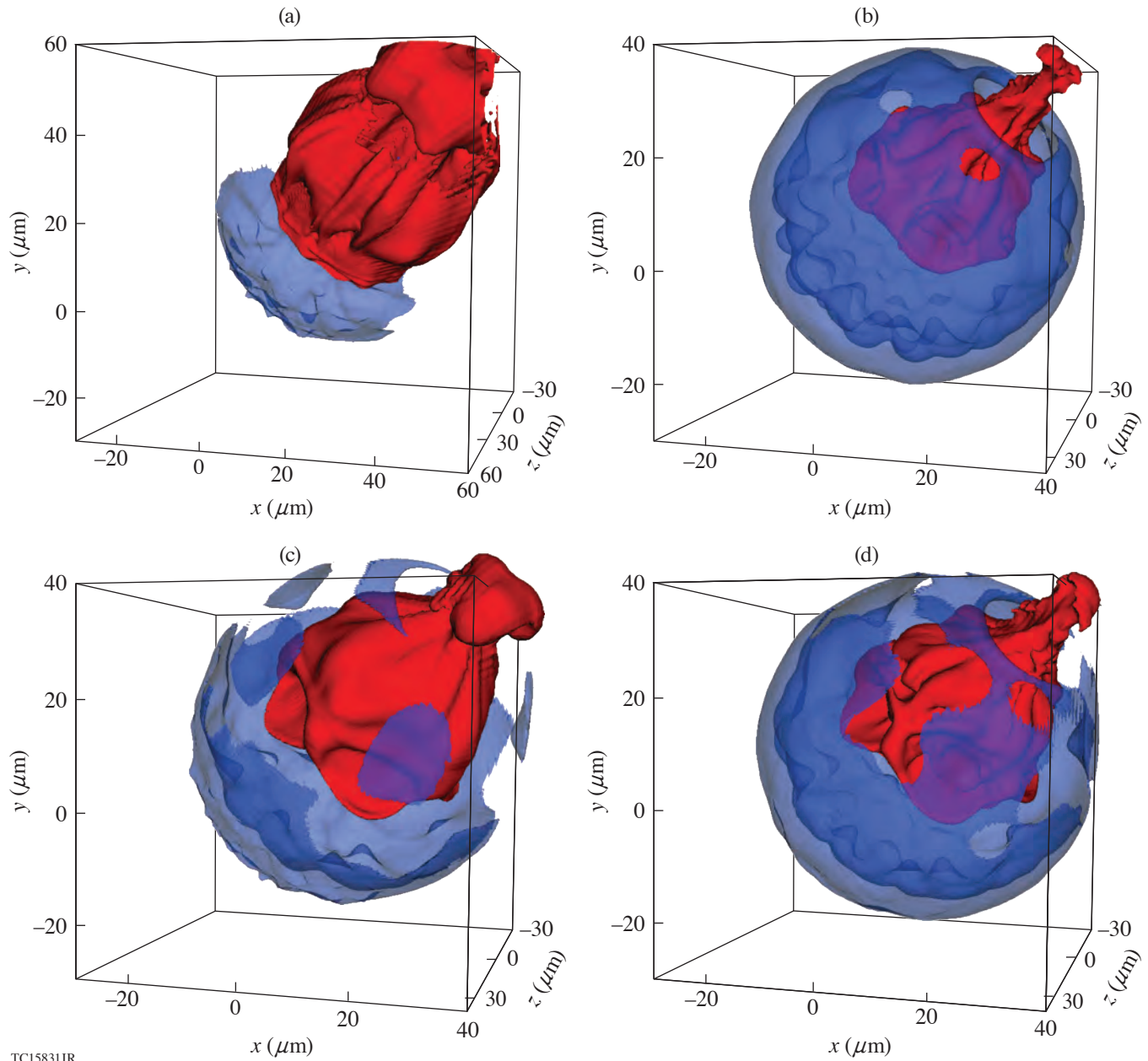
Our algorithm differs significantly from other methods implemented in RH codes on several key points: First, we make use of inverse ray tracing (IRT) to compute the laser propagation, as opposed to the method of forward ray tracing (FRT), which is usually employed. This is the first time an IRT method has been used for laser calculations coupled to plasma hydrodynamics in

RH fusion codes. Second, we decouple the laser grid from the hydrodynamics grid. This allows us to tailor a grid that is optimized for the resolution of the ray equations, leading to a better load balance for parallel computations. In addition, the laser grid itself is split into two grids: one for calculating ray electric fields and one for calculating ray trajectories. Furthermore, we employ a geodesic laser grid structure, contrary to the standard polar grids employed in 3-D RH codes. It is the first time that such a three-grid scheme has been employed for laser calculations. Third, we make use of the Etalon Integral method to compute laser fields in places where the GO framework breaks down.⁸ This is also a new technique for RH codes, which is enabled by the use of IRT and allows us to remove the free parameters used in standard codes to set caustic fields. Fourth, the fields reconstructed from GO using IRT are at a higher order in space than conventional grid binning methods used to compute absorption and fields. While it is possible to achieve a higher order in space for fields using FRT through interpolation or local derivative estimation, the IRT method natively obtains this higher order. This is an important point in 3-D ICF implosions, where noise issues stemming from low convergence in the number of rays per cell for some FRT schemes, or low-order field estimation methods, will often be detrimental. Fifth, the laser code and the RH codes are also decoupled in time, allowing both codes to iterate asynchronously. Indeed, laser computations are often more costly than hydrodynamic ones (when including LPI's) but do not need updating as often. This is also the first time a RH code implements a desynchronized laser scheme. Finally, the use of IRT has additional advantages: e.g., it allows a native separation of the laser field between the various reflected components (so-called "sheets") that, for example, enable one to precisely account for self-interaction of the incident and reflected fields of beams through CBET. It also considerably speeds up pump-depletion iterations in CBET algorithms by allowing us to update only part of the ray equations.

Applications to direct-drive implosions for ICF have been considered for which a geodesic icosahedron grid is implemented in *IFRIIT*. The performances of the *ASTER/IFRIIT* coupling have been demonstrated by conducting simulations of cryogenic implosions performed on the OMEGA Laser System, in the presence of various sources of 3-D effects: laser port geometry, cross-beam energy transfer, beam imbalance, and target misalignment [see Fig. 1, (p. 136)]. The code was found to have sufficiently low numerical noise to accurately model the high-convergence ICF implosions without introducing spurious modes. A comparison with neutron data for a cryogenic implosion experiment has also shown excellent agreement for the laser-plasma coupling (notably the measured bang time). More-recent developments (to be published in an upcoming paper) include the modeling of the polarized CBET interaction. In the latter case, simulations with the full post-shot data allow the magnitude of the measured DT flow to be reproduced, as well as approaching the measured direction of the flow.

This material is based upon work supported by the Department of Energy National Nuclear Security Administration under Award Number DE-NA0003856, the University of Rochester, and the New York State Energy Research and Development Authority. This work was granted access to the HPC resources of TGCC computer cluster (Ref. 9) under the allocation 2020-A0070506129 and 2021-A0090506129 made by GENCI.

1. R. Betti and O. A. Hurricane, *Nat. Phys.* **12**, 435 (2016).
2. W. L. Kruer, *The Physics of Laser Plasma Interactions*, 1st ed. (CRC Press, Boca Raton, FL, 2003).
3. D. Batani *et al.*, *Nucl. Fusion* **54**, 054009 (2014).
4. T. B. Kaiser, *Phys. Rev. E* **61**, 895 (2000).
5. P. Michel *et al.*, *Phys. Plasmas* **16**, 042702 (2009).
6. I. V. Igumenshchev *et al.*, *Phys. Plasmas* **23**, 052702 (2016).
7. T. R. Boehly *et al.*, *Opt. Commun.* **133**, 495 (1997).
8. A. Colaitis *et al.*, *Phys. Plasmas* **26**, 032301 (2019).
9. Très Grand Centre de calcul du CEA (TGCC), Accessed 6 October 2021, <http://www-hpc.cea.fr/en/complexe/tgcc.htm>.



TC15831JR

Figure 1

Academic test case of the effect of large offset and beam imbalance on cryogenic targets, illustrating how CBET can mitigate such effects. [(a),(b)] The target at stagnation in the presence of a 40- μm positioning offset in the $\theta = 65, \varphi = 45$ direction, and [(c),(d)] a 5% beam imbalance imposing a mode 1 in the same direction as the target offset. Run results without [(a),(c)] and with [(b),(d)] CBET enabled. In all figures, the 100-g/cm³ density isocontour is shown in blue, the 50/50 DT ice/gas fractional volume isocontour is shown in red, and the axis ticks are in units of microns. The simulation setup is that of shot 94712.

Experimentally Inferred Fusion-Yield Dependencies of OMEGA Inertial Confinement Fusion Implosions

A. Lees,^{1,2} R. Betti,^{1,2,3} J. P. Knauer,¹ V. Gopalaswamy,^{1,2} D. Patel,^{1,2} K. M. Woo,¹ K. S. Anderson,¹ E. M. Campbell,¹ D. Cao,¹ J. Carroll-Nellenback,¹ R. Epstein,¹ C. J. Forrest,¹ V. N. Goncharov,¹ D. R. Harding,¹ S. X. Hu,¹ I. V. Igumenshchev,¹ R. T. Janezic,¹ O. M. Mannion,^{1,3} P. B. Radha,¹ S. P. Regan,¹ A. Shvydky,¹ R. C. Shah,¹ W. T. Shmayda,¹ C. Stoeckl,¹ W. Theobald,¹ and C. A. Thomas¹

¹Laboratory for Laser Energetics, University of Rochester

²Department of Mechanical Engineering, University of Rochester

³Department of Physics and Astronomy, University of Rochester

Inertial confinement fusion¹ implosions are complex nonlinear processes that are highly sensitive to many input parameters. The lack of an accurate simulation capability, the low shot rate of laser implosion facilities, and the effects of shot-to-shot variations make it difficult to extract single parameter dependencies, thereby preventing guided improvements in implosion performance. In this summary, the different dependencies of the fusion yield are extracted from the OMEGA² experimental database of 177 implosions. The importance of these results is twofold: First, they identify the degradation mechanisms; second, they enable predictions of how the yield improves if each degradation is mitigated. When applied to OMEGA implosions the results indicate that the highest yield achievable on OMEGA should exceed 2×10^{14} neutrons with only minor adjustment to the laser pointing and by reducing the fill age. Yields close to 3×10^{14} are predicted if the degradation from R_b/R_t is mitigated.

Generalizing the conclusions of Ref. 3 to include the effects of variable systematic nonuniformity seeds and experimental input parameters that are not included in 1-D simulations, a physics-based statistical mapping model [see Eq. (1)] is derived for the measured fusion yield Y^{exp} . The yield is assumed to be dominated by the implosion velocity, which is typically well simulated by the 1-D code *LILAC*,⁴ as indicated by shell trajectory measurements;⁵ therefore, the yield is expected to depend on the simulated 1-D yield Y_{1-D}^{sim} . The statistical model is written in terms of the yield-over-clean (YOC), leading to the following intuitive formulation of the fusion yield:

$$Y^{\text{exp}} = \text{YOC}^{\text{exp}} Y_{1-D}^{\text{sim}} \quad (1)$$

$$\text{YOC}^{\text{exp}} \approx \text{YOC}_h \text{YOC}_f \text{YOC}_b \text{YOC}_{\ell=1} \text{YOC}_{\text{res}},$$

where the degradation due to hydrodynamic instabilities from systematic nonuniformities is denoted as YOC_h ; YOC_f is the degradation due to DT fill age, tritium damage, and ³He accumulation; YOC_b is the degradation from finite laser beam size; and $\text{YOC}_{\ell=1}$ is the degradation from the $\ell = 1$ mode. YOC_{res} denotes a weak ($\leq 15\%$ over the entire database) residual size scaling not captured by 1-D hydrocodes^{6,7} and is approximately constant for high-performance OMEGA implosions. Each YOC term is analyzed and extracted by mapping onto the experimental database.

The yield degradation from $\ell = 1$ can be approximated as a power law of the temperature ratio between the maximum and minimum apparent ion temperature $R_T = T_1^{\text{max}}/T_1^{\text{min}}$ (Ref. 8). Since the T_i measurement error is about 10%, only implosions with R_T greater than a minimum threshold $R_T^{\text{min}} \approx 1.1$ are expected to exhibit detectable degradation. Therefore, the degradation from the $\ell = 1$ mode is approximated as

$$\text{YOC}_{\ell=1} \sim \hat{R}_T^\mu, \hat{R}_T \equiv \max \left[1, \frac{R_T}{R_T^{\min}} \right]. \quad (2)$$

Here the values of μ and R_T^{\min} are obtained through the global mapping onto the data.

YOC_f depends on the time between the DT fill and the shot time (fill age) as well as the tritium and deuterium concentrations (θ_T and θ_D , respectively). Instead of the fill age, one can use the 1-D-simulated yield degradation $\xi_{\text{He}} = Y_{1\text{-D,He}}^{\text{sim}}/Y_{1\text{-D}}^{\text{sim}}$, where $Y_{1\text{-D,He}}^{\text{sim}}$ includes the ${}^3\text{He}$ produced over the course of the fill age, all of which is assumed to be accumulated in the vapor region. Power-law dependencies are assumed, leading to

$$\text{YOC}_f \sim \theta_T^\delta \theta_D^\nu \xi_{\text{He}}^\phi. \quad (3)$$

The degradation from finite laser spot size YOC_b can be approximated through a power of laser beam to target radius R_b/R_t :

$$\text{YOC}_b \sim (R_b/R_t)^\gamma \quad (4)$$

with $\gamma \approx 2.4$ in 3-D simulations.⁹ Here, as for all the other degradations, the exponent γ is determined by the mapping to the data.

A functional relation of simulated 1-D parameters that best maps the degradation from hydrodynamic instabilities, YOC_h is constructed by combining in-flight aspect ratio (IFAR) and the shell adiabat $\alpha_F = P_a/P_F$ (ratio of the ablation pressure to the Fermi degenerate pressure), into a single parameter $I_\alpha \equiv (\alpha_F/3)^{1.1}/(\text{IFAR}/20)$ as indicated in Refs. 10 and 11. The convergence ratio (CR) is added to better account for the degradation from low- and mid-mode asymmetries. To account for inaccuracies in modeling shock transit, the shell thickness is included through the dimensionless parameter $\hat{D} \equiv R_{\text{out}}/R_{\text{in}}$ representing the ratio between the outer and inner shell radii. Therefore YOC_h is approximated as $\text{YOC}_h \sim I_\alpha^\eta \text{CR}^{2\omega} D^\epsilon$. At sufficiently large adiabats and low IFAR's, implosions become stable to short-wavelength modes and the benefits of higher adiabat and low IFAR are expected to decrease.¹⁰ Therefore, a piecewise value of η is used above and below a critical value (I_c) of I_α . The final form of the hydrodynamic degradation is then written as

$$\text{YOC}_h \sim \hat{I}_\alpha^\eta C_R^\omega D^\epsilon, \quad (5)$$

where $\hat{I}_\alpha = I_\alpha/I_c$ and $\eta = \eta_{<} \Theta(1 - \hat{I}_\alpha) + \eta_{>} \Theta(\hat{I}_\alpha - 1)$ with $\Theta(x)$ representing the Heaviside step function.

The power indices in Eqs. (2)–(5) are determined by χ^2 minimization over the entire OMEGA implosion database and the two threshold parameters R_T^{\min} , I_c were chosen to minimize the cross-validation error. The results are summarized in Table I including the 95% confidence level for each exponent. Each dependence can be visualized by isolating the corresponding YOC and comparing with the power-law approximation:

$$\text{YOC}_j^{\text{exp}} \equiv \frac{\text{YOC}_j^{\text{exp}}}{\prod_{i \neq j} \text{YOC}_i} \rightarrow \text{YOC}_j. \quad (6)$$

The plots in Fig. 1 show the comparison in Eq. (6) for the dependencies in Eq. (1).

General conclusions can be readily extracted from this analysis. First, the degradation from the $\ell = 1$ is as predicted by the 3-D simulations with a power index $\mu \approx -1.44$ and a threshold factor $R_T^{\min} = 1.14$ from the T_i measurement error. Such a good agreement with the simulations confirms the accuracy of the mapping technique to extract the correct trends from the data. Reasonable agreement with 1-D-simulated degradation due to ${}^3\text{He}$ accumulation is indicated by $\phi \approx 1.39$ close to unity. Furthermore, the degradation in two extremely long fill age targets (45 and 90 days) is well predicted as shown by the two points farthest to the left on Fig. 1(b), adding confidence that the model is correctly accounting for the effect of ${}^3\text{He}$ accumulation. As a result of this

Table I: Power indices and confidence intervals for all the degradation terms as a result of fitting the model in Eq. (1) to the OMEGA database.

Parameter	Power index	95% confidence interval
\hat{R}_T^μ	$\mu = -1.44$ $R_T^{\min} = 1.14$	$\mu = -1.61$ to -1.28
ξ_{He}^ϕ	$\phi = 1.39$	$\phi = 1.25$ to 1.54
θ_T^δ	$\delta = 1.97$	$\delta = 1.00$ to 2.90
θ_D^ν	$\nu = 1.16$	$\nu = 0.54$ to 1.79
$(R_b/R_t)^\gamma$	$\gamma = 2.97$	$\gamma = 2.72$ to 3.24
\hat{I}_α^η	$\eta_< = 1.06$ $\eta_> = 0.45$ $I_c = 0.8$	$\eta_< = 0.91$ to 1.21 $\eta_> = 0.40$ to 0.49
C_R^ω	$\omega = -0.97$	$\omega = -1.05$ to -0.89
\hat{D}^ε	$\varepsilon = -3.35$	$\varepsilon = -4.11$ to -2.58

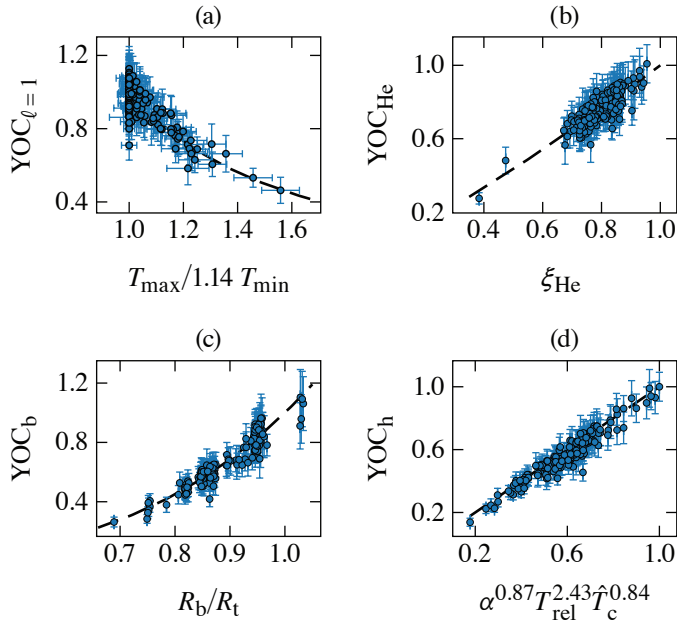


Figure 1
The individual degradations due to (a) $\ell = 1$ mode, (b) ^3He accumulation in the vapor, (c) finite beam size, and (d) hydrodynamic instabilities extracted from the OMEGA database according to Eq. (6). The dashed lines indicate the power laws from the model; the power indices are given in Table I.

TC15691JR

analysis, OMEGA shot 96806 was designed with the shortest-ever fill age of 3 days, achieving the highest performance on OMEGA at the time with a neutron yield of 1.53×10^{14} and an areal density of $157 \pm 15 \text{ mg/cm}^2$ at a laser energy of 27.3 kJ.

Shot 96806 was subsequently repeated with a fill age of 8 days (shot 96808) resulting in a 14% reduction in fusion yield, as predicted by the statistical model (13%). Another conclusion can be drawn about the isotopic composition of the DT ice layer since maximizing the term $\theta_T^{1.97} (1 - \theta_T)^{1.16}$ gives the optimal tritium concentration at $\theta_T \approx 0.6$. The mapping to data reveals a strong R_b/R_t correlation with a power index of $\gamma = 2.97$, which is stronger than indicated by 3-D simulations of the beam mode in Ref. 9. Furthermore, the highest-performing implosions with $R_b/R_t \approx 0.87$ show a significant (35%) degradation from this mechanism,

whereas post-shot 3-D simulations show negligible degradation due to the beam mode. This indicates that new physics is at play, which is an active area of research, and it can include new sources of nonuniformities from the laser beam geometry as well as 1-D physics model deficiencies most likely related to the reduction of cross-beam energy transfer, when $R_b < R_t$. Lastly, the mapping model indicates strong degradation due to hydrodynamic effects (YOC_h) at low adiabat, high convergence, and high IFAR [Fig. 1(d)]. The results indicate that the highest yields can be achieved only at high adiabat and low IFAR with the maximum yield occurring at adiabats >4.5 .

This material is based upon work supported by the Department of Energy National Nuclear Security Administration under Award Number DE-NA0003856, the University of Rochester, and the New York State Energy Research and Development Authority.

1. J. Nuckolls *et al.*, *Nature* **239**, 139 (1972).
2. T. R. Boehly *et al.*, *Opt. Commun.* **133**, 495 (1997).
3. V. Gopalaswamy *et al.*, *Nature* **565**, 581 (2019).
4. J. Delettrez *et al.*, *Phys. Rev. A* **36**, 3926 (1987).
5. D. T. Michel *et al.*, *Phys. Rev. Lett.* **114**, 155002 (2015).
6. W. Theobald *et al.*, “OMEGA Subscale Cryogenic Implosions in Symmetric and Polar-Direct-Drive Beam Geometry,” presented at the 62nd Annual Meeting of the American Physical Society Division of Plasmas Physics, Memphis, TN, 9–13 November 2020.
7. C. A. Thomas *et al.*, “Quantifying the Effects of Scale and Illumination Geometry in Laser Direct Drive,” presented at the 62nd Annual American Physical Society Division of Plasma Physics, Memphis, TN, 9–13 November 2020.
8. K. M. Woo *et al.*, *Phys. Plasmas* **27**, 062702 (2020).
9. V. Gopalaswamy *et al.*, “Using Statistics to Predict, Design, and Understand Fusion Experiments,” submitted to *Physics of Plasmas*.
10. V. N. Goncharov *et al.*, *Phys. Plasmas* **21**, 056315 (2014).
11. H. Zhang *et al.*, *Phys. Plasmas* **27**, 122701 (2020).

Density Evolution After Shock Release from Laser-Driven Polystyrene Targets in Inertial Confinement Fusion

A. Shvydky,¹ D. Haberberger,¹ A. V. Maximov,¹ R. Boni,¹ D. Cao,¹ J. Carroll-Nellenback,¹ D. H. Froula,¹ V. N. Goncharov,¹ S. X. Hu,¹ I. V. Igumenshchev,¹ S. T. Ivancic,¹ V. V. Karasiev,¹ J. P. Knauer,¹ P. M. Nilson,¹ P. B. Radha,¹ S. P. Regan,¹ J. R. Rygg,¹ T. C. Sangster,¹ M. D. Rosen,² and V. A. Smalyuk²

¹Laboratory for Laser Energetics, University of Rochester

²Lawrence Livermore National Laboratory

In laser-driven inertial confinement fusion (ICF), a cryogenically cooled spherical shell of deuterium–tritium (DT) fuel is imploded and compressed by material ablation to form a high-areal-density confinement around a central spot where conditions for ignition are created.^{1,2} At the beginning of the implosion, multiple shocks are launched into the ablator and DT-ice shell. After the shocks break out of the shell into the gas, the shell starts to accelerate inward. The density gradient at the inner part of the shell, formed by the shock release, controls the dynamics of shell deceleration and limits the final hot-spot convergence ratio and peak fuel areal density.

To have predictive capability for ICF implosions it is important that radiation-hydrodynamic codes are able to accurately simulate the density profile of the material release ahead of the high-density shell under conditions relevant to ICF implosions (zero to a few-times solid-state density, a few to tens of eV temperature, and a few to tens of megabars of pressure). It is very difficult to probe the density profile in the material released from the inner side of the DT shell because of the low opacity of DT and various complications due to geometry. While techniques are being developed for direct density measurements during a cryogenic implosion, several key questions relevant to material release can be studied using planar foils. In recent experiments³ release plasma profiles in planar foils were measured for the first time using optical interferometry. Results indicate that material release is enhanced in experiments compared to that predicted by radiation-hydrodynamics simulation and that the low-density part of the plasma profile in the release strongly depends on conditions at the back (opposite to the laser drive) surface right before the shock breakout. A density gradient at the back surface enhances the expansion compared to that in a classical release from a sharp foil–vacuum interface. It was hypothesized^{4,5} that the formation of a density gradient at the back surface prior to shock arrival is the result of an early expansion caused by coronal x-ray preheating.

In this study, the underlying mechanisms for the enhanced release observed in experiments are examined through a systematic comparison of the experiments to radiation-hydrodynamic simulation using various thermal- and radiation-transport models and opacity and equation-of-state (EOS) tables. We find that the rarefaction-wave expansion is highly sensitive to the radiation-transport model used in the simulations. When radiation transport was treated using the S_n radiation-transport method⁶ the release experiments⁵ were consistently explained within the framework of radiation hydrodynamics.

The shock-release experiment carried out on the OMEGA EP Laser System used a 37- μm -thick, 4-mm-diam hemispherical CH shell (to prevent parallax in line-integrated diagnostics) and was irradiated from its inner side (front side for the laser) by two ultraviolet (UV) laser beams with a wavelength of 351 nm [see Fig. 1(a)]. With a combined laser energy of 6 kJ in a 5-ns square pulse, an overlapped intensity of 3×10^{14} W/cm² was obtained in a 750- μm -diam eighth-order super-Gaussian spot created using distributed phase plates. The two laser beams heated the front surface of the foil, creating ~ 30 -Mbar ablative pressure that drove an ~ 65 -km/s shock through the foil. At about 670 ps from the start of the laser pulse, the shock broke out from the back side of the foil and formed a rarefaction wave that expanded into the vacuum. The foil started to accelerate at about 1.3 ns, the time at

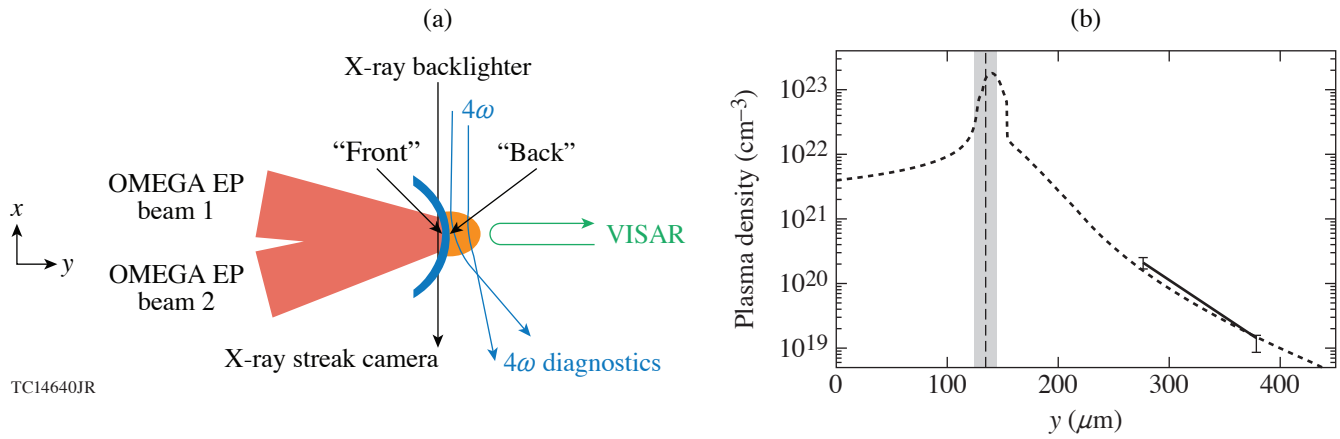


Figure 1

(a) The experimental setup used two 5-ns beams to drive a hemispherical CH shell; x-ray streaked radiography was used to measure the in-flight shell position; 4ω laser interferometry to measure the low-density profile in the rarefaction wave; and the velocity interferometry system for any reflector (VISAR) to measure the motion of the back surface of the shell. (b) The measured (solid line) and simulated (dotted curve) plasma density profiles at 2 ns. The vertical dashed line represents the peak shell positions as measured by the streak camera (with error bars shown by the shaded regions).

which the head of the rarefaction wave reached the front of the foil. The 4ω (263-nm-wavelength) interferometer⁷ captured the rarefaction wave's plasma-density profile at 1, 2, 3, and 4 ns. Due to noise limitations this profile is accurate only in the low-density region measured by the 4ω probe from $\sim 10^{19} \text{ cm}^{-3}$ to $\sim 10^{20} \text{ cm}^{-3}$; the measured density profile is further limited by the collection angle of the 4ω probe lens. As an example, Fig. 1(b) (solid line) shows the lineout of the plasma density inferred from the 2-ns interferogram taken along the middle of the drive ($x = 0$). For convenience in comparing the time evolution of the low-density part of the rarefaction wave to simulations, we extract the positions of the 10^{19}-cm^{-3} and 10^{20}-cm^{-3} plasma density locations along the middle of the drive and plot them versus time as shown in Fig. 2.

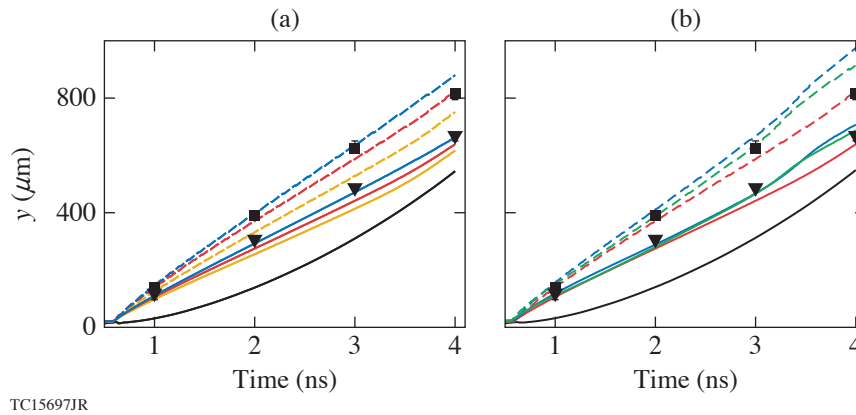


Figure 2

(a) Positions of 10^{19}-cm^{-3} - (dashed curves) and 10^{20}-cm^{-3} (solid curves) plasma density versus time from simulations performed with S_n and AOT (red), S_n and CRE (blue), and MGD and AOT (yellow); all with *SESAME* EOS. (b) Positions of 10^{19}-cm^{-3} (dashed curves) and 10^{20}-cm^{-3} (solid curves) plasma density versus time are from simulations performed with *SESAME* (red), QEOS (blue), and the ideal-gas (green) EOS; all with S_n and AOT. In (a) and (b), black squares (triangles) mark 10^{19}-cm^{-3} (10^{20}-cm^{-3}) plasma density positions and the solid black curve marks the shell trajectory.

Simulations were performed with the 1-D Lagrangian radiation-hydrodynamic code *LILAC*. The laser drive was adjusted to account for transverse thermal losses, which are not modeled in 1-D simulations, and to match the foil trajectory, which was experimentally measured and accurately simulated with the 2-D radiation-hydrodynamic code *DRACO*. An example of the simu-

lated plasma density profile taken at 2 ns is shown in Fig. 1(b) (dotted curve). The density peak ($\sim 1.8 \times 10^{23} \text{ cm}^{-3}$ at $y = 140 \text{ }\mu\text{m}$) corresponds to the shell, the rising part of the density profile on the left of the shell corresponds to the corona, and the decaying part of the density profile on the right of the shell corresponds to the rarefaction wave. The simulated scale length and extent of the density profiles at all four times are in good agreement with the measurements and show a weak dependence on the opacity and EOS tables as illustrated in Fig. 2. This insensitivity indicates that radiation-hydrodynamic simulations capture essential physics in the evolution of the low-density part of the plasma profiles in the release from a CH foil into vacuum. The simulations in Fig. 2 use astrophysical opacity tables (AOT's), collisional-radiative-equilibrium (CRE) opacity tables, *SESAME* (table 7593), quotidian equation of state (QEOS), and the ideal-gas EOS models. Simulations in previous studies reported in Ref. 3, which showed much shorter expansion and scale length of the electron density profile in the release [see yellow curves in Fig. 2(a)], used a flux-limited multigroup diffusion (MGD) method⁸ to model the radiation transport. MGD is the standard method for modeling radiation transport in ICF radiation-hydrodynamic codes because of its computational efficiency. The simulations shown in red, blue, and green in Fig. 2 use a more-accurate, albeit more computationally expensive, multigroup S_n radiation-transport method (method of ordinates).⁶

In summary, we have presented a consistent interpretation of the experimental results (the shock breakout time, shell trajectory, and rarefaction-wave plasma density profile) within the framework of radiation hydrodynamics: (1) The simulations showed that the low-density part of the plasma profile in the rarefaction wave formed when a shock is released from the back surface of a CH foil strongly depends on conditions at the back surface right before the shock breakout. A density gradient at the back surface enhances the expansion of the rarefaction wave compared to that in a classical release from a sharp foil–vacuum interface. When the shock travels over the low-density part of the gradient, it heats the material to higher temperatures than when the shock travels over the bulk of the shell. The higher temperature increases the sound speed of the shocked material, resulting in an enhanced release. (2) Simulations predict an early expansion (during the shock transit time) of the back surface of the foil caused by preheat by coronal x rays. Experiments using the VISAR diagnostic measured movement of the back surface of the foil during the shock transit time. The essential role of coronal x-ray preheat in the release was verified by experiments with a buried Au layer that showed a significantly reduced rarefaction-wave expansion in comparison with the baseline experiments. (3) To predict the low-density profile in the rarefaction wave, radiation-hydrodynamic simulations must accurately model preheat of the back surface of the foil by coronal x rays and the early back-surface expansion. This requires the S_n radiation transport model to accurately describe the passage of the coronal radiation through CH material under the drive conditions.

This material is based upon work supported by the Department of Energy National Nuclear Security Administration under Award Number DE-NA0003856, the University of Rochester, and the New York State Energy Research and Development Authority.

1. R. S. Craxton *et al.*, *Phys. Plasmas* **22**, 110501 (2015).
2. E. M. Campbell *et al.*, *Matter Radiat. Extremes* **2**, 37 (2017).
3. D. Haberberger *et al.*, *Phys. Rev. Lett.* **123**, 235001 (2019).
4. A. Shvydky *et al.*, *Bull. Am. Phys. Soc.* **64**, BAPS.2019.DPP.NO5.8 (2019).
5. M. D. Rosen, *Bull. Am. Phys. Soc.* **65**, BAPS.2020.DPP.CP17.3 (2020).
6. S. Chandrasekhar, *Radiative Transfer* (Dover Publications, New York, 1960).
7. A. Howard *et al.*, *Rev. Sci. Instrum.* **89**, 10B107 (2018).
8. D. Mihalas and B. Weibel-Mihalas, *Foundations of Radiation Hydrodynamics* (Oxford University Press, New York, 1984).

Experimental Characterization of Hot-Electron Emission and Shock Dynamics in the Context of the Shock-Ignition Approach to Inertial Confinement Fusion

A. Tentori,¹ A. Colaitis,¹ W. Theobald,^{2,3} A. Casner,¹ D. Raffestin,¹ A. Ruocco,^{1,4} J. Trela,¹ E. Le Bel,¹
 K. S. Anderson,² M. S. Wei,² B. J. Henderson,² J. L. Peebles,² R. Scott,⁴ S. Baton,⁵ S. A. Pikuz,⁶
 R. Betti,^{2,3,7} M. Khan,⁸ N. Woolsey,⁸ and D. Batani¹

¹Centre Lasers Intenses et Applications, CELIA, Université Bordeaux, France

²Laboratory for Laser Energetics, University of Rochester

³Department of Mechanical Engineering, University of Rochester

⁴Central Laser Facility, STFC Rutherford Appleton Laboratory, United Kingdom

⁵Laboratoire pour l'Utilisation des Lasers Intenses, CNRS-Ecole Polytechnique-CEA-Sorbonne Universités, France

⁶Joint Institute for High Temperatures of Russian Academy of Sciences, Russia

⁷Department of Physics and Astronomy, University of Rochester

⁸York Plasma Institute, Department of Physics, University of York, United Kingdom

Shock ignition (SI) is an alternative approach to direct-drive inertial confinement fusion based on the separation of the compression and the ignition phases.^{1,2} The high laser intensity required in the ignition phase exceeds the thresholds for the generation of laser-plasma instabilities,³ generating a large amount of suprathermal electrons. Depending on their characteristics these electrons could preheat the hot spot with detrimental effects for the SI scheme, or assist in generating a strong shock.⁴

Here we report on a planar target experiment conducted on the OMEGA EP Laser System aimed at characterizing the hot-electron source and the shock dynamics using laser parameters relevant for SI. A UV ($\lambda = 351$ -nm) laser beam was tightly focused on planar multilayer targets, providing a nominal vacuum laser intensity of $\sim 10^{16}$ W/cm² with a pulse duration of ~ 1 ns. The laser energy delivered was ~ 1250 J. The planar targets consisted of 500- μ m-diam disks with two layers (175 or 250 μ m of CH, or 20 or 10 μ m of Cu). These were mounted on a 50- μ m-thick CH slab intended to inhibit hot-electron recirculation. The UV interaction laser impinged on the front of the CH ablator, generating a strong shock and large amounts of hot electrons. The shock propagation was monitored using x-ray time-resolved radiographs; the x-ray source was created by focusing a second laser beam (4×10^{14} W/cm², 3-ns pulse duration) on a V foil. This scheme allows production of copious amounts of V K_{α} x rays that pass through the target; the x rays are then detected by a four-strip x-ray framing camera (XRFC).⁵ The camera was equipped with a 4×4 array of 20- μ m-diam pinholes, capturing 16, 2-D images of the shock front at different times with $6\times$ magnification (Fig. 1).

Hot electrons were characterized using separate x-ray spectrometers. The hot-electron-produced bremsstrahlung radiation was diagnosed by two time-integrating hard x-ray spectrometers (BMXS's).⁶ The instruments are composed of a stack of 15 imaging plates alternated by filters of different metals. The total yield of Cu K_{α} was measured by an absolutely calibrated zinc von Hamos x-ray spectrometer (ZnVH).⁷

The post-processing of the spectrometers relies on cold Monte Carlo methods [Geant4 (Ref. 8)] in which the electron transport and the x-ray generation on the diagnostics are simulated. In particular, electrons are assumed to be energetically described by a 2-D Maxwellian function:

$$f_e(E) = \frac{N_e}{T_h} e^{-E/T_h}.$$

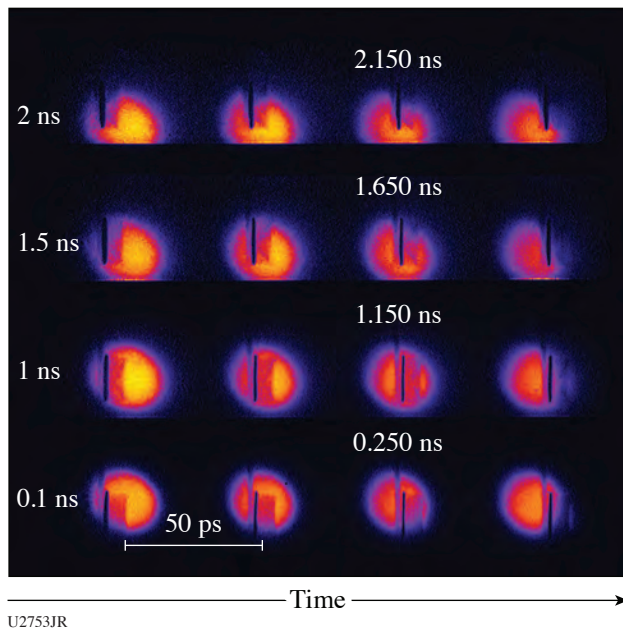


Figure 1
 Array of 2-D radiographs captured at various times by the XRFC
 for shot 28407. Line spacing between each image is 50 ps.

The parameters N_e and T_h that reproduce both the experimental bremsstrahlung spectrum and the K_α signal detected by the BMXS's and the ZnVH are calculated. A large uncertainty on the values of N_e and T_h arises because of the disagreement among the results from different shots and because of the systematic disagreement between the two diagnostics. A disagreement of $\sim 25\%$ is also noted in the simulations of the K_α signal using two different libraries of Geant4.^{9,10} As such, T_h ranges from 20 keV up to 50 keV and N_e from 4×10^{16} down to 5×10^{15} . It is therefore necessary to consider the hydrodynamic evolution of the target to reduce these large ambiguities. In particular, we considered three representative hot-electron distribution functions to use as input in the hydrodynamic simulations to determine which *combination* of laser to hot-electron energy conversion efficiency η and average temperature T_h better reproduces the experimental behavior observed in the radiographs. The three representative $f_e(E)$ are reported in Table I.

Table I: Parameters of Maxwellian functions $f_e(E)$ obtained from post-processing the BMXS and ZnVH diagnostic data for shot 28407, used as input in *CHIC*.

$f_e(E)$			
	T_h (keV)	N_e (10^{16})	η (%)
$f_{e1}(E)$	26	3.4	11
$f_{e2}(E)$	35	1.4	6
$f_{e3}(E)$	45	0.5	3

The radiation-hydrodynamic simulations were performed with the code *CHIC*,¹¹ in which a model of hot-electron transport is included.¹² The shock position and the copper plate expansion are the figures of merit used to characterize the hot-electron source. Different intensities and kinetic energies of the hot-electron beam will strongly affect the variation in time of these two quantities. The simulations showed that an electron beam described by $f_{e1}(E)$ and $f_{e2}(E)$ allows reproduction of the experimental behavior.

According to the simulations hot electrons with these characteristic values of η and T_h increase the shock pressure up to 150 Mbar, 25 Mbar more than the value predicted by simulations without the hot-electron beam included. The effects of such an electron distribution function on a typical SI imploded target¹³ were evaluated using a simple ideal-gas equation-of-state model. An increase of the shell adiabat was calculated using the high conversion efficiency found in the experiment, which could represent an issue for the SI scheme.

This material is based upon work supported by the Department of Energy National Nuclear Security Administration under Award Number DE-NA0003856, the University of Rochester, and the New York State Energy Research and Development Authority.

1. V. A. Shcherbakov, *Sov. J. Plasma Phys.* **9**, 240 (1983).
2. R. Betti *et al.*, *Phys. Rev. Lett.* **98**, 155001 (2007).
3. W. L. Kruer, *The Physics of Laser Plasma Interactions*, edited by D. Pines, 1st ed. (CRC Press, Boca Raton, FL, 2003).
4. S. Gus'kov *et al.*, *Phys. Rev. Lett.* **109**, 255004 (2012).
5. D. K. Bradley *et al.*, *Rev. Sci. Instrum.* **63**, 4813 (1992).
6. C. D. Chen *et al.*, *Rev. Sci. Instrum.* **79**, 10E305 (2008).
7. L. C. Jarrott *et al.*, *Rev. Sci. Instrum.* **88**, 043110 (2017).
8. S. Agostinelli *et al.*, *Nucl. Instrum. Methods Phys. Res. A* **506**, 250 (2003).
9. F. Salvat, *PENELOPE 2018: A Code System for Monte Carlo Simulation of Electron and Photon Transport*, Nuclear Energy Agency (OECD Publishing, Paris, France, 2019).
10. S. T. Perkins *et al.*, Lawrence Livermore National Laboratory, Livermore, CA, Report UCRL-50400 (1991).
11. J. Breil, S. Galera, and P.-H. Maire, *Comput. Fluids* **46**, 161 (2011).
12. A. Colaitis *et al.*, *Phys. Rev. E* **92**, 041101(R) (2015).
13. A. Colaitis *et al.*, *Phys. Plasmas* **23**, 072703 (2016).

Experimental Observations of Laser-Driven Tin Ejecta Microjet Interactions

A. M. Saunders,¹ C. V. Stan,¹ K. K. Mackay,¹ B. Morgan,¹ J. A. K. Horwitz,¹ S. J. Ali,¹ H. G. Rinderknecht,² T. Haxhimali,¹ Y. Ping,¹ F. Najjar,¹ J. Eggert,¹ and H.-S. Park¹

¹Lawrence Livermore National Laboratory

²Laboratory for Laser Energetics, University of Rochester

The study of metal ejecta microjet interactions has broad applicability to fields ranging from planetary formation¹ to cloud interaction dynamics.² An ejecta microjet forms when a strong shock travels through a metal sample and, upon reaching the opposite side, interacts with a micron-scale surface perturbation, such as a dent or a groove. The surface perturbation then inverts to form a jet of micron-scale material traveling at a high velocity, often exceeding 1 km/s (~ 2200 mi/h) (Ref. 3). The jet is comprised of particles with average diameters of ~ 1 μm (Ref. 4). While extensive work has been performed to understand microjet formation and evolution, collisions of interacting microjets have been neglected. We present the first measurements of interaction behavior between two high-velocity tin ejecta microjets as captured through sequences of x-ray radiography images from experiments on the OMEGA EP laser.

Figure 1(a) shows a schematic of the ejecta platform. The targets consist of two tin foils with an angle of 130° between target normals. The foils have grooves carved into their interior surfaces, which traverse the entire foils and are 45 μm deep with 60° opening angles. Figure 1(b) shows a photo of the assembled targets. The tin foils are 100 μm thick with 30 - μm -thick plastic ablaters on their front surfaces to increase laser drive efficiency. They are irradiated with two 8-ns square laser pulses with tunable energy, driving shock waves into the tin. Figure 1(c) shows pressure profiles from radiation-hydrodynamic simulations performed using Ares⁵ at three different times for the sample case of a 11.7-GPa shock. After a delay, a 500-J, 100-ps short-pulse laser heats a 20- μm titanium microwire as a bright x-ray point source to image along the axis perpendicular to the flow of both planar microjets with a resolution of 20 μm . Figures 1(d) and 1(e) show analyzed radiographs of interacting jets from targets with laser drives of 70 J and 1200 J, producing shock pressures of 11.7 GPa and 116 GPa, respectively. We observe densities up to 30 and 150 mg/cm^3 for the two cases. The density relates linearly to the packing density (or “volume fraction”) of particles within the jetting material. From our analysis, the volume fractions in the microjets reach up to 0.3% for the lower-pressure drive and 1.5% for the higher-pressure drive. Analysis of the lower-pressure jets shows that the jets pass through each other unattenuated, maintaining the same velocity and density distributions. In comparison, the higher-pressure jets generate a cloud of material upon interaction, suggesting a higher probability of particle collisions.

Simulations of the jetting tin identified three different regimes: a low-energy regime where material strength inhibits jet formation, a moderate-energy regime where the tin is a mixed solid–liquid material, and a high-energy regime where the tin is expected to be fully melted.⁶ The 11.7-GPa and 116-GPa cases are in the moderate- and high-energy regimes, respectively. Simulations of two interacting microjets for a 11.7-GPa shock exhibit the same unattenuated behavior that is observed in the experiments. Figure 2 shows simulated jet interactions from 116-GPa shocks. We characterize the spread of the interaction cloud for both the simulations and the data in the R - and the S -directions indicated in Fig. 2(a). The spread along R [Fig. 2(b)] corresponds with the extent of the cloud from the center of the interaction point in the direction of jet propagation and assesses how much the jet slows in its original direction of propagation. The spread in the S direction [Fig. 2(c)] quantifies the vertical extent of the projection onto the center axis of symmetry. Both are defined as the widths between a volume fraction cutoff of 0.1%. The hypothetical linear extents for unattenuated jets are depicted with dashed orange lines. The simulation captures the observed slowing from

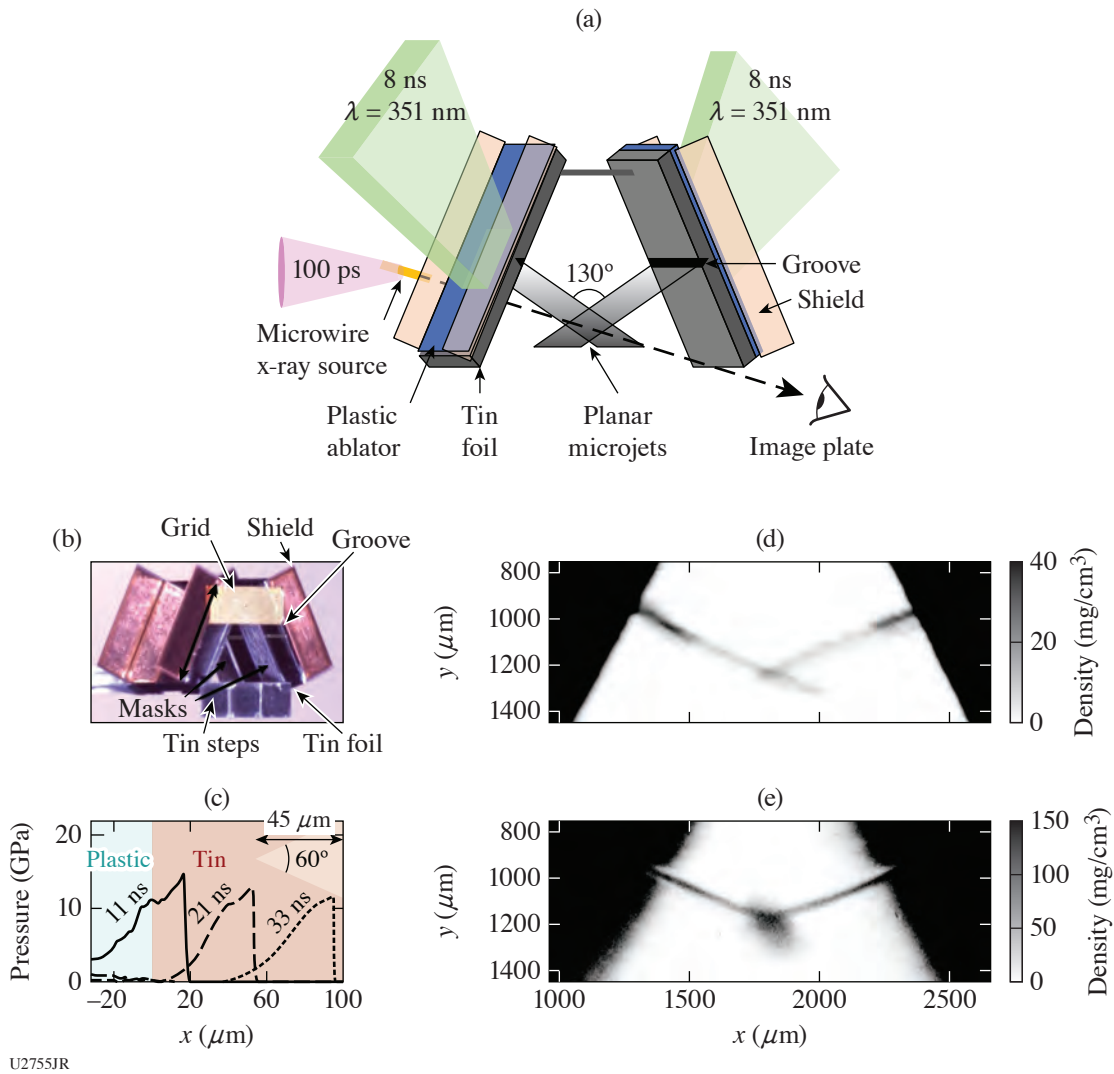


Figure 1

(a) Schematic of the tin microjet interaction platform. Two long-pulse lasers drive shocks into tin foils with grooves carved into their rear surfaces. A short-pulse laser on a microwire generates x rays for radiography. (b) Photo of the target indicating key elements and dimensions. Tin steps of known thicknesses are used for density calibration in radiographs. Masks limit the jet region that propagates to the interaction point. (c) Simulated spatial variations of pressure at three times. Groove schematic is overlaid on simulation results. [(d),(e)] Two analyzed radiographs from drive pressures of 11.7 and 116.0 GPa, respectively. The higher-pressure drive results in densities that are 5× higher than the lower-pressure case.

6.5 km/s to 4.5 km/s after interaction in Fig. 2(b); the collisions between particles result in altered mass-velocity distributions of the particles such that the particles travel in many directions, generating a cloud. Figure 2(c), however, shows that the observed vertical extent of the cloud exceeds the predicted value. Lineouts of the spread in both the R and S directions for the data and simulations show similar qualitative characteristics, with higher-density regions at the center of interaction followed by densities tapering with increased distance from the center. However, the simulations show up-to 30% higher density at the center point of interaction, again suggesting that the simulations do not capture the full spread behavior.

More experiments are needed to understand both the collision model deficiencies and the onset of interaction behavior as a function of shock pressure, but these experiments provide the first data on interacting ejecta microjet behavior and a novel methodology to observe the interactions of high-velocity, particle-laden flows, which opens many more avenues for detailed study.

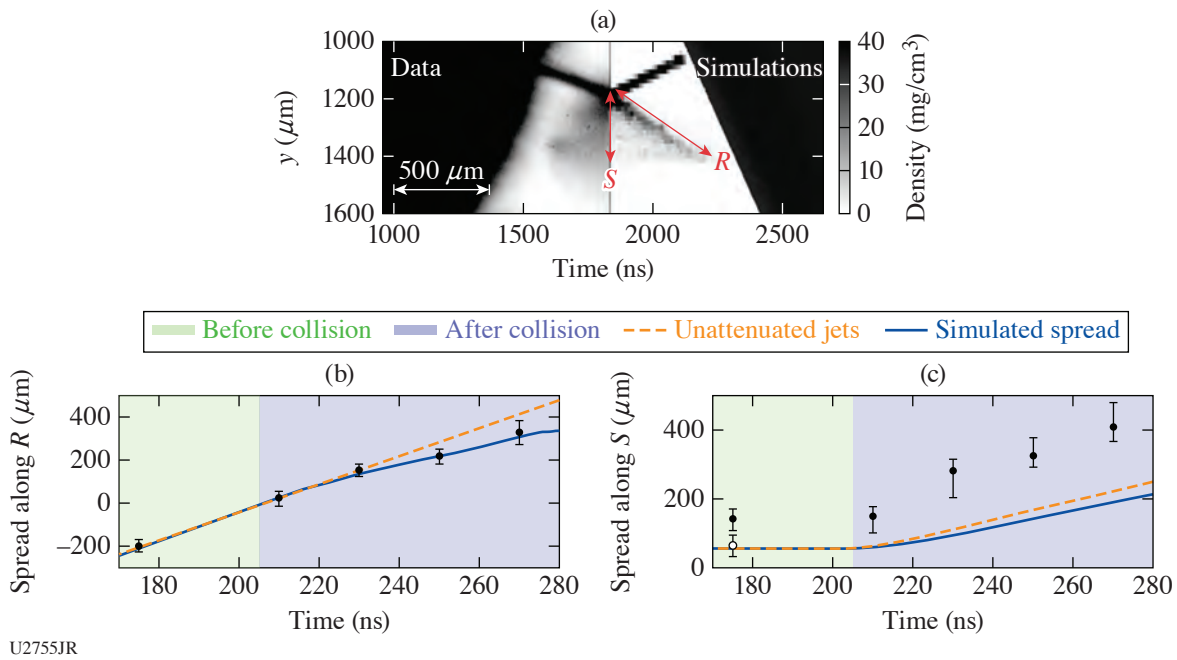


Figure 2
 High-pressure shock data and simulations for particle spread. (a) Density maps for the data (left) and simulations (right). Spread as measured along the R and S directions is indicated. (b) The spread of the microjet cloud in the direction of jet propagation as measured from the center point of the interaction (R direction): simulations (blue line), experiments (black points). (c) The projection of jet extent onto the axis of symmetry (S direction). The points before collision indicate the vertical extent of a single jet: the bulk of the jet (white) and the small bulbous region near the front of the jet (black). The orange lines indicate the hypothetical linear extent of unattenuated jets.

This material is based upon work supported by the Department of Energy National Nuclear Security Administration under Award Number DE-NA0003856, the University of Rochester, and the New York State Energy Research and Development Authority.

1. M. Lambrechts and A. Johansen, *Astron. Astrophys.* **544**, A32 (2012).
2. Z. Warhaft, *Fluid Dyn. Res.* **41**, 011201 (2008).
3. K. O. Mikaelian, *Phys. Rev. Lett.* **80**, 508 (1998).
4. D. S. Sorenson *et al.*, *J. Appl. Phys.* **92**, 5830 (2002).
5. R. M. Darlington, T. L. McAbee, and G. Rodrigue, *Comp. Phys. Commun.* **135**, 58 (2001).
6. K. K. Mackay *et al.*, *J. Appl. Phys.* **128**, 215904 (2020).

Optical Shock-Enhanced Self-Photon Acceleration

P. Franke,^{1,2} D. Ramsey,^{1,2} T. T. Simpson,^{1,2} D. Turnbull,¹ D. H. Froula,^{1,2} and J. P. Palastro^{1,3,4}

¹Laboratory for Laser Energetics, University of Rochester

²Department of Physics and Astronomy, University of Rochester

³Department of Mechanical Engineering, University of Rochester

⁴Institute of Optics, University of Rochester

Photon accelerators can spectrally broaden laser pulses with high efficiency in moving electron density gradients driven in a rapidly ionizing plasma. When driven by a conventional laser pulse, the group-velocity walk-off experienced by the accelerated photons and deterioration of the gradient from diffraction and plasma-refraction limit the extent of spectral broadening. Here we show that a laser pulse with a shaped space–time and transverse intensity profile overcomes these limitations by creating a guiding density profile at a tunable velocity. Self-photon acceleration in this profile leads to dramatic spectral broadening and intensity steepening, forming an optical shock that further enhances the rate of spectral broadening. In this new regime, multi-octave spectra extending from 400-nm to 60-nm wavelengths, which support near-transform-limited <400-as pulses, are generated over <100 μm of interaction length.

Broadband sources of coherent radiation find utility across diverse scientific disciplines as experimental drivers and diagnostic tools. State-of-the-art supercontinuum sources, which primarily achieve spectral broadening through Kerr-induced self-phase modulation of ultrashort laser pulses in either gas-filled fibers¹ or self-guided filaments,² routinely generate multi-octave spectra in the infrared (IR) to ultraviolet (UV) wavelength range (15 μm to 100 nm).^{3–7} Such sources have thus far been limited to wavelengths >100 nm, due to a lack of dispersion control and strong absorption in the extreme ultraviolet (XUV) ($\lambda = 10$ nm to 100 nm). Extending coherent broadband sources into the extreme ultraviolet would open new wavelength regimes for spectroscopy and increase the achievable spatial and temporal resolution for applications including single-shot spectral interferometry,⁸ transient spectroscopy,⁹ and coherence tomography.¹⁰

Photon accelerators can spectrally broaden laser pulses with high efficiency in moving electron density gradients.^{11,12} When driven by a conventional laser pulse, the group velocity walk-off experienced by the accelerated photons and deterioration of the gradient from diffraction and refraction limit the extent of spectral broadening [Figs. 1(a) and 2(f)],^{13–16} Here we introduce a scheme [Fig. 1(b)] that largely eliminates the adverse effects of diffraction, refraction, and dephasing by combining spatiotemporal^{17–20} and transverse intensity profile shaping of the laser pulse.^{21–23} This structured flying-focus (SFF) pulse drives a guiding plasma density profile that moves at a tunable focal velocity v_f . When a properly designed SFF pulse propagates in a homogeneous, partially ionized plasma, it undergoes extreme self-steepening and spectral broadening, culminating in the formation and collapse of an optical shock.

From 2-D finite-difference time-domain simulations, we discover that this novel self-shocked photon acceleration can produce multi-octave spectra extending well into the XUV (400 nm to 60 nm) over <100 μm of interaction length. The incident pulse had a central wavelength of 400 nm, a total energy of 53 μJ , and a total duration of 12 fs, values compatible with a tabletop Ti:Sa laser system. The intensity peak produced by the spatiotemporal shaping had a duration of 3.3 fs. The incident pulse was compressed considerably during the interaction, such that an isolated 700-as pulse was obtained at the accelerator output (90- μm interaction length). A simple short-pass filter can isolate even shorter 1.3 \times transform limited, highly focusable, coherent, high-intensity

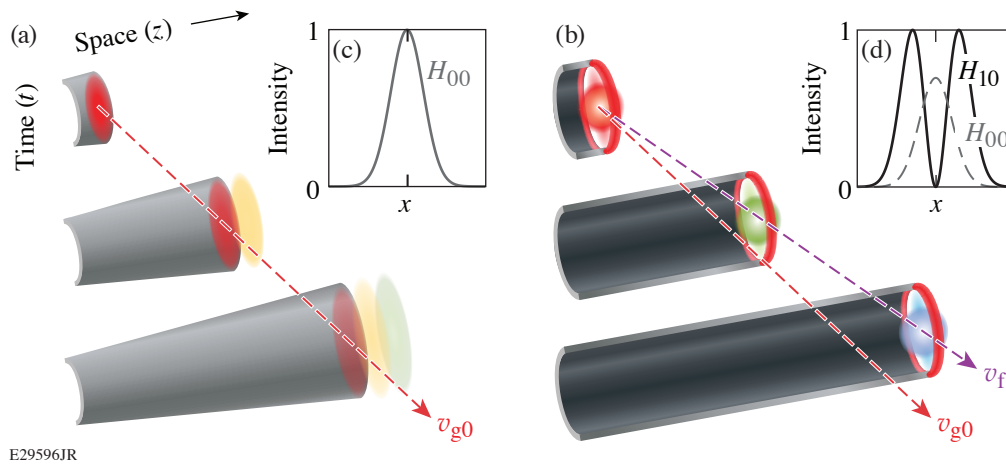


Figure 1

(a) A Gaussian beam drives a (gray) radially convex ionization front at the group velocity of light over approximately a Rayleigh length. Photons diverge from the optical axis due to diffraction and plasma refraction. Frequency upshifted photons dephase from the ionization front due to group velocity walk-off, limiting the system to relatively small frequency shifts. (b) A SFF pulse drives a concave ionization front at a tunable focal velocity $v_f \gtrsim v_{g0}$ over a distance much greater than a Rayleigh length. Photons are concentrated near the optical axis and stay in phase with the ionization front, resulting in many photons undergoing a large frequency shift. Transverse intensity profiles of a typical (c) Gaussian pulse and (d) SFF pulse used in 2-D simulations. Spatiotemporal shaping causes the intensity peak of the SFF to propagate at a tunable velocity in the far field. The guiding-transverse profile is achieved by combining orthogonally polarized Laguerre-Gaussian spatial modes.

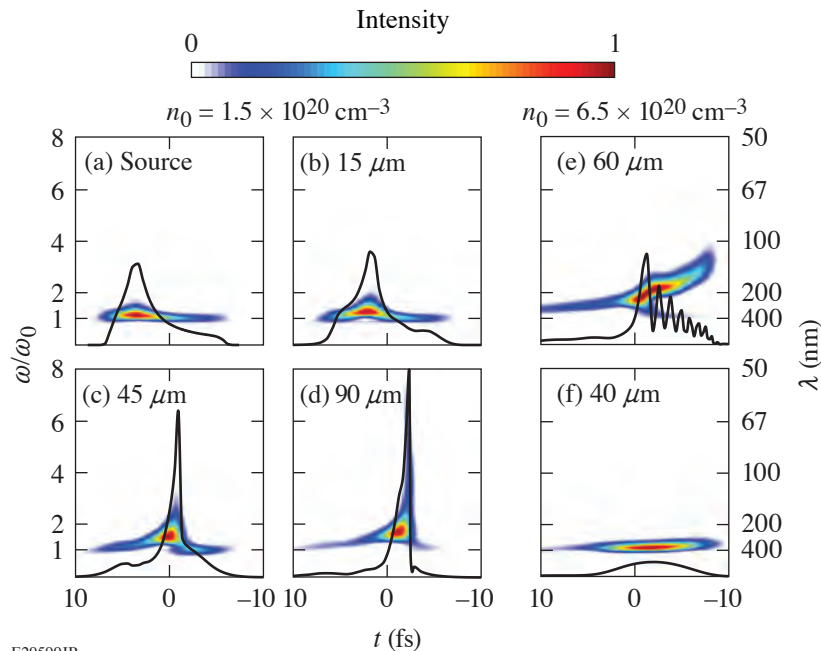


Figure 2

Spectrograms obtained by wavelet transform of the electric field on the optical axis for a SFF pulse at (a) the source input plane, (b) $15 \mu\text{m}$, (c) $45 \mu\text{m}$, and (d) $90 \mu\text{m}$, with $v_f = 1.015 v_{g0} = 0.9817 c$, and an initial neutral density $n_0 = 1.5 \times 10^{20} \text{cm}^{-3}$. For comparison, the spectrograms at higher density ($n_0 = 6.5 \times 10^{20} \text{cm}^{-3}$) are shown for (e) a SFF pulse with $v_f = 1.030 v_{g0} = 0.8740 c$, and (f) a standard Gaussian pulse focused at $z = 10 \mu\text{m}$. The color scale in each plot is normalized to the peak intensity. On-axis intensity profiles (black) are normalized to 10^{17}W/cm^2 .

($>10^{15} \text{W/cm}^2$), subfemtosecond pulses (350 as, $9\times$ temporal compression) from the accelerator output without the need for post compression. Spectral filtering could be achieved by allowing the output pulse to naturally diffract out of the end of the accelerator, collimating it with an appropriate curved reflector,²⁴ and then allowing it to pass through a 200-nm-thick magnesium foil.²⁵ The filtered pulse could then be refocused on target using another curved reflector.

Spatiotemporal shaping produces a focal region much longer than a Rayleigh length and allows the peak laser intensity to move through the accelerator at a velocity $v_{g0} < v_f < c$, where v_{g0} is the initial group velocity of the pulse. Under these condi-

tions, the intensity peak moves forward within the pulse's temporal envelope, such that self-accelerated photons at the back of the pulse catch up to and remain in phase with the intensity peak formed by the unshifted photons as they come into focus. The transverse intensity profile of the pulse has higher off-axis intensity. The resulting optical field ionization creates a guiding, radial electron density gradient that dynamically forms just ahead of the central axial density gradient responsible for the photon acceleration. Accelerated photons, thus confined near the optical axis, overlap temporally and spatially with other photons of varying frequency. This local increase in bandwidth and photon density leads to dramatic self-steepening and elevated amplitude of the main intensity peak. The resulting sharpened axial gradient causes faster frequency shifting and more sharpening, which in turn causes even faster frequency shifting [Figs. 2(a)–2(d)]. Eventually, optical wave breaking terminates the self-steepening and limits the maximum extent of spectral broadening. Increasing the initial density of the target increases the group-velocity dispersion, leading to shorter wave-breaking distances and smaller maximum frequency shifts [Fig. 2(e)].

The unique combination of compact size, short wavelength, broad bandwidth, and high coherence distinguishes this approach from other currently available sources. An experimental realization would provide a novel tabletop source of coherent broadband radiation and attosecond pulses in the XUV that could eventually scale to a tabletop source of coherent soft x rays. Democratizing access to extreme light through the development of radiation sources, such as that described here, could lead to an increased rate of scientific progress across fields that have far-reaching and positive impacts in fields such as material science, biology, and clean energy.

This material is based upon work supported by the Office of Fusion Energy Sciences under Award Number DE-SC0019135, the Department of Energy National Nuclear Security Administration under Award Number DE-NA0003856, the University of Rochester, and the New York State Energy Research and Development Authority.

1. J. M. Dudley, G. Genty, and S. Coen, *Rev. Mod. Phys.* **78**, 1135 (2006).
2. A. Couairon and A. Mysyrowicz, *Phys. Rep.* **441**, 47 (2007).
3. K. Jiao *et al.*, *Opt. Lett.* **44**, 5545 (2019).
4. F. Belli *et al.*, *Optica* **2**, 292 (2015).
5. A. Ermolov *et al.*, *Phys. Rev. A* **92**, 033821 (2015).
6. J. C. Travers *et al.*, *Nat. Photon.* **13**, 547 (2019).
7. N. Aközbebek *et al.*, *New J. Phys.* **8**, 177 (2006).
8. H. Mashiko *et al.*, *Opt. Express* **28**, 21025 (2020).
9. K. Ramasesha, S. R. Leone, and D. M. Neumark, *Annu. Rev. Phys. Chem.* **67**, 41 (2016).
10. F. Wiesner *et al.*, *Optica* **8**, 230 (2021).
11. S. C. Wilks *et al.*, *Phys. Rev. Lett.* **62**, 2600 (1989).
12. J. T. Mendonça, *Theory of Photon Acceleration*, Series in Plasma Physics (Institute of Physics Publishing, Bristol, England, 2001).
13. J. M. Dias *et al.*, *Phys. Rev. E* **66**, 056406 (2002).
14. N. C. Lopes *et al.*, *Europhys. Lett.* **66**, 371 (2004).
15. J. M. Dias *et al.*, *Phys. Rev. Lett.* **78**, 4773 (1997).
16. A. Howard *et al.*, *Phys. Rev. Lett.* **123**, 124801 (2019).
17. D. H. Froula *et al.*, *Nat. Photonics* **12**, 262 (2018).
18. A. Sainte-Marie, O. Gobert, and F. Quéré, *Optica* **4**, 1298 (2017).
19. J. P. Palastro *et al.*, *Phys. Rev. Lett.* **124**, 134802 (2020).
20. T. T. Simpson *et al.*, *Opt. Express* **28**, 38516 (2020).
21. M. W. Beijersbergen *et al.*, *Opt. Commun.* **112**, 321 (1994).
22. Y. Shen *et al.*, *Light Sci. Appl.* **8**, 90 (2019).
23. A. Longman *et al.*, *Opt. Lett.* **45**, 2187 (2020).
24. C. Bourassin-Bouchet *et al.*, *Opt. Express* **21**, 2506 (2013).
25. G. D. Tsakiris *et al.*, *New J. Phys.* **8**, 19 (2006).

Nonlinear Thomson Scattering of Spatiotemporally Shaped Laser Pulses

D. Ramsey,¹ B. Malaca,² A. Di Piazza,³ M. Formanek,³ P. Franke,¹ D. H. Froula,¹ M. Pardal,² T. T. Simpson,¹
J. Vieira,² K. Weichman,¹ and J. P. Palastro¹

¹Laboratory for Laser Energetics, University of Rochester

²Instituto de Plasmas e Fusão Nuclear-Laboratório Associado, Portugal

³Max-Planck-Institut für Kernphysik, Germany

Bright sources of high-energy photons lead to advancements in a range of disciplines including ultrafast biology and material science, nonlinear quantum electrodynamics, nuclear spectroscopy, and radiotherapy. The brightest sources currently reside at large accelerator facilities in the form of x-ray free-electron lasers or synchrotrons. While laser-driven sources promise a smaller-scale, widely accessible alternative, challenges in achieving the required photon number, energy, and coherence have held these sources back. Of the potential candidate laser-driven schemes, nonlinear Thomson scattering (NLTS) can produce extremely high energy, collimated radiation in a relatively controlled setting. NLTS, however, has inherent constraints that currently impede its realization as a practical light source.

In NLTS a relativistic electron collides with a laser pulse traveling in the opposite direction [Fig. 1(a)]. The electron rapidly oscillates in the fields of the pulse, reflecting and reradiating the incident photons. The properties of the radiation depend on the laser intensities and frequency of the pulse and the initial electron energy. Maximizing the radiated power requires large laser intensities. In these strong fields, the ponderomotive force of the pulse appreciably decelerates the electron and increases the amplitude of its oscillations along the direction of its initial motion. This red shifts the emitted frequencies and widens the emission angle.¹ The trade-off between the power, spectrum, and emission angle constrains the utility of NLTS.

Spatiotemporal pulse shaping provides control over the ponderomotive force, which can compensate for the ponderomotive deceleration in NLTS. As an example, the chromatic aberration from a diffractive optic and a chirp can be used to control the location and time at which each temporal slice within a pulse comes to its focus, respectively. By adjusting the chirp the resulting intensity peak, and therefore the ponderomotive force, can travel at any velocity with respect to the phase fronts (forward or backward) over distances much longer than a Rayleigh range.² Aside from extending the interaction length, a ponderomotive force that counter-propagates with respect to the phase fronts can *accelerate* an electron in NLTS.³

Here we describe novel regimes of nonlinear Thomson scattering that exploit the ponderomotive control afforded by spatiotemporal pulse shaping to substantially enhance the scaling of power, emission angle, and frequency with laser intensity. For high-intensity pulses, these regimes exhibit orders-of-magnitude-higher radiated powers and smaller emission angles than conventional NLTS. Further, the improved scaling with laser intensity allows for lower electron energies, relaxing the requirements on the electron accelerator.

Figure 1 contrasts backscattering configurations for conventional NLTS and NLTS with ponderomotive control (NPC). Conventional NLTS employs a standard laser pulse with an intensity peak and phase that counter-propagate at the vacuum speed of light with respect to a relativistic electron. NPC employs a spatiotemporally shaped pulse with an intensity peak that counter-propagates with respect to its phase fronts and co-propagates with respect to the electron. In both cases, as the electron enters the leading edge of the intensity peak, it begins oscillating in the polarization (transverse) and propagation (longitudinal) directions.

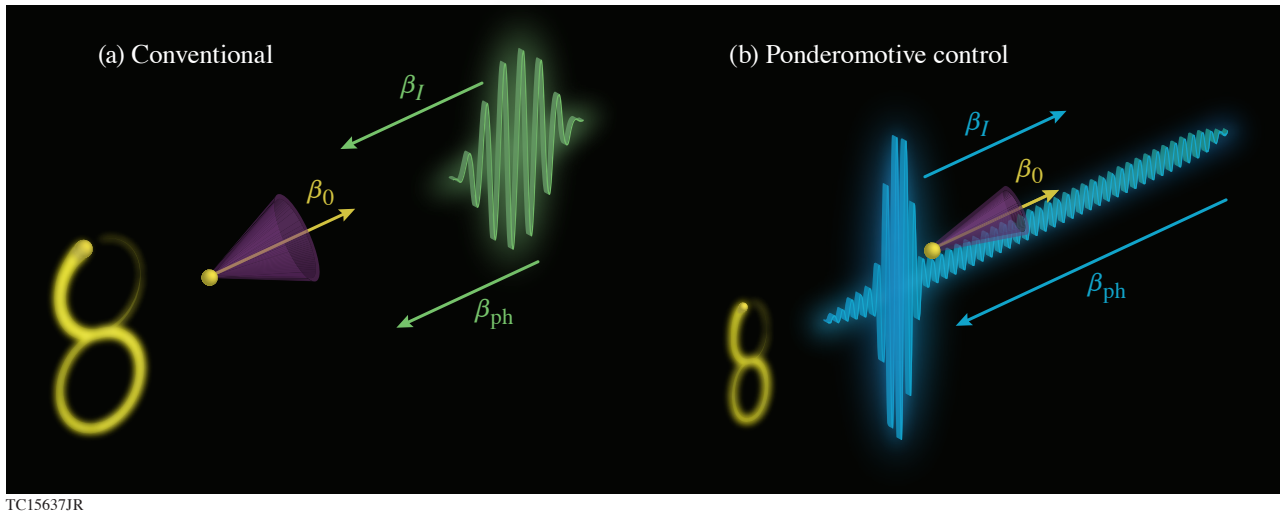


Figure 1

(a) A conventional NLTS configuration in which the intensity peak and phase fronts of a laser pulse travel in the opposite direction of the electron. At the rising edge of the intensity peak, the ponderomotive force decelerates the electron, red shifting the emitted frequencies and widening their emission angle (purple cone). (b) NLTS with ponderomotive control aligns the velocities of the intensity peak and the electron. Here the ponderomotive force of the intensity peak increases or maintains the electron velocity, allowing for higher-frequency emission into a smaller angle. The electron trajectory in its average rest frame (figure-eight motion) is depicted to the left of each case.

In NPC as the co-propagating intensity peak begins to overtake the initially slower moving electron, the electron is ponderomotively *accelerated* by the co-traveling intensity peak of the pulse—in the direction opposite to the phase velocity. The electron momentum increases as the electron enters regions of higher intensity. The acceleration enhances the overall radiation properties: emitted frequencies are now blue shifted and the radiation cone narrows. Ultimately, NPC switches the burden of accelerating electrons from an external source to the laser pulse itself—a situation ideal for existing and emerging high-energy, high-power laser facilities. Nonlinear Thomson scattering with ponderomotive control can produce extremely high energy photons with a spectrum that can be tuned through the initial electron energy, the laser amplitude, and, now, the ponderomotive velocity. The added flexibility enabled by ponderomotive control eliminates the tradeoffs inherent to conventional NLTS.

This material is based upon work supported by the Office of Fusion Energy Sciences under Award Number DE-SC0019135 and DE-SC00215057, the Department of Energy National Nuclear Security Administration under Award Number DE-NA0003856, the University of Rochester, and the New York State Energy Research and Development Authority.

1. E. Esarey, S. K. Ride, and P. Sprangle, *Phys. Rev. E* **48**, 3003 (1993).
2. D. H. Froula *et al.*, *Nat. Photonics* **12**, 262 (2018).
3. D. Ramsey *et al.*, *Phys. Rev. E* **102**, 043207 (2020).

Kinetic Simulation Study of Magnetized Collisionless Shock Formation on a Terawatt Laser System

Y. Zhang,^{1,2} J. R. Davies,^{1,2} P. V. Heuer,¹ and C. Ren^{1,2,3}

¹Laboratory for Laser Energetics, University of Rochester

²Department of Mechanical Engineering, University of Rochester

³Department of Physics and Astronomy, University of Rochester

In the cosmos, magnetized collisionless shocks such as termination shocks and bow shocks are ubiquitous. These shocks are usually magnetized by astronomical objects and are believed to be an important source of nonthermal particles in the universe. High-power laser systems are capable of reproducing these conditions in the laboratory and enable the systematic study of the underlying physics. It is well known that collisionality is very low due to low plasma density in space; collisions therefore cannot provide efficient dissipation for the shock. A modified two-stream instability (MTSI) has been proposed as the main dissipation mechanism for (quasi-) perpendicular collisionless shocks.^{1,2} Previous kinetic particle-in-cell (PIC) simulations used reduced ion–electron mass ratio, an unrealistic high magnetic field, or reduced speed of light to save computational resources; these concessions may alter the relative importance of different physical processes. In this summary our simulations use realistic and experimentally accessible parameters to capture true physics and provide a direct reference for experiments.

In the experimental setup shown in Fig. 1(a), a laser-driven solid-density piston is launched to drive a collisionless shock in a premagnetized ambient hydrogen or neon plasma. The external magnetic field is applied by MIFEDS (magneto-inertial fusion electrical discharge system).³ In the simulations, as seen in Fig. 1(b), the piston is idealized by a fixed reflecting wall on the right boundary. The ambient plasma drifts toward the wall, which leads to a clear shock downstream free of the influence from the piston. This drifting velocity V_d in the simulation frame is identical to the piston velocity V_p in the lab frame.

To create a collisionless shock the ion collisional mean free path between piston ions and ambient ions must be much larger than the shock width L , and the piston velocity must be supermagnetosonic. These two conditions constrain the ambient plasma density,

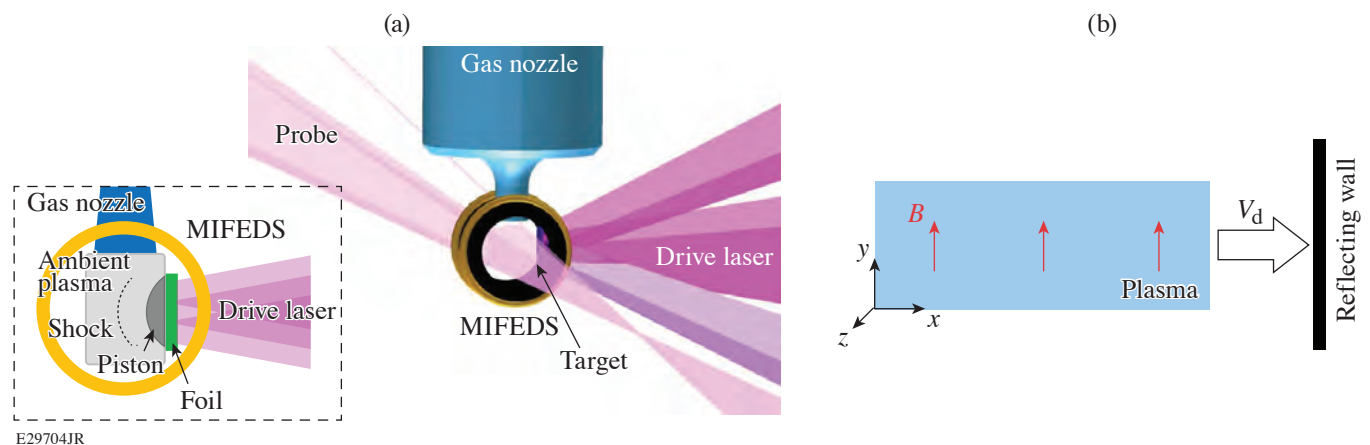


Figure 1

(a) Experimental setup and top-down schematic; (b) reflecting wall simulation setup.

$$\frac{27Z_i \left(\frac{B_1^T}{50}\right)^2}{56 \frac{m_i}{m_H} \left(\frac{V_p^{\text{km/s}}}{500}\right)^2 - Z_i \frac{T_{e1}^{\text{eV}}}{50} - \frac{T_{i1}^{\text{eV}}}{50}} < n_{e1}^{10^{19} \text{ cm}^{-3}} \ll \frac{131}{\ln \Lambda} \left(\frac{m_i}{m_H}\right)^2 \frac{1}{Z_i^3} \left(\frac{L^{\mu\text{m}}}{100}\right)^{-1} \left(\frac{V_p^{\text{km/s}}}{500}\right)^4, \quad (1)$$

where m , n , Z are the particle mass, density, charge number, respectively; B is the magnetic field; V_p is the piston velocity; subscripts i , H , and e denote ion, proton, and electron, respectively; 1 (2) represents the upstream (downstream) direction; and the superscripts indicate the units of the parameters.

The growth of MTSI has been used to find suitable parameter space for OMEGA EP⁴ experiments. The dispersion relation of MTSI is written as⁵

$$1 + \frac{\omega_{pe}^2}{k^2 v_{\text{the}}^2} \left[1 - \exp(-\lambda_e) \sum_{m=-\infty}^{\infty} I_m(\lambda_e) \frac{\omega}{\omega + m\Omega_{ce}} \right] - \sum_{s=\text{in, re}} \frac{\omega_{ps}^2}{2k^2 v_{\text{the}}^2} Z'(\xi_s) = 0, \quad (2)$$

where ω_{ps} is the plasma frequency for species s (e for electrons, in for incoming ions, and re for reflected ions), $v_{\text{ths}} = (T_s/m_s)^{1/2}$ is the thermal velocity, Ω_{cs} is the gyrofrequency, k is the mode number, $\lambda_e = k^2 v_{\text{the}}^2 / \Omega_{ce}^2$, I_m is the modified Bessel function of the first kind, Z is the plasma dispersion function, and $\xi_s = (\omega - kV_{xs}) / \sqrt{2} k v_{\text{ths}}$, where v_{xs} is the bulk velocity of the two ion species. Equation (2) can be solved numerically for $\omega = \omega_r + i\omega_i$, from which the maximum growth rate $\gamma_{\text{MTSI}} = [\omega_i]_{\text{max}}$, and the corresponding, most-unstable mode k_{MTSI} , and wavelength $\lambda_{\text{MTSI}} \equiv 2\pi/k_{\text{MTSI}}$ can be found. Under zero-current condition and the assumptions $n_{in}/n_{re} = 3$, $V_{in} = V_d/4$, $V_{re} = 3V_d/4$, it is found that the maximum growth rate of MTSI is much larger than the ion gyrofrequency when $M_{s1} \geq 4$ for hydrogen and $M_{s1} \geq 2$ for neon, indicating a shock can be readily formed within a few tenths of an ion gyration period. Alternately, with an achievable applied magnetic field of only tens of tesla, it is possible to create a shock within a few tenths of a nanosecond. Typical parameter ranges achievable on the OMEGA EP/MIFEDS platform are given in Table I. Based on the conditions discussed in this section we chose upstream parameters listed in Table I for our PIC simulations to study shock formation in more detail. The MTSI, collisionality parameters, and some dimensionless quantities are also shown in Table I.

Hydrogen and neon shocks both form within $\sim \gamma_{\text{MTSI}}^{-1}$. Figure 2 shows the hydrogen shock as an example. At $t = 0.126$ ns ($\approx 0.10 T_{\text{ci1}} \approx 1.1/\gamma_{\text{MTSI}}$), a shock with a compression ratio of $r \approx 2.35$ [Fig. 2(a)] is formed by the $M_{\text{sp}} = 3.5$ ideal piston. The presence of reflected ions [the density hump in the upstream region in Fig. 2(a) and the lower prong of the tuning fork structure in Fig. 2(b)] indicates the supercriticality of the formed shock. MTSI is induced by the interaction between the incoming ion and shock-reflected ion in the background magnetic field. Nonzero modes in the Fourier spectrum of E_x [modes 1 and 2 in Fig. 2(c)] further confirm MTSI is the operating instability, in good agreement with the solutions of the dispersion relation.

The reflected ions are accelerated in both shock normal and tangential directions by the electrostatic field and the motional electric field, respectively, to 6.6 to 9.7 keV (average ~ 8 keV) in the lab frame. These ions accumulate in the upstream and participate in shock-front reformation (on the time scale of a few Ω_{ci}^{-1}) in later times. Our results using realistic parameters substantially separate the shock-formation time from Ω_{ci}^{-1} versus previous simulations using reduced m_i/m_e , showing that these shocks are formed via MTSI. Electrons are heated isotropically to $T_{e2} \approx 200$ eV. Additional 1-D simulations further confirm that the shock is indeed collisionless and the reflecting wall is a good approximation of a realistic piston. The formed shocks are also well described by Rankine–Hugoniot jump conditions.

This material is based upon work supported by the Department of Energy National Nuclear Security Administration under Award No. DE-NA0003856, Department of Energy Award No. DE-SC0020431, and the resources of the National Energy Research Scientific Computing Center (NERSC), a U.S. Department of Energy Office of Science User Facility located at Lawrence Berkeley National Laboratory. The authors thank the UCLA-IST OSIRIS consortium for the use of OSIRIS.

Table I: Parameters for the OMEGA EP/MIFEDS platform and the hydrogen/neon simulations, with corresponding MTSI growth rate/mode number of the most-unstable mode and some key dimensionless quantities. The plasma beta is $\beta = 2\mu_0(n_i T_i + n_e T_e)/B^2$, $\tau = \omega_{pe}^2/\Omega_{ce}^2$ is the magnetization parameter. The piston velocity range is from *HYDRA*⁶ simulations of the proposed experimental setup.

		OMEGA EP/MIFEDS	Hydrogen	Neon (Ne ⁸⁺)
Upstream				
Density	n_{e1}	10^{18} to 10^{20} cm ⁻³	10^{19} cm ⁻³	6×10^{18} cm ⁻³
Temperature	T_1	40 to 400 eV	50 eV	160 eV
B field	B_1	≤ 50 T	50 T	50 T
Piston velocity	V_p	≤ 500 km/s	442 km/s	375 km/s
Ion gyroradius	ρ_{i1}		92.3 μ m	195.7 μ m
Ion gyroperiod	T_{ci1}		1.3 ns	3.3 ns
MTSI				
Maximum growth rate	γ_{MTSI}		8.8 ns ⁻¹	6.7 ns ⁻¹
Most-unstable mode	λ_{MTSI}		10.7 μ m	14.2 μ m
Dimensionless				
Piston sonic Mach number	M_{sp}		3.50	3.50
Alfvénic Mach number	M_{Ap}		1.28	1.33
Magnetosonic Mach number	M_{msp}		1.20	1.25
Ion mean free path	$\lambda_{ii}/\lambda_{\text{MTSI}}$		74	40
MTSI growth rate	$\gamma_{\text{MTSI}}/\Omega_{ci1}$		11.5	21.9
Plasma beta	β_1		0.16	0.17
Magnetization	τ_1		421	247

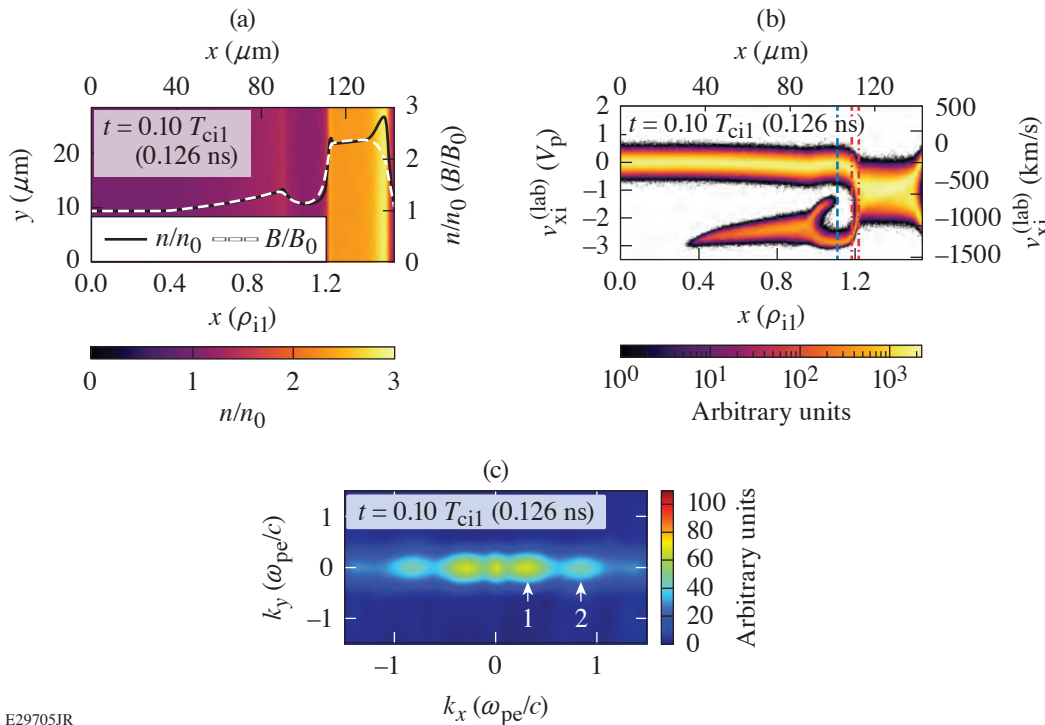


Figure 2
 (a) Hydrogen ion density (2-D and y averaged) and magnetic field (y averaged) at $t = 0.10 T_{ci1}$; (b) Ion $v_{xi}^{(\text{lab})}$ - x phase space in the lab frame; (c) Fourier spectrum of E_x . The modes labeled with 1 and 2 are $k_x \approx 0.33$ and $0.86 \omega_{pe}/c$, respectively.

E29705JR

1. J. Park *et al.*, Phys. Plasmas **19**, 062904 (2012).
2. J. Park *et al.*, Astrophys. J. **765**, 147 (2013).
3. D. H. Barnak *et al.*, Rev. Sci. Instrum. **89**, 033501 (2018).
4. D. N. Maywar *et al.*, J. Phys.: Conf. Ser. **112**, 032007 (2008).
5. S. P. Gary, *Theory of Space Plasma Microinstabilities*, Cambridge Atmospheric and Space Science Series (Cambridge University Press, Cambridge, 1993).
6. M. M. Marinak *et al.*, Phys. Plasmas **8**, 2275 (2001).

Relativistically Transparent Magnetic Filaments: Scaling Laws, Initial Results, and Prospects for Strong-Field Quantum Electrodynamics Studies

H. G. Rinderknecht,¹ T. Wang,² A. Laso Garcia,³ G. Bruhaug,¹ M. S. Wei,¹ H. J. Quevedo,⁴ T. Ditmire,⁴
J. Williams,⁵ A. Haid,⁵ D. Doria,⁶ K. M. Spohr,⁶ T. Toncian,³ and A. Arefiev²

¹Laboratory for Laser Energetics, University of Rochester

²University of California, San Diego

³Helmholtz-Zentrum Dresden-Rossendorf, Germany

⁴University of Texas, Austin

⁵General Atomics, San Diego

⁶ELI-NP & IFIN-HH, Bucharest-Magurele, Romania

Relativistic electron motion and volumetric laser–plasma interaction at supercritical densities create a novel phenomenon: the relativistically transparent magnetic filament. A sufficiently intense laser in an overdense plasma induces a relativistic current filament that moves axially with the laser field. This current generates a quasi-static azimuthal magnetic field with strength comparable to the laser field. Surrounding the filament with a higher-density channel wall optically guides the laser pulse, allowing intense laser–plasma interaction over many Rayleigh lengths. This system operates as a relativistic plasma rectifier for laser light that efficiently converts the laser’s electric and magnetic fields into a direct filamentary current and associated magnetic field. Electrons oscillate within the confining azimuthal magnetic field, facilitating direct energy gain from the laser and acceleration to hundreds of MeV. At the same time, the electron deflections within the magnetic field cause them to emit photons. Simulations predict that the azimuthal field strength reaches the megatesla level and the effective acceleration gradient exceeds 10^5 MeV/cm in the multipetawatt regime. The extreme magnetic-field strength and electron energy boost the radiated photon energy and the radiative power such that the magnetic filaments become efficient radiators of MeV photons.

We derived analytical scaling laws for the radiative properties of the magnetic filament phenomenon in terms of four parameters: the normalized laser amplitude $a_0 = |e|E/m\omega c$, a relativistic transparency parameter $S_\alpha \equiv n_e/n_c a_0$ with electron density n_e and critical plasma density n_c , the normalized laser focal radius $R_\lambda = (R/\lambda)$, and the normalized laser pulse duration $\tau_\nu = c\tau/\lambda$. To derive these laws, we made the following assumptions: First, the electrons are represented by a thermal distribution, with the number of accelerated electrons $N_e = n_e \pi R^2 c \tau$. Second, the characteristic temperature of the electron distribution scales linearly with time and can be represented as $T(t) = C_T a_0 m c^2 (ct/\lambda)$ for a constant of acceleration C_T . Third, the azimuthal magnetic field is produced by a relativistic, uniform current density as $B(r) = B_0 \pi(r/\lambda) S_\alpha$ for the laser’s magnetic-field amplitude B_0 . Fourth, the radiation power per electron is given by the synchrotron power spectrum and is evaluated using $B(r)$ at either the laser radius or a magnetic boundary $r_{mb} = \lambda f_i^{1/2} S_\alpha^{-1/2} \pi^{-1}$, which is a maximum radius that electrons can reach with a given initial momentum $\gamma_i \equiv f_i a_0$ for a constant f_i of order unity.¹ Fifth, the electrons radiate during a fraction of their orbit f_i . Lastly, the interaction ends by depletion of the laser pulse at a time $t_{cut} = f_i t_{max}$ for a constant factor f_i in the range (0, 1) and t_{max} represents the time at which the energy in the electron population equals the initial laser energy. These assumptions result in scaling laws for photon energy $\langle \epsilon^* \rangle$, total radiated energy $E_{\gamma, tot}$, number of photons N_γ , and efficiency η_γ as shown in Table I.

The scaling laws were compared to the results of 3-D particle-in-cell (PIC) simulations, as shown in Fig. 1. The PIC simulations used laser amplitude $a_0 = 190$ (intensity 5×10^{22} W/cm²), $S_\alpha = 0.105$ ($n_e = 20 n_c$), $\tau = 35$ fs, and focal radius $R = 0.65, 0.95, 1.35, 1.6,$ and $2.1 \mu\text{m}$ (Ref. 2). The acceleration constant C_T was inferred to have a value of approximately 0.08 from simulated

Table I: Scaling laws for relativistically transparent magnetic filaments.

Limit	$R < r_{\text{mb}}$	$R > r_{\text{mb}}$
$\langle \varepsilon_* \rangle / mc^2$	$\approx 1.4 \times 10^{-5} f_i a_0^2 R \lambda_{\mu\text{m}}^{-1}$	$\approx 4.4 \times 10^{-7} f_i^{1/2} f_t^2 a_0^3 S_\alpha^{-3/2} \lambda_{\mu\text{m}}^{-1}$
$\frac{E_{\gamma, \text{tot}}}{mc^2}$	$\approx 7.7 \times 10^2 f_i^3 f_r C_T^{-1} a_0^5 R \lambda_{\mu\text{m}}^4 \tau_\nu$	$\approx 7.8 \times 10^1 f_i f_t^3 f_r C_T^{-1} a_0^5 S_\alpha^{-1} R \lambda_{\mu\text{m}}^2 \tau_\nu$
N_γ	$\approx 5.6 \times 10^8 f_i f_r C_T^{-1} a_0^2 S_\alpha R^3 \tau_\nu \lambda_{\mu\text{m}}$	$\approx 1.8 \times 10^8 f_i^{1/2} f_t f_r C_T^{-1} a_0^2 S_\alpha^{1/2}$
η_γ	$\approx 2.9 \times 10^{-7} f_i^3 f_r C_T^{-1} a_0^3 R \lambda_{\mu\text{m}}^{-1}$	$\approx 2.9 \times 10^{-8} f_i f_t^3 f_r C_T^{-1} a_0^3 S_\alpha^{-1} \lambda_{\mu\text{m}}^{-1}$

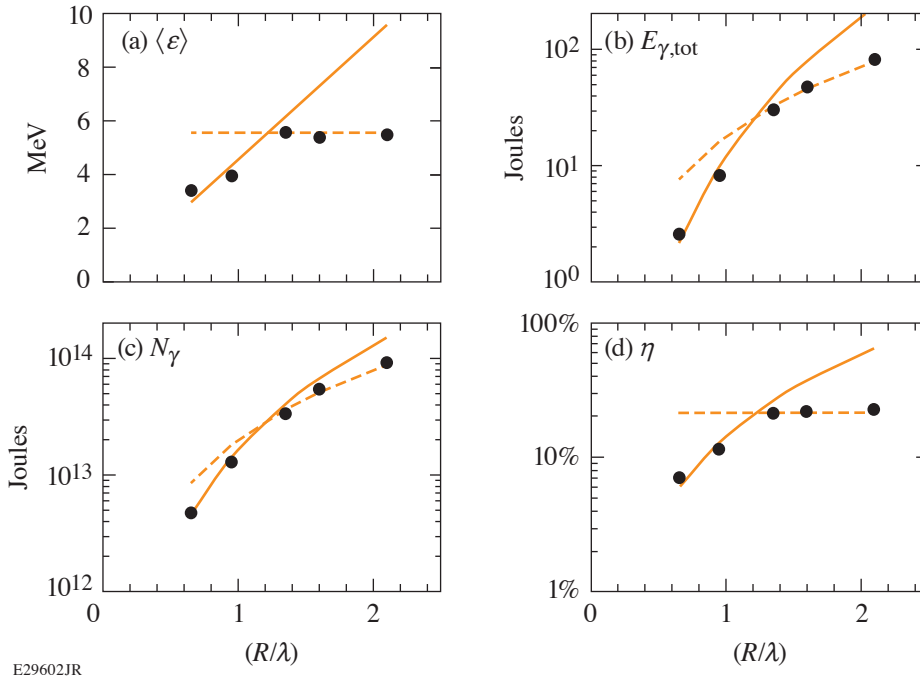


Figure 1

Comparison of derived scaling laws in the limit $R < r_{\text{mb}}$ (solid line) and $R > r_{\text{mb}}$ (dashed line) with 3-D PIC simulations in Ref. 2 (circles). (a) Characteristic photon energy, (b) total radiated energy, (c) total number of photons, and (d) radiation efficiency. Simulation results are for photons with energy above 1 MeV. Model coefficients are $f_i = 1.53$, $f_t = 0.31$, $f_r = 0.19$, and $C_T = 0.08$.

electron spectra; this value was used without loss of generality as the laws depend only on the composite constant (f_r/C_T) . The scaling laws agree with the 3-D PIC simulations with reasonable values for the constants $f_i = 1.53$, $f_t = 0.31$, and $f_r = 19\%$.

Initial experiments were performed on the Texas Petawatt Laser to study this phenomenon. A peak intensity of $1.1 \times 10^{21} \text{ W/cm}^2$ ($a_0 = 29.9$) was focused onto arrays of microchannels laser drilled in Kapton with a $6\text{-}\mu\text{m}$ inner diameter and filled with low-density CH foam with a density of 15 and 30 mg/cm^3 (5 and $10 n_c$, respectively). Elevated electron temperatures were observed in two of eight shots with good laser–target alignment, in agreement with predictions from 3-D PIC simulations of laser–channel interaction, as shown in Fig. 2. This fraction is consistent with the likelihood of laser–channel interaction, given the

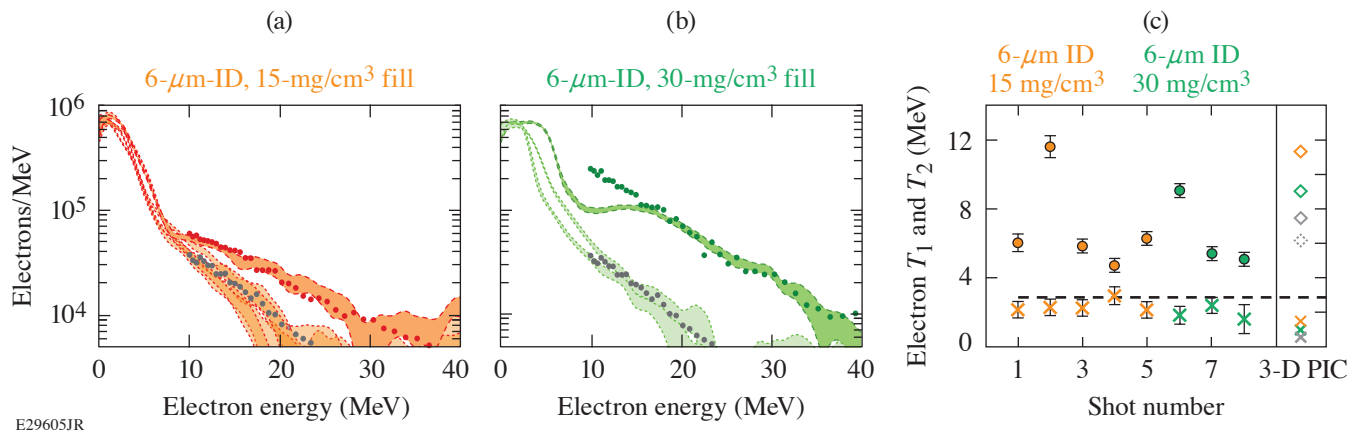


Figure 2

[(a),(b)] Electron spectra recorded on TPW experiments (curves) and from 3-D PIC simulations (circles). (c) Inferred electron temperatures on shots (circles) and from 3-D PIC simulations (diamonds). Channels with 5- n_c fill (orange), with 10- n_c fill (green), and planar 200- n_c target (gray).

pointing stability of 5- μm rms. We infer that the predicted magnetic filament phenomenon was observed in these experiments. The scaling laws will be used to design optimal targets for future experiments. At 10-PW laser facilities, efficiency approaching 50% is predicted for MeV photons.

This material is based upon work supported by the Department of Energy National Nuclear Security Administration under Award Number DE-NA0003856, the University of Rochester, and the New York State Energy Research and Development Authority.

1. Z. Gong *et al.*, Phys. Rev. E **102**, 013206 (2020).
2. T. Wang *et al.*, Phys. Rev. Applied **13**, 054024 (2020).

Ramp-Compressed Sodium at 480 GPa: A Dense Plasma Electride

D. N. Polsin

Laboratory for Laser Energetics, University of Rochester

The limiting high-pressure behavior of matter suggests that some materials transform into simple dense-packed structures with free-electron metallic behavior; examples include the ultradense solids of planetary cores and the hot plasmas of thermonuclear reactions and stellar interiors. This model breaks down at significant compressions where valence–valence and valence–core electron overlap are responsible for the chemical and electronic properties, bringing quantum behavior to the macroscale and giving rise to exotic phases such as high-temperature superconductors, quantum Hall insulators, and electriles. Sodium is the ideal material to explore such behavior due to its remarkable transformation at just 200 GPa from a free-electron simple metal to a structurally complex transparent electride,¹ where electrons are localized in interstitial positions due to the density-driven quantum mechanical constraints on the electronic wave functions.² Studies of high-temperature (>1000-K) electride behavior in the solid, liquid, and plasma phases have largely been limited to theoretical studies with no data on the kinetics of these phase transformations on nanosecond time scales.^{3,4} Here we report on measurements of the structural and electronic properties of Na in an unexplored regime, where the nearest Na–Na distance approaches the 3s orbital radius. Lasers are used as high-pressure drivers to ramp compress Na up to 480 GPa and ~2000 K. X-ray diffraction measurements at these unprecedented pressures and temperatures reveal that the *hP4* electride phase is stable even in a dense plasma state and on nanosecond time scales. At intermediate pressures (242 to 292 GPa), new complex phases with diffraction peaks unaccounted for by the *hP4* structure are observed. The new phase is not transparent—in striking contrast to static compression studies—but a significant decrease in the conductivity is consistent with a transformation to a high-temperature electride phase. Interactions between core electrons occur in all materials at extreme densities and pressures; the formation and understanding of these novel quantum materials in their transient states are the first steps to a new generation of high-energy-density quantum matter.

Sodium's intriguing high-pressure behavior is evident upon inspection of its phase diagram shown in Fig. 1. Sodium transforms from simple cubic structures to at least seven complex, low-symmetry phases near the minimum of the melting curve (blue circles and blue curves) at 118 GPa and room temperature.^{5,6} At 147 GPa, it transforms into an incommensurate host–guest structure—a complex structure consisting of two interpenetrating host and guest structures—as the melting temperature begins to increase.^{7,8}

This series of high-pressure phase transformations is associated with remarkable transformations in Na's electronic properties with a transition from a mirrorlike metal at ambient pressure to a dark, nonreflecting *tI19* phase at 147 GPa to a transparent insulator at 200 GPa with a band gap of at least 1.3 eV (Refs. 1 and 9). Guided by first-principles structure searching results, the x-ray diffraction pattern from the transparent phase is a distorted double hexagonal close-packed (dhcp) *hP4* electride structure¹ that, together with the interstitial quasi-atoms form the binary Ni_2In structure, shown in Fig. 1 (structural model).

Simultaneous x-ray diffraction (XRD) and reflectivity measurements were performed on the OMEGA EP laser that ramp compressed Na to nearly 500 GPa (Ref. 10). At 409 ± 15 GPa, the diffraction pattern has four peaks, consistent with the *hP4* phase reported in previous room-temperature static compression experiments by Ma *et al.*,¹ but at higher temperatures and under dynamic compression. We index the four lines as the *hP4* (010), (011), (012), and (110), giving lattice parameters $a = b = 2.75 \pm 0.03$ Å and $c/a = 1.35 \pm 0.02$. Compared to the ideal dhcp lattice, with $c/a = 3.27$ for hard spheres, the *hP4* structure is highly distorted and not close packed because the electride nature of this structure stabilizes a more open structure to accommodate the local-

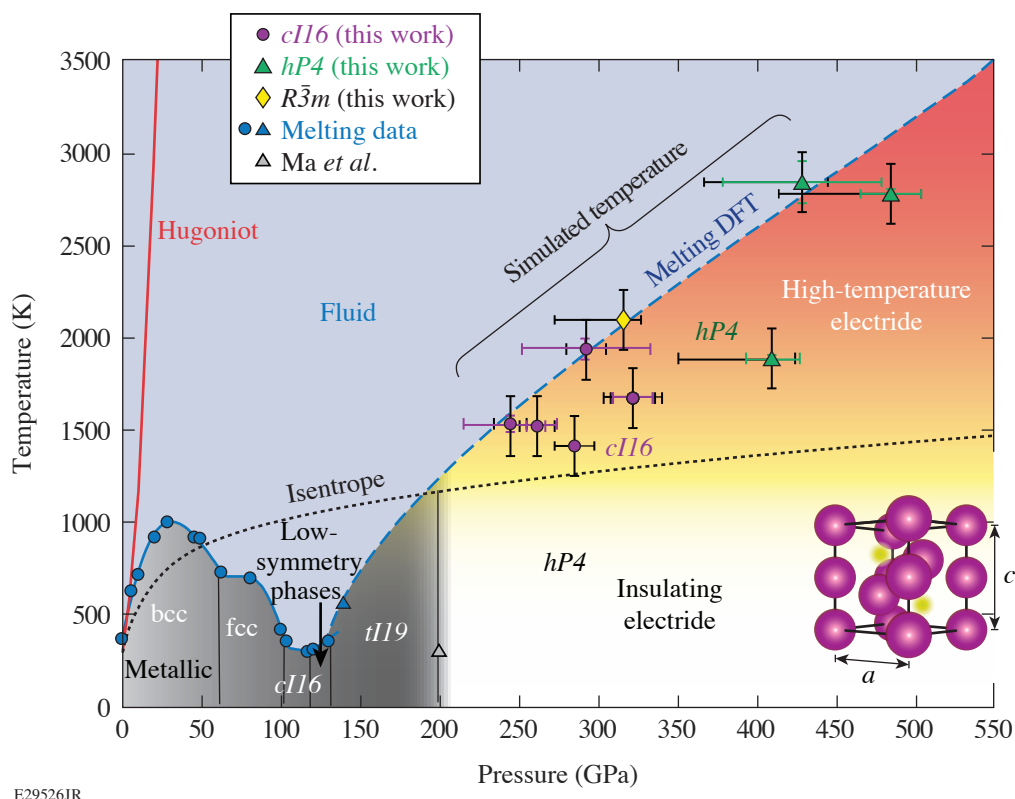


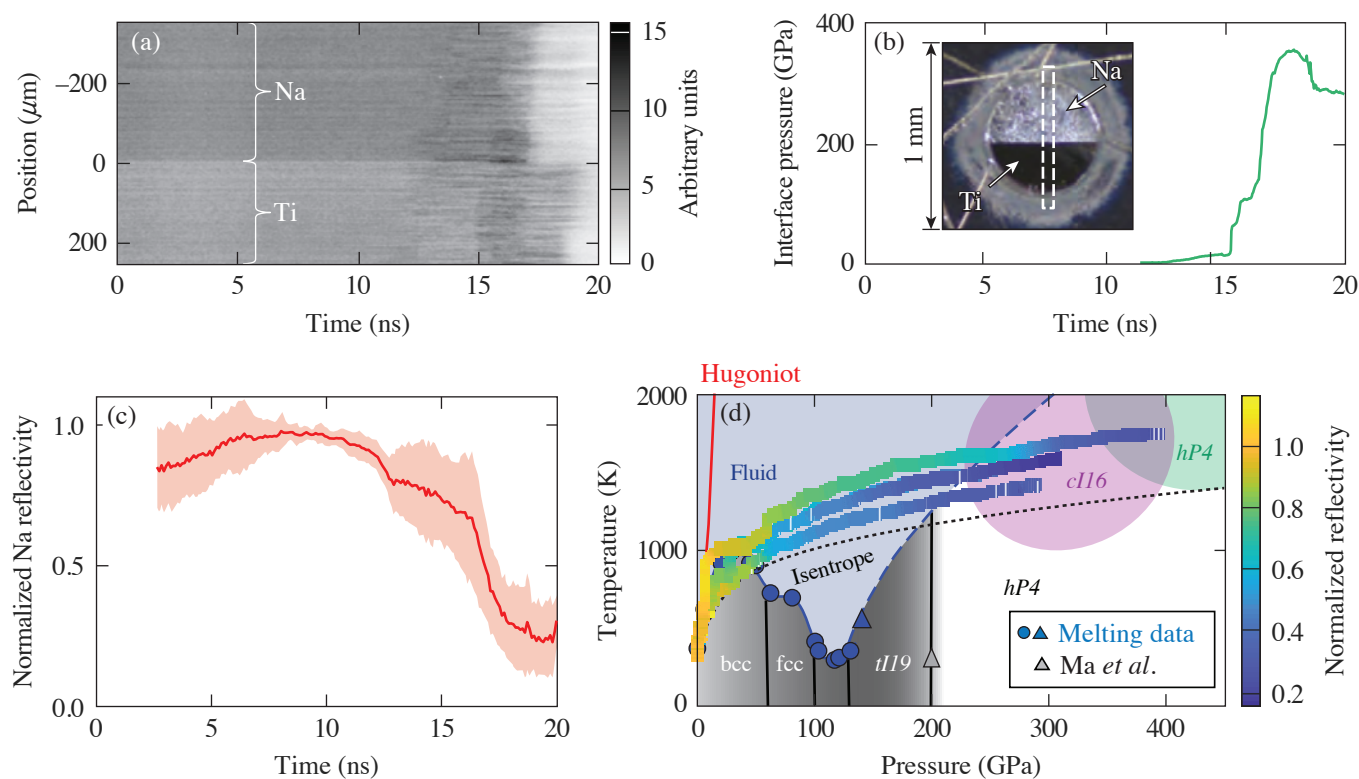
Figure 1

The high-pressure phase diagram of Na based on our laser-driven ramp compression data (purple circles, yellow diamond, and green triangles; black error bars represent systematic and random uncertainties; color “error” bars represent standard deviation in pressure and temperature states within the sample) and previous work from Refs. 1, 5, 6, 8, and 11. The data are compared to the theoretical principal Hugoniot and isentrope. The melting curve data from Refs. 6 and 8 are shown (blue circles and triangle) along with density-functional-theory (DFT) calculations¹¹ for the melting curve (blue dashed line) above 130 GPa in the *hP4* phase [structural model (bottom right): Na⁺ ions (purple), localized electrons (yellow)]. Three different phases of Na, *cI16*, *R3m* and *hP4*, are observed. The temperatures are estimated from hydrodynamics simulations.

ized valence electron charge.¹ Compared to the static compression data ($c/a = 1.46$), we observe a decrease in the c/a ratio with increasing pressure that agrees well with the density functional theory predictions and implies a stronger electron localization.¹

At pressures between 242 and 292 GPa, the XRD pattern is consistent with a complex *cI16* phase. This is isostructural with the *cI16* phase of sodium near the minimum of the melting curve at lower temperatures and pressures (108 GPa, room temperature)¹² and lithium (40 GPa, 180 K).¹³ The *cI16* structure (space group: $I43d$, 220) is a body-centered-cubic (bcc) superstructure with 16 atoms on the 16c Wyckoff site. The diffraction pattern has five peaks with a clearly different symmetry than the *hP4* structure, which was observed at these pressures in room-temperature experiments.¹ In one experiment at 315 ± 11 GPa (shot 26479), a diffraction pattern distinct from both *cI16* and *hP4* was observed. The diffraction pattern was compared to those from theoretically predicted structures and other structures observed in alkali metals including *oP8*, *oC16*, *tI4*, and *tI19*, but none were found to match the observed diffraction pattern. A Bravais lattice and space group search¹⁴ suggest a rhombohedral structure (space group: $R\bar{3}m$, 166). This is the same structure observed in As, Sb, and Bi (Ref. 15).

Figure 2(c) shows the average Na reflectivity as a function of time. As seen in both the raw data and the average across all experiments, the Na reflectivity drops to about $23\% \pm 4\%$ of its initial value. The temperature–pressure paths of the reflectivity measurements are shown in Fig. 2(d), where hydrocode simulations are used to estimate the temperatures. The reflectivity is tracked through the bcc phase into the stability region of the fluid phase, and at the highest pressures, in the *cI16* phase and approaching the *hP4* phase where it is dark and nonreflective. A threefold drop in electrical conductivity is expected in the low-coordinated



E29558JR

Figure 2

(a) A non-fringing VISAR (velocity interferometer system for any reflector) image for a Na target using a transparent MgO window and containing Ti coatings to detect changes in reflectivity (shot 27971). The non-fringing image is generated by blocking one arm of the VISAR interferometer, and shows no evidence of the pre-imposed striped reflectance pattern with a $150\text{-}\mu\text{m}$ period behind the Na layer. (b) (inset) A microscope image through the high-Z pinhole shows the Na layer (top) and the half-Ti overcoat (bottom) with the VISAR field of view overlaid (dashed box). The interface pressure of the shot shown in (a) shows that the drop in reflectivity is coincident with the increasing pressure. (c) Average (red curve) and standard deviation (red shaded region) of all Na reflectivity data normalized to the Ti reflectivity behind the transparent window. (d) The temperature–pressure phase diagram of Na with the simulated ramp-compression path (multicolor curves) for three reflectivity experiments.

liquid sodium between 40 and 80 GPa (Ref. 16). Similarly in liquid potassium, atomistic simulations predict a continuous transition from a free-electron metal to an electrider liquid at pressures corresponding to the melting curve maximum and the onset of electrider formation [10 to 20 GPa (K); 30 to 200 GPa (Na)] that manifests as a dip in the reflectivity similar to that observed here.¹⁷ Reduced reflectance is consistently observed in host–guest structures in Na and K at lower pressure.^{1,7,18}

Using laser-driven ramp compression, XRD measurements of sevenfold compressed Na are made in a regime where core overlap is thought to stabilize the formation of electrider states. The observation of the *hP4* phase at 480 GPa and ~ 3000 K, which was previously observed to be transparent at 200 GPa and room temperature, implies that electrider formation is possible on nanosecond time scales and at higher temperatures. At intermediate pressures, two additional unexpected phases of Na are observed. The reflectivity in both the liquid and solid stability regions is observed to continuously decrease where theory predicts a liquid–liquid phase transition to an electrider fluid in alkali metals.^{11,17} Interactions between core electrons occur in all materials at extreme densities and pressures, and these results give insight into the structural complexity and core-electron chemistry in Na—the most-striking example of a high-pressure electrider.

This material is based upon work supported by the Department of Energy National Nuclear Security Administration under Award Number DE-NA0003856, the University of Rochester, and the New York State Energy Research and Development Authority.

1. Y. Ma *et al.*, *Nature* **458**, 182 (2009).
2. M.-S. Miao and R. Hoffmann, *Account. Chem. Res.* **47**, 1311 (2014).
3. X. Dong *et al.*, *Nat. Chem.* **9**, 440 (2017).
4. J. Dai *et al.*, *Phys. Rev. Lett.* **109**, 175701 (2012).
5. E. Gregoryanz *et al.*, *Science* **320**, 1054 (2008).
6. E. Gregoryanz *et al.*, *Phys. Rev. Lett.* **94**, 185502 (2005).
7. L. F. Lundegaard *et al.*, *Phys. Rev. B* **79**, 064105 (2009).
8. M. Marqués *et al.*, *Phys. Rev. B* **83**, 184106 (2011).
9. A. Lazicki *et al.*, *Proc. Nat. Acad. Sci.* **106**, 6525 (2009).
10. D. D. Meyerhofer *et al.*, *J. Phys.: Conf. Ser.* **244**, 032010 (2010).
11. R. Paul *et al.*, *Phys. Rev. B* **102**, 094103 (2020).
12. M. I. McMahon *et al.*, *Proc. Nat. Acad. Sci.* **104**, 17,297 (2007).
13. M. Hanfland *et al.*, *Nature* **408**, 174 (2000).
14. B. Toby and R. Dreele, *J. Appl. Crystallogr.* **46**, 544 (2013).
15. O. Degtyareva, M. I. McMahon, and R. J. Nelmes, *High Pressure Res.* **24**, 319 (2004).
16. J.-Y. Raty, E. Schwegler, and S. A. Bonev, *Nature* **449**, 448 (2007).
17. H. Zong *et al.*, *Nat. Phys.* **17**, 955 (2021).
18. K. Takemura and K. Syassen, *Phys. Rev. B* **28**, 1193(R) (1983).

On the Liquid–Liquid Phase Transition in Dense Hydrogen

V. V. Karasiev,¹ J. Hinz,¹ S. X. Hu,¹ and S. B. Trickey²

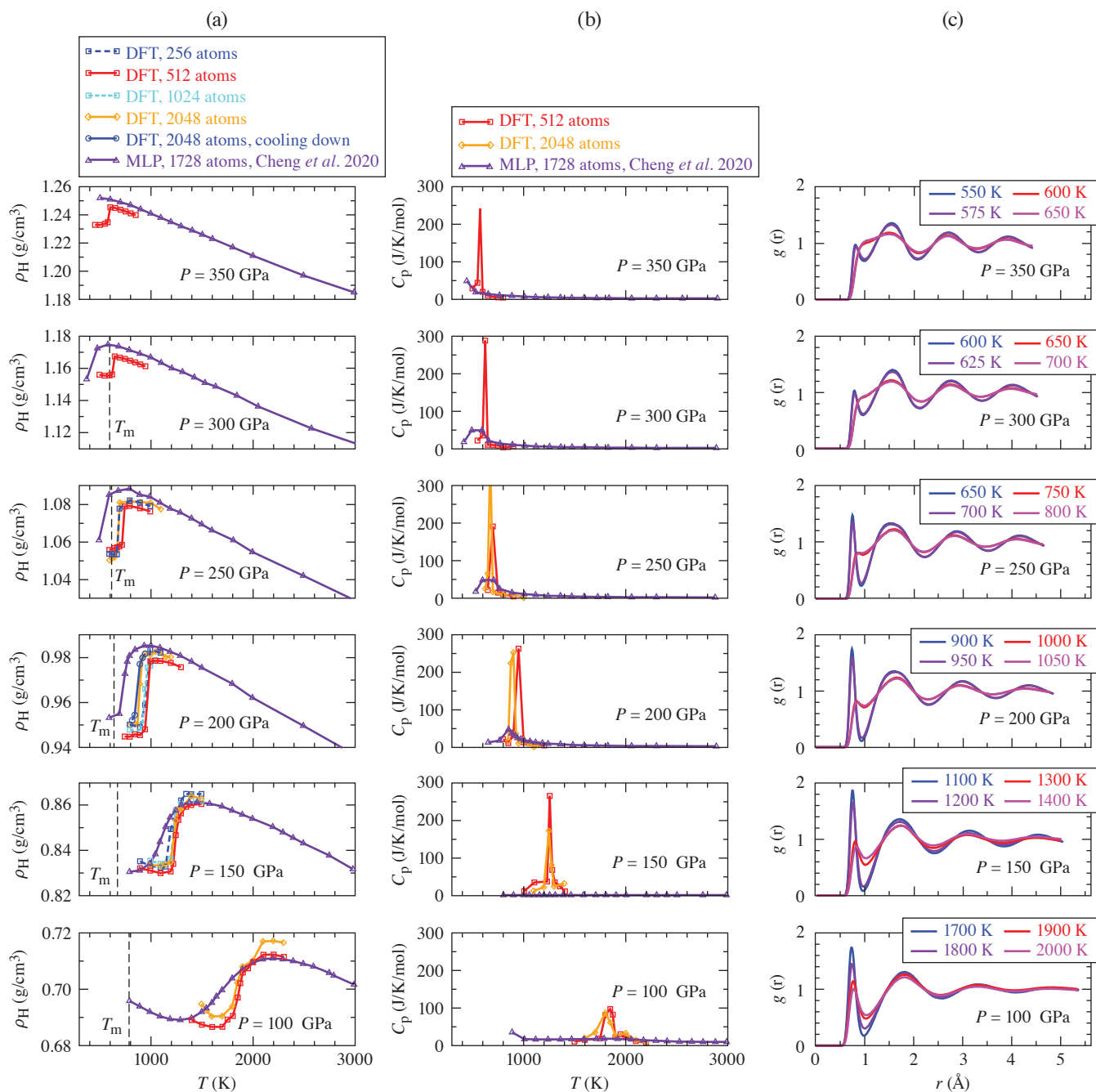
¹Laboratory for Laser Energetics

²Quantum Theory Project, Department of Physics, University of Florida

Determining the liquid–liquid phase transition (LLPT) in high-pressure hydrogen is a longstanding challenge with notable variation in experimental and calculated results (see Refs. 1–5 and citations therein). Until recently, the computational consensus was for a first-order transition. Calculated values differed but, for example, our results on $700 \leq T \leq 3000$ K are a curve along $320 \geq P \geq 70$ GPa (Ref. 2). Driven by molecular H₂ dissociation, transition signatures include density jumps, qualitative and sharp changes in ionic pair correlation functions (PCF's), and abrupt dc conductivity and reflectivity changes. In distinct contrast, Cheng *et al.*⁶ used molecular dynamics (MD) driven by a machine-learned potential (MLP) and found a continuous molecular-to-atomic liquid transformation that goes supercritical above $P \approx 350$ GPa, $T \approx 400$ K. They attributed the qualitative difference from MD-DFT (density functional theory) to (a) finite size effects that foster the formation of defective solids, with the common use of *NVT* dynamics tending to increase defect concentration relative to *NPT* ensemble results and (b) much shorter simulation times in the MD-DFT calculations than in the MD-MLP ones. Conceptually, the issue is whether a single MLP can correctly represent two chemically distinct regimes (molecular, atomic). An unambiguous test is to perform longer MD-DFT runs on significantly larger systems. If the MD-MLP represents the underlying theory (*ab initio* MD) faithfully and if the diagnosis based on MD-MLP is correct, results from the two simulation types should match. To test that, we have done much larger, longer MD-DFT calculations. The results are consistent with earlier MD-DFT calculations, thus qualitatively different from the MD-MLP results. Neither the large-system nor longer-run diagnosis from MD-MLP is sustained. Our *NPT* MD simulations were driven by DFT forces with Perdew–Burke–Ernzerhof (PBE) exchange correlation (XC).⁷ (Reference 6 used PBE to train the MLP.) We used from 256 through 2048 atoms per cell. Brillouin zone sampling used the Baldereschi mean value point for the simple cubic crystal structure $\mathbf{k} = (1/4, 1/4, 1/4)$ (Ref. 8). *VASP*^{9,10} was used for 1024 and 2048 atom systems, while the *i-PI* interface¹¹ with *Quantum Espresso*¹² was used for 256 and 512 atoms. Consistent results from the two confirm that the MD code and technical choices (thermostat, barostat, etc.) are inconsequential.

Our new large-system MD-DFT results agree with prior MD-DFT and coupled electron–ion Monte Carlo simulations:^{2,3,13} there is a sharp molecular-to-atomic transition. Figure 1 shows the qualitatively different character versus the MD-MLP prediction. Figure 1(a) shows density profiles $\rho_{\text{H}}(T)$ along isobars. At 300 and 350 GPa, the large-scale MD-DFT $\rho_{\text{H}}(T)$ values jump $\approx 1\%$ near $T = 650$ K. At 300 GPa, that is above the experimental melting temperature T_{m} (Ref. 14). In contrast, the 300-GPa MD-MLP isobar has a steep density increase near $T = 500$ K (in the stable solid phase),⁶ but it passes smoothly through both the melt line and the LLPT. Except for a systematic offset, the MD-MLP $\rho_{\text{H}}(T)$ matches the MD-DFT $\rho_{\text{H}}(T)$ in the atomic fluid region.

The molar heat capacity from MD-DFT as a function of T is shown in Fig. 1(b). All the isobars exhibit divergent heat capacity character across the transition. Evidently finite-size effects on T_{LLPT} are small and do not modify that character. To check on the possibility that finite-size effects trapped our simulations in defective solid configurations, we calculated the mean-squared displacement (MSD) of the 512 atom systems as a function of time along the 150- and 200-GPa isobars for $1100 \leq T \leq 1400$ K and $900 \leq T \leq 1200$ K, respectively. The MSD (not shown here) grows near linearly with time, as is characteristic of a liquid but not a solid.



TC15635JR

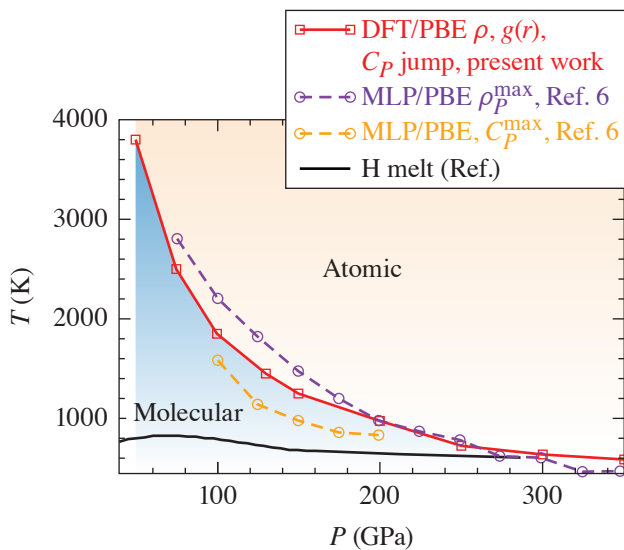
Figure 1

Comparison of MD results from the PBE XC-based MLP and *ab initio* MD-DFT (DFT) *NPT* simulations. (a) Hydrogen density as a function of T along six isobars. Experimental melting temperature T_m for each isobar is shown by a vertical dashed line.¹⁴ (b) Molar heat capacity as a function of T along the isobars. (c) PCF for each isobar for two temperatures below the density jump and two temperatures above the density jump.

Figure 1(c) shows the PCF on each isobar at temperature pairs below and above the density jump. Above, the first PCF peak virtually disappears, confirmation of the density jump being in conjunction with the molecular dissociation.²

To test possible long simulation duration effects on T_{LLPT} or its character, we performed six sequential MD-DFT runs of roughly 1.8-ps duration each for a total of ≈ 10 -ps duration and at 200 GPa with 512 and 2048 atoms. There were no meaningful differences in the results in either case. This outcome agrees with that of Geng *et al.*¹⁵ who performed runs up to 6 ps and found no meaningful differences with respect to 1.5 ps (after equilibration). To investigate whether the nanosecond time scale might make the simulated transition smooth, we performed a set of 2048-atom MD-DFT *NPT* simulations beginning with the atomic fluid at 200 GPa. Starting at 950 K, we cooled the system in sequential runs to 899, 849, and 824 K with simulation duration around 8 ps for each temperature. If the nanosecond time scale were to yield a smooth transition, the hydrogen density during such a fast cooling curve would not drop sharply below the hypothetical smooth long-duration curve. But, as evident in the Fig. 1(a) density plot at 200 GPa, the cooling curve (thin blue curve, circles) is almost identical to the one from MD-DFT simulations when the molecular fluid T is increased gradually (sharp transition shown by the solid orange curve).

Figure 2 shows the LLPT curves associated with density jumps, heat capacity peaks, and PCF peak disappearance. For the new large-scale MD-DFT calculations, those three criteria give one curve shown in red with squares at data points. With virtually identical P, T values; small differences in the transition temperature (less than 100 K for $P \leq 150$ GPa) are caused by numerical errors in calculating the molar heat capacity using finite differences. Two MD-MLP curves emerge from the analysis, however, one for the location of molar heat capacity maxima, C_P^{max} , and another for the maximum density, ρ_P^{max} . Consistent with the foregoing discussion, there are striking differences. The MLP C_P^{max} curve lies well below the MD-DFT curve. The MLP ρ_P^{max} curve is flatter than the MD-DFT reference curve and lies close to it only at about $P = 70$ GPa, $T = 2800$ K and then again for P between about 170 and 300 GPa.



TC15636JR

Figure 2

The LLPT boundary from the present large-scale MD-DFT (DFT/PBE) simulations compared to MLP (MLP/PBE) C_P^{max} and ρ_P^{max} curves.

Given that neither the finite-size nor simulation duration diagnosis advanced in Ref. 6 is sustained by direct-calculation of chemically distinct regimes (molecular, atomic) of the hydrogen, we conclude that the MD-MLP results for the LLPT do not reproduce the fundamental MD-DFT results as they should. Up to 2048 atoms and 10-ps simulation duration, our results are consistent with the earlier subcritical behavior predictions.

V. V. Karasiev, J. Hinz, and S. X. Hu were supported by the Department of Energy National Nuclear Security Administration Award Number DE-NA0003856 and U.S. National Science Foundation PHY Grant No. 1802964. S. B. Trickey was supported by Department of Energy Grant DE-SC0002139. This research used resources of the National Energy Research Scientific Computing Center, a DOE Office of Science User Facility supported by the Office of Science of the U.S. Department of Energy under Contract No. DE-AC02-05CH11231. Part of the computations were performed on the Laboratory for Laser Energetics HPC systems.

1. E. Gregoryanz *et al.*, *Matter Radiat. Extremes* **5**, 038101 (2020).
2. J. Hinz *et al.*, *Phys. Rev. Research* **2**, 032065(R) (2020).
3. G. Rillo *et al.*, *Proc. Natl. Acad. Sci.* **116**, 9770 (2019).
4. B. Lu *et al.*, *Chin. Phys. Lett.* **36**, 103102 (2019).
5. C. Pierleoni *et al.*, *Proc. Natl. Acad. Sci.* **113**, 4953 (2016).
6. B. Cheng *et al.*, *Nature* **585**, 217 (2020).
7. J. P. Perdew, K. Burke, and M. Ernzerhof, *Phys. Rev. Lett.* **77**, 3865 (1996); **78**, 1396(E) (1997).
8. A. Baldereschi, *Phys. Rev. B* **7**, 5212 (1973).
9. G. Kresse and J. Furthmüller, *Phys. Rev. B* **54**, 11,169 (1996).
10. G. Kresse and D. Joubert, *Phys. Rev. B* **59**, 1758 (1999).
11. V. Kapil *et al.*, *Comput. Phys. Commun.* **236**, 214 (2019).
12. P. Giannozzi *et al.*, *J. Phys.: Condens. Matter* **29**, 465901 (2017).
13. W. Lorenzen, B. Holst, and R. Redmer, *Phys. Rev. B* **82**, 195107 (2010).
14. C. S. Zha *et al.*, *Phys. Rev. Lett.* **119**, 075302 (2017).
15. H. Y. Geng *et al.*, *Phys. Rev. B* **100**, 134109 (2019).

Impact of Electrode Geometry on the Efficiency of Metal–Semiconductor–Metal AlGaN Ultraviolet Photodiodes

S. F. Nwabunwanne and W. R. Donaldson

Laboratory for Laser Energetics, University of Rochester

Fast aluminum-gallium-nitride ($\text{Al}_x\text{Ga}_{1-x}\text{N}$)–based metal–semiconductor–metal (MSM) ultraviolet (UV) photodiodes (PD's) have been successfully designed, fabricated, and characterized using conventional photolithography techniques. Various electrode geometries were fabricated to investigate the influence of metal contact shapes on device performance indices with emphasis on the response speed and bias-voltage–independent efficiency. Peak response times from the best devices were evaluated with a bias-voltage–independent, external quantum efficiency of 1198% at 19.5 V and 70% at 60 V for *n*-doped and intrinsic devices, respectively. Based on the measured mobility, these devices should be capable of a response time as short as 1.31 ps.

$\text{Al}_x\text{Ga}_{1-x}\text{N}$ -based UV PD's have been the subject of active research due to their intriguing material properties. Sustained interest in $\text{Al}_x\text{Ga}_{1-x}\text{N}$ photodetectors stems from their impressive characteristics such as a wide and tunable direct band gap, thermal resistivity, radiation sturdiness, and electrical robustness. The ability to easily select the detected wavelength by simply varying the aluminum content of $\text{Al}_x\text{Ga}_{1-x}\text{N}$ is a significant advantage of these group III–V compounds. Also, $\text{Al}_x\text{Ga}_{1-x}\text{N}$ photodetectors can be specifically designed to look at specific spectral windows.^{1,2}

Intrinsic and Si-doped wafers obtained from KYMA Technologies were prepared by metal organic chemical-vapor deposition (MOCVD). A thin AlN layer serves to minimize the lattice constant mismatch between intrinsic/*n*-doped AlGaN thin films and the sapphire substrate. Si-doped wafers have a carrier density of $1 \times 10^{18} \text{ cm}^{-3}$, while the intrinsic wafers have a carrier density of $1 \times 10^{17} \text{ cm}^{-3}$. The Hall-effect measurements of Si-doped $\text{Al}_{0.1}\text{Ga}_{0.9}\text{N}$ thin films using the van der Pauw³ geometry configuration resulted in a carrier mobility of $127 \text{ cm}^2\text{V}^{-1}\text{s}^{-1}$, a carrier density of $2 \times 10^{18} \text{ cm}^{-3}$, and a resistivity of $0.0243 \text{ }\Omega\text{cm}$. Similarly, for Si-doped $\text{Al}_{0.2}\text{Ga}_{0.8}\text{N}$ thin film, the carrier mobility was measured as $10.4 \text{ cm}^2\text{V}^{-1}\text{s}^{-1}$, the carrier density as $1 \times 10^{18} \text{ cm}^{-3}$, and resistivity as $0.5656 \text{ }\Omega\text{cm}$. We investigated the defect densities of the wafers using x-ray rocking-curve measurements, which yielded $1.4398 \times 10^6 \text{ cm}^{-2}$ and $1.9288 \times 10^6 \text{ cm}^{-2}$ dislocation densities for intrinsic $\text{Al}_{0.1}\text{Ga}_{0.9}\text{N}$ and $\text{Al}_{0.2}\text{Ga}_{0.8}\text{N}$ thin films, respectively. For *n*-doped wafers, dislocation densities were $1.0201 \times 10^6 \text{ cm}^{-2}$ and $1.4702 \times 10^6 \text{ cm}^{-2}$ for $\text{Al}_{0.1}\text{Ga}_{0.9}\text{N}$ and $\text{Al}_{0.3}\text{Ga}_{0.7}\text{N}$, respectively. These numbers are among the lowest reported dislocation densities in AlGaN thin films; typically dislocation densities are of the order of 10^7 to 10^8 cm^{-2} (Refs. 2 and 4).

Two different electrode geometries were fabricated on the Pt and Au devices. There are a total of five interdigitated fingers for each device configuration, which consists of $1 \times 5\text{-}\mu\text{m}$ -wide electrodes that are spaced at $2\text{-}\mu\text{m}$ and $3\text{-}\mu\text{m}$ intervals. The electrodes on our previous devices covered 50% (Ref. 1) of the active area but these devices' electrodes cover about 30% of the active area. This implies ~20%-more incident UV light will be absorbed by the PD, resulting in improved sensitivity. An antireflection (AR) layer consisting of 44 nm of SiO_2 was designed for near-zero reflectivity at 262 nm, contributing ~20% improvement in the external quantum efficiency (EQE) of the PD's.

The light source was a 262-nm *Q*-switched Crystalaser with 10-ns pulse duration and 4.5 nJ of energy, externally clocked at 2.5 kHz. The beam diameter of the laser at the PD was $138 \text{ }\mu\text{m}$. Approximately 0.05 nJ per pulse reached the active area of the device. A Si-biased PD was employed as a reference detector to account for variation in the pulse energy. A half-wave plate combined with the UV polarizer was employed to control the amount of UV energy reaching both diodes during the reference

diode calibration. A 12.5-GHz Tektronix oscilloscope served as the primary measurement tool for the MSM AlGaIn PD's, which introduced a bandwidth constraint on our ability to measure the intrinsic impulse response of these devices.

With the electrode's geometry varied to facilitate absorption of 20% more of the incident photons as well as a strong electric field of 1×10^7 V/m at 20-V bias voltage, which is 40% greater than the electric field in the previous devices, we observed for the first time with these PD's, a bias-voltage-independent EQE of 1198% at 19.5 V and 70% at 60 V for the best-performing *n*-doped and intrinsic devices, respectively. As evidenced by the long tail in response, the Pt device must be in photoconductive mode, causing a multiplication of carriers that accounts for the superhigh EQE. While we desire efficient devices, the photoconductive gains of some of these devices are unsuitable for ultrafast laser pulse characterization due to their long tails. The EQE of the AlGaIn devices, which is the ratio of the number of photogenerated carriers to the number of incident photons, was calculated using

$$QE(\eta) = \frac{I_{ph}/e}{P/h\nu}, \quad (1)$$

where I_{ph} is the photocurrent (A) obtained by averaging the diode's voltage response measured over time and multiple acquisitions and dividing by 50- Ω oscilloscope's impedance; e is the charge; P denotes the optical power (W) of the incident light; h is Planck's constant; and ν is the frequency (Hz) of the input light. The voltage response curves were acquired ten times at each bias voltage and then integrated over 1.5-ns time interval. The efficiency of a PD is shown in Fig. 1. This represents a significant improvement over previous devices. A plausible contribution to the improvement in the EQE is the elevated electric field that drove the photogenerated carriers to saturation velocity, thereby preventing their recombination before they could be removed at the contacts. We estimate that the elevated electric field contributed about 30% to the boost in the EQE. Furthermore, the low number of defects in the $Al_xGa_{1-x}N$ thin films translated to a reduced number of trap sites that impede the free flow of carriers when photoexcited. This improved the mobility of the carriers, leading to a pronounced 30% increase in the EQE. Finally, the Schottky contacts formed with Pt and Au have been reported to reduce UV detection since they cast opaque shadows on the semiconductor, thereby reducing the efficiency of UV absorption.⁵⁻⁷ We reduce this impact of Pt and Au electrodes by making them thinner and fewer in number. Also, Schottky contacts block current from -5 V to 5 V, which is less than -8 V to 8 V in the previous devices, thereby leading to a rise in the photocurrent and contributing ~20% to the jump in the EQE. Finally, it is evident that some photoconductive gain mechanisms could have added to the photogenerated current accounting for about 10% elevation in the EQE for intrinsic devices and adding >50% in *n*-doped devices.

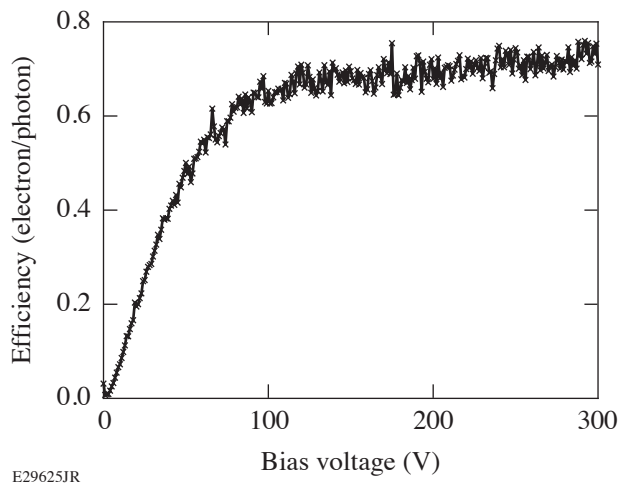


Figure 1
External quantum efficiency of AlGaIn PD as a function of bias voltage with saturation beginning at 75 V.

This material is based upon work supported by the Department of Energy National Nuclear Security Administration under Award Number DE-NA0003856, the University of Rochester, and the New York State Energy Research and Development Authority.

1. Y. Zhao and W. R. Donaldson, IEEE J. Quantum Electron. **56**, 4000607 (2020).
2. Y. Zhao and W. R. Donaldson, IEEE Trans. Electron Devices **65**, 4441 (2018).
3. D. M. Boerger, J. J. Kramer, and L. D. Partain, J. Appl. Phys. **52**, 269 (1981).
4. R. Gaska *et al.*, Appl. Phys. Lett. **72**, 707 (1998).
5. S. Wang *et al.*, IEEE Photon. Technol. Lett. **33**, 213 (2021).
6. P. C. Chang *et al.*, J. Alloys Compd. **504**, S429 (2010).
7. F. Bouzid, L. Dehimi, and F. Pezzimenti, J. Electron. Mater. **46**, 6563 (2017).

Impact of Boundary Sharpness on Temporal Reflection in Dispersive Media

J. Zhang,¹ W. R. Donaldson,² and G. P. Agrawal^{1,2}

¹The Institute of Optics, University of Rochester

²Laboratory for Laser Energetics, University of Rochester

In this summary, we investigate the impact of the finite rise time of a temporal boundary inside a dispersive medium used for temporal reflection and refraction of optical pulses. We develop a matrix approach in the frequency domain for analyzing such temporal boundaries and use it to show that the frequency range over which reflection can occur is reduced as the rise time increases. We also show that total internal reflection can occur even for shallow boundaries. This feature suggests that temporal waveguides can be realized through cross-phase modulation, even when pump pulses have relatively long rise and fall times. In past studies, the moving temporal boundary was assumed to be infinitely sharp such that the refractive index changes instantaneously at the boundary location. In practice, any temporal boundary will have a finite rise time. One expects the results obtained for a sharp boundary to remain valid as long as the rise time is much shorter than other time scales of interest (such as the width of the pulse being reflected at the boundary). It is not known, however, how the results obtained for a sharp boundary need to be modified when the rise time of the temporal boundary is non-negligible.

We assume that a temporal boundary, moving at the speed V_B , has been created inside the dispersive medium using a suitable technique (e.g., cross-phase modulation with a pump pulse) so that the refractive index of the medium differs by a small amount Δn on the two sides of the boundary. In most previous studies on temporal reflection, $s(t)$ is taken to be a step function of the form $h(t-T_B)$, assuming an infinitely sharp boundary located at $t = T_B$. In this work, we consider temporal boundaries with a finite rise time T_r ; in particular, $s(t)$ was considered to be a super-Gaussian of order m , $e^{-[(t-T_B)/T_0]^{2m}}$, where $T_r \sim T_0/m$.

For a sharp boundary with $T_r = 0$, it is known that a pulse splits into two parts after it arrives at the boundary, which can be identified as the reflected and transmitted parts.¹ Their spectra are shifted from the spectrum of the incident pulse in such a way that the reflected part never crosses the boundary. We extend this approach to temporal boundaries of arbitrary shapes by making a reasonable approximation. We divide the boundary region into N segments, each of finite duration such that $s(t)$ can be treated as a constant inside the segment. In other words, we replace the actual shape of the boundary with a staircase. This can be done for a boundary of any shape if we make N large enough that $s(t)$ does not vary much inside each segment. Consider one spectral component of the pulse before the first segment with the frequency $\omega = \omega_0 + \delta_0$. It propagates as a plane wave $A_0 e^{i(Kz - \delta_0 t)}$. As this plane wave traverses the boundary region, its frequency changes from one segment to the next, but K remains the same because of momentum conservation at any temporal boundary.¹ At the same time, a reflected wave is produced with a shifted frequency. As a result, two plane waves exist in the n th segment, where $s(t) = s_n$ is a constant.

Our approach is similar to that used for calculating the reflectivity of a stack of multiple dielectric layers.² We use the transfer and propagation matrices to cross all segments, starting from the far end of the last segment. The resulting matrix of the entire temporal boundary is the product of $2N + 1$ matrices. In terms of the four elements of this matrix, the incident, reflected, and transmitted waves are related as

$$\begin{pmatrix} A_{\text{in}} \\ A_{\text{R}} \end{pmatrix} = \begin{pmatrix} M_{11} & M_{12} \\ M_{21} & M_{22} \end{pmatrix} \begin{pmatrix} A_{\text{T}} \\ 0 \end{pmatrix}.$$

The reflectivity and transmissivity of the temporal boundary are given by $R = |M_{21}/M_{11}|^2$ and $T = |1/M_{11}|^2$, where the matrix elements can be computed using the group velocity, the group velocity dispersion, and the frequency shift across the boundary. One interesting feature of an infinitely sharp temporal boundary is that the analog of total internal reflection (TIR) can occur, i.e., it is possible to have the situation where the faster-propagating probe pulse never overtakes the slower-moving pump because the frequency of the probe pulse changes. We can normalize the parameter $(\omega_0/c) \Delta n$ to the minimum value for TIR to occur. Physically, this normalized parameter B represents the value of the index change relative to the value required for TIR to occur.

As seen in Fig. 1, TIR occurs for Δf values below 0.3 THz. The reason it ceases to occur for larger values of Δf is related to a larger speed mismatch between the wave relative to the moving boundary. As Δf increases beyond 0.3 THz, change in the propagation constant continues to increase, which decreases the reflectivity further. The rate of decrease depends on the boundary's rise time, and it becomes more rapid as T_r increases (or m decreases). For a Gaussian-shaped boundary with $m = 1$, the reflectivity becomes nearly a step function of Δf . In practical terms, for such boundaries, a narrowband signal is either totally reflected or fully transmitted, depending on its frequency. We considered two cases with $B = 0.95$ and $B = 1.05$, where $B = 1$ is required for TIR to occur. In the first case ($B = 0.95$), 96% of the pulse energy crosses the boundary. For $B = 1.05$, all the energy is reflected because the index change across the boundary is larger by 10% and exceeds the TIR threshold of $B = 1$. These results show that a relatively small change in the refractive index can produce large changes in the transmitted energy of a probe pulse when pump pulses are used to create a moving temporal boundary using the Kerr nonlinearity of an optical fiber.

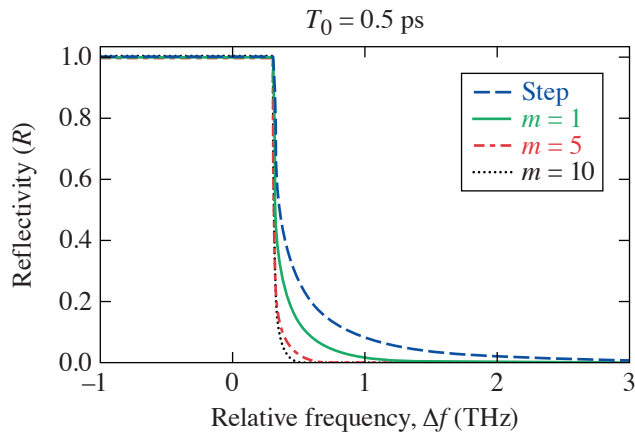


Figure 1
Dependence of the reflectivity spectrum on the rise time of a temporal boundary ($T_0 = 0.5$ ps) is shown using three values of m . The dashed curve shows, for comparison, the case of a step-function boundary.

E29700JR

This material is based upon work supported by the National Science Foundation (ECCS-1933328).

1. B. W. Plansinis, W. R. Donaldson, and G. P. Agrawal, *Phys. Rev. Lett.* **115**, 183901 (2015).
2. S. J. Orfanidis, *Electromagnetic Waves and Antennas* (2016) [Online], Chap. 6. Available: <https://www.ece.rutgers.edu/~orfanidi/ewa/>.

Time-Domain Fabry–Perot Resonators Formed Inside a Dispersive Medium

J. Zhang,¹ W. R. Donaldson,² and G. P. Agrawal^{1,2}

¹The Institute of Optics, University of Rochester

²Laboratory for Laser Energetics, University of Rochester

In this summary, we show that the temporal analog of a Fabry–Perot resonator (FPR) can be realized by using two moving temporal boundaries inside a dispersive medium, such as an optical fiber.^{1–3} In practice, such boundaries are created by using a pump–probe configuration in which one or more short pump pulses are launched together with a probe pulse. Each pump pulse increases the refractive index of the single mode of the fiber through the nonlinear Kerr effect, but this increase occurs only over the duration of the pump pulse. The temporal FPR can be probed by an optical pulse that is injected into the fiber after the pump pulse is injected. The frequency of the probe pulse must be such that it propagates faster than the pump pulse. Physically, when the probe pulse crosses the pump pulse (the temporal slab), a part of the probe pulse changes its frequency such that it speeds up and travels ahead of the pump pulse, while part of the probe changes frequency so that it appears to move more slowly than the pump pulse. Inside this slab, the index change is small, 3×10^{-7} , and can be realized in practice using a short, intense 1-ps pump pulse. To calculate the transmissive properties of time-domain FPR's, we develop a transfer-matrix method similar to that used for analyzing the reflectivity of a spatial structure containing multiple thin films. We show that this method can be used for calculating the transfer matrix of pump pulses of any shape. As a simple example, we first consider a temporal slab formed by using a single pump pulse with sharp leading and trailing edges (rectangular shape pulse) and acting as a simple FPR. We found that such an FPR has several transmission peaks corresponding to resonances similar to spatial FPR's. If the frequency of the probe pulse is at the peak of the first resonance, more than 90% of the pulse energy is transmitted through the slab. Reflective losses (about 7%) occur due to the finite distance it takes for the probe pulse to cross the slab. Indeed, we see two reflected pulses that correspond to reflections at the two interfaces of the slab. If the probe pulse is centered on the first minimum of the temporal FPR, the reflected pulse contains most of the input energy. The bandwidth (or Q factor) and contrast of these peaks, however, decrease rapidly with increasing frequency. In contrast with spatial FPR's, for which mirror reflectivity remains constant over a wide bandwidth, temporal reflection is very sensitive to the frequency of incident light.

We propose an improved design for time-domain FPR's by using two temporally separated pump pulses such that each pump pulse acts as a reflective element of the FPR. We apply our transfer-matrix method to this design for pulses of arbitrary shapes and obtain an expression for the transmissivity of such FPR's that appears identical to the corresponding result for space-domain FPR's. To illustrate the performance of the proposed FPR, we consider a practical configuration: The pump pulses' wavelength is in the anomalous dispersion region of the optical fiber while the probe pulse is in the normal dispersion region. Two pump pulses propagate as two optical solitons and their center is delayed by T_c (Ref. 4). A high-index region forms over the width of each pulse because of a Kerr-induced increase in the refractive index of the fiber's mode. Choosing the pump pulses to have a secant-squared temporal shape with a width of 90 fs (FWHM) and a separation of 1.4 ps with an intensity such that $\Delta n = 3 \times 10^{-7}$, we calculated the transmission characteristics for the two cases of the input spectrum center at the first maximum of the zeroth-order peak, and input spectrum at the first minimum below the zeroth order peak. These results are shown in Fig. 1.

We also show that temporal FPR's formed in the anomalous group-velocity dispersion region of optical fibers by using two short solitons to form multiple sharp transmission peaks with relatively high Q factors. We verified the results of the transfer-matrix method by directly solving the pulse-2 propagation equation with the split-step Fourier method. We showed that a probe pulse can

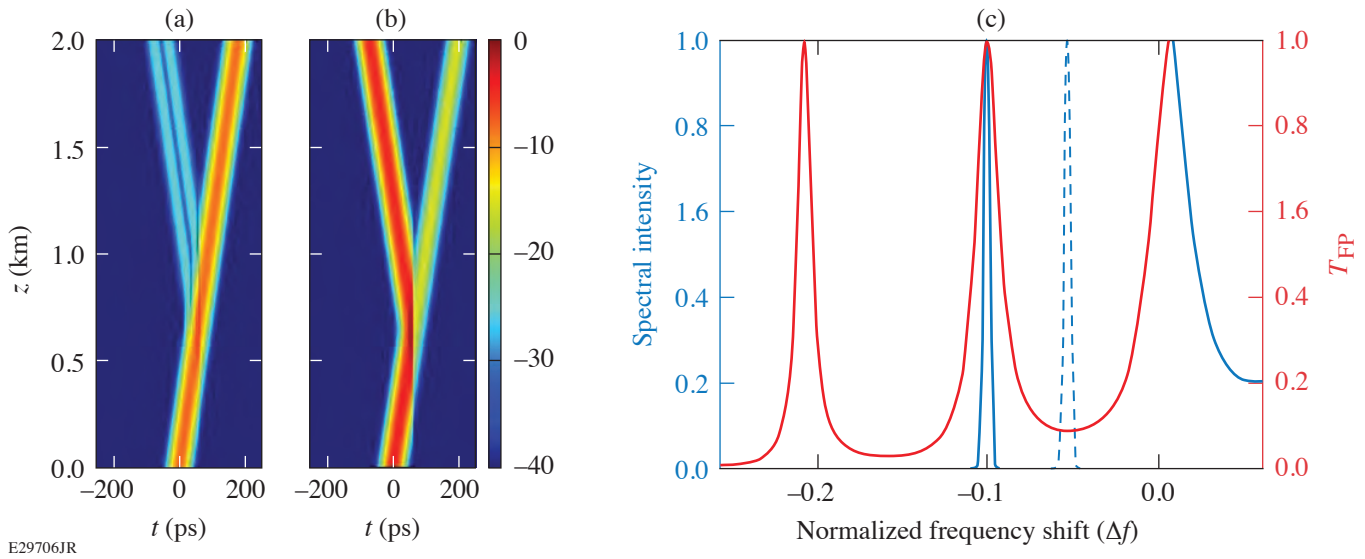


Figure 1

Temporal evolution of a 20-ps Gaussian pulse when its spectrum is centered at (a) a transmission peak and (b) a transmission valley. (c) Location of pulse spectra within the transmission curve (red) of the FPR. The solid blue curve is the incident spectrum in (a) and the dashed line is the incident spectrum in (b); spectral intensity is plotted. Both blue curves plot the spectral intensity.

be fully transmitted through such an FPR when its spectrum overlaps with that of a transmission peak of the FPR. If the spectral bandwidth is larger than the transmission peak width, the temporal FPR acts as an optical filter, analogous to spatial FPR's.

This material is based upon work supported by the National Science Foundation (ECCS-1933328).

1. J. T. Mendonça and P. K. Shukla, *Phys. Scr.* **65**, 160 (2002).
2. B. W. Plansinis, W. R. Donaldson, and G. P. Agrawal, *Phys. Rev. Lett.* **115**, 183901 (2015).
3. J. Zhang, W. R. Donaldson, and G. P. Agrawal, *J. Opt. Soc. Am. B* **38**, 997 (2021).
4. G. P. Agrawal, *Nonlinear Fiber Optics*, 6th ed. (Academic Press, Boston, 2019).

MTW-OPAL: A Technology Development Platform for Ultra-Intense All-OPCPA Systems

J. Bromage, S.-W. Bahk, I. A. Begishev, S. Bucht, C. Dorrer, C. Feng, B. N. Hoffman, C. Jeon, C. Mileham, J. B. Oliver, R. G. Roides, M. J. Shoup III, M. Spilatro, B. Webb, and J. D. Zuegel

Laboratory for Laser Energetics, University of Rochester

Ultra-intense laser systems are being developed by several institutions to use the full potential of deuterated potassium dihydrogen phosphate (DKDP) for high-energy optical parametric chirped-pulse amplification (OPCPA).¹⁻⁴ Noncollinear optical parametric amplifiers (NOPA's) using DKDP can support broadband gain for supporting pulses as short as 10 fs. Large-aperture DKDP crystals (>400 mm) make it possible to use Nd:glass lasers as kilojoule pump sources.⁵ Although OPCPA is now routinely used as a broadband front-end technology for many hybrid systems, scaling OPCPA to energies >100 J is still an active area of laser research and development. This summary reports on the MTW-OPAL Laser System, a mid-scale optical parametric amplifier line pumped by the Multi-Terawatt laser, as a platform for the laser technology development with a long-term goal of building EP-OPAL, a femtosecond-kilojoule system within the Omega Laser Facility.⁶

The MTW-OPAL Laser System is shown schematically in Figs. 1 and 2, and described in more detail in Ref. 7. The ultra-broadband front end produces stretched pulses using white-light continuum generation and a series of three NOPA's using beta

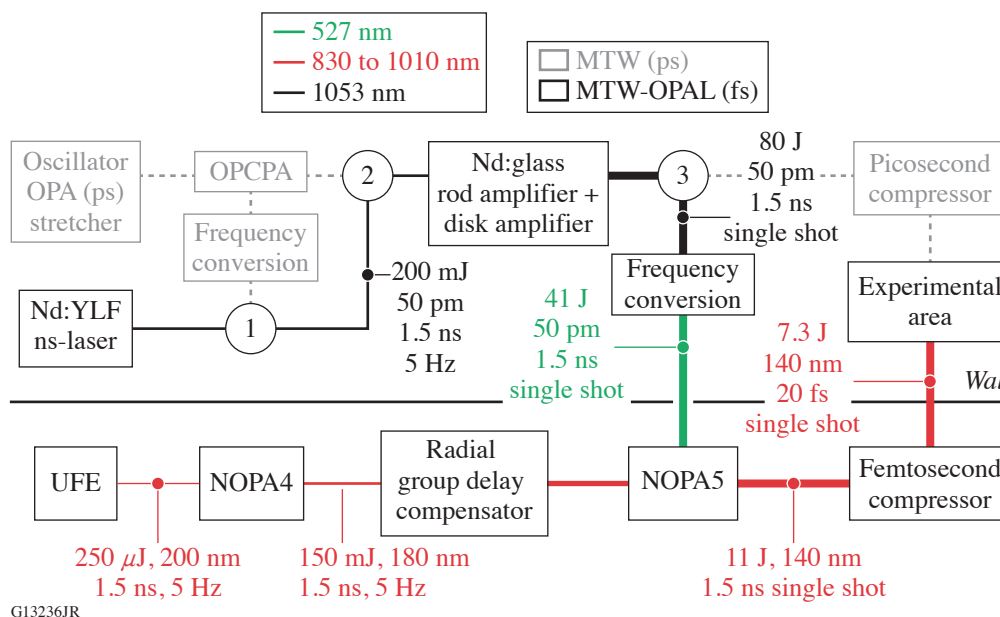


Figure 1
Schematic of the MTW-OPAL Laser System. UFE: ultra-broadband front end.

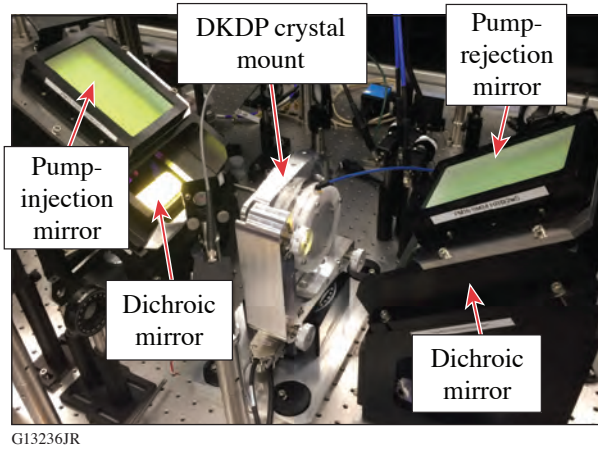


Figure 2
NOPA5 amplifier showing surrounding optics.

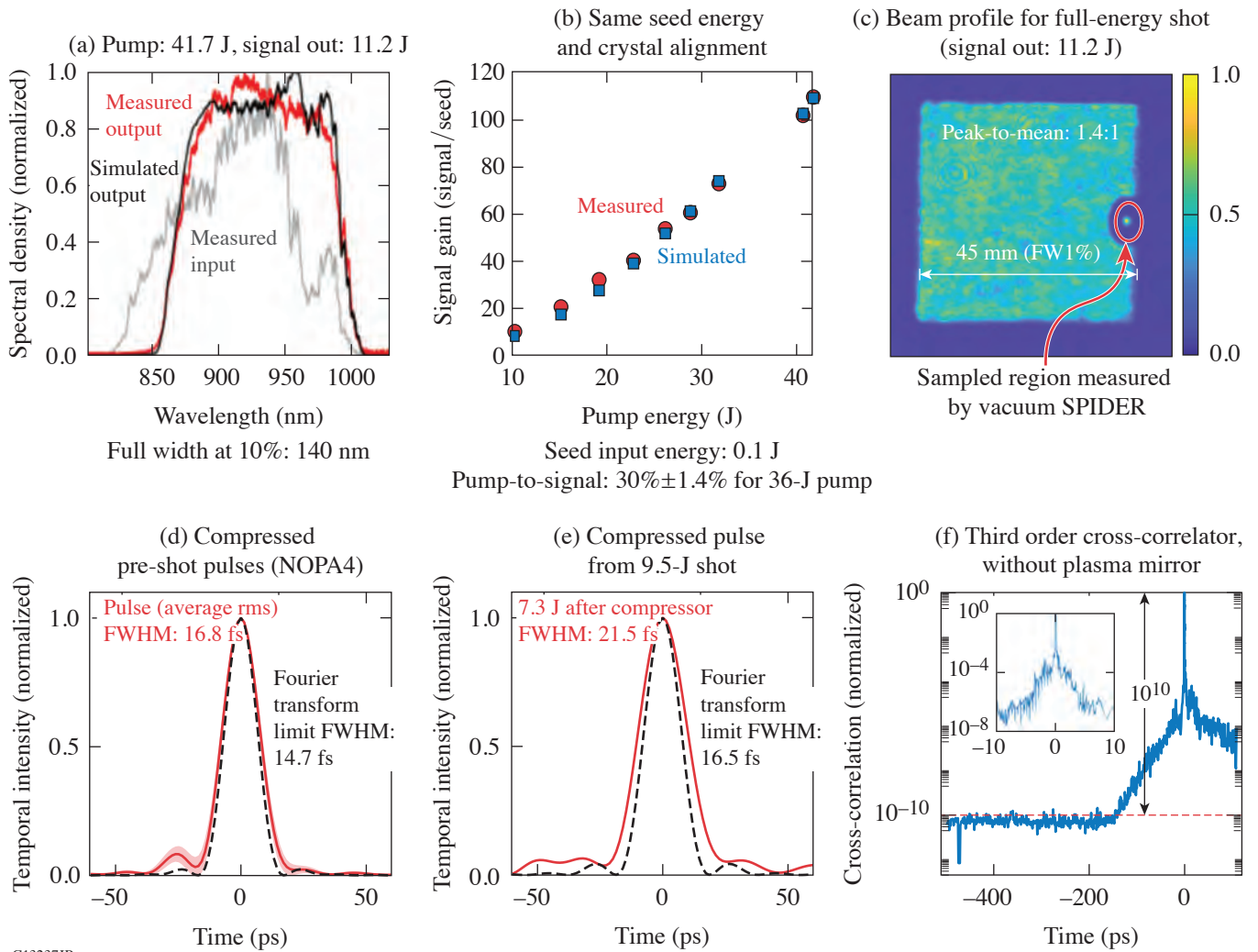
barium borate (BBO) crystals that are pumped with picosecond pulses for maximum temporal contrast. The pulse is stretched to 1.5 ns and matched to the pump pulse for the two NOPA4 stages (also BBO crystals) and the pump for the final NOPA5 stage (DKDP); the NOPA5 pump pulse is produced by the MTW laser configured in a narrowband mode. Radial group-delay compensation is used to minimize temporal broadening from refractive telescopes that image each amplifier stage to the next. A femtosecond compressor with a suite of laser diagnostics is used to compress the pulse to <20 fs before transport in vacuum to the experimental area.

Demonstrating large-aperture OPCA is a primary goal of the MTW-OPAL project. NOPA5 uses $63 \times 63 \times 52\text{-mm}^3$ 70% deuterated DKDP crystals to amplify 45-mm-sq beams with gains of ~ 100 , producing 11-J broadband pulses with up to 40% pump-to-signal transfer efficiency.⁸ Another primary goal is demonstrating a scalable four-grating compressor, transport optics, and diagnostics suitable for EP-OPAL. An all-reflective achromatic telescope has been developed for relay imaging NOPA5 to the final grating. Hybrid coatings (metal and multilayer dielectric) suitable for 200-nm bandwidth are being evaluated for use in the vacuum compressor chamber for both *s*- and *p*-polarized beams.

Figure 3 shows a summary of the primary results from the “First-Light” Campaign in March 2020 along with the subsequent campaigns to ramp the energy through the compressor to achieve 0.35 PW. These campaigns show that the laser design is fundamentally sound, and optimization continues as we prepare for “First Focus” campaigns later this year.

This material is based upon work supported by the Department of Energy National Nuclear Security Administration under Award Number DE-NA0003856, the University of Rochester, and the New York State Energy Research and Development Authority.

1. I. N. Ross *et al.*, *Opt. Commun.* **144**, 125 (1997).
2. V. V. Lozhkarev *et al.*, *Opt. Express* **14**, 446 (2006).
3. C. N. Danson *et al.*, *High Power Laser Sci. Eng.* **7**, e54 (2019).
4. V. V. Lozhkarev *et al.*, *Laser Phys.* **15**, 1319 (2005).
5. J. B. Hu *et al.*, *Appl. Opt.* **60**, 3842 (2021).
6. J. H. Kelly *et al.*, *J. Phys. IV France* **133**, 75 (2006).
7. J. Bromage *et al.*, *High Power Laser Sci. Eng.* **7**, e4 (2019)
8. I. A. Begishev, *et al.*, *Proc. SPIE* **11666**, 1166607 (2021).



G13237JR

Figure 3

(a) NOPA5 spectral measurements for a full-energy shot (input, output, and simulated). (b) Signal gain measured after NOPA5, with a maximum signal energy of 11.2 J. (c) Full-energy NOPA5 output beam. (d) SPIDER measurement statistics (50 shots) and Fourier transform limit for compression without pumping NOPA5. (e) Vacuum SPIDER measurement of spatially sampled beam with the full-energy output from NOPA5. (f) Temporal contrast measurements of compressed NOPA5 seed pulses.

Alignment Tolerance Analysis for Divided-Pulse Nonlinear Compression

G. W. Jenkins,^{1,2} C. Feng,¹ and J. Bromage^{1,2}

¹Laboratory for Laser Energetics, University of Rochester

²Institute of Optics, University of Rochester

Recent work has pushed self-phase modulation (SPM)-based spectral broadening to higher pulse energies and peak powers in both hollow-core fiber (HCF)¹ and multipass cells (MPC's).² While these demonstrations have shown that spectral broadening using gas-based SPM can handle very high pulse energies, they also show that the process is limited by gas ionization. They must therefore employ large-core fibers or large focal spots in the MPC to avoid gas ionization.

This work is focused on a more-scalable method to improve the energy limits of SPM-based pulse compression: divided-pulse nonlinear compression (DPNLC) (illustrated in Fig. 1). In DPNLC, a high-energy pulse is divided into multiple low-energy pulses that are spectrally broadened, recombined back into a high-energy pulse, and then compressed to a short duration.³ The low-energy pulses have peak intensity below the gas ionization intensity threshold. As demonstrated in our previous work, DPNLC has the advantage of preserving the amount of spectral broadening, whereas the large-core fibers and large MPC modes reduce the amount of broadening obtained.⁴

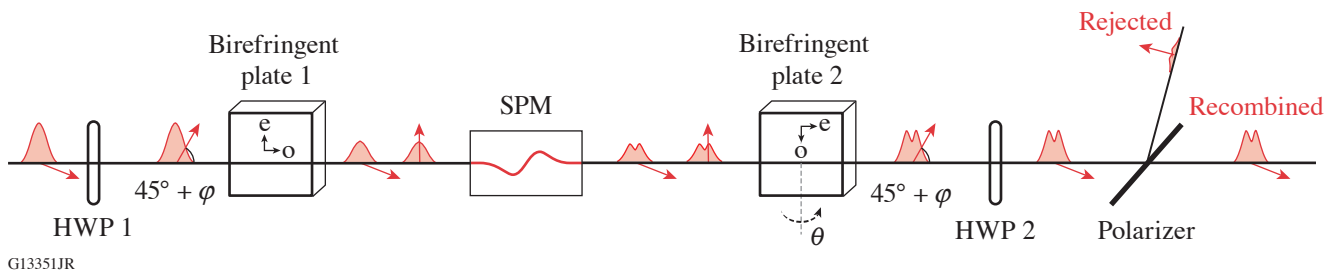


Figure 1

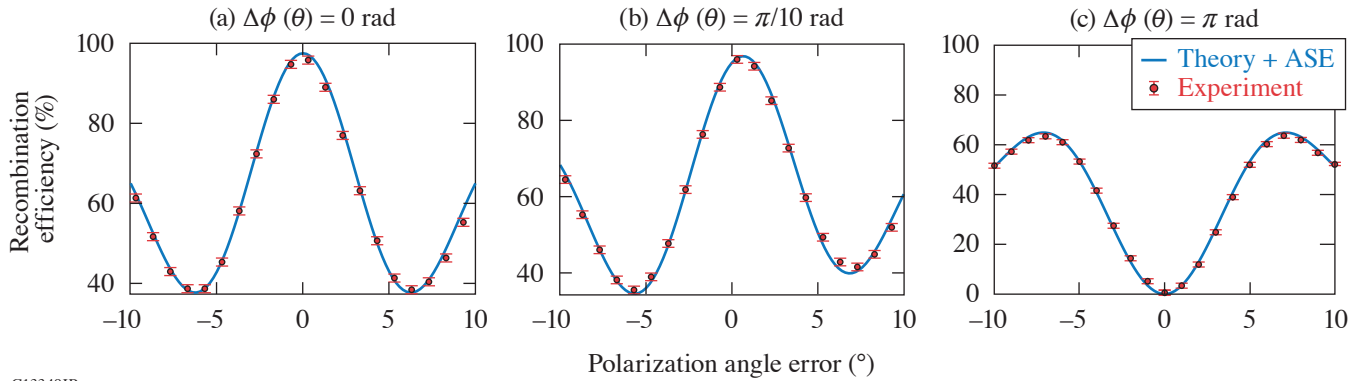
Apparatus for divided-pulse nonlinear compression analyzed in this summary. Birefringent plates with extraordinary axis “e” and ordinary axis “o” are used to divide one pulse into two low-energy, orthogonally polarized pulses. Red arrows indicate the pulse’s polarization, and the distorted pulse shape after the SPM stage indicates an arbitrary reshaping by nonlinear processes in the SPM stage. The angles φ and θ represent angular errors in polarization and crystal AOI, respectively.

The alignment of the birefringent plates must be quite precise to divide and recombine the pulses with high efficiency. Previous authors have analyzed the precise alignment tolerances with computationally expensive numeric solutions of the nonlinear Schrödinger equation.^{5,6} We have developed an analytic model that describes the output pulse from a DPNLC system that we expect to be a faster, more-flexible tool for tolerancing such systems. The most-sensitive alignment errors are errors φ in the incoming pulse polarization angle (equivalent to an error of φ in the birefringent plate axes) and errors θ in birefringent plate 2’s angle of incidence (AOI) [which is modeled as a retardance $\Delta\phi(\theta)$]. We developed an analytic expression for the recombination efficiency of two-pulse DPNLC after accumulating Φ_{NL} nonlinear phase, which is shown in Eq. (1). The infinite sum can be simplified, as in Eq. (2), to quickly prescribe angular tolerances by using the $n = 0$ and the $n = 1$ terms and a small angle approximation for the retardance.

$$\eta = \frac{1}{2} \left\{ 1 + \sin^2(2\varphi) + \cos^2(2\varphi) \cos[\Delta\phi(\theta)] \sum_{n=0}^{\infty} \frac{(-1)^n [2\Phi_{\text{NL}} \sin(2\varphi)]^{2n}}{(2n)! \sqrt{2n+1}} - \cos^2(2\varphi) \sin[\Delta\phi(\theta)] \right. \\ \left. \times \sum_{n=0}^{\infty} \frac{(-1)^n [2\Phi_{\text{NL}} \sin(2\varphi)]^{2n+1}}{(2n+1)! \sqrt{2n+2}} \right\}. \quad (1)$$

$$\eta_{\text{small}} = 1 - \frac{\cos^2(2\varphi)}{2} \left[\frac{2\Phi_{\text{NL}}^2 \sin^2(2\varphi)}{\sqrt{3}} + \frac{2\Phi_{\text{NL}} \Delta\phi(\theta) \sin(2\varphi)}{\sqrt{2}} + \frac{\Delta\phi(\theta)^2}{2} \right]. \quad (2)$$

We have experimentally verified the validity of the model by measuring the recombination efficiency across angular errors with excellent agreement, as shown in Fig. 2. The figure plots the results of recombining our homebuilt 1.2-ps, 10-mJ pulses at a wavelength of 1030 nm after the accumulation of nonlinear phase in an HCF and division and recombination using 12-mm-thick, x -cut calcite plates. We should also note that a correction for amplified spontaneous emission (ASE) and pre-/postpulses is included in the plots in Fig. 2 because the ASE does not acquire significant nonlinear phase in the HCF and therefore has a different recombination efficiency.



G13349JR

Figure 2

Experimental confirmation of angular tolerances model. The recombination efficiency is measured with errors in both the incoming polarization angle and AOI on plate 2 and is found to agree well with Eq. (1).

A useful consequence of the recombination efficiency expression is that the AOI can be used to compensate for polarization errors. The polarization angle tolerance becomes quite tight for large nonlinearity. For the 8.4-rad nonlinearity demonstrated in our lab and prescribing the angular tolerance to maintain >95% recombination efficiency, AOI compensation can loosen our angular tolerance from 1.0° to 2.8° , a tolerance that is easy to meet by hand.

This material is based upon work supported by the Department of Energy National Nuclear Security Administration under Award Number DE-NA0003856, the University of Rochester, and the New York State Energy Research and Development Authority.

1. G. Fan *et al.*, Opt. Lett. **46**, 896 (2021).
2. M. Kaumanns *et al.*, Opt. Lett. **46**, 929 (2021).
3. H. Jacquemin *et al.*, J. Opt. Soc. Am. B **32**, 1901 (2015).
4. G. W. Jenkins, C. Feng, and J. Bromage, Opt. Express **28**, 31,943 (2020).
5. F. Guichard *et al.*, IEEE J. Sel. Top. Quantum Electron. **20**, 619 (2014).
6. M. Kienel *et al.*, Opt. Express **21**, 29,031 (2013).

Eddy Killing from Global Satellite Observations

S. Rai,¹ M. Hecht,² M. Maltrud,² and H. Aluie^{1,3}

¹Department of Mechanical Engineering, University of Rochester

²Los Alamos National Laboratory

³Laboratory for Laser Energetics, University of Rochester

While wind is the primary driver of the oceanic general circulation, we find that it kills the ocean’s most-energetic motions—its mesoscale eddies—at an average rate of 50 GW. We used satellite observations and a recent method to disentangle multiscale processes in spherical systems, including in an inertial confinement fusion implosion.¹ To our knowledge, a length-scale analysis of air–sea energy transfer on the entire globe had not been previously undertaken. In fact, we show that the temporal mean-eddy decomposition (i.e., Reynolds averaging) commonly used in oceanography fails to unravel eddy killing. Our results present the first evidence that eddy killing is a major seasonal sink for the oceanic eddies, peaking in winter. We find that eddy killing removes a substantial fraction (up to 90%) of the wind power input in western boundary currents such as the Gulf Stream and Kuroshio. This process, often overlooked in analyses and models, is a major dissipation pathway for mesoscales—the ocean’s most-energetic scales.

At the surface of the ocean, wind deposits kinetic energy at the rate of $\tau \cdot u_o$, where τ is the wind stress at the surface of the ocean and u_o is the surface ocean velocity.² The power deposited in eddies, smaller than the size of l , is captured by Eq. (1). The overline represents the coarse-graining operation at length-scale l .

$$EP_l^{\text{Cg}} = \overline{\tau \cdot u_o} - \bar{\tau} \cdot \bar{u}_o. \quad (1)$$

Equation (1) is analogous to the frequently used wind power input from Reynolds decomposition³ as given in Eq. (2). The angled brackets represent temporal averaging and the primes represent deviation from temporal averaging.

$$EP^{\text{Rey}} = \langle \tau \cdot u \rangle - \langle \tau \rangle \cdot \langle u_o \rangle = \langle \tau' \cdot u'_o \rangle. \quad (2)$$

Studies using Reynolds decomposition, for example in Ref. 4, find that global power inputs to the eddies as measured from Eq. (2) are positive. Our work shows that eddy killing is an inherently spatial process and requires a spatial scale analysis to unravel it [Eq. (1)]. We find that wind power input is negative for length scales smaller than 260 km, implying eddy killing at those scales [see Fig. 1(b)]. Eddy killing is especially pronounced in Western Boundary Currents (WBC’s) (e.g., the Gulf Stream and Kuroshio) and the Antarctic Circumpolar Current (ACC), while the remainder of the ocean has negligible eddy killing [see Fig. 1(a)]. Figure 1(c) reproduces the temporal analysis of previous studies and highlights the stark contrast with a spatial analysis, where we see a dominance of positive wind power input into the ocean, falsely suggesting a lack of eddy killing. This is contrasted by a dominance of negative values in Fig. 1(a).

This research was funded by U.S. NASA grant 80NSSC18K0772 and a grant from LANL’s Center for Space and Earth Science. H. Aluie was also supported by U.S. Department of Energy grants DE-SC0014318, DE-SC0020229, and DE-SC0019329; NSF grant PHY-2020249; and U.S. Department of Energy National Nuclear Security Administration under Awards DE-NA0003856 and DE-NA0003914. Computing time was provided by NERSC under contract no. DE-AC02-05CH11231 and NASA’s HEC Program through NCCS at Goddard Space Flight Center.

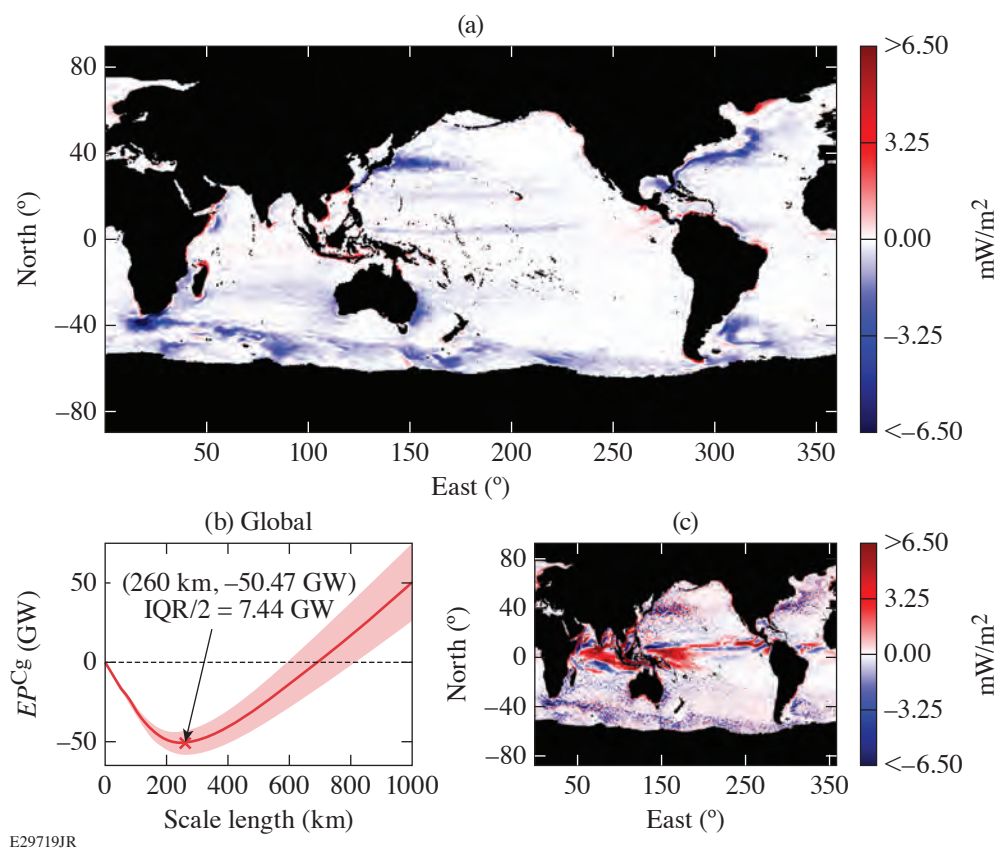


Figure 1

Direct measurement of eddy killing by coarse-graining satellite observations. (a) Wind power input (in mW/m^2) to the flow at scales <260 km using our measure EP^{Cg} in Eq. (1). We are able to clearly detect eddy killing (negative values) throughout the global ocean, especially in WBC's and the ACC. Areas in black include land and ocean regions with seasonal or permanent ice coverage. (b) Performing a scan over an entire range of length scales to unravel scales at which eddy killing operates globally, in addition to its magnitude. This is a key advantage of coarse graining. At any scale l , the plot shows wind power input to all scales smaller than l . By attaining a minimum at $l = 260$ km, it implies that eddies only at scales smaller than 260 km (but not larger) are losing energy to the wind, on average. The envelope shows interquartile range (IQR) (25th to 75th percentiles, Q1 to Q3) of temporal variation about the weekly climatology (as calculated from the seven years of data) of EP^{Cg} , and $IQR/2 = (Q3 \text{ to } Q1)/2$. For reference, $IQR/2 = 95.63$ GW for the global $\tau \cdot u_o$ without any decomposition. (c) Reproducing eddy killing using the traditional Reynolds (or temporal) decomposition, EP^{Rey} , as in prior studies. It shows a stark contrast to our measure EP^{Cg} , with sporadic values of mixed sign without a clear indication of eddy killing. The two decompositions differ starkly in the tropics but agree near some land boundaries, where we expect winds to drive small-scale currents.

1. H. Aluie, GEM-International Journal on Geomathematics **10**, 9 (2019).
2. C. Xu, X. Zhai, and X.-D. Shang, Geophys. Res. Lett. **43**, 12,174 (2016).
3. L. Renault, J. C. McWilliams, and S. Masson, Sci. Rep. **7**, 17747 (2017).
4. C. W. Hughes and C. Wilson, J. Geophys. Res. Oceans **113** (2008).

The 12th Omega Laser Facility Users Group Workshop

J. A. Frenje,¹ S. Ali,² E. Merritt,³ K. Falk,⁴ S. Finnegan,³ M. Gatu Johnson,¹ M. P. Valdivia,⁵ L. Willingale,⁶ and J. P. Knauer⁷

¹Massachusetts Institute of Technology

²Lawrence Livermore National Laboratory

³Los Alamos National Laboratory

⁴Helmholtz-Zentrum Dresden-Rossendorf

⁵Johns Hopkins University

⁶University of Michigan

⁷Laboratory for Laser Energetics, University of Rochester

The 12th Omega Laser Facility Users Group (OLUG) Workshop was held virtually 27–30 April 2021. Over 200 researchers from 40 institutions in the U.S., China, France, Germany, Italy, Japan, Russia, and the UK registered for the meeting. This all-time attendance record for the OLUG Workshop was due to the absence of the on-site space limitations at LLE. The main goal of every OLUG Workshop is to facilitate a continuing dialog among OMEGA users; between the Users and LLE management; and between the Users and the broader scientific community. A major part of OLUG’s responsibility is to also enhance the Omega Facility and its capabilities by defining a set of Findings and Recommendations (F&R’s) each year. In addition, the workshop offers opportunities for students and young researchers to present their research in an interactive, yet informal, setting. This OLUG Workshop program included talks, posters, students and postdoc sessions, and a discussion of F&R’s. In total, OLUG collectively submitted 29 F&R’s to LLE management. The 13th OLUG Workshop will be held at LLE on 27–29 April 2022.

Introduction

The impact of the Omega Laser Facility on the fields of high-energy-density physics and inertial confinement fusion (ICF) is substantial in terms of both breadth and depth. Omega offers tremendous opportunities for programmatic and basic-science research through NNSA’s National Laser User Facility (NLUF) and Laboratory Basic Science (LBS) programs. These programs play central roles in providing researchers with unique opportunities to conduct science in the areas of laboratory astrophysics, hydrodynamics and atomic physics, hydrodynamic instabilities and radiation hydrodynamics, materials physics and behavior of the equation-of-state under extreme conditions, relativistic laser–plasma interactions and magnetized plasmas, advanced/alternative inertial fusion concepts, nuclear physics, atomic physics and spectroscopy, and advanced diagnostics capabilities. Additionally, these programs play an important role in the student and postdoc training. The annual OLUG Workshop brings users together from all over the world, facilitating a vibrant dialog among them about their experiences running experiments through the NLUF and LBS Programs at the Omega Laser Facility. It also facilitates a dialog between users and the LLE management focused on enhancing the Omega Facility and its capabilities, resulting in a set of well-defined F&R’s each year, thus encouraging collaborations that could be undertaken.

The Workshop Program

The OLUG Program included the following invited science talks: “JASRI Experimental Platforms Using High-Power Optical Lasers at X-Ray Free Electron” (Toshinori Yabuuchi), “Overview of 2020 Royal Society Meeting to Update the EU/UK Roadmap for Inertial Fusion Energy” (Peter Norreys), “Findings from the Brightest Light Initiative Workshop” (Roger Falcone), “NNSA Internal 2020 Review of the Different ICF Approaches and Where We Are on the Road to Ignition” (Sean Regan), “Where’s the Fusion? Overcoming Unexpected Challenges and the Road to Solutions for Ignition and Beyond” (Sean Finnegan), “Exploring Stellar Nucleosynthesis and Basic Nuclear Science Using High-Energy-Density Plasmas at OMEGA and the NIF” (Maria Gatu



U2752JR

Figure 1
A photo (computer screen shot) of some of the 2021 OLUG Workshop participants.

Johnson), and “Microphysics of Ultra-Dense Solids Common to Giant Planet Interiors and Macrophysics of Hot Plasmas Typical of Stellar Interiors” (Gilbert Collins). In addition, Ann Satsangi, Kramer Akli, and Slava Lukin presented National Nuclear Security Administration’s, Office of Fusion Energy Sciences’, and the National Science Foundation’s perspectives on the role of the Omega Facility and Users in their programs. Other highlights included the talk “Commissioned MTW-OPAL Laser and Proposed 2×25 PW EP-OPAL Laser” by Jake Bromage (LLE); the facility talk “Omega Facility Update and Progress on OLUG Recommendations” by Sam Morse (LLE); and an update on NLUF/LBS/LaserNetUS activities by Mingsheng Wei (LLE). A student/postdoc panel discussion was led by Suzanne Ali (LLNL). A discussion of OLUG’s Findings and Recommendations with LLE management was led by Liz Merritt (LANL) and Mario Manuel (GA). A roundtable discussion on “Careers in HED Science” was led by Suzanne Ali (LLNL). Student, postdoc, scientist, and facility posters totaling 50 poster presentations were organized in three poster sessions. Out of these posters, 37 of them were presented by graduate students, postdocs, and undergraduate students.

Nominations and Election

An election was held in 2020 but due to the COVID-19 pandemic, there was no election in 2021. A nominating committee was formed in November 2019 to request January nominations for the February 2020 election of four new OLUG Executive Committee (ExCom) members. Johan Frenje (Chair, MIT), Will Fox (PPPL), and Paul Keiter (LANL) formed the election committee. From a four-candidate ballot, Maria-Pia Valdivia (Johns Hopkins University) and Louise Willingale (University of Michigan) were elected as University representatives to replace Mark Koepke (West Virginia University) and Petros Tzeferacos (formerly University of Chicago); Alison Saunders (LLNL) was elected as national lab representative to replace Mario Manuel (GA); and Katerina Falk (HZDR, Dresden Rossendorf, Germany) was elected as the non-U.S. representative to replace Alexis Casner (CEA, France). For the May 2021–April 2022 period, the OLUG ExCom members are (a) four from U.S. university/small business: Johan Frenje (MIT, Chair), Maria-Pia Valdivia (Johns Hopkins, Vice Chair) Maria Gatu Johnson (MIT), and Louise Willingale (University of Michigan); (b) three from national laboratory/major business: Liz Merritt (LANL), Sean Finnegan (LANL), and Alison Saunders (LLNL); (c) one non-U.S. researcher: Katerina Falk (HZDR, Dresden Rossendorf, Germany); (d) one from the Junior Researcher list: Suzanne Ali (LLNL); and (e) LLE, ex-officio: Jim Knauer. The OLUG ExCom thanks Mark Koepke, Petros Tzeferacos, Mario Manuel, and Alexis Casner for their service and excellent work making OLUG such a vibrant community.

Summary of Findings and Recommendations

An important outcome of the annual workshop is the list of F&R's that OLUG submits to the LLE management. The 2021 F&R's are summarized below, categorized as Documentation (#1–#5), Calibration (#6–#9), Diagnostics (#10–#22), Target Capability (#23), Laser Systems (#24–#28), and Codes (#29). An update on the implementation of these F&R's will be presented by the LLE management at the OLUG satellite meeting on 9 November 2021 at the APS–DPP conference in Pittsburgh.

1. Ensure that users have access to detailed and up-to-date documentation on diagnostics.
2. Improve navigation on the diagnostic usage page (add links to the shot days for easier navigation to RID's with diagnostic setups).
3. Make OMEGA EP UV optics transmission measurements readily available to Users.
4. Improve Dante maintenance and documentation.
5. Make calibration data readily available on the PI portal.
6. Characterize gas-jet nozzles.
7. Characterize standard proton source on OMEGA EP.
8. Calibrate CPS1, CPS2, and MagSPEC with a Ra-221 source.
9. Bragg crystal inventory and characterization for streaked x-ray spectrometer.
10. Add a timing fiducial to Dante.
11. Fix SIM streak camera A (SSCA) UV timing fiducial.
12. Add an active shock breakout diagnostic (ASBO)/streak optical pyrometer on OMEGA EP TIM-14.
13. Add an optical Thomson scattering (OTS) diagnostic to OMEGA EP.
14. Provide more streak camera options for time-resolved x-ray spectroscopy.
15. Upgrade detector-finger holders for CPS1 and CPS2.
16. Time-resolved x-ray history measurements in high-neutron-yield environments.
17. Add the capability to infer directional flow vector on D₂-gas-filled or low-DT-yield implosions.
18. Add a third VISAR leg on ASBO on OMEGA EP and/or OMEGA.
19. Add photocathode options for PJX2 and PJX3.
20. Improve accuracy of SSCA data acquisition time.
21. Provide a new sector-magnet electron–positron–proton spectrometer for use in a wide-range of HEDS experiments on OMEGA/OMEGA EP.
22. Implement quick-look for CR-39–based proton radiography.
23. Add planar cryo on OMEGA EP.
24. Increase UV power on OMEGA EP.
25. OMEGA: Any beam, any delay (or at least a third leg).
26. Add opposing OMEGA EP beams.
27. Add smaller distributed phase plates on OMEGA EP.
28. Add smoothing by spectral dispersion on OMEGA EP.
29. Shared VisRad license.

This OLUG Workshop was made possible in part by the Laboratory for Laser Energetics at the University of Rochester for the use and availability of critical resources and support. In addition, OLUG thanks the LLE management for their exceptional responsiveness to our F&R's.

FY21 Q3 Laser Facility Report

J. Puth, M. Labuzeta, D. Canning, and R. T. Janezic

Laboratory for Laser Energetics, University of Rochester

During the third quarter of FY21, the Omega Facility conducted 296 target shots on OMEGA and 225 target shots on OMEGA EP for a total of 521 target shots (see Tables I and II). OMEGA averaged 10.0 target shots per operating day, averaging 87.2% Availability and 94.3% Experimental Effectiveness. OMEGA EP averaged 8.4 target shots per operating day, averaging 94.1% Availability and 92.6% Experimental Effectiveness.

Table I: OMEGA Laser System target shot summary for Q3 FY21.

Program	Laboratory	Planned Number of Target Shots	Actual Number of Target Shots
ICF	LLE	99	83
	LLNL	11	7
ICF Subtotal		110	90
HED	LLE	44	42
	LANL	11	13
	LLNL	38.5	46
	SNL	22	21
HED Subtotal		115.5	122
LBS	LLE	5.5	6
	LLNL	5.5	5
LBS Subtotal		11	11
AIBS		22	24
APL		11	10
CMAF		11	12
NLUF		22	21
Calibration	LLE	0	6
Grand Total		302.5	296

AIBS: Academic and Industrial Basic Science

APL: Applied Physics Labs (Johns Hopkins University)

CMAF: Center for Matter at Atomic Pressures

LBS: Laboratory Basic Science

NLUF: National Laser Users Facility

Table II: OMEGA EP Laser System target shot summary for Q3 FY21.

Program	Laboratory	Planned Number of Target Shots	Actual Number of Target Shots
ICF	LLE	28	24
	LLNL	21	21
ICF Subtotal		49	45
HED	LLE	35	50
	LANL	7	8
	LLNL	21	23
HED Subtotal		63	81
LBS	LLNL	14	14
LBS Subtotal		14	14
AIBS		7	9
CMAP		14	25
LaserNetUS		14	17
NLUF		7	10
Calibration	LLE	0	24
Grand Total		168	225

The OMEGA stage-F alignment sensor package upgrade project was completed on all 60 beams. This project provides higher resolution of alignment and spatial profile information for the alignment beam. With this system now in place, automated alignment algorithms are being developed for improved consistency. Additionally, the stage-C alignment sensor packages were augmented with appropriate filtration to take on shot measurements, improving system characterization.

The OMEGA de-ionized water-cooling system for the amplifiers has been augmented with a degassing system to reduce the oxidization of components and reduce the resulting contamination in the coolant flow. This is anticipated to reduce the amount of maintenance required on the amplifiers and may increase the transmission of flash-lamp light to the amplifier disks.

Computational and Experimental Evidence of Species Separation in CH Shock Release

S. Zhang,¹ D. E. Fratanduono,² M. C. Marshall,¹ J. R. Rygg,¹ A. E. Lazicki,² A. Shvydky,¹ D. Haberberger,¹ V. N. Goncharov,¹ T. R. Boehly,¹ G. W. Collins,¹ and S. X. Hu¹

¹Laboratory for Laser Energetics, University of Rochester

²Lawrence Livermore National Laboratory

Materials shock release, such as that of the CH ablator into the DT fuel or that of DT ice into gas, is involved in different stages of inertial confinement fusion (ICF) and can affect performance but is challenging to quantify both experimentally and theoretically. Typically, the design of ICF experiments relies on single-fluid hydrodynamic simulations. On occasion, however, such simulations omit the microscopic chemistry and physics that play an important role. For example, Thomson-scattering experiments¹ have shown that the fractions of carbon and hydrogen species on the laser-ablation side of a CH₂ foil are different from the initial target composition. Another set of experiments² based on optical interferometry measurements of CH shock release found low-density plasmas at locations far ahead of hydrosimulation predictions. Interestingly, when considering radiation transport and pre-expansion at the rear surface of CH before shock arrival, improved agreements with experiments were reached.² Follow-up studies,³ however, indicate that inconsistency remains between simulation and experiments that used a gold shield to prevent radiation preheat.

Recently, S. Zhang and S. X. Hu employed a large-scale molecular-dynamics (MD) approach to simulate the release of strongly shocked CH polystyrene.⁴ They found species separation and hydrogen streaming ahead of carbon that produce low-density plasmas whose velocities and scale lengths both match experimental observations. This demonstrates MD as a promising approach for simulating nonequilibrium processes, such as shock release, under extreme conditions. One advantage of the MD approach is that any atomic level kinetic effect is explicitly taken into account. In addition, our calculations show that existing reactive force fields for CH can be readily used for high-pressure applications involving CH and produce post-shock equations of state that are similar to the known Hugoniot of CH in a broad range of pressures (deviations are less than 20% for pressures up to 135 Mbar).

We performed extensive MD simulations and designed new laser-driven experiments by considering different shock strengths to further clarify the microscopic shock-release physics of CH. Our experimental design prevents radiation preheat of the sample and employs a thin (~50-nm) Si₃N₄ foil to witness the release of shocked CH across a vacuum gap [Fig. 1(a)]. Interestingly, we observe VISAR (velocity interferometer system for any reflector) reflectivity changes before fringe shifts [Fig. 1(b)] and similarly for all glow-discharge polymer and CH experiments when shocked to above 550 GPa, but not in the experiments of pure diamond or beryllium. These observations are all consistent with our MD-predicted species separation and hydrogen streaming, which are clearly seen upon shock breakout and during the release of CH under strong shocks (350 GPa or higher) but absent for weak shocks (160 GPa or lower) [Figs. 1(c) and 1(d)]. Furthermore, our experiments show that the velocity of the Si₃N₄ foil jumps up earlier in the case of a stronger shock [Fig. 1(f)]. This is also consistent with our MD results, which show that species momentum ramps up (when hydrogen arrives) before jumping up (as carbon arrives) and that this momentum jumping happens at earlier times for stronger shocks [Fig. 1(e)].

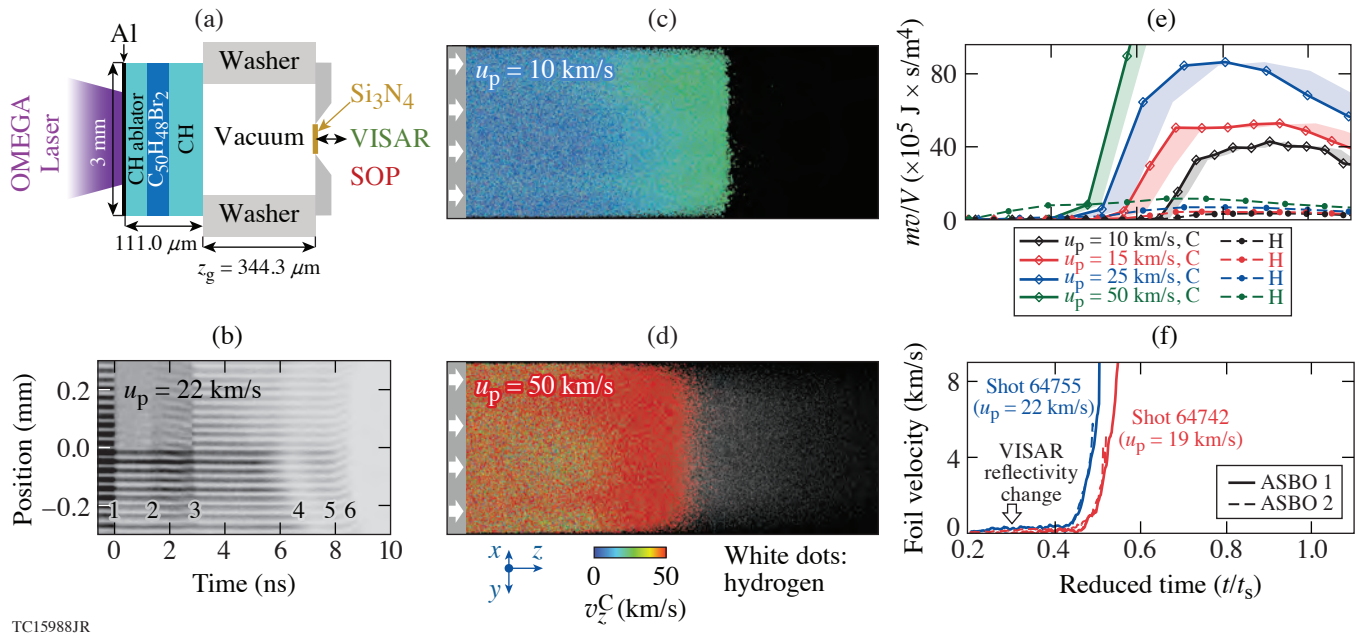


Figure 1

(a) A schematic of the target design and (b) a representative VISAR image of our CH shock-release experiment. An aluminum overcoat and a brominated CH layer are used to prevent radiation preheat of the CH sample. The upper half of the Si₃N₄ foil is coated with titanium. In (b), the numbers “1” to “6” denote the times that the laser turns on, first visibility of the shock front, shock breakout of the CH sample, the reflectivity change of the Si₃N₄ foil, fringe shift indicating motion of the foil, and blackout of fringes, respectively. [(c),(d)] Snapshots of our MD simulations during the release. Carbon atoms are color coded according to their z -component velocities, and hydrogen atoms are shown as white dots. Species separation is clearly observable for strong shocks but absent for weak shocks. (e) Species momentum at the position of a “witness foil” and (f) experimentally measured foil velocities after breakout of shocks with different strength. Time in (e) and (f) is originated from the moment of shock breakout and reduced by the scaling factor $t_s = z_g/u_s$, where z_g is the thickness of the vacuum gap and u_s is the velocity of shock upon breakout. In (e), shaded areas denote the estimated uncertainties in time bounded by the post-shock and first-principles⁵ Hugoniot values of u_s . In (f), the time of VISAR reflectivity change in shot 64755 is indicated with an arrow; u_p is the particle velocity in experiments or piston velocity in simulations. ASBO: active shock breakout.

We also quantified the effect of hydrogen isotopes on CH shock release by comparing the results from CH, CD, and CT calculations. We found lighter hydrogen isotopes stream farther away from carbon, while the spatial velocity profiles of different species are similar. This results in higher momentum and energy (by one to two orders of magnitude) of the lighter species/isotopes at the release front of the heavier species. Such differences in streaming rate of different isotopes could lead to degradation of the final compression in ICF experiments, as well as discrepancies between hydrodynamic predictions and experiments.

To understand the effect of radiation preheat on the shock release, we simulated preheated CH by considering samples with different thicknesses. Our calculations show species velocities increase with both the cell size and the degree of preheat, more so for hydrogen than carbon. We also found that the scale length of the species increases with cell size but is not sensitive to preheat. By extrapolating these results to the experimental sample size with 10% thermal expansion (as predicted by hydrodynamic simulations with radiation transport³), we can expect the velocity and scale length of the carbon species (or electrons if considering average ionization $\langle Z \rangle \sim 1$) to become comparable to those measured in experiments,² which would reconcile the findings from hydrodynamic simulations. Under our established understanding of species separation, however, we must expect that hydrogen runs ahead at much faster velocities and longer scale lengths than carbon. Therefore, we conclude that pre-expansion, if it occurred in the experiment conducted by Haberberger *et al.*,² would be much less than 1 μm. This is in clear contrast to hydro-predictions and can be tested by future experiments.

This material is based upon work supported by the Department of Energy National Nuclear Security Administration under Award Number DE-NA0003856, the University of Rochester, and the New York State Energy Research and Development Authority.

1. J. S. Ross *et al.*, *Rev. Sci. Instrum.* **83**, 10E323 (2012).
2. D. Haberberger *et al.*, *Phys. Rev. Lett.* **123**, 235001 (2019).
3. A. Shvydky *et al.*, *Phys. Plasmas* **28**, 092703 (2021).
4. S. Zhang and S. X. Hu *et al.*, *Phys. Rev. Lett.* **125**, 105001 (2020).
5. S. Zhang *et al.*, *Phys. Rev. E* **96**, 013204 (2017); S. Zhang *et al.*, *J. Chem. Phys.* **148**, 102318 (2018).

Nonuniform Absorption and Scattered Light in Direct-Drive Implosions Driven by Polarization Smoothing

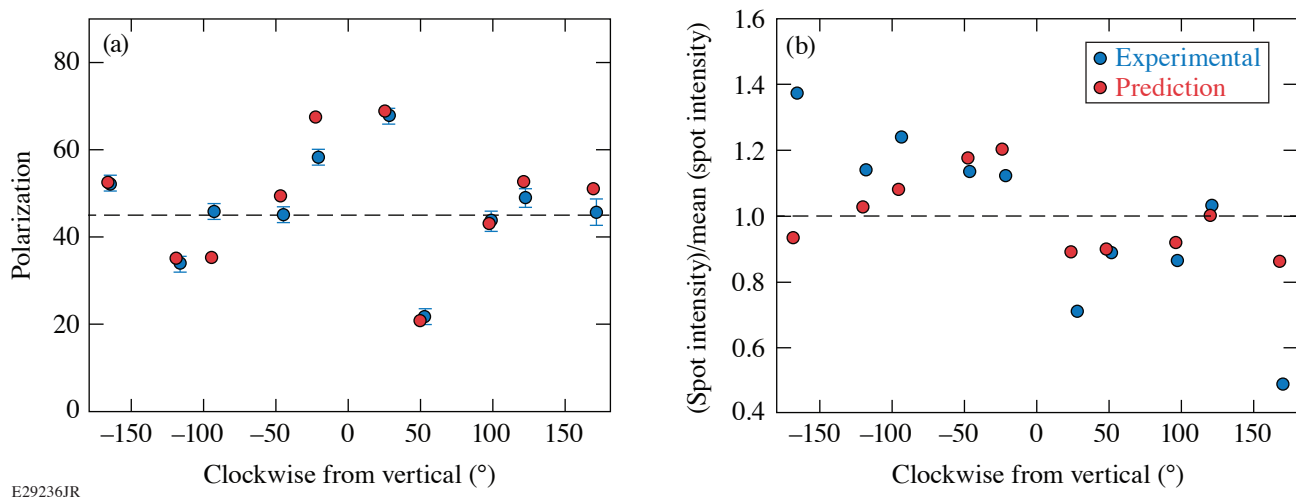
D. H. Edgell, P. B. Radha, J. Katz, A. Shvydky, D. Turnbull, and D. H. Froula

Laboratory for Laser Energetics, University of Rochester

Laser-direct-drive symmetric implosions on OMEGA illuminate a target with 60 laser beams and are designed to produce spherical implosions. Simulations suggest that direct-drive laser irradiation nonuniformity must be below the 1% rms level to minimize low-mode nonuniformities and hydrodynamic instabilities that quench the implosion.¹ Observations of light scattered from OMEGA implosions do not show the expected symmetry and have a much larger variation than standard predictions. For the first time, we have quantified the scattered-light nonuniformity from individual beams and identified cross-beam energy transfer (CBET)² between the polarization components produced by OMEGA's polarization smoothing as the source of the enhanced nonuniformity.

The 3ω gated optical imager (3ω GOI), scattered-light diagnostic^{3,4} was developed to image the light scattered from an implosion. The scattered light appears as a symmetric pattern of 60 distinct spots, each corresponding to a beamlet of light collected from one of the 60 beams. Each beamlet originates from a specific point in the far-field profile of a beam, and as it refracts through the plasma, its intensity varies due to absorption and CBET until it ultimately reaches the diagnostic collection optic. An important feature of the 3ω GOI is a Wollaston prism that splits the collected light into orthogonal horizontal and vertical polarization components that are imaged simultaneously.

In a symmetric implosion, all beamlets collected from beams at the same angular distance from the diagnostic are imaged at the same radial distance from the center of the spot pattern. Figure 1 shows the observed variation (blue circles) in beamlet



E29236JR

Figure 1

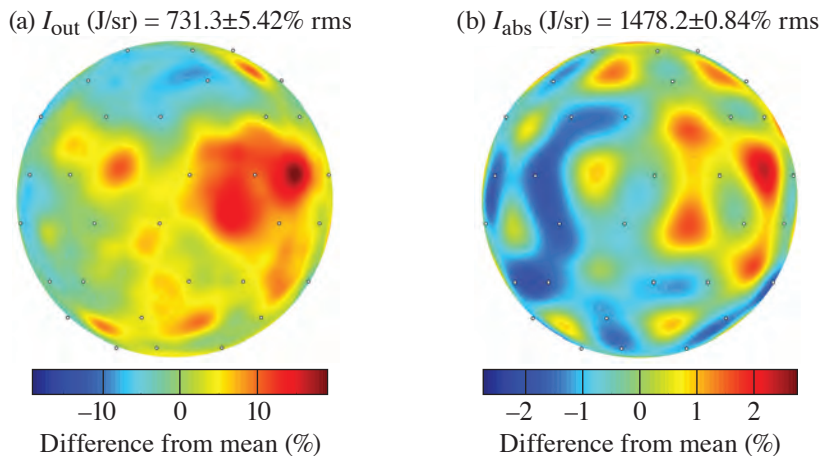
The measured (blue circles) and predicted (red circles) values for the beamlet (a) polarization and (b) intensity as a function of angle from vertical are plotted for a radial beam group.

polarization and total relative intensity for a radial group of beamlets. Truly symmetric laser absorption and CBET should produce constant relative intensity [dashed line in Fig. 1(b)]. Energy exchange due to CBET can rotate the polarization components in the beams,⁵ but in a symmetric implosion, the polarization would be altered identically for each beamlet and the polarizations recorded by the 3ω GOI would show symmetry about the vertical and horizontal axes due to the Wollaston prism orientation. No such symmetry about these axes ($0^\circ/180^\circ$ and $+90^\circ/-90^\circ$, respectively) is observed in Fig. 1(a). Both the observed intensity and polarization of the beamlets indicate that the scattered light from an OMEGA implosion is highly asymmetric.

On OMEGA, each beam is polarization smoothed by passing the laser beams through distributed polarization rotators (DPR's)⁶ that split it into two orthogonal polarizations. The split beams exit the DPR with a minute difference in direction that results in an on-target offset of $90\ \mu\text{m}$. The total on-target overlapped far-field beam profile has two opposite regions in the direction of the offset where the light is mostly linearly polarized. A 3-D CBET model⁷ was developed to follow the evolution of the polarization of each split beam as it propagates through the plasma and interacts with crossing beams. When both the DPR-produced polarizations and offsets were used to predict the beamlet polarizations and intensities (red circles in Fig. 1), the measured variation in both was explained. The high correlation between the measured and predicted polarization of the beamlets in Fig. 1(a) demonstrates the accuracy of the modeling, while the correlation between the measured and predicted intensity of the beamlets provides confirmation that the DPR's are responsible for the observed asymmetry in the scattered light.

Enhanced CBET in the strongly polarized regions created by the DPR split offset is a source of asymmetry during an implosion. To illustrate the magnitude of this effect, the 3-D CBET + DPR model was applied to a typical OMEGA cryogenic target implosion and the total time-integrated nonuniformity was calculated. Figures 2(a) and 2(b) show that the total time-integrated nonuniformity over the entire course of an implosion due to CBET and the DPR-polarization split is predicted to be significant for an otherwise symmetric implosion. Figure 2(a) shows the calculated total scattered light over the inner surface of the target chamber wall. The predicted variation in radial exposure is 5.4% rms with a peak to valley over 30%. This large variation demonstrates the significance of this effect on scattered light. Measurements must account for the effect of the DPR offsets to accurately infer laser absorption during implosions on OMEGA.

A relatively simple solution to the issue of DPR + CBET-induced nonuniformity is to fabricate and deploy new DPR's with a decreased spot separation of $10\ \mu\text{m}$ in the far field, which the model predicts will reduce the scattered-light rms variation by a factor of more than 5 to only 0.92%.



E29548JR

Figure 2

Predicted variation from mean of the (a) scattered light and (b) absorption radiant exposure (J/sr) distributions over a spherical surface for an OMEGA cryogenic implosion using the current DPR's that create a $90\text{-}\mu\text{m}$ offset on target chamber center between the polarization split sub-beams.

This material is based upon work supported by the Department of Energy National Nuclear Security Administration under Award Number DE-NA0003856, the University of Rochester, and the New York State Energy Research and Development Authority.

1. V. N. Goncharov *et al.*, Plasma Phys. Control. Fusion **59**, 014008 (2017).
2. W. L. Kruer *et al.*, Phys. Plasmas **3**, 382 (1996).
3. D. H. Edgell *et al.*, Rev. Sci. Instrum. **89**, 10E101 (2018).
4. D. H. Edgell *et al.*, Rev. Sci. Instrum. **92**, 043525 (2021).
5. P. Michel *et al.*, Phys. Rev. Lett. **113**, 205001 (2014).
6. T. R. Boehly *et al.*, J. Appl. Phys. **85**, 3444 (1999).
7. D. H. Edgell *et al.*, Phys. Plasmas **24**, 062706 (2017).

Feasibility Study of Diagnosing In-Flight Shell Thickness for Laser-Direct-Drive DT Cryogenic Implosions on OMEGA

J. Baltazar,^{1,2} R. C. Shah,¹ S. X. Hu,^{1,2} K. Churnetski,^{1,2} R. Epstein,¹ V. N. Goncharov,^{1,2} I. V. Igumenshchev,¹ T. Joshi,¹ W. Theobald,^{1,2} and S. P. Regan^{1,2}

¹Laboratory for Laser Energetics, University of Rochester

²Department of Mechanical Engineering, University of Rochester

During the deceleration phase of laser-direct-drive inertial confinement fusion experiments, the shell acts as a piston on the fuel, converting its kinetic energy into internal energy of the hot spot and the main fuel. The shell applies a pressure (p_{sh}) on the hot-spot plasma that depends on the in-flight shell thickness (ΔR_i), mass of the shell (M), and velocity of the shell (v), with the relation $p_{\text{sh}} \sim (M/\Delta R_i^3)v^2$ (Ref. 1). The final hot-spot pressure (p_{hs}) scales with the compressive work of the shell, giving $p_{\text{hs}} \sim p_{\text{sh}}^{5/3}$ [Eq. (62) in Ref. 1]. Many factors in the experiment such as single-beam nonuniformity (laser imprint), target surface debris, and ice roughness, among others, can lead to asymmetric implosions, which perform worse than symmetric implosions. Ablation-surface modulations caused by target features and laser nonuniformity imprint can become the seed for the Rayleigh–Taylor (RT) instability, which further evolves surface modulations at the ablation front during the acceleration phase and decompresses the shell (increases ΔR_i^3), leading to a reduction of the final compression of hot-spot plasma. Surface modulations can be reduced by increasing the shell's entropy, characterized by the shell adiabat $\alpha \sim P/P_F$ and set by the initial picket in the laser pulse (where P_F is the Fermi-degenerate pressure), but there is a trade-off² in overall performance. A higher α results in larger ablation velocities and better stability due to increased RT stabilization effects, but with reduced compression achieved in the implosion.²

An adiabat study (Refs. 3 and 4), $\alpha \sim 2$ to 6, of plastic-shell implosions using 2-D *DRACO* simulations without laser imprint showed the trend that as the adiabat decreased the shell thickness decreased. When laser imprint was introduced to the 2-D simulations, a decompression of the shell (increase in the shell thickness) was observed and became more prominent as the adiabat decreased due to the decrease in RT stabilization effects. Self-emission measurements taken on OMEGA matched the decompression of the shell observed in the simulations and thus, it was determined that laser imprint explained the decompression of the shell in plastic-shell implosions. A separate adiabat study of DT cryogenic implosions⁵ with $\alpha \sim 2$ to 5 using 3-D *ASTER* simulations without laser imprint exhibited a similar trend in the shell thickness to plastic-shell implosions as the adiabat decreased. When laser imprint was introduced to the 3-D *ASTER* low-adiabat ($\alpha \sim 2$) and mid-adiabat ($\alpha \sim 3$) implosions, the shell decompression followed a similar trend to the plastic implosion simulations and measurements. However, measurements of the DT cryogenic implosions did not match the mid-adiabat ($\alpha \sim 3$) implosion simulation; they only matched the low-adiabat implosions ($\alpha \sim 2$). Therefore, it was suggested that additional perturbations or 1-D effects not captured accurately in hydro-simulations may be present in experiments.⁵ It is still not clear where the origin of these perturbations occurs; however, some possible sources include the rise of ³He bubbles in the ice layer due to tritium decay, target defects from the cryogenic filing process,⁶ and microscopic defects on the ablator surface that were characterized using atomic force microscopy.⁷ This motivated an investigation to determine if it was feasible to extend the technique to infer the shell thickness from the self-emission^{3,4} of DT cryogenic implosions in order to better understand the effects of laser imprint on shell decompression.

In this work, shell decompression is diagnosed in DT cryogenic implosions from brightness profiles of the coronal plasma and hot-spot emission. Simulations of DT cryogenic implosions are used to study the x-ray signatures for the compressed DT shell. The simulations are post-processed using *Spect3D* to obtain gated images of the x-ray self-emission from the implosion. In experiments,

this is accomplished by recording time-resolved images of x-ray emission from the imploding target using a filtered, 16-pinhole array imager and an x-ray framing camera.⁸ The x-ray images are angularly averaged, and the shell thickness is inferred from the separation between the edge of the hot-spot emission and the emission from the outer peak signal, which corresponds with the location of the ablation front. The radial shape from the measurements is dependent on the material of the compressing shell and hot-spot plasma. Therefore, a different analysis is required when analyzing either plastic or cryogenic implosions.

X-ray self-emission measurements of DT cryogenic implosions on OMEGA are simulated using 1-D (*LILAC*) and 3-D (*ASTER*) hydrodynamic codes to study the effects of laser imprint. Metrics for the shell locations were developed by comparing *LILAC* simulations to angularly averaged self-emission profiles.

A 1-D simulation highlighting how the technique is applied to DT cryogenic measurements is shown in Fig. 1. During the acceleration phase, the outer-shell trajectory is obtained by tracking the outer maximum signal point in synthetic gated x-ray images. This signal is blurred by the instrument response function (IRF) and masked by the signal from the hot spot during the deceleration phase; therefore, the trajectory is extrapolated from the acceleration phase to follow a free-fall line in the deceleration phase, where the hot-spot signal has increased and becomes brighter than the signal at the ablation front. The experimental signature for the inner shell turns on after the onset of hot-spot x-ray emission. From comparing the steep gradients in temperature and density from the *LILAC* simulations with the self-emission brightness profiles, it was determined that the inner-shell trajectory is tracked using the 20% intensity from the edge of the hot-spot signal [$I_{20} = 0.20(I_{\max} - I_{\min}) + I_{\min}$]. The 20% intensity point matched the inner-shell location, determined from the hydrodynamic profiles, for different adiabats and target sizes. Taking the difference between the extrapolated and the inner-shell trajectory provides the measurement of the shell thickness over different times.

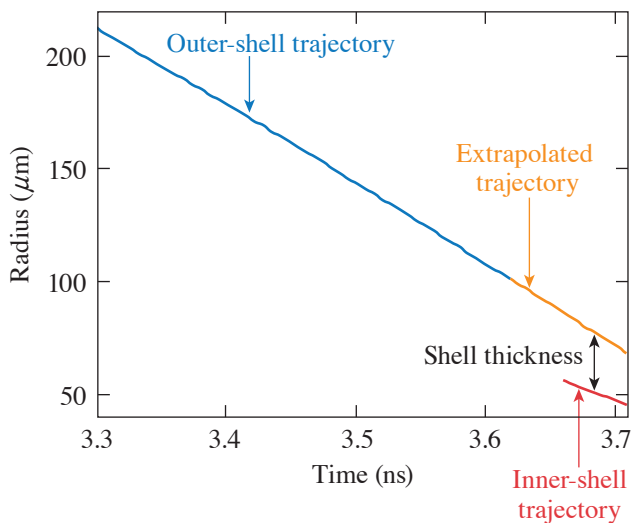


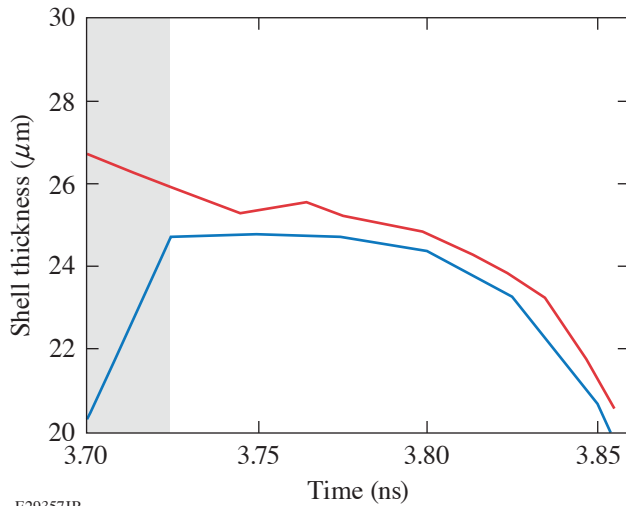
Figure 1

Results from 1-D *LILAC* simulations ($\alpha \sim 2$) and the post-processed (*Spect3D*) measurements show how shell measurements are obtained in the implosion. The outer shell (blue) is tracked using the maximum signal point and is extrapolated to follow a free-fall line (orange) after the laser is turned off. The shell thickness is obtained when the hot spot turns on and the inner-shell (red) trajectory can be tracked.

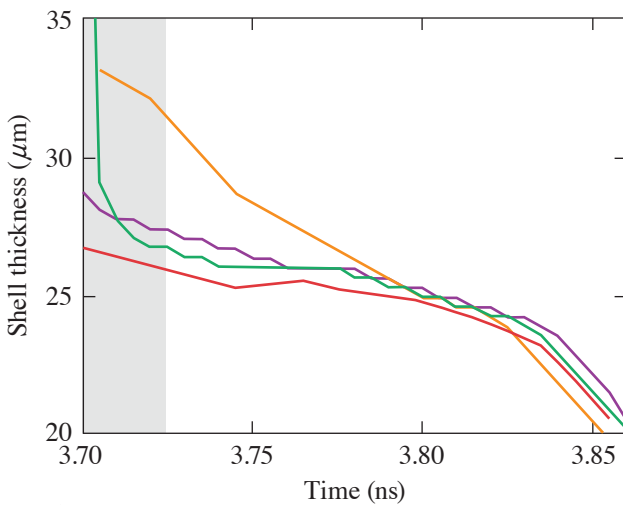
E29359JR

A comparison of the x-ray-inferred thickness, without applying any spatial or temporal blurring, and the hydrodynamic quantity is shown in Fig. 2. The shell thickness in the 1-D simulation is inferred by tracking the largest gradients in the density profile through measuring the distance between the position of the positive gradient for the inner shell and the negative gradient for the outer shell. In Fig. 2, the gray-shaded region shows that the rebounding shock has not yet collided with the high-density shell. In this time range, the hot spot has not been heated by the shock and the hot-spot emission is low compared to the ablation front. After the shock hits the shell, indicated by the white region in Fig. 2, the hot-spot emission becomes prominent and the x-ray-inferred shell thickness measurements are in agreement with the simulations.

The diagnostic requirements to obtain shell measurements within $\sim 3 \mu\text{m}$ are ≤ 10 -ps integration and a point spread function with $\text{FWHM} \leq 5 \mu\text{m}$. The IRF for a pinhole array imager and an x-ray framing camera ($20\text{-}\mu\text{m}$ spatial blurring and 40-ps integration), along with other camera parameters, are applied to the synthetic x-ray measurements in Fig. 3 to determine the diagnostic



E29357JR



E29675JR

Figure 2

The shell thickness obtained from tracking the hydrodynamic gradients (blue) shows a $1\text{-}\mu\text{m}$ correspondence with shell measurements (without IRF, gray region) after the shock reaches the shell (white region). The temporal and spatial finiteness of the simulations are ~ 5 ps and ~ 1 μm , respectively. In the gray region, the rebounding shock has not traversed through the incoming compressing shell; therefore, the emission of the hot spot at this time is low compared to the ablation-front emission.

Figure 3

The x-ray measurement without the IRF is shown by gray shading. Various IRF's were applied to the x-ray measurement to determine the diagnostic requirement: 40-ps integration and 20- μm spatial blurring (orange curve), 10-ps integration and 5- μm spatial blurring (purple curve), and 10-ps integration and 1- μm spatial blurring (green curve). As the spatial and temporal blurring increases the x-ray measurement is affected. The diagnostic requirement (purple curve) followed a similar trajectory to the best-case scenario (without spatial and temporal blurring).

requirements to infer the shell thickness. Applying a temporal blurring of 40 ps showed that the x-ray-inferred shell thickness is increased by ~ 4 μm but follows the same trajectory as the case without any temporal blurring. Therefore, the measurements are not as sensitive to the temporal blurring compared to the spatial blurring of the instrument. The effect from the spatial blurring has a larger effect on the measurements and leads to a reduction in the inferred shell thickness when the spatial blurring increases, as shown in Figs. 4(a) and 4(b). Application of this technique with the current resolution does not give an accurate measurement of the shell thickness; however, this technique can be used to analyze trends in the shell thickness.

Using the current camera parameters (i.e., a spatial resolution of 20 μm and a temporal resolution of 40 ps) on OMEGA,⁹ it was determined that the trend in the shell thickness should be analyzed as opposed to the shell thickness alone. An adiabat study was conducted to demonstrate the effectiveness of the analysis technique on 3-D *ASTER* simulations, with and without laser imprint. A range of shell thickness measurements for implosions of $\alpha \sim 1.7$ to 2.8 is shown in Fig. 5. The low-adiabat ($\alpha = 1.7$) implosion with laser imprint shows a clear increase in the trend when compared with the uniform case, while the high-adiabat ($\alpha = 2.8$) implosion shows only a slight increase in comparison, which is expected due to the higher stability. Additionally, the laser-imprint case of the low-adiabat implosion exhibited an advancement of the hot-spot emission, while the high-adiabat case showed no major discrepancy in the onset of the hot-spot emission. The criteria for the onset of hot-spot emission are defined by the time when the hot-spot signal is $\sim 50\%$ of the peak signal. The early hot-spot emission agrees with a previous analysis of the same campaign⁵ and is consistent with what was observed in low-adiabat plastic-shell implosions,^{3,4} where the advancement of

the onset of hot-spot emission is caused by the laser-imprint-induced RT instability that causes spikes at the ablation front and bubbles to break through the shell, which drives the inner shell farther toward the center during the acceleration phase. This technique will be applied to experimental data⁵ and used to further our understanding of laser imprint on DT cryogenic implosions.

This material is based upon work supported by the Department of Energy National Nuclear Security Administration under Award Number DE-NA0003856, the University of Rochester, and the New York State Energy Research and Development Authority.

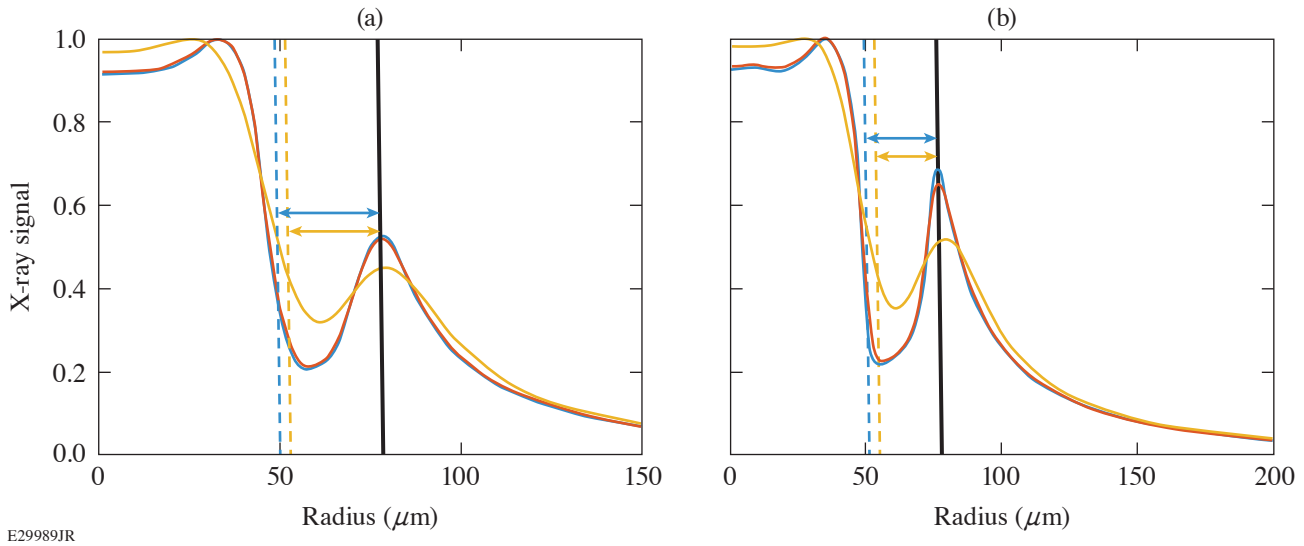


Figure 4
 (a) Simulated x-ray brightness profiles obtained in the deceleration phase of a DT cryogenic implosion are shown with an IRF that includes a temporal blurring of 40 ps and a spatial blurring of 1 μm (blue), 5 μm (red), and 20 μm (yellow). The location of the hot-spot boundary was in the same vicinity for the 1- μm and 5- μm cases. Therefore, the location for the hot-spot boundary is shown as dashed lines for the 5- μm (red), and 20- μm (blue) case. (b) Simulated x-ray brightness profiles obtained in the deceleration phase of a DT cryogenic implosion are shown with an IRF that includes a temporal blurring of 10 ps and a spatial blurring of 1 μm (blue), 5 μm (red), and 20 μm (yellow). Increasing the spatial blurring will decrease the inferred shell thickness due to the widening of the diagnosed image of the emission signal profile caused by instrumental effects. Furthermore, the spatial blurring's effect on the measurement is dominant when compared to the effects from the temporal blurring.

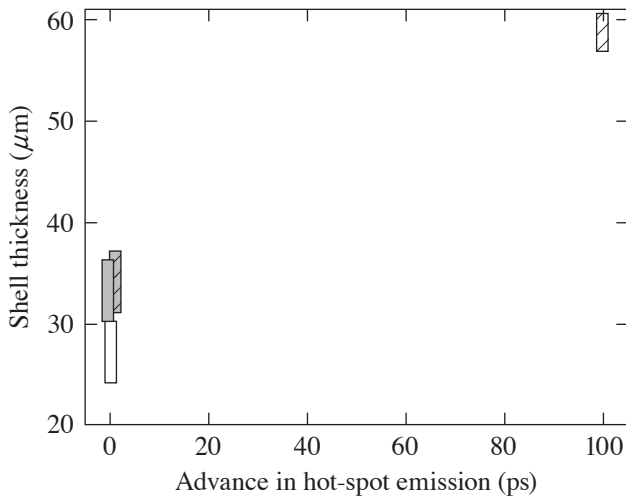


Figure 5
 The calculated shell thickness from 3-D *ASTER* x-ray simulations with the IRF of 40-ps temporal resolution and 20- μm spatial resolution for two implosions without (solid color) and with (striped) the effects of laser imprint included: $\alpha = 1.7$ (white box/striped white box) and $\alpha = 2.8$ (gray box/striped gray box). The low-adiabat implosion with laser imprint shows an overall increase in the shell-thickness trend and an advancement in time of the hot-spot emission.³⁻⁵ Both of these characteristics agree with what was observed in plastic-shell implosions. The high-adiabat implosion is less sensitive to the laser-imprint effects and exhibits only a slight increase in the shell thickness and a negligible advancement in time of the hot-spot emission.

1. V. N. Goncharov *et al.*, Phys. Plasmas **21**, 056315 (2014).
2. R. S. Craxton *et al.*, Phys. Plasmas **22**, 110501 (2015).
3. S. X. Hu *et al.*, Phys. Plasmas **23**, 102701 (2016).
4. D. T. Michel *et al.*, Phys. Rev. E **95**, 051202(R) (2017).
5. R. C. Shah *et al.*, Phys. Rev. E **103**, 023201 (2021).
6. I. V. Igumenshchev *et al.*, Phys. Plasmas **20**, 082703 (2013).
7. S. P. Regan *et al.*, Nucl. Fusion **59**, 032007 (2019).
8. D. K. Bradley *et al.*, Rev. Sci. Instrum. **63**, 4813 (1992).
9. A. K. Davis, "Laser Ablation and Hydro-Efficiency of Capsules Imploded in a Direct-Drive Inertial-Confinement-Fusion Configuration," Ph.D. thesis, University of Rochester, 2017.

Shock-Ignition Laser-Plasma Interactions in Ignition-Scale Plasmas

R. H. H. Scott,¹ K. Glize,¹ L. Antonelli,² M. Khan,² W. Theobald,³ M. S. Wei,³ R. Betti,³ C. Stoeckl,³ A. G. Seaton,⁴ T. D. Arber,⁵ D. Barlow,⁵ T. Goffrey,⁵ K. Bennett,⁵ W. Garbett,⁶ S. Atzeni,⁷ A. Casner,⁸ D. Batani,⁸ C. Li,⁹ and N. Woolsey²

¹Central Laser Facility, STFC Rutherford Appleton Laboratory, UK

²York Plasma Institute, Department of Physics, University of York, UK

³Laboratory for Laser Energetics, University of Rochester

⁴Los Alamos National Laboratory

⁵University of Warwick, UK

⁶Atomic Weapons Establishment, UK

⁷Dipartimento SBAI, Università di Roma “La Sapienza,” Italy

⁸CELIA, University of Bordeaux, France

⁹Massachusetts Institute of Technology

The 30-kJ OMEGA—a sub-ignition-scale laser—and a novel shallow-cone target are currently being used to study laser-plasma interactions at ablation-plasma density scale lengths and laser intensities anticipated for direct-drive shock-ignition implosions at National Ignition Facility scale. Our results show that, under these conditions, the dominant instability is convective stimulated Raman scattering (SRS) with experimental evidence of two-plasmon decay (TPD) only when the density scale length is reduced. Particle-in-cell (PIC) simulations indicate that this is due to TPD being shifted to lower densities, removing the experimental backscatter signature, and reducing the hot-electron temperature. The experimental laser-energy coupling to hot electrons was found to be 1% to 2.5%, with electron temperatures between 35 and 45 keV. Radiation-hydrodynamic simulations employing these hot-electron characteristics indicate that they should not preheat the fuel in MJ-scale shock-ignition experiments.

This work describes the first laser-plasma interaction experiment performed at ignition scale and at laser intensities of relevance to shock ignition. A novel target design was created in order to reproduce the anticipated ablation-plasma conditions for an ignition-scale laser-direct-drive implosion using a sub-ignition facility. Planar targets have an infinite radius of curvature and, therefore, the potential for long density scale lengths. Twenty of OMEGA’s 60 beams can be coupled onto a planar target and arranged as cones with incidence angles of 23°, 48°, and 62°. Ten of these 20 beams (5 kJ) are used to create a long-density-scale-length ablation plasma, with the remaining ten beams (5 kJ) driving a “shock-ignition” pulse into this preformed ablation plasma. The 62° cone of beams has a high angle of incidence (θ) on target, resulting in beam reflection at low density ($n_{\text{refl}} = n_c \cos^2 \theta$, where n_{refl} is the electron density where reflection occurs), which, in turn, results in inefficient laser absorption. Simulations indicate that the absorption is as low as 60%, reducing the ablation rate and forming short density scale lengths of $\sim 200 \mu\text{m}$.

Laser-target coupling is improved using a novel flat-tipped, shallow-cone target and repointing the low-intensity laser beams beyond the cone axis of symmetry. The conical target has the effect of reducing the beams’ effective angle of incidence, θ , significantly improving the predicted absorption to 90%. A schematic of the target and example beam position is shown in Fig. 1(a). Furthermore, the conical geometry acts to reduce the divergence of the ablation-plasma flow, further increasing the density scale length. Moreover, maintaining an open-cone geometry avoids on-axis plasma flow convergence and jet formation. Simulations used the 2-D, cylindrically symmetric Lagrangian radiation-hydrodynamic code *H2D*, with 3-D laser ray tracing, *SESAME* equations of state, multigroup diffusive radiation transport, and flux-limited thermal conductivity. The calculated density scale

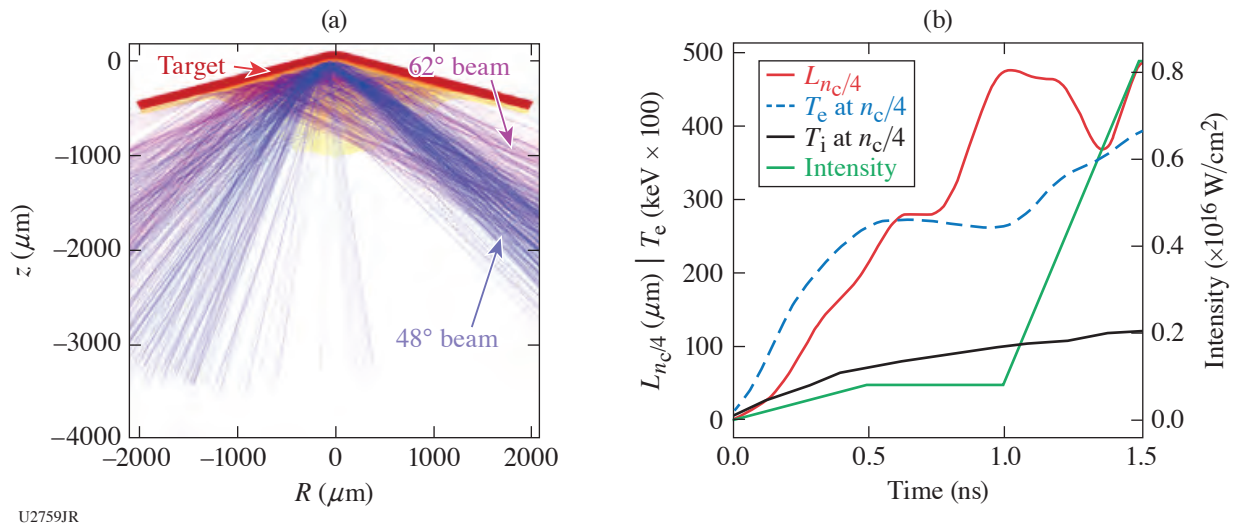


Figure 1

(a) The open-cone target design employed to generate large ablation-plasma scale lengths, shown just before the high-intensity beams switch on at 1 ns. Only two low-intensity beams are shown for clarity. (b) Simulated density scale length, electron temperature, and intensity at $n_c/4$ as a function of time using the open-cone target.

length $L_{n_c/4}$ and electron temperature T_e at the quarter-critical surface, shown in Fig. 1(b), predict ignition-scale density scale lengths of $450 \mu\text{m}$ and $T_e = 3 \text{ keV}$ at 1 ns (the time at which the high-intensity interaction commences).

The target (Fig. 1) is comprised of a 3.6-mm-diam cone with 152° opening angle and a $100\text{-}\mu\text{m}$ -diam flat tip. The laser was incident on a $40\text{-}\mu\text{m}$ -thick CH plastic ablator, backed with a $5\text{-}\mu\text{m}$ Cu diagnostic layer, followed by $30 \mu\text{m}$ of CH to tamp target expansion and prevent electron refluxing. By varying the power in the high-intensity beams on a given shot, a range of peak intensities, corrected for inverse bremsstrahlung absorption, from 8×10^{14} to $8.3 \times 10^{15} \text{ W/cm}^2$ was incident on the $n_c/4$ surface, which simulations indicate was located $\sim 200 \mu\text{m}$ from the target's front surface. The nominal delay between low- and high-intensity beams was 1 ns. A total of 12 target shots were performed.

Laser light backscattered into two of the high-intensity beams on the 23° beam cone was temporally and spectrally resolved using the full-aperture backscatter (FABS) diagnostic. Backscattered light not entering the beam port was imaged using the near backscatter imager and filtered to distinguish stimulated Brillouin scattering ($\sim 351 \text{ nm}$) and SRS and/or TPD (400 to 700 nm) components. Hot-electron production was diagnosed from Cu K-shell line emission using an absolutely calibrated zinc von Hamos (ZVH) spectrometer across the spectral region of 8 to 9 keV and a spherically bent quartz crystal imager (SCI) aligned to the Cu K_α spectral line at 8047.8 eV. The SCI has a narrow spectral window of 8047 to 8054 eV and records data onto an image plate (IP). The hot-electron temperature was inferred from bremsstrahlung emission using a nine-channel, differentially filtered, IP-based, time-integrated hard x-ray image plate (HXIP) over the range of 10 to 200 keV.

Figure 2(a) is an example of the backscattered light spectra with an $\sim 450\text{-}\mu\text{m}$ density scale length. The early-time ($< 1\text{-ns}$) backscatter signal is attributed to TPD: the narrowband spectral features above and below 702 nm have previously been shown to be indicative of TPD. As the high-intensity beams ramp up after 1 ns, a broad, bright spectral feature is seen across the 475- to 600-nm range. This broad feature is consistent with backscattered light caused by convective SRS: the backscattered light originates from densities in the range of 0.04 to $0.16 n_c$ —well below the ~ 0.22 to $0.25 n_c$ range where TPD is able to occur.¹ The dashed white line indicates the normalized SRS threshold (I_{thSRS}) assuming a linear density profile. This was found to consistently predict the onset of convective SRS. SRS reflectivity measured in one high-intensity beam port (B25) as a function of single-beam intensity is shown in Fig. 3(b). During the high-intensity part of the drive, no clear evidence of TPD nor absolute SRS was observed. The sharp cutoff in the signal below $\sim 480 \text{ nm}$ is not unexpected because the lower densities reduce convective SRS gain and enhance Landau damping; however, it may also be a signature of SRS rescatter.

Bremsstrahlung radiation emission produced via collisions of hot electrons within the target make it possible to estimate the hot-electron temperature. Measurements from the time-integrated HXIP instrument are interpreted using a Geant4-derived instrument response function² and χ^2 minimization techniques. Any low-energy x rays from the ablation plasma and/or Cu K-shell emission were removed by excluding the two lower-energy HXIP channels. The inferred hot-electron temperatures are in the range ~35 to 45 keV, as shown by the red \times 's in Fig. 3(a).

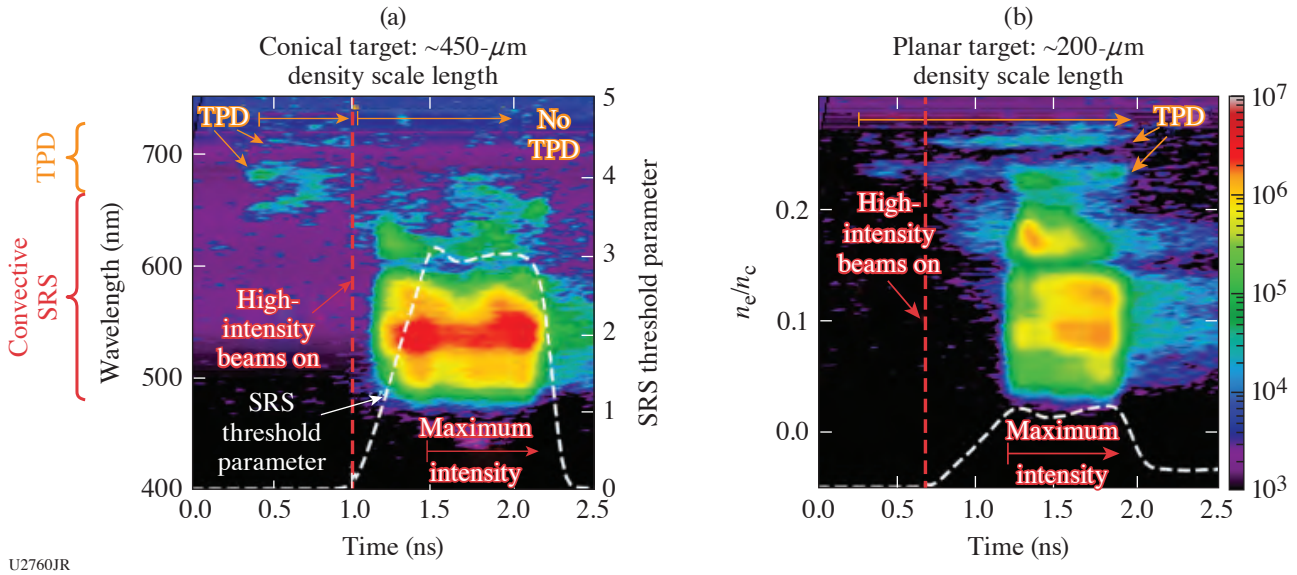


Figure 2 FABS streaked backscatter spectra: (a) Typical long-density-scale-length data: TPD is visible at early time, while during the high-intensity pulse convective SRS dominates. (b) Reduced density scale length with a planar target: TPD is visible throughout. In both cases, the low-intensity beams ramp up from 0 to 0.5 ns, while the maximum intensity is 8.5×10^{15} W/cm². The y axes and color scale apply to both plots with densities assuming a temperature of 3 keV. Dashed white lines indicate the SRS threshold parameter (>1 is above threshold), dashed red lines indicate the point at which the high-intensity beams turn on. In the small density scale-length case (where SRS is just above threshold), TPD is visible throughout. This is not the case in the long scale length when SRS is well above threshold. The FABS data were highly reproducible.

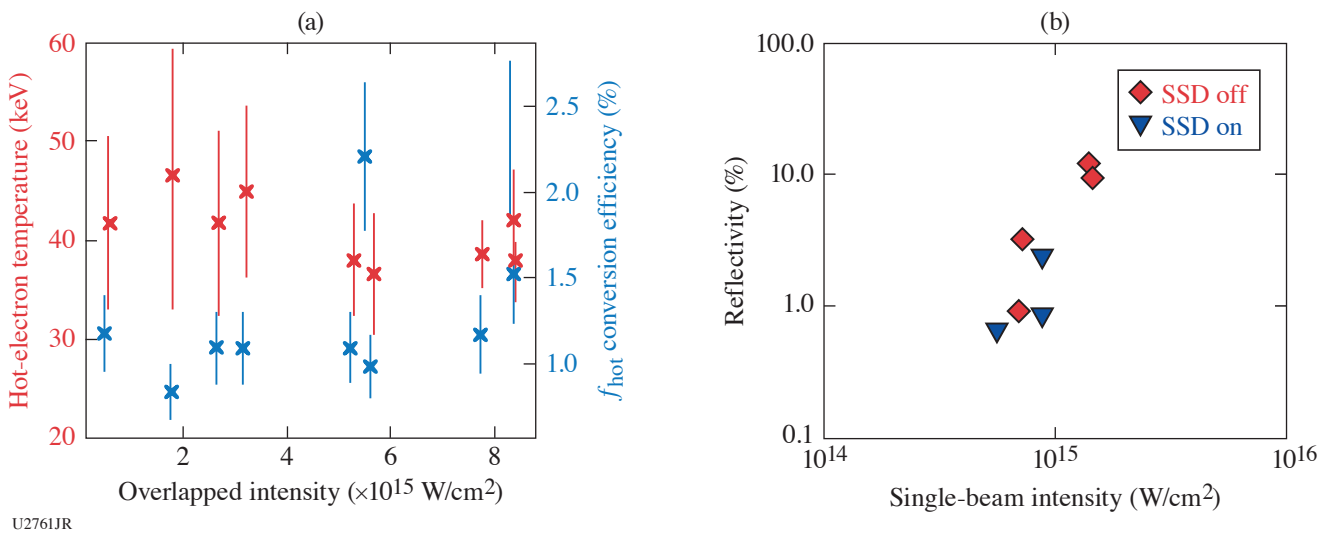


Figure 3 (a) Hot-electron temperature and total laser energy conversion to hot electrons as a function of intensity. (b) SRS reflectivity from (high-intensity) Beam 25.

The fraction of total laser energy converted to hot electrons was inferred from the K_{α} yield, as measured using the ZVH diagnostic. The number of K_{α} photons was extracted from background-subtracted ZVH data and then converted into hot-electron energy using Geant4 Monte Carlo simulations that use the cold target geometry and a 40-keV Maxwellian hot-electron population. A conversion efficiency between 1% and 2.5% [blue \times 's in Fig. 3(a)] is inferred, with some suggestion of an intensity dependence. Modeling indicates that laser-ablation-induced x-ray emission did not contribute to the signal. These data are consistent with SCI K_{α} images.

A comparison measurement at shorter density scale lengths is possible by reducing the delay of the high-intensity beams with respect to the low-intensity beams to 0.7 ns. This limits the plasma expansion duration, reducing the quarter-critical density scale length to $\sim 300 \mu\text{m}$ [see Fig. 1(b)]. An alternative to laser retiming is to switch to a planar target, which further reduces the density scale length to $\sim 200 \mu\text{m}$. Radiation-hydrodynamic simulations predict a reduction in the electron temperature to 2.5 and 2 keV, respectively, for these two cases. At the shortest density scale length [see Fig. 2(b)], TPD is visible throughout the interaction during the low- and high-intensity parts of the laser pulse. Moreover, SRS is just above threshold during the high-intensity interaction. This contrasts with the long-scale-length case, where TPD is not observed and the high-intensity interaction significantly exceeds the SRS threshold. This suggests a transition from a small-scale-length, TPD-dominated regime to a long-scale-length regime, which appears to be dominated by convective SRS.

To investigate the relative roles of TPD and convective SRS in these experiments, 2-D plane-wave PIC simulations were performed with the code *EPOCH*³ in a density scale length, electron (ion) temperature, and intensity regime of direct relevance to this experiment: 0.1 to 0.26 n_c , 600 μm , 4.5 (2.25) keV, and $2 \times 10^{15} \text{ W/cm}^2$, respectively. These simulations show qualitative agreement with the experiments. Detailed examination of the simulations reveals that the electron plasma waves (EPW's) in the region from 0.20 to 0.24 n_c are principally caused by TPD, which explains the lack of reflected light emitted from this region and provides a compelling explanation for the ‘‘Raman gap.’’ The occurrence of TPD at these densities is attributed to convective TPD. The low (32-keV) hot-electron temperature in the simulations—in approximate agreement with experiments—is ascribed to the fact that EPW phase velocities increase rapidly as n_c approaches $n_c/4$. As the EPW wave spectrum, which is comprised of TPD EPW's and low-density SRS EPW's, is shifted below $n_c/4$, EPW phase velocities are limited; consequently, the hot-electron temperature is reduced. At the simulated intensity, convective SRS is just above threshold; therefore, at higher intensities it would be expected that pump depletion, due to convective SRS at lower densities, would play an increasing role in governing the competition between TPD and SRS.⁴ Nevertheless, we have shown that a significant factor in the dynamics observed experimentally and via simulation is likely explained by the shifting of TPD to lower densities. This shift removes the experimental $\omega_0 = 2$ ‘‘doublet’’ diagnostic feature, prevents convective SRS backscatter from ~ 0.20 to 0.24 n_c , and reduces the hot-electron temperature.

To assess the impact that the hot electrons observed in these experiments have on an implosion, we performed 2-D arbitrary Lagrangian–Eulerian radiation-hydrodynamic simulations of a 500-kJ shock-ignition implosion using the code *ODIN*. During the laser ray trace, energy is extracted from the laser (2.5%) and hot electrons are launched from the $n_c/4$ surface with a 40-keV temperature in a 45° cone. A Monte Carlo approach (benchmarked against MCNP) was used for hot-electron transport, scattering, and energy deposition. Using these experimentally measured hot-electron characteristics, the generated pressure is unaffected by the hot electrons with very little degradation in the density profile—an encouraging result for future MJ-scale shock-ignition experiments.

In summary, using a novel target design fielded on the 30-kJ OMEGA Laser System, we have found that for ablation-plasma conditions of relevance to shock ignition, the hot-electron temperature remains relatively low at 35 to 45 keV, with up to $\sim 2.5\%$ of the laser energy converted to hot electrons. Hydrodynamic simulations indicate the low observed hot-electron number and temperature are compatible with shock ignition at MJ scales.

This work was funded by EPSRC Grant Nos. EP/P023460/1, EP/P026486/1, and EP/P026486/1. This work has been carried out within the framework of the EUROfusion Consortium and has received funding from the EuroFUSION research and training programme under Grant Agreement Number 633053. The views and opinions expressed herein do not necessarily reflect those of the European Commission. The involved teams have operated within the framework of the Enabling Research Project: ENR-IFE19.CEA-01 Study of Direct Drive and Shock Ignition for IFE: Theory, Simulations, Experiments, Diagnostics Development.

1. W. Seka *et al.*, Phys. Plasmas **16**, 052701 (2009).
2. M. Stoeckl and A. A. Solodov, Nucl. Instrum. Methods Phys. Res. A **931**, 162 (2019).
3. T. D. Arber *et al.*, Plasma Phys. Controlled Fusion **57**, 113001 (2015).
4. C. Z. Xiao *et al.*, Nucl. Fusion **60**, 016022 (2019).

Hot-Electron Preheat and Mitigation in Polar-Direct-Drive Experiments at the National Ignition Facility

A. A. Solodov,¹ M. J. Rosenberg,¹ M. Stoeckl,¹ A. R. Christopherson,² R. Betti,¹ P. B. Radha,¹ C. Stoeckl,¹ M. Hohenberger,² B. Bachmann,² R. Epstein,¹ R. K. Follett,¹ W. Seka,¹ J. F. Myatt,³ P. Michel,² S. P. Regan,¹ J. P. Palastro,¹ D. H. Froula,¹ E. M. Campbell,¹ and V. N. Goncharov¹

¹Laboratory for Laser Energetics, University of Rochester

²Lawrence Livermore National Laboratory

³Department of Electrical and Computer Engineering, University of Alberta

The direct-drive approach to laser fusion is susceptible to hot-electron preheat due to the long-scale-length plasma conditions near the quarter-critical density of the target $n_c/4$ [where $n_c \approx 1.1 \times 10^{21} \lambda_0^{-2} \text{cm}^{-3}$ is the critical density and λ_0 (in μm) is the laser wavelength]. This plasma is susceptible to parametric instabilities, such as stimulated Raman scattering (SRS),¹ that generate electrostatic plasma waves capable of accelerating electrons. For full-scale, direct-drive-ignition experiments, it is estimated that the target adiabat and performance will be negatively affected if more than $\sim 0.15\%$ of the laser energy is coupled into the cold fuel in the form of hot electrons.²

In this summary, we report measurements of hot-electron energy deposition in National Ignition Facility (NIF)-scale implosions. Surrogate $\sim 2.4\text{-mm}$ -diam fuel capsules are driven in the polar-direct-drive (PDD) NIF geometry, which are only $\sim 30\%$ smaller than targets for the proposed ignition NIF PDD design.³ We employ the multilayered target platform to study the hot-electron energy deposition profile in the imploding shell,⁴ using mass-equivalent plastic targets with inner Ge-doped layers. Figure 1 shows (a) the laser power shape and [(b),(c)] targets with CH ablators and CH(Ge) payload. Different thicknesses of the Ge-doped layer ($35 \mu\text{m}$ to $59 \mu\text{m}$) were used, and the hard x-ray (HXR) emission was compared to the HXR emission from the reference all-CH target. The HXR emission was measured using the ten-channel NIF filter-fluorescer x-ray diagnostic.⁵

NIF target implosions were simulated using the 1-D hydrodynamic code *LILAC*.⁶ *LILAC* simulations predict similar coronal conditions for all of the mass-equivalent targets, with a density scale length at the $n_c/4$ surface of $420 \mu\text{m}$, an electron temperature of 3.5 keV , and an overlapped intensity of $4.5 \times 10^{14} \text{ W/cm}^2$. Similar coronal conditions indicate similar laser-plasma interaction and hot-electron generation. Indeed, the measured SRS scattered-light spectra were almost identical in the experiments. The Monte Carlo code Geant4 (Ref. 7) modeled hot-electron transport, energy deposition, and bremsstrahlung emission in the imploding shell. Hot electrons were injected at the $n_c/4$ surface with a Maxwellian energy distribution and the temperature (T_{hot}), total energy, and divergence half-angle ($\theta_{1/2}$) were varied to best match the measured HXR spectra; $\theta_{1/2}$ was found to exceed 40° to 45° , the half-angle at which the dense shell is seen from the $n_c/4$ surface during the implosion.

Figure 1(d) shows the HXR spectra measured in the experiments and their best fits using the simulated spectra. The inferred hot-electron temperature is $T_{\text{hot}} = 56 \pm 2 \text{ keV}$. The hot-electron energy deposition profile for the all-CH target, based on the simulation that best fits the data, is plotted in Fig. 1(e). It shows the cumulative hot-electron energy fraction in percent of the laser energy ($E_L = 720 \text{ kJ}$) plotted as a function of the radial coordinate in the unimploded shell, measured from the inner shell radius. The inset shows the energy deposition in the unablated part of the shell in more detail. The red circles show the hot-electron energy deposition in the Ge-doped layers in the simulations of the multilayered targets plotted versus the mass-equivalent radius in the all-CH target. The inferred energy depositions in the multilayered and all-CH targets are in good agreement. Most of the hot-electron energy is deposited in the plasma that is ablated during the implosion. The energy deposited in the unablated shell ($R - R_{\text{inner}} < 79.5 \mu\text{m}$) is $0.4 \pm 0.05\%$ of E_L , with only about half of this energy deposited in the inner 80% of the unablated shell.

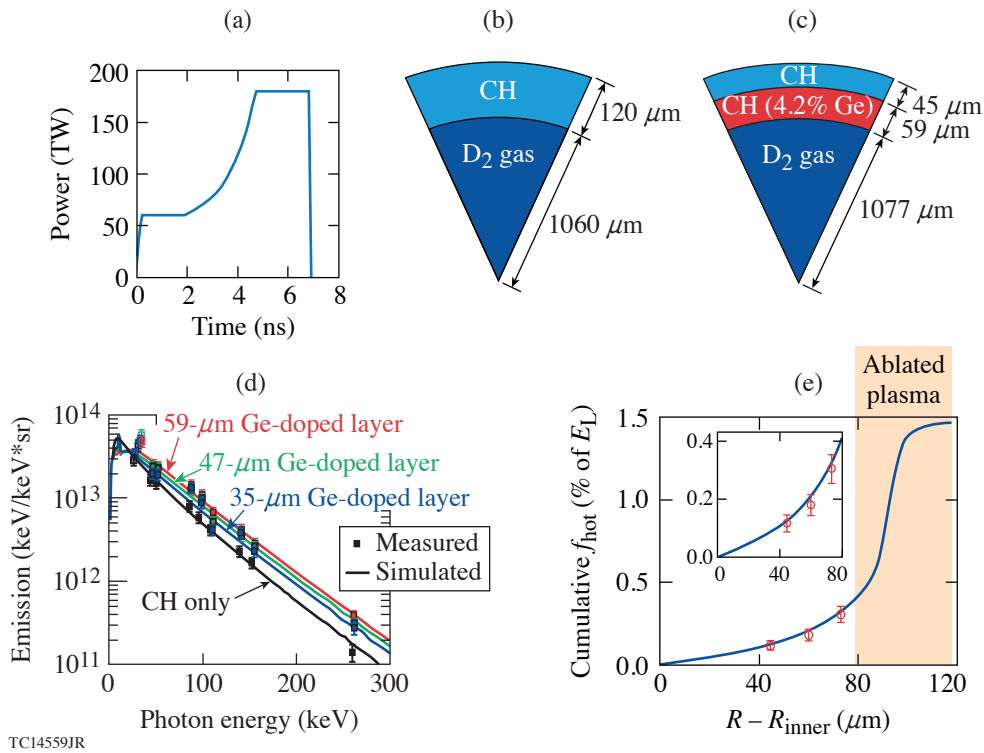


Figure 1

(a) The total laser power profile; [(b),(c)] design of targets with CH ablators; (d) measured and simulated time-integrated HXR spectra; (e) the cumulative hot-electron energy fraction for the all-CH target as function of the radial coordinate in the unimploded shell.

Thin layers of mid-Z material, such as Si, strategically placed in the ablator, can mitigate SRS and reduce hot-electron preheat. Figures 2(a) and 2(b) show the mass-equivalent targets having a buried Si layer in the ablator, designed to pass through the $n_c/4$ region during the laser flattop. This configuration shows significant reduction of SRS compared to the experiment without a Si layer. The inferred hot-electron temperature is $T_{\text{hot}} = 52 \pm 2$ keV. With a Si layer, hot-electron energy deposition in the unablated shell is reduced by about a factor of 2, demonstrating an important mitigation effect of the Si layer and providing a promising preheat-mitigation strategy that can expand the ignition-design space to higher intensities. Preheat extrapolation to ignition-scale cryogenic DT implosions on the NIF shows that by using a Si layer, preheat levels can be acceptable for on-target intensities close to 10^{15} W/cm².

This material is based upon work supported by the Department of Energy National Nuclear Security Administration under Award Number DE-NA0003856, the University of Rochester, and the New York State Energy Research and Development Authority.

1. W. Seka *et al.*, Phys. Fluids **27**, 2181 (1984); H. Figueroa *et al.*, Phys. Fluids **27**, 1887 (1984); C. S. Liu, M. N. Rosenbluth, and R. B. White, Phys. Fluids **17**, 1211 (1974).
2. J. A. Delettrez, T. J. B. Collins, and C. Ye, Phys. Plasmas **26**, 062705 (2019).
3. T. J. B. Collins *et al.*, Phys. Plasmas **19**, 056308 (2012); T. J. B. Collins and J. A. Marozas, Phys. Plasmas **25**, 072706 (2018).
4. A. R. Christopherson *et al.*, Phys. Rev. Lett. **127**, 055001 (2021).
5. M. Hohenberger *et al.*, Rev. Sci. Instrum. **85**, 11D501 (2014).
6. J. Delettrez *et al.*, Phys. Rev. A **36**, 3926 (1987).
7. S. Agostinelli *et al.*, Nucl. Instrum. Methods Phys. Res. A **506**, 250 (2003).

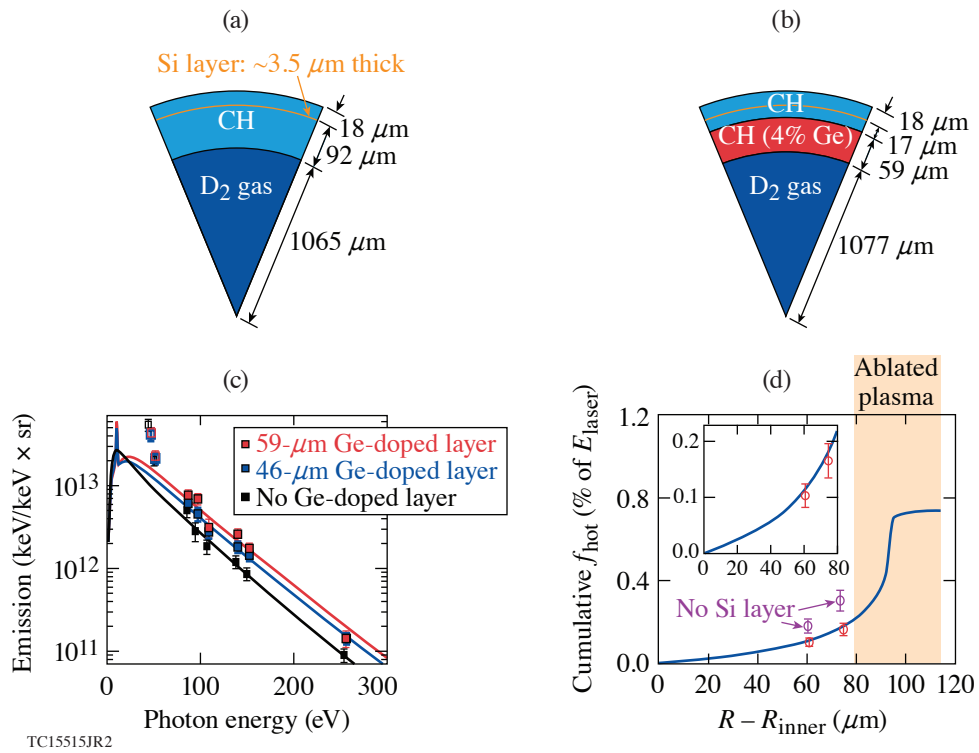


Figure 2

[(a),(b)] Targets with a Si layer in the ablator. (c) Measured and simulated time-integrated HXR spectra. (d) The cumulative hot-electron energy fraction for the target with a Si layer shown in (a) as a function of the radial coordinate in the unimploded shell.

Thermal Decoupling of Deuterium and Tritium During the Inertial Confinement Fusion Shock-Convergence Phase

N. V. Kabadi,¹ R. Simpson,¹ S. Atzeni,² J. Eriksson, P. J. Adrian,¹ A. Bose,¹ J. A. Frenje,¹ M. Gatu Johnson,¹ B. Lahmann,¹ C. K. Li,¹ C. E. Parker,¹ F. H. Séguin,¹ G. D. Sutcliffe,¹ C. J. Forrest,³ S. Fess,³ V. Yu. Glebov,³ R. T. Janezic,³ O. M. Mannion,³ H. G. Rinderknecht,³ M. J. Rosenberg,³ C. Stoeckl,³ G. Kagan,⁴ M. Hoppe,⁵ R. Luo,⁵ M. Schoff,⁵ C. Shulberg,⁵ H. W. Sio,⁶ J. Sanchez,⁶ L. Berzak Hopkins,⁶ D. Schlossberg,⁶ K. Hahn,⁶ C. Yeaman,⁶ and R. D. Petrasso¹

¹Plasma Science and Fusion Center, Massachusetts Institute of Technology

²Dipartimento SBAI, Università degli Studi di Roma "La Sapienza," Italy

³Laboratory for Laser Energetics, University of Rochester

⁴Centre for Inertial Fusion Studies, The Blackett Laboratory, Imperial College, UK

⁵General Atomics

⁶Lawrence Livermore National Laboratory

A series of experiments using DT gas-filled, shock-driven implosions was carried out at the Omega Laser facility. The capsules were nominally 2.3- μm -thick glass shells with an 860- μm outer diameter that were driven by a 0.6-ns square laser pulse delivering 15 kJ. Both the initial fill densities (0.2 to 4 mg/cm^3) and fill ratios (40% to 97% D) were varied. These experiments generated conditions relevant to the shock-convergence phase of hot-spot ignition experiments such as those conducted at the National Ignition Facility (NIF), without being complicated by a subsequent compression phase. With a high ablation rate and minimal residual shell mass, implosions of this type are insensitive to hydrodynamic instabilities. Data from shock-driven, indirect-drive exploding pushers (IDEP's) conducted on the NIF are also used. In these experiments, the spectral DTn and DDn ion temperatures (T_{sDTn} and T_{sDDn}) are inferred from the width of the produced neutron spectra as measured by neutron time-of-light diagnostics. To infer the level of thermal decoupling, the apparent species temperatures (T_{T} and T_{D}) can be inferred directly from the measured spectral temperatures based on the species masses (m_{D} and m_{T}) without accounting for emission weighting due to temperature profiles:

$$T_{\text{D}} = T_{\text{sDDn}}, \quad (1)$$

$$T_{\text{T}} = T_{\text{sDTn}} + \frac{m_{\text{D}}}{m_{\text{T}}}(T_{\text{sDTn}} - T_{\text{sDDn}}). \quad (2)$$

The differential equation governing the evolution of the ratio of two-ion temperatures due to ion-ion equilibration is given by

$$\frac{d}{dt} \frac{T_2}{T_1} = -\frac{1}{\tau_{12}} \left(\frac{T_2}{T_1} \right)^2 + \left(\frac{1}{\tau_{12}} - \frac{1}{\tau_{21}} \right) \frac{T_2}{T_1} + \frac{1}{\tau_{21}}, \quad (3)$$

where τ_{21} is the characteristic time at which species 2 equilibrates with species 1, which can be calculated from observables. The solution to this equation, when ignoring the weak dependence on species fraction, can be written as

$$\frac{T_2}{T_1} = \tanh \left[\frac{t}{\tau_{ii}} + \text{atanh}(R_0) \right], \quad (4)$$

where the integration constant R_0 is the temperature ratio as t goes to 0 and the total equilibration time is given by the harmonic mean of the τ_{12} and τ_{21} :

$$\tau_{ii} = 2 \left[\frac{1}{\tau_{12}} + \frac{1}{\tau_{21}} \right]^{-1}. \quad (5)$$

This dynamic model can be applied to the average observables from an implosion. For the average time scale, τ_N is calculated from the measured DT neutron emission time τ_{DTn} :

$$\tau_N = \frac{\tau_{DTn}}{\tau_{ii}}. \quad (6)$$

Figure 1 shows the apparent ratio of T_T to T_D plotted versus τ_N for three different D:T fill ratios. The observed trend is consistent for all fill fractions and well described by the equation

$$\frac{T_T}{T_D} = \tanh \left[\tau_N + \operatorname{atanh}(1.52 \pm 0.04) \right], \quad (7)$$

indicating a trend that begins at ≈ 1.5 and decays to 1 (or thermal equilibrium) at a rate determined by τ_N . Since the initial temperature ratio will be dominated by shock coupling based on ion-species properties, we conclude that the shock coupling scales linearly with mass (D and T have identical charge), $T_i \propto m_i$. Coupling directly proportional to mass is consistent with the rebounding shock stagnating the incoming flow and converting the flow energy of a species into thermal energy. It is also consistent with predictions for the mass dependence of shock coupling^{1,2} and recent astrophysical observations of collisionless shock heating.³

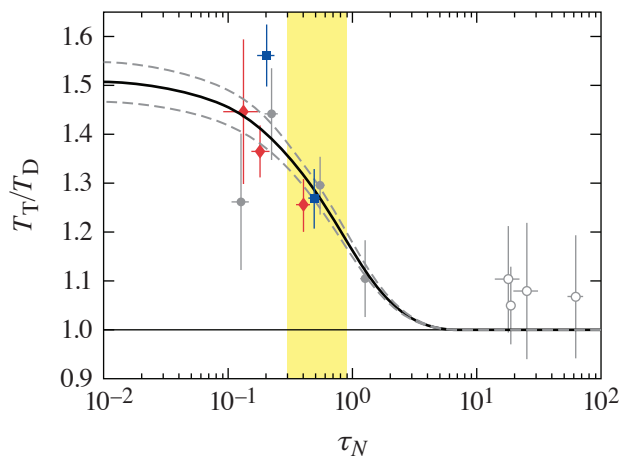


Figure 1

Apparent temperature ratio versus the normalized equilibration time scale for DT gas-filled implosions. Red diamonds are 97:3, gray circles 50:50, and blue squares 40:60 D:T atomic fill ratio. The open gray circles are from NIF IDEP's. All points are consistent with the equation $T_T/T_D [\tau_N + \operatorname{atanh}(1.52 \pm 0.04)]$, shown by the solid black curve with dashed 95% confidence interval. The reduced χ^2 statistic for this fit is 0.96. The yellow-shaded region represents the conditions most relevant to the shock-convergence phase in NIF ICF implosions.

U2762JR

This material is based upon work supported by the Department of Energy, National Nuclear Security Administration under Awards No. DE-NA0003868 and No. DE-NA0003938.

1. Ya. B. Zel'dovich and Yu. P. Raizer, in *Physics of Shock Waves and High-Temperature Hydrodynamic Phenomena*, edited by W. D. Hayes and R. F. Probstein (Dover, Mineola, NY, 2002), Chap. VII, pp. 515–520.
2. B. D. Keenan *et al.*, *Phys. Plasmas* **25**, 032103 (2018).
3. M. Miceli *et al.*, *Nat. Astron.* **3**, 236 (2019).

Enhanced Laser–Energy Coupling with Small-Spot Distributed Phase Plates (SG5-650) in OMEGA DT Cryogenic Target Implosions

W. Theobald,^{1,2} D. Cao,¹ R. C. Shah,¹ C. A. Thomas,¹ I. V. Igumenshchev,¹ K. A. Bauer,¹ R. Betti,^{1,2,3} M. J. Bonino,¹
E. M. Campbell,¹ A. R. Christopherson,¹ K. Churnetski,^{1,2} D. H. Edgell,¹ C. J. Forrest,¹ J. A. Frenje,⁴ M. Gatu Johnson,⁴
V. Yu. Glebov,¹ V. N. Goncharov,¹ V. Gopalaswamy,¹ D. R. Harding,¹ S. X. Hu,^{1,2} S. T. Ivancic,¹ D. W. Jacobs-Perkins,¹ R. T.
Janezic,¹ T. Joshi,¹ J. P. Knauer,¹ A. Lees,^{1,2} R. W. Luo,⁵ O. M. Mannion,¹ F. J. Marshall,¹ Z. L. Mohamed,^{1,2} S. F. B. Morse,¹
D. Patel,^{1,2} J. L. Peebles,¹ R. D. Petrasso,⁴ P. B. Radha,¹ H. G. Rinderknecht,¹ M. J. Rosenberg,¹ S. Sampat,¹ T. C. Sangster,¹
W. T. Shmayda,¹ C. M. Shulberg,⁵ A. Shvydky,¹ C. Sorce,¹ C. Stoeckl,¹ M. D. Wittman,¹ and S. P. Regan^{1,2}

¹Laboratory for Laser Energetics, University of Rochester

²Department of Mechanical Engineering, University of Rochester

³Department of Physics and Astronomy, University of Rochester

⁴Plasma Science and Fusion Center, Massachusetts Institute of Technology

⁵General Atomics, San Diego

Cryogenic deuterium–tritium ice target implosions on OMEGA with new small-spot (“SG5-650”) distributed phase plates (DPP’s) achieved an $(11\pm 4)\%$ increase in energy coupling compared to implosions with standard-spot DPP’s by decreasing the ratio R of the laser spot diameter to the target diameter from 0.93 to 0.75. The ratio R of the laser spot diameter to target diameter is an important parameter for increasing the hydrodynamic efficiency. A significant increase in hydrodynamic efficiency is expected for smaller R . The hydrodynamic efficiency η is defined as the ratio of the kinetic energy of the imploding shell at the end of the acceleration phase and the laser energy, $\eta = (1/2)m\bar{v}^2/E_L$, where m is the mass of the unablated shell (determined from simulations), \bar{v} is the shell velocity (determined from shell trajectory measurements), and E_L is the laser energy. The SG5-650 DPP’s provide a smaller focal spot size of $674\ \mu\text{m}$, defined as the diameter that encircles 95% of the measured beam energy compared to $834\ \mu\text{m}$ for the SG5-850. The hydrodynamic efficiency, defined as the ratio of the kinetic energy in the imploding shell to the laser energy, increased from 4.5% to 5.0% based on radiation-hydrodynamic calculations benchmarked to shell trajectory and bang-time measurements. Higher energy coupling came at the expense of increased hot-electron production as well as increased hydrodynamic instabilities seeded by a larger mode-10 amplitude from the beam port geometry, both of which may have reduced the fusion neutron production and areal density.

The shell trajectory from a cryogenic DT target implosion was recorded with the technique described in Ref. 1 for a single-picket–pulse implosion. Figure 1(a) shows the measured trajectory (red crosses) of the imploding shell for shot 91837 compared to simulated trajectories from 1-D radiation-hydrodynamic simulations using *LILAC*,² assuming the use of SG5-650 DPP’s (black curve). *LILAC* includes a 3-D ray-trace model taking the exact shape of the focal spot into account, a nonlocal electron thermal conduction model,³ a cross-beam energy transfer model,⁴ and first-principles equations of state.⁵ In addition, the blue curve shows the predicted trajectory as if the experiment had been performed with SG5-850 DPP’s. Similar trajectory measurements driven by laser beams equipped with SG5-850 DPP’s are in excellent agreement with the calculated trajectory assuming SG5-850 DPP’s in a *LILAC* simulation.⁶ As expected, the measured shell trajectory in Fig. 1(a) agrees much better with the simulation for $R = 0.75$ (SG5-650) than for $R = 0.9$ (SG5-850). The simulation with the SG5-850 DPP’s shows a delayed shell trajectory. Consequently, the shell implodes faster with the SG5-650 DPP, indicating a higher hydrodynamic efficiency η .

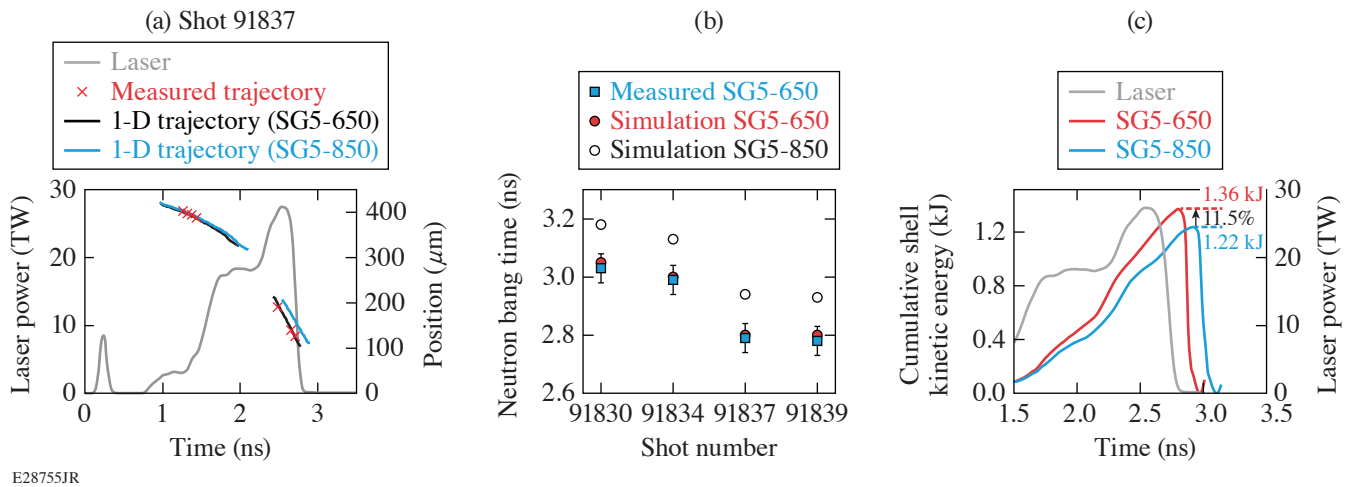


Figure 1

(a) Measured trajectory (red crosses) of the imploding DT cryogenic target shell for shot 91837 in comparison to simulated trajectories assuming SG5-650 DPP's (black curve) and SG5-850 DPP's (blue curve). The gray curve represents the laser pulse. (b) Measured neutron bang time (blue squares) compared to simulated values with SG5-650 (red circles) and SG5-850 (open circles); (c) calculated cumulative shell kinetic energy versus time for shot 91837.

The measured neutron bang time and the absorbed laser-energy fraction support the inferred enhanced energy coupling with SG5-650 DPP's. Figure 1(b) shows the measured neutron bang time (blue squares) compared to simulated values with SG5-650 (red circles) and SG5-850 (open circles). For example, for shot 91837, the measured bang time is 2.79 ± 0.05 ns compared to a predicted bang time of 2.80 ns. Repeating the simulations with SG5-850 DPP's shows that the predicted bang time is later (2.94 ns). The same trend is observed for the other three shots. Knowing that the calculated $(\Delta\eta)_{\text{calc}}$ for shot 91837 is 5.0×10^{-3} and the calculated bang-time shift is 140 ps, the measured bang-time shift of (150 ± 50) ps yields $(\Delta\eta)_{\text{exp}} = (5.5 \pm 1.8) \times 10^{-3}$. Similar values are obtained for the other three shots since the measured bang-time shifts agree very well with the calculated bang-time shifts. Therefore, the relative increase $(\Delta\eta/\eta)_{\text{exp}}$ is $(11 \pm 4)\%$ for all four shots and is in agreement with the trajectory measurement and the theoretical value. Figure 1(c) displays the calculated cumulative shell kinetic energy versus time for shot 91837. The energy reaches 1.36 kJ for SG5-650 at bang time and 1.22 kJ for SG5-850; therefore, an 11.5% calculated increase in the kinetic energy of the imploding shell from the smaller-spot DPP. The calculated hydrodynamic efficiency increased from 4.5% with SG5-850 to 5.0% with SG5-650.

Although the experiment provides encouraging results from an increased energy coupling, the overall implosion performance in terms of neutron yield and areal density is poorer compared to other high-performing shots with the SG5-850 DPP's.⁶ The smaller DPP focal spots likely limit the implosion performance due to increased hydrodynamic instabilities seeded by low- and mid-mode laser illumination nonuniformity. Three-dimensional hydrodynamic simulations with the code *ASTER*⁷ for SG5-650, $R = 0.75$ implosions show a higher susceptibility to low- and mid-mode perturbations induced by target offset, beam mispointing, and power balance compared to similar implosions with SG5-850 and $R = 0.9$. In addition, the beam-port geometry produces, in SG5-650, $R = 0.75$ implosions, a dominant contribution from mid-mode $\ell = 10$.

This material is based upon work supported by the Department of Energy National Nuclear Security Administration under Award Number DE-NA0003856, the University of Rochester, and the New York State Energy Research and Development Authority.

1. D. T. Michel *et al.*, Rev. Sci. Instrum. **83**, 10E530 (2012).
2. J. Delettrez *et al.*, Phys. Rev. A **36**, 3926 (1987).
3. V. N. Goncharov *et al.*, Phys. Plasmas **13**, 012702 (2006).

4. I. V. Igumenshchev *et al.*, *Phys. Plasmas* **17**, 122708 (2010).
5. S. X. Hu *et al.*, *Phys. Rev. E* **92**, 043104 (2015).
6. W. Theobald *et al.*, “Enhanced Laser-Energy Coupling with Small-Spot Distributed Phase Plates (SG5-650) in OMEGA DT Cryogenic Target Implosions,” to be published in *Physics of Plasmas*.
7. I. V. Igumenshchev *et al.*, *Phys. Plasmas* **23**, 052702 (2016).

The Benefits of Spin Polarization for Fusion Propulsion

G. Bruhaug^{1,2} and A. Kish^{1,3}

¹Laboratory for Laser Energetics, University of Rochester

²Department of Mechanical Engineering, University of Rochester

³Department of Physics and Astronomy, University of Rochester

Nuclear fusion has long been considered an ideal method of space propulsion due to the extremely high fuel-specific energy ($\sim 2 \times 10^6$ greater than the best chemical fuels) and exhaust velocity ($\sim 4\%$ of the speed of light versus ~ 4 km/s for the best chemical fuels). This high performance will allow for rapid interplanetary missions as well as interstellar missions within the lifetime of the researchers involved.¹ Fusion propulsion suffers, however, from two primary complications: the difficulty of igniting a self-sustaining fusion chain reaction and the large amount of ionizing radiation generated by the reaction, which requires a considerable mass of shielding to protect against this radiation.¹ This summary describes the ability of a unique, yet well known, nuclear physics technique known as “spin polarization” to lower both the ignition requirements and the flux of ionizing radiation that the spacecraft must handle.

All nuclei possess an inherent angular momentum known as “spin” that plays a significant role in nuclear reactions, especially nuclear fusion. Spin polarization is the process of aligning the nuclear spin vectors of the fusion reactants prior to the reaction. For five-nucleon fusion reactions, notably DT (deuterium and tritium) and D³He (deuterium and helium-3), spin polarization serves to increase the cross section for fusion and force the reaction products to emit anisotropically. Increasing the reaction cross section lowers the requirements to reach fusion ignition, allowing the spacecraft to use less energy for ignition and requiring less total circulating power during operation. This will decrease both the fusion reactor equipment mass and radiator mass. Additionally, the anisotropic emission of reaction products allows a substantial fraction (up to 80%) of the neutron radiation to be directed away from the spacecraft, reducing the required shielding mass.²

Several methods for producing spin-polarized nuclei have been considered and tested for the purposes of nuclear physics experiments and producing beams of spin-polarized particles in particle colliders. For fusion reactors that require a constant stream of gaseous fusion fuel, various optical pumping techniques provide options for creating jets or beams of polarized fusion fuel. These techniques are technologically mature, but they do suffer from various polarization-loss mechanisms, e.g., contact with the walls of the fuel transport system. For fusion reactors that can operate with frozen-fuel injection, spin polarization can be achieved via super chilling of the fuel and/or the application of a strong (>10 -T) magnetic field. These methods allow for pellets of prepolarized fuel to be created and stored before injection into the reactor.²

A limiting factor on the utility of spin-polarized fuel is the depolarization rate in the fusion reactor.² For rapidly pulsed fusion reactors with no significant magnetic fields, the rate of depolarization can be far slower than the expected reaction time. In long-pulse or steady-state fusion reactors, the recycling of fuel from the reactor walls can significantly deplete the population of polarized fuel. Additionally, the presence of an external magnetic field can quickly depolarize the fuel depending on the alignment of the spin polarization with the magnetic field. Such reactor analysis is beyond the scope of this summary, but the authors recommend fusion concepts such as inertial confinement fusion to capitalize on the benefits of spin polarization based on this preliminary analysis.

A unique aspect of spin-polarized DT fusion is the anisotropic emission of the neutrons and alpha particles. This emission profile, seen in Fig. 1 for neutrons, can be leveraged to significantly reduce the neutron radiation impacting the ship while also providing more propulsive efficiency due to the favorable emission profile of the alpha particles (the inverse profile of the neutrons). Figure 2 shows an artistic conception of the change in neutron emission profile on the famous VISTA inertial fusion-powered spacecraft design.

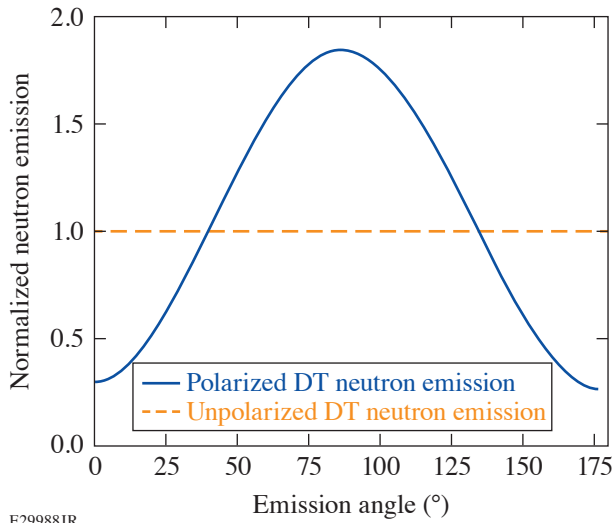


Figure 1
Neutron angular emission profile for polarized and unpolarized DT fuel in the center of mass frame.

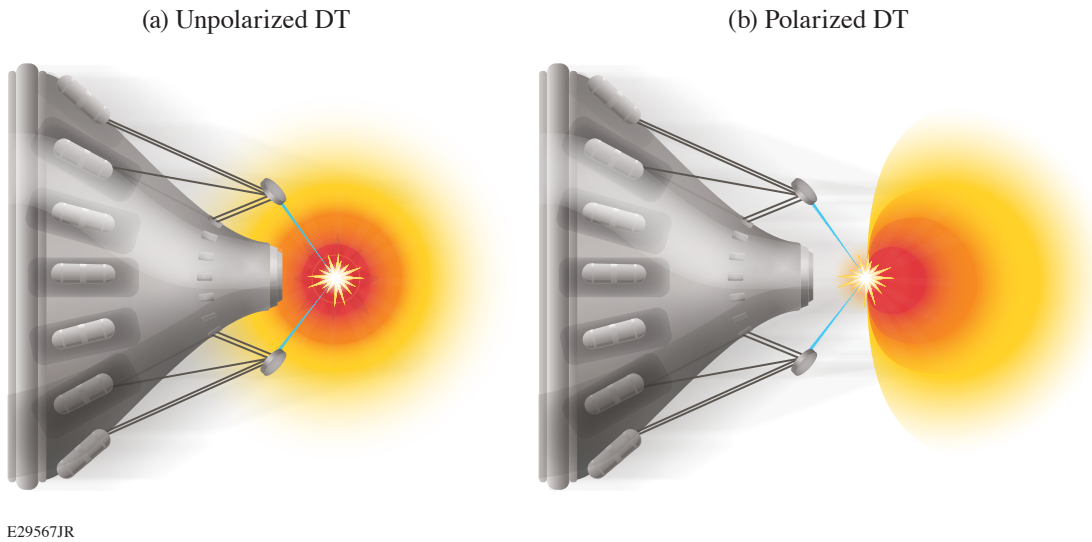


Figure 2
(a) Neutron emission profile from unpolarized DT; (b) Neutron emission from polarized DT.

A conservative analysis was performed to estimate the required radiation shielding, fusion ignition energy, and propulsive efficiency for spacecraft using both spin-polarized DT and spin-polarized D³He fusion fuel. Based on this analysis we estimate >20% reduction in ignition requirements, ~45% more fusion burnup, ~2% reduction in radiation shielding mass, and >30% increase in propulsive efficiency of the fusion rocket. DT fusion provides the greatest benefits; polarizations >60% were found to provide less radiation flux onto the spacecraft than similarly polarized D³He fuel. This surprising result shows the incredible potential of spin-polarized DT to act as a power source for future spacecraft.

The authors recommend that future research into fusion spacecraft consider the potential of spin-polarized fuel to improve the structure and performance of spacecraft propulsion and shielding.

1. C. D. Orth, Lawrence Livermore National Laboratory, Livermore, CA, Report UCRL-TR-110500 (2005).
2. G. Ciullo *et al.*, in *Nuclear Fusion with Polarized Fuel*, Springer Proceedings in Physics (Springer International Publishing, Switzerland, 2016), Vol. 187, pp. 1–13.

Scaling of Turbulent Viscosity and Resistivity: Extracting a Scale-Dependent Turbulent Magnetic Prandtl Number

X. Bian,¹ J. K. Shang,¹ E. G. Blackman,² G. W. Collins,^{1,2,3} and H. Aluie^{1,3}

¹Department of Mechanical Engineering, University of Rochester

²Department of Physics and Astronomy, University of Rochester

³Laboratory for Laser Energetics, University of Rochester

It is widely believed that turbulence plays an important role in the outward transport of angular momentum in accretion disks for inward mass accretion.¹ The simplest conceptual framework is to think of turbulence as an effective (or turbulent) viscosity v_t , which leads to the “turbulent diffusion” of angular momentum at scales far larger than viscous scales; this description has long shaped our thinking of accretion disk dynamics.² Similarly, magnetic fields can be transported outward by an effective (or turbulent) resistivity η_t . In this way, the magnetic-field configuration in accretion disks may be influenced by a balance between the inward advection by accretion and the outward diffusion by turbulent resistivity. This balance between the competing effects of v_t and η_t is captured by the turbulent magnetic Prandtl number $\text{Pr}_t \equiv v_t/\eta_t$.

In this summary, we develop a new approach to determine these “effective transport” coefficients acting at different length scales. To our knowledge, our work is the first to calculate the turbulent magnetic Prandtl number as a function of length scale. Our results indicate that it has values of ≈ 1 to 2 at the smallest ideal hydrodynamic scales, increasing to ≈ 5 to 10 at the largest scales.

We analyze the coarse-grained kinetic energy (KE) and magnetic energy (ME) density balance of the incompressible magnetohydrodynamic (MHD) equations³ and extract the effective transport coefficients v_t , η_t , and Pr_t as a function of length scale. We analyze the energy budgets resulting from the eddy viscosity model. Within our coarse-graining framework, this is equivalent to having the rate of energy cascading to scales smaller than l equal to a turbulent dissipation acting on scales $> l$:

$$2v_t \langle |S_\ell|^2 \rangle \equiv \langle \bar{\Pi}_\ell^u \rangle, \eta_t \langle |\mathbf{J}_\ell|^2 \rangle \equiv \langle \bar{\Pi}_\ell^b \rangle. \quad (1)$$

It is possible to relate v_t and η_t to energy spectra. Indeed, the space-averaged turbulent dissipation can be expressed in terms of energy spectra:

$$\langle \bar{\Pi}_\ell^u \rangle = 2v_t \langle |\bar{\mathbf{S}}_\ell|^2 \rangle = 2v_t \int_0^k k'^2 E^u(k') dk', \langle \bar{\Pi}_\ell^b \rangle = \eta_t \langle |\mathbf{J}_\ell|^2 \rangle = 2\eta_t \int_0^k k'^2 E^b(k') dk'. \quad (2)$$

The kinetic and magnetic energy spectra scale as

$$E^u(k) \propto k^{-2\sigma_u-1}, \quad E^b(k) \propto k^{-2\sigma_b-1}. \quad (3)$$

The exponents σ_u and σ_b in the scaling of spectra are related to the scaling of velocity and magnetic-field increments:³

$$\delta u(\ell) \propto \ell^{\sigma_u}, \quad \delta B(\ell) \propto \ell^{\sigma_b}. \quad (4)$$

For sufficiently high Reynolds number flows, X. Bian and H. Aluie⁴ showed that $\langle \overline{\Pi}_\ell^u \rangle$ and $\langle \overline{\Pi}_\ell^b \rangle$ become constant, independent of scale in the so-called “decoupled range.” From definitions in Eq. (1), and considering the scaling relations discussed above, we can infer that the turbulent transport coefficients vary with scale in the decoupled range as follows:

$$v_t \propto k^{-2(1-\sigma_u)}, \quad \eta_t \propto k^{-2(1-\sigma_b)}, \quad \text{Pr}_t \propto k^{-2(\sigma_b-\sigma_u)}. \quad (5)$$

We conducted pseudo-spectral direct numerical simulations of MHD turbulence using hyperdiffusion with grid resolutions up to 2048^3 . Figure 1 shows the effective transport coefficients as a function of scale calculated using their respective definitions in Eq. (1). We can see that $v_t(k) \sim k^{-5/3}$ and $\eta_t(k) \sim k^{-4/3}$ are consistent with relation in Eq. (5) when $\sigma_u = 1/6$ and $\sigma_b = 1/3$, as in our simulations. Moreover, we see that $\text{Pr}_t(k) \sim k^{1/3}$, which is also consistent with the derived scaling in Eq. (5) with $\sigma_u = 1/6$ and $\sigma_b = 1/3$ in our simulated flows. For accretion disks, this indicates that the flow may be more efficient at accreting large-scale magnetic fields radially inward than diffusing them outward.

Analyzing the kinetic and magnetic energy cascade rates, we infer power-law scaling in Eq. (5) for v_t , η_t , and Pr_t given our definitions of those transport coefficients. This approach circumvents relying on particular values for the spectral scaling exponents (σ_u and σ_b) from a specific MHD phenomenology—whether it exists or not—by relying on results from X. Bian and H. Aluie⁴ of conservative KE and ME cascades.

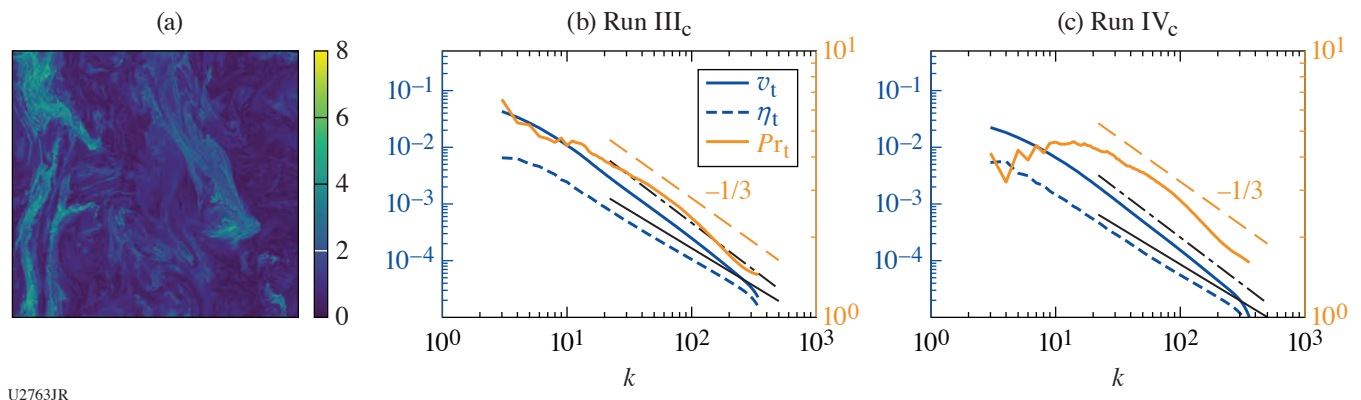


Figure 1

(a) A 2-D slice from a 3-D simulation of turbulent flow subject to a strong external magnetic field in the vertical. It highlights the anisotropic and complex transport in such flows. [(b),(c)] Plots of v_t , η_t , and Pr_t at different scales for two cases at the highest resolution. Three reference lines with a slope of $-1/3$, $-5/3$ (dashed-dotted black curve), and $-4/3$ (solid black curve) are added.

This research was funded by DOE FES grants DE-SC0014318 and DE-SC0020229. Partial funding for this research was provided by the Center for Matter at Atomic Pressures (CMAP), a National Science Foundation (NSF) Physics Frontier Center, under Award PHY-2020249.

1. S. A. Balbus and J. F. Hawley, *Rev. Mod. Phys.* **70**, 1 (1998).
2. N. I. Shakura and R. A. Sunyaev, *Astron. Astrophys.* **24**, 337 (1973).
3. H. Aluie, *New J. Phys.* **19**, 025008 (2017).
4. X. Bian and H. Aluie, *Phys. Rev. Lett.* **122**, 135101 (2019).

First Demonstration of a Triton Beam Using Target Normal Sheath Acceleration

A. K. Schwemmlin,^{1,2} C. Stoeckl,¹ C. J. Forrest,¹ W. T. Shmayda,¹ S. P. Regan,¹ and W. U. Schröder^{1,2}

¹Laboratory for Laser Energetics, University of Rochester

²Departments of Physics and Chemistry, University of Rochester

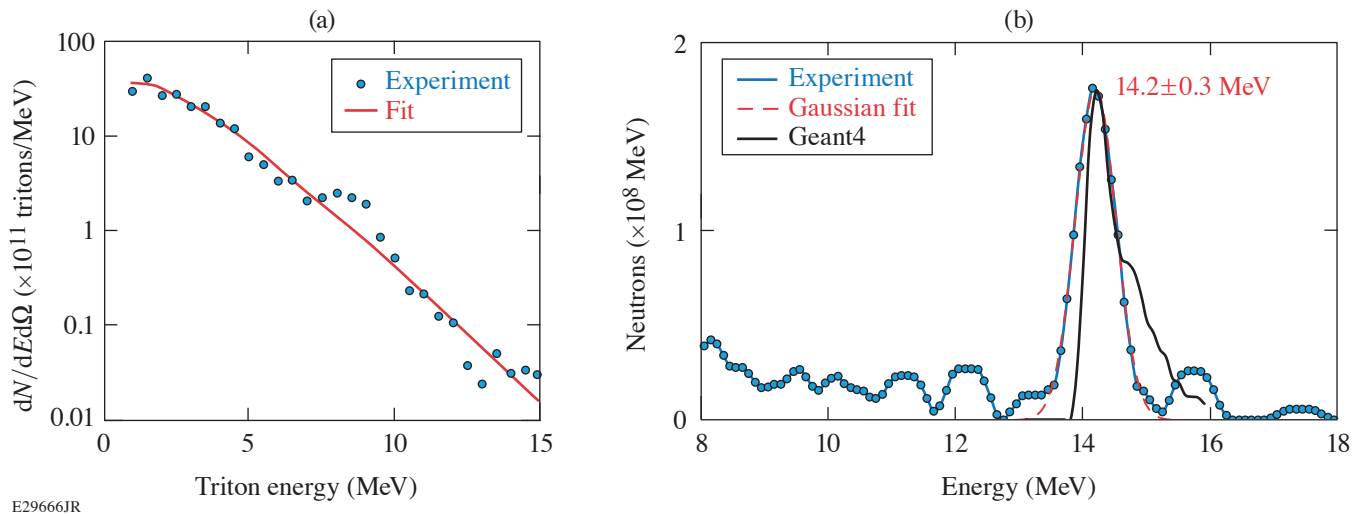
Triton beams provide unique experimental opportunities to study reactions between light nuclei. Of particular interest is the tritium–tritium reaction $T(t, 2n)\alpha$, which may produce the exotic compound nucleus ${}^6\text{He}$ in an excited state. However, populating the excited state of ${}^6\text{He}$ closest to the entrance configuration of two tritons requires a bombarding energy of at least 2.3 MeV (Ref. 1), which has never been reached experimentally. The results will improve the understanding of both the structure of ${}^6\text{He}$ and the T–T reaction mechanism.

Triton beams up to energies of about 1 MeV have been generated from the 1950s to 1980s in accelerator facilities,^{2–4} but tritium contamination of the exposed infrastructure led to a cessation of such experiments. Target normal sheath acceleration⁵ (TNSA) isolates the necessary tritium in a small ($500 \times 500 \times 25\text{-}\mu\text{m}^3$) target. When exposed to a high-intensity ($>10^{16}\text{ W/cm}^2$) laser beam, the target emits energetic ($\sim 1\text{-MeV}$) electrons, which establish a strong (TV/m) electric field that accelerates ions from the target surface. Previous studies using deuterated targets on OMEGA EP⁶ demonstrated that deuteron energies of up to 12 MeV are achievable with this technique.

For this study, titanium targets were exposed to approximately 1 bar of 99.97% pure tritium gas at 225°C for 2 h. Several targets were examined separately to determine their tritium content by a thermal desorption process,⁷ revealing an activity of $500 \pm 10\ \mu\text{Ci}$ or approximately 10^{16} tritons. In a first experiment, one target was irradiated by a short (10-ps) OMEGA EP pulse (1.25-kJ, 30- μm focal-spot diameter). The spectra of the emitted ions were analyzed using Thomson parabola ion energy (TPIE⁸) to reveal the triton spectrum shown in Fig 1(a). The experimental data (blue circles) can be fitted reasonably well with a Maxwell–Boltzmann distribution (red curve) and an effective temperature of $1.4 \pm 0.1\text{ MeV}$. This shape is typical for the TNSA process using planar targets. The total integrated yield of tritons was 3×10^{12} , corresponding to a laser-to-triton energy conversion efficiency of approximately 0.04%.

In a proof-of-principle nuclear reaction experiment, a secondary 100- μm -thick deuterated polyethylene (CD) target was arranged parallel to the tritiated target generating the triton beam 5 mm behind the CD target. A standard OMEGA neutron time-of-flight detector,⁹ positioned 13.4 m away from the target at 79° to the target normal, was utilized to detect any deuterium–tritium (D–T) fusion neutrons. The neutron spectrum, corrected for instrument and attenuation effects, is shown in Fig. 1(b). The experimental data (blue circles) can be fitted well with a Gaussian (dashed red curve) with parameters $14.2 \pm 0.3\text{ MeV}$ (mean \pm stdev). A Geant4 (Ref. 10) simulation of the experiment is shown by the black curve and accounts for the energy loss of tritons in the CD target and applicable kinematics. The simulation reveals that scattering angles close to 90° greatly reduce the effect of the projectile energy since the momentum transfer from projectile to ejectile becomes very inefficient. In these cases, the Q value of the reaction dominates, and a narrow peak is generated. A total of approximately 10^8 neutrons were produced, in good agreement with predictions by Geant4.

Future experiments will catch the triton beam in a tritiated secondary target to induce T–T reactions at the high energies required to populate the mentioned excited state of ${}^6\text{He}$. A rapid increase in cross section with triton energy is expected once the state can



E29666JR

Figure 1

(a) The triton beam spectrum (blue circles) as delivered by TPIE, together with a fit (red curve) to a Maxwell–Boltzmann distribution. (b) The neutron spectrum produced by the D–T reaction experiment (blue circles), together with a Gaussian fit (dashed red curve) and a Geant4 simulation (solid black curve).

be populated, and the shape of the neutron spectrum will reveal details about the reaction mechanism.¹¹ Further experiments are planned with secondary lithium and beryllium targets to produce exotic, neutron-rich isotopes of these elements via di-neutron transfers. These isotopes are of interest to *ab initio* structure modeling^{12,13} and reaction networks in stars.¹⁴

This material is based upon work supported by the Department of Energy National Nuclear Security Administration under Award Number DE-NA0003856, the University of Rochester, and the New York State Energy Research and Development Authority.

1. TUNL Nuclear Data Evaluation, Energy Level Diagrams for $A = 6$, Accessed 30 November 2021, <https://nucldata.tunl.duke.edu/nucldata/figures/06figs/menu06.shtml>.
2. C. Wong, J. D. Anderson, and J. W. McClure, *Nucl. Phys.* **71**, 106 (1965).
3. A. A. Jaffe *et al.*, *Proc. Phys. Soc.* **76**, 914 (1960).
4. R. Woods, J. L. McKibben, and R. L. Henkel, *Nucl. Instrum. Methods* **122**, 81 (1974).
5. S. C. Wilks *et al.*, *Phys. Plasmas* **8**, 542 (2001).
6. C. Stoeckl *et al.*, *Nucl. Instrum. Methods Phys. Res. B* **453**, 41 (2019).
7. C. Fagan *et al.*, *Fusion Sci. Technol.* **76**, 424 (2020).
8. J. A. Cobble *et al.*, *Rev. Sci. Instrum.* **82**, 113504 (2011).
9. C. J. Forrest *et al.*, *Rev. Sci. Instrum.* **83**, 10D919 (2012).
10. GEANT4: A Simulation Toolkit, CERN Accelerating Science, Accessed 2 Aug 2021, <https://geant4.web.cern.ch/node/1>.
11. B. Lacina, J. Ingley, and D. W. Dorn, Lawrence Livermore National Laboratory, Livermore, CA, Report UCRL-7769 (1965).
12. C. Cockrell, J. P. Vary, and P. Maris, *Phys. Rev. C* **86**, 034325 (2012).
13. C. Forssén *et al.*, *Phys. Rev. C* **71**, 044312 (2005).
14. M. Terasawa *et al.*, *Astrophys. J.* **562**, 470 (2001).

Spatiotemporal Control of Laser Intensity Through Cross-Phase Modulation

T. T. Simpson, D. Ramsey, P. Franke, K. Weichman, M. V. Ambat, D. Turnbull, D. H. Froula, and J. P. Palastro

Laboratory for Laser Energetics, University of Rochester

Spatiotemporal pulse shaping provides control over the trajectory and range of an intensity peak. While this control can enhance laser-based applications, the optical configurations required for shaping the pulse can constrain the transverse or temporal profile, duration, or orbital angular momentum (OAM). Here we present a novel technique for spatiotemporal control that mitigates these constraints by using a “stencil” pulse to spatiotemporally structure a second primary pulse through cross-phase modulation (XPM) in a Kerr lens. The temporally shaped stencil pulse induces a time-dependent focusing phase within the primary pulse. This technique, the “flying-focus X,” allows the primary pulse to have any profile or OAM, expanding the flexibility of spatiotemporal pulse shaping for laser-based applications. As an example, simulations show that the flying-focus X can deliver an arbitrary-velocity, variable-duration intensity peak with OAM over distances much longer than the Rayleigh range.

Spatiotemporal pulse shaping offers a new paradigm for controlling laser intensity. By exploiting space–time correlations in the amplitude or phase of a laser pulse, a number of recent techniques have created arbitrary-velocity intensity peaks that remain nearly propagation invariant over distances much longer than the Rayleigh range. These features promise to revolutionize a wide range of laser-based applications, including high-power amplifiers and compact accelerators. Nevertheless, each of the existing techniques requires an optical configuration that constrains properties of the intensity peak, such as its transverse or temporal profile, duration, or OAM. As an example, the original “chromatic” flying focus uses a chirp and a chromatic lens to control the time and location at which each temporal slice of a laser pulse comes to focus, respectively. While this technique offers some flexibility to shape the transverse profile of the far field, the chromatic aberration and chirp can place a lower bound on the duration of the intensity peak that is much larger than the transform-limited duration.^{1,2} An alternative technique, the “achromatic” flying focus, employs the spherical aberration of an axiparabola to focus different annuli in the near field to different axial locations in the far field and an echelon to adjust their relative timing.^{3,4} Here, the intensity peak can have a near-transform-limited duration, but the flattop transverse profile required in the near field and the spherical aberration of the axiparabola fully determine the far-field profile.

We describe a novel technique for spatiotemporal control: the “flying-focus X,” which combines temporal pulse shaping with XPM to produce an ultrashort, arbitrary-velocity intensity peak, with or without OAM, over distances far greater than the Rayleigh range. Specifically, a temporally shaped, high-intensity “stencil” pulse induces the time-dependent focusing of a second “primary” pulse through XPM in a medium with an intensity-dependent refractive index (Kerr lens) (Fig. 1). The minimum and maximum intensity of the stencil pulse set the focal range of the primary pulse, while its duration sets the velocity of the resulting intensity peak. Use of a stencil pulse mitigates the constraints on the primary pulse, allowing for spatiotemporal control independent of properties such as the far-field duration, transverse profile, or OAM. In effect, these constraints are offloaded onto the stencil pulse. As a result, flying-focus X provides unprecedented flexibility for structuring the far-field properties of the intensity peak, promising to further enable or enhance a wide range of laser-based applications.

Figure 1 illustrates how temporal pulse shaping and XPM can be used to control the trajectory and range of an intensity peak. A stencil pulse and a primary pulse, overlapped in space and time, co-propagate along the z axis and enter a convex, parabolic

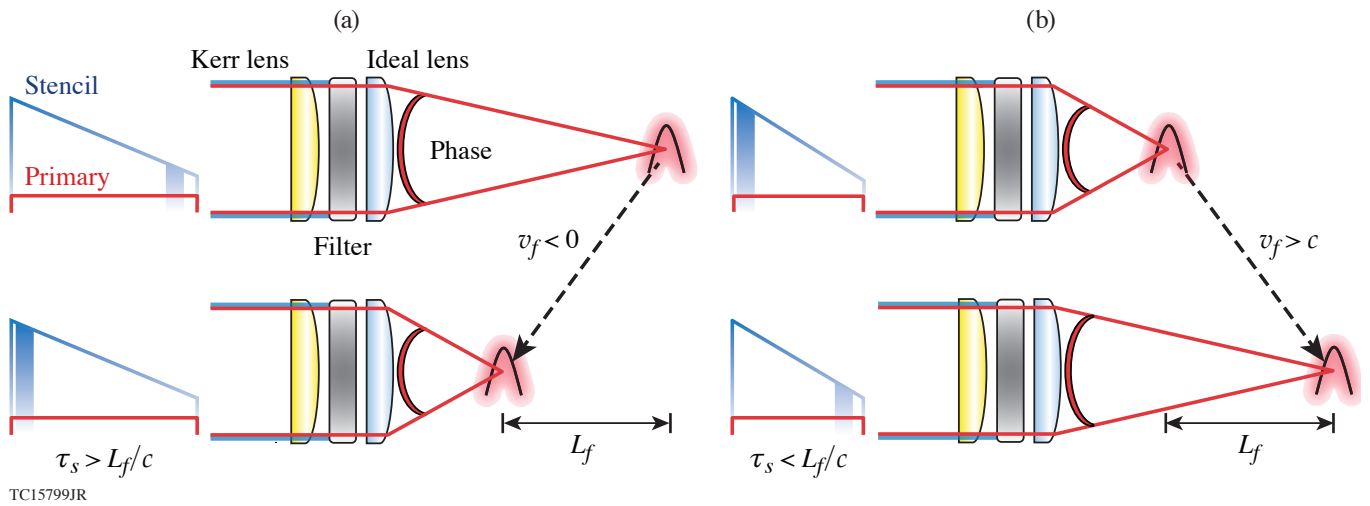


Figure 1

A schematic of the flying-focus X. A high-intensity stencil pulse with a flat-top transverse and shaped temporal profile co-propagates with a low-intensity primary pulse. The stencil induces a time-dependent focusing phase on the primary in a parabolic Kerr lens. A filter removes the stencil, while an ideal lens provides additional focusing for the primary. The resulting focus travels over a distance L_f at a velocity v_f , both of which can be tuned by shaping the temporal profile of the stencil. A stencil pulse with an intensity that ramps up in time can produce either (a) negative or (b) positive superluminal focal velocities depending on its duration τ_s .

Kerr lens. The two pulses have distinct wavelengths or polarization vectors, and the stencil intensity is much greater than the primary intensity. The stencil pulse has a flat-top transverse profile, which, in combination with the parabolic shape of the Kerr lens, ensures that the primary pulse acquires an aberration-free wavefront curvature. The instantaneous intensity of the stencil dictates the time dependence of that curvature, with high stencil intensities inducing greater curvature. The time-dependent wavefront curvature is equivalent to that applied by an ideal lens with a time-dependent focal length. As a result, the primary pulse can have any transverse profile or orbital angular momentum, in addition to the extended focal range and velocity control afforded by previous spatiotemporal pulse-shaping techniques.

Simulations show that the flying-focus X can create an ultrashort-duration intensity peak traveling near the vacuum speed of light over many Rayleigh ranges (Fig. 2)—a configuration ideal for advanced accelerators.^{5,6} To produce the desired focal velocity, the stencil intensity ramps up linearly in time over ~ 330 fs. In the far field, the ≈ 10 -fs intensity peak maintains its diffraction-limited Gaussian spot over the entire focal range ($L_f = 1$ cm), while traveling at a focal velocity $v_f = 1.01 c$.

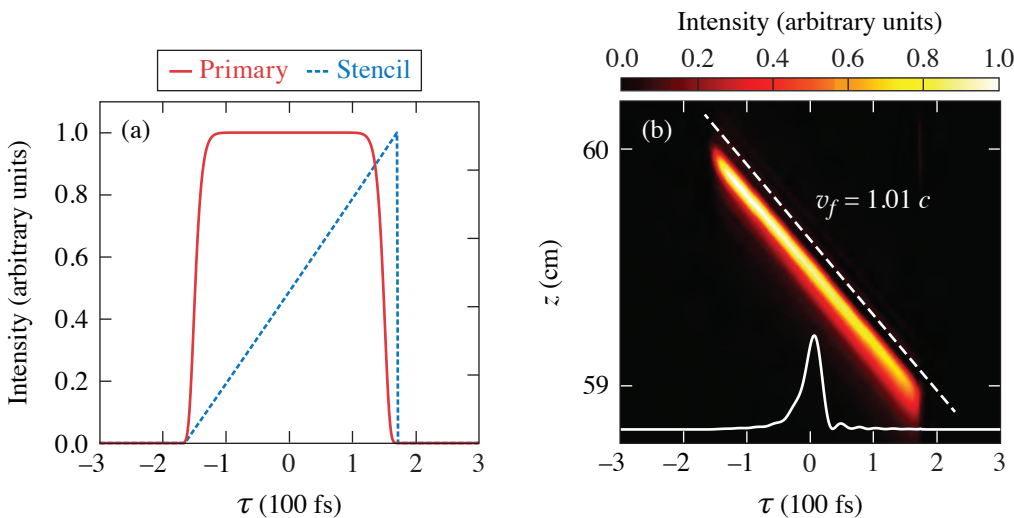


Figure 2

Simulation results for a flying-focus X pulse with $v_f = 1.01 c$, demonstrating velocity control, an ultrashort duration, and near propagation invariance through the focal range. (a) The temporal profile of the stencil and primary pulses at the entrance of the Kerr lens. (b) The maximum intensity of the primary pulse in the far field and a lineout of its temporal profile. All values are normalized to their respective maxima and $\tau = t - z/c$.

TC15801JR

The work published here was supported by the U.S. Department of Energy Office of Fusion Energy Sciences under contract No. DE-SC0016253, the Department of Energy under Cooperative Agreement No. DE-NA0003856, the University of Rochester, and the New York State Energy Research and Development Authority.

1. D. H. Froula *et al.*, *Nat. Photonics* **12**, 262 (2018).
2. A. Sainte-Marie, O. Gobert, and F. Quéré, *Optica* **4**, 1298 (2017).
3. J. P. Palastro *et al.*, *Phys. Rev. Lett.* **124**, 134802 (2020).
4. C. Caizergues *et al.*, *Nat. Photonics* **14**, 475 (2020).
5. P. Franke *et al.*, *Phys. Rev. A* **104**, 043520 (2021).
6. J. P. Palastro *et al.*, *Phys. Plasmas* **28**, 013109 (2021).

Improved Equation-of-State Table of Deuterium for High-Energy-Density Applications

D. I. Mihaylov, V. V. Karasiev, S. X. Hu, J. R. Rygg, V. N. Goncharov, and G. W. Collins

Laboratory for Laser Energetics, University of Rochester

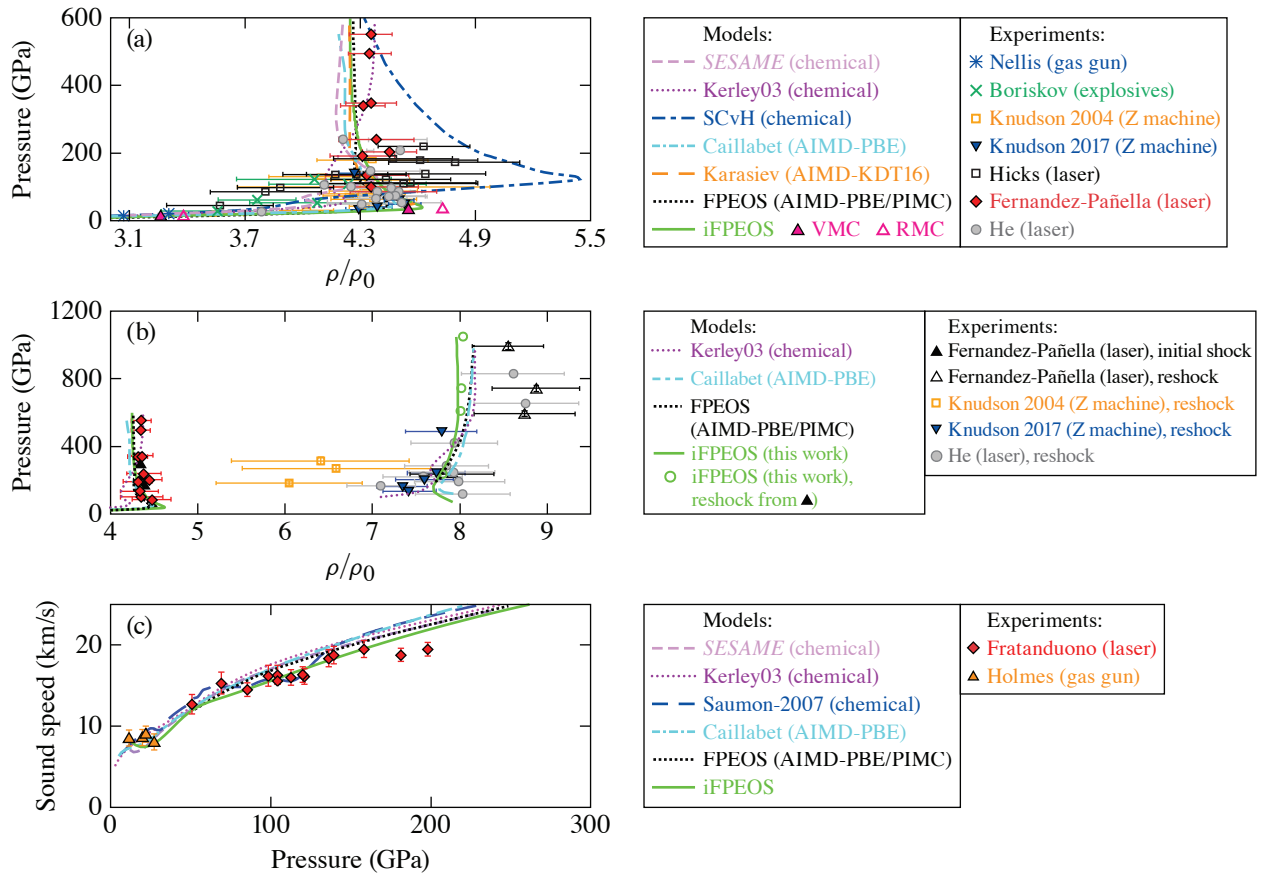
We present an improved first-principles equation-of-state (iFPEOS) table of deuterium that is an update on the previously established FPEOS table^{1,2} by introducing (1) fully consistent molecular dynamics (MD) driven by density functional theory (DFT) treatment for all ρ - T points, (2) a universal treatment of exchange-correlation (XC) thermal effects, and (3) quantum treatment of ions. This new iFPEOS includes ρ points in the range of $1 \times 10^{-3} \leq \rho \leq 1.6 \times 10^3 \text{ g/cm}^3$ and T points in the range of $800 \text{ K} \leq T \leq 256 \text{ MK}$, thereby covering the challenging warm-dense-matter regime.

For an improved description of the electronic structure at high T , iFPEOS employs newly developed T-SCAN-L (Ref. 3), which is a free-energy XC density functional with explicit temperature dependence at the meta-generalized gradient approximation (meta-GGA) level of DFT. Previous models such as FPEOS and other popular DFT-based models⁴ rely on the zero- T , GGA-level XC functional PBE (Perdew–Burke–Ernzerhof). Therefore, iFPEOS provides an improvement in accuracy by taking into account important XC thermal effects⁵ and including the higher-level, more-accurate treatment of the XC interaction. In addition, we combine T-SCAN-L with the rVV10 XC functional in order to account for van der Waals interactions. Recently, Hinz *et al.* demonstrated the success of DFT with SCAN-L+rVV10 XC in predicting the molecular dissociation boundary in dense D (Ref. 6). This accuracy of the SCAN-L+rVV10 functional, in combination with the development of T-SCAN-L, is the main motivation for constructing iFPEOS.

In the high- T regime, above $T \approx 250,000 \text{ K}$, standard Kohn–Sham (KS) DFT calculations become prohibitively expensive due to the high number of thermally occupied orbitals; therefore, we use orbital-free (OF) DFT. In OF DFT, the KS orbital-dependent kinetic energy functional is approximated by a density-dependent one. Here we use the newly developed noninteracting free-energy density functional LKTF γ TF, which is a one-parameter, tunable, convex combination of the Luo–Karasiev–Trickey free energy density functional (LKTF)⁷ and Thomas–Fermi functional. We tune the γ parameter and various densities spanning iFPEOS and also perform overlapping KS and OF calculations for T point in the region of switching from OF to KS in order to verify that results for pressure and energy agree to within 1% between the two methods.

Finally, nuclear quantum effects (NQE's) are accounted for via path-integral molecular dynamics (PIMD) calculations.⁸ Since PIMD calculations are much more computationally demanding, they are performed for only select ρ - T points for conditions in which NQE's are relevant. Results have been compared to those from classical MD and applied to the full iFPEOS as NQE's corrections. For computational details regarding KS, OF, and PIMD calculations, see Secs. III and IV in Ref. 9.

We compare iFPEOS to the latest results from experimental measurements of shock-compressed D, reporting principal and reshock Hugoniot¹⁰ and sound speed along the principal Hugoniot.¹¹ We performed an extra calculation at initial density $\rho_0 = 0.173 \text{ g/cm}^3$, $T = 19 \text{ K}$ so that initial conditions for solving the Rankine–Hugoniot equations are consistent with those reported in Ref. 10. The main conclusions from comparing the iFPEOS principal Hugoniot to experiment and other models is that iFPEOS provides an improvement in accuracy in the low-pressure ($P < 200 \text{ GPa}$), low- T regime ($T < 60,000 \text{ K}$), but at higher pressure and temperatures, the iFPEOS Hugoniot joins those predicted by other first-principles models that predict significantly lower compressibility [see Fig. 1(a)].



TC15795JR

Figure 1

(a) Pressure versus compression along the principal Hugoniot of shocked D as predicted by iFPEOS and other popular first-principles and chemical EOS models and calculations along with the latest experimental data. (b) Pressure versus compression in reshocked D. Collection of points and curves below compression of 5 is select principal Hugoniot data corresponding to (a). Data above compression of 5 correspond to latest experimental measurements along with various EOS models including iFPEOS reshock Hugoniot launched off of iFPEOS principal Hugoniot (solid green curve) and iFPEOS reshock states launched off of initial states corresponding to the ones reported in Ref. 10 (green circles) and determined via impedance matching with a-quartz. Green circles serve as a more direct comparison with latest experiments (black upright open triangles). (c) Sound speed along the principal Hugoniot as predicted by iFPEOS and other popular EOS models and according to latest experimental measurements. AIMD: *ab initio* molecular dynamics; KDT: Karasiev–Dufty–Trickey; PIMC: path-integral Monte Carlo; VMC: variational Monte Carlo.

Similar trends are seen in comparing iFPEOS reshock Hugoniot to experimental measurements [Fig. 1(b)], where for pressures $P > 600$ GPa, we see 6% to 11% underestimation of the compression in reshocked D. In the low-pressure regime of the reshocked Hugoniot, we see good agreement between different models that are all in good agreement with the latest experimental measurements considering the relatively larger error bars compared to measurements of principal Hugoniot. For $P > 600$ GPa, however, iFPEOS predicts even stiffer (1% to 3%) behavior than other models.

Finally, we compare iFPEOS to experimental measurements and other EOS model predictions of Eulerian sound speed along the principal Hugoniot [Fig. 1(c)]. This comparison further verifies the conclusions reached in Hugoniot comparisons, namely that iFPEOS provides slightly better agreement with experimental data in the low-pressure, low- T regime, but for $P > 200$ -GPa, iFPEOS, as well as other first-principles models, significantly disagrees with experiment by overestimating the sound speed. The excellent agreement with experimental gas-gun measurements at $P < 50$ GPa is expected since this is the region of molecular dissociation, which is accurately captured by the T-SCAN-L+rVV10 functional. The improved agreement with laser-shock

experimental data at $50 < P < 200$ GPa [red diamonds in Fig. 1(c)] is attributed to the improved treatment of XC thermal effects by T-SCAN-L, which are expected to be most important in these particular thermodynamic conditions ($20,000 < T < 80,000$ K).

This material is based upon work supported by the Department of Energy National Nuclear Security Administration under Award Number DE-NA0003856, U.S. National Science Foundation PHY Grant No. 1802964, the University of Rochester, and the New York State Energy Research and Development Authority.

1. S. X. Hu *et al.*, Phys. Rev. B **84**, 224109 (2011).
2. S. X. Hu *et al.*, Phys. Plasmas **22**, 056304 (2015).
3. V. V. Karasiev, D. I. Mihaylov, and S. X. Hu, “Meta-GGA Exchange-Correlation Free Energy Density Functional to Achieve Unprecedented Accuracy for Warm-Dense-Matter Simulations,” submitted to Physical Review Letters.
4. L. Caillabet, S. Mazevet, and P. Loubeyre, Phys. Rev. B **83**, 094101 (2011).
5. V. V. Karasiev, L. Calderín, and S. B. Trickey, Phys. Rev. E **93**, 063207 (2016).
6. J. Hinz *et al.*, Phys. Rev. Research **2**, 032065(R) (2020).
7. K. Luo, V. V. Karasiev, and S. B. Trickey, Phys. Rev. B **101**, 075116 (2020).
8. M. Ceriotti *et al.*, J. Chem. Phys. **133**, 124104 (2010).
9. D. I. Mihaylov *et al.*, Phys. Rev. B **104**, 144104 (2021).
10. A. Fernandez-Pañella *et al.*, Phys. Rev. Lett. **122**, 255702 (2019).
11. D. E. Fratanduono *et al.*, Phys. Plasmas **26**, 012710 (2019).

An X-Ray Penumbra Imager for Measurements of Electron-Temperature Profiles in Inertial Confinement Fusion Implosions on OMEGA

P. J. Adrian,¹ J. A. Frenje,¹ B. Aguirre,² B. Bachmann,³ A. Birkel,¹ M. Gatu Johnson,¹ N. V. Kabadi,¹ B. Lahmann,¹ C. K. Li,¹ O. M. Mannion,⁴ W. Martin,² Z. L. Mohamed,⁴ S. P. Regan,⁴ H. G. Rinderknecht,⁴ B. Scheiner,⁵ M. J. Schmitt,⁵ F. H. Séguin,¹ R. C. Shah,⁴ H. Sio,³ C. Sorce,⁴ G. D. Sutcliffe,¹ and R. D. Petrasso¹

¹Plasma Science and Fusion Center, Massachusetts Institute of Technology

²Sandia National Laboratories

³Lawrence Livermore National Laboratory

⁴Laboratory for Laser Energetics, University of Rochester

⁵Los Alamos National Laboratory

One of the main challenges of inertial confinement fusion is symmetry control of the implosion. Asymmetries reduce implosion performance and generate bulk flows that degrade the conversion of shell kinetic energy into hot-spot thermal energy. Recently, penumbra imaging of hot-spot x-ray emission was used at the National Ignition Facility to simultaneously measure hot-spot shape and temperature to assess asymmetry in different implosion designs,¹ as well as spatially resolve electron temperature to quantify mix-induced radiative cooling.² Penumbra imaging is a coded imaging technique, where a source of size S is imaged with an aperture of radius R_{app} such that $2R_{\text{app}} > S$. This imaging technique is used when signal statistics prevent the use of conventional pinhole imaging ($2R_{\text{app}} \ll S$). Information about spatial distribution of the emitting source is encoded in the penumbra.

We developed and fielded a new penumbra imager at the Omega Laser Facility, with 6- μm resolution, to image x rays in the energy range of 10 to 30 keV. This system is based on the existing penumbra charged-particle imaging system (PCIS).³ Three imagers can be fielded in different ten-inch diagnostic manipulators (TIM's) to study 3-D asymmetries. We record images in different x-ray energy bands using a filtered stack of FujiTM image plates and present a technique to infer the radially dependent electron temperature $T_e(r)$.

The PCIS detectors are TIM-based diagnostics that hold an aperture 4.2 cm from the target chamber center and a detector 59 cm from the aperture, yielding a magnification of ~ 14 . Three types of apertures are used: $1 \times 2000 \mu\text{m}$, $19 \times 400 \mu\text{m}$, or $151 \times 100 \mu\text{m}$ (number of pinholes \times diameter) made from a substrate of 500- μm -thick Ta, 125- μm -thick W, or 125- μm -thick W, respectively. All apertures are circular to less than 3 μm . The detector is an array of FujiTM SR x-ray image plates interspersed with x-ray filters. Each subsequent image plate is sensitive to a higher-energy portion of the x-ray spectrum: typical values for peak sensitivity range from 10- to 30-keV x rays. The image plates are scanned with 25- μm resolution. The spatial resolution of the system at a magnification of 14 is 6 μm and is limited by the combination of detector resolution and x-ray diffraction.

A burn-averaged T_e is extracted from the inferred x-ray spectrum, which is derived from the energy deposited in each penumbra image. The image-plate scanner measures the photostimulated luminescence (PSL), which is related to the energy deposited in the phosphor layer. The PSL recorded in the umbra of the k th image plate is calculated as

$$\text{PSL}_k = \int_0^\infty \frac{\text{IP}_{\text{sen}}(E)}{F_k(t)} \frac{j(E)}{E} T_k(E) dE, \quad (1)$$

where E is the x-ray energy, $IP_{\text{sen}}(E)$ is the image-plate sensitivity in PSL/photon, $F_k(t)$ represents the fading of the image plate when it is scanned t minutes after exposure, $j(E)/E$ is the photon emission in photons/keV, and $T_k(E)$ is the transmission function of all filters in front of the k th image plate. The spectrum is modeled as a single-temperature bremsstrahlung emission $j(E) = A \exp(-E/T_e)$, where A and T_e are the fit variables. The main sources of error in this analysis were due to photon statistics and uncertainty in the fade curve of each image plate.

The source profile is reconstructed from the measured penumbral image using an iterative deconvolution approach based on the Lucy–Richardson algorithm.⁴ On each iteration the source image is convolved with the aperture function and compared against the measured penumbral image using a χ^2 metric. Iterations stop once the reduced χ^2 metric is of the order of unity or lower. For x-ray penumbral imaging, we have found that signal statistics are excellent for x rays in the energy range of 10 to 30 keV for most implosions of interest.

Figure 1 shows [(a),(b)] penumbral images and [(c),(d)] reconstructions from a SiO_2 capsule with 422- μm radius, 2.4- μm shell thickness, gas fill of 10 atm D_2 , 15 atm ^3He , and ~ 0.04 atm T_2 , and imploded with 15.6 kJ of laser energy in a 0.6-ns square pulse. Both reconstructions converged in 100 iterations and show a ring-like structure resulting from the unablated glass shell that surrounds the hot spot.

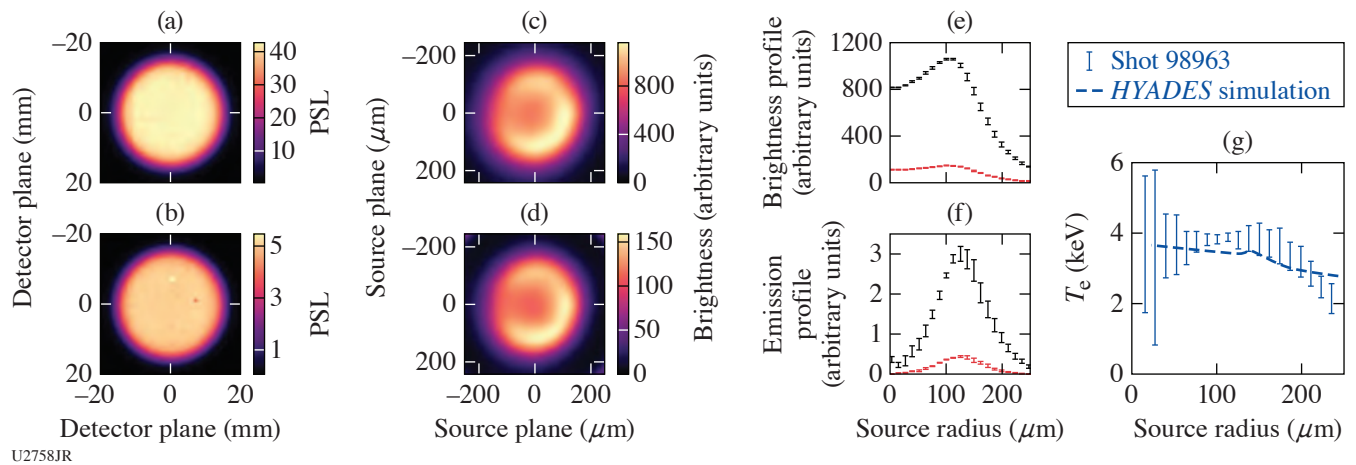


Figure 1

Data from shot 98963. The x-ray penumbral imager used a 1000- μm -radius aperture. (a) Recorded x-ray penumbral image closest to target chamber center (TCC) with 15 μm Ta + 3000 μm CR-39 ($\text{C}_{12}\text{H}_{18}\text{O}_7$) + 100- μm Al filtering. (b) X-ray penumbral image for the image plate farthest from TCC with additional 150- μm Al filtering [(c),(d)]. Reconstructed x-ray emission obtained from (a) and (b), respectively. (e) Azimuthally averaged brightness profiles (chord integrated) from (c) and (d) in black and red, respectively. (f) Radial emission profiles calculated from the surface brightness profiles in (e) via Abel inversion. (g) Measured $T_e(r)$ for shot 98963 (blue error bars). A post-shot *HYADES* simulation is shown (dashed blue line). The simulated T_e is an x-ray emission averaged over the entire implosion time.

From these measurements, the radial profile of T_e is determined. We assume spherical symmetry of the source, which allows us to azimuthally average the reconstructed x-ray images to get the brightness profile shown in Fig. 1(e). The errors in the brightness profiles are determined from the azimuthal variation in each radial bin. To extract $T_e(r)$, we calculate the radial emission from the brightness profiles by an inverse Abel transform [Fig. 1(f)]. We use a discrete version of the Abel transform proposed by Yoshikawa and Suto.⁵

The relative amplitude of the radial emission profiles is used to infer T_e in each radial bin by using Eq. (1) and filtering of the two images. A post-shot simulation of this implosion was performed using the *HYADES* 1-D radiation-hydrodynamics code,⁶ and the emission-averaged $T_e(r)$ is shown in Fig. 1(g) for comparison. The measured $T_e(r)$ agrees with the simulation. The average uncertainty in $T_e(r)$ is 10%. The best inference of the temperature is where the most x-ray emission occurs. However, there are

large uncertainties at small radii due to low levels of emission occurring at those small radii. In the future, this technique will be extended to utilize three simultaneous lines of sight to reconstruct 3-D maps of electron temperature.

This material is based upon work supported by the Department of Energy National Nuclear Security Administration under Award Number DE-NA0003856, the University of Rochester, and the New York State Energy Research and Development Authority.

1. B. Bachmann *et al.*, Rev. Sci. Instrum. **87**, 11E201 (2016).
2. B. Bachmann *et al.*, Phys. Rev. E **101**, 033205 (2020).
3. F. H. Séguin *et al.*, Rev. Sci. Instrum. **75**, 3520 (2004).
4. W. H. Richardson, J. Opt. Soc. Am. **62**, 55 (1972).
5. K. Yoshikawa and Y. Suto, Astrophys. J. **513**, 549 (1999).
6. J. T. Larsen and S. M. Lane, J. Quant. Spectrosc. Radiat. Transf. **51**, 179 (1994).

Advanced Laser Development and Plasma-Physics Studies on the Multi-Terawatt Laser

I. A. Begishev,¹ V. Bagnoud,² S.-W. Bahk,¹ W. A. Bittle,¹ G. Brent,¹ R. Cuffney,¹ C. Dorrer,¹ D. H. Froula,¹ D. Haberberger,¹
C. Mileham,¹ P. M. Nilson,¹ A. V. Okishev,^{1,†} J. L. Shaw,¹ M. J. Shoup III,¹ C. R. Stillman,^{1,3} C. Stoeckl,¹ D. Turnbull,¹
B. Wager,¹ J. D. Zuegel,¹ and J. Bromage¹

¹Laboratory for Laser Energetics, University of Rochester

²GSI - Helmholtzzentrum für Schwerionenforschung GmbH, Germany

³Image Science, Space and Airborne System, L3Harris Technologies

[†]Deceased

The Multi-Terawatt (MTW) laser, built initially as the prototype front end for a petawatt laser system, is a 1053-nm hybrid system with gain from optical parametric chirped-pulse amplification (OPCPA) and Nd:glass. Compressors and target chambers were added, making MTW a complete laser facility (output energy up to 120 J, pulse duration from 20 fs to 2.8 ns) for studying high-energy-density physics and developing short-pulse laser technologies and target diagnostics. Further extensions of the laser support the ultrahigh-intensity laser development of an all-OPCPA system and a Raman plasma amplifier.

Fundamental research in high-energy-density physics¹ and materials science² has accelerated the development of kilojoule and megajoule lasers;^{3–9} however, the deployment of these lasers is limited because of the cost and complexity of construction and operation. The low repetition rates (typically a few shots per day) hinders the mapping of large parameter spaces and statistical averaging. Midscale lasers producing hundreds of joules with subpetawatt peak power provide more flexibility and user access at higher repetition rates. Lasers at this scale enable technologies to be developed and tested before they are implemented on large-scale facilities. They also serve as experimental platforms for scientific research in their own right.

This summary describes LLE's MTW laser, a midscale laser system built initially as the prototype front end for OMEGA EP.⁴ Currently, MTW operates at 1053 nm, where gain is provided by a combination of optical parametric amplification in nonlinear crystals and laser amplification in neodymium-doped glass. A pulse compressor and three target chambers have been added, making MTW a complete facility for plasma-physics research and laser science, as well as a development platform for laser technologies, large-area damage tests, and target diagnostics. MTW is also open for external users to conduct experiments.

Separate broadband and narrowband front ends produce synchronized nanosecond pulses for the OPCPA seed and pump, respectively. The narrowband pulse is amplified in three Nd:YLF amplifiers and frequency doubled before it pumps the OPCPA crystals. The resulting broadband signal pulse is further amplified in two Nd:glass amplifiers. After the picosecond compressor, pulses can be directed to the spherical target chamber (STC), the cylindrical target chamber (CTC), or the underdense plasma (UDP) chamber. As an option, the picosecond compressor can be bypassed to allow nanosecond pulses to propagate directly to each target chamber.

MTW can also be configured in a narrowband mode. In this case, the output of the Nd:YLF amplifiers goes directly to the Nd:glass amplifiers. This mode is mainly used to pump the final stage of an ultra-broadband optical parametric amplifier line (OPAL) after second-harmonic generation. It supports the generation of >10-J, >140-nm pulses,¹⁰ which are compressed in the femtosecond compressor and delivered to the UDP chamber. Table I summarizes the range of parameters and applications of the broadband and narrowband modes of operation for the MTW Laser System. A general view of the MTW Laser System from the end of the system shows the picosecond grating compressor chamber (ps-GCC), the STC, and the CTC (Fig. 1).

Table I: Parameters and main applications of the MTW laser.

Mode	Application	λ (nm)	E (J)	τ (ps)
Broadband	Large-area damage tests	1053	120	2400
	High-energy-density physics, x-ray and neutron diagnostics	1053, 527	35 to 50	0.5 to 100
	Raman plasma amplification	1053, 527	35 to 40	0.5 to 100
	Ultrafast streak-camera development	1053, 264	0.1 (5 Hz)	0.5 to 100
Narrowband	Pump for all OPCPA lasers	527	50	1600
	5ω generation development	527, 263, 211	1.2 (5 Hz)	1000 to 2800

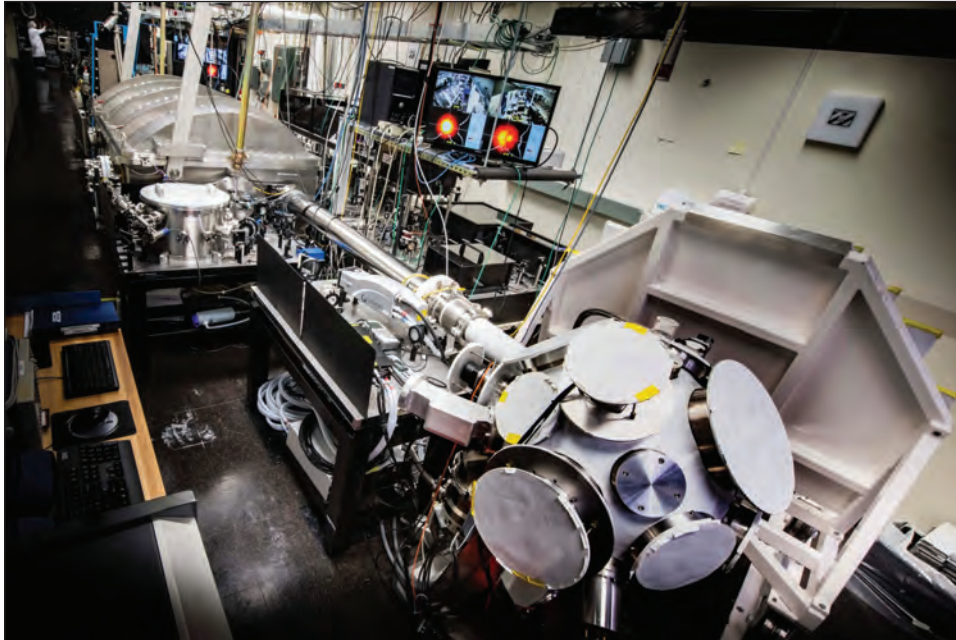


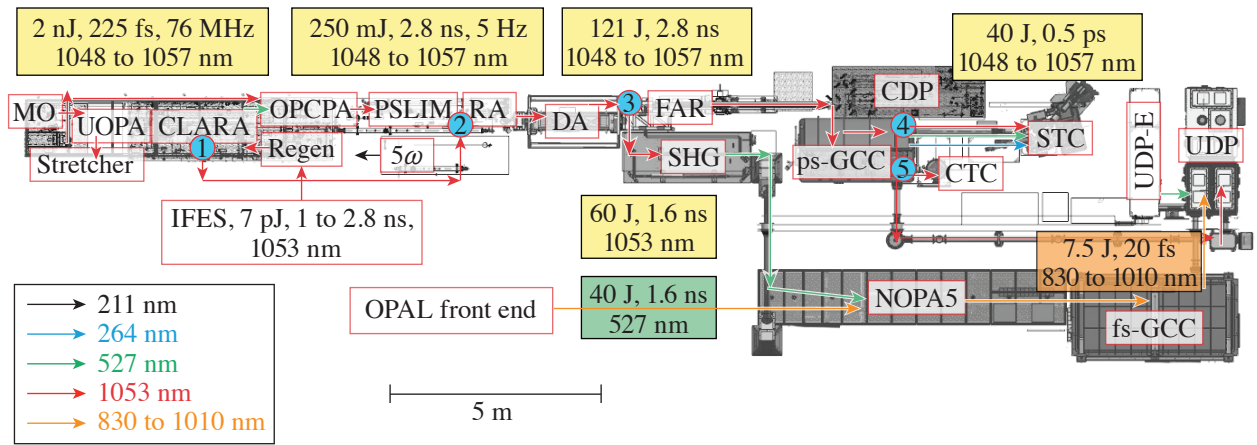
Figure 1
General view of the MTW Laser System from the spherical target chamber side.

G13292JR

A detailed layout of the MTW laser is shown in Fig. 2. Depending on the desired operation mode, switchyards (SY's) 1 to 5 (indicated as blue circles) using mirrors on kinematic or translation stages send beams along different paths. The broadband front end consists of a commercial femtosecond master oscillator, an ultrafast optical parametric amplifier (UOPA) for increased temporal contrast, and a pulse stretcher. The narrowband front end includes a pulse-shaping system,¹¹ a diode-pumped regenerative amplifier (regen),¹² and a crystal large-aperture ring amplifier (CLARA),¹³ all operating at 1053 nm. The amplified narrowband beam is frequency converted to the second harmonic to pump the OPCPA stages,¹⁴ which are seeded by the broadband front end. The UOPA provides approximately four-orders-of-magnitude energy amplification while restricting the associated parametric fluorescence to a few picoseconds around the output pulse.¹⁵ This makes it possible to reduce the required gain in the OPCPA stages, where the pump pulse has a duration of a few nanoseconds, and therefore significantly reduces the level of contrast degradation resulting from nanosecond fluorescence.

The OPCPA output signal beam is shaped by a programmable spatial light modulator (PSLIM) and amplified in a Nd:glass rod amplifier (RA) and disk amplifier (DA). The pulse is then compressed in the ps-GCC and can be delivered to one of three target chambers. For solid-target experiments, the STC or CTC are typically used; gas-jet and gas-cell experiments are conducted in the UDP chamber.

In the narrowband operation mode, the switchyard mirrors send the CLARA output beam directly for amplification by the RA and DA. To pump the final noncollinear optical parametric amplifier for the OPAL system, switchyard 3 is used to send the pulse



G12322JR

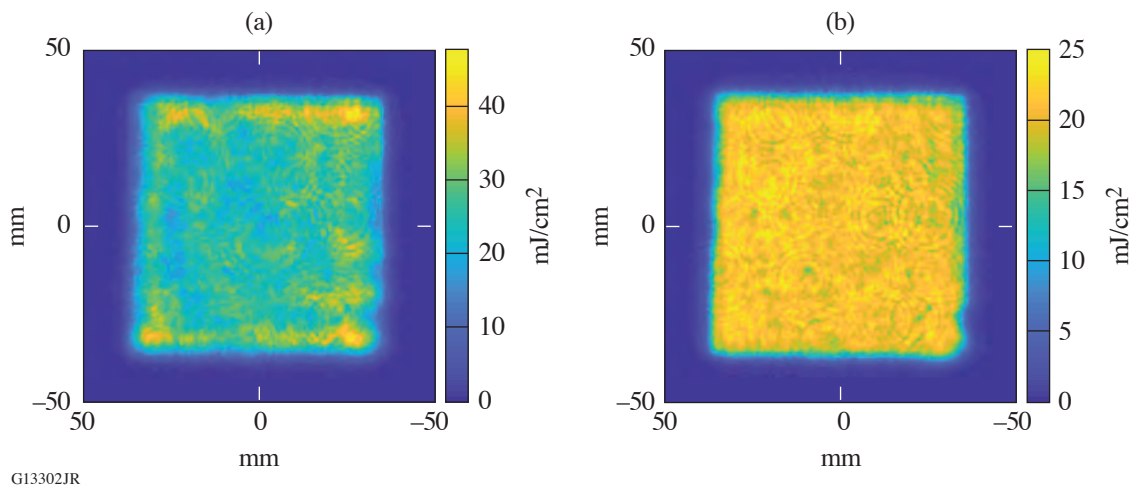
Figure 2

MTW laser layout. MO: master oscillator; IFES: integrated front-end system; 5ω : fifth-harmonic-generation table; FAR: Faraday isolator; CDP: compressor diagnostics package; NOPA5: the fifth nonlinear optical parametric amplifier stage; UDP-E: UDP laser; 1–5: switchyards.

to the second-harmonic-generation (SHG) table before propagating to the OPAL area. Here it is overlapped in time and space at the OPCPA crystal with the ultra-broadband seed pulse from the OPAL front end.¹⁰ The amplified signal pulse is compressed in the femtosecond grating compressor chamber (fs-GCC) and sent to the UDP chamber.

The narrowband mode has also been used to develop technologies for the fifth-harmonic generation of joule-class, near-infrared pulses. For this, the CLARA output can be sent with or without amplification in the RA to the 5ω table, where several studies using cascades of nonlinear crystals have been performed.^{16,17}

The gain nonuniformity of the RA can be precompensated by PSLIM.¹⁸ Figure 3(a) shows the profile of the MTW output beam when the PSLIM is bypassed. Figure 3(b) shows that PSLIM can correct the mode to a flat, near-uniform beam profile. The high performance in the uniformity is the result of closed-loop operation of the PSLIM algorithm.



G13302JR

Figure 3

Rod amplifier beam profiles measured at the plane equivalent to the last hit of the beam on the grating in the compressor (a) without and (b) with PSLIM correction.

The on-shot MTW output energy is measured using pickoff calorimeters, which are cross-calibrated with a large-aperture calorimeter that covers a large energy range (1.5 J to 1000 J). Figure 4 demonstrates the MTW energy map at different voltages for the RA and DA. Curves show the increase in output energy versus RA input energy for different RA and DA voltages. Each point has a shot number, energy density, and peak-to-mean beam modulation.

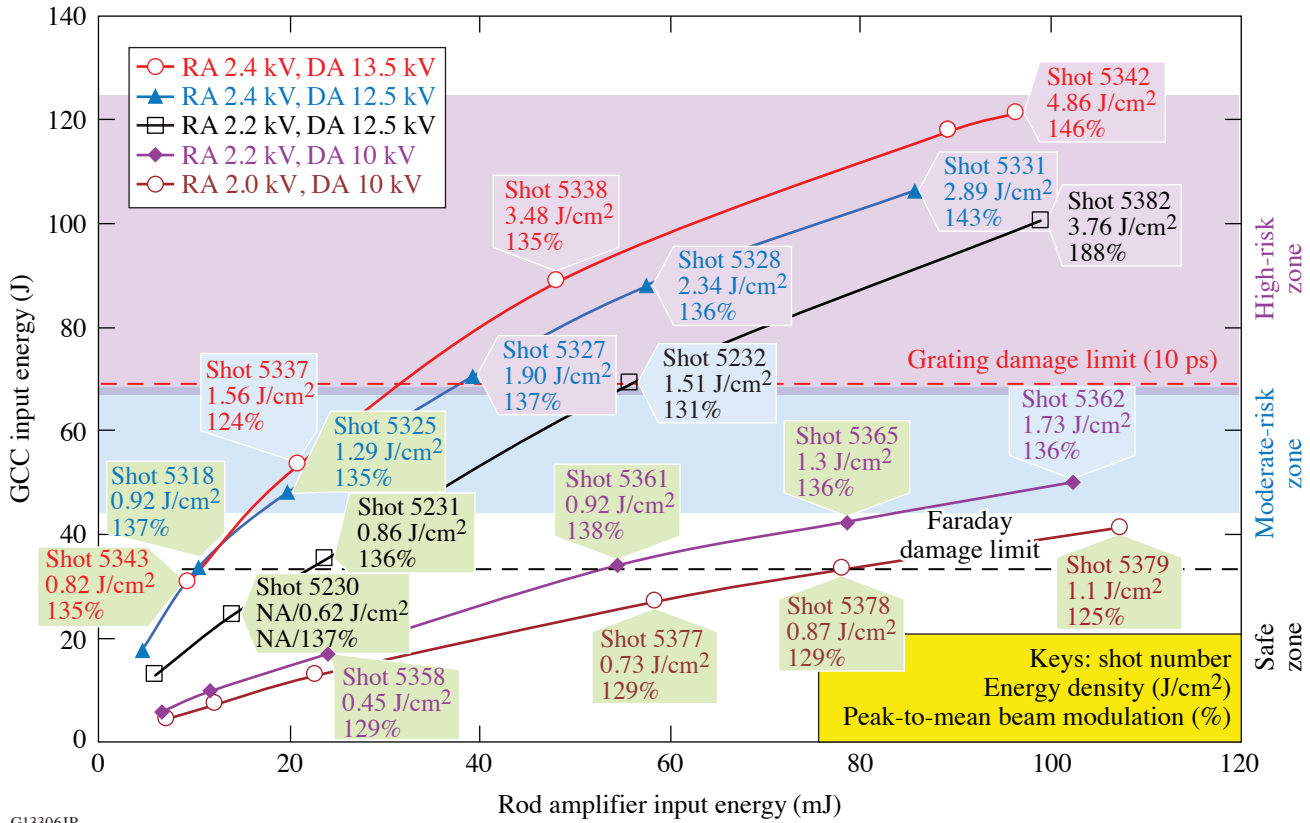


Figure 4 MTW output energy for a range of RA input energies and operating voltages for the rod and disk amplifiers. Dashed lines are damage limits imposed by the final Faraday isolator and the gratings for 10-ps pulses.

The beam propagating to the GCC and on toward the CTC and STC has two major limitations in energy; these limitations arise from the Faraday isolator and the gratings used in the compressor. The 50-J limit is set by the terbium glass damage threshold of 2 J/cm². The energy range below 50 J is shown in Fig. 4 as the safe zone (no shading). Because the Faraday isolator is installed before the compressor in the stretched pulse, the isolator energy limitation does not depend on the pulse duration after the compressor.

The second energy limitation is set by the damage threshold of compressor gratings, where the last hit on G1/G4 dominates. This limit does depend on the pulse duration; for example, at 10 ps, the measured damage threshold is 1.7 J/cm², which corresponds to the limit of output energy of 85 J. In practice, safe operation must also consider beam modulation and a safety factor of 20%, which results in a maximum energy on the final grating of approximately 70 J. The zone between 50 J and 70 J is the moderate-risk zone (blue shading), while above 70 J is the high-risk zone (purple shading). The energy on target for a 10-ps pulse is typically kept below 36 J and below 18 J for the best compression at 500 fs.

The maximum energy produced by MTW is 120 J. This is acceptable for the all-OPCPA beam path because SY3 (Fig. 2) picks the full energy beam before the last Faraday isolator.

The stretcher varies the MTW pulse duration and the sign of the chirp. A second-order scanning autocorrelator (SAC) is routinely used with the 5-Hz OPCPA beam prior to full-energy shots to measure the pulse autocorrelation width with subpicosecond precision, covering a range up to 100 ps. An autocorrelation trace of the shortest pulse is shown in Fig. 5(a) and has 497 fs at FWHM, which corresponds to a pulse duration of ~ 369 fs. It is shown along with a simulated autocorrelation function calculated for a transform-limited pulse based on the OPCPA's output spectrum. Both autocorrelation traces overlap well with only a 4.8% mismatch between the FWHM's.

TESSA, a time-expanded single-shot autocorrelator, is required to measure picosecond pulses when the Nd:glass amplifiers are used. It has a limit of 40 ps set by the clear aperture of the noncollinear autocorrelation crystal. Figure 5(b) shows a typical series (not taken at best compression) of single-shot autocorrelation traces, which demonstrates a highly stable operation of the MTW laser.

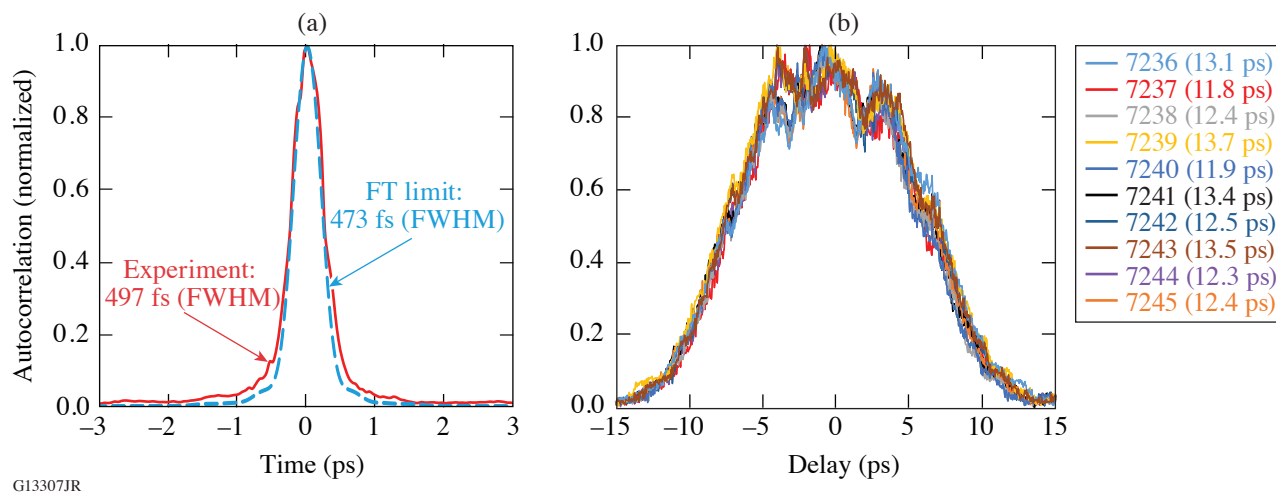


Figure 5

(a) The measured best-compression autocorrelation function and the simulated corresponding autocorrelation function calculated for a transform-limited pulse based on the OPCPA's output spectrum. (b) Single-shot autocorrelation traces taken by TESSA in a series of full-energy, not-the-best compression MTW shots.

To measure relatively long compressed pulses, a high-bandwidth 55-GHz photodiode and a 45-GHz oscilloscope are used. The duration of the resulting impulse response at 1053 nm is 17 ps, which overlaps with short compressed pulse diagnostics based on second-order autocorrelations. The real-time oscilloscope allows for single-shot acquisition; therefore, the diagnostic can be used on high-energy shots. The gain narrowing in the RA and the DA modifies the spectrum of the MTW beam. The changes on the spectrum and, therefore, on the recompressed pulse duration depend on the voltage from each amplifier and OPCPA output energy. Figure 6 shows pulse durations after the picosecond compressor measured with different diagnostics, depending on the stretcher translation stage position referenced to its position for best compression.

The nonlinear cross-correlator provides MTW temporal contrast information with high temporal resolution over an ~ 200 -ps temporal window [Fig. 7(a)], while the high-contrast photodiode provides single-shot contrast information over a much larger temporal window with resolution limited by the bandwidth of the photodetector and oscilloscope, approximately 200 ps [Figs. 7(b) and 7(c)].

The focal spot of the MTW output beam is measured at the focus of the $f/2$ off-axis parabola in the center of the STC using a 12-bit camera and a $10\times$ objective microscope. An attenuation of 10^6 is achieved using two 0.1% leaky wedged mirrors installed in an "antiparallel" configuration inside the GCC. Additional attenuation is provided using neutral-density filters. A typical focal spot is shown in Fig. 8(a) and has a slightly elliptical shape with major and minor axes widths of $6\ \mu\text{m}$ and $5\ \mu\text{m}$, respectively; 85% of the energy is contained in a circle with a $5\text{-}\mu\text{m}$ radius [Fig. 8(b)].

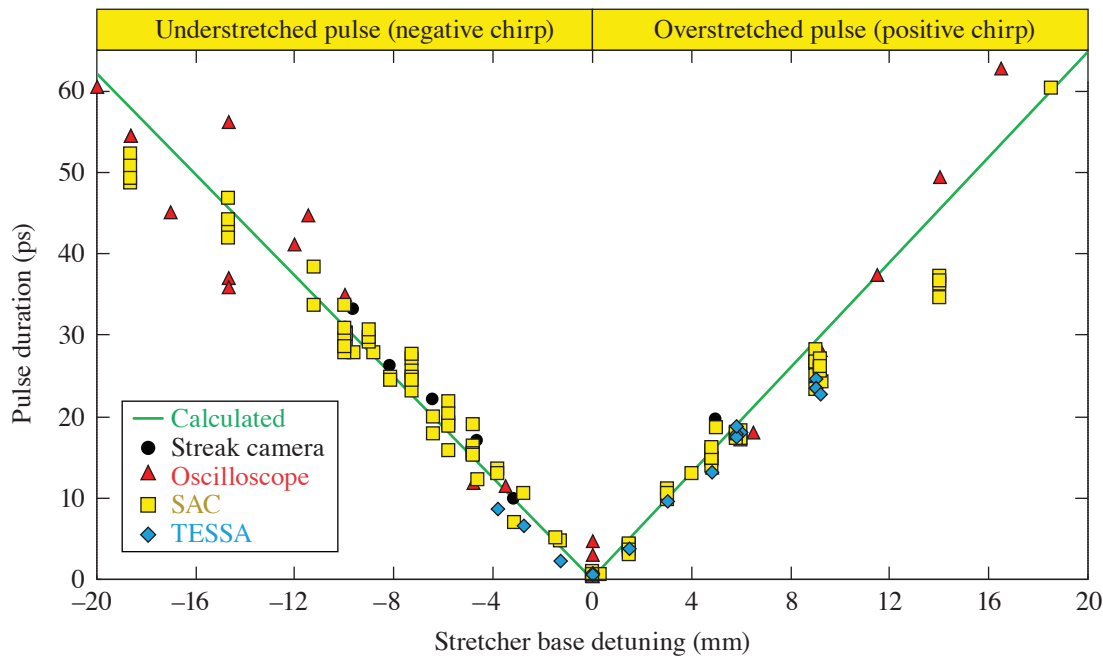
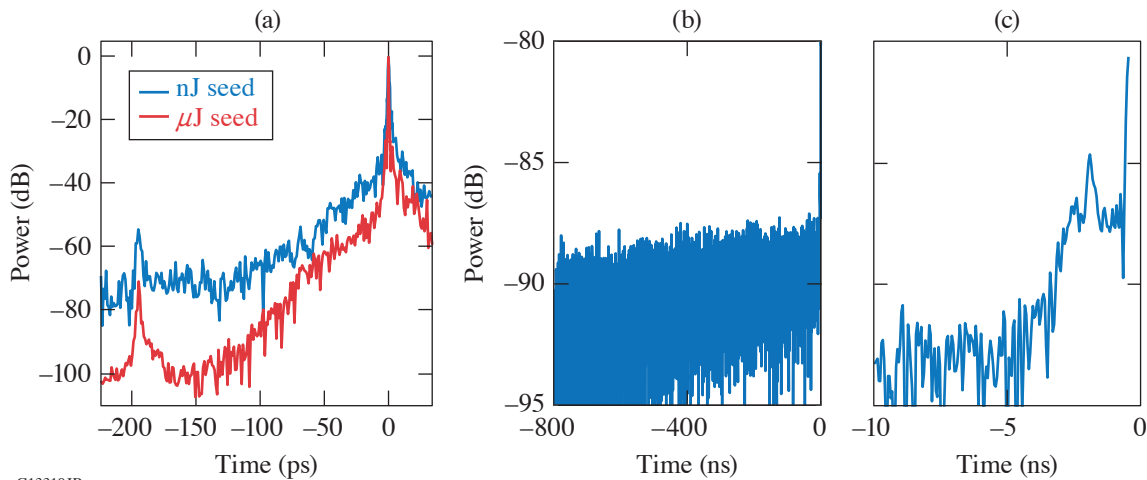


Figure 6
Compressed pulse duration adjustment by the stretcher.

G13309JR



G13310JR

Figure 7
Temporal contrast of the compressed MTW pulse measured with (a) the nonlinear cross-correlator and [(b),(c)] with a photodiode and oscilloscope. In (a), the temporal contrast is shown before and after UOPA deployment.

The MTW wavefront is measured by a wavefront sensor. This measurement requires careful calibration of non-common-path wavefront aberrations in the diagnostic path and a determination of the single-pass contribution through the compressor. A typical MTW wavefront for a single pass through the GCC is shown in Fig. 9 and has a peak-to-valley (p-v) variation of 0.15λ over 98% of the MTW beam.

The main applications of the MTW laser include high-energy-density science,^{19,20} x-ray spectrometers,²¹ neutron diagnostic development,²² and “flying focus”—a concept where the combination of temporal chirp and longitudinal chromatic aberration

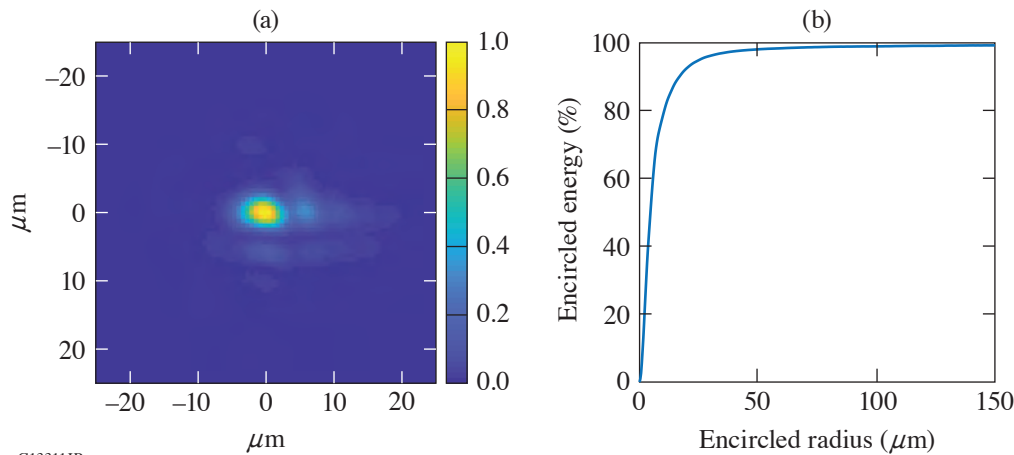


Figure 8
Focal spot of an MTW beam.

G13311JR

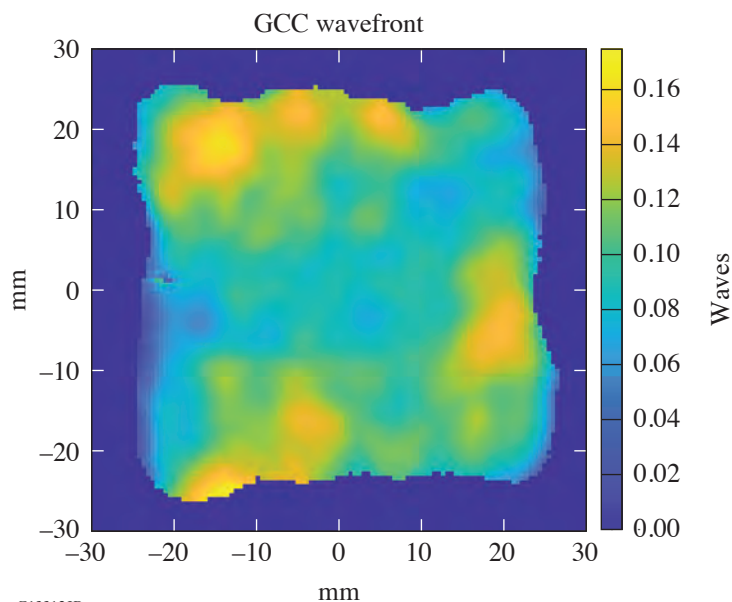


Figure 9
MTW output wavefront, with a 0.15λ (p-v) modulation.

G13312JR

provides unprecedented spatiotemporal control over the velocity of a high-intensity focal spot over distances far exceeding the Rayleigh length.²³ Efforts are underway to use MTW for parametric amplification; using stimulated Raman scattering in a plasma which could be an enabling technology in the generation of ultrahigh-power laser pulses.²⁴

Many experiments on MTW require wavelengths different from the 1053-nm fundamental. For example, picosecond time-resolved measurements of dense plasma line shifts²⁵ require the second harmonic. Timing calibration of x-ray streak cameras requires short subpicosecond pulses in the deep-UV region. Fifth-harmonic generation is necessary for many plasma diagnostics.^{26,27} To satisfy these requirements and to increase the temporal contrast of compressed pulses,²⁸ the MTW output beam can be converted into the second, fourth, and fifth harmonics.

MTW was built based on the most-recent laser technologies and continues to develop novel ideas in laser science and engineering while also providing a flexible platform for development of frontier laser and plasma diagnostics.

This material is based upon work supported by the Department of Energy National Nuclear Security Administration under Award Number DE-NA0003856, the University of Rochester, and the New York State Energy Research and Development Authority.

1. S. Gales *et al.*, Rep. Prog. Phys. **81**, 094301 (2018).
2. A. L. Kritcher *et al.*, Nature **584**, 51 (2020).
3. G. H. Miller, E. I. Moses, and C. R. Wuest, Opt. Eng. **43**, 2841 (2004).
4. J. H. Kelly *et al.*, J. Phys. IV France **133**, 75 (2006).
5. J. Ebrardt and J. M. Chaput, J. Phys.: Conf. Ser. **244**, 032017 (2010).
6. C. N. Danson *et al.*, Nucl. Fusion **44**, S239 (2004).
7. G. Xu *et al.*, Rev. Laser Eng. **36**, 1172 (2008).
8. V. V. Lozhkarev *et al.*, Laser Phys. Lett. **4**, 421 (2007).
9. C. N. Danson *et al.*, High Power Laser Sci. Eng. **7**, e54 (2019).
10. J. Bromage *et al.*, High Power Laser Sci. Eng. **7**, e4 (2019).
11. J. R. Marciante and J. D. Zuegel, Appl. Opt. **45**, 6798 (2006).
12. A. V. Okishev *et al.*, in Advanced Solid-State Lasers, edited by M. E. Fermann and L. R. Marshall, OSA TOPS Vol. 68 (Optical Society of America, Washington, DC, 2002), pp. 418–422.
13. V. Bagnoud *et al.*, Appl. Opt. **44**, 282 (2005).
14. V. Bagnoud *et al.*, Opt. Lett. **30**, 1843 (2005).
15. C. Dorrer, A. V. Okishev, and J. D. Zuegel, Opt. Lett. **32**, 2143 (2007).
16. I. A. Begishev *et al.*, Opt. Lett. **43**, 2462 (2018).
17. I. A. Begishev *et al.*, Opt. Express **29**, 1879 (2021).
18. S.-W. Bahk, I. A. Begishev, and J. D. Zuegel, Opt. Commun. **333**, 45 (2014).
19. P. M. Nilson *et al.*, J. Phys. B: At. Mol. Opt. Phys. **48**, 224001 (2015).
20. M. Storm *et al.*, Rev. Sci. Instrum. **79**, 10F503 (2008).
21. C. R. Stillman *et al.*, Rev. Sci. Instrum. **87**, 11E312 (2016).
22. C. Stoeckl *et al.*, Rev. Sci. Instrum. **87**, 053501 (2016).
23. D. H. Froula *et al.*, Nat. Photonics **12**, 262 (2018).
24. D. Turnbull *et al.*, Plasma Phys. Control. Fusion **61**, 014022 (2019).
25. C. R. Stillman *et al.*, Phys. Rev. E. **95**, 063204 (2017).
26. J. S. Ross *et al.*, Rev. Sci. Instrum. **81**, 10D523 (2010).
27. V. V. Ivanov, A. A. Anderson, and I. A. Begishev, Appl. Opt. **55**, 498 (2016).
28. D. Hillier *et al.*, Appl. Opt. **52**, 4258 (2013).

Analytic Phase Solutions of Three-Wave Interactions

S.-W. Bahk

Laboratory for Laser Energetics, University of Rochester

Analytic solutions for three- and four-wave nonlinear interactions have long been available since the very early discussion of this phenomena.¹ The original approach provided amplitude and relative phase solutions as well as a general methodology based on utilizing constants of motion. The conservation laws involving the total and relative powers and relative phase between these waves provide an efficient way of solving the coupled-wave equations. The phase solution provided by Ref. 1 is the relative phase solution between interacting waves, but *no closed-form phase solution of an individual wave* has been presented over the last six decades. Smith and Bowers have shown that one of the interacting waves that starts from zero intensity always develops a phase that is linearly proportional to wave-vector mismatch.² Buchvarov *et al.* derived phase solutions by approximating the intensity solutions using an approximate form of the elliptic sinus function.³ Marhic found analytic phase solutions for four-wave interactions but did not extend the work to three-wave mixing.⁴ Ross *et al.* found phase solutions under nondepleted pump assumption.⁵ The authors also provided the integral form of the phase solution as a function of pump depletion in a pump-depletion regime.⁶ A survey of these works reveals that complete analytic phase solutions for three-wave mixing have not been previously published, while the necessity of the phase solutions has been mostly addressed by numerical methods.⁷ In this summary, analytic phase solutions are shown to exist for three-wave mixing, expressible using standard mathematical functions. The solution provided by Ross *et al.*⁶ does not explicitly show the functional dependence of phase on the wave-vector mismatch, Δk . It rather shows a linear dependence of Δk with residual terms hidden in the integral. The integral also does not provide an advantage in calculation speed over a direct numerical integration of differential equations.

Despite the availability of numerical approaches for directly solving differential equations with a minimum number of approximations, analytic solutions are still powerful tools in calculating optical parametric chirped-pulse-amplification (OPCPA) performance where the group delay and walk-off terms are often negligible. The temporal slice or the corresponding frequency slice of a stretched signal pulse interacts with the concurrent portion of the pump pulse, independent of other frequency slices. The local approximation approach allows one to apply analytic solutions at each wavelength slice. This computational efficiency allows for fast estimation and optimization of the phase performance in the amplified signal beam. Phase performance is becoming increasingly important in ultra-broadband, large-scale OPCPA systems since they are associated with the performance of pulse compression and focusing.

The equations for three interacting waves inside a second-order nonlinear medium in a normalized electric field (E') unit are written as

$$\frac{dE'_s}{dz} = iE'_i{}^* E'_p \exp(-i\Delta kz), \quad \frac{dE'_i}{dz} = iE'_s{}^* E'_p \exp(-i\Delta kz), \quad \frac{dE'_p}{dz} = iE'_s E'_i \exp(i\Delta kz),$$

where the subscripts s, i, and p indicate signal, idler, and pump fields. The z axis is defined to be normal to the crystal surface and Δk is measured along the z axis, i.e., $\Delta k = k_{s,z} + k_{i,z} - k_{p,z}$. Normalized electric fields are defined as

$$E'_s = \frac{d}{c} \sqrt{\frac{\omega_i \omega_p}{n_i n_p}} E_s = \sqrt{u} \exp(i\phi_s), \quad E'_i = \frac{d}{c} \sqrt{\frac{\omega_s \omega_p}{n_s n_p}} E_i = \sqrt{v} \exp(i\phi_i), \quad E'_p = \frac{d}{c} \sqrt{\frac{\omega_s \omega_i}{n_s n_i}} E_p = \sqrt{w} \exp(i\phi_p).$$

The constants d and c are the second-order effective nonlinear coefficient and speed of light. It can be shown that there are four constants of motion: $p = u + w$, $q = v + w$, $r = u - v$, and $s = \sqrt{uvw} \cos(\Delta kz + \phi_s + \phi_i + \phi_p) - (1/2)\Delta k w_0$. Since these are constants, we can set these values using the initial intensity and phase values, e.g.,

$$p = u_0 + w_0, \quad s = \sqrt{u_0 v_0 w_0} \cos(\phi_{s,0} + \phi_{i,0} - \phi_{p,0}) - \frac{1}{2} \Delta k w_0, \text{ etc.}$$

The 0 subscript indicates the initial value at $z = 0$.

The solutions in the case of $v_0 = 0$ (no idler input) will be shown here without derivation. This case covers the most-practical case for optical parametric amplification. The intensity solutions are

$$w(z) = w_c - \frac{w_c - w_0}{\text{dn}^2(z/z_d, m)}, \quad u(z) = p - w(z), \quad v(z) = q - w(z),$$

where $z_d = 1/\sqrt{w_c - w_a}$ and $m = (w_b - w_a)/(w_c - w_a)$. The three pump parameters (w_a, w_b, w_c) are calculated as

$$w_a = (1/2)(p' - \sqrt{p'^2 - \Delta k^2 w_0}), \quad w_b = w_0, \quad \text{and} \quad w_c = (1/2)(p' + \sqrt{p'^2 - \Delta k^2 w_0}),$$

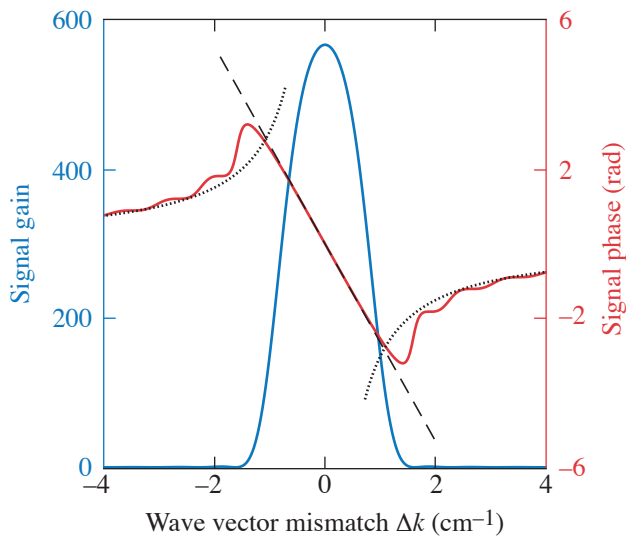
with $p' = p + \Delta k^2/4$. The function dn is one of the Jacobi elliptic functions. The unit of normalized intensity is in (distance unit of z)⁻². The pump depletion distance, which is of the order of z_d , is easily estimated from the initial normalized pump intensity or vice versa.

The phase solutions are

$$\begin{aligned} \phi_s(z) &= \phi_s(0) - \frac{\Delta k}{2} \left(\frac{w_c - w_0}{w_c - p} \right) \left\{ z - z_d \Pi \left[\frac{(w_c - p)}{-u_0} m; \text{am}(z/z_d, m), m \right] \right\}, \\ \phi_i(z) &= \pi/2 - \phi_s(0) + \phi_p(0) - \frac{1}{2} \Delta k z, \\ \phi_p(z) &= \phi_p(0) + \frac{\Delta k}{2} \left(\frac{w_c - w_0}{w_c} \right) \left\{ z - z_d \Pi \left[\frac{w_c}{w_0} m; \text{am}(z/z_d, m), m \right] \right\}. \end{aligned} \quad (1)$$

Here, $\Pi(\dots)$ and $\text{am}(\dots)$ are an elliptic integral of the third kind and the Jacobi amplitude function, respectively.

The signal gain $[u(z)/u(0)]$ and phase plots are shown in Fig. 1 for a 6.8-cm KDP crystal with its c axis oriented at 41.06° with respect to the z axis. The initial signal and pump intensities are 1 MW/cm^2 at $0.930 \mu\text{m}$ and 1 GW/cm^2 at $0.527 \mu\text{m}$, respectively. The phase plot shows linear behavior within the amplification bandwidth, which can be approximated to $-\Delta k/2 [z - \tanh(\sqrt{w_0} z)/\sqrt{w_0}]$ (dashed line). In the depletion regime for a 20-dB amplifier, $\sqrt{w_0} z \sim 3.68$, so phase in the linear regime can be further approximated to $-0.36 \Delta k z$. Outside the gain bandwidth the phase asymptotically approaches $-w_0 z/\Delta k$ (dotted line). The signal beam in this regime therefore has a pump-beam-intensity-dependent phase profile, which can be used to produce an instantaneous phase profile. This behavior is similar to the cascaded nonlinearity.⁸



G13366JR

Figure 1
Intensity and phase response with respect to wave-vector mismatch Δk .

These results provide convenient tools to estimate the phase performance of an OPA in either spatial or temporal domains. The analytic phase solutions for the case of nonzero idler input and for the case of sum-frequency and second-harmonic generation are discussed in detail in Ref. 9.

This material is based upon work supported by the Department of Energy National Nuclear Security Administration under Award Number DE-NA0003856, the University of Rochester, and the New York State Energy Research and Development Authority.

1. J. A. Armstrong *et al.*, Phys. Rev. **127**, 1918 (1962).
2. A. V. Smith and M. S. Bowers, J. Opt. Soc. Am. B **12**, 49 (1995).
3. I. Buchvarov *et al.*, Opt. Commun. **141**, 173 (1997).
4. M. E. Marhic, J. Opt. Soc. Am. B **30**, 62 (2013).
5. I. N. Ross *et al.*, Opt. Commun. **144**, 125 (1997).
6. I. N. Ross *et al.*, J. Opt. Soc. Am. B **19**, 2945 (2002).
7. I. Jovanovic *et al.*, J. Opt. Soc. Am. B **26**, 1169 (2009).
8. R. DeSalvo *et al.*, Opt. Lett. **17**, 28 (1992).
9. S. W. Bahk, Opt. Lett. **46**, 5368 (2021).

Overcoming Gas-Ionization Limitations with Divided-Pulse Nonlinear Compression. II. Experimental Demonstration

G. W. Jenkins,^{1,2} C. Feng,¹ and J. Bromage^{1,2}

¹Laboratory for Laser Energetics, University of Rochester

²Institute of Optics, University of Rochester

Recent work has pushed self-phase modulation (SPM)-based spectral broadening to higher pulse energies and peak powers in both hollow-core fibers (HCF's)¹ and multipass cells (MPC's).² While these demonstrations have shown that spectral broadening using gas-based SPM can handle very high pulse energies, they also show that the process is limited by gas ionization. SPM-based pulse compressors must therefore employ large-core fibers or large focal spots in the MPC to avoid gas ionization.

This work demonstrates a more-scalable method to improve the energy limits of SPM-based pulse compression: divided-pulse nonlinear compression (DPNLC) (illustrated in Fig. 1). In DPNLC, a high-energy pulse is divided into multiple low-energy pulses that are spectrally broadened, recombined back into a high-energy pulse, and then compressed to a short duration.³ The low-energy pulses have peak intensities below the gas-ionization intensity threshold and can pass through the HCF with high efficiency, while the original high-energy pulse would suffer significant ionization losses.

We demonstrated the advantages of DPNLC by spectrally broadening 1030-nm, 1.2-ps laser pulses in a 300- μ m inner-diam, xenon-filled HCF. Xenon was chosen for its low ionization threshold to make the ionization effects strong. The advantage of

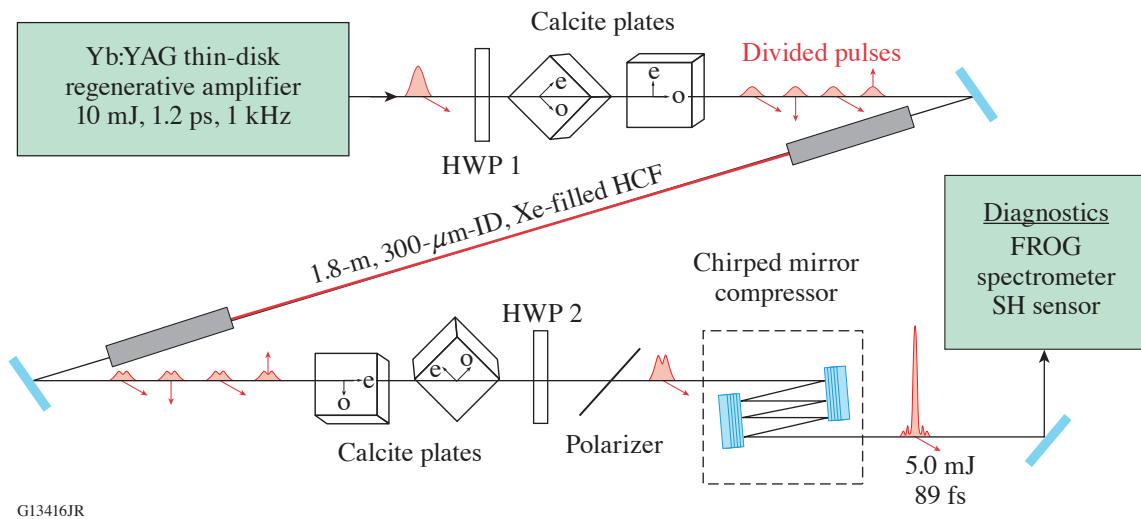


Figure 1

Apparatus for divided-pulse nonlinear compression analyzed in this summary. Birefringent plates with extraordinary axis “e” and ordinary axis “o” are used to divide one pulse into multiple low-energy, orthogonally polarized pulses. Red arrows indicate the pulse’s polarization, and the distorted pulse shape after the SPM stage indicates an arbitrary reshaping by nonlinear processes in the SPM stage. FROG: frequency-resolved optical gating; HWP: half-wave plate; SH: Shack–Hartmann wavefront sensor.

DPNLC was immediately obvious based on the output energy from the HCF, as shown in Fig. 2. We measured a near-constant 67% transmission through the evacuated HCF for all input pulse energies, but once the HCF was filled with xenon, the transmission became a strong function of input energy. Above an input energy of 4 mJ, the xenon started ionizing, reducing the fiber throughput dramatically. HCF is a loosely guiding structure so plasma defocusing after the onset of ionization defocused energy out of the HCF and created large energy losses. Larger input energies did not yield larger output energies beyond exceeding the ionization threshold; the ionization clamped the output to approximately 2 mJ, consistent with previous observations of ionization in HCF.^{1,4} By dividing the input into two pulses, the cumulative energy threshold for ionization nearly doubled and good HCF throughput was measured up to 8-mJ input energy. Finally, by dividing into four pulses, the full 10-mJ pulse energy of our laser can be broadened in the fiber without ionization losses; we measured 6.6-mJ output (four pulses with 1.65 mJ each).

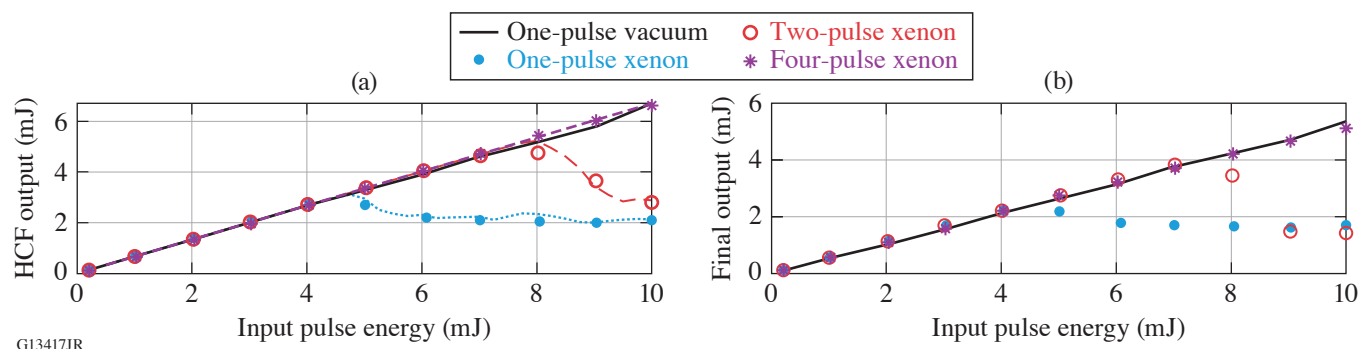


Figure 2

HCF throughput using one, two, and four divided pulses (a) immediately after the HCF and (b) after recombination and compression. Data markers plot the experimentally measured energies and dotted and dashed curves in (a) plot the simulated output energy using the model in our previous work.⁵

After the HCF, the divided and SPM-broadened pulses were recombined using a set of calcite plates identical to the dividing plates. High recombination efficiency was measured. For two pulses, the recombination efficiency was near perfect (>97% limited by the 2.5% polarization reflection on the polarizer) for all energies before the onset of gas ionization. After the onset of ionization, phase artifacts from the gas-plasma mixture prevented good recombination, and we measured losses as great as 50%. For four pulses, recombination efficiency was high for all input energies; we measured only a slow decrease with pulse energy down to 89% efficiency at 10-mJ input. We attribute this decrease to a small misalignment of the first calcite plate.

After recombination, DPNLC produces a high-quality output beam. The measured spectra are significantly broadened and agree with the side-lobed structure produced by SPM-based spectral broadening. The beam profile is high quality, with a measured M^2 of 1.21 and 1.20 along the x and y axes of the beam, respectively. M^2 did not change significantly with pulse energy, or the number of pulse divisions, or ionization plasma effects. We attribute the M^2 invariance to the modal-cleaning properties of the HCF;⁶ only the fundamental mode of the fiber has significant energy at the end of the fiber and the fundamental mode sets the beam profile.

Finally, the recombined pulse was compressed with chirped mirrors to a shorter duration. In the best case (10-mJ input with four-pulse division), the pulse was compressible to 89 fs (FWHM), a compression factor of 13.4 \times . We estimate this pulse has 5.0 mJ of pulse energy at 91% of the transform-limited pulse's peak power. We expect this work will motivate DPNLC for use on higher-energy systems. DPNLC can enable large factors without the need for switching gases or making the system prohibitively large.

This material is based upon work supported by the Department of Energy National Nuclear Security Administration under Award Number DE-NA0003856, the University of Rochester, and the New York State Energy Research and Development Authority.

1. G. Fan *et al.*, Opt. Lett. **46**, 896 (2021).
2. M. Kaumanns *et al.*, Opt. Lett. **46**, 929 (2021).
3. H. Jacqmin *et al.*, J. Opt. Soc. Am. B **32**, 1901 (2015).
4. O. Hort *et al.*, J. Opt. Soc. Am. B **32**, 1055 (2015).
5. G. W. Jenkins, C. Feng, and J. Bromage, Opt. Express **28**, 31,943 (2020).
6. P. Patimisco *et al.*, J. Appl. Phys. **118**, 113102 (2015).

Electric-Field Enhancement Caused by Subwavelength-Sized Particles Located on the Surface of Multilayer Dielectric Mirrors

H. Huang, K. R. P. Kafka, and S. G. Demos

Laboratory for Laser Energetics, University of Rochester

An important factor that limits the output performance of laser systems is the coupling of energy from the laser beam into localized areas of its constituent optical components, which leads to permanent modification of the affected localized regions (commonly referred to as laser-induced damage). There are a number of underlying mechanisms that introduce such localized damage precursors that are typically associated with the introduction of impurities during the manufacturing process, during handling and installation of the optic, or due to contamination during operation. While this problem has been extensively investigated for large-aperture nanosecond laser systems, the impact of particle contamination on the laser-damage performance of short-pulse laser systems has only recently received attention.^{1,2} Whereas most of the optics of concern in nanosecond laser systems are transmissive, optical elements for short-pulse laser systems are typically reflective and are based on metal or multilayer dielectric (MLD) coating designs. A laser pulse impinging on the surface of an optical component can interact with particles, such as contamination debris, to produce a scattered electric field. The coherent superposition of this scattered field with the incident laser field can significantly increase the local field intensity. This effect can be of critical importance because it can reduce the laser-induced-damage threshold of the affected component. To address this issue, a combination of experimental and modeling effort is required to assess the specific features of such contamination particles that pose a high risk for the lifetime and performance of the optics. These features include the size of the particles in combination with their shape and their optical and thermomechanical properties.

In this work, we use a field-propagation code to determine the magnitude and location of the electric-field enhancement arising from the presence of small particles located on the surface of MLD mirrors. In our modeling we consider a steady-state, monochromatic electric-field distribution within the volume of interest. Taking into account the 20 to 30 fs required for fields to propagate throughout the simulated volume, the results are directly applicable to laser pulse durations longer than that time. For shorter pulses, we would need to consider the time-dependent nature of the electric-field distribution. The monochromatic nature of the simulations also neglects potential effects due to broad bandwidths of ultrashort pulses. Here we study the following variables:

- Particle material: transparent dielectric or metal with high reflectivity
- Particle size $\lambda/8$ to 2λ (for laser wavelength λ)
- Particle shape: regular (spherical, cubic, triangular) or irregular
- Region of interest: particle surface, inside the particle, and inside the coating
- Particle density: coherent effects arising from adjacent particles

The model estimates the peak electric-field intensity as a function of the particle size normalized by the incident wavelength. Two particle shapes (rectangle and triangle) and two classes of material optical properties (dielectric/transparent and metal/absorbing) are considered. Figure 1 summarizes the modeling results providing the maximum field intensity values and their general location separated into four general categories: inside the MLD layers, inside the particles, below the surface of the optic (within the MLD layers), and on the surface of the particle. The shape and material optical properties of the particle (such as the reflectance by the particle surface and its absorption properties) govern this interaction. Furthermore, the locations and value of

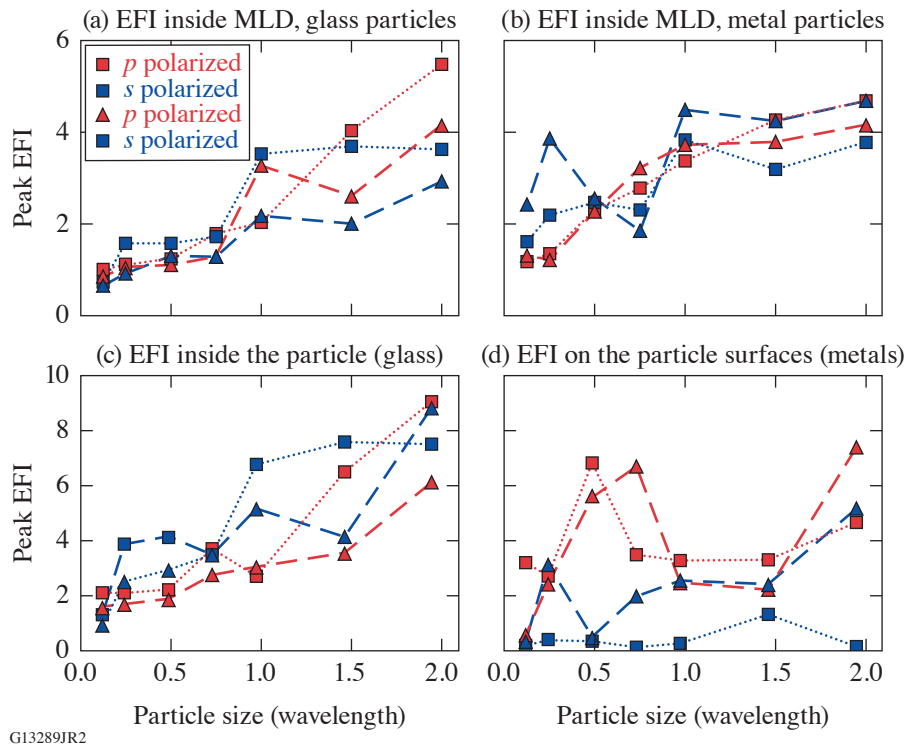


Figure 1

The peak electric-field intensity (EFI) as a function of the ratio between the particle size and the incident wavelength for two particle shapes (rectangle and triangle depicted as solid squares and triangles, respectively) using p -polarized and s -polarized (red and blue shapes, respectively) laser beams inside the MLD for (a) glass and (b) metal particles, (c) inside the bulk for glass, and (d) on the surface for metal particles.

maximum field intensity are indicators of the locations of damage initiation and the corresponding reduction of the laser-damage threshold in the presence of debris particles, respectively.

The results suggest that particle sizes as small as $1/4$ of the laser wavelength can introduce a field enhancement that is higher than that inherent to the coating-design parameters. Such particles would be very difficult to detect after the installation of the optic; therefore, an effective way for detecting particles smaller than wavelength may be needed. Understanding the field enhancement on laser optics caused by contamination particles located on the surface is important in terms of estimating the associated reduction of the laser-induced-damage threshold. On the other hand, understanding of the field enhancement on the particles help understand secondary contamination effects^{1,2} that can also have detrimental effect on the damage resistance of the optic. Although this study is limited by the resolution and the nature of the 2-D modeling, we expect that the general conclusions are still valid. We plan further studies using more advanced modeling capabilities to further study specific cases that are relevant to the performance and lifetime of optics located inside the grating compressor chamber in the OMEGA EP Laser System. Quantitative modeling of this effect provides guidance to determine quality control for fabrication, handling, and maintenance of optics.

This material is based upon work supported by the Department of Energy National Nuclear Security Administration under Award Number DE-NA0003856, the University of Rochester, and the New York State Energy Research and Development Authority.

1. K. R. P. Kafka and S. G. Demos, *Opt. Lett.* **44**, 1844 (2019).
2. K. R. P. Kafka *et al.*, *Opt. Eng.* **60**, 031009 (2020).

Central Density and Low-Mode Perturbation Control of Inertial Confinement Fusion Dynamic Shell Targets

W. Trickey,¹ V. N. Goncharov,^{1,2} I. V. Igumenshchev,¹ A. Shvydky,¹ T. J. B. Collins,¹ and E. M. Campbell¹

¹Laboratory for Laser Energetics, University of Rochester

²Department of Mechanical Engineering, University of Rochester

The dynamic shell is a new class of target in inertial confinement fusion (ICF).¹ ICF targets require a high-density outer shell to contain a fusion burn triggered by the ignition of a central low-density fuel. Traditionally, this outer shell is formed during capsule production by the manufacture of a solid, cryogenic deuterium–tritium (DT) layer. In the dynamic shell target, the high-density outer layer is formed dynamically in-flight via a series of laser pulses that compress the target, allow it to rebound, and then decelerate the expanding plasma, forming a shock that develops into the shell. In this summary, we first consider control of the fuel density in the central region, set by the initial profile of the laser pickets. By controlling the central density, it is possible to modify the convergence ratio (CR) of the implosion. Secondly, we consider how best to minimize low-mode perturbation through the choice of beam-port configuration.

In conventional targets, CR is determined mainly by the implosion velocity and shell adiabat. High convergence ratios require high implosion velocities; such implosions are susceptible to hydrodynamic instabilities formed during the acceleration of the shell. However, CR can additionally be controlled by changing the initial density of the central vapor region. In conventional targets this is limited by the operational temperature range of the DT ice. The dynamic shell target can access a broader range of central densities by controlling the laser pickets. Longer pulses allow for longer periods of expansion and therefore lower central densities. This is plotted in Fig. 1, where two pulses are shown to have a central density range of nearly an order of magnitude, 0.1 to 0.8 mg/cm³.

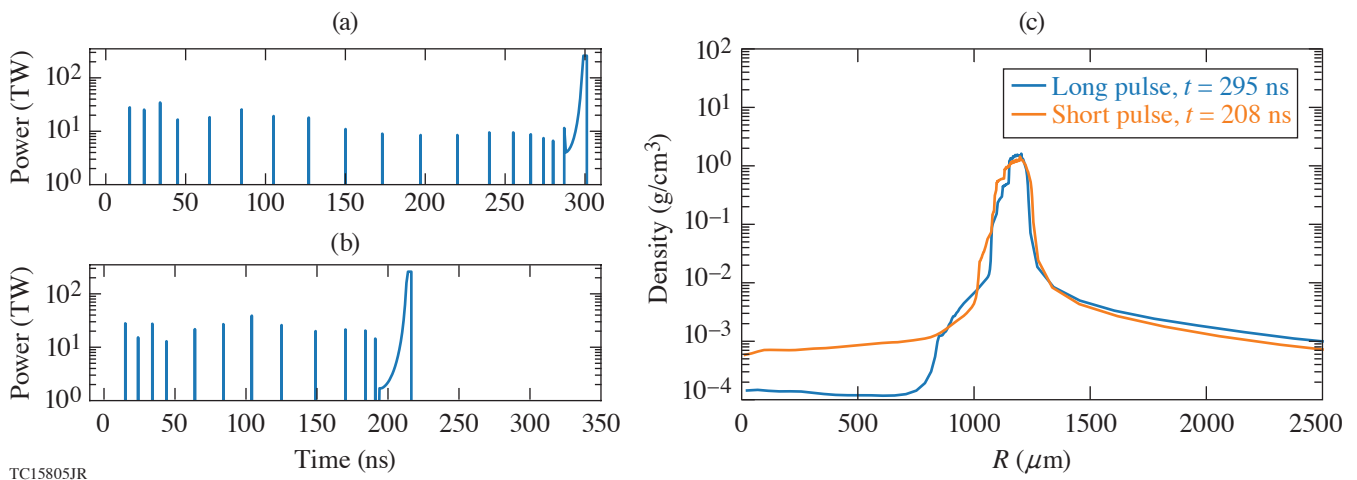


Figure 1

Time profiles of the laser profile for a (a) long- and (b) short-pulse dynamic shell target. (c) The mass-density profiles from a LILAC simulation, taken at the point of shell formation.

In the formation of the dynamic shell, there are three sequences of hydrodynamic implosion, expansion, and implosion again. The long periods involved allow ample time for low-mode ($\ell \leq 20$) perturbations to form, threatening the stability of the shell. Beam-port geometry is a major contributor to these perturbations. Previous work by Murakami *et al.*² has shown that high-performing configurations can be found using a technique where each port is modeled as a charged particle fixed to the surface of a sphere. In a numerical simulation initialized with a random configuration, the particles are allowed to repel up to the point where they reach a minimum Coulomb potential across the surface of a sphere. Using this technique it was found that configurations with certain beam numbers produced “particularly symmetric” configurations, which are observed as sharp drops in the root-mean-square perturbation in Fig. 2.

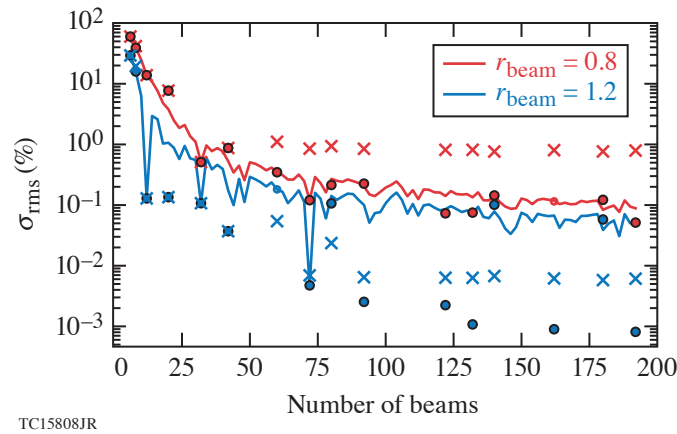


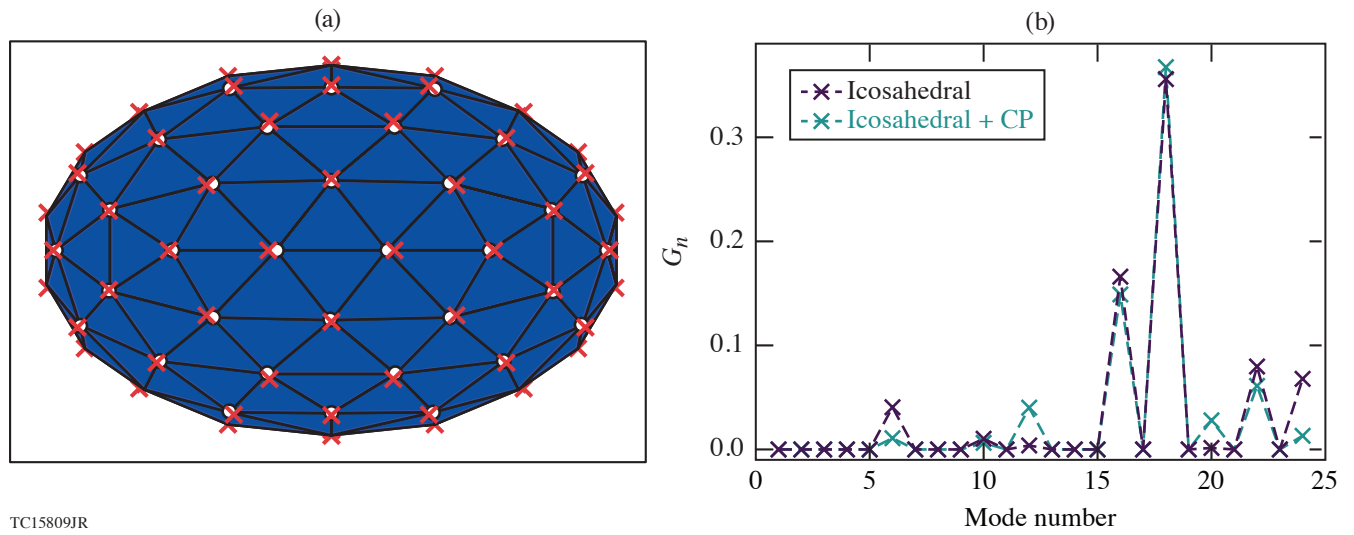
Figure 2

The root-mean-square perturbation as a function of beam number for two sets of super-Gaussian beam parameters. The solid curves show the performance of charged-particle configurations. Icosahedral configurations are shown as 'x's. Icosahedral initialized charged-particle configurations are shown as circles.

In the present work, it is shown that high performance occurs when the charged-simulation naturally tends toward a polyhedral shape, namely the geodesic icosahedron. These icosahedral configurations have a spectral mode structure where the majority of the nonuniformity is supplied by only a select number of modes and all other modes contribute negligible perturbation. This is in contrast to a typical charged-particle configuration that will have similar contributions from all modes up to a dominant beam mode. The main contributing mode in icosahedral configurations is $\ell = 6$; high performance comes when the beam shape suppresses the $\ell = 6$ mode. A further improvement can be made when icosahedral configurations are optimized using a charged-particle simulation. The effect is to reduce the $\ell = 6$ mode while sacrificing increased contribution from other less-significant modes. Different geometries and spectral mode structures of the configurations are shown in Fig. 3. In Fig. 2, it can be seen that the icosahedral configurations optimized with the charged-particle method achieve the lowest nonuniformity of all the configurations.

This material is based upon work supported by the Department of Energy National Nuclear Security Administration under Award Number DE-NA0003856, the University of Rochester, and the New York State Energy Research and Development Authority.

1. V. N. Goncharov *et al.*, Phys. Rev. Lett. **125**, 065001 (2020).
2. M. Murakami and D. Nishi, Matter Radiat. Extremes **2**, 55 (2017).



TC15809JR

Figure 3

Comparisons between icosahedral and icosahedral initialized, charged-particle configurations. (a) The blue surface and white circles show the position of beam ports for a 92-beam icosahedral configuration, the red x's show where the beam ports move under a charged-particle simulation. (b) The change in the geometric factors between the two configurations.

High Yields in Direct-Drive Inertial Confinement Fusion Using Thin-Ice DT Liner Targets

C. A. Williams,^{1,2} R. Betti,^{1,2,3} V. Gopalaswamy,^{2,3} and A. Lees^{2,3}

¹Department of Physics and Astronomy, University of Rochester

²Laboratory for Laser Energetics, University of Rochester

³Department of Mechanical Engineering, University of Rochester

Achieving the thermonuclear instability known as “ignition” in inertial confinement fusion implosions requires high levels of compression and large fusion yields.¹ This summary centers around a new target design—the thin-ice DT liner—that is intended to greatly increase neutron yields from direct-drive implosions on OMEGA.

Nominal OMEGA cryogenic implosions are able to produce implosion velocities v_{imp} within the range of 350 to 450 km/s, which generate ion temperatures ~ 5 keV when the deuterium–tritium (DT) shell stagnates at the target center.² The implosion velocity can be increased to over 650 km/s by driving large-outer-diam targets ($\sim 1010 \mu\text{m}$) with thinner DT ice layers ($\sim 34 \mu\text{m}$), with the target in Fig. 1(a) serving as an example. The implosion velocity scales as

$$v_{\text{imp}} \propto \sqrt{\frac{P_a}{\rho_0} \left(\frac{R_0}{\Delta_0} \right)}, \quad (1)$$

where P_a is the ablation pressure, ρ_0 is the initial density of the shell, R_0 is the initial shell radius, and Δ_0 is the initial shell thickness.³ Therefore, large initial aspect ratios (R_0/Δ_0) allow DT liners to be imploded quickly without increasing laser intensity, which is preferred since intensities above 10^{15} W/cm^2 excite deleterious laser–plasma interactions that reduce laser absorption and limit compression.⁴

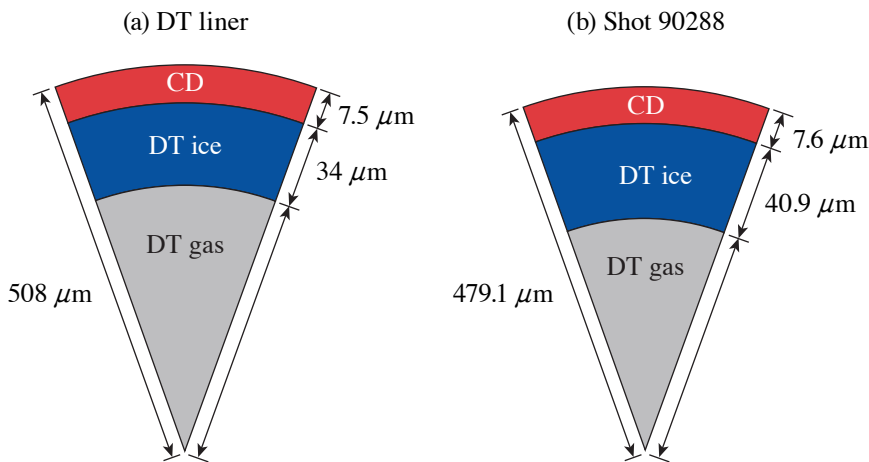


Figure 1
A target geometry comparison between (a) a thin-ice DT liner and (b) the capsule of shot 90288, a more-conventional direct-drive target. Note that the DT liner is 6% larger in diameter, yet, its fuel layer is 17% thinner, which raises v_{imp} according to Eq. (1).

TC15763JR

One-dimensional simulations of DT liners exhibit neutron-averaged ion temperatures just below 9 keV and core temperatures up to 14 keV. These elevated temperatures greatly augment the fusion reaction rate, which leads directly to an increase in fusion yield. Statistical models predict DT liner yields to exceed 3.5×10^{14} fusion reactions when driven with ~ 30 kJ of 351-nm laser light.

Historically, thin and fast implosions are degraded by hydrodynamic instabilities that jeopardize the integrity of the shell during the acceleration phase of the implosion.⁵ Furthermore, the instabilities that grow while the shell accelerates can feed through the shell to its inner surface and perturb it. During deceleration, the inner shell surface is unstable and the seeded perturbations are free to grow, which leads to reduced temperatures and pressures in the stagnating fusion fuel. The designs of this work promote stability during shell acceleration by raising the laser power early in the pulse, as shown in Fig. 2. This causes strong shock waves to travel through the shell, creating entropy and density profiles that are conducive for ablative stabilization of the in-flight shell.⁶ In fact, strong ablative stabilization results in a 25% decrease in the cutoff wave number of DT liners compared to shot 90288, a previous high-performing implosion performed on OMEGA. Due to the high temperature of the hot spot and low density of the confining shell, DT liners benefit greatly from ablative stabilization during deceleration as well.⁷ The temporally shaped pulses presented in this work demonstrate cutoffs in the unstable spectrum at lower modes than nominal implosions; they cut off at $\ell \approx 35$ for DT liners compared to a cutoff at $\ell \approx 45$ for shot 90288. The square pulse shape produces a more-extreme spectrum than the temporally shaped laser pulses; it has its cutoff mode number at $\ell \approx 15$, corresponding to greatly improved deceleration phase stability.

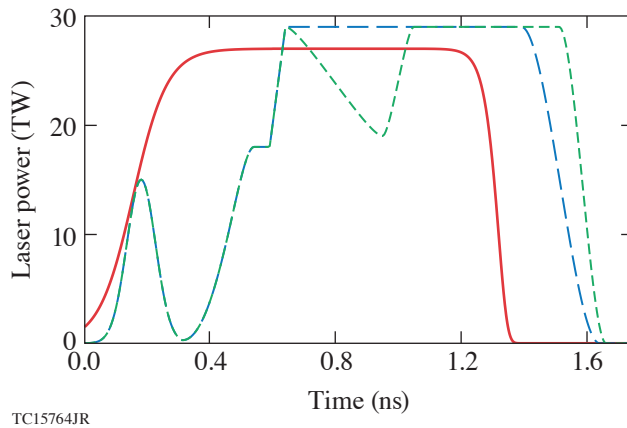


Figure 2

The laser pulse shapes used to irradiate the target described in Fig. 1(a). The laser energy of the square (solid red curve), flattop (long dashed blue curve), and double-spike (short dashed green curve) pulses is 31 kJ each.

Simulations of thin-ice DT liners show them to possess unique properties apart from their ability to produce high yields. For instance, higher mass ablation at the hot spot/cold shell interface during deceleration leads to a substantial accumulation of mass in the hot spot. At the time of peak neutron-production rate (the bang time), roughly 60% of the total areal density comes from the hot-spot plasma, with the remaining 40% provided by the cold tamping shell. In contrast, for high-convergence implosions such as shot 90288, only $\sim 40\%$ of the total areal density comes from the hot spot. The cold shell accounts for the remaining 60%.

The distinction between hot spot and cold shell vanishes as the in-flight shell entropy is increased, a regime easily accessed by using square pulses. Instead of two distinct regions at bang time, the unablated mass is nearly constant density and the temperature gradient becomes smoother, with temperatures above 6 keV persisting up to $25 \mu\text{m}$ from the target center. Implosions of this kind resemble those of volume ignition designs, in which all of the unablated mass acts as a hot spot.

An additional consequence of the thin ice layer in DT liner targets is that by starting with less ice at the beginning of the implosion, most of the fuel mass (up to 70% in the reported designs) has been ablated by bang time. This allows the return shock rebounding off the target origin to pass through almost all of the final fuel mass. Since most of the piston-like compression work is done by the shocked portion of the shell, DT liners act as efficient pistons with very little residual kinetic energy in the unshocked “free-fall” portion of the shell.⁸

The designs for thin-ice DT liner targets show that fusion energies above 1 kJ can be attained with only ~30 kJ of laser energy. If validated experimentally, this would be the first demonstration of capsule gain for an implosion on the 60-beam OMEGA laser, with capsule gain defined as the ratio of fusion energy yield to in-flight shell kinetic energy. Realizing the record yields that DT liners are predicted to produce will help LLE shot designers find an optimum between the high-yield, low-convergence DT liners and more-conventional designs that have greater areal densities but lower yields.

This material is based upon work supported by the Department of Energy National Nuclear Security Administration under Award Number DE-NA0003856, the University of Rochester, and the New York State Energy Research and Development Authority.

1. J. Nuckolls *et al.*, *Nature* 239, **139** (1972).
2. R. Betti and O. A. Hurricane, *Nat. Phys.* **12**, 435 (2016).
3. R. S. Craxton *et al.*, *Phys. Plasmas* **22**, 110501 (2015).
4. W. Seka *et al.*, *Phys. Plasmas* **16**, 052701 (2009).
5. Lord Rayleigh, in *Scientific Papers* (Cambridge University Press, Cambridge, England, 1900), Vol. II.
6. K. Anderson and R. Betti, *Phys. Plasmas* **10**, 4448 (2003).
7. V. Lobatchev and R. Betti, *Phys. Rev. Lett.* **85**, 4522 (2000).
8. R. Betti *et al.*, *Phys. Plasmas* **9**, 2277 (2002).

LLE's Summer High School Research Program

R. S. Craxton

Laboratory for Laser Energetics, University of Rochester

During the summer of 2021, eight students from Rochester-area high schools participated in the Laboratory for Laser Energetics' Summer High School Research Program. This was the 32nd year of the program, which started in 1989. The 2020 program was unfortunately canceled because of the Covid pandemic. In 2021, LLE held a fully virtual program for students who had applied and been interviewed for the 2020 program. The program started earlier than usual (in the middle of June rather than after July 4) and finished earlier (in the middle of August) to meet the schedules of the graduating seniors. The program comprised nine weeks rather than the usual eight.

The goal of LLE's program is to excite a group of highly motivated high school students about careers in the areas of science and technology by exposing them to research in a state-of-the-art environment. Too often, students are exposed to "research" only through classroom laboratories, which have prescribed procedures and predictable results. In LLE's summer program, the students experience many of the trials, tribulations, and rewards of scientific research. By participating in research in a real environment, the students often become more excited about careers in science and technology. In addition, LLE gains from the contributions of the many highly talented students who are attracted to the program.

The students spent most of their time working on their individual research projects with members of LLE's technical staff. The projects were related to current research activities at LLE and covered a broad range of areas of interest including experimental diagnostic development, computer modeling of implosion physics, experimental design, plasma-physics simulations, physical chemistry, future laser system design, and scientific data management (see Table I).

The students attended weekly seminars on technical topics associated with LLE's research. Topics this year included laser physics, fusion, nonlinear optics, nuclear physics, pulsed power, fiber optics, and LLE's cryogenic target program. The students also learned how to give scientific presentations and were introduced to LLE's computational resources.

The program culminated on 11 August with the virtual "High School Student Summer Research Symposium," at which the students presented the results of their research to an audience including parents, teachers, and LLE staff. The students' written reports will be made available on the LLE Website and bound into a permanent record of their work that can be cited in scientific publications.

Three hundred and ninety-nine high school students have now participated in the program. This year's students were selected from nearly 70 applicants to the canceled 2020 program. LLE is planning a normal, in-person program for 2022.

This material is based upon work supported by the Department of Energy National Nuclear Security Administration under Award Number DE-NA0003856, the University of Rochester, and the New York State Energy Research and Development Authority.

Table I: High School Students and Projects—Virtual Program, Summer 2021.

Name	High School	Supervisor	Project Title
Semma Alfatlawi	Victor	C. J. Forrest	Inferring a Neutron Yield from Nuclear Activation Techniques
Felix Huang	Webster Schroeder	H. G. Rinderknecht	Uniformity of X-Ray Prepulses for Imprint Mitigation in Directly Driven Implosions
Audrey Kohlman	Churchville-Chili	R. S. Craxton	Polar-Direct-Drive Designs for the Laser Megajoule
Meghan Marangola	Brighton	R. S. Craxton	Optimization of Direct-Drive Designs for a Proposed Dual Direct-/Indirect-Drive Laser
Tyler Petrillo	Webster Schroeder	R. S. Craxton	Development of a Polar-Direct-Drive Design for a Large-Diameter Beryllium Target on the National Ignition Facility
Leo Sciortino	School of the Arts	R. W. Kidder	Data Services to Improve Access to Scientific Image Data
Aditya Srinivasan	Pittsford Sutherland	A. B. Sefkow and M. Lavell	Exploration of Collision Models for Hybrid Fluid-Kinetic Simulations
Andrew Wu	Pittsford Mendon	K. L. Marshall	Computational Modeling of the Polarizability of Liquid Crystals

FY21 Q4 Laser Facility Report

J. Puth, M. Labuzeta, D. Canning, and R. T. Janezic

Laboratory for Laser Energetics, University of Rochester

During the fourth quarter of FY21, the Omega Facility conducted 304 target shots on OMEGA and 257 target shots on OMEGA EP for a total of 561 target shots (see Tables I and II). OMEGA averaged 10.1 target shots per operating day, averaging 88.1% Availability and 93.9% Experimental Effectiveness. OMEGA EP averaged 8.7 target shots per operating day, averaging 91.0% Availability and 97.1% Experimental Effectiveness.

Table I: OMEGA Laser System target shot summary for Q4 FY21.

Program	Laboratory	Planned Number of Target Shots	Actual Number of Target Shots
ICF	LLE	66	67
	LANL	11	11
	LLNL	22	22
	SNL	11	9
ICF Subtotal		110	109
HED	LLE	16.5	16
	LANL	11	7
	LLNL	55	44
	SNL	11	11
HED Subtotal		93.5	78
LBS	LLE	11	12
	LLNL	11	10
LBS Subtotal		22	22
AIBS		11	9
APL		11	14
OFES		11	14
CMAP		11	11
NLUF		60.5	47
Grand Total		330	304

AIBS: Academic and Industrial Basic Science

APL: Applied Physics Labs (Johns Hopkins University)

CMAP: Center for Matter at Atomic Pressures

LBS: Laboratory Basic Science

NLUF: National Laser Users Facility

OFES: Office of Fusion Energy Sciences

Table II: OMEGA EP Laser System target shot summary for Q4 FY21.

Program	Laboratory	Planned Number of Target Shots	Actual Number of Target Shots
ICF	LLE	31.5	49
	LLNL	21	21
ICF Subtotal		52.5	70
HED	LLE	14	20
	LANL	14	13
	LLNL	38.5	42
	SNL	7	8
HED Subtotal		73.5	83
LBS	LLNL	14	18
LBS Subtotal		14	18
AIBS		14	19
CMAP		14	18
LaserNetUS		21	23
NLUF		17.5	18
Calibration	LLE	7	8
Grand Total		213.5	257

During this quarter, the port H2 neutron time-of-flight diagnostic was installed and activated on OMEGA to add additional views to the neutronics suite of diagnostics. This additional view has allowed scientists to measure variations in ion temperature along a previously uncharacterized axis.

The Gas-Jet Target System, a ten-in. manipulator (TIM)-based payload that injects a plume of gas into the vacuum of the target chamber immediately prior to laser shot arrival and allows for the formation of a low-density plasma, has been upgraded to provide up to 1500 psia of pressure. The design of the nozzle controls the speed and pattern of the gas plume and configurations allowing Mach numbers in the range of 3 to 8 have been characterized at this point. With adequate design time, users may request additional nozzle designs.

National Laser Users' Facility and External Users' Programs

M. S. Wei

Laboratory for Laser Energetics, University of Rochester

Under the facility governance plan implemented in FY08 to formalize the scheduling of the Omega Laser Facility as a National Nuclear Security Administration (NNSA) User Facility, Omega Facility shots are allocated by programs following NNSA guidance. NNSA funds about 190 shot days each year on the OMEGA and OMEGA EP Laser Systems for experiments. The majority (~68%) of these shot days are committed to the national Inertial Confinement Fusion (ICF) Program and the High-Energy-Density (HED) Program with shots conducted by scientists from Lawrence Livermore National Laboratory (LLNL), Los Alamos National Laboratory (LANL), Sandia National Laboratories (SNL), the Naval Research Laboratory (NRL), and LLE. In FY21, the Omega Laser Facility delivered a total of 2098 shots over 206.5 days, among which 1326 target shots were conducted for the ICF and HED campaigns including calibration shots (112). The successful completion of the large number of experiments at the Omega Laser Facility during the COVID-19 global pandemic is attributed to the “*RemotePI*” operation protocol that has enabled all experimental principal investigators (PI's) and collaborators to safely and effectively conduct experiments via remote access.

The Fundamental Science Program at the Omega Laser Facility, with projects selected through open-call and peer-reviewed processes, is typically allotted between 25% to 29% of the total NNSA-funded Omega Facility shot days. The program has two distinct components: (1) the National Laser Users' Facility (NLUF) experiments (~18% of the NNSA-funded shot time) led by researchers from U.S. academia and business; and (2) the Laboratory Basic Science (LBS) experiments (with ~11% of the NNSA-funded shot time) that are led by the NNSA ICF laboratories including LLNL, LANL, SNL, NRL, and LLE and the Office of Science laboratories such as SLAC National Accelerator Laboratory, Princeton Plasma Physics Laboratory (PPPL), and Lawrence Berkeley National Laboratory (LBNL). In FY21, the NLUF and LBS programs obtained 360 and 231 target shots, respectively, and together accounted for ~28% of the overall facility shots.

Since FY20, LLE has provided a few additional shot days each year on OMEGA EP to the users of the newly established LaserNetUS network funded by the DOE Office of Fusion Sciences (FES) with user experimental proposals annually solicited and selected by a fully independent proposal review panel process. The LaserNetUS program obtained 29 target shots on OMEGA EP in FY21.

Since FY21, a few additional shot days each year at the Omega Laser Facility have also been made available to the University of Rochester (UR)-hosted Center for Matter at Atomic Pressure (CMAP), a new Physics Frontier Center funded by the National Science Foundation (NSF). CMAP is a collaboration among faculty, scientists, researchers, and students at UR, Massachusetts Institute of Technology, Princeton University, the University of California at Berkeley and Davis, the University of Buffalo, and LLNL. CMAP researchers conduct laboratory-based exploration of planets and stars throughout the universe and obtained 43 target shots in FY21.

During FY21, the Omega Laser Facility had also been used to support research grants led by LLE scientists and funded by FES (14 target shots on OMEGA) and Advanced Research Projects Agency–Energy (ARPA-E) (24 target shots on OMEGA) and for other externally funded programs led by teams from the Johns Hopkins University's Applied Physics Laboratory (APL) (24 target shots on OMEGA) and Marvel Fusion, a German fusion start-up company (24 target shots on OMEGA EP). These externally

funded experiments are conducted at the facility on the basis of special agreements put in place by UR/LLE and participating institutions with the endorsement of NNSA.

The facility users who conducted experiments during this year included 17 collaborative teams participating in the NLUF Program including the one-time Academic and Industrial Basic Science Program using the NLUF facility time allocation from the FY20–FY21 awards; 21 teams led by scientists from LLNL, LANL, LLE, and LBNL participating in the LBS Program; three project teams participating in the LaserNetUS Program; six project teams from the CMAP; many collaborative teams from the national laboratories (LLNL, SNL, NRL) and LLE conducting ICF experiments; investigators from LLNL, LANL, SNL, and LLE conducting experiments for HED campaigns; and researchers from APL and Marvel Fusion.

A critical part of the NLUF program and the LaserNetUS program is the education and training of graduate students in high-energy-density (HED) and plasma physics. In addition, graduate students can also access the Omega Laser Facility to conduct their theses research through collaborations with national laboratories and LLE. In total, 66 graduate students (see Table I) from 20 other universities have participated in these external user-led research projects with experiments at the Omega Laser Facility, among which nine students successfully defended their Ph.D. theses in calendar year 2021 (see the highlighted names in Table I). It is worth noting that 18 of these students are new to the Omega Laser Facility.

Table I: Graduate students from 20 universities who have conducted research utilizing the Omega Laser Facility through NLUF, LBS, LaserNetUS, and/or via collaborations with national labs and LLE in FY21. Five students successfully defended their Ph.D. theses during calendar year 2021 (see the shaded cells).

Name	University	Advisor(s)	Notes
A. Aghedo	Florida A&M University	Albert (LLNL)	New–LLNL collaboration
C. Bruulsema	University of Alberta	Rozmus	New–LLE collaboration (PI: D. Froula)
E. Grace	Georgia Tech (GT)	Trebino (GT)/ Ma (LLNL)	LLNL collaboration
J. Gonzalez-Quiles	Johns Hopkins University (JHU)	Wicks	
Y. Li	JHU	Wicks	New
T. Perez	JHU	Wicks	
Z. Ye	JHU	Wicks	
A. Palmer	Michigan Tech.	–	New–LANL collaboration (PI's: Rasmus and Flippo)
P. J. Adrian	Massachusetts Institute of Technology (MIT)	Petrasso/Frenje/Li	
C. Chang	MIT	Petrasso/Frenje/Li	New
S. Dannhoff	MIT	Petrasso/Frenje/Li	New
T. Evans	MIT	Petrasso/Frenje/Li	New
T. M. Johnson	MIT	Petrasso/Frenje/Li	
N. V. Kabadi	MIT	Petrasso/Frenje/Li	Defended Ph.D. thesis in November 2021 (now an Assistant Scientist at CMAP)
J. Kunimune	MIT	Petrasso/Frenje/Li	
B. Lahmann	MIT	Petrasso/Frenje/Li	Defended Ph.D. thesis in February 2021 (now a postdoc at LLNL)
J. Percy	MIT	Petrasso/Frenje/Li	
B. Reichelt	MIT	Petrasso/Frenje/Li	
G. Sutcliffe	MIT	Petrasso/Frenje/Li	

Table I: Graduate students from 20 universities who have conducted research utilizing the Omega Laser Facility through NLUF, LBS, LaserNetUS, and/or via collaborations with national labs and LLE in FY21. Five students successfully defended their Ph.D. theses during calendar year 2021 (see the shaded cells) (continued).

Name	University	Advisor(s)	Notes
R. Simpson	MIT	Winslow (MIT)/Ma (LLNL)	LLNL Collaboration
A. Chien	Princeton	Ji	Defended Ph.D. thesis in August 2021
D. Kim	Princeton	Duffy	
S. Han	Princeton	Duffy	
I. Ocampo	Princeton	Duffy	
K. Lezhnin	Princeton	–	New–NLUF/AIBS (PI's: D. Schaeffer and W. Fox)
K. Perez	Rice University	Liang	
W. Riedel	Stanford	Cappelli	
M. Harwell	University of California, Davis	Stewart	CMAP
R. Lee	University of California, Los Angeles	Mori	NLUF/AIBS (PI: M. Manuel)
M. Sinclair	University of California, Los Angeles	Joshi	LLNL collaboration including LBS (PI: F. Albert)
K. Bhutwala	University of California, San Diego (UCSD)	Beg	
A. Bogale	UCSD	Beg	New–LaserNetUS (PI: M. Manuel)
T. Cordova	UCSD	Beg	New–LaserNetUS (PI's: K. Matsuo and F. Beg)
J. Vaughan	UCSD	Beg	
J. Strehlow	UCSD	Beg	
J. Saret	UCSD	Beg	New
R. Turner	UCSD	Beg	New–LaserNetUS (PI's K. Matsuo and F. Beg)
D. Zimmer	UCSD	Beg	
G. Righi	UCSD	Meyers	LLNL collaboration (PI's: C. Stan and H.-S. Park) and LaserNetUS (PI: G. Righi)
A. Angulo	University of Michigan	Kuranz	
K. Bryant	University of Michigan	Kuranz	
S. Coffing	University of Michigan	Drake	LANL collaboration (PI's: P. Kozlowski and H. Johns)
C. Fiedler-Kawaguchhi	University of Michigan	Kuranz	New–LANL collaboration (PI's: A. Rasmus and K. Flippo)
K. Kelso	University of Michigan	Kuranz	
H. Lefevre	University of Michigan	Kuranz	Defended Ph.D. thesis in April 2021 (now an NSF Postdoc Fellow at University of Michigan)
K. Ma	University of Michigan	Kuranz	
M. Springstead	University of Michigan	Kuranz	
R. Vandervort	University of Michigan	Drake	

Table I: Graduate students from 20 universities who have conducted research utilizing the Omega Laser Facility through NLUF, LBS, LaserNetUS, and/or via collaborations with national labs and LLE in FY21. Five students successfully defended their Ph.D. theses during calendar year 2021 (see the shaded cells) (continued).

Name	University	Advisor(s)	Notes
B. Russell	University of Michigan	Krushelnick/Willingale	
J. Latham	University of Michigan	Willingale	New
H. Tang	University of Michigan	Willingale	
M. Wadas	University of Michigan	Johnsens	LLNL collaboration including LBS (PI: M. Milliot)
E. Gallardo-Diaz	University of Nevada, Reno (UNR)	Mancini	New–NLUF and LLE collaboration
J. Rowland	UNR	Mancini	New
C. Allen	UNR	White	LLNL collaboration including LBS shots and NLUF
J. J. Donaghy	University of New Hampshire	Fox	LaserNetUS
P. King	University of Texas (UT), Austin	Hegelich/Albert	LLNL collaboration including LBS (PI: F. Albert)
I. Pagano	UT, Austin	Downer/Albert	New–LLNL collaboration including LBS (PI: F. Albert)
S. Myren	Virginia Tech	–	New–LANL collaboration (PI's: A. Rasmus and K. Flippo)
C. Samulski	Virginia Tech	Srinivasan	GA collaboration (AIBS, PI: M. Manuel)
V. Bouffetier	University of Bordeaux	Casner	LLE collaboration including LBS (PI: W. Theobald) and LANL LBS (PI: T. E. Weber); Defended Ph.D. thesis in December 2021 (now a postdoc at European X-Ray Free-Electron Laser Facility)
C. Vlachos	University of Bordeaux	Santos	NLUF UCSD collaboration
T. Campbell	Oxford	Gregori	NLUF and LLE collaboration
H. Poole	Oxford	Gregori	NLUF and LLE collaboration
A. Dearing	University of York	Woolsey	LLE collaboration (PI: W. Theobald)
M. Khan	University of York	Woolsey	Rutherford Appleton Laboratory/ University of York (PI: R. Scott) and LLE (PI: W. Theobald) collaboration

FY21 National Laser Users' Facility Program

M. S. Wei

Laboratory for Laser Energetics, University of Rochester

FY21 was the second year of a two-year period of performance for the 21 National Laser Users' Facility (NLUF) projects (Table I) including ten Academic and Industrial Basic Science (AIBS) experiments approved for the FY20–FY21 shot allocation at the Omega Laser Facility. In total, 360 target shots were taken for 17 NLUF projects during FY21. These NLUF experiments conducted at the facility during FY21 are summarized in this section.

Table I: Twenty-one NLUF (in blue) and AIBS (in gray) projects approved for the FY20–FY21 Omega Laser Facility shot allocations.

Principal Investigator	Institution	Title
F. N. Beg*	University of California, San Diego	Charged-Particle Transport and Energy Deposition in Warm Dense Matter With and Without an External Magnetic Field
C. M. Krauland	General Atomics	Characterization of the Nonlinear Laser–Plasma Interaction in Electron-Assisted Shock Ignition
K. Krushelnick*	University of Michigan	The Dynamics of Strong Magnetic Fields Generated by Relativistic Laser–Plasma Interactions Using OMEGA EP
E. Liang*	Rice University	Collision of Two Magnetized Jets Created by Hollow Ring Lasers
R. C. Mancini*	University of Nevada, Reno	A Laboratory Photoionized Plasma Experiment on OMEGA EP
C. McGuffey*	University of California, San Diego	Driving Compressed Magnetic Fields to Exceed 10 kT in Cylindrical Implosions on OMEGA
R. D. Petrasso*	Massachusetts Institute of Technology	High-Energy-Density Physics, Laboratory Astrophysics, and Student Training on OMEGA
P. Tzeferacos/D. Lamb*	University of Chicago	Fundamental Astrophysical Processes in Radiative Supersonic Magnetohydrodynamic Turbulence
M. Valdivia*	Johns Hopkins University	Demonstration of Monochromatic Talbot–Lau X-Ray Deflectometry Electron Density Diagnostic in Laser–Target Interactions
J. Wicks	Johns Hopkins University	High Pressure and Temperature Polymorphism of a Key Super-Earth Mantle Material: MgO
L. Willingale*	University of Michigan	Direct Laser Acceleration of Electrons for Bright, Directional Radiation Sources
M. Cappelli*	Stanford University	Hydrodynamic Versus Kinetic Atomic Mix in Deflagrating Converging Plasmas
T. Duffy*	Princeton University	Phase Transitions in Planetary Materials at Ultrahigh Pressures
W. Fox*	Princeton University	Magnetic Reconnection in High-Energy-Density Plasmas
R. Jeanloz*	University of California, Berkeley	Multi-Compression and Chemical Physics of Planetary Interiors

Table I: Twenty-one NLUF (in blue) and AIBS (in gray) projects approved for the FY20–FY21 Omega Laser Facility shot allocations (continued).

Principal Investigator	Institution	Title
H. Ji*	Princeton University	Study of Particle Acceleration from Magnetically Driven Collisionless Reconnection at Low Plasma Beta Using Laser-Powered Capacitor Coils
C. C. Kuranz*	University of Michigan	Experimental Astrophysics on the OMEGA Laser
M. J.-E. Manuel	General Atomics	B-Field Effects on Laser–Plasma Instabilities
D. Schaeffer*	Princeton University	Particle Heating by Collisionless Shocks in Magnetized High-Energy-Density Plasmas
B. Srinivasan	Virginia Tech	Investigation of Feasibility of the $11\text{B}(\text{P},3\alpha)$ Reaction in Inertial Confinement Fusion Settings
W. Theobald	University of Rochester	Quantifying Turbulent Rayleigh–Taylor Mixing with X-Ray Phase-Contrast Imaging

*PI’s project conducted shots at the Omega Laser Facility in FY21.

Developing Krypton L-Shell Spectroscopy to Study Ion–Electron Equilibration High-Energy-Density Plasmas on OMEGA (ieRate-21A)

Principal Investigators: P. J. Adrian, N. V. Kabadi, C. K. Li, F. H. Séguin, R. D. Petrasso, and J. A. Frenje (Plasma Fusion Science Center, MIT); E. Gallardo-Diaz and R. C. Mancini (University of Nevada, Reno); R. Florido (Universidad de Las Palmas de Gran Canaria); and V. Yu. Glebov, S. P. Regan, and A. Sorce (LLE)

MIT graduate student P. J. Adrian and collaborators led an NLUF experiment to study the physics of ion–electron equilibration in high-energy-density plasmas (HEDP’s). The experiments conducted involved the implosion of thin-glass capsules filled with D^3He gas and a trace amount of krypton on the OMEGA Laser System. The implosions produce high density and temperature conditions at peak compression for ion–electron equilibration studies. The primary goal of this study was to develop a new diagnostic technique for determining the electron density (n_e) and electron temperature (T_e) at peak compression through krypton L-shell spectroscopy. The multilayer monochromatic imager (MMI)¹ diagnostic was utilized to measure krypton L-shell lines resolved in time and space. Unfortunately, on this day severe complications with the framing camera used by the MMI prevented the acquisition of critical data of spatially resolved krypton L-shell emission measurements. Time-resolved x-ray spectroscopy data were measured, however, and are shown in Fig. 1. Analysis of the data is still ongoing and will be used in future publications to detail the utilization of krypton L-shell spectroscopy.

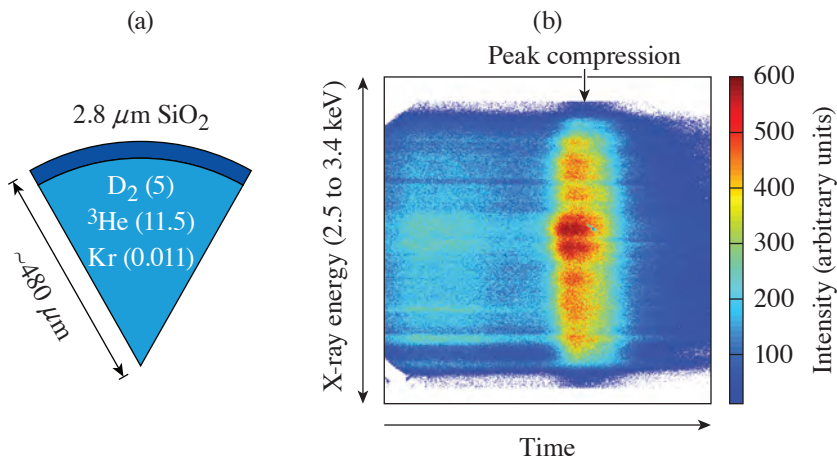


Figure 1
 (a) Diagram of the imploded capsule. The gas fills for this experiment were 5 atm of D_2 , 11.5 atm of ^3He , and 0.011 atm of krypton. (b) Time-resolved x-ray spectrum in an energy band of 2.5 to 3.4 keV. The x-ray spectrometer clearly resolves x-ray emission at peak compression where the krypton L-shell should be strongly emitting.

U2775JR

This work was supported in part by the National Laser Users' Facility under Contract DE-NA0003938, Laboratory for Laser Energetics under Contract 417532G/UR FAO GR510907. P. J. Adrian was also supported with a DOE SSGF Fellowship under contract DE-NA0003960.

Developing Krypton L-Shell Spectroscopy to Study Ion–Electron Equilibration High-Energy-Density Plasmas on OMEGA (ieRate-21A2)

Principal Investigators: P. J. Adrian, N. V. Kabadi, C. K. Li, F. H. Séguin, R. D. Petrasso, and J. A. Frenje (Plasma Fusion Science Center, MIT); E. Gallardo-Diaz and R. C. Mancini (University of Nevada, Reno); R. Florido (Universidad de Las Palmas de Gran Canaria); and V. Yu. Glebov, S. P. Regan, and A. Sorce (LLE)

Measurements of ion–electron equilibration in the high-density ($>10^{23}\text{-cm}^{-3}$) and high-temperature ($>1\text{-keV}$) regime are necessary to constrain theories on ion–electron transport. This work continues experimental measurements of ion–electron equilibration in this regime. The goal of these experiments was to acquire krypton L-shell emission data from an implosion to determine the electron density (n_e) and electron temperature (T_e) during peak compression. This measurement is critical for determining the plasma conditions achieved in the implosion for the study of ion–electron equilibration. Previous experiments attempting this measurement indicated the krypton L-shell signal to background needed to be increased. To increase the signal, the gas fill of krypton was increased to 0.014 atm, as shown in Fig. 2(a), from previous studies that used 0.011 atm. In addition, a significant background source was x rays from thermal bremsstrahlung emission of the corona. On this day the laser pulse was optimized so that the coronal x-ray emission did not contribute to the x-ray signal during peak compression. The x-ray emission history was measured with a prototype x-ray emission history diagnostic² shown in [Fig. 2(b)]. The data clearly indicate that x-ray emission from peak compression is separated from the coronal emission, which decays after the laser turns off. The MMI³ diagnostic was utilized to measure krypton L-shell lines resolved space at peak compression. Figure 2(c) displays images of the implosion recorded with MMI at peak compression. The data are still under analysis and will be used to diagnose the plasma conditions during peak compression of the implosion, which is critical for studying ion–electron equilibration. Presentations about these experiments are being given at the APS Division of Plasma Physics meeting in 2021.

This work was supported in part by the National Laser Users' Facility under Contract DE-NA0003938, Laboratory for Laser Energetics under Contract 417532G/UR FAO GR510907. P. J. Adrian was also supported with a DOE Stewardship Science Graduate Fellowship (SSGF) under contract DE-NA0003960.

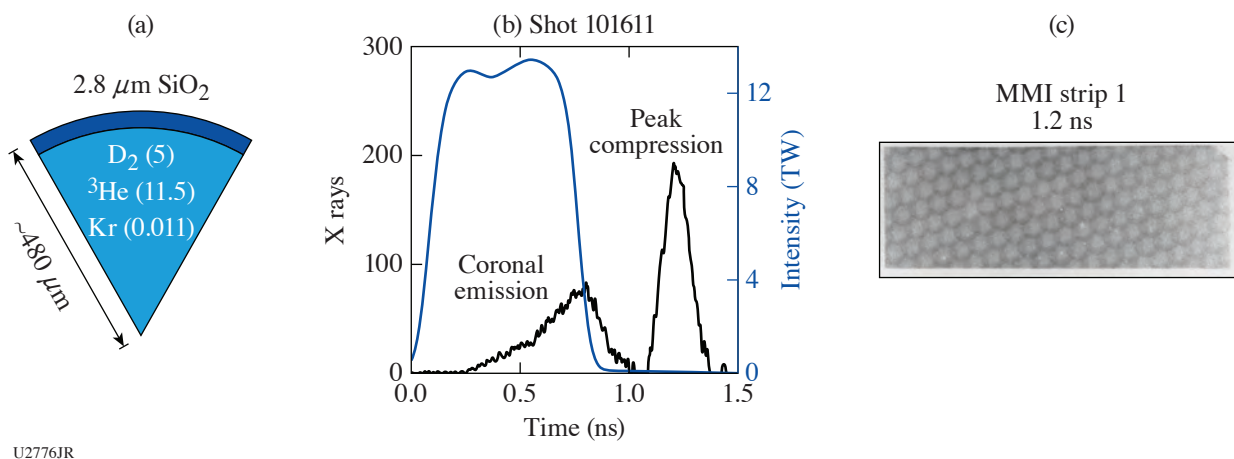


Figure 2

(a) Diagram of the imploded capsule. The gas fills for this experiment were 5 atm of D₂, 11.5 atm of ³He, and 0.014 atm of krypton. (b) Measurement of x-ray emission history relative to the laser pulse. (c) Example MMI data taken during peak compression around 1.2 ns. Data from shot 101611.

Energy Deposition in Magnetized Dense Plasma by Laser-Driven Relativistic Electrons

Principal Investigators: M. Bailly-Grandvaux, K. Matsuo, J. Kim, D. Kawahito, and F. N. Beg (Center for Energy Research, University of California, San Diego); C. McGuffey (General Atomics); J. L. Peebles, J. R. Davies, M. S. Wei, and S. Muller Fess (LLE); P. Gourdain (Department of Physics and Astronomy, University of Rochester), J. Honrubia (Universidad Polit cnica de Madrid, Spain); and J. J. Santos (CELIA, University of Bordeaux, France)

Understanding the role of the magnetic field is important for advanced fusion schemes such as fast-ignition inertial confinement fusion and magnetized liner inertial fusion. Here, we report on energy deposition in dense matter by intense laser-driven relativistic electrons with and without an external magnetic field. Thirty-six UV beams with a total energy of ~ 13.5 kJ are delivered in 1.5 ns to compress a 100-mg/cm³ CH foam cylinder doped with 1 at. % of Ti. On joint shots, the OMEGA EP beam is injected along the cylinder axis near stagnation time, delivering ~ 840 J in 10 ps. The magneto-inertial fusion electrical discharge system (MIFEDS) pulsed-power coil provides an external magnetic field of ~ 18 T at the cylinder target position, which reaches ~ 1 kT at maximum compression.

In the previous experiment in FY20, the idea was to record, on the same x-ray spectral range (no crystal swap required), both the Ti-dopant emission from the imploded foam and the K-shell emission from fast electrons knocking the two Fe/Cr foils attached on each cylinder end. However, the streaked x-ray spectrometer (SXS) and the time-integrated x-ray spectrometer (XRS) experienced significant background issues when OMEGA EP was fired due to the high noise generated by relativistic electrons. Nevertheless, referring to last year's report, we obtained high-quality measurements of the implosion trajectories and stagnation conditions from the x-ray framing camera (XRFC) and the XRS diagnostic in implosion-only shots. The shots were also highly reproducible, allowing us to benchmark our radiation-hydrodynamic simulations with 2-D *FLASH* and successfully compare implosion trajectories with XRFC results and compressed core conditions with XRS, respectively [see Figs. 3(a) and 3(b)].

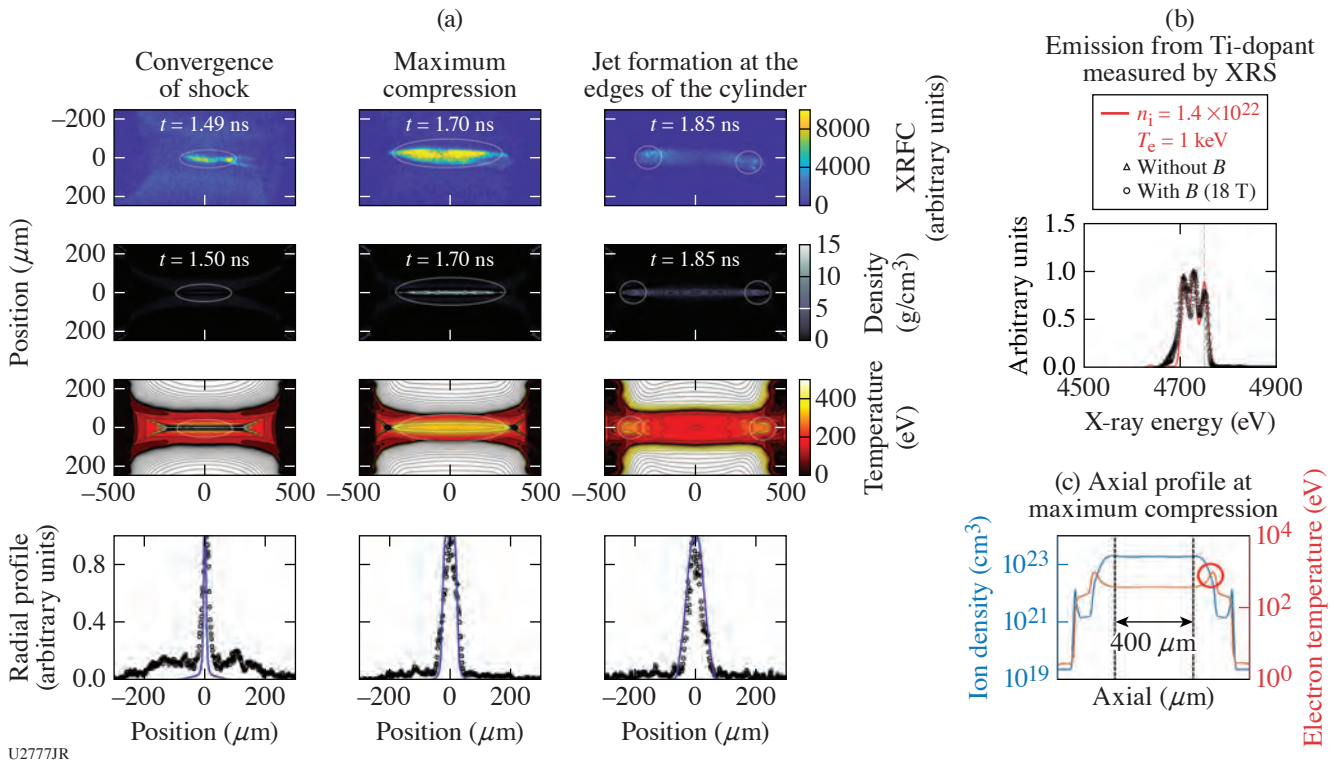


Figure 3

(a) XRFC result (applied $B = 18$ T) compared with 2-D *FLASH*. (b) XRS titanium-dopant K-shell spectra for $B = 0$ T and applied $B = 18$ T, compared to (c) *FLYCK* calculations using the density and temperature extracted from *FLASH* at the edge of the compressed core.

Note that the x-ray emission from the Ti dopant cannot escape from the inside of the compressed core due to opacity effects. Given that the XRS line of sight was along the cylinder's axis, the emission from the edge of the compressed core is the highest contribution to the measured spectra. This hypothesis is validated by the very good agreement between the experimental spectra and the core edge conditions extracted from *FLASH* [Fig. 3(c)].

In the RelEPlasma-21A experiment, we used higher-Z foils (Zn/Cu) attached to each end of the cylinder and fielded the radiation-hardened zinc von Hamos (ZVH) spectrometer tuned to Zn/Cu K-shell emission. The experimental setup and target description are given in Figs. 4(a) and 4(b), respectively. Despite the very high background associated with the joint shots, we successfully recorded Zn and Cu K-shell emission for $B_0 = 0$ T and $B_0 = 18$ T [Fig. 4(d)]. The OMEGA EP beam is injected at $t = 1.65$ ns, which is near maximum compression. We observe an increase of the Zn K_α /Cu K_α ratio for the magnetized shot, which indicates that fewer electrons reached the exit (Cu) side of the cylinder.

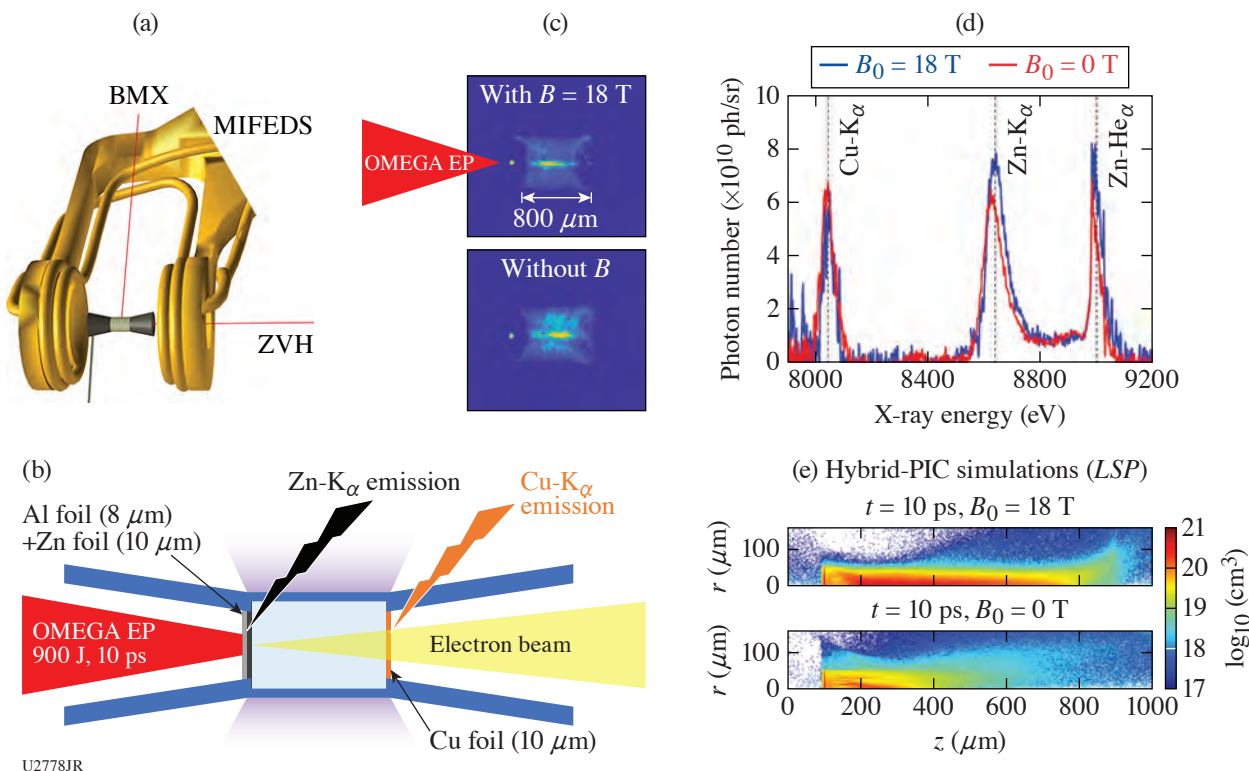


Figure 4

(a) Sketch of the RelEPlasma-21A experimental setup, using the time-integrated ZVH spectrometer, that is shielded against background radiation. (b) Description of the cylinder target for electron transport measurements. (c) X-ray pinhole camera results for joint shots with and without applied B field (18 T). (d) Zn and Cu K-shell emission recorded by the ZVH spectrometer on joint shots. (e) Hybrid-PIC simulations of the electron transport in the compressed cylinder, with and without applied B field. The hybrid-PIC simulations use maps of the plasma density and temperature extracted from *FLASH* near maximum compression ($t = 1.65$ ns).

To unravel the electron transport behavior with and without an applied B field, we carried out 2-D hybrid-PIC (particle-in-cell) simulations using the *LSP* code. The OMEGA EP electron source was previously characterized using full-PIC simulations and compared with results from an electron spectrometer.⁴ We imported the maps of hydrodynamic plasma quantities from the 2-D *FLASH* simulations for $t = 1.65$ ns. The *FLASH* simulations were performed for both $B_0 = 0$ T and $B_0 = 18$ T, including the magnetohydrodynamic (MHD) packages in *FLASH* to compute the compressed B field. The background resistivity of the CH at various temperature (and densities) called for the use of advanced resistivity models in *LSP*. As discussed in Ref. 4, the compressed magnetic field of ~ 1 kT is strong enough to guide ~ 5 -MeV electrons in the compressed core of ~ 15 - μm radius. Consequently, the fast electrons can propagate deeper into the compressed core when the cylinder is magnetized, enabling more

efficient energy deposition via collisions with the dense compressed core. On the other hand, in the unmagnetized cylinder, the fast electrons are mirrored or scattered near the compressed core edges and reach the rear side primarily through the low-density outer part of the cylinder (at higher radii), therefore without experiencing a strong drag. This can be qualitatively observed in the x-ray pinhole camera images shown in Fig. 3(c), where more emission is seen outside the core versus inside the core for the unmagnetized shot versus the magnetized shot. Overall, the number of electrons reaching the rear side of the cylinder will be reduced in the magnetized case due to the enhanced energy deposition. Figure 3(e) shows snapshots of the fast-electron density for the unmagnetized and magnetized cases. The above-described fast-electron-transport behavior between magnetized and unmagnetized targets is clearly observed in simulations.

The remaining analysis involves calculating the synthetic time-integrated K_{α} emission from the Zn and the Cu channel using the fast-electron macroparticle information from the hybrid-PIC simulations. It requires consideration of the bulk temperature, density, and kinetic energy dependence of the K_{α} cross sections, as well as optical depth effects of the Zn emission radiation transport through the compressed cylinder.

This work was supported by the National Nuclear Security Administration through the National Laser Users' Facility Program NA0003943.

Deposition of Intense Proton Beams in Cu and Resultant Heating

Principal Investigators: M. Bailly-Grandvaux, K. Bhutwala, and F. N. Beg (Center for Energy Research, University of California, San Diego); C. McGuffey (General Atomics); D. Mariscal and T. Ma (LLNL); and P. M. Nilson and W. Theobald (LLE)

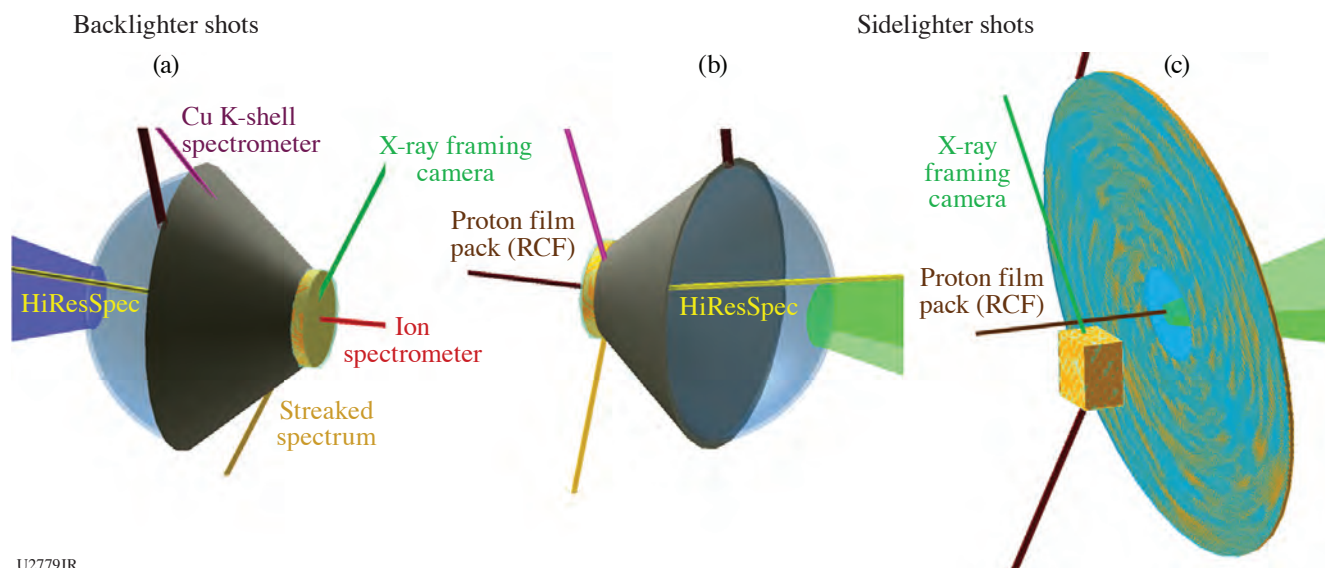
The OMEGA EP short-pulse laser can deliver proton and ion beams with tens of joules that can then deposit their energy in bulk samples, leading to rapid, uniform heating. ProtonWDM-EP-21A is the second shot day of a pair of NLUF shot days studying energy deposition of proton beams in solid matter. On the first shot day in FY20, a thin Si wafer was heated by protons and probed by x-ray absorption spectroscopy using a short-pulse-driven continuum backlighter. It was observed that Si K-shell absorption evolved from a single K-edge feature to a blurred K edge to a sequence of up to a dozen absorption features within a matter of 100 ps (Ref. 5) In the upcoming shot day, protons will be focused into Cu disks (10 or 25 μm thick \times 200 μm diameter), and x-ray emission diagnostics will observe the heating of the disk, which is expected to reach $\gg 100$ eV through proton then ion heating. The samples are much thicker than the thin Si foils used in FY20. The thicker samples will produce sufficient emission for line spectroscopy and imaging; however, they are still expected to be heated uniformly in depth with minimal self-absorption. Proton beam transport in an even-thicker material (plastic foam) has also been studied by this group using OMEGA EP.⁶

Unlike in ProtonWDM-EP-20A and pIsoHeat, a steep-walled hollow cone will be attached to the rear of the target foil and the front of the Cu sample. Such a cone has been shown to funnel the proton beam into a small spot.⁷ The cone has a 100- μm opening at the tip. The target and diagnostic lines of sight for these shots are shown in Figs. 5(a) and 5(b). Another type of shot is planned for the shot day in which the proton beam will be incident, without strong focusing in this case, onto a bulk Cu slab. The slab will catch only half of the beam, and radiochromic film will measure the unblocked and transmitted portions. This will be this group's first attempt to measure energy deposition of the OMEGA EP-driven proton beam with absorption directly in the intense beam on a single shot. This configuration is shown in Fig. 5(c). New hardware for the radiochromic film, developed through the Omega Laser Facility Users Group (OLUG) recommendations process, will be fielded on this shot day.

This work was supported by the National Nuclear Security Administration through the National Laser Users' Facility Program NA0003943.

Cylindrical Compressions with Embedded B Fields to Characterize Strongly Magnetized Hot Dense Plasmas

Principal Investigators: M. Bailly-Grandvaux and F. N. Beg (Center for Energy Research, University of California, San Diego); R. Florido (University of Las Palmas de Gran Canaria, Spain); G. Perez-Callejo, J. J. Santos, and C. Vlachos (CELIA, University of Bordeaux, France); C. A. Walsh (LLNL); F. Suzuki-Vidal (Imperial College, UK); C. McGuffey (General Atomics); R. C. Mancini (University of Nevada, Reno); M. A. Gigosos (Universidad of Valladolid, Spain); and J. L. Peebles, J. R. Davies, and S. Muller-Fess (LLE)



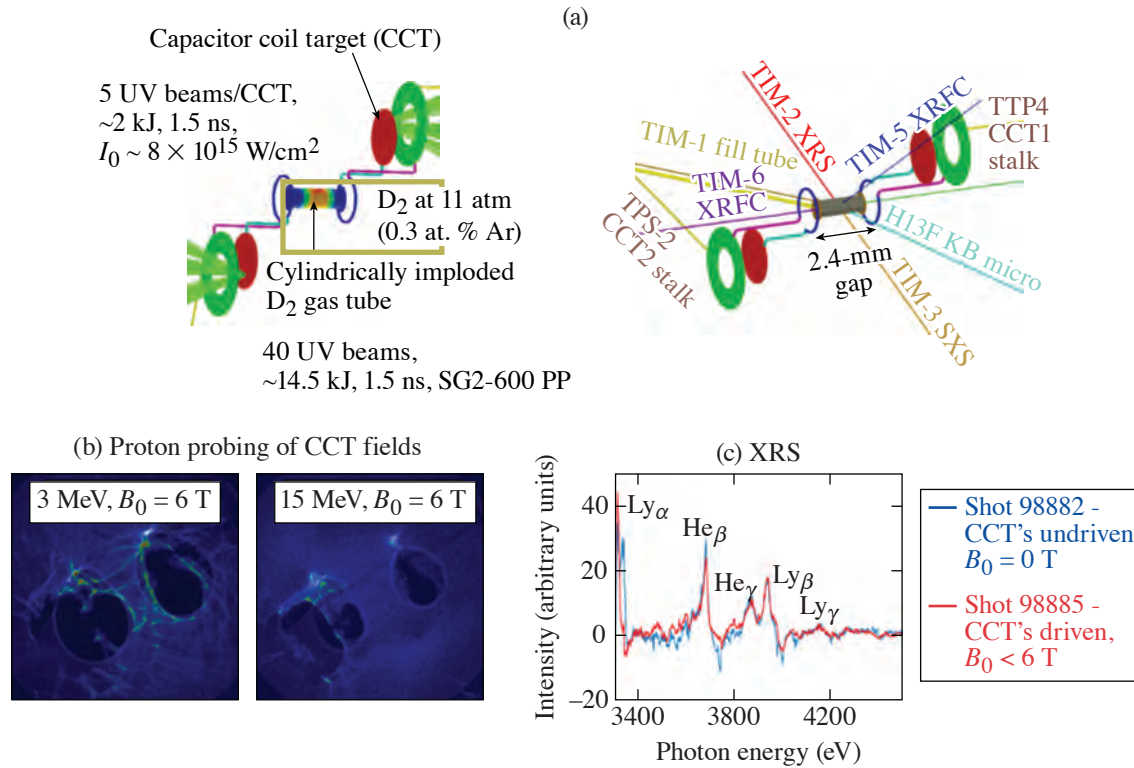
U2779JR

Figure 5

[(a),(b)] Experimental configurations for the Cu disk heating experiment and (c) the proton energy deposition measurement. The first two configurations will use the same laser and target conditions but have complementary diagnostics. Configuration (c) will provide a simple measurement of energy deposition as well as time-resolved images of the top Cu face, giving a cross-sectional view of the emission profile.

The use of external magnetic fields in inertial confinement fusion (ICF) has been identified as a promising way to assist ignition. In this relatively new area of research, the magnetic-field transport during compression and related magnetized plasma dynamics must be studied. We proposed a platform for the OMEGA laser to study MHD effects in cylindrical implosions at regimes of large magnetic pressure and magnetization. Cylindrical targets were filled with Ar-doped D_2 gas and symmetrically imploded using a 40-beam, 14.5-kJ, 1.5-ns laser drive. To investigate the effects of magnetization, implosions were characterized using x-ray imaging and Ar K-shell line-emission spectroscopy. Two-dimensional simulations using the MHD code *GORGON* predicted that a seed B field of 30 T should be compressed to ~ 30 kT. As a result, the characteristic conditions of the compressed core and the emitted Ar spectrum are expected to be modified.⁸ We performed implosions with a seed B-field induced from (or using) laser-driven coils [Fig. 6(a)] and MIFEDS [Fig. 7(a)]. According to proton probing results, the B-field generated seed with laser-driven coils was < 6 T [Fig. 6(b)] during the BCoilCompress-20A shot day, likely due to the large inductance of the coils. This seed B field was too low to affect the core conditions [Fig. 6(c)]. A dual-MIFEDS design provided a seed B field of ~ 25 T in the recent BCoilCompress-21A shot day; the result was observation of systematic changes in the Ar spectra between unmagnetized and magnetized shots [Fig. 7(c)]. Carrying out such magnetized implosion experiments will advance the modeling of B-field compression and diffusion along with the benchmarking of atomic kinetics and line shape calculations in magnetized plasmas relevant to complex ICF-related experiments with embedded B fields.

In the latest BCoilCompress-21A Campaign, eight target shots were taken, including two pointing shots at the beginning of the shot day. Four shots were magnetized with a seed B field of ~ 25 T and two were unmagnetized, i.e., MIFEDS was not charged. In Fig. 7(b), we present a typical x-ray framing camera result. Before 1.3 ns, we can see solely the emission from the plastic shell moving inward at a velocity evaluated around ~ 230 km/s. After 1.3 to 1.4 ns, the core is being assembled along the central axis, with a peak emission (\sim max compression) occurring around 1.5 to 1.6 ns. Those numbers are in line with previous cylindrical implosion data from the SmallMagLIF Campaigns, noting that our shell thicknesses were between 18 and 20 μm during our FY21 shot day. In addition, measurements from the fixed, gated x-ray imager diagnostic found a compressed core radius of 12 to 15 μm , which corresponds to a convergence ratio (CR) of ~ 20 . This is $\sim 30\%$ of what simulations predict: a similar observation as in Ref. 9. Accordingly, assuming mass conservation, the compressed core density is ~ 1 g/cm³, in agreement with the inferred electron density from the Ar K-shell spectra of the XRS time- and space-integrated spectrometer.



U2780JR

Figure 6

(a) Experimental setup of the BCoinCompress-20A shot day, using laser-driven capacitor coil targets (CCT's) to generate the seed B field. (b) Overlay of experimental and synthetic (for $B_0 = 6$ T) proton deflectometry images, showing some current asymmetry in the coils and matching prediction for $B_0 < 6$ T. (c) Ar x-ray line emission for undriven (blue) and driven (red) CCT's.

Despite the lower convergence ratio than in simulations and shell thickness variations of the order of $\pm 1 \mu\text{m}$ across our target batch, a high reproducibility of the Ar spectra recorded with XRS was observed for each of the two distinct scenarios, unmagnetized or magnetized. More interestingly, regardless of the small differences in the target shell thickness, several systematic observations are seen in the time-integrated Ar spectra [Fig. 7(c)]. For the magnetized shots, the following line-intensity ratios are higher: (a) $\text{Ly}\beta/\text{He}\beta$, (b) $\text{Ly}\alpha/\text{He}$ -like satellites, and (c) $\text{He}\alpha/\text{Li}$ -like satellites, therefore suggesting a higher electron temperature for the magnetized implosion core. These observations are consistent with the impact of the compressed B field on the core conditions and have been predicted, at least in a qualitative manner, by our synthetic spectra simulations. Finally, note that the Ar line emission is dominated by the core conditions, as seen in the time-resolved spectra of Fig. 7(d). This indicates that there is no impact in the XRS data from Ar contamination in the shell nor is there evidence of a premature breakup of the shell.

We also observed a systematic increase of the neutron yield and neutron-inferred ion temperatures when adding the B field. The shot-to-shot variability of neutron diagnostics is higher, however, than what we observed from the Ar spectra in the same conditions. It points toward the use of x-ray emission diagnostics with a dopant in the gas to extract global trends of a magnetic field (or else) on the core formation and thereby alleviate the large variability associated with neutron measurements. The combination of the two types of measurements is very valuable, particularly considering that, due to opacity effects, the emission spectroscopy results might be more sensitive to the core edge compared to neutron measurements.

More analysis is needed to weigh the effects of nonuniform plasma conditions on the spectroscopy data and to assess the significance of the neutron-inferred quantities at this yield level. In a future experiment, we will focus on optimizing the laser pointing and target alignment, as well as the target quality and variability, to reach higher convergence ratios and thereby lower plasma β .

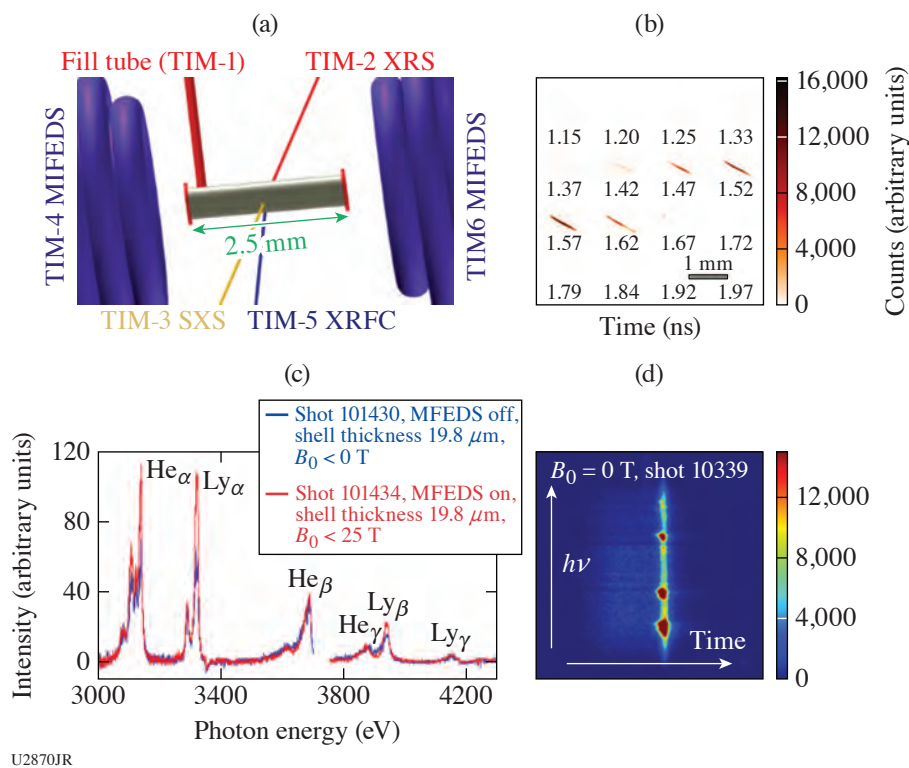


Figure 7

(a) Experimental setup of the BCoilCompress-21A shot day, using dual MIFEDS to generate an ~ 25 -T seed B field. (b) Example result from the XRFC, monitoring the implosion trajectories. (c) Ar x-ray line-emission spectra for a pair of unmagnetized (blue) and magnetized (red) shots; the comparison is consistent with higher T_e with the field. (d) A time-resolved Ar x-ray line-emission spectrum, which shows that the Ar spectra are dominated by the core emission.

The magnetic pressure should have a greater effect on the assembled core density, leading to the rise of specific extended-MHD effects of great interest for magneto-inertial fusion, namely induced currents and nonlocal electron transport (discussed in Ref. 8).

In parallel, we will further pursue our investigation of laser-driven coil designs for OMEGA. Our first experiment confirmed the critical importance of the large coil inductance at the imposed 1.5-ns irradiation duration (which needed to be the same as the implosion drivers). We are exploring designs with lower inductance that would still be compatible with the constraints of cylindrical compressions and could potentially produce B fields higher than MIFEDS.

This work was supported by the NNSA/NLUF Grant DE-NA0003940. M. Bailly-Grandvaux received a new grant (DE-SC0022250) for this project from DOE Office of Science High-Energy-Density Laboratory Plasmas (HEDLP) Program for FY21–FY24.

Studies of Strongly Magnetized Electrons and Ions on Heat Flow and Symmetry in Shock-Driven Implosions

Principal Investigators: J. A. Frenje, C. Chang, N. V. Kabadi, and P. J. Adrian (MIT); J. L. Peebles (LLE); and C. A. Walsh (LLNL)

The MagImp-21 Campaign included two half-day experiments (MagImp-21A and 21B) on OMEGA to study the impact of strongly magnetized electrons and ions on electron thermal transport (and asymmetries in the thermal transport), ion Knudsen number, and ion and electron viscosity. This campaign is a central part of MIT student C. Chang's Ph.D. thesis.

These experiments used thin-glass capsules filled with 90% D_2 and 10% 3He gas driven by a 1-ns square pulse delivering about 16 kJ to the capsule. Since the glass shell was ablated at peak compression in these experiments, the observables are mainly

due to the shock-driven plasma conditions. MIFEDS was used to apply an initial B field to the implosion. A large set of nuclear and x-ray diagnostics was used to measure yield, electron temperature and electron-temperature profiles, implosion trajectory, implosion size, and x-ray emission source profiles in different energy bands. The MagImp-21A experiment conducted at an initial B field of 50 T generated some great data. For example, the nuclear emission history increased by 20% in the magnetized case than in the nonmagnetized reference case. In addition, the electron temperature and electron-temperature profile went up 10% and steepened 3×, respectively. These examples shown in Fig. 8 highlight the results from the MagImp-21A experiment. Detailed data analysis is ongoing, and results will be prepared for publication. In contrast, MagImp-21B, which was to be executed at 20 T, did not occur because of MIFEDS failure just before the first magnetized experiment. The hope is to have the MagImp-21B rescheduled in FY22.

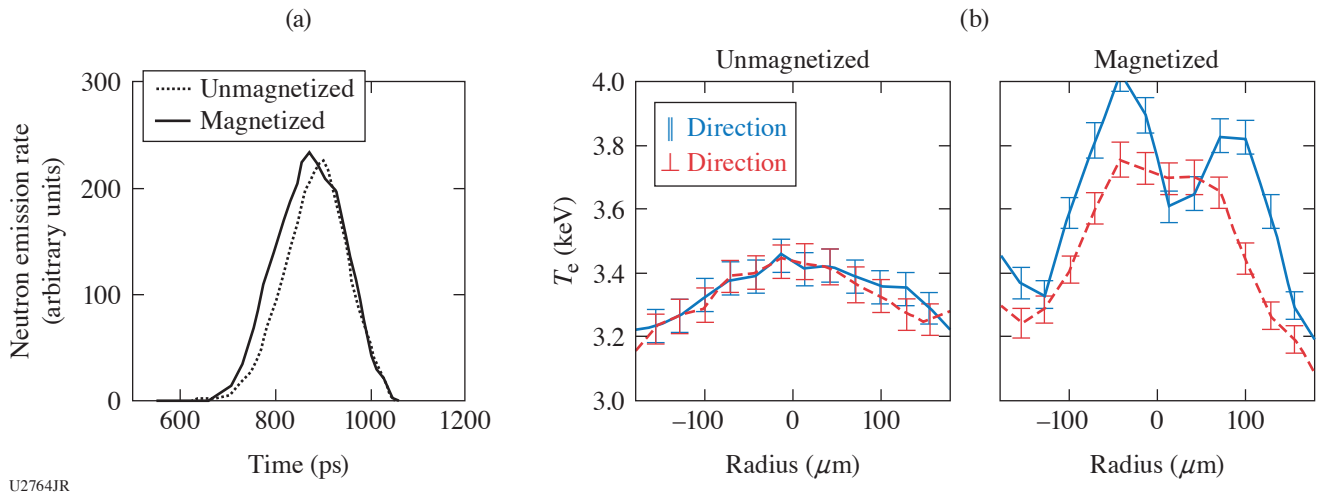


Figure 8

Main results from the MagImp-21A experiments. (a) Nuclear-emission history for the 50-T magnetized case (solid curves) and unmagnetized case (dotted curves). (b) Electron-temperature profiles for the unmagnetized and the 50-T magnetized case. The red and blue curves indicate the electron-temperature profiles in the direction perpendicular and parallel to the magnetic-field lines, respectively.

This work was supported in part by the National Laser Users' Facility under Contract DE-NA0003938, and Laboratory for Laser Energetics under contract 417532G/UR FAO GR510907.

The NuclSyn-21 Campaign for Measurements of the $^3\text{He}^3\text{He}$ Proton Spectrum and Platform Development for CNO Studies

Principal Investigators: M. Gatu Johnson, P. J. Adrian, J. A. Frenje, T. M. Johnson, N. V. Kabadi, J. Kunimune, C. K. Li, J. Pearcy, F. H. Séguin, G. D. Sutcliffe, and R. D. Petrasso (MIT); B. D. Appelbe, A. J. Crilly, and G. Kagan (Imperial College, UK); C.J. Forrest, V. Yu. Glebov, O. M. Mannion, F. J. Marshall, and C. Stoeckl (LLE); L. M. Green, B. M. Haines, B. D. Keenan, and W. T. Taitano (LANL); and H. W. Sio (LLNL)

The NuclSyn-21 Campaign included two half-day OMEGA experiments: (1) N_2D_2 and (2) $^3\text{He}^3\text{He}$, with the broad joint goal of furthering efforts to study nucleosynthesis-relevant nuclear reactions using the ICF Platform.

The goals of the N_2D_2 experiment were to test the feasibility of using the ICF platform for carbon-nitrogen-oxygen (CNO)-cycle-relevant nuclear studies and also to study shock coupling physics. The shots used thin plastic shell capsules filled alternatively with an N_2D_2 gas mixture or pure D_2 gas to test the impact of adding the heavier N ions on the performance of shock-driven implosions. A large set of nuclear and x-ray diagnostics was brought to bear to study yield, ion temperature (T_i) and electron temperature, implosion size, and x-ray emission. T_i inferred from the DD-n neutron spectrum from the N_2D_2 -gas-filled implosions was found to be slightly higher than for the D_2 -only implosions. The DD-n yield from the D_2 -only implosions was found

to be $\sim 6\times$ higher than the yield from the mix-fill implosion, with a factor of 4 expected based on the difference in deuterium number density only. These results suggest that the shock-driven ICF platform will be feasible for CNO experiments. Detailed data analysis is ongoing, and results will be prepared for publication.

The ${}^3\text{He} + {}^3\text{He} \rightarrow \alpha + \text{p} + \text{p}$ reaction is the main energy-producing step in our sun, and the basic nuclear physics governing this reaction are not well understood. An improved understanding of the fusion-product spectrum for this reaction can substantially impact inference of its S-factor from accelerator experiments, which will feed directly into solar models, impact predicted rates of solar neutrinos, and thus constrain modeling of solar dynamics. The goal of the ${}^3\text{He}{}^3\text{He}$ experiment was to extend earlier OMEGA experiments where the ${}^3\text{He}{}^3\text{He}$ proton spectrum was measured at proton energy $E_p > 6$ MeV [Fig. 9(a)]¹⁰ with a measurement of the lower-energy protons at $1.5 < E_p < 6$ MeV. Such data would much better constrain modeling of this reaction [Fig. 9(a)]. Two new diagnostics were brought to bear to make this measurement: a new MagSpec spectrometer [Fig. 9(b)] and an optimized step-range-filter design [Fig. 9(c)].¹¹ Data analysis is still in progress but initial results look promising, suggesting data were obtained at least down to $E_p = 1.5$ MeV.

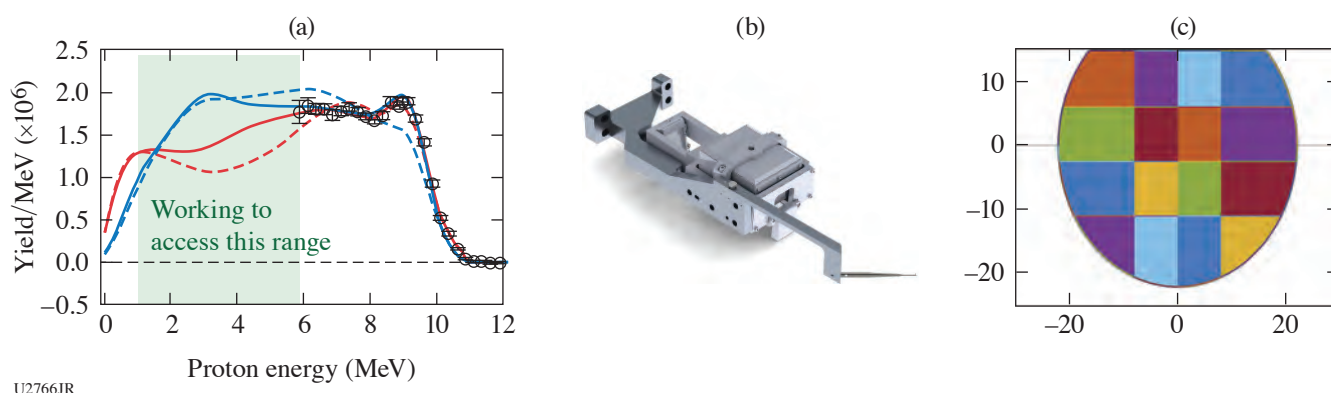


Figure 9

(a) Proton spectrum from the ${}^3\text{He}{}^3\text{He}$ reaction previously measured on OMEGA as published in Ref. 10. Until NuclSyn-21, the spectrum was only measured at proton energy $E_p > 6$ MeV. Data below 6 MeV are required to strongly constrain modeling of the reaction, as can be understood from looking at the colored lines that represent different models. The NuclSyn-21 experiments aimed to access the range highlighted in green through the use of two new diagnostic capabilities: (b) MagSpec, which consists of an aperture fielded in a ten-inch manipulator (TIM) at 20 cm from target chamber center (TCC) for high detection efficiency, a bending magnet, and a CR-39 detector, and (c) a new, optimized step-range-filter design, with 16 tantalum filters of various thickness fielded in front of a piece of CR-39 to allow inference of the full broad proton spectrum from ~ 1.5 to 12 MeV (Ref. 11).

This work was supported in part by the National Laser Users' Facility under Contract DE-NA0003938, Laboratory for Laser Energetics under Contract 417532G/UR FAO GR510907, and Lawrence Livermore National Laboratory under Contract B640112.

Performance Scaling of Inverted-Corona Neutron Sources

Principal Investigator: M. Hohenberger (LLNL)

Co-investigators: N. Meezan and A. J. Mackinnon (LLNL); J. Percy and N. V. Kabadi, (Plasma Science and Fusion Center, MIT); W. Riedel and M. Cappelli (Stanford University); S. H. Glenzer (Stanford University); and C. J. Forrest (LLE)

Experiments were performed on the OMEGA laser to study the performance of the inverted-corona neutron platform. Laser beams were incident onto the inside surface of a sphere through laser entrance holes, thereby ablating a layer of fusion fuel, e.g., a CD liner.¹² Fuel may also be provided as a gas fill.¹³ In either case, the fuel plasma stagnated on center and was heated to fusion conditions. Such targets have shown promise as neutron sources for high-energy-density applications, and experiments at the National Ignition Facility (NIF) are planned to apply this platform to radiochemistry applications such as neutron cross-section measurements. Previous experiments performed on OMEGA demonstrated a surprising yield dependence on the CD-liner thickness, indicating mix in the ablating plasma. Experiments with D_2 -gas-filled, CH-wall targets also indicated mix

of the wall material into the gas fill as a potential limiting factor in the performance. This suggested that the addition of a CD liner to gas-filled targets should mitigate some of the mix-induced yield degradation,^{13,14} as was confirmed computationally in PIC simulations modeling the gas–ablator interface.¹⁵

Targets were 1.8-mm-diam capsules driven by 40 OMEGA beams (1-ns square pulses, ~19 kJ) [see Fig. 10(a)]. The shot day comprised three parts: (1) yield scaling with CD-liner thickness in a vacuum target; (2) D₂-gas-filled targets with a CD liner; and (3) CD-lined targets with a ³He fill to diagnose gas–ablator mix via proton emission from D–³He reactions. The vacuum target performance scaled as expected and was consistent with previous data [Fig. 10(b)],^{12,13} although no yield improvements were observed for a CD-liner thickness >2 μm. Adding a CD liner to gas-filled targets increased the yield by ~2× from $Y_n \sim 3.2 \times 10^{10}$ to $Y_n \sim 1.5 \times 10^{10}$ compared to a CH-only capsule [Fig. 10(c)]. Finally, no correlation was observed between proton or D–D neutron yield and CD-liner thickness in ³He-filled targets. In contrast to previous data, these results suggest that only the innermost few microns of wall material affect the hot-spot conditions.

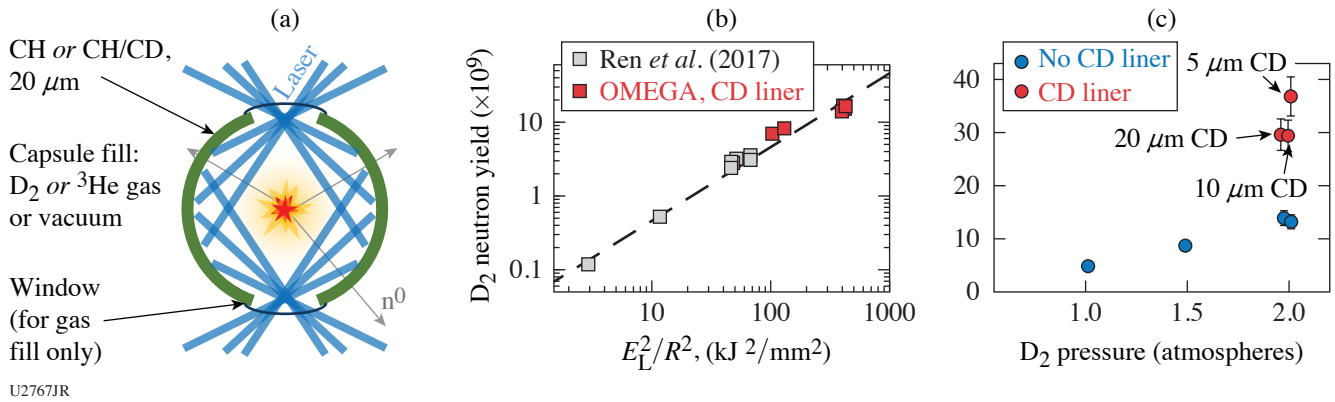


Figure 10

(a) The capsule is laser irradiated on the inside surface via two laser entrance holes. (b) In CD-lined targets, the neutron yield scaled as expected with laser energy and target size. (c) Adding a CD liner significantly increased the neutron yield from D₂-gas-filled targets.

Gas-Jet Collisionless Shock Experiments on OMEGA

Principal Investigators: T. M. Johnson, G. D. Sutcliffe, J. A. Percy, A. Birkel, N. V. Kabadi, B. Lahmann, P. J. Adrian, B. L. Riechelt, J. Kunimune, and C. K. Li (Plasma Science and Fusion Center, MIT); H. Chen (LLNL); J. Katz (LLE); and V. T. Tikhonchuk (Université de Bordeaux, Eli Beamlines)

Collisionless shocks are a common phenomena in the universe that are not well understood. They can be found inside our solar system, in supernova remnants, and in active galactic nuclei. When two collisionless plasma sheets collide at high velocity, instabilities redistribute kinetic energy by generating electromagnetic fields. These fields in turn interact with the plasma, forming a shock and dissipating even more energy in field generation, plasma heating, and particle acceleration. Recent pMagShock-21A experiments on the OMEGA laser, which is part of MIT student T. M. Johnson's Ph.D. thesis, successfully created collisionless shocks. In this experiment, lasers drive a CH hemispherical target to launch a supersonic plasma flow (>1500 km/s). This supersonic plasma flow collides with a volume of hydrogen gas provided by the gas-jet system. A schematic drawing of the experiment is shown in Fig. 11(a). The hydrogen gas is ionized by reflected laser light and bremsstrahlung from the plasma flow. When these two plasmas collide, a collisionless shock is formed. We diagnosed this system using imaging 2ω Thomson scattering, D³He backlit proton radiography, and electron spectroscopy [Osaka University electron spectrometer (OU-ESM) and electron–positron–proton soectrometer (EPPS)]. In total, our experiment consisted of 13 shots split between a Thomson-scattering configuration and a proton radiography configuration.

Thomson scattering provided very valuable information about the spatial structure of the collisionless shock. Namely, we observed large increases in density and temperature, as shown in Figs. 11(b) and 11(c), respectively. This gives a measurement of

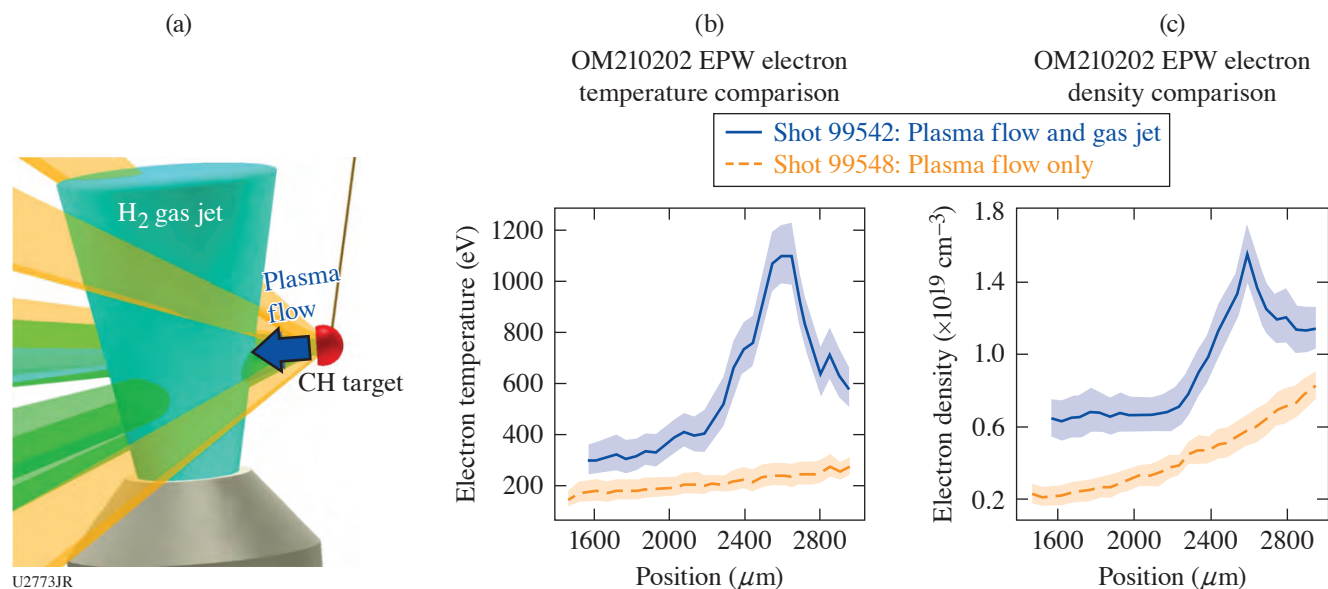


Figure 11

(a) A CAD rendering of the experimental configuration. (b) Imaging Thomson-scattering-measured electron temperature. The comparison is between shots without the gas jet (not interaction) and shots with both the gas jet and plasma flow (with interaction). A large increase in temperature is observed, indicating shock formation. (c) Imaging Thomson-scattering-measured electron density. Similar to the electron temperature, an increase in density is observed. EPW: electron plasma wave.

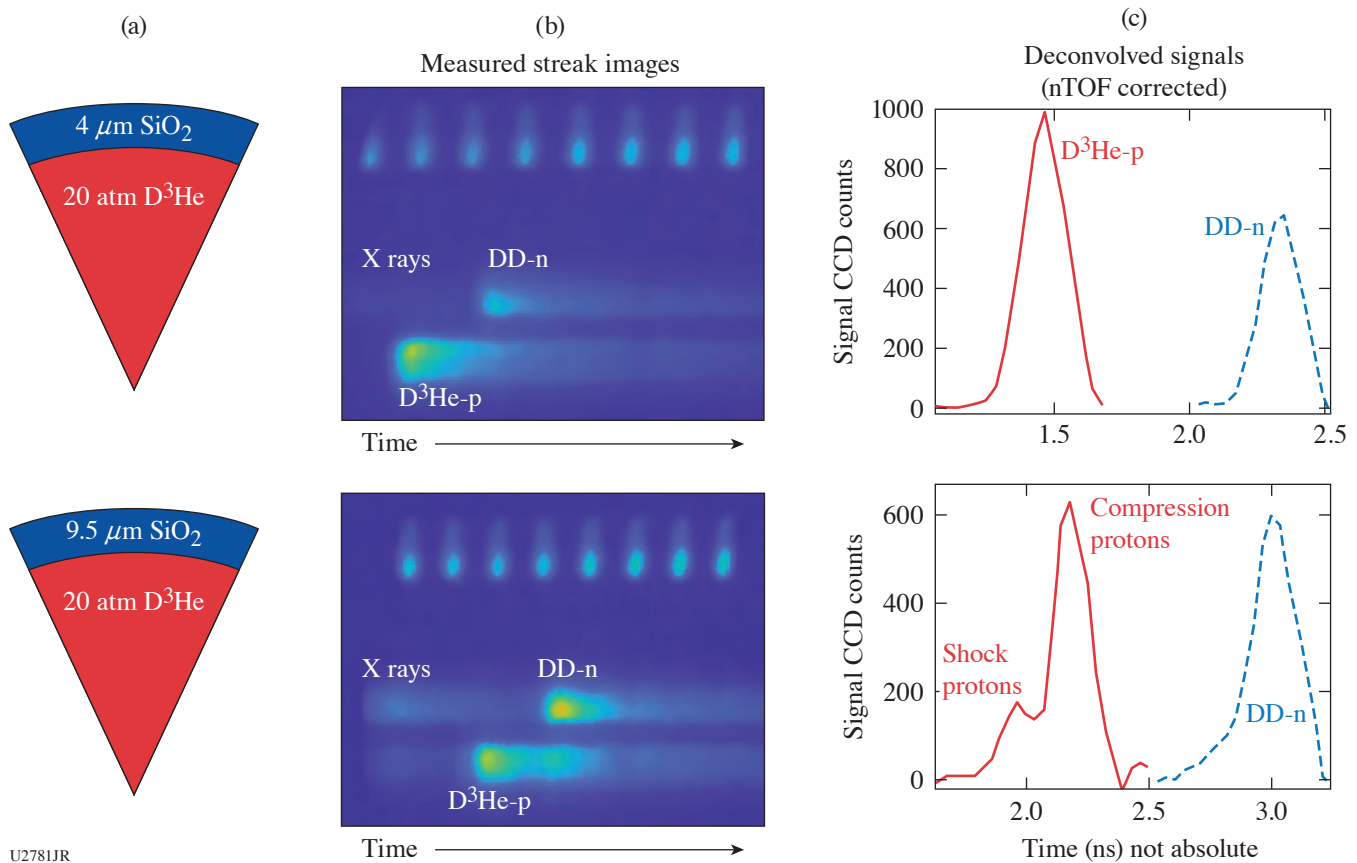
the size of the shock. The Thomson-scattering data also provided a measurement of the flow velocity, which confirms that our system has very low collisionality. Additionally, proton radiography measurements show a clear shock structure, and electron spectroscopy measurements show that electrons are accelerated into a power-law distribution. Work is ongoing to finalize the analysis of these data and to perform comprehensive MHD and PIC simulations.

This work was supported in part by the National Laser Users' Facility under Contract DE-NA0003938 and Laboratory for Laser Energetics under Contract 417532G/UR FAO GR510907.

Measurement of Multiple Nuclear Emission Histories in the Transition from Shock to Compression-Dominated Implosions

Principal Investigators: N. V. Kabadi, P. J. Adrian, and J. A. Frenje (Plasma Science and Fusion Center, MIT)

The primary goal of these experiments was to collect data related to multi-ion and kinetic effect in the transition from shock-dominated to compression-dominated implosions by varying the shell thickness in glass capsules. It was previously found that ion species separation and thermal decoupling between ion species impact nuclear emission during the shock-convergence and rebound phases.¹⁶ The experiments were designed to determine if these effects impact the subsequent compression phase. The primary data for this investigation are the DD-n yields and ion temperatures from neutron times of flight (nTOF's), D³He-p yields and spectra from the wedge-range filter spectrometers, and simultaneous measurement of the DD-n and D³He-p emission histories on the particle x-ray temporal diagnostic (PXTD). The PXTD data collected on shots with a 4-μm-thick shell show a fully shock-dominated emission history as shown in Fig. 12, while data collected with 9.5-μm-thick shells have separate D³He-p shock and compression components as also shown in Fig. 12. The arrival histories at the scintillator 3 cm from target chamber center (TCC) can also be seen in Fig. 12. These will be corrected for the particles' times of flight pending CR-39 processing. The two emission histories will be determined with ~10-ps cross timing uncertainty. The ratio of the DD-n to D³He-p emission histories in combination with the total yields and burn-averaged ion temperatures will be used to determine if the data are consistent with average-ion hydrodynamics.



U2781JR

Figure 12

Examples of the PXTD data collected on the OMEGA shot day PXTD-20A, delayed to FY21. Using the PXTD, the DD-n and D3He-p emission histories were captured on a single diagnostic, allowing detailed comparison of their relative timing. The implosion with a 4- μm -thick shell shows D³He-p and DD-n histories dominated by a shock flash component while the 9- μm -thick shells produced DD-n dominated by compression and D³He-p with both shock and compression components.

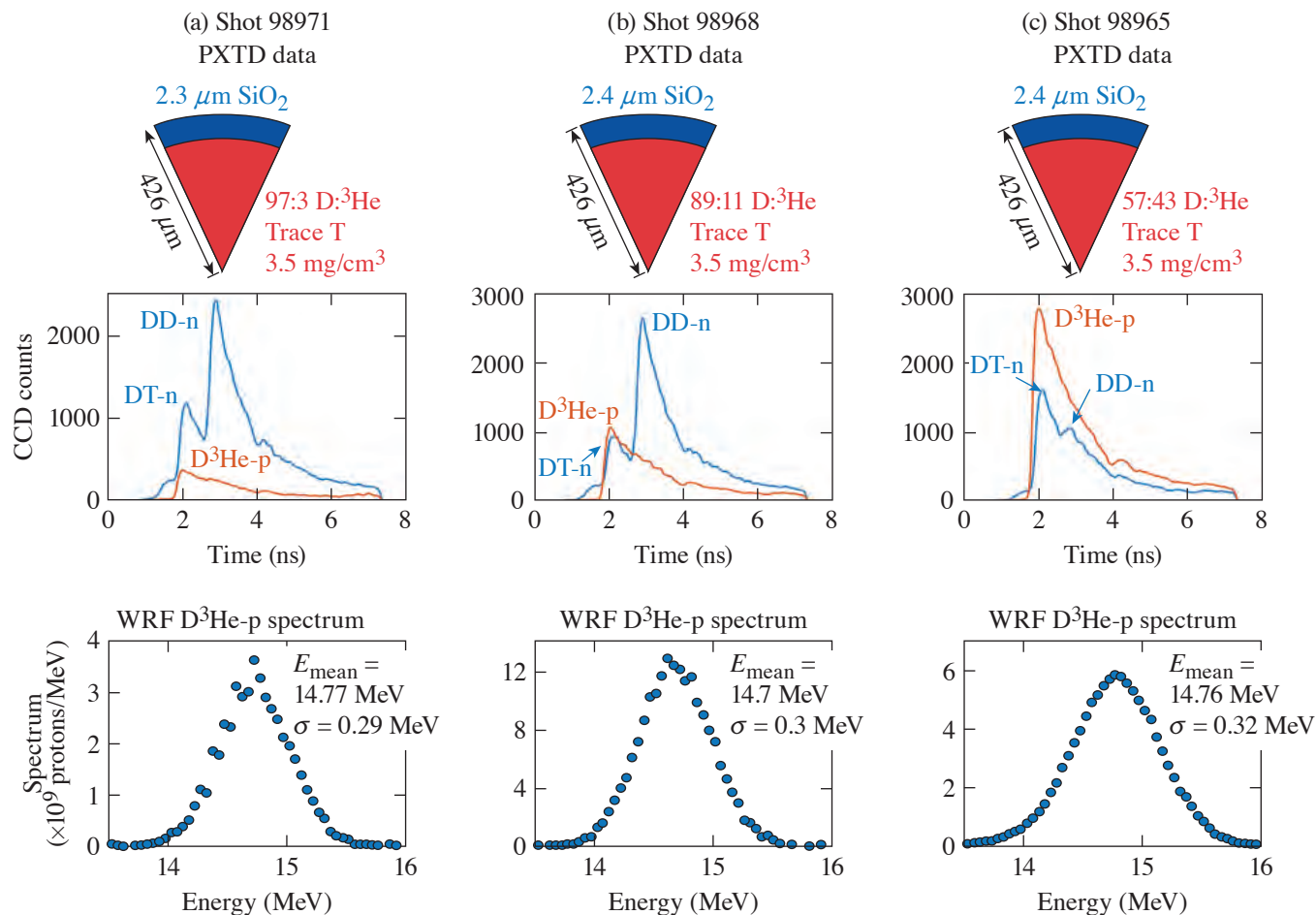
This material is based upon work supported by the Department of Energy, National Nuclear Security Administration under Award Nos. DE-NA0003868 and DE-NA0003938.

Measurement of Multiple Nuclear Emission Histories in Hydro-Equivalent Shock-Driven Implosions

Principal Investigators: N. V. Kabadi, P. J. Adrian, and J. A. Frenje (Plasma Science and Fusion Center, MIT)

The goal of this study is to better understand the previously observed multi-ion dynamics during the shock convergence phase of ICF implosions.^{17,18} These experiments used thin glass shells filled with high-density, 3.5-mg/cm³ gas comprised of mainly deuterium and ³He with a trace amount of tritium. More details of the experimental configurations are shown in Fig. 13. The initial gas density was held constant while varying the D:³He fill ratio, making the implosions hydrodynamically equivalent. The fill ratios allow simultaneous measurement of the DD-n, DT-n, and D³He-p emission histories with the PXTD.¹⁷ By measuring all three histories on a single diagnostic, they can be compared with ~ 10 -ps relative timing accuracy. An example of this data is shown in Fig. 13. PXTD uses fast-rise scintillators coupled to an optical streak camera so all of the information is encoded in the rising edges. To interpret the PXTD data, the emitted D³He-p spectrum measured with wedge-range-filter (WRF) spectrometers is also critical; example spectra are included in Fig. 13. From these data, the source of previously observed bang-time separation can be determined. It will be attributed to multi-ion diffusion, kinetics, or hydrodynamics based on how the bang-time separation varies with initial fill ratio. Analysis and preparation for publication are ongoing.

This work was supported in part by the National Laser Users' Facility under Contract DE-NA0003938, Laboratory for Laser Energetics under Contract 417532G/UR FAO GR510907.



U2782JR

Figure 13

Examples of the PXTD and WRF data collected on the OMEGA shot day PXTD-20B, delayed to FY21. Using the PXTD the DD-n, DT-n, and D³He-p emission histories were all captured on a single diagnostic, allowing detailed comparison of their relative timing. Direct measurement of the D³He-p spectrum with WRF's is critical to interpreting this data.

Germanium Dioxide Under Ramp Compression to Extreme Conditions: Phase Transitions in a SiO₂ Analog

Principal Investigators: D. Kim, I. K. Ocampo, and T. S. Duffy (Princeton University); and R. F. Smith and F. Coppari (LLNL)

The high-pressure behavior of AO₂ compounds is of long-standing importance due to their extensive polymorphism and varied transformation pathways. In particular, GeO₂ is one of a family of dioxides whose high-pressure behavior has been of interest as an analog for the behavior of SiO₂ in the deep mantles of terrestrial-type exoplanets. Pressures in the mantles of such exoplanets are expected to exceed 1 TPa, which is far in excess of those attainable in standard static high-pressure experiments. Ramp compression combined with *in-situ* x-ray diffraction (XRD) using the Omega Laser Facility allows one to observe the structure behavior, phase transitions, and kinetics of planetary materials at these conditions.

SiO₂ is expected to adopt low-symmetry crystal structures including the cubic pyrite-type ($Pa\bar{3}$) phase at high pressure and the hexagonal Fe₂P-type or orthorhombic cotunnite-type structures (coordination number of 9). These phases of GeO₂ are predicted

to be stable at lower pressures than in SiO_2 as a consequence of the larger ionic radius of Ge^{4+} relative to Si^{4+} . The challenges in investigating oxide minerals using *in-situ* XRD measurements under dynamic compression are their weak diffraction signal resulting from low-symmetry structures and the low atomic number constituents. In this study, we have examined the high-pressure behavior of GeO_2 under extreme conditions under ramp loading using OMEGA and OMEGA EP lasers.

Sixteen shots on GeO_2 were performed. Polycrystalline α -quartz GeO_2 was compressed to 3 GPa in a diamond-anvil cell producing 10- to 19- μm -thick pellets. The sample pellet was glued between a diamond ablator and either a LiF window for low-pressure experiments (<400 GPa) or a diamond window for high-pressure experiments (>400 GPa). The target assembly was backed by a metal foil with a pinhole material that serves to collimate the x-ray beam. The ramp-shaped laser pulses were used to generate strong compression waves, producing a series of reverberations at layer boundaries in the target package to produce uniform high-pressure conditions in the sample. At predicted peak pressure, a 1- to 2-ns x-ray pulse was generated by irradiating metal foils, and diffracted x rays were recorded on the image plates behind the sample. The velocity at the interface between the sample and LiF window or the free-surface velocity of the rear diamond was measured to determine the stress history within the sample.

We have examined the crystal structure of GeO_2 up to 882 GPa under ramp loading, higher stress than previous studies by a factor of 5. One to five sample diffraction lines were observed from 154 to 882. Our study of GeO_2 shows that pyrite-type GeO_2 occurs from 154 GPa to 436 GPa, which extends to higher pressure than that predicted by theory (~ 300 GPa). Above 436 GPa, we observe evidence for a post-pyrite phase in GeO_2 . Based on the diffraction data, the best candidate for this new phase is the cotunnite-type structure, which has been predicted to be a stable phase of GeO_2 above 300 GPa (Fig. 14). Our results demonstrate that ramp compression can be an effective technique for synthesizing and characterizing dense phases in oxides. Furthermore, we show that ramp compression may also be used to identify lower-symmetry phases in oxide materials. This analog study offers a test of theoretical calculations as well as the crucial information to explore high-pressure behavior of SiO_2 .

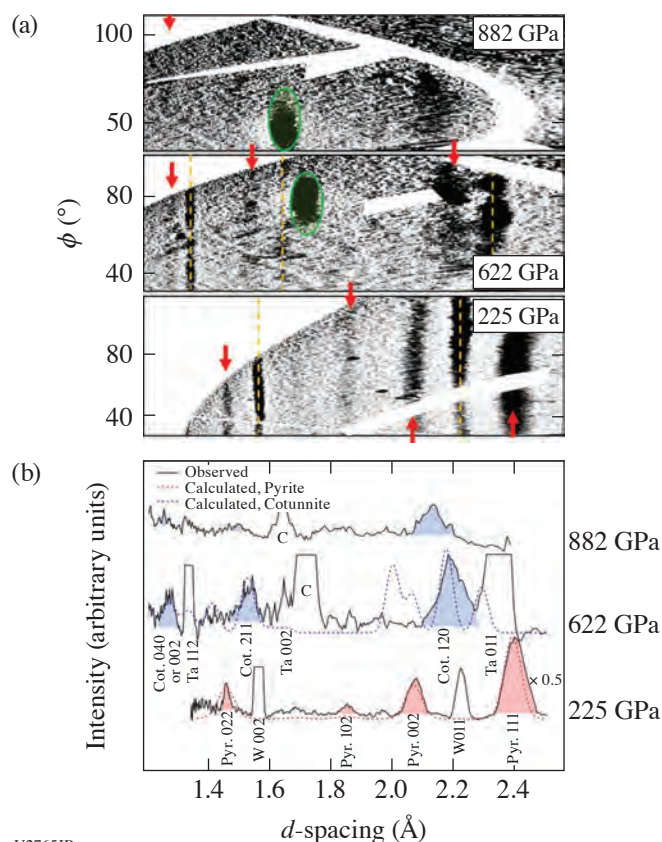


Figure 14

Representative (a) XRD images and (b) integrated 1-D diffraction patterns for ramp-compressed GeO_2 . (a) The red arrows indicate the diffraction peaks from the sample. The green ellipses show single-crystal Laue diffraction from diamond that can be identified as highly textured, localized peaks compared to the extended lines of GeO_2 . Yellow dashed lines denote diffraction from the pinhole substrate. (b) Pink- and blue-shaded peaks show the observed GeO_2 diffraction lines compared with the calculated diffraction pattern for the pyrite-type structure at 225 GPa (dashed red line) and cotunnite-type structure at 622 GPa (dashed blue line), respectively. The observed diffraction lines at 882 GPa are consistent with the cotunnite phase but could not be calibrated precisely due to the lack of recorded pinhole diffraction signal. "C" denotes a single-crystal spot corresponding to the green ellipse.

U2765JR

Developing Multipurpose Capsule Backlighters

Principal Investigators: C. C. Kuranz, H. J. LeFevre, and K. V. Kelso (University of Michigan)

Many experiments use capsule implosions as x-ray backlighters.^{19,20} As x-ray sources, they are bright, short-duration emitters of continuum soft x rays below 10 keV with small spatial extent. With a large physics target, however, it can be difficult to direct beams to the capsule uniformly, and an understanding of the influence of the laser irradiation pattern on the backlighter performance is necessary. Keiter *et al.* addressed this issue in work to observe the duration and spectral content of capsule backlighters with anisotropic laser patterns.²¹

A case can also be made that the capsule backlighters are not being used to their full potential. The capsule implosion, which creates the backlighter, contains a considerable amount of energy and heats the stagnated plasma to kilovolt temperatures with densities significantly above solid density. This is a useful set of conditions and with the appropriate target geometry could create a source that has bright continuum and line emission that would be capable of making two measurements with a single source.

On recent OMEGA shot days, with the participation of graduate student K. V. Kelso and postdoctoral research fellow H. J. LeFevre, we explored capsule backlighters with anisotropic laser irradiation patterns and specifications to produce useful line and continuum emission. The experiments used multiple spectrometers along with framing cameras to diagnose the emission from the capsule. The work on anisotropic laser irradiation patterns expands the work of Keiter *et al.* through the development of a metric to characterize the initial laser pattern on a capsule.

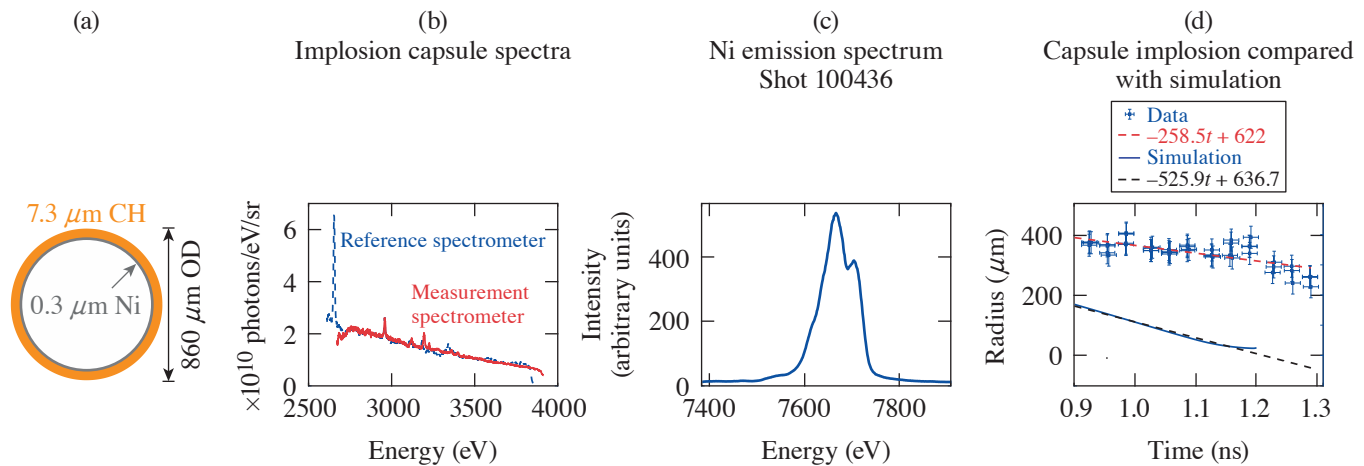
$$\phi = \frac{1}{N_{\text{LOS}}} \sum_i^{N_{\text{LOS}}} e^{-\left|1 - \frac{I_{\text{LOS},i}}{\bar{I}}\right|}, \quad (1)$$

where ϕ is the metric to determine the laser pattern anisotropy, N_{LOS} is the number of lines of sight in the capsule model, $I_{\text{LOS},i}$ is the rms intensity for a particular line of sight, and \bar{I} is the average intensity over the entire capsule surface. This parameter is one where the laser intensity is uniformly distributed over the surface of the capsule and zero when the intensity is localized to very small spots on the capsule. For laser irradiation patterns using VisRad,²² the value of ϕ is 0.9983 for a 60-beam illumination on OMEGA and 0.9424 for the experiments presented here.

This work creates a dual-source backlighter using a nickel layer on the interior surface of a standard CH vacuum capsule. The thicknesses of the layers are adjusted to keep the mass of the capsule identical to the typical 9- μm wall thickness and 860- μm outer diameter of the commonly used vacuum capsules. This should produce continuum emission in the 2- to 5-keV range, which would be useful as an absorption probe for features near the Ar K-shell and line emission from the Ni K-shell near 7.8 keV. The line emission could act as a pump for fluorescence measurements or as a probe for x-ray Thomson scattering with the correct experimental design. Figure 15(a) shows the capsule specification for the dual-source design.

Spectral measurements using an XRS in ten-inch manipulators TIM-1 and TIM-3 provide some understanding of the uniformity of the emission from these backlighters. Figure 15(b) compares x-ray spectra between two lines of sight using a CH vacuum capsule and time-integrated, flat crystal spectrometers observing emission in the 2- to 4-keV range. The analysis converts the image plate readout to an absolute photon spectrum using a common approach,¹⁹ but it is important to point out that this is only accurate to the image-plate sensitivity, crystal rocking curve, and filter attenuation, which were all calculated and not measured in this work.

The emission from the nickel-lined capsules used the SXS, the imaging x-ray Thomson scattering (IXTS) spectrometer, and an XRS to monitor the line emission. Figure 15(c) shows the Ni K-shell emission from the XRS clearly indicating the presence of bright lines that have similar contrast to laser-irradiated foil targets. Data from the SXS and IXTS confirm these findings and show that the line emission does not extend outside the original bounds of the capsule, but this is not shown here. This may indicate the hot electrons and high-energy photons from the laser-plasma interactions are interacting with the nickel early in time. Figure 15(d) compares the outer diameter of the imploding capsule as a function of time from framing-camera measurements with



U2788JR

Figure 15

(a) The specified dimensions of the Ni-lined capsules used to produce an x-ray source that has a tailored spectrum to produce line and continuum emissions that are useful for measurements. (b) A comparison of two time-integrated spectrometers viewing an evacuated, CH capsule from TIM-1 and TIM-3 on the same shot. The text provides caveats to the accuracy of the photon number spectrum. (c) The Ni K-shell using an XRS from an experiment using a lined capsule that shows the bright, high-contrast lines that could provide an additional probe for a diagnostic. (d) A comparison of the outer diameter of a Ni-lined capsule implosion between 1-D simulation results and framing-camera data. The difference in the minimum diameter could be due to the 3-D nature of the experiment from the anisotropic laser irradiation pattern.

1-D simulation results. The framing camera used here had an 8×-16 nose cone with a 50-ps pulse forming module (PFM) on a charge-coupled device (CCD). There was also a pair of filters, 10 μm Ni and 12.5 μm Mo, that restricted the transmitted light to the spectral range of the nickel K-shell. This analysis draws circles around the framing-camera images with a threshold for the average pixel to determine the outer boundary of the capsule. The error bars in this figure use the pinhole and motion blurring for the spatial dimension and the PFM and bias voltage for the time axis. This shows that the simulations are reaching a much smaller minimum radius than the experiments. There are many possible reasons for this: The anisotropic nature of the laser irradiation pattern will create a very nonuniform implosion that causes the stagnated plasma to be highly aspherical. Additionally, there is the potential for hydrodynamic instabilities to develop at the interfaces, which will reduce the inward velocity of the nickel flow, resulting in lower compression. These are also 1-D simulations of a problem that will have significant 3-D effects, leading one to expect differences when comparing with experimental results.

This work is funded by the U.S. Department of Energy NNSA Center of Excellence under Cooperative Agreement number DE-NA0003869 and the National Laser User Facility Program.

Collision of Two Magnetized Jets Created by Hollow Ring Lasers

Principal Investigator: E. Liang (Rice University); and H. Ji and L. Gao (Princeton Plasma Physics Laboratory)

The goal of this proposal is to take advantage of the 60 OMEGA laser beams to create and study strong, magnetized, high beta shocks by colliding head-on two supersonic MG magnetized jets created by irradiating flat plastic targets with a hollow ring of laser beams. In our previous OMEGA experiments, we have successfully demonstrated creation of a narrowly collimated plasma jet with MG-level magnetic fields around the jet by irradiating 20 OMEGA beams onto a flat plastic target in a ring pattern.²³ The jet properties were characterized as a function of ring radius d and target composition (pure CH versus 2% Fe-doped CH). The strong MG poloidal magnetic field of these jets is created via the Biermann battery mechanism by the collisions of individual beam blowoffs and compressed by the on-axis flow. The field gets stronger, more ordered, and persists to greater distances from the target as d is increased from 0 to 1200 μm. During FY21, we successfully carried out two OMEGA experiments (one OMEGA only and one joint experiment) to study collision of two such counter-propagating jets and the formation of shocks.

Figure 16 is a sketch of the OMEGA-only experimental setup where 19 OMEGA beams from each of the OMEGA hemispheres irradiated a flat CH target with a hollow ring pattern having an 800- μm ring radius. The jet properties in terms of collimation, flow speed, and magnetic-field generation were optimal in our previous campaigns. The two jets were separated by 6.4 mm. We employed three main diagnostics to characterize the properties and evolution of the collision region near TCC: Thomson scattering (TS), proton radiography, and an XRFC. The TS diagnostic measures the time evolution of density, electron and ion temperatures, and flow velocity at TCC, at 0.15 mm, and 0.25 mm from TCC along the jet axis. Beam 25 was used for TS. For the OMEGA-only experiment, monoenergetic protons generated from D^3He implosions with the rest of the 21 OMEGA beams were used to probe the magnetic-field geometry and magnitude. The primary difference between the OMEGA-only and joint experiments was the proton radiography diagnostic. For the joint experiment, broadband protons generated by intense laser–solid interactions using the OMEGA EP beam were used for proton radiography. The XRFC was used to capture time-lapse x-ray images of the entire domain. We obtained excellent data from all diagnostics for both experiments.

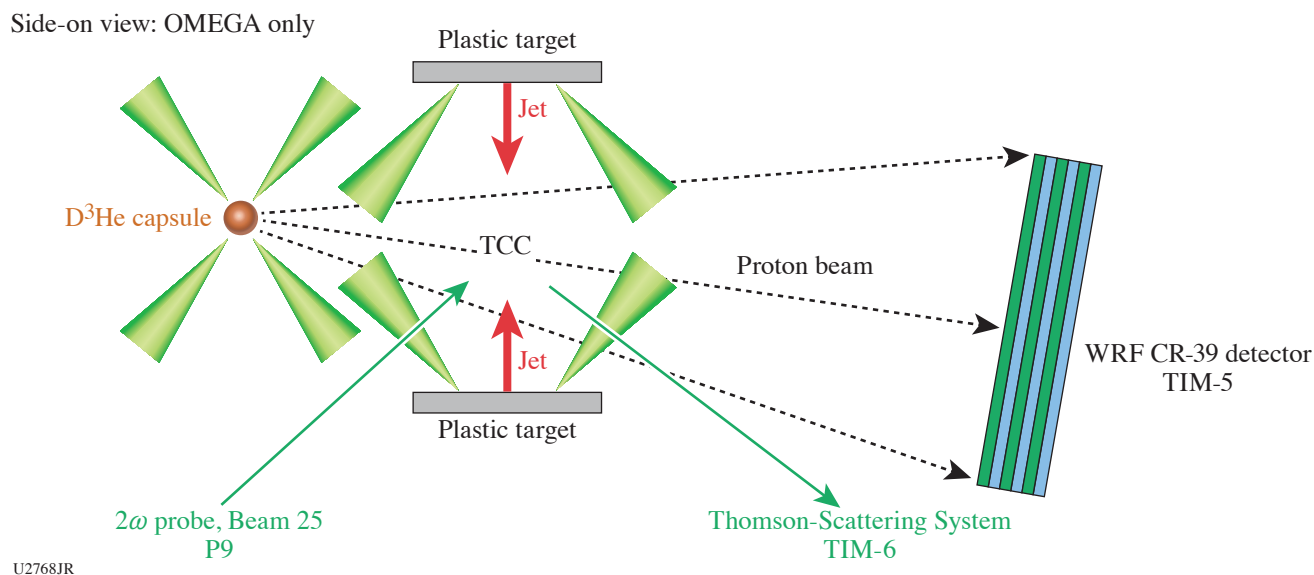


Figure 16
Sketch of the experimental setup for two colliding magnetized jets.

Figure 17 shows the measured XRFC data as a function of time in direct comparison with 3-D *FLASH* simulations. The experimental data show very nicely the jet formation and collision and the shock formation. Because of the assumption of Spitzer electron thermal conductivity in *FLASH*, the electron thermal conduction fronts run far ahead of the shocks. The quasi-isothermal electron temperature profile away from TCC is much hotter than the ion temperature. By comparing the *preliminary* TS, proton radiography (Prad), and XRFC data with 3-D *FLASH* predictions, we arrive at the following tentative conclusions:

1. The XRFC images show that the morphology of the shocked region strongly resembles those predicted by 3-D *FLASH*. The shocked region appears well defined and largely orthogonal to the jet axis as predicted, with only a slight tilt, due to the (unavoidable) small misalignment of the two jets.
2. The TS data at TCC agree very well with 3-D *FLASH* predictions for density, electron, and ion temperatures. This gives us comfort in the performance of 3-D *FLASH* simulations.
3. The TS-derived electron temperature at 0.15 mm below TCC appears, however, *much lower* than 3-D *FLASH* predictions, which was based on Spitzer (2006) electron thermal conductivity. This suggests that the *true electron thermal conductivity*

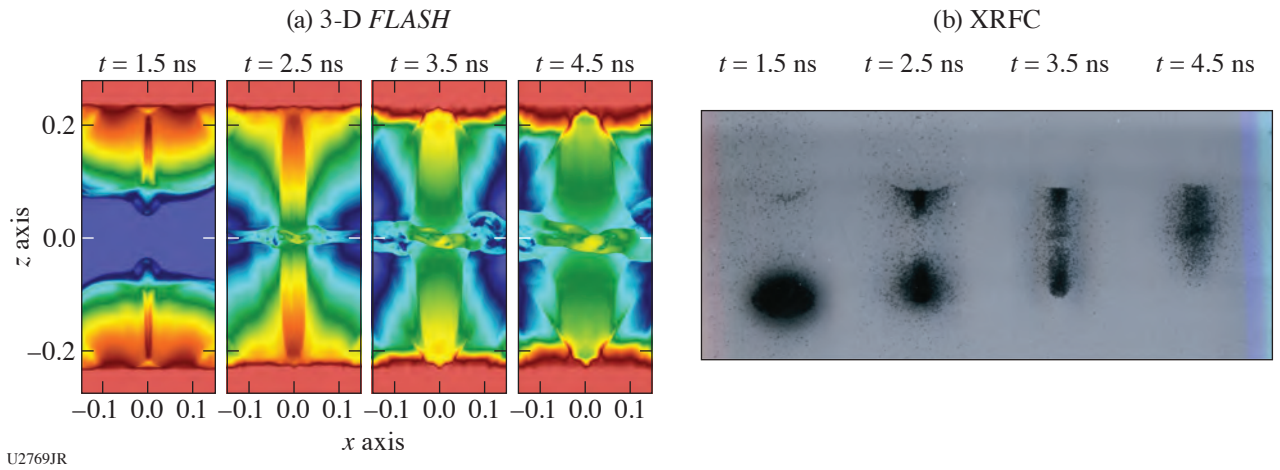


Figure 17

(a) Three-dimensional *FLASH* predictions of the jet and shock morphology largely resemble (b) the XRFC images. Both the simulated and XRFC images show a slight tilt of the shocked region due to the imperfect alignment of the two colliding jets.

ity must be lower than predicted by the Spitzer model, most likely due to strong magnetic fields orthogonal to the jet axis, which inhibit electron transport along the flow. Further study using a modified *FLASH* code with *self-consistent* magnetized anisotropic electron transport is in progress.

The Prad data of Fig. 18 shows that, while the fields far from the contact surface remain parallel to the jet axis as in previous single-jet Prad images, *in the region between the shocks, the fields appear to be largely parallel to the contact surface and orthogonal to the jet axis*. This is consistent with *FLASH* predictions. The field direction appears to turn somewhere between the shock and the electron-conduction front positions. We emphasize that our field patterns are completely different from those created by Weibel (1959) instability in the collisionless regime.

This work was supported by the National Laser Users' Facility under Grant No. DOE DE-NA0003942.

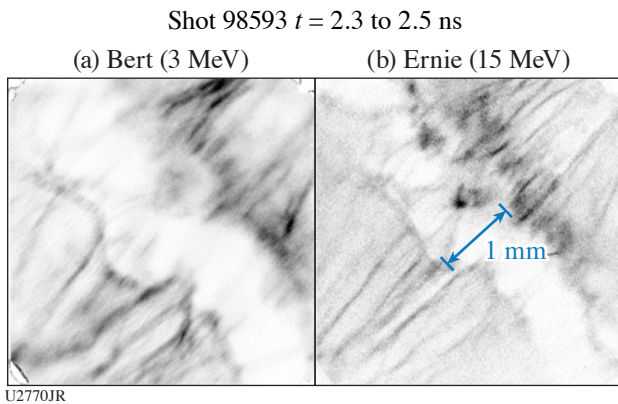


Figure 18
Sample proton images; jet axes run from lower left to upper right.

A Laboratory Photoionized Plasma Experiment on OMEGA EP

Principal Investigators: R. C. Mancini (University of Nevada, Reno); R. F. Heeter and D. Liedahl (LLNL); and S. P. Regan (LLE)

Photoionized plasmas are widespread in the universe, e.g., active galactic nuclei, warm absorbers, x-ray binaries, and the accreting disks surrounding black holes. The focus of this project is to study in the laboratory the heating, temperature, and

charge-state distribution of photoionized plasmas driven by a broadband intense flux of x rays. Most laboratory work performed to date on laboratory plasmas pertains to collisional plasmas, i.e., those where electron collisional processes play a dominant role in the plasma ionization and atomic physics. Relatively little attention has been paid, however, to understanding the basic properties of laboratory photoionized plasmas where both photoionization and photoexcitation, driven by a broadband x-ray flux, become dominant. The quantitative information that we obtain from these objects is based mainly on the analysis of spectroscopic observations made by orbiting telescopes such as Chandra and XMM-Newton. The complexities of the astrophysical environment make the spectral analysis challenging, however, and laboratory experiments are critically needed to benchmark analysis codes.

We have established a new experimental platform for OMEGA EP that uses a plastic-tamped silicon sample driven by the 30-ns-duration, broadband x-ray flux produced by the Gatling-gun radiation source. This source is comprised of three copper hohlraums that are sequentially driven by three OMEGA EP beams, each one delivering 4 kJ of UV energy in a 10-ns square pulse shape. Each copper hohlraum has a length of 2.8 mm and an inner diameter of 1.4 mm and is filled with TPX foam. The laser beams sequentially illuminate one hohlraum at a time, thus producing an x-ray flux characteristic of 90-eV radiation temperature for a time period of 30 ns. The relatively long duration of the Gatling-gun radiation source is critical to producing a plasma in photoionization equilibrium where photoionization is counterbalanced by radiative and dielectronic recombination.

The experimental setup has three components: (1) the Gatling-gun x-ray source, (2) a tamped silicon sample, and (3) a titanium backlit source. The silicon sample has a diameter of 2 mm and is placed at a distance of 7 mm from the source. It has an initial thickness of 0.2 or 0.4 μm and is coated on both sides with submicron-thick, 2.5-mm-diam layers of parylene plastic. Heated by the x-ray flux, the tamped silicon sample expands and ionizes into the L-shell range of silicon ions; i.e., neon- to lithium-like ions, thereby producing a photoionized plasma in steady state with an atom number density of a few times 10^{18} atoms/cm³ and a relatively uniform spatial distribution.

The spatial extension of the blow-off TPX/copper plasma from the copper hohlraums is monitored with the 4ω probe laser to make sure that it does not reach the silicon sample. The silicon photoionized plasma is probed with L-shell self-emission spectra recorded with a grating spectrometer and K-shell line absorption spectra recorded with a KAP crystal streaked spectrometer. The latter is afforded by a 1-ns-duration, separate titanium backlight source driven by the fourth laser beam of OMEGA EP. This laser beam delivers 1 kJ of UV energy onto a titanium slab target in a 1-ns square pulse shape. The radiative recombination continuum emission photons of the titanium laser-produced plasmas backlight and probe the photoionized plasma via absorption spectroscopy. From this measurement, the charged-state distribution and electron temperature of the plasma can be extracted.

Figure 19 displays the transmission spectra recorded in a series of nominally identical experiments where the titanium backlight source was fired at three different times relative to the beginning of the x-ray drive. The Gatling-gun x-ray flux starts at $t = 0$ ns

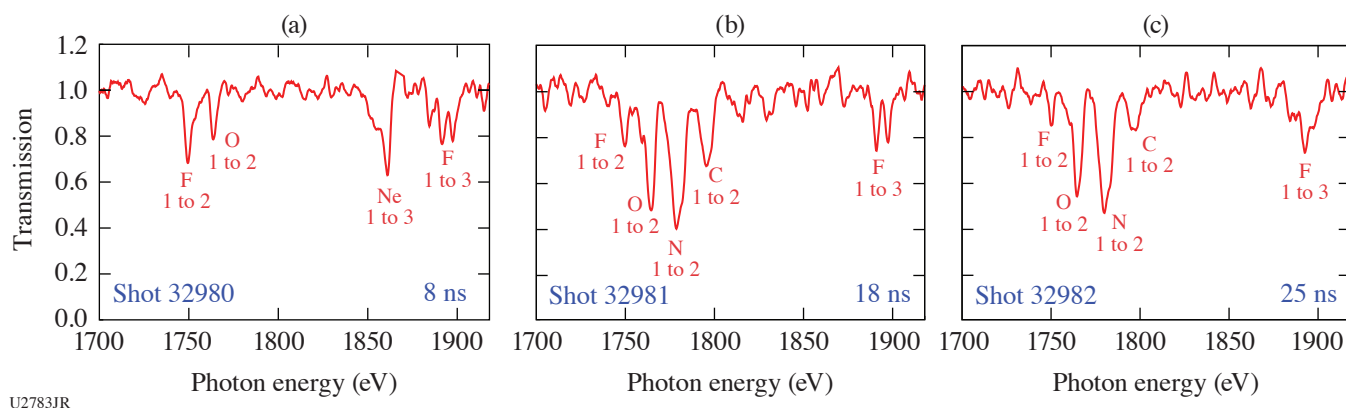


Figure 19

K-shell transmission spectra of the silicon photoionized plasma at (a) $t = 8$ ns, (b) 18 ns, and (c) 25 ns recorded in three nominally identical experiments on OMEGA EP. Shot numbers and line absorption transitions in Ne-, F-, O-, N- and C-like Si ions are indicated in the plots.

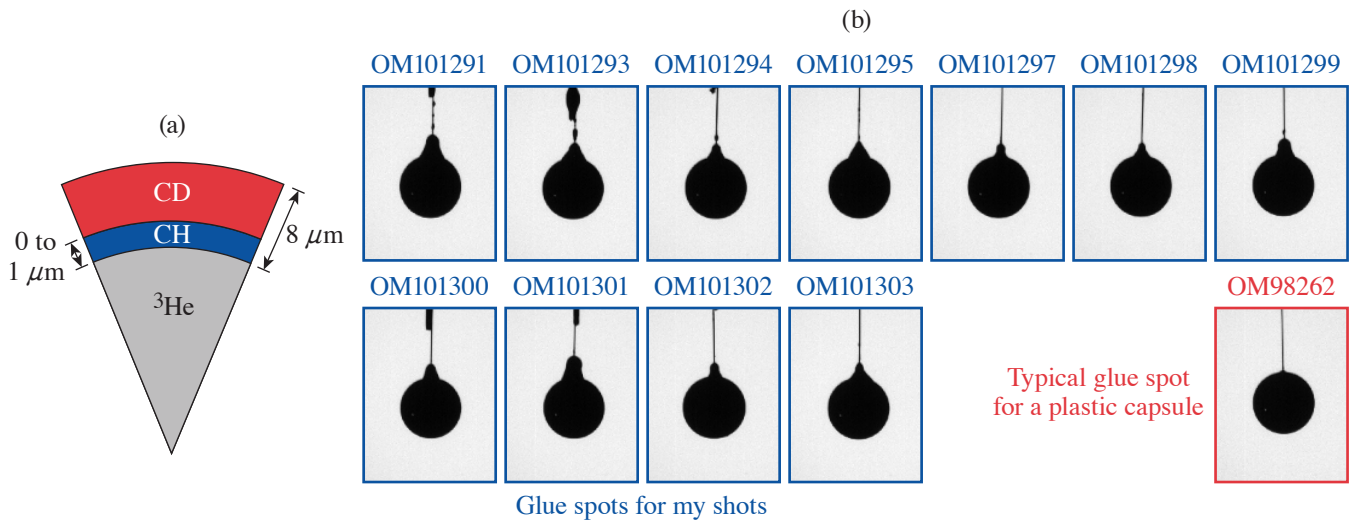
and lasts until $t = 30$ ns. The tamped silicon sample was $0.4\text{-}\mu\text{m}$ thick and tamped on both sides with $0.5\ \mu\text{m}$ of parylene. The data show $n = 1$ to $n = 2$ line absorption transitions in F-, O-, N- and C-like silicon ions as well as $n = 1$ to $n = 3$ in Ne- and F-like ions. On one hand, the observation at $t = 8$ ns is characteristic of the end of the initial phase of heating and ionization. It displays a silicon plasma that is just beginning to populate the range of L-shell ions. On the other hand, the transmission spectra recorded at $t = 18$ ns and $t = 25$ ns are nearly identical and dominated by $n = 1$ to $n = 2$ transitions in F-, O-, N- and C-like silicon ions. These nearly identical measurements demonstrate that a photoionized plasma in steady state has been produced in the laboratory for the first time. The latter is critical to compare with and benchmark the astrophysical modeling codes that are employed in the analysis and interpretation of x-ray astronomy observations.

Measurement of Kinetic Mix Mechanisms Using Separated Reactant Experiments in an Exploding-Pusher Regime

Principal Investigators: B. Reichelt, P. J. Adrian, N. V. Kabadi, C. K. Li, M. Gatu Johnson, and J. A. Frenje (MIT)

The goal of this campaign was to perform measurements of non-hydrodynamic mix mechanisms in exploding-pusher-type targets. Traditionally, ICF design has been chiefly driven by hydrodynamic simulations that have no models implemented to describe mixing of one material into another. During shock propagation, however, the high temperatures reached by ions challenges this assumption and can lead to situations where diffusion is the predominant source of mix, rather than hydrodynamic instabilities like Rayleigh–Taylor and Richtmyer–Meshkov. This work attempted to probe this effect using a CD shell with an inner CH offset of varying thickness and a ^3He fill, so that $\text{D}^3\text{He-p}$ observed must come through diffusion from the CD layer into the hot spot [Fig 20(a)]. The setup was similar to previous work done by Meany *et al.*²⁴ but extended to lower fill pressures and capsule thicknesses in order to capture a more exploding-pusher-like regime where a kinetic description of mix becomes necessary. Unfortunately, when the capsules were glued to the stalks, the glue spots were made out of spec and much too large [Fig 20(b)]. Since large glue spots introduce hydrodynamic mix mechanisms, it is nearly impossible to disentangle the cause of observed yields, so the physics goals of the experiments were compromised. The Omega scheduling facility has recognized this and has been working with us to schedule contingency shots to rectify this issue.

This material is based upon work supported by the Department of Energy, National Nuclear Security Administration under Award Nos. DE-NA0003868 and DE-NA0003938.



U2784JR

Figure 20

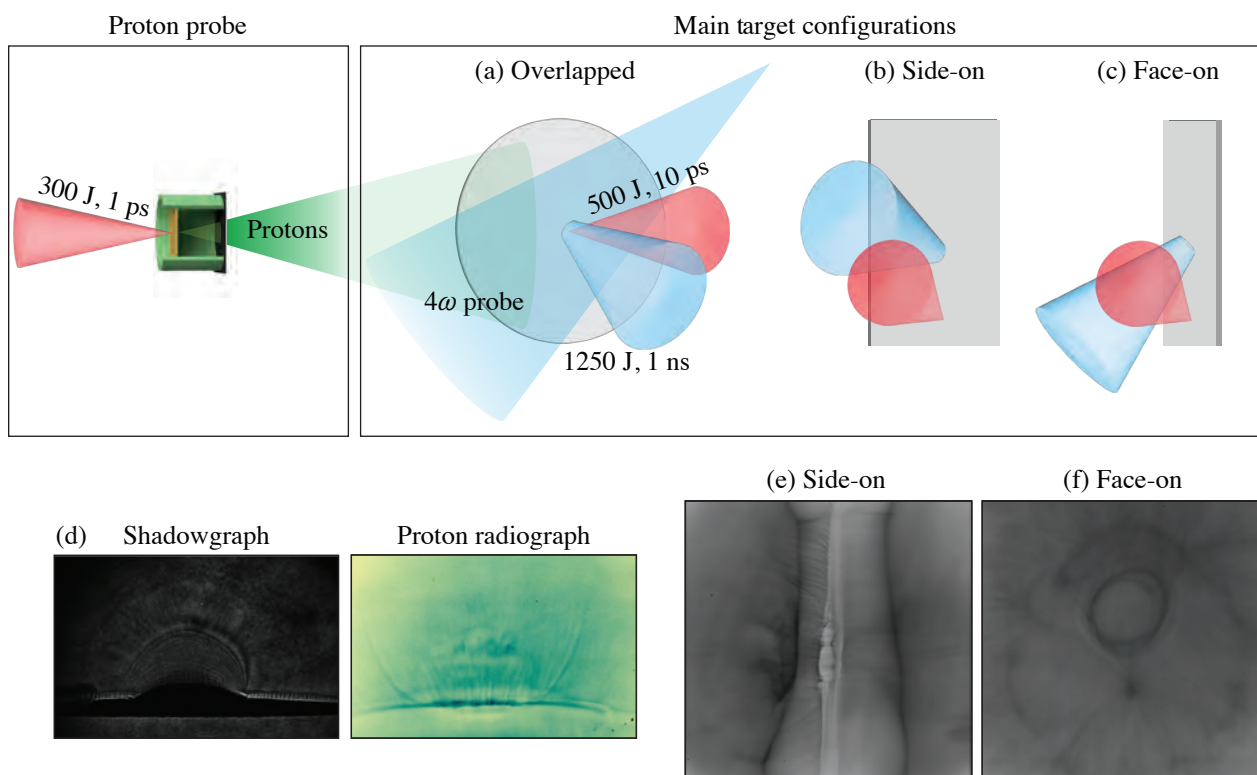
(a) A pie diagram illustrating the target design used for this set of experiments; (b) an illustration of the large glue spots that compromised the physics goals of this campaign.

The Dynamics of Magnetic Fields and Relativistic Electrons in Solid Target Interactions Using OMEGA EP

Principal Investigators: B. K. Russell, P. T. Campbell, G. Fiksel, H. Tang, A. G. R. Thomas, L. Willingale, and K. Krushelnick (G rard Mourou Center for Ultrafast Optical Science, University of Michigan); C. Dong (Princeton Plasma Physics Laboratory); C. A. Walsh (LLNL); and P. M. Nilson (LLE)

The strong magnetic fields produced during the interaction of lasers with solid-density targets have been used to study many processes in the laboratory including magnetic reconnection. The standard reconnection geometry uses two laser pulses interacting on a target to produce expanding plasma plumes with azimuthal magnetic fields.²⁵ These fields expand with the plumes and are antiparallel, allowing them to reconnect. Several experiments have been performed in this geometry with moderate intensity pulses studying reconnection dynamics including those in asymmetric reconnection.²⁶ Much higher intensity pulses have also been used, generating relativistic magnetized electrons that reconnected in the first demonstration of relativistic electron-driven magnetic reconnection.²⁷ On our first OMEGA EP shot day of FY21, we combined these ideas using a moderate intensity pulse and a relativistic intensity pulse to generate a highly asymmetric interaction. On our second OMEGA EP shot day, we explored a slight modification of this geometry with overlapped pulses similar to what has been used in studies for fast-ignition fusion.²⁸

We explored two geometries using interactions with foil targets: an asymmetric magnetic reconnection geometry and an overlapped short-pulse/long-pulse geometry. In the reconnection geometry, a 1-ns UV pulse was focused to an intensity of $\sim 10^{14}$ W/cm² on thin CH foils, 750 ps before the arrival of a short 500-J, 10-ps IR pulse with an intensity $>10^{18}$ W/cm² focused at various separation distances from the long-pulse focus. In the overlapped geometry, these same pulses were used; however, the short pulse was focused to the same position on the target as the long pulse [Fig. 21(a)] and CH and Cu foils were used. In



U2785JR

Figure 21

Main target configurations used in our two shot days in FY21 including (a) overlapped, (b) side-on, and (c) face-on. (d) The overlapped configuration allowed for simultaneous probing by the 4ω probe and protons. The (e) side-on and (f) face-on configurations show the fields in the interaction of the strongly magnetized relativistic electrons with the long-pulse plasma plume.

both geometries, protons were accelerated from Cu foils by a short-pulse 300-J, 1-ps laser and used to probe the interactions.²⁹ The protons were detected on a radiochromic film (RCF) stack, producing a time series of data on each shot. In the overlapped geometry, the 4ω probe was used to probe the interaction through polarimetry, shadowgraphy, and angular filter refractometry.

In the reconnection geometry, protons were used to image the fields with probing directions normal or transverse to the target surface [Figs. 21(b) and 21(c)], giving us a detailed picture of the interaction. Initially, the long-pulse laser produced a plasma plume with azimuthal magnetic fields generated by the Biermann battery mechanism, $\partial B/\partial t \propto \nabla T_e \times \nabla n_e$ (Ref. 30). The short-pulse then interacted with the foil at separation distances from the long-pulse focus of 1.25 to 2.65 mm, generating strongly magnetized relativistic electrons that expanded from the focal region. On the time scale of the relativistic electron expansion, the long-pulse plume is effectively a stationary magnetized obstacle. In the proton images, we see the formation of bow-shock-like features [Figs. 21(e) and 21(f)]. To understand these features, we performed a massive 3-D particle-in-cell simulation using the code *OSIRIS*^{31,32} on the NASA Pleiades supercomputer using ~ 2.5 M core hours. To reduce computation time, the long-pulse plasma plume was initialized in the simulation by fitting to the data obtained from extended-MHD simulations using the code *GORGON*.³³ Additionally, we have been using particle-tracking codes to generate synthetic radiographs of the simulation data. Analysis of the experimental and simulation data is ongoing.

On our most-recent shot day, we explored the interaction in the overlapped geometry shown in Fig. 21(a). A similar setup was used by Ivancic;³⁰ however, in our shot day, we used proton radiography to study the interaction in addition to the 4ω probe diagnostics. This allowed us to obtain information on both the density and fields in the interaction [Fig. 21(d)]. Shots were taken on Cu and CH, allowing us to study the effects of target material. The delay of the 4ω probe was varied, allowing us to observe the propagation of the short pulse into the long-pulse-generated plume. Analysis similar to that performed for the reconnection geometry will be performed for these data.

This material is based upon work supported by the Department of Energy, National Nuclear Security Administration under Award No. DE-NA0003954. P. T. Campbell is supported by the U.S. Department of Energy Fusion Energy Sciences Postdoctoral Research Program administered by the Oak Ridge Institute for Science and Education (ORISE) for DOE. ORISE is managed by Oak Ridge Associated Universities (ORAU) under DOE Contract No. DE-SC0014664. B. K. Russell acknowledges support from National Science Foundation (NSF) Grant No. 1751462.

Particle Heating by Collisionless Shocks in Magnetized High-Energy-Density Plasmas

Principal Investigators: D. B. Schaeffer (Princeton University)

Co-investigators: W. Fox and S. Malko (Princeton Plasmas Physics Laboratory); G. Fiksel (University of Michigan); and P. V. Heuer (LLE)

Magnetized collisionless shocks, in which the shock forms in a pre-existing magnetic field, appear in many space and astrophysical environments, including planetary shocks, supernovae remnants, and galaxy clusters. Of particular interest are high-Mach-number shocks, which are a key component of astrophysical plasmas and have been associated with extremely high-energy cosmic rays. These strongly driven shocks employ fundamentally different dissipation mechanisms compared to low-Mach-number shocks, resulting in a critical outstanding problem in shock physics: How is energy partitioned among particle populations across high-Mach-number shocks? Despite decades of *in-situ* studies by spacecraft, telescope observations, and corresponding numerical simulations, there remains a lack of understanding of the mechanisms by which particles are heated.

Through the AIBS Program, we carried out two experiments to study particle heating by magnetized collisionless shocks: one shot day on OMEGA and one shot day on OMEGA EP. In the OMEGA shots (MagShkHeat-21A), an external magnetic field was provided by MIFEDS-powered coils (similar in design to the “racetrack” coils used in previous shots^{34,35}), a background plasma was produced by ablating a CH foil, and the shock was driven by ablating a second CH foil to drive a piston plasma through the magnetized background plasma [see Fig. 22(a)]. The goals of the OMEGA shots were to measure electron and ion heating with Thomson-scattering diagnostic along two directions and to test the use of a gas jet. The Thomson-scattering diagnostic was set up to probe either parallel or perpendicular to the external magnetic field in order to measure the corresponding parallel or perpendicular heating. A third configuration replaced the background CH foil with a gas jet to test if the gas jet could provide a

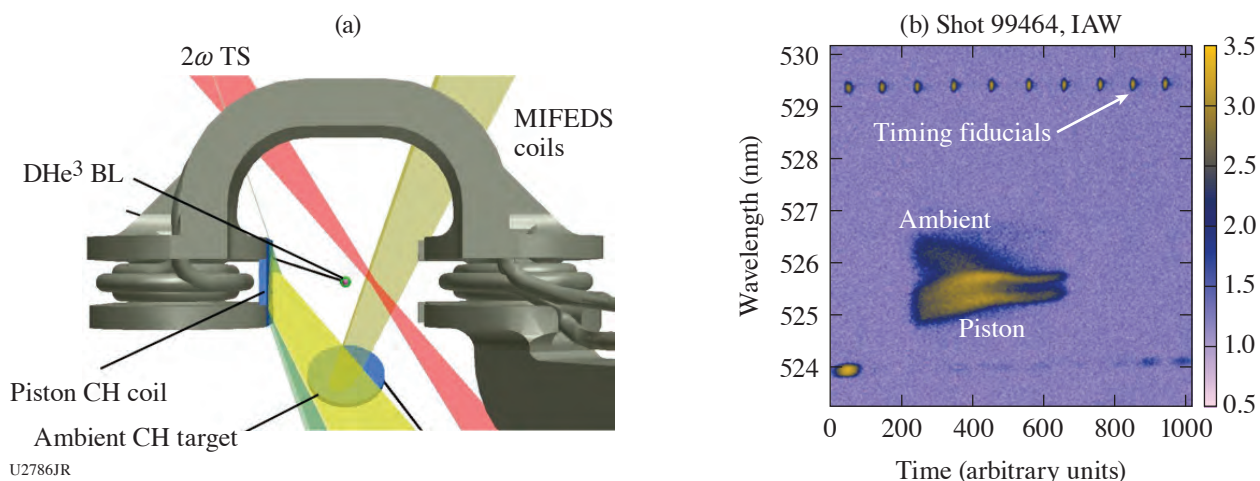


Figure 22

(a) Schematic of the experimental setup on OMEGA for probing perpendicular to the background magnetic field with Thomson scattering. By rotating the MIFEDS coils 90°, the Thomson-scattering diagnostic probed parallel to the field. The ambient CH target was replaced with a gas jet on some shots. (b) Example ion-acoustic wave (IAW) spectrum from the Thomson-scattering diagnostic.

better magnetized background plasma. We successfully acquired Thomson-scattering data in all three configurations, shown in Fig. 22(b). The data are currently being analyzed.

For the shot day on OMEGA EP (MagShkHeat-EP-21A), we designed a brand new MIFEDS-based platform [see Fig. 23(a)], with the goal of providing a more-uniform magnetized ambient plasma and larger magnetized system size. Instead of racetrack coils, we used a Helmholtz coil design, which allowed us to create large fields (~ 10 T) over several millimeters. The ambient plasma was created by ionizing the gas from a gas jet. Together, this platform allowed us to drive more-uniform shocks over much longer lengths and time scales than what we could achieve previously. The goals of the OMEGA EP shots were to validate this new platform and measure shock spatial scales as a function of shock speed (Mach number). The primary diagnostics were refracting imaging using the 4ω probe beam and proton deflectometry using short-pulse-driven TNSA (target normal sheath acceleration) protons. We also placed an image plate at the back of the proton RCF stack to capture an *in-situ* x-ray reference image of the mesh, which could then be compared to the proton image of the mesh to directly measure the proton deflections.

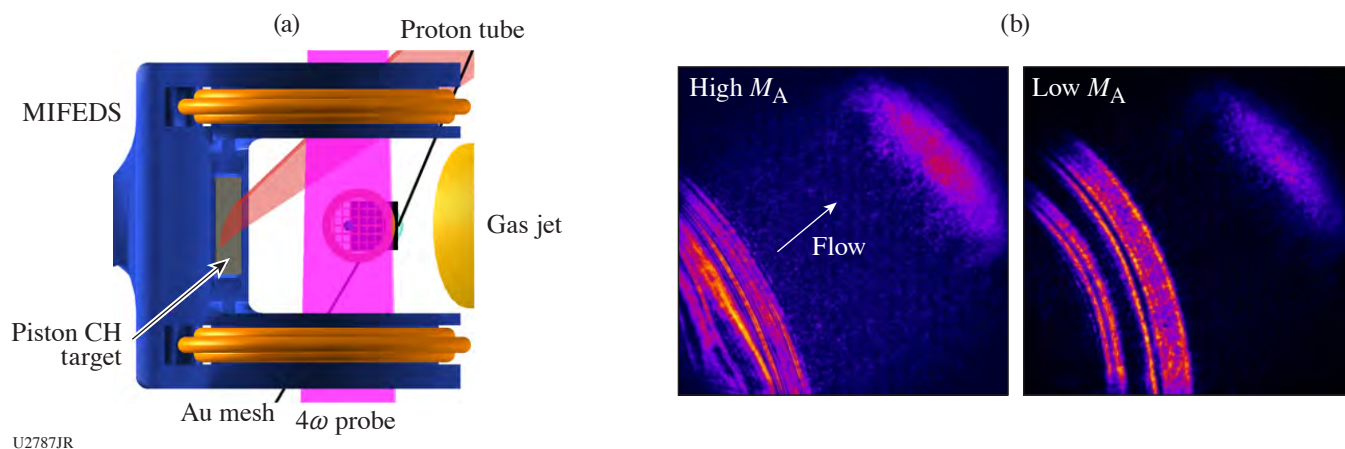


Figure 23

(a) Schematic of the experimental setup on OMEGA EP. (b) Example angular filter refractometry images for two shock Mach numbers.

We successfully demonstrated that the gas jet was compatible with the MIFEDS coils, although the coils were perturbed slightly by the gas pressure. We also successfully demonstrated for the first time that we could acquire a high-contrast *in-situ* x-ray reference image of a mesh.³⁶ We could only test this on one shot, however, since the gas pressure pushed the mesh into the proton tube. We nonetheless acquired excellent proton images (without mesh) on the remaining shots, as well as excellent shadowgraphy and angular filter refractometry images of the shock for several Mach numbers [see Fig. 23(b)]. There are clear variations in the shock structure with a Mach number, which we are currently analyzing.

This work was conducted at the Omega Laser Facility and funded under the auspices of the U.S. Department of Energy by the University of Rochester's Laboratory for Laser Energetics under Contract No. DE-NA0003856. This work was also supported by NASA under Grant No. 80NSSC19K0493.

Investigation of Hydrodynamics and Magnetic-Field Saturation in Foam-Lined Interfaces

Principal Investigators: G. D. Sutcliffe, T. Johnson, J. Percy, B. Lahmann, P. J. Adrian, N. V. Kabadi, M. Gatu Johnson, R. D. Petrasso, and C. K. Li (MIT); B. Pollock and J. Moody (LLNL); and J. Katz (LLE)

In ICF hohlraums, prior configurations used gas-filled hohlraums to slow the expansion of high- Z -ablated wall material into the path of the laser beams. This gas-fill technique has largely been abandoned on the NIF because it gives rise to large laser-plasma interactions. Other techniques have been proposed to counteract the expansion of the wall material, including foam-lined hohlraums.

Magnetic fields generated by the interaction of \sim ns lasers with foam-lined hohlraums could give rise to magnetic-field saturation, which scales differently than typically seen in experiments with solid-density targets.³⁷ When the target material is solid density, the ablated plasma exists in the "convective regime" of magnetic-field saturation, where $L/d_i > 1$ and peak magnetic fields are proportional to d_i/L (where d_i is the ion inertial length and L is the temperature-gradient length scale). When plasmas are generated from a foam material, the length scales can approach a different regime: a resistive dissipation regime, where $L/d_i \lesssim 1$ and the peak field goes as L/d_i . Pre-shot *FLASH* simulations of such a configuration corroborated this intuition: regions of Biermann magnetic-field generation have L/d_i of the order of unity, as seen in Fig. 24.

An example target can be seen in Fig. 25(a). Key diagnostics in this experiment are proton radiography to measure magnetic fields and Thomson scattering to measure plasma conditions. Time-staggered proton radiography shots characterize the instantaneous magnetic fields at a variety of times. Imaging Thomson-scattering data were acquired to characterize instantaneous density

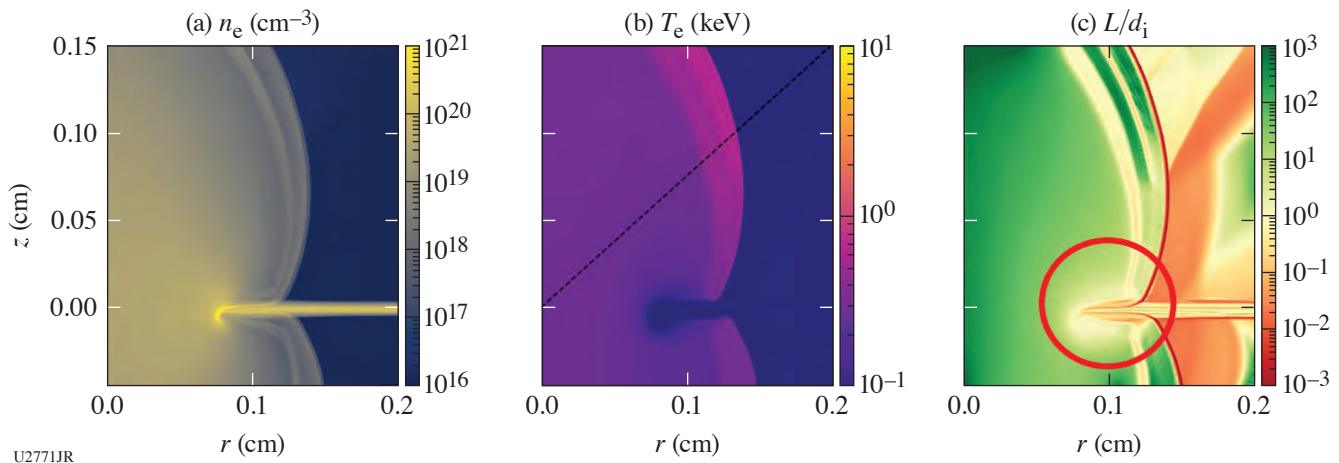
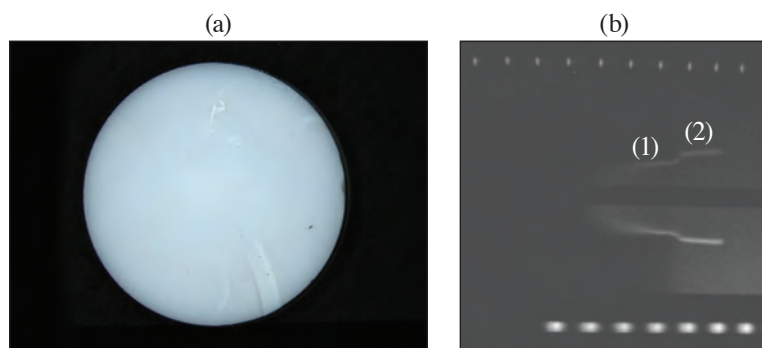


Figure 24

FLASH simulations showing the expected (a) electron density, (b) electron temperature, and (c) normalized length scale (L/d_i). In the region where Biermann fields are generated, L/d_i is of the order of unity.



U2772JR

Figure 25

(a) One of the 50-mg/cm³ foam targets, viewed face-on. (b) Thomson-scattering electron plasma wave data showing the evolution of plasma density in the region above the foil surface. At (1), we see the low-density material ablating from the foam portion of the target. In (2), the bubble is shocked by the ablation of the solid-density backing material expanding into the earlier bubble.

and temperature profiles in the ablated plasma region. The processing of proton radiography CR-39 detector data is underway. Interesting shock features can be seen in the Thomson-scattering data [Fig. 25(b)], which match *FLASH* simulations where a solid-density backing was included. Combined analysis of proton radiographs, Thomson-scattering data, and *FLASH* simulations is underway.

This work was supported in part by the National Laser Users Facility under Contract DE-NA0003938.

Relativistic Intensity Laser Channeling and Direct Laser Acceleration of Electrons from an Underdense Plasma

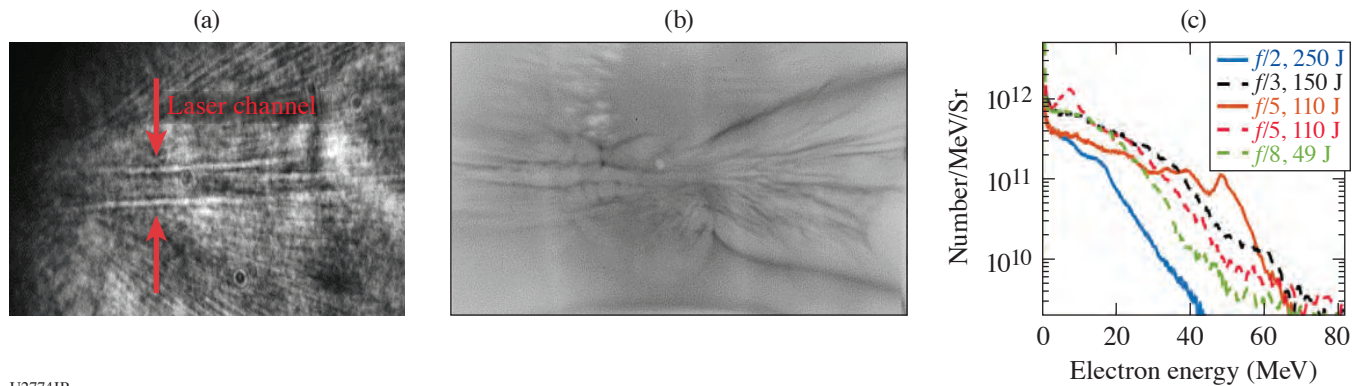
Principal Investigators: H. Tang, A. McKelvey, P. T. Campbell, B. K. Russell, Y. Ma, A. G. R. Thomas, and L. Willingale (University of Michigan); J. L. Shaw and P. M. Nilson (LLE); H. Chen and F. Albert (LLNL); and A. V. Arefiev (University of California, San Diego)

Laser-plasma interactions generate high-energy electrons, which have a number of applications, including generating secondary sources like x-ray radiation, electron-positron pairs, ion acceleration, or neutron generation. Direct laser acceleration (DLA) is one mechanism for producing these relativistic high-energy electrons. The transverse electric field of the laser pulse accelerates electrons too close to the speed of light, and the $v \times \mathbf{B}$ force converts electron transverse momentum to longitudinal momentum. If the interaction occurs within an underdense plasma, the localized electric and magnetic fields of the laser channel can significantly enhance the electron energy gain.^{38,39} Our experiments aim to understand the dynamic and complex DLA mechanism to optimize the high-energy electron beam production. During two shot days in FY21, we performed a series of shots to investigate the effects of the f number, laser pulse duration, and plasma density.

A backlighter short laser pulse with a 1053-nm wavelength was focused onto the edge of a 2-mm-diam helium gas-jet target. The backing pressure to the gas jet was varied to adjust the plasma density of the interaction. The laser pulse duration was varied between 1 to 5 ps, and the beam was apodized to alter the f number (and therefore the focal-spot size). The generated hot electrons were measured by a laser-axis EPPS and a transverse EPPS. The 4ω optical probe was employed to map the plasma density profile. The quasi-static electric- and magnetic-fields evolution of the plasma channel was observed using proton deflectometry. The proton probe was generated using the 1-ps sidelighter beam and a 50- μ m Cu foil. To improve the temporal resolution of proton radiography, we used a customized RCF pack.

A laser channel is observed in the 4ω shadowgraph shown in Fig. 26(a). The laser is propagating from the left to the right. The proton probe beams deflected by the fields of the channel are shown in an example RCF image [Fig. 26(b)]. The laser creates a clean channel through the plasma, and filaments surround the main channel and expand to a goblet shape. For a pulse with a longer duration like 3 ps and 5 ps, the extended time of the pulse's existence in the plasma prevents electrons from moving back from the upper and lower walls to the channel, leading to a wider and more-uniform main channel and more-confined filaments.

Figure 26(c) shows the electron spectra from the laser-axis EPPS. The solid and dashed curves represent two shot series using different gas nozzles. Due to a reduced aperture size for the large apodizer, the laser energy for a large f number is smaller. Despite



U2774JR

Figure 26

(a) A 4ω shadowgraph image from shot 35722. The laser is propagating from the left to the right and the channel walls are between the arrows. (b) The raw RCF image from shot 35722 illustrates the deflections in the proton beam caused by the channel fields. (c) Electron spectra for various focusing geometries.

the reduction in laser energy, and therefore intensity, the mean electron energy with a large f number does not drop significantly for these conditions. The electron acceleration was likely affected by the size of the laser focal spot. We are conducting PIC simulations to investigate the effects of focal-spot size, density, and laser pulse duration.

This material is based upon work supported by the DOE/NNSA under Award Number DE-NA0003944.

Fundamental Astrophysical Processes in Radiative Supersonic Magnetohydrodynamic Turbulence

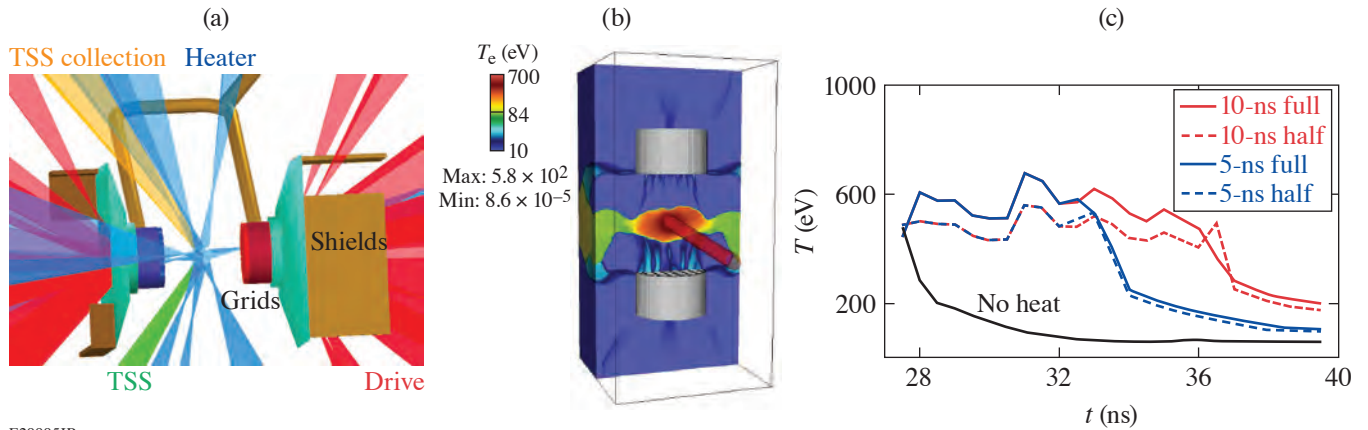
Principal Investigators: P. Tzeferacos,*§ A. Reyes, Y. Lu, K. Moczulski,* P. Farmakis,* and A. Armstrong* (Flash Center for Computational Science, University of Rochester); C. Palmer (Centre for Plasma Physics, School of Mathematics and Physics, Queen's University, Belfast); A. F. A. Bott (Department of Astrophysical Sciences, Princeton University); H. Poole and G. Gregori (Department of Physics, University of Oxford); D. H. Froula and J. Katz (LLE); A. Birkel, C. K. Li, and R. D. Petrasso (Plasma Science and Fusion Center, MIT); J. S. Ross and H.-S. Park (LLNL); and D. Lamb (Department of Astronomy and Astrophysics, University of Chicago)

*Also LLE

§Also Department of Physics, University of Oxford

Magnetic fields are ubiquitous in the universe and are salient agents in numerous astrophysical processes;⁴⁰ however, their origin is not fully understood. The consensus among cosmologists and astrophysicists is that cosmic magnetic fields are the result of dynamo amplification of tiny seed fields in turbulent magnetized plasmas.⁴¹ The turbulent dynamo mechanism eluded experimental demonstration for decades, while theoretical and numerical studies largely relied on simplified models⁴² that steer clear of realistic magnetized compressible turbulence, where strong density fluctuations, shocks, filamentation, and radiative effects complicate the picture and confound the analysis. This project aims to demonstrate and characterize fluctuation dynamo in compressible, radiative plasmas in a controlled laboratory environment. The experiments exploit the mature TDYNO experimental platform we developed⁴³ for the Omega Laser Facility and demonstrated turbulent dynamo in the laboratory for the first time⁴⁴ and it was meticulously characterized.⁴⁵ The experiments also build on the experience we have gained in designing and interpreting laser-driven experiments using validated simulations created with *FLASH*,⁴⁶ a highly capable radiation MHD code we have developed that is able to simulate a wide range of high-energy-density physics experiments.⁴⁷ The project establishes a basis for laboratory investigations on the nature of the saturated MHD turbulent state in radiative, compressible turbulence.

The second shot day of our OMEGA campaign was carried out on 15 July 2021 and was geared toward measuring (1) the plasma viscosity using the spectral cutoff of the density fluctuations and (2) the self-emitted fusion protons in the plasma due to D–D reactions. The platform deployed is shown in Fig. 27(a) and is similar to the one we fielded at Omega for our previous suc-



E29995JR

Figure 27

Turbulent dynamo experiments at Omega. (a) VISRAD schematic of the TDYNO platform for OMEGA to study the viscous cutoff in the power spectrum of the turbulent plasma. (b) FLASH simulation of the experiment showing one of 11 heater beams heating the turbulent plasma (electron temperature rendering, eV). (c) Temporal profiles for different heater-beam configurations showing the plasma temperatures (eV) that the turbulent interaction region can sustain.

successful TDYNO campaigns. The assembly is comprised of two composite targets and two grids that are connected by a pair of cylindrical shields. The composite targets are 3 mm in diameter and consist of a 50- μm -thick deuterated polystyrene foil (CD) and a 240- μm -thick polystyrene washer. The polystyrene washers were machined to have a 400- μm -diam cylindrical “well” in their centers. The two targets are mounted 8 mm apart and the pair of grids is placed between them. The two grids are made of polyimide and are mounted 4 mm apart—each of them 2 mm away from the respective proximate face of the foil target. The 3-mm-diam, 230- μm -thick grids consist of 300- μm -wide holes and 100- μm wires, offset with respect to each other to break the mirror symmetry of the assembly: grid A (red) has a hole in the center, while grid B (blue) does not. Rectangular cones on each target shield the diagnostics from the intense x-ray emission produced when a sequence of ten 1-ns-duration laser beams coming from different angles illuminate each target. The two targets are driven for 10 ns, delivering a total of 5 kJ per target on an area defined by the laser’s SG5 phase plates. The temporal profile of the drive is a flat-top profile. As shown in the FLASH simulation we performed for the platform design, the beams drive a pair of counter-propagating, high magnetic Reynolds number R_m plasma flows that carry the seed magnetic fields generated by a Biermann battery. The flows propagate through a pair of grids that destabilize the flow and define the driving scale of the turbulence (L). The flows then meet at the center of the chamber to form a hot, turbulent interaction region [Fig. 27(b)], where the magnetic fields are amplified to saturation values. After its formation, the interaction region is also illuminated with a sequence of 11 heater beams (Fig. 27), time staggered for 9 ns, capable of delivering a total of 1.7 kJ. The heater beam configuration can maintain high plasma temperatures for the duration of the illumination [Fig. 27(c)], which alters the plasma viscosity, increases the length scale of the viscous cutoff of the power spectrum, and boosts the yield of DD protons generated in the deuterated plasma.

To measure the turbulent spectrum using x-ray imaging and capture the viscous scale where the turbulent kinetic energy dissipates into heat, we fielded two x-ray framing cameras, one with $2\times$ magnification viewing the turbulent plasma edge-on [Figs. 28(a) and 28(b)], and another with $12\times$ magnification viewing the interaction region at an angle (i.e., our main diagnostic for the viscous length scale). Unfortunately, the $12\times$ magnification camera worked only for the first shot of the day, which significantly impacted the shot rate for the remainder of the experiment and compromised our ability to achieve our scientific objectives. Despite numerous attempts to troubleshoot the high-resolution framing camera problem, we were unable to use our main plasma diagnostic. Nevertheless, the heater beams were, in fact, able to significantly increase the plasma temperature. The 4ω Thomson-scattering diagnostic [Fig. 27(a)] yielded detailed information about the plasma state (ion and electron temperatures, bulk flow velocity, turbulent velocity, and electron density). More specifically, it revealed that we sustained ion temperatures of ~ 500 eV and electron densities of $\sim 5 \times 10^{19} \text{ cm}^{-3}$. For moderate to large fluid Reynolds numbers (Re) periodic box simulations, the viscous cutoff is shown to satisfy

$$kL/2\pi \sim 0.2 \text{Re}^{3/4},$$

where k is the wave number and L is the driving scale of the turbulence. For our experimental conditions, we have

$$\text{Re} \sim 130 \left(\frac{T_i}{500 \text{ eV}} \right)^{-5/2} \left(\frac{n_e}{10^{20} \text{ cm}^{-3}} \right) \sim 50,$$

which is consistent with the reduction we see in relative intensity fluctuations [Figs. 28(c) and 28(d)] and brings the cutoff to $l_{\text{visc}} > 50 \mu\text{m}$; i.e., above the resolution limit of the $2\times$ magnification framing camera, also shown in the shift toward larger scales of the spectral peak in Figs. 27(e) and 27(f). This preliminary analysis is encouraging and builds confidence for our next shot day, where we expect to have the high-resolution framing camera issues resolved. Finally, we were able to measure the signal on the EPPS diagnostic for two of the shots. Further analysis of the signal, combined with measurements with the proton core imaging spectrometer (PCIS) CR-39, will be used to determine the utility of the signal for benchmarking the DD proton production in the experiment. Despite the complexity of the experimental platform and the experimental diagnostic problems, with the help of LLE personnel, we were able to perform nine shots during this shot day.

The research leading to these results has received funding from the European Research Council (ERC) under the European Community's Seventh Framework Programme (FP7/2007-2013)/ERC Grant Nos. 256973 and 247039, DOE NNSA under Contract No. B591485 to LLNL, Field Work Proposal No. 57789 to Argonne National Laboratory (ANL), Subcontract No. 536203

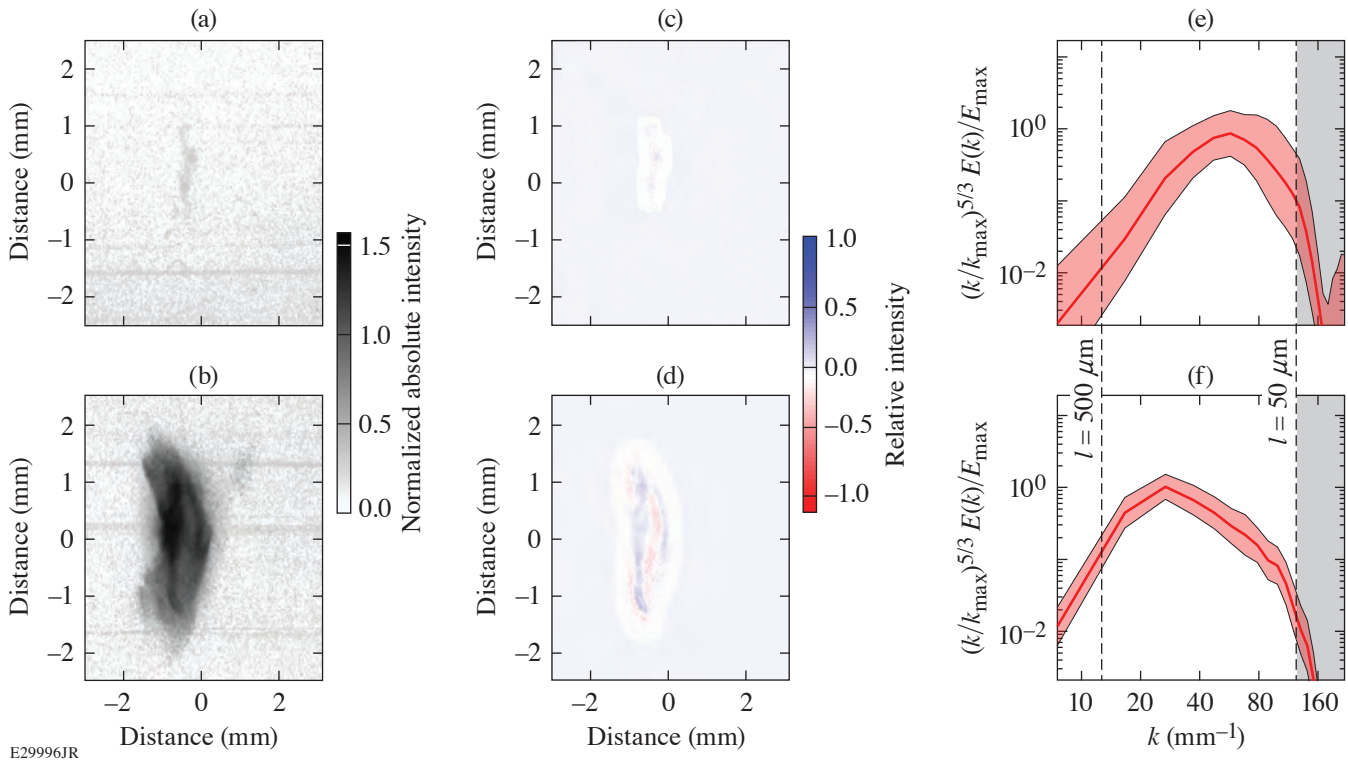


Figure 28

Experimental results. (a) X-ray image of the turbulent interaction region from the $2\times$ magnification framing camera, without the heater beams, at 32.5 ns. (b) Same as (a) but with the heater beams turned on. (c) Relative intensity showing the fluctuations in the turbulent plasma. (d) Same as (c) but with the heater beams turned on. (e) Preliminary power spectra of the turbulent kinetic energy for the two cases in (c) and (d), normalized by the peak energy and boosted by $k^{-5/3}$ (i.e., Kolmogorov scaling) to better display the viscous cutoff. (f) Same as (e) but with the heater beams turned on.

with Los Alamos National Laboratory, Subcontract B632670 with LLNL, and grants No. DE-NA0002724, DE-NA0003605, and DE-NA0003934 to the University of Chicago, DE-NA0003868 to the Massachusetts Institute of Technology, and Cooperative Agreement DE-NA0003856 to the Laboratory for Laser Energetics, University of Rochester. We acknowledge support from the U.S. DOE Office of Science Fusion Energy Sciences under grant No. DE-SC0016566 and the National Science Foundation under grants No. PHY-1619573, PHY-2033925, and AST-1908551. Awards of computer time were provided by the U.S. DOE ASCR Leadership Computing Challenge (ALCC) program, using resources at ANL, which is supported by the U.S. DOE Office of Science under contract No. DE-AC02-06CH11357. We acknowledge funding from grants 2016R1A5A1013277 and 2017R1A2A1A05071429 of the National Research Foundation of Korea. Support from AWE plc., the Engineering and Physical Sciences Research Council EP/M022331/1, EP/N014472/1, and EP/R034737/1, and the U.K. Science and Technology Facilities Council is also acknowledged.

Implementation of a Monochromatic Talbot–Lau X-Ray Deflectometer for Electron Density Diagnostics in High-Energy-Density Physics

Principal Investigators: M. P. Valdivia, D. Stutman, and M. K. Schneider (Johns Hopkins University); V. Bouffetier, G. Perez-Callejo, and A. Casner (Universite de Bordeaux-CNRS-CEA, CELIA)

Co-investigators: C. Stoeckl, C. Mileham, T. Filkins, S. Fess, and M. Romanofsky (LLE)

The proper characterization of the underdense plasma conditions in laser–plasma interactions is key to the study of high-energy-density-physics.⁴⁸ Laser–plasma instabilities have been observed to negatively impact hohlraum performance in ICF, for example. These instabilities and their growth depend on the density profile of coronal plasma. Therefore, many experiments performed in large laser facilities, such as LLE, will benefit from accurately measuring electron density profiles in the corona, where the laser–plasma interactions are most active. Moreover, measurements above critical density would help benchmark codes and simulations that currently fail to accurately predict the plasma ablation dynamics of thin foils irradiated by nanosecond pulse lasers. An NLUF experiment proposed the continuation of previous OMEGA EP campaigns that aimed to characterize the ablation front of laser-irradiated foils by mapping x-ray refraction angle and measuring electron density ($n_e \approx 10^{23} \text{ cm}^{-3}$) through Talbot–Lau x-ray deflectometry (TXD).⁴⁹ The latest experiment tested a monochromatic version of the OMEGA EP TXD diagnostic (Fig. 29) developed by Johns Hopkins University under NNSA (HEDLP and NLUF) and LaserNetUS grants.⁵⁰

Copper wire and oil targets were driven by 10-ps laser pulses of 150 to 450 J (~ 1 to $9 \times 10^{17} \text{ W/cm}^2$) to obtain K_α emission. The x-ray backlighting from the targets enabled monochromatic TXD moiré imaging at 8 keV. The diagnostic performance was

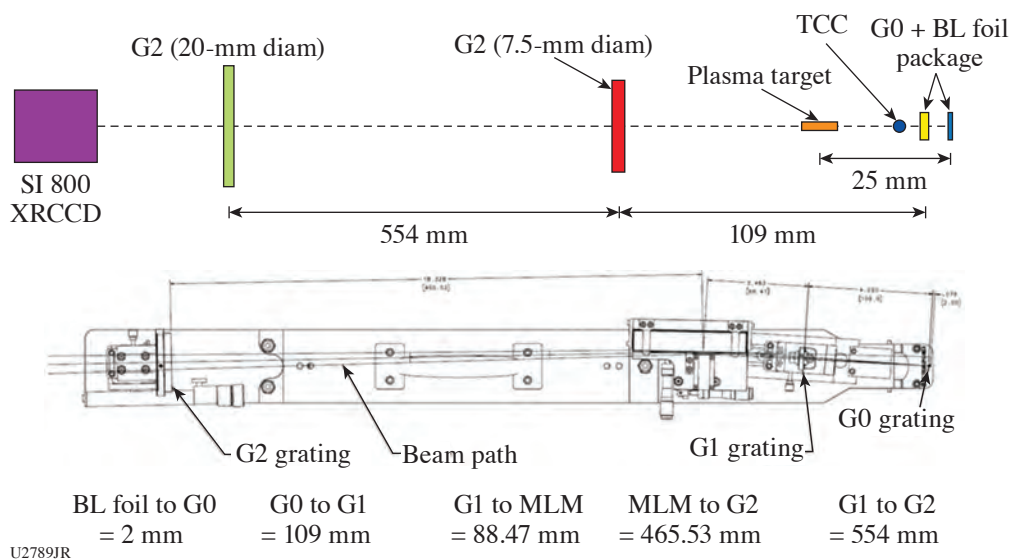


Figure 29
Schematic of the Talbot–Lau interferometer monochromator configuration (EP-M-TXD) including a multilayer mirror selecting 8-keV x rays.

compromised by the low photon flux measured at the detector surface. In view of these first results, photon flux optimization was prioritized over plasma ablation imaging in this campaign. Moiré images of ~ 70 counts were acquired by an x-ray CCD (Fig. 30), equivalent to ~ 50 photons per pixel calculated assuming $\sim 7 \times 10^{-4}$ conversion efficiency of laser light into Cu K_{α} photons, CCD with quantum efficiency $>50\%$ at 8 keV, interferometer transmission of $\sim 20\%$, and an attenuation factor of 6 in the blast shield, detector light-blocking filter, and the CH target. Based on previous experiments,⁴⁹ at least 300 counts were expected on the CCD surface when considering $\sim 25\%$ mirror reflectivity. From these results, it was concluded that new source grating fabrication methods reduced transmission by a factor of ~ 3 to 4 (Ref. 50). Foil targets irradiated normally with an additional 5° increased counts on shot 34898 when compared to shot 34889 [Fig. 30(a)]. Moreover, 6.9% contrast was measured for shot 34898 versus 4.7% for shot 34889 [Fig. 30(b)]. The improved fringe contrast may be attributed to the specific source grating used since they are replaced on each shot. When performing *ex-situ* alignment with a Cu anode x-ray tube, measured moiré fringe contrast was higher for the specific rail and source grating used in shot 34898 when compared to shot 34889 (26% versus 19%). Furthermore, moiré fringe contrast and transmission differed for each source grating. Nevertheless, monochromatic TXD diagnostic procedures for *ex-situ* multilayer mirror and grating alignment were successful. The demonstration of reference moiré image acquisition through phase stepping is an important campaign outcome since it will allow for accurate attenuation, phase, and scatter retrieval through TXD methods not requiring an additional laser shot to obtain a reference image.⁵¹

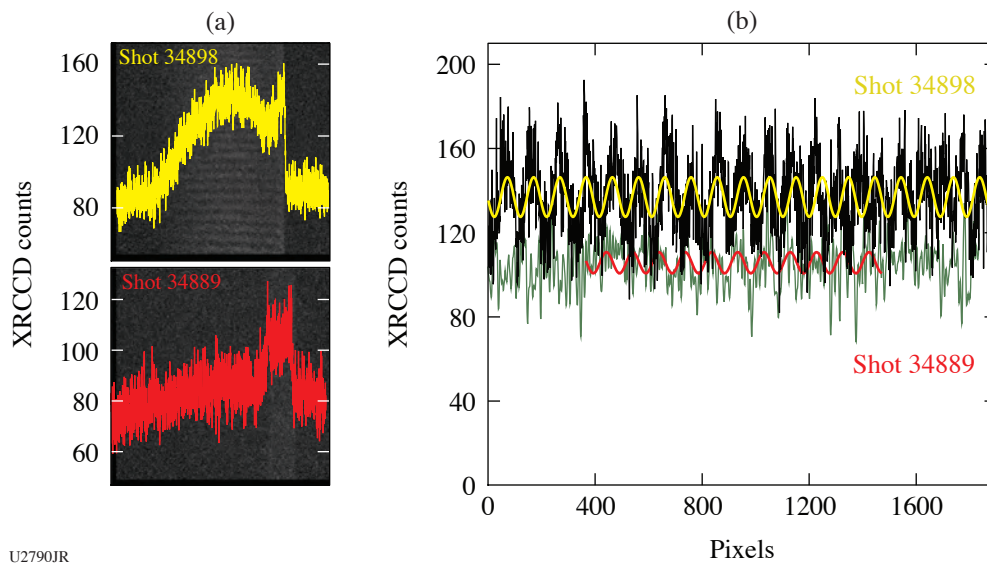


Figure 30

(a) Monochromatic TXD experimental moiré images from the NLUF (FY21) Campaign. X-ray backlighting was provided by irradiating Cu foils at ~ 150 J, 11 ps, $72\text{-}\mu\text{m}$ spot size for shots 34898 and 34889. Shot 34889 shows a $200\text{-}\mu\text{m}$ Ta slab placed in the middle of the image; no object is present for shot 34898. (b) Moiré fringe profiles used to measure fringe contrast of $\sim 5\%$ for shot 34898 and $\sim 7\%$ for shot 34889.

Optimal conditions for generating x-ray backlighters suitable for TXD will be pursued in future experiments. Spatial resolution and flux optimization will be performed on the Multi-Terawatt (MTW) laser by varying the laser pulse length and energy as well as Cu backlighter target geometry, using source gratings with higher transmission. Monochromatic x-ray backlighting optimization on MTW will inform an upcoming OMEGA EP experiment with the goal to map electron density from a laser-produced plasma object. Note, a recent Laboratory Basic Science Campaign used standard TXD diagnostics to probe the ablation front of an irradiated CH foil. Moiré fringe shifts were observed and 2-D maps of phase, transmission, and dark field were retrieved using an *ex-situ* reference image obtained through phase-stepping. Therefore, once x-ray backlighter optimization is achieved, higher moiré fringe contrast from the monochromatic TXD diagnostics presented here will enable improved electron density, scatter, and elemental composition diagnostic capabilities for HEDP.

This work was supported by U.S. DOE/NNSA HEDLP: DE-NA0003882 and NLUF: DE-NA0003941.

Electron Exhaust Jet and Kinetic Instabilities in a Magnetic Reconnection Experiment Using Laser-Driven Capacitor Coils

Principal Investigators: S. Zhang, A. Chien, and H. Ji* (Princeton University); L. Gao (Princeton Plasma Physics Laboratory); E. G. Blackman (Department of Physics and Astronomy, University of Rochester); R. K. Follett, D. H. Froula, and J. Katz (LLE); W. Daughton (LANL); C. K. Li, A. Birkel, and R. D. Petrasso (MIT); and J. Moody and H. Chen (LLNL)

*Also Princeton Plasma Physics Laboratory

Magnetic reconnection is a dramatic conversion of magnetic-field energy to plasma flows and energetic particles via a change of magnetic-field topology. In collisionless plasmas, current-driven instabilities may lead to thermalization and electron-ion coupling, providing a major pathway for dissipation in magnetic reconnection. The development of laser-driven capacitor coils in HEDP experiments has provided an unprecedented avenue to study laboratory plasma magnetic reconnection. Kilojoule lasers can drive 10- to 100-kA current in the coils and generate >100-T magnetic fields, producing magnetic-pressure-dominant plasmas akin to the solar corona or magnetosphere. In this OMEGA experiment, we combined the laser-driven capacitor-coil experiments with time-resolved collective Thomson scattering to study the kinetic physics in the collisionless reconnection, including the evolution of the non-Maxwellian velocity distribution function, electron jets, and the kinetic instabilities.

The experimental platform is shown in Fig. 31. The capacitor-coil target is made of a 50- μm -thick Cu foil. The 600- μm -diam coils have 500- μm -long legs and are separated by 600 μm . The magnetic field generated by the capacitor-coil targets is profiled by proton radiography.^{52–54} The upstream magnetic-field strength is ~ 40 T at 6 ns after the laser's onset. The proton radiography also shows the center feature indicating the reconnection current sheet.

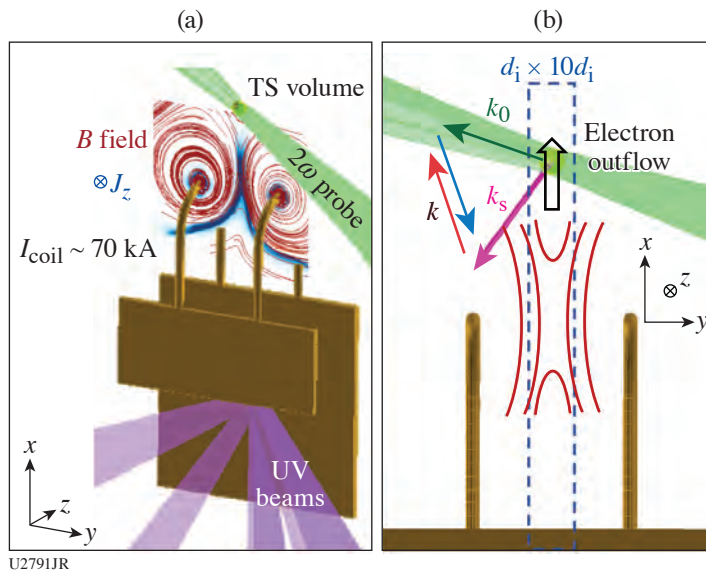
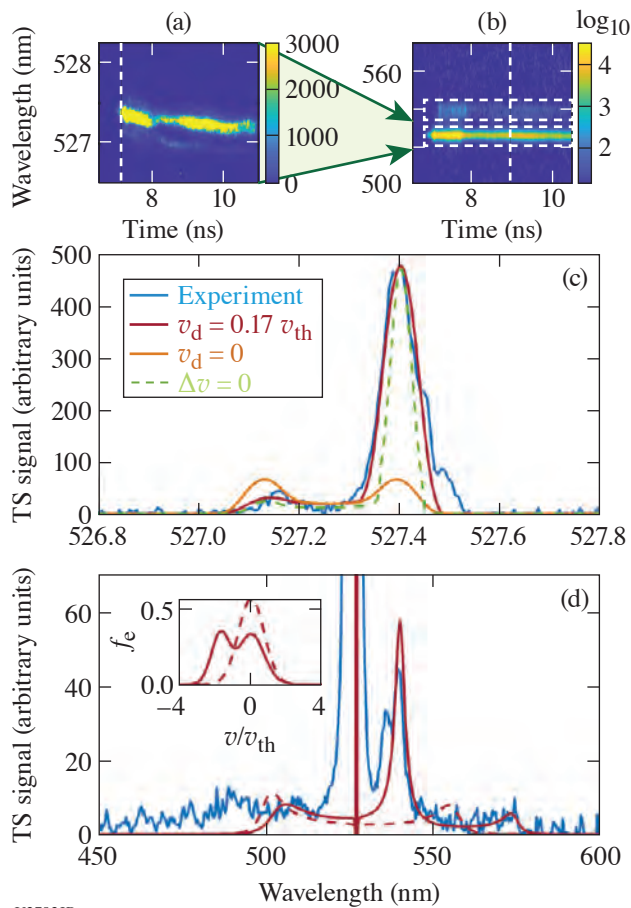


Figure 31

Experimental setup. Six beams of a 500-J, 1-ns UV laser are used to irradiate the back plate of the capacitor, driving current in the coils with $I_{\text{coil}} \sim 70$ kA. *FLASH* MHD simulation results are overlapped in (a) to show the structure of the magnetic field (red lines) and the out-of-plane current density (blue) in the z direction. A 2 ω (527 nm) TS beam (green) probes the reconnection exhaust region, 600 μm above the center point between the top of the coils. The k_0 and k_s in (b) are the wave vectors of the probe beam and the collected scattered light. The red and blue arrows indicate wave vectors (k) of waves in plasma that scatter the probe light to the collector. These k 's are in the x - y plane and 17° off the outflow direction.

The non-Maxwellian distribution and the kinetic instabilities of the reconnection exhaust are shown in the spectrogram of the Thomson scattering. As shown in Fig. 32(a), the IAW-resonant scattering is bursty and asymmetric. The asymmetric IAW spectrum before the bursts can be reproduced in the synthetic TS spectrum with relative drift between electrons and ions as shown in Fig. 32(c). The bursts confirm the existence of the current-driven ion-acoustic instabilities. Figure 32(b) shows that the asymmetric IAW peaks are accompanied with an electron-acoustic wave (EAW) resonant peak, which needs a two-stream distribution to reproduce as shown in Fig. 32(d).

We acknowledge the Omega Laser Facility staff at the Laboratory for Laser Energetics. This work was performed under the auspices of U.S. DOE NNSA under the AIBS program, and the DOE Office of Science under the HEDLP program with award No. DE-SC0020103.



U2792JR

Figure 32

[(a),(b)] Time-resolved TS at $t = 7$ to 10 ns. The IAW resonant peaks in (a) are highly asymmetric (10:1 to 100:1). (c) The spectrum along the vertical dashed line of (a) before the IAW bursts and the comparison with the synthetic TS spectra. The highly asymmetric IAW's can be reproduced with electrons streaming relative to ions with $v_d \sim 0.17 v_{th}$. (b) The EAW peak along with the IAW feature. The spectrum at 9 ns [along the vertical dashed line of (b)] is plotted in (d) with a fitted synthetic spectrum (solid red line). A two-stream electron distribution is needed to reproduce the strong EAW signal. The distribution is shown as the solid line in the inserted plot. For reference, the synthetic TS spectrum from a Maxwellian distribution is shown as the dashed line.

1. H. Sio *et al.*, Rev. Sci. Instrum. **87**, 11D701 (2016).
2. N. Kabadi *et al.*, Rev. Sci. Instrum. **92**, 023507 (2021).
3. T. Nagayama *et al.*, Phys. Plasmas **21**, 050702 (2014).
4. D. Kawahito *et al.*, Phil. Trans. R. Soc. A **379**, 20200052 (2021).
5. C. McGuffey *et al.*, Bull. Am. Phys. Soc. **65** (2020).
6. K. Bhutwala *et al.*, "Transport of an Intense Proton Beam from a Cone-Structured Target Through Plastic Foam with Unique Proton Source Modelling," submitted to Physical Review E.
7. C. McGuffey *et al.*, Sci. Rep. **10**, 9415 (2020).
8. C. A. Walsh *et al.*, Plasma Phys. Control. Fusion **64**, 025007 (2022).
9. J. R. Davies *et al.*, Phys. Plasmas **26**, 022706 (2019).
10. A. B. Zylstra *et al.*, Phys. Rev. Lett. **119**, 222701 (2017).

11. B. Lahmann *et al.*, Rev. Sci. Instrum. **92**, 083506 (2021).
12. G. Ren *et al.*, Phys. Rev. Lett. **118**, 165001 (2017).
13. M. Hohenberger *et al.*, Rev. Sci. Instrum. **92**, 033544 (2021).
14. W. Riedel *et al.*, High Energy Density Phys. **37**, 100861 (2020).
15. W. M. Riedel *et al.*, Phys. Plasmas **28**, 122702 (2021).
16. H. G. Rinderknecht *et al.*, Phys. Rev. Lett. **114**, 025001 (2015).
17. H. Sio *et al.*, Phys. Plasmas **26**, 072703 (2019).
18. H. Sio *et al.*, Phys. Rev. Lett. **122**, 035001 (2019).
19. A. Krygier *et al.*, Rev. Sci. Instrum. **89**, 10F114 (2018).
20. Y. P. Opachich *et al.*, Phys. Plasmas **24**, 063301 (2017).
21. P. A. Keiter and R. P. Drake, Rev. Sci. Instrum. **87**, 11E338 (2016).
22. J. J. MacFarlane, J. Quant. Spectrosc. Radiat. Transf. **81**, 287 (2003).
23. L. Gao *et al.*, Astrophys. J. Lett. **873**, L11 (2019).
24. K. D. Meaney *et al.*, Bull. Am. Phys. Soc. **65** (2020).
25. P. M. Nilson *et al.*, Phys. Rev. Lett. **97**, 255001 (2006).
26. M. J. Rosenberg *et al.*, Nat. Commun. **6**, 6190 (2015).
27. A. E. Raymond *et al.*, Phys. Rev. E **98**, 043207 (2018).
28. S. Ivancic, "Channeling Experiments on OMEGA EP," Ph.D. thesis, University of Rochester, 2015.
29. N. L. Kugland *et al.*, Rev. Sci. Instrum. **83**, 101301 (2012).
30. L. Biermann and A. Schlüter, Phys. Rev. **82**, 863 (1951).
31. R. A. Fonseca *et al.*, in *Computational Science – ICCS 2002*, edited by P. M. A. Sloot *et al.*, Lecture Notes in Computer Science, Vol. 2331 (Springer, Berlin, 2002), pp. 342–351.
32. R. G. Hemker, Ph.D thesis, UCLA, 1999.
33. P. T. Campbell *et al.*, Phys. Rev. Lett. **125**, 145001 (2020).
34. D. B. Schaeffer *et al.*, Phys. Rev. Lett. **119**, 025001 (2017).

35. D. B. Schaeffer *et al.*, Phys. Rev. Lett. **122**, 245001 (2019).
36. S. Malko *et al.*, Appl. Opt. **61**, C133 (2022).
37. M. G. Haines, Phys. Rev. Lett. **78**, 254 (1997).
38. A. V. Arefiev *et al.*, Phys. Plasmas **23**, 056704 (2016).
39. A. E. Hussein *et al.*, New J. Phys. **23**, 023031 (2021).
40. E. N. Parker, *Cosmical Magnetic Fields: Their Origin and Their Activity*, The International Series of Monographs on Physics (Clarendon Press, Oxford, 1979).
41. R. M. Kulsrud *et al.*, Astrophys. J. **480**, 481 (1997).
42. A. Brandenburg and Å. Nordlund, Rep. Prog. Phys. **74**, 046901 (2011).
43. P. Tzeferacos *et al.*, Phys. Plasmas **24**, 041404 (2017).
44. P. Tzeferacos *et al.*, Nat. Commun. **9**, 591 (2018).
45. A. F. A. Bott *et al.*, Proc. Natl. Acad. Sci. **118**, e2015729118 (2021).
46. B. Fryxell *et al.*, Astrophys. J. Suppl. Ser. **131**, 273 (2000).
47. P. Tzeferacos *et al.*, High Energy Density Phys. **17**, 24 (2015).
48. R. Paul Drake, *Introduction to High-Energy-Density Physics*, High-Energy-Density Physics: Foundation of Inertial Fusion and Experimental Astrophysics, edited by R. P. Drake (Springer International Publishing, Cham, 2018), pp. 1–20.
49. M. P. Valdivia *et al.*, Rev. Sci. Instrum. **87**, 11D501 (2016).
50. M. P. Valdivia *et al.*, Rev. Sci. Instrum. **91**, 023511 (2020).
51. M. P. Valdivia *et al.*, Appl. Opt. **57**, 138 (2018).
52. L. Gao *et al.*, Phys. Plasmas **23**, 043106 (2016).
53. A. Chien *et al.*, Phys. Plasmas **26**, 062113 (2019).
54. A. Chien *et al.*, Phys. Plasmas **28**, 052105 (2021).

FY21 Laboratory Basic Science Program

M. S. Wei

Laboratory for Laser Energetics, University of Rochester

The Laboratory Basic Science (LBS) Program awarded 22 projects with a total allocation of 23 shot days for a full year schedule at the Omega Laser Facility in FY21. Due to the delays of five FY20 LBS projects into FY21 as a result of the COVID-19 pandemic-caused disruption in FY20, six FY21 LBS projects were subsequently delayed into FY22. A total of 231 target shots were conducted over 21 days for 21 LBS projects including five from the FY20 program and 16 from the FY21 program. These experiments were led by scientists from Lawrence Livermore National Laboratory (LLNL), Los Alamos National Laboratory (LANL), Lawrence Berkeley National Laboratory (LBNL), and LLE (see Table I).

During FY21, LLE issued a solicitation for LBS proposal for beam time in FY22. A total of 27 proposals were submitted, requesting a total of 36 Omega shot days, exceeding the available LBS allocation by 232%, showing strong interest and high demand of Omega facility time for basic high-energy-density (HED) science experiments from the National Nuclear Security Administration Inertial Confinement Fusion (NNSA ICF) laboratories and the Office of Science laboratories. An independent LBS Proposal Review Panel (PRP) consisting of ten subject-matter experts from university, national laboratories, and industry reviewed and ranked the proposals. Based on the LBS PRP's recommendation, 15 FY22 LBS proposals were selected and allocated a total of 15.5 shot days for experiments at the Omega Laser Facility in FY22, as shown in Table II. With the six carryovers from the FY21 LBS program (shown in Table I), a total of 22 shot days are allocated for LBS experiments in FY22. The LBS experiments conducted in FY21 are summarized here.

Table I: LBS projects with experiments conducted at the Omega Laser Facility in FY21, including five carryovers from the FY20 LBS Program. The blue shaded cells are the five projects from the FY20 program. The gray shaded cells are the FY21 LBS projects postponed with shots rescheduled in FY22.

Principal Investigator	Institution	Title
F. Coppari	LLNL	The Atomic Structure and Melting of New Solid and Superionic Water Ices at Multi-Megabar Pressures: Searching for Ice XIX
Z. L. Mohamed	LLE	Study of Gamma-Ray Products from Reactions Relevant to Big-Bang Nucleosynthesis
A. Pak/N. Lemos	LLNL	Proton Radiography of Target Normal Sheath Acceleration Fields in the Long-Pulse Regime
H. G. Rinderknecht	LLE	Measuring the Triton Breakup Reaction $T(n,2n)D$
J. R. Rygg/H. Poole	LLE	Optical and X-Ray Scattering Measurements of Dense Silicon
F. Albert	LLNL	X-Ray Radiography with Sources Driven by Laser Wakefield Acceleration
F. Coppari	LLNL	Melting, Polymorphism, and Kinetics of Crystallization of Superionic Ice
T. Döppner	LLNL	Developing Fresnel Diffractive Radiography for Mutual Diffusion Measurements
D. E. Fratanduono/M. Millot	LLNL	Investigating Giant Impacts on Rocky Planets with High-Pressure Melting and Shock Equation-of-State Measurements on Complex Silicates

Table I: LBS projects with experiments conducted at the Omega Laser Facility in FY21, including five carryovers from the FY20 LBS Program. The blue shaded cells are the five projects from the FY20 program. The gray shaded cells are the FY21 LBS projects postponed with shots rescheduled in FY22 (continued).

Principal Investigator	Institution	Title
N. Lemos	LLNL	Proton Radiography of a Hybrid Laser Wakefield Accelerator Driven by a Picosecond–Kilojoule-Class Laser
L. Masse/S. Khan	LLNL	Evidencing the Transition from Landau–Darrieus Instability to Ablative Richtmyer–Meshkov Using Low-Density Foam Targets on OMEGA EP
P. M. Nilson/S. X. Hu	LLE	Atomic Physics at Petapascal Pressures
J. L. Peebles	LLE	Comparison and Validation of Dynamic Magnetic-Field Diagnostics on Laser-Driven Coils and MIFEDS
S. Singh	LLNL	Determination of High-Pressure Phase Transformation Mechanisms at the Atomic Scale
V. Smalyuk/H. Sio	LLNL	Kelvin–Helmholtz Instability with a Magnetic Twist
C. Stoeckl	LLE	Development of New Experimental Platform LIANS on OMEGA EP for Deuteron and Triton-Induced Nuclear Reactions
G. Tabak	LLE	Extreme Physics of Hydrogen and Water in Planetary Interiors
W. Theobald	LLE	X-Ray Phase-Contrast Imaging of Imploding Strong Shock Waves
T. J. Weber/M. P. Valdivia	LANL	Understanding Collisional Interpenetration of Ion Species with Talbot–Lau Interferometry
S. Zhao/C. Stan	LBNL	Extreme Deformation of High-Entropy Alloys
H. Chen/M. Edwards	LLNL	Developing a Magnetic Mirror Trap for Laser-Produced Relativistic Electron–Positron
H. Chen	LLNL	Measuring Particle Transport in Turbulent Plasmas
L. Gao	PPPL	Investigation of Magnetic-Field Generation with Short-Pulse Laser-Powered Capacitor Coils
Y.-J. Kim	LLNL	Extreme Chemistry Inside the Icy Planets: Shock Compression of Precompressed Ammonia–Water Mixtures
H. G. Rinderknecht	LLE	A Plasma Rectifier for Extreme Magnetic Fields, Efficient Electron Acceleration, and Bright X-Ray Sources
A.B. Zylstra	LLNL	Big-Bang Nucleosynthesis Relevant to the Primordial ⁷ Li Problem

PPPL: Princeton Plasma Physics Laboratory.

Expanding Our Understanding of Warm Dense Water Ices

Principal Investigators: F. Coppari (LLNL)

Co-investigators: Y.-J. Kim, J. H. Eggert, and M. Millot (LLNL)

Water exhibits a complex polymorphism at high pressures and temperatures. Twenty different forms of ice have been found experimentally, and more have been predicted to become stable at pressure exceeding 400 GPa. In 2021, we were allocated two shot days (one from the previous year’s LBS allocation, delayed because of COVID-19) on the OMEGA EP Laser, where we collected a total of 15 shots in the two campaigns. The goal of these experiments was to expand our understanding of the structural properties of water ices in the warm-dense-matter regime relevant to planetary interiors. This research built on the success of a previous work performed on the OMEGA 60 laser that led to the discovery of a new form of ice (Ice XVIII) with superionic properties.^{1,2}

Table II: LBS Program approved target shots at the Omega Laser Facility in FY22.

Principal Investigator	Institution	Title
F. Albert	LLNL	High-Precision X-Ray Radiography Driven by Laser Wakefield Acceleration
G. Bruhaug	LLE	Relativistic THz-Matter Interactions
S. Clarke	LLNL	The Effect of Ni Concentration on Phase Transformation Dynamics in the Fe-Ni Binary System
G. W. Collins	LLE	Quantum States of Hydrogen: Toward a Superconducting Superfluid
A. Gleason	SLAC	Viscosity Measurements Using Tracer Particles
I. V. Igumenshchev	LLE	Formation of Dynamic Shells Using Foam Ball Targets
J. Jeet	LLNL	Cross-Calibrations of the DT γ -to-Neutron and D- ^3He γ -to-Proton Branching Ratios Against the $^{12}\text{C}(n,n')\gamma$ Reaction
A. Krygier	LLNL	The Strength of Fe and Fe-Si 16 wt% at the Conditions in Earth's Core
S. Malko	PPPL	Detailed Benchmarking of the Nernst Effect in a Magnetized HED Plasma
J. L. Peebles	LLE	Probing In-Flight Vacuum Magnetic-Field Compression on OMEGA
M. J. Rosenberg	LLE	Electron Energization in Colliding and Reconnecting Magnetized Plasmas
M. B. Schneider	LLNL	Using Isoelectronic Line Ratios to Measure Density in Nonlocal Thermodynamic Equilibrium Plasmas
R. Smith	LLNL	Measuring the Viscosity of Silicates at Lower-Mantle Conditions
C. Stoeckl	LLE	Development of New Experimental Platform LIANS on OMEGA EP for Deuteron and Triton-Induced Nuclear Reactions
G. Swadling	LLNL	Angular Momentum Transport in Disk-Jet Transitions

Two laser beams were used to compress a thin liquid water layer to different pressures and temperatures, and two additional beams were used to generate a quasi-monochromatic x-ray source that enabled us to collect x-ray diffraction patterns, revealing the crystalline structure of water ices at extreme conditions, using the powder x-ray diffraction image plate (PXRDIIP) diagnostic.³

In addition to the challenges related to the scientific goals of this campaign (i.e., obtaining a diffraction signal off a low scattering material and accurately designing the target geometry and pulse shape to reach specific pressure/temperature conditions), we had to overcome technical difficulties related to the confinement of a thin liquid water layer for a sufficiently long time (at least one week, from filling to shot time). Accurate metrology of the target was done prior to and after filling (in Livermore) and prior to the shot (in Rochester)⁴ to ensure that the target was still holding water at shot time. We obtained excellent data (Fig. 1), whose analysis is underway, and will allow us to elucidate the complex behavior of warm dense water ices at extreme conditions.

Developing Fresnel Diffractive–Refractive Radiography for Experimental Measurements of Mutual Diffusivity in Warm Dense Matter

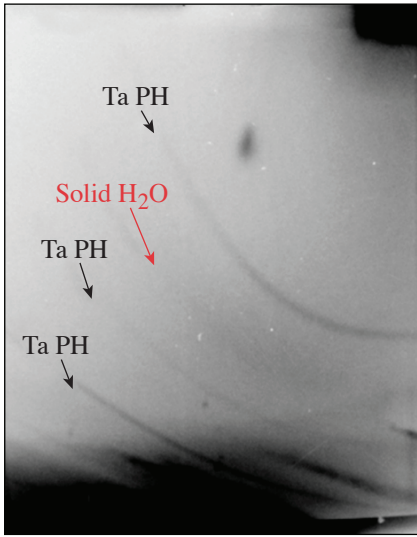
Principal Investigators: T. Döppner (LLNL)

Co-investigators: L. Divol, A. Kemp, O. L. Landen, Y. Ping, and M. Schölmerich (LLNL); T. G. White and C. H. Allen (University of Nevada, Reno); M. Oliver (Central Laser Facility, UK); and W. Theobald (LLE)

The experimental measurement of concentration-driven diffusion between two species in warm dense matter (WDM) is important for benchmarking instability growth simulations in ICF experiments.⁵ The scale length of this mutual diffusion is of the order of $1\ \mu\text{m}$, necessitating a diagnostic tool that can resolve density gradient changes with submicron resolution. For FY21, we had a full shot day on OMEGA (MutualDiffusivity-21A), where we refined our Fresnel diffractive–refractive radiography imaging platform by measuring dynamic density gradients in WDM material, improving our previous results from FY20.

The development of this platform has progressed from imaging cold wire targets to sampling driven dynamic WDM systems, looking at the interface of isochorically heated W and fluorinated CH (Fig. 2). Our preliminary analysis shows significant expansion

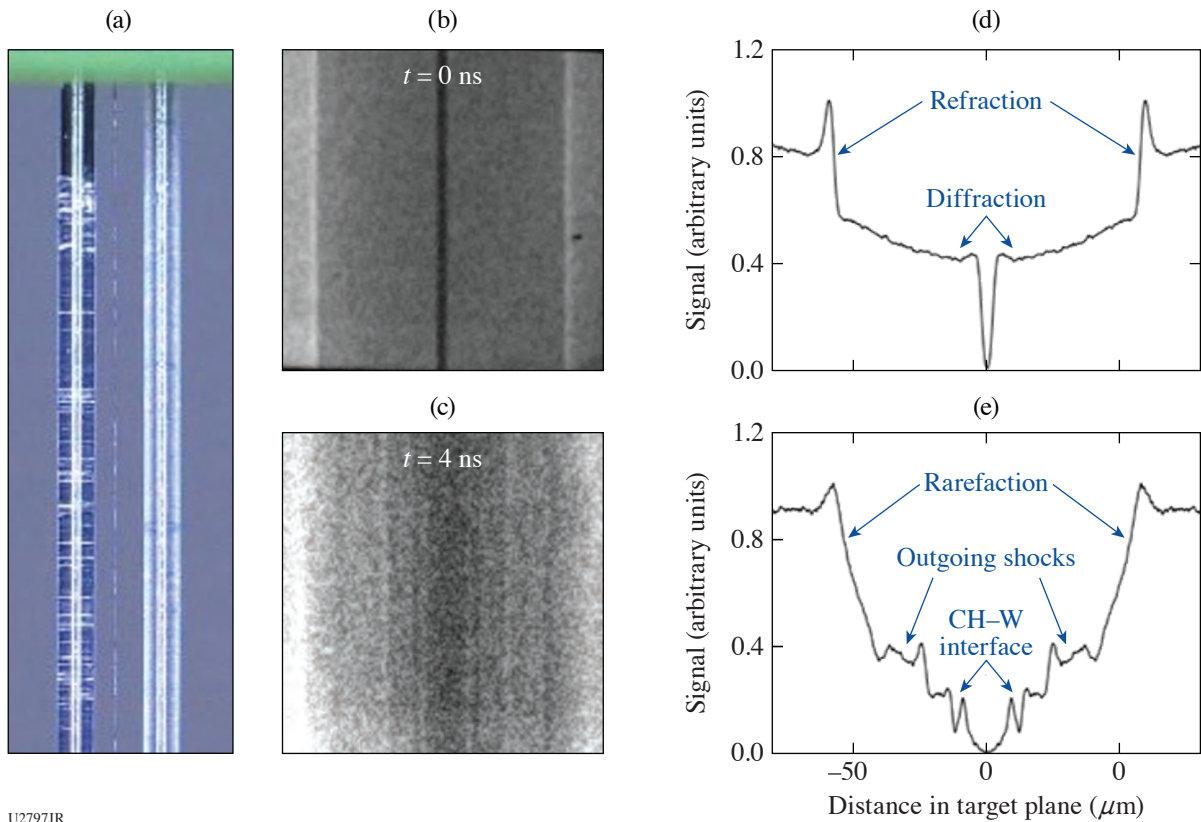
in the W wire and shocks launched into the CH that evolve over time. We had nine target shots over the course of our shot day, five of which used our monolithic target⁶ on OMEGA's planar cryocart mounts.



U2796JR

Figure 1

Example x-ray diffraction data. The red arrow points to the diffraction signal from water ice solidified by the laser-driven compression. Black arrows indicate diffraction signals from Ta at ambient conditions that allow us to accurately determine the geometry of the diffraction experiment.



U2797JR

Figure 2

(a) Samples of our plastic-coated W wires alongside an uncoated W wire in between. These wires were coated via physical vapor deposition (PVD) at the Central Laser Facility (CLF), UK. [(b),(c)] Radiographs and [(d),(e)] lineouts of a cold target and a driven target, respectively. The clear change in the features is evident in the lineouts, showing the explosion of the W wire and the expanded CH-W interface as well as a shock wave launched into the CH.

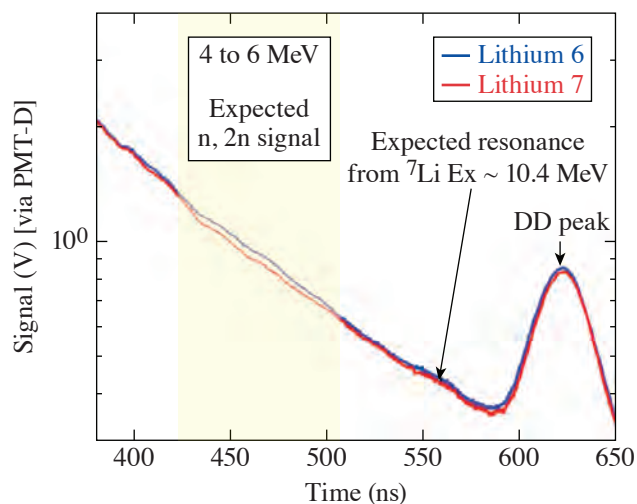
Inelastic Reactions of $^{6(7)}\text{Li}$ from 14-MeV Neutrons Using an Inertial Confinement Fusion Platform

Principal Investigators: C. J. Forrest, J. P. Knauer, P. B. Radha, V. Yu. Glebov, Z. L. Mohamed, S. P. Regan, and C. Stoeckl (LLE); and W. U. Schröder (LLE, Department of Chemistry and Physics, University of Rochester)

High-energy-density laboratory plasmas (HEDLP) is an established experimental platform that is used to address opportunities in a number of fields of scientific research.⁷ Recently, HEDLP plasmas generated on the OMEGA laser⁸ have been used to conduct basic nuclear science experiments. These facilities present viable and interesting alternatives to experimental accelerator-based platforms. In fact, primary yields are at the levels required to begin investigating fundamental nuclear reactions including neutron-induced breakup reactions of light nuclei. For these reasons, new fields of scientific exploration have been initiated for both nuclear interactions and high-energy-density plasmas.

The experimental campaign that was conducted in FY21 is part of an ongoing series of cross-section measurements using a platform for weapons-relevant, light-ion nuclear reaction experiments on OMEGA. A DT gas-filled implosion produces a point source of neutrons, and a heavily shielded neutron time-of-flight (nTOF) spectrometer measures the neutron spectrum from a sample along the line of sight to the detector. Four targets were imploded with an ^6Li sample and five with an ^7Li sample. Two targets were imploded with no sample to record the incident neutron source spectrum. A preliminary comparison of the (n,2n) spectra from ^6Li and ^7Li in the 4- to 6-MeV range shows the expected enhancement in the ^6Li signal, as shown in Fig. 3. However, the predicted resonance for ^7Li at $E_x \sim 10.4$ MeV (a scattered neutron energy of ~ 3 MeV) was not apparent in the spectrum, suggesting that the state is either below the detection threshold (i.e., the cross section is below 10 millibarns) or the scattering resonance line width is too narrow to be resolved with the current diagnostic setup. The rich data set will be further analyzed in the coming weeks.

This material is based upon work supported by the Department of Energy National Nuclear Security Administration under Award Number DE-NA0003856, the University of Rochester, and the New York State Energy Research and Development Authority.



E30004JR

Figure 3

The double-differential cross section has been measured using a high-yield 14-MeV neutron source incident on $^{6(7)}\text{Li}$. A preliminary comparison of the (n,2n) spectra from ^6Li and ^7Li in the 4- to 6-MeV range shows the expected enhancement in the ^6Li signal.

Radiography Development for the Landau–Darrieus Instability

Principal Investigators: S. F. Kahn (LLNL)

Co-investigators: D. A. Martinez and V. A. Smalyuk (LLNL); and T. Goudal, G. Perez, L. P. Masse, L. Ceurvorst, and A. Casner (CELIA, University of Bordeaux, France)

The Landau–Darrieus Instability (LDI)⁹ is an instability inherent to mediums undergoing combustion. Our experiments on OMEGA EP and the National Ignition Facility (NIF) aim to observe LDI with laser ablation¹⁰ for the first time. The experi-

ments' laser intensity is too low (1.25 TW/cm^2) to reduce Rayleigh–Taylor instability growth. On OMEGA EP, we are attempting to observe perturbation growth early in time (up to 10 ns). Additionally, we will measure the shock-/ablation-front velocities. To develop our experiments on the NIF where we will observe LDI at later stages ($>30 \text{ ns}$), we will test two backlighter choices (molybdenum and tantalum) that will optimize our radiography intensity and contrast.

In the experiments, we drive 100-mg/cm^3 foams made of carbonized resorcinol formaldehyde (CRF), with a 10-ns-long UV laser and radiograph from both the face and side of the target (see Fig. 4). The foam targets have machined oscillations with 100- and $50\text{-}\mu\text{m}$ wavelengths (see Fig. 5). The face radiograph is intended to measure the instability growth of those preimposed ripples. As the amplitude of the ripples grow, the optical depth will correspondingly increase. For the side radiographs, we oriented the target so that the ripples are along the diagnostic line of sight. In this way, the ripple growth could also be observed from the side if aligned. Additionally, using a time-gated detector, we can generate the shock-/ablation-front velocities. The 2-D shape of the front would be curved since the beam spot is smaller than the target face.

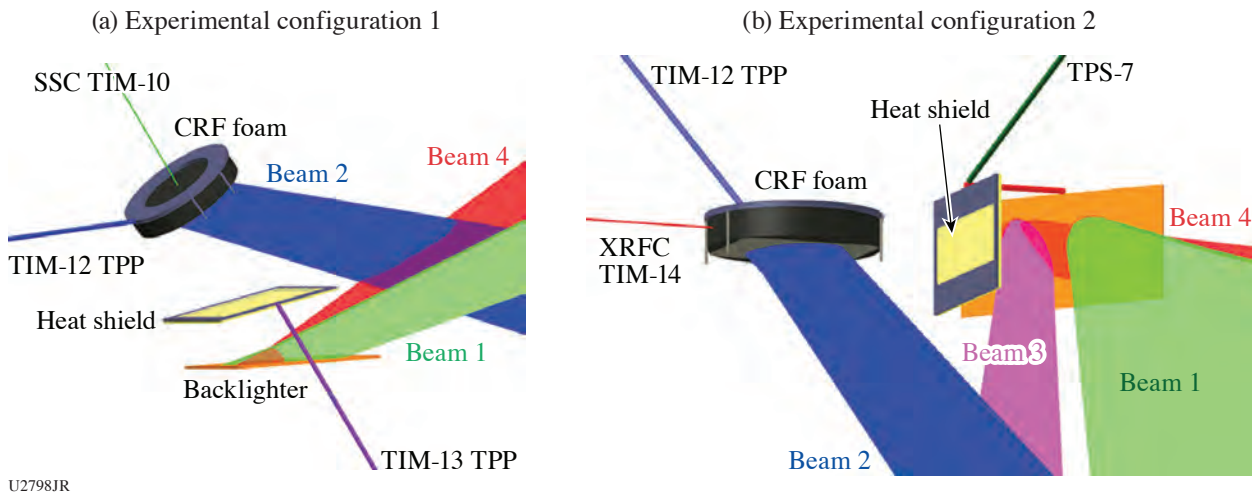


Figure 4
Two configurations were used. (a) The face-on configuration that used an Mo or Ta backlighter activated using two beams with a long-duration picketed pulse. One-dimensional radiographs are recorded onto an x-ray streak camera. A heat shield protects the foam from low-energy radiation from the backlighters. (b) Configuration 2 radiographs the target from the side using a vanadium backlighter onto an x-ray framing camera (XRFC). SCC: Sydor streak camera; TIM: ten-inch manipulator; TPP: two-photon polymerization; TPS: Target Positioning System.

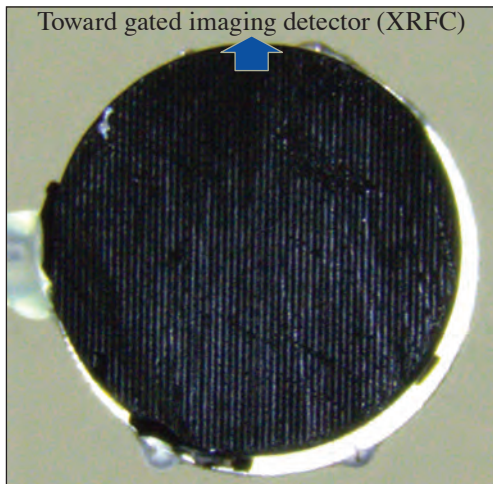


Figure 5
Photograph of one of the CRF foam targets with $100\text{-}\mu\text{m}$ -wavelength machined oscillations. The 6-mm-diam, 0.5-mm-thick target is oriented so that the ripples are along the imaging diagnostic line of sight.

Data from the streak camera (Configuration 1) did not show the expected results (see Fig. 6). We did not observe a discernable contrast across the ripples (horizontal direction). We saw oscillations in the time direction that are much lower frequency than the oscillations observed in the measured laser pulse. The current hypothesis is that the target and streak camera orientation was not aligned so that the 1-D image was smeared.

Excellent data was obtained, however, from the gated imager (Configuration 2), as shown in Fig. 7. Here, there are four time snaps starting at 3.5-ns and 2-ns intervals (drive duration is 0 to 10 ns). The ablation front is curved since the laser beam intensity decreases within the area of the target. The velocity of the shock was measured as $\sim 18 \mu\text{m/ns}$ and matches the simulations to within $5 \mu\text{m/ns}$. In the middle frames, it appears that ripple oscillations are visible in a few of the machined ripples. When we perform this experiment on the NIF, we will optimize to see this (increase magnification and radiograph contrast).

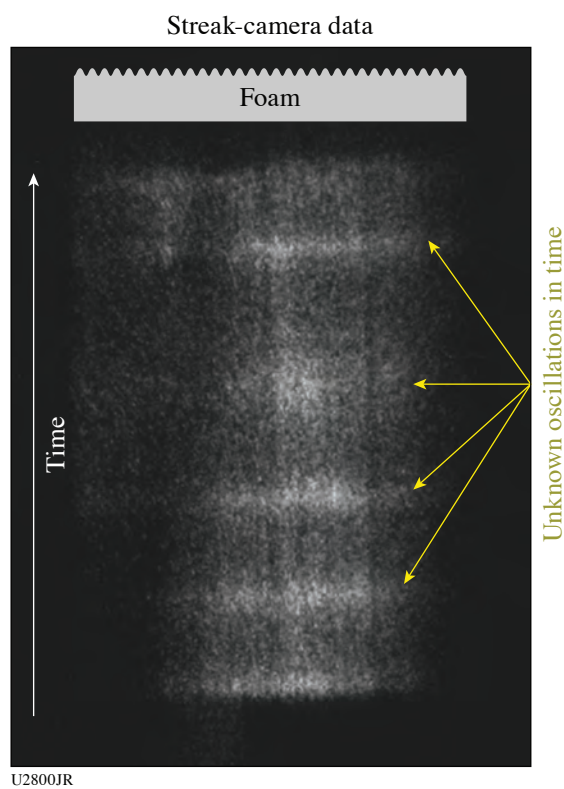


Figure 6
Data (shot 34687) from the SSC. Time goes in the vertical direction, while space is in the horizontal direction. The orientation and size of the expected ripple pattern are shown at the top of the image. The expected oscillations for the ripple pattern are missing. The bright horizontal lines are oscillations in time with an unknown origin. The vertical features are variations in the streak cameras photocathode sensitivity as these variations are seen in several shots at exactly the same location.

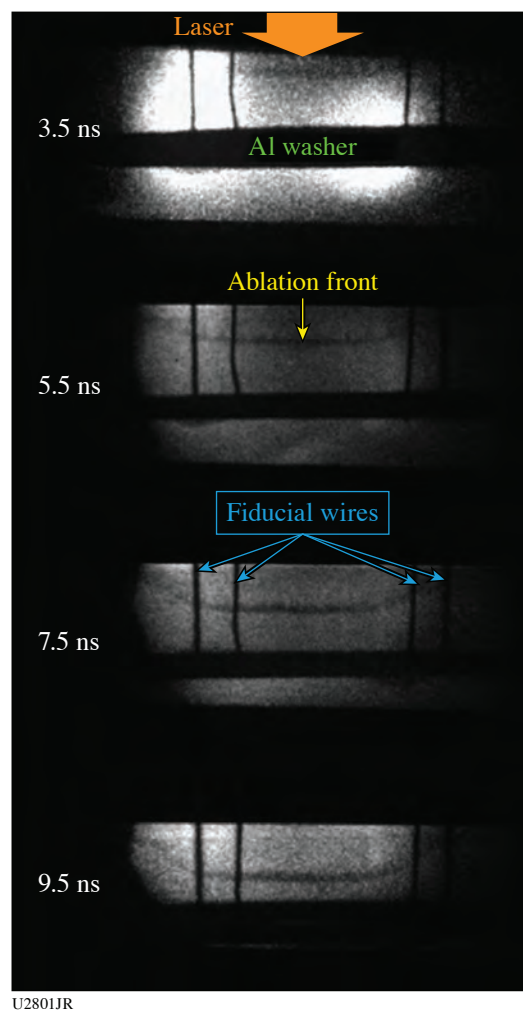


Figure 7
Data (shot 34692) from the Sydor framing camera. There are four time strips with the first strip on top at 3.5 ns and the other three strips recording at 2-ns intervals with 400-ps time gating. In the images, the laser irradiates the target from above. We use four wires as fiducials to set the space scale. The ablation front is the curved darker region that appears mostly across the images. It moves away from the laser as time increases at $\sim 18 \mu\text{m/ns}$.

Finally, we determined that the molybdenum backlighter was superior compared to the tantalum backlighter for x rays (2 to 3 keV). The signal from Mo was about $5\times$ brighter and produced lower-energy x rays as desired for better contrast.

These experiments helped us to determine the course and configuration for our upcoming NIF experiments. The shock-velocity measurement validated our simulations. The trouble we saw with the streak camera influenced our decision to use a gated 2-D imager in our NIF experiments along with a molybdenum backlighter.

This work was performed under the auspices of the U.S. Department of Energy by Lawrence Livermore National Laboratory under contract DE-AC52-07NA27344, Lawrence Livermore National Security, LLC.

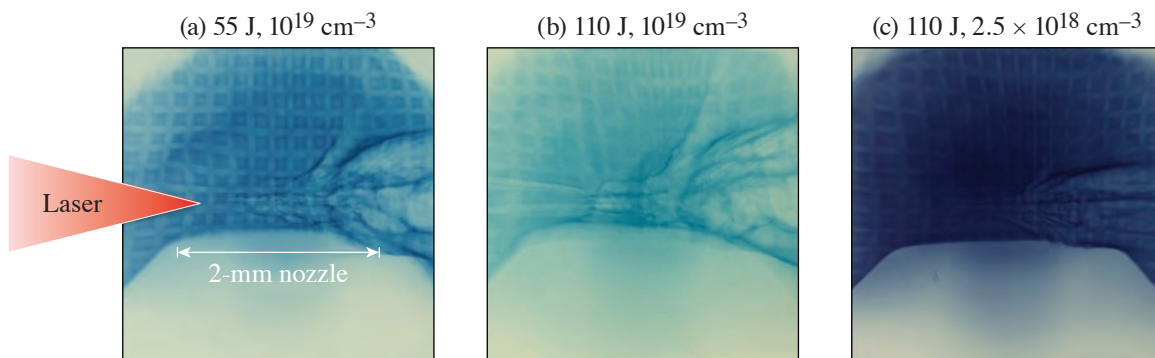
Proton Radiography of a Hybrid Laser Wakefield Accelerator Driven by a Kilojoule, Picosecond-Class Laser

Principal Investigators: N. Lemos, R. Simpson, P. King, and F. Albert (LLNL); and J. L. Shaw (LLE)

This work aimed to characterize the field’s structure and time evolution of a hybrid laser wakefield accelerator (H-LWFA) driven by a kilojoule, picosecond-class laser using proton radiography. We measured for the first time the field’s structure at the end of the interaction, i.e., at the plasma vacuum boundary. We observed the generation of large azimuthal magnetic fields that were confirmed by our quasi-3-D particle-in-cell simulations.

When the laser crosses the plasma–vacuum boundary, it leaves behind the blow-out region that is positively charged with a narrow central filament of ions and electrons.^{11,12} When the electron bunch gets to the plasma–vacuum boundary, the most-energetic electrons escape the plasma, setting up a plasma potential barrier. This in turn confines the lower-energy electrons. As these electrons are pulled back into the plasma (return current), they form a vortex with an accompanying magnetic field that can reach tens of megagauss in magnitude. By Faraday’s law, this magnetic field in turn produces a longitudinal electric field that will accelerate ions. This slowly varying longitudinal accelerating electric field can reach tens of GV/m. In this case, the B field has a defocusing effect that is negligible compared to the focusing force generated by the electric field. In this manner, the ion filament is maintained until the magnetic field decays over time. Typically, LWFA’s are driven with low-energy (a few joules), femtosecond laser pulses and produce a small amount of accelerated charge (~ 1 nC). Here, using a kilojoule-class laser, we have already shown¹³ that we can produce electron beams with hundreds on nC that will reinforce the vortex fields, making this the perfect platform to study this acceleration mechanism.

Due to its characteristics and the unique geometry of two orthogonal high-energy short pulses, OMEGA EP offers the perfect setup to perform a pump–probe experiment. We drove the H-LWFA with one beam and with the orthogonal beam generated a proton beam, through target normal sheath acceleration, that probed the H-LWFA. As it crosses the H-LWFA, the proton beam will be deflected by the magnetic and electric fields, creating a unique radiographic pattern on the proton detector (Fig. 8). Since



U2802JR

Figure 8
Proton radiography images 10 ps after the H-LWFA was formed.

different proton energies probe the H-LWFA at different times due to the different time of flight of each proton energy, it was also possible to record the time evolution of these fields on a single shot. Plasma density and laser energy scans were performed (Fig. 8), where it was possible to identify that the magnitude and spatial dimensions of the magnetic fields increased with plasma density and laser energy.

This work was supported by DOE Office of Science Early Career Research Program (Fusion Energy Sciences) under SCW1575-1.

Investigating Giant Impacts Between Rocky Planets with Shock Equation-of-State Measurements on Natural Silicates

Principal Investigator: M. Millot (LLNL)

Co-investigators: D. E. Fratanduono (LLNL); and B. A. Chidester (University of California, Davis)

The Earth and other rocky planets likely formed after a series of energetic collisions in the early solar system. Simulations of these impacts rely on accurate equations of state and phase diagrams of natural materials to determine the amount of melting, vaporization, and mixing that occurs in the aftermath of a giant impact. Combined with data collected at the Sandia Z Machine, this study is the first to measure the principal pressure–density–temperature (P - ρ - T) Hugoniot of Fe-bearing orthopyroxene [bronzite, $(\text{Mg}_{0.9}\text{Fe}_{0.1})\text{SiO}_3$] to conditions relevant to giant impacts. To complement this data, we extended the experimental Hugoniot of Fe-free enstatite (MgSiO_3) to 1700 GPa, over twice the previously reported pressure. Additionally, we collected shock data for bronzite and olivine $[(\text{Mg}_{0.9}\text{Fe}_{0.1})_2\text{SiO}_4]$ at lower pressures to constrain the onset of melting for these materials.

We completed ten shots on OMEGA EP in the one-day allocation, using alternating beams to increase the shot rate. Those data are combined with data collected in a previous shot allocation (FY19,20-SilicateEOS). As shown in Fig. 9, the enstatite compression curve from OMEGA EP closely matches data from the Z machine (this study), several previous experimental studies,^{14,15} and molecular-dynamics (MD) calculations.¹⁶ On the other hand, the bronzite compression curve diverges from the enstatite calculations, suggesting that even a small amount of Fe can affect the shock compressibility of silicate materials. All of these data, along with the melting curve information, will be incorporated into analytical equations of state for use in planetary impact simulations.

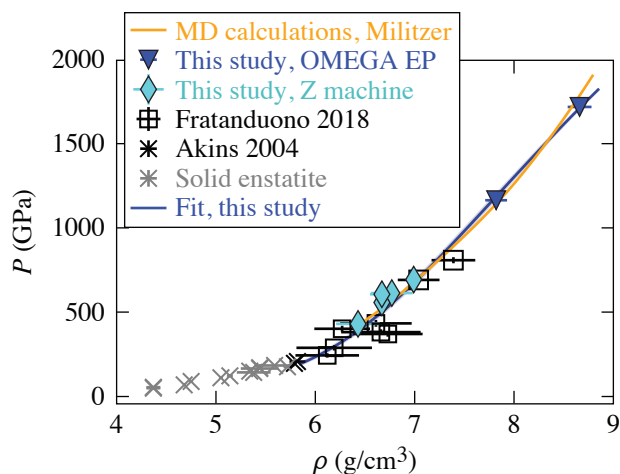


Figure 9
Preliminary P - ρ data for Fe-free enstatite (light gray symbols) and Fe-bearing bronzite (blue triangles). The enstatite data match *ab initio* estimates well, while the bronzite data diverge from these estimates at high pressure.

S Factor for $H(T, ^4\text{He})\gamma$ at Low Center-of-Mass Energies

Principal Investigators: Z. L. Mohamed and J. P. Knauer (LLE); Y. H. Kim, H. Geppert-Kleinrath, and K. D. Meaney (LANL); and M. S. Rubery and A. B. Zylstra (LLNL)

While deuterium–tritium and deuterium–deuterium fusion are the most commonly studied fusion reactions due to their high cross sections, several lower-cross-section reactions are of interest to the fusion community as well as the nuclear physics and astrophysics communities due to their relevance to big-bang nucleosynthesis. Even though several such reactions have been studied

in accelerator experiments, ICF facilities offer a unique opportunity to study these reactions in a plasma environment that can directly produce astrophysically relevant temperatures, pressures, and electron screening effects that beam-based accelerator experiments cannot. This particular experiment focused on the $H(T, {}^4\text{He})\gamma$ reaction, which produced a 19.8-MeV gamma. In addition to its relevance to big-bang nucleosynthesis, the $H(T, {}^4\text{He})\gamma$ reaction is also of interest to the ICF community due to its use in mix experiments.

The goal of this experiment was to measure gamma rays on several HT implosions at different ion temperatures to determine an S factor for this reaction as a function of center-of-mass (CM) energy. The S factor is generally used to represent the rate of fusion reactions as they occur in high-density astrophysical environments and is considered to isolate the nuclear component of the cross section such that

$$S(E_{\text{CM}}) = \frac{E_{\text{CM}}}{\exp\left(-\frac{2\pi Z_1 Z_2 \alpha e^2}{\hbar v}\right)} \sigma(E_{\text{CM}}), \quad (1)$$

where E_{CM} is the CM energy, σ is the cross section, Z_1 and Z_2 are the atomic numbers of the interacting nuclei, α is the fine structure constant, e is the charge of an electron, \hbar is the reduced Planck constant, and v is the relative velocity between the two nuclei. As HT-filled targets contain a small amount of D as contamination in the T part of the fill, D–T reactions also occurred in these “HT” experiments. The D–T neutrons from the $D(T, {}^4\text{He})n$ reaction could therefore be used to measure a D–T neutron yield and ion temperature. The S factor for $D(T, {}^4\text{He})n$ is considered to be well-known to within a few percent,¹⁷ so the S factor for $H(T, {}^4\text{He})\gamma$ can be calculated in relation to the $D(T, {}^4\text{He})n$ reaction such that

$$S_{\text{HT}\gamma} = S_{\text{DTn}} \frac{Y_{\text{HT}\gamma}}{Y_{\text{DTn}}} \left[\frac{n_{\text{D}} A_{\text{HT}} \xi_{\text{DT}}^2 \exp(-3\xi_{\text{DT}})}{n_{\text{H}} A_{\text{DT}} \xi_{\text{HT}}^2 \exp(-3\xi_{\text{HT}})} \right], \quad (2)$$

where $Y_{\text{HT}\gamma}$ and Y_{DTn} represent gamma and neutron yields, A_{HT} and A_{DT} represent the reduced mass numbers for the HT and DT reactions, and ξ_{HT} and ξ_{DT} are functions of Z_1 , Z_2 , reduced mass number, and ion temperature.¹⁸

The experiment included six HT targets at various fill pressures and shot with various laser configurations as well as six analogous H_2 targets that were used to investigate the contribution of any non-nuclear background. Cherenkov detectors including the Atomic Weapons Establishment diagnostic for areal density (DAD) and the LANL gas Cherenkov detectors (GCD-1 and GCD-3) were used to measure gammas. The DAD uses a quartz radiator, which can detect gammas down to 0.4 MeV. GCD-1 and GCD-3 both used CO_2 at different pressures for gamma energy thresholds of 6.3 and 12 MeV, respectively. No non-nuclear background was observed on any of these detectors; however, the GCD-3 signals showed unexpected oscillations that were thought to be associated with the photomultiplier tube, while the DAD measurement was thought to be contaminated by gammas from the remaining glass shell due to its very low threshold. The GCD-1 data were therefore considered to be the most reliable for use in the S factor analysis.

Because the total gamma signal in these implosions includes gammas from both $H(T, {}^4\text{He})\gamma$ and $D(T, {}^5\text{He})\gamma$ in similar amounts, the $D(T, {}^5\text{He})\gamma$ component must be subtracted from the total signal to isolate the HT gamma. The DT γ signal area per D–T neutron as measured by GCD-1 in Ref. 19 was used to perform this subtraction along with neutron yields as measured by nTOF detector 12mntofN. Ion temperatures were also measured from 12mntofN. Shots of similar ion temperature were grouped together and considered to represent a single data point with an average ion temperature and gamma yield.

The final data set used to calculate the S factor included average ion temperatures of 4.6, 9.0, and 12.7 keV, which correspond to CM energies of 16, 25, and 32 keV. The inferred S factors at these CM energies were 2.9 ± 0.6 , 3.4 ± 0.6 , and 4.4 ± 0.9 eV*barn as calculated using the GCD-1 gamma signal, DT neutron yields as measured by 12mntofN, and reference D–T neutron S factor from Ref. 17. The error bars on these measurements include uncertainties on the number of Cherenkov photons generated in the

detector as calculated using Geant4 simulations performed by collaborator M. S. Rubery. At present, the only accelerator data available for comparison are that from Ref. 20, which include two data points at CM energies of 12.3 and 31.2 keV as well as a fit to these two data points and accelerator data collected at higher energies. Figure 10 shows the data points and best-fit line from Ref. 20 plotted along with the data points from the OMEGA measurement. The OMEGA data points appear to be 25% to 70% higher than the best-fit line from Ref. 20; however, they appear to be in approximate agreement with the two individual accelerator data points from Ref. 20 within their error bars. Overall, further investigation of the $H(T, {}^4\text{He})\gamma$ reaction seems to be warranted considering the lack of accelerator data for comparison at these low CM energies.

This material is based upon work supported by the Department of Energy National Nuclear Security Administration under Award Number DE-NA0003856, the University of Rochester, and the New York State Energy Research and Development Authority.

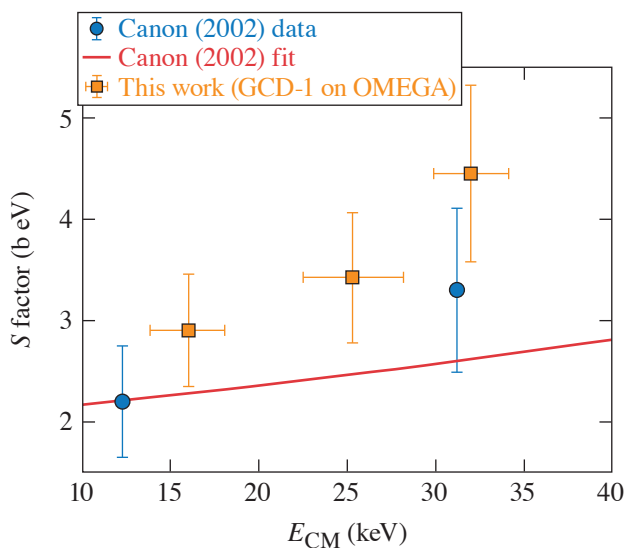


Figure 10

Comparison between GCD-1 data points from this work (yellow) and data points from Ref. 20. These two data points were the only accelerator data points available at these low CM energies. Reference 20 also provides a best-fit line to these data points and accelerator data at much higher energies (red line). The mean values of the GCD-1 data points appear to be 25%–75% higher than the best-fit line provided by Ref. 20; however, they appear to be in agreement with the two individual data points from Ref. 20 within their error bars.

E29997JR

Atomic Physics at Petapascal Pressures

Principal Investigators: P. M. Nilson, S. X. Hu, D. T. Bishel, and D. A. Chin (LLE); and S. B. Hansen (SNL)

Under HED conditions, the building blocks of matter (atoms) experience tremendous pressures, ranging from millions to many trillions of atmospheres (1 million atm = 1 Mbar = 10^{11} Pa; 1 PPa = 10 Gbar). Understanding how atomic physics may be altered in these conditions is fundamentally important to the exploration of stellar interiors and brown/white dwarfs, planetary cores, and ICF implosions. The LBS campaign (PetapascalAtmPhys-21A) was successfully carried out on 18 February 2021 and used our recently developed platform for implosion spectroscopy on OMEGA. In this campaign, we used Cu-doped CH capsules with a 30- μm -thick shell, which are filled with 20 atm of D_2 gas and 1% Ar by atomic fraction [see Fig. 11(a)]. These targets were imploded by 60 OMEGA laser beams with a 1-ns square pulse, having a total laser energy of ~ 27 kJ on target. When the imploding shell stagnates, a hot spot is formed, which “backlights” the compressed Cu-doped CH shell ($\rho = 10$ to 20 g/cm^3 , $kT = 50$ to 500 eV). Both time-resolved and time-integrated x-ray spectra are recorded by high-resolution spectrometers. A typical time-resolved spectrum is shown in Fig. 11(b), in which both the K_α line emission and $1s-2p$ absorption of Cu are presented. In FY21, we developed the density functional theory (DFT)-based kinetic modeling code *VERITAS* to self-consistently understand these experimental measurements. A preliminary comparison of time-integrated experimental data (solid red line) with *VERITAS* (solid blue line) and traditional collision-radiative-equilibrium (CRE) model predictions (dashed green line) is illustrated in Fig. 11(b). It is shown that the traditional CRE models failed to reproduce the pronounced $1s-2p$ absorption feature that is observed in the experiment, while the DFT-based *VERITAS* modeling gives an overall good account of the $1s-2p$ absorption in Cu (although some minor detailed discrepancies exist). *VERITAS* modeling reveals that the dominant $1s-2p$ absorption was caused by the $2p$ level

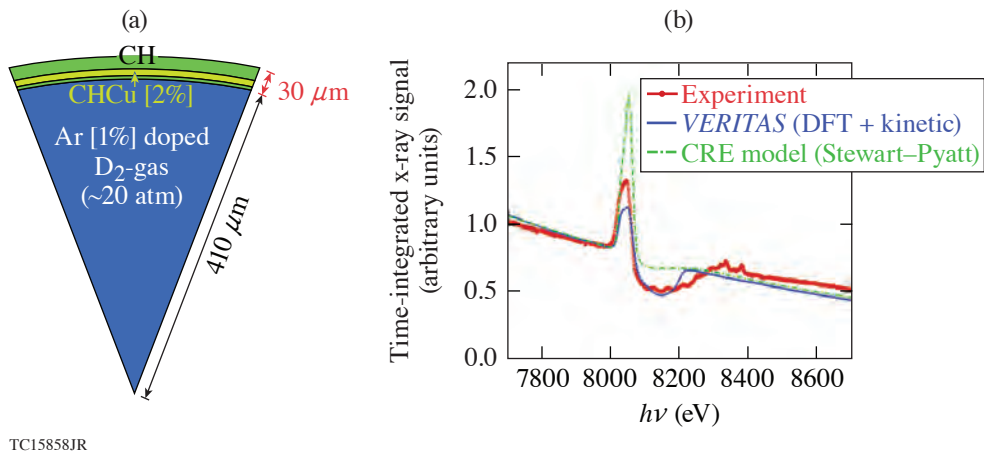


Figure 11

(a) Schematic of the implosion target that was used in these experiments, which includes a buried Cu-doped plastic layer inside the shell and a D_2 Ar (1 at. %)-filled core. (b) An example comparison of a measured time-integrated x-ray spectrum with *VERITAS* and CRE model predictions.

depletion of Cu due to heating of the CHCu layer by a thermal wave originating from the hot implosion core. This comparison highlights the necessity for a self-consistent treatment of atomic ionization in these dense plasma conditions. A quantitative comparison of time-resolved spectra with *VERITAS* model predictions is underway, and a manuscript reporting these findings is in preparation.

Comparison and Validation of Dynamic Magnetic-Field Diagnostics on Laser-Driven Coils and MIFEDS

Principal Investigators: J. L. Peebles, J. R. Davies, D. Barnak, R. B. Spielman, and R. Betti (LLE)

The initial objectives of the LBS shot day were as follows: (1) compare diagnostic responses between laser-driven coils (LDC's) and the known fields of the magneto-inertial fusion electrical discharge system (MIFEDS) and a separate fast rise pulser; (2) fully map (in 3-D) the electric and magnetic fields for a laser-driven coil at different times during the driving laser interaction; and (3) compare the measurements collected by B-dot probing, Faraday rotation, and proton radiography.

All the campaign objectives were met with a single shot day and two additional shots afforded by the facility during short-pulse/long-pulse timing qualification. These two additional shots allowed us to demonstrate the axial proton radiography technique using the known 40-T central field of a MIFEDS coil. The axial radiography technique utilizes weaker radial fields to cause a rotation effect in the proton radiograph proportional to the square root of the proton energy. There were some doubts about the technique since in the paraxial approximation no rotation should be seen (since the radial field changes sign on either side of the coil). With these shots, however, we demonstrate that in reality a significant rotation can be measured and scales exactly as expected with proton energy. These shots also helped to verify the proton spectrum, where the first two films in Fig. 12 contain mainly shadows of 9-MeV protons that were primarily deposited on the third film. Two shots were conducted in this configuration, the second of which reversed the field, which reversed the rotation direction of the radiograph. The axial probe was then applied to laser-driven coils, along with a simultaneous transverse probe. These measurements demonstrated that double-plate, "capacitor"-style, laser-driven coils developed very weak fields, with currents of the order of 2.5 kA (Fig. 13). The single-plate coil styled in a helical pattern showed slightly larger currents at around 15 kA close to the driven plate and 5 kA further away.

For these experiments a new diagnostic platform was developed called the Mini B-dot probe. While B-dots are nothing new in terms of technology for time-resolved measurements of magnetic fields, we wanted to develop our own platform that could be customized and calibrated for use on OMEGA EP. These B-dots were calibrated using the 1-kA, high-repetition-rate pulser shown in Fig. 14, which demonstrated their sensitivity to low-mode dc perturbations. In the experiments, the B-dot probes could distinguish the two laser pulses [long pulse (LP) driving the LDC, short pulse (SP) for creating protons] and showed an order-of-

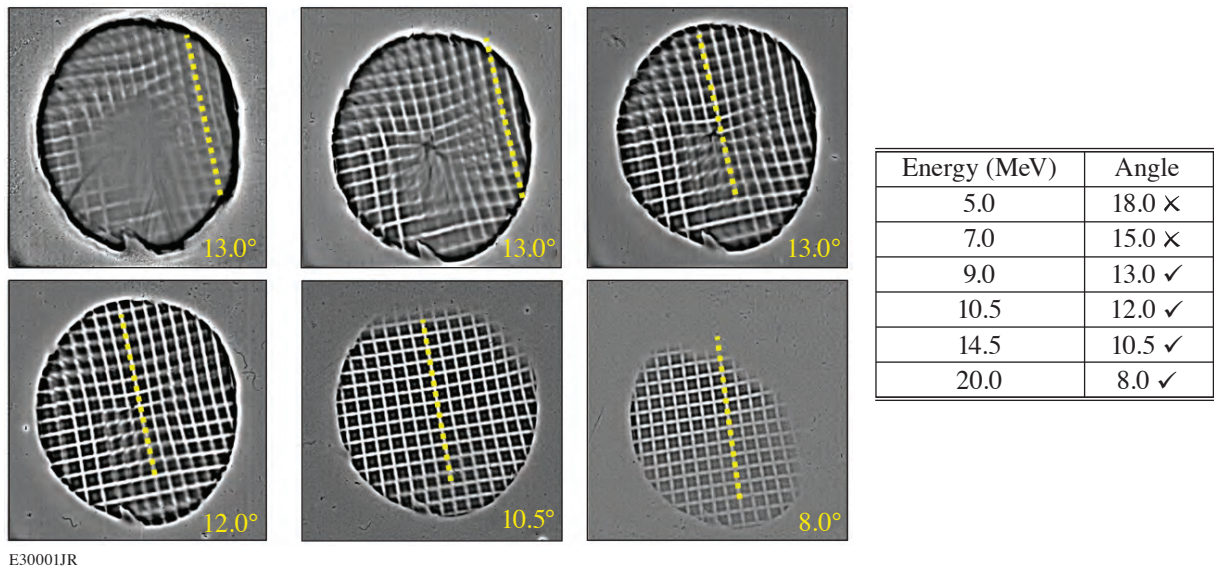


Figure 12

Axial proton radiography data taken from a MIFEDS reference shot. Protons passing through the coil receive an azimuthal kick as they pass the radial magnetic field. They travel on this altered trajectory until they receive an opposing kick from the field upon leaving the coil, resulting in a net spatial rotation in the radiograph related to the time of flight (and therefore energy) of the proton.

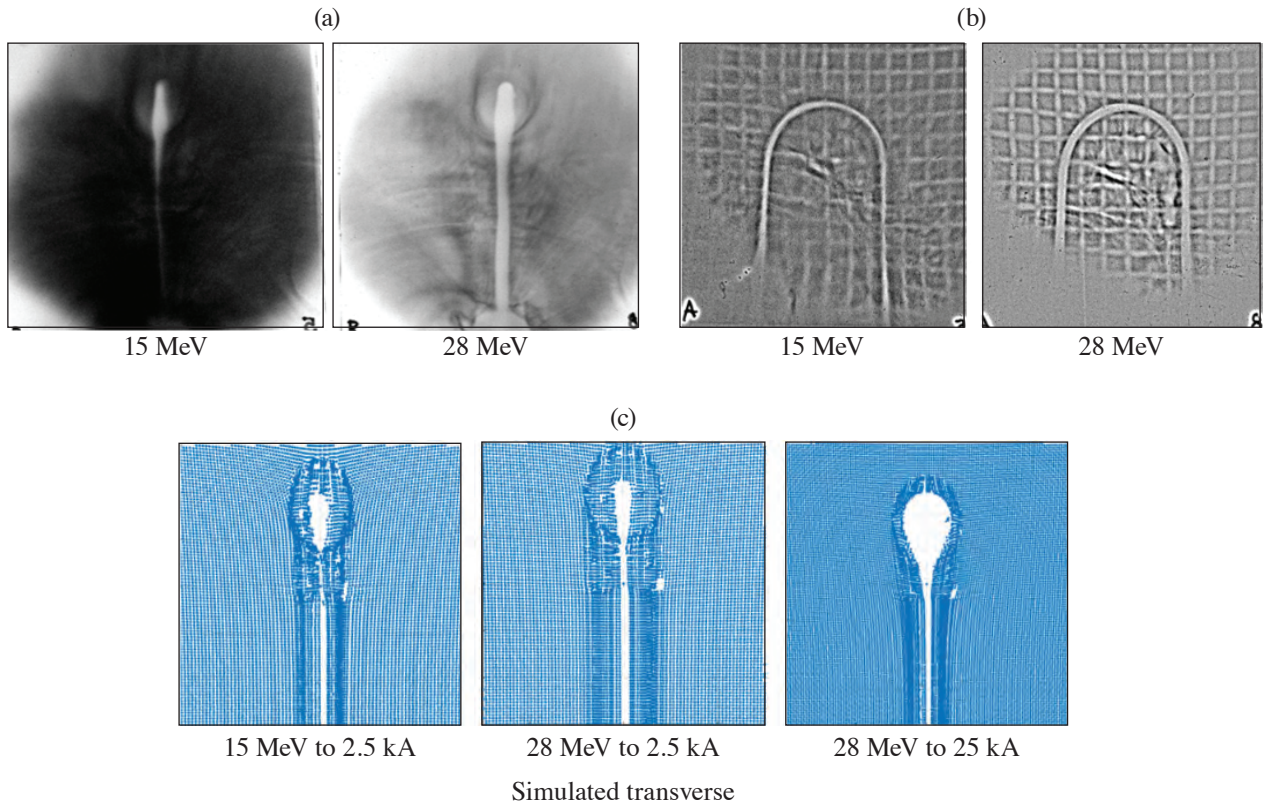


Figure 13

Transverse, axial, and simulated radiography data of double-plate LDC targets. Transverse radiographs are very sensitive to small currents and are required to reach 2.5 kA of current in the LDC. The current is too small to create any sort of resolvable rotation in the axial probe compared to the MIFEDS test shot. As an example, 25 kA of current creates voids far larger on the transverse radiograph than were measured, indicating no presence of a strong magnetic field.

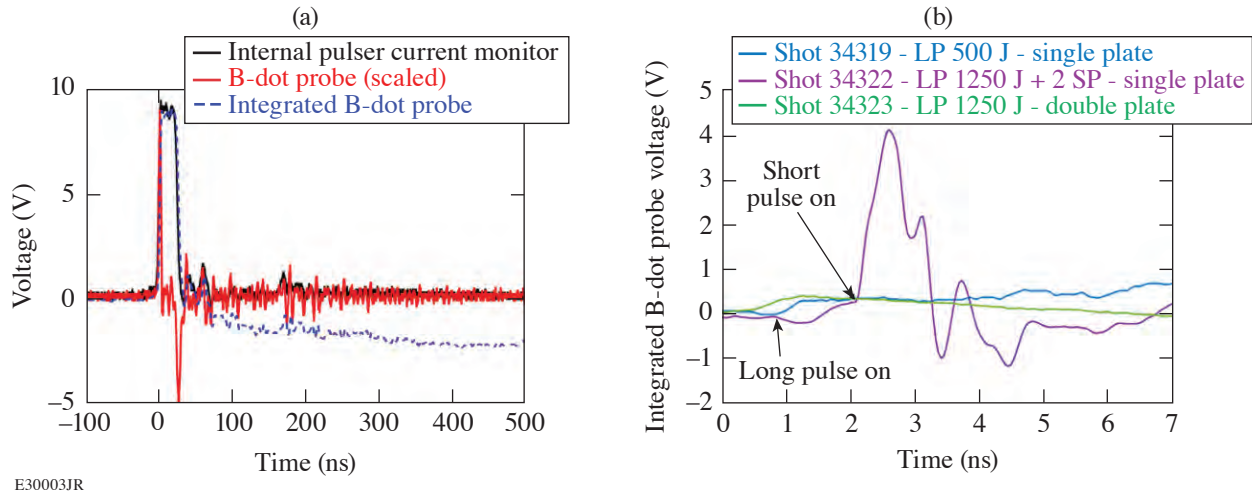


Figure 14

(a) Calibration data from the B-dot probe mathematically integrated and compared against the internal pulser current measurement. During the current pulse there is near-perfect agreement, although on longer time scales a dc offset causes significant error in the integrated measurement. (b) During experimental measurements, the long pulse and short pulse were offset by 1 ns, with additional delays due to signal time of flight between laser incidence locations. If assumed to be from magnetic field only, the long-pulse signal corresponded to an upper limit of 50 kA of current and the short pulse roughly 500 kA (an unphysical value by energy conservation).

magnitude-larger signal when the SP was active. By energy conservation we can understand that the signal on the B-dot probe from the short pulse was not from the magnetic field. This tells us that the B-dot probe measurement provides an upper limit on magnetic-field measurements since it is unable to discriminate between magnetic and electric fields. This also suggests that previous experiments that produced very high field measurements using a B-dot probe may have had their results skewed by short-pulse interactions in the experiment.

Measurements of Warm-Dense-Matter Silicon Based on Angularly and Spectrally Dispersed X-Ray Scattering

Principal Investigators: H. Poole and G. Gregori (Department of Physics, University of Oxford); M. K. Ginnane, D. N. Polsin, S. X. Hu, S. P. Regan, and J. R. Rygg (LLE); and T. White (University of Nevada, Reno)

To improve the modeling of WDM silicon, we investigated the plasma conditions seen at 1.1-Mbar compression using active shock breakout (ASBO), angularly resolved x-ray diffraction, and spectrally resolved inelastic x-ray Thomson scattering (XRTS) on the OMEGA EP Laser. Current experimental data^{21–23} have led to contradictory conclusions regarding the best model for predicting ionization potential depression.

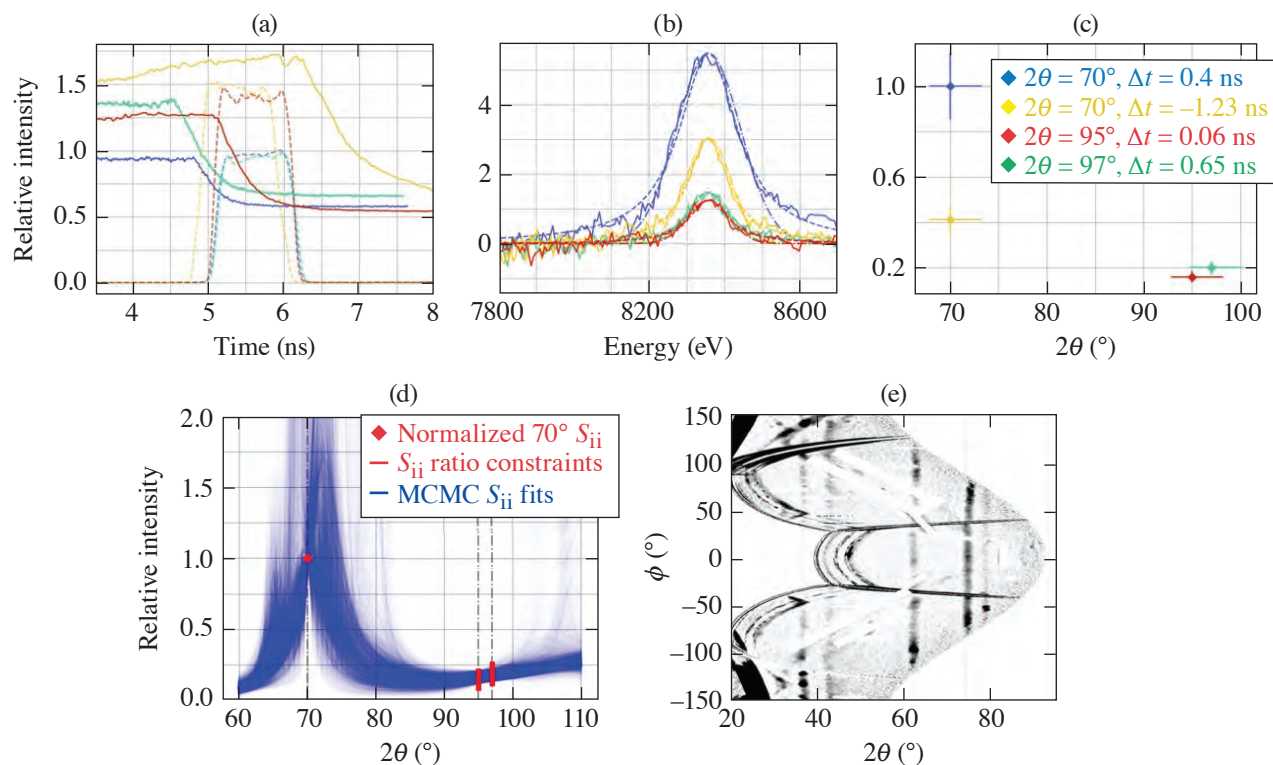
The total dynamic structure factor is given by²⁴

$$S(k, \omega) = |f(k) + q(k)|^2 S_{ii}(k, \omega) + Z_f S_{ee}^0(k, \omega) + Z_b \int \tilde{S}_{ce}(k, \omega - \omega') S_S(k, \omega') d\omega',$$

where $S_{ii}(k, \omega) \sim S_{ii}(k) \delta(\omega)$ is the ion–ion dynamic structure factor and Z_b and Z_f are the number of bound and free electrons, respectively. In the investigated XRTS scattering regime, the noncollective, unknown terms are $S_{ii}(k)$, $q(k)$, and Z_f . Angularly resolved x-ray diffraction provides, in mid- to high- Z materials, a direct measurement of $|f(k), q(k)|^2 S_{ii}(k) \sim Z_b^2$, which therefore leaves XRTS sensitive only to the ionization state, Z_f .

The experimental design used a variant of the PXRDIIP platform on OMEGA EP, which allowed for simultaneous characterization of the compressed Si sample using ASBO, PXRDIIP, and XRTS, using the ZSPEC diagnostic. The investigated pressure was 1.1 Mbar, with x-ray scattering recorded at 70° and 97°.

As shown in Fig. 15, current analysis of the relative elastic scattering peaks across the two angles collected on this shot day, alongside a 95° shot from a previous campaign date, indicates a relative S_{ij} ratio between the lower and higher scattering angles. It should be noted that the second 70° shot (yellow curve) is omitted from the analysis. This is because, as seen in Fig. 15(a) and in the legend, $\Delta t = -1.23$ ns, the x rays scattered while silicon was still partially in the solid state. In Fig. 15(d), the accepted XRTS shots were fed into a Monte Carlo Markov Chain²⁵ (MCMC) analysis code that produces a range of accepted S_{ij} fits and posterior parameter distributions (shown in Fig. 16) based on the experimental data. To produce these fits, the 70° is normalized to 1, and the 95° and 97° points are restrained to within some ratio band as shown in Fig. 15(d).



U2794JR

Figure 15

(a) Solid curves: profile of shock breakout determined from active shock breakout (ASBO) analysis. Dashed curves: relative intensity of the laser profiles incident on Cu x-ray backlighter. The time between shock breakout and the x-ray source is indicated in the legend. (b) X-ray Thomson scattering (XRTS) profiles from varied scattering angles. The elastic scattering peaks have been fit with Gaussian and Lorentzian curves shown as dashed and dashed-dotted lines, respectively. (c) Area of elastic scattering against scattering angle. The area error is determined as the difference between Gaussian and Lorentzian fits seen in (b). (d) Attempt at S_{ij} Monte Carlo Markov Chain (MCMC) fitting. (e) Powder x-ray diffraction image plate (PXRDIP) analysis isolating the Ag pinhole diffraction lines.

The current parameter distributions from this MCMC analysis is indicated in Table III. Information has been obtained on the mass density and silicon ionization, but the electron temperature remains broadly distributed. These results need to be compared to accurate simulations. Additionally, further constraints could be applied to these conditions as a result of further PXRDIP analysis.

Table III: MCMC parameter distributions for predicted Si mass density and ionization. The normal distributions are visualized in Fig. 16.

Parameter	MCMC analysis
Mass density (g/cm^3)	2.0 ± 0.2
Ionization	6 ± 2

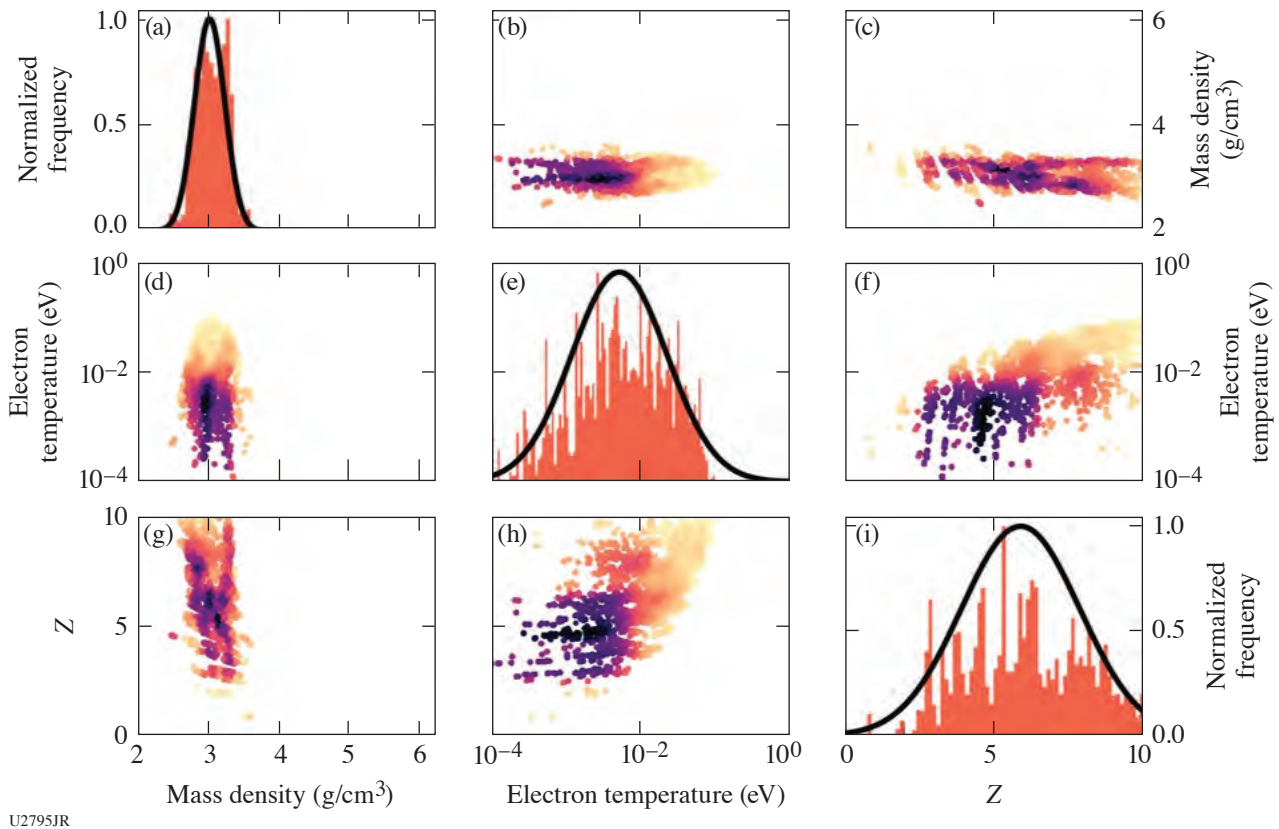


Figure 16

MCMC analysis for S_{ii} data obtained from elastic XRTS peaks shown in Fig. 15(c). The upper and lower quadrants show the density maps for the relation between the different fitted plasma parameters. The central plots are the normalized parameter histograms with normal distributions fitted over them.

This material is based upon work supported by the Department of Energy National Nuclear Security Administration under Award Number DE-NA0003856.

Measurement of the ${}^3\text{H}(n,2n){}^2\text{H}$ Breakup Cross Section Using Direct-Drive Inertial Confinement Fusion Implosions

Principal Investigators: H. G. Rinderknecht and C. J. Forrest (LLE); and M. Gatu Johnson (MIT)

Nuclear reactions involving small numbers of nucleons are of great interest to modern nuclear physics theory because they constrain low-energy reactions important to nuclear astrophysics. Low-energy light-ion reactions challenge the current capabilities of nuclear physics simulations in a regime where full-physics simulations are plausible. ICF implosions have been used to measure the differential cross section for low-energy light-ion reactions including elastic scattering of deuterons and tritons by 14.1-MeV D-T fusion neutrons,²⁶ six-nucleon fusion reactions,²⁷ and the deuteron breakup reaction $\text{D}(n,2n)\text{p}$ (Ref. 28). However, almost no published data exist for the triton three-body breakup reaction $\text{T}(n,2n)\text{D}$, and what data exist are of extremely poor quality.²⁹ The relatively low cross section of this reaction (~ 50 mb) has made it difficult to assess in implosions not specifically designed to measure this process.

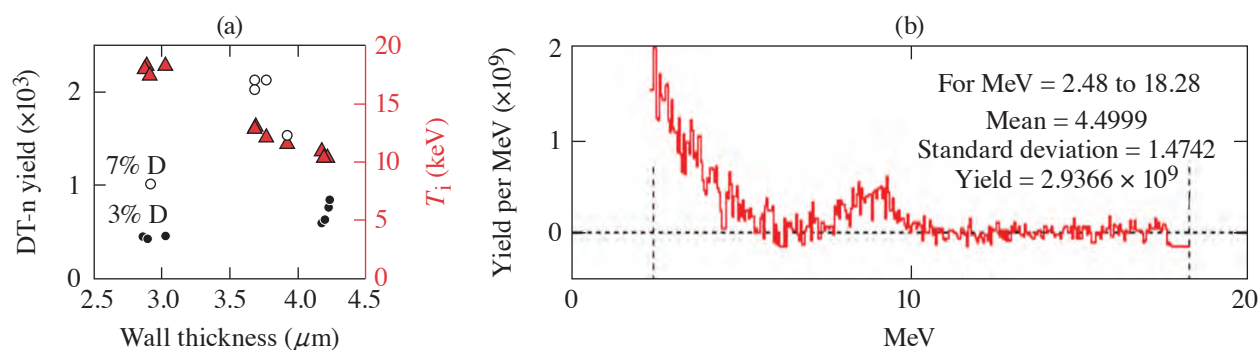
We performed a series of direct-drive implosion experiments using the OMEGA laser to measure the first high-quality deuteron spectra from the triton-breakup reaction. Targets were filled with tritium-rich fuel [$f_{\text{T}} = n_{\text{T}}/(n_{\text{T}} + n_{\text{D}}) = 93\%$ or 97%] designed to balance the requirement of a high yield of D-T fusion neutrons and a low background of elastically scattered deuterons. The implosions were SiO_2 spheres with $3\text{-}\mu\text{m}$ or $4\text{-}\mu\text{m}$ walls and $1070\text{-}\mu\text{m}$ outer diameter. These were predicted to generate moderate areal density ($\rho R = 5$ to 10 mg/cm^2) in symmetric implosions, limiting deuteron energy loss on the way out of the fuel. The

targets were imploded with 0.6-ns and 0.9-ns square pulses, respectively, to match the predicted bang time and reduce the effect of capsule charging on the charged-particle spectra. Neutron yields of 0.4 to 2.1×10^{13} were observed, as shown in Table IV and plotted in Fig. 17. The primary diagnostic was the magnetic recoil spectrometer (MRS) used in charged-particle mode to record deuteron spectra, which was expected to observe between 2 and 9×10^3 deuterons per shot. Secondary diagnostics included the charged-particle spectrometer (CPS2) to measure elastically scattered (n,t) tritons.

Analysis of the CPS2 diagnostic shows elastically scattered triton spectra that are consistent in magnitude and spectral shape with implosion areal density of the order of 1 to 10 mg/cm^2 , as shown in Fig. 17. Both deuteron and triton signals were observed in the MRS data. Interpretation of the data has been more difficult than anticipated due to the co-location of substantial (n,t) triton and D-T fusion α backgrounds with the (n,d) and (t,n,2n)t signals of interest. The alpha, triton, and deuteron signals are separable in principle since different particle species produce different track diameters in the CR-39 detection medium; however, this work

Table IV: Experimental design and results from the TBreak-20A Campaign. Two wall thicknesses (3.0 and $4.0 \mu\text{m}$) and two fuel D:T ratios (7% and 3% deuterium) resulted in four implosion types. Neutron yields in the range 4 to 21×10^{12} were observed, resulting in a predicted 2 to 9×10^3 triton-breakup deuterons observed by the MRS in each implosion.

Shot number	RID	Pulse shape	Wall (μm)	Deuterium %	$Y_{\text{DTn}} (10^{12})$	$\langle T_i \rangle$ keV	$Y_{\text{T}(n,2n)\text{D}} (10^8)$	$*N_{\text{detected}} \text{T}(n,2n)\text{D}$
98789	79825	SG06v001	3.0	7%	10.1	17.5	7.3	5210
98790	79953	SG06v001	3.0	3%	4.5	18.1	3.3	2250
98791	79956				4.3	18.4	3.2	2160
98792	79957				4.6	18.4	3.4	2290
98794	79297				SG09v002	4.0	7%	15.3
98795	79958	21.3	13.0	14.2				9040
98796	79959	21.3	12.2	14.2				9040
98797	79960	20.3	13.2	13.5				8610
98799	79954	SG06v001	3.0	3%	6.0	11.1	4.0	2690
98800	79962				7.6	10.5	5.1	3410
98802	79963				6.4	10.5	4.3	3410
98803	79964				8.4	10.5	5.6	3750



E30010JR

Figure 17

(a) Observed D-T fusion neutron yield (black) and burn-averaged ion temperature (red) from the Tbreak-20A Campaign. Fuel mixtures with 3% deuterium and 7% deuterium are shown as filled and open circles, respectively. (b) Elastically scattered triton spectrum measured by CPS2 on shot 98794. The spectral shape and yield are consistent with an areal density in the range of 1 to 10 mg/cm^2 .

is ongoing. We anticipate that we will be able to precisely infer areal density using the MRS (n,t) triton spectra. We will then use the differing spectral shape of the (n,d) and t(n,2n)d deuteron spectra on each shot to infer what fraction of the deuterons is produced from triton breakup and use this value to constrain the cross section of the t(n,2n)d breakup process.

This material is based upon work supported by the Department of Energy National Nuclear Security Administration under Award Number DE-NA0003856, the University of Rochester, and the New York State Energy Research and Development Authority.

Proton Radiography of Target Normal Sheath Acceleration Fields in the Long-Pulse Regime

Principal Investigators: R. Simpson, N. Lemos, D. Mariscal, E. Grace, G. Scott, J. Kim, and T. Ma (LLNL); and J. L. Shaw (LLE)

In this experimental campaign we performed a time-dependent radiograph of the surface fields (front and back) of a laser-irradiated solid target while varying the laser pulse length. The goal was to investigate the increased coupling and higher-energy target normal sheath acceleration (TNSA) proton that have been reported when using picosecond laser pulse durations (low and high intensity)³⁰ as opposed to when using tens of femtosecond laser pulses.

In the TNSA mechanism, a high-power laser is incident upon the front side of a thin (~μm scale) solid target where electrons are efficiently heated to high energies. These heated electrons traverse through the target and set up a sheath field on the back side, which accelerates ions from the rear surface (Fig. 18). This sheath field is generated by the electron pressure gradient and has accelerated ions up to ~100 MeV (Ref. 31). Both short-pulse beamlines of OMEGA EP were used to simultaneously create and probe the TNSA fields. A thin Cu foil was driven by one laser beam, creating the TNSA fields at the back of the target. A second laser beam irradiating a thin gold foil generated a proton beam that probed the TNSA fields generated by the first laser pulse. Different proton energies probed the TNSA fields at different times due to the different time of flight of each proton, so it was possible to record the time evolution of these fields on a single shot (Fig. 18). A parameter scan over several pulse durations (keeping the laser intensity constant) showed that the maximum proton energy was achieved for a laser pulse duration >10 ps. Figure 18 shows the time evolution of a Cu foil expanding from 0 to 50 ps for a laser pulse duration of 0.6 ps. At longer pulse

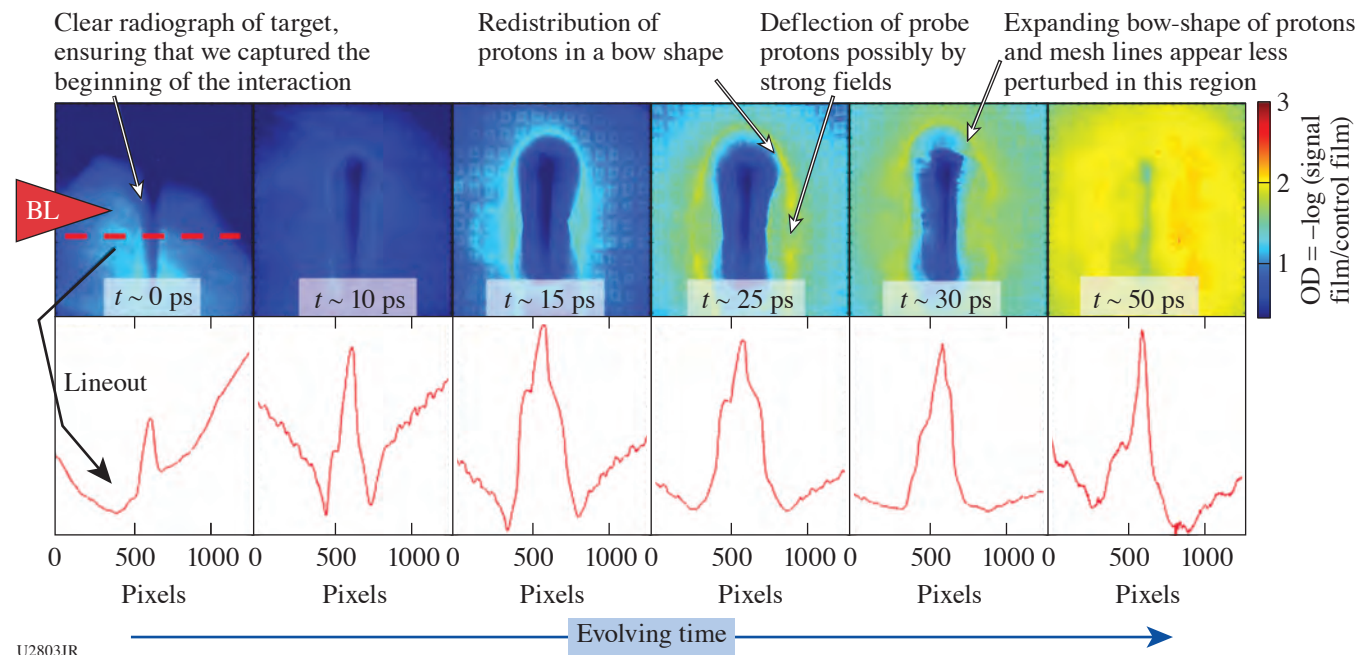


Figure 18 Single-shot proton radiography of an expanding Cu foil irradiated by a 0.6-ps, 34-J laser pulse. The top row images show the radiochromic film signal from 0 to 50 ps. The bottom row shows the horizontal lineouts at the center of the Cu foil.

lengths, which are most relevant to our work on the NIF-ARC (Advanced Radiographic Capability Laser), we missed time = 0 (when laser pulse one irradiates the Cu foil). We will extend this work beyond these preliminary shots to capture these dynamics in the multipicosecond regime.

The DOE NNSA Laboratory Residency Graduate Fellowship Program was provided under Cooperative Agreement number DE-NA0003960.

Determination of High-Pressure Phase Transformation Mechanisms at the Atomic Scale

Principal Investigators: S. Singh, R. F. Smith, J. H. Eggert, and J. McNaney (LLNL); and J. Wicks (Johns Hopkins University)

For many materials, the application of pressure results in an atomic rearrangement into a lower-energy crystal structure that is accompanied by an associated volume collapse. Such phase transformations are commonplace in nature and can fundamentally alter the transport, chemical, and mechanical characteristics of a solid. Reconstructive phase transformations—which is a type of transformation in which no group–subgroup relationship between the parent and transformed phase exists—constitutes an important class of such phase transitions. Determining the sequence of atomic movements that facilitate pressure-induced phase transformations has been a great challenge in the field of high-pressure physics, toward the goal of developing predictive time-dependent and mechanistic atomic-pathway-dependent models. Despite decades of research, these processes remain poorly defined and largely restricted to theoretical study.^{32–35}

We designed a series of shock-compression shots to explore the melt curve of FeO and texture evolution in SiC. The pressure was tuned by changing the laser power, and samples were probed just before shock breakout using x-ray diffraction. Figure 19(a) shows the target pressure states for the FeO sample.³⁶ Several experimentally measured phase boundaries, as well as the theoretically predicted melt curve, are also shown.

By using a multilayered target package, we were able to obtain high-quality diffraction data between 200 and 360 GPa. Examples of raw and integrated data are shown in Fig. 19(b). VISAR (velocity interferometer for any reflector) was employed as

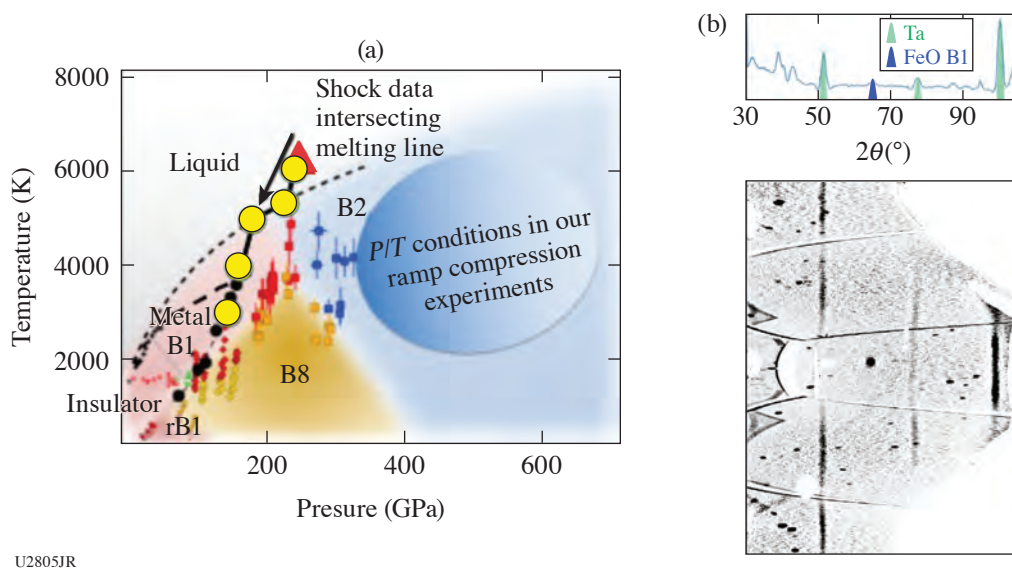


Figure 19

(a) The phase diagram of FeO with theoretically predicted phase boundaries and data from previous studies is shown. Target pressures proposed during the campaign are shown with the yellow circles. (b) The diffraction data corresponding to the red triangle (~230 GPa). Raw (lower) and integrated (upper) data from the FeO target package are shown. The powder lines are from the W pinhole. There is diffraction recorded from the B1 phase, which is well above the theoretically calculated melt curve on the FeO Hugoniot.

a secondary diagnostic in the campaign to allow pressure determination. Over one shot day, we took 11 shots and successfully characterized the structural behavior of FeO and SiC at several different pressure and temperature states. Crystalline diffraction from the FeO B1 phase was observed at pressures well above the theoretical melt curve and presents an interesting avenue for future experiments.

OMEGA EP NuclTNSA Campaign

Principal Investigator: C. Stoeckl (LLE)

The 26 January LBS campaign on OMEGA EP aimed to characterize the TNSA deuteron beam emitted from 25- μm -thick titanium targets exposed to 1 atm of D_2 at 350°C for 24 h. The OMEGA EP laser with intensities between 1 and $7 \times 10^{17} \text{ W/cm}^2$ was directed onto these targets, and the profile and energy spectrum of the emitted deuteron beam was measured using radiochromic film (RCF) and Thomson parabola ion energy (TPIE).³⁷ In separate experiments, the deuteron beam was directed onto deuterated polyethylene (CD) targets to induce D–D fusion and test the feasibility of this platform for nuclear reaction studies. The existing nTOF detectors at 90° and 130° were employed to detect any D–D fusion neutrons.

Insights from these experiments are utilized to produce tritiated titanium targets, which have been demonstrated to emit a comparable tritium beam when irradiated by OMEGA EP. This platform is currently the only one worldwide to deliver a multi-MeV triton beam for nuclear experiments.

1. Deuteron Beam Characteristics

This campaign featured for the first time a step absorber for TPIE to remove the heavy C^{n+} and O^{n+} contaminants in the deuteron beam. Aluminum foils of thicknesses between 10 and 100 μm were arranged in bands directly in front of the image plate, with the thicker foils in regions where higher ion energies are expected. The results are shown in Fig. 20(a), where the left panel demonstrates that even an untreated Ti target produces various lines associated with surface contaminants. These can be removed from the beam with the step filter, as shown in the center, such that the deuterated target on the right produces only D^+ and H^+ lines.

The corresponding deuteron spectra for several energies are shown in Fig. 20(b). In general, the spectra have an exponential shape with cutoff energies around 10 MeV. It is evident that the deuteron beam spectrum can be controlled coarsely by increasing

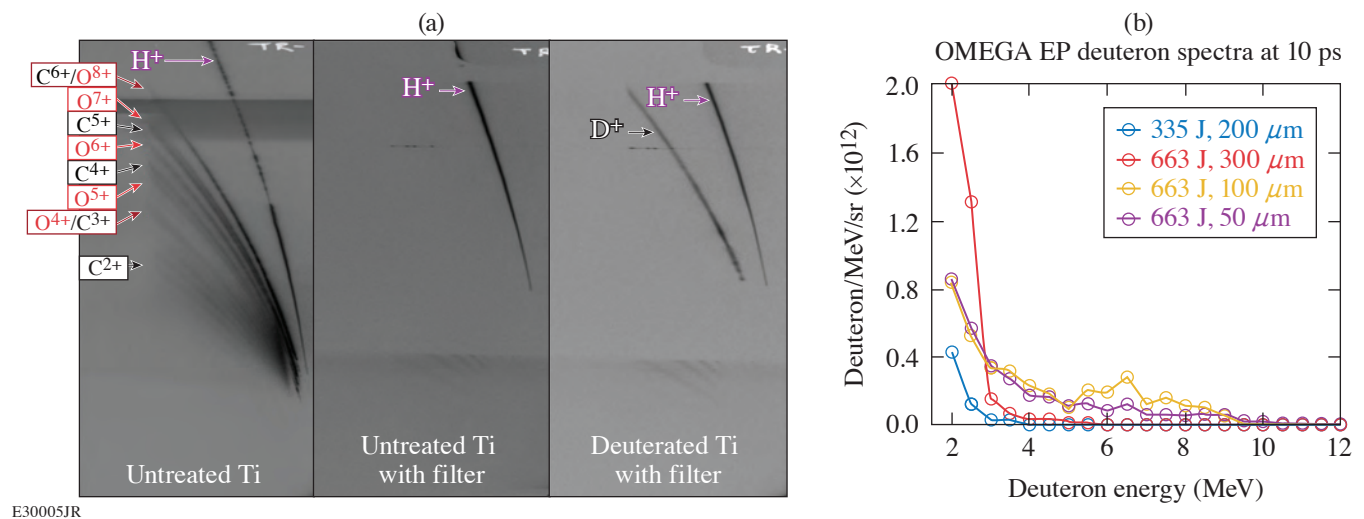
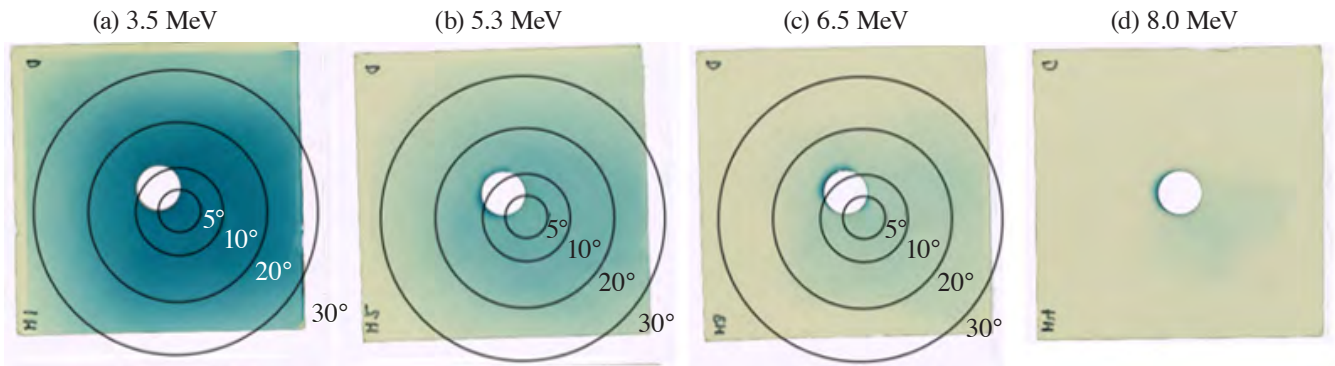


Figure 20
 (a) Raw TPIE image plates with and without the described filter. (b) Corresponding deuteron spectra.



E30006JR

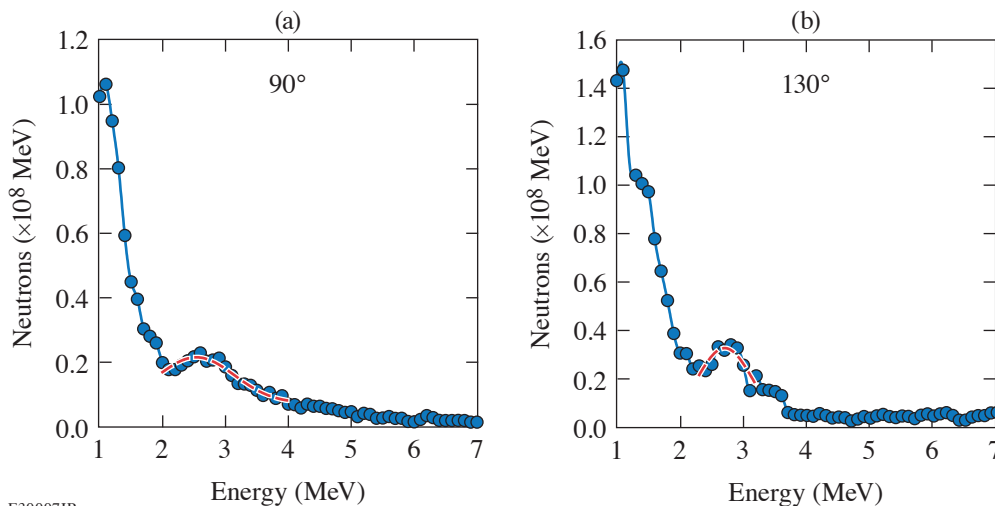
Figure 21
Raw RCF images. High-energy ions tend to be closer to the beam axis.

the laser energy, which increases the deuteron cutoff energies and total yields at all energies. Prior experiments with CD targets³⁸ suggested that further beam shaping is possible with additional laser beams, which will be examined in a planned campaign.

The RCF measurement delivered a spatial beam profile consistent with expectations from other TNSA experiments.^{38,39} Figure 21 shows that the low-energy ions tend to be emitted at angles of up to 30°, whereas the high-energy ions tend to stay close to the center.

2. Pilot Nuclear Experiment

The described deuteron beam was directed onto a secondary CD target 5 mm behind the first, and two nTOF detectors were employed to look for any D–D fusion neutrons. The neutron spectra, corrected for instrument responses and attenuation effects and calibrated against ICF experiments, are shown in Fig. 22. Two peaks at 2.5 MeV (90°) and 2.7 MeV (130°) are evident, which is consistent with kinematically shifted D–D fusion neutrons.



E30007JR

Figure 22
Neutron time-of-flight spectra at two different angles, featuring a small D–D fusion peak.

Prior campaigns³⁸ suggested that the signal-to-background ratio can be improved by enclosing the primary target in a plastic cylinder that shields the target chamber from high-energy protons. The neutrons produced by the associated (p, n) reactions with the chamber walls increase the background substantially. A follow-up campaign is planned to investigate this hypothesis and improve the neutron signals from these experiments.

Report for H₂-H₂O-DAC-21A

Principal Investigator: G. Tabak (LLE)

Co-investigators: G. W. Collins and J. R. Rygg (LLE); and R. Dias (University of Rochester)

The purpose of this campaign was to study hydrogen-rich systems with planetary science applications in mind. Both hydrogen and water are major components of ice giant interiors, and a recent work predicts that at extreme pressures an H₂O structure will form, which would have implications for planetary interior modeling.⁴⁰ While hydrogen and water are immiscible at ambient conditions, it is known that they can mix in certain ratios at ~1 GPa and higher pressures, a range accessible by the diamond-anvil cell (DAC) platform, which is now standard at the Omega Laser Facility.⁴¹ This experiment required several new developments for the team, including a new liquid–gas filling technique as well as reaching 3 to 5 GPa, which is a higher pressure range than what had been achieved in previous experiments with these cells. The filled DAC's would then be shock-compressed on OMEGA 60 and taken to the several-100-GPa range. VISAR and a streaked optical pyrometer (SOP) is used to directly measure the shock velocity, reflectivity, and self-emission. Impedance matching with a quartz standard is used to measure the pressure and density, while the self-emission is referenced to quartz to infer the shock temperature, giving a full equation of state. The evolution of pressure, density, temperature, and reflectivity along the Hugoniot would then be explored for potential signatures of phase changes and novel chemistry at extreme conditions.

Unfortunately, after this proposal was submitted, the gas loader unexpectedly broke down and repairs were completed a week before the shot day. It was impossible to fully develop the new techniques as originally planned, so the cells were filled with pure methane (CH₄), which contributed to an ongoing effort to understand this material. CH₄ is another hydrogen-rich system that is also a major constituent of giant planets and is, therefore, closely related to the original goal. It is predicted to have an intricate phase diagram at pressures of several 100 GPa, including eventual separation into diamond and hydrogen, and elucidating the properties of methane at these extreme conditions would provide internal insight into the ice layer of giant planets such as Uranus and Neptune.⁴² After some improvements to the target preparation process, methane DAC's were prepared with pressures reaching 4 to 5 GPa, which is the pressure range that was desired for the hydrogen–water mixture.

High-quality data on methane were obtained at the challenging precompression of 4 to 5 GPa, bringing the experimental conditions closer to planetary interior conditions. While the 100- to 400-GPa range is easy to reach with shocks, high precompression

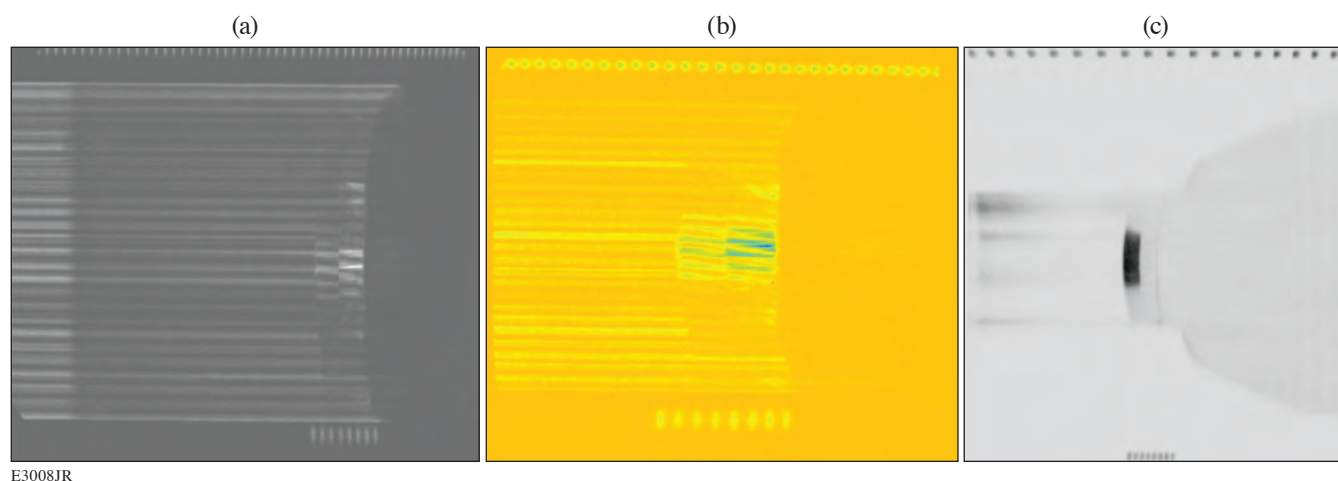


Figure 23

(a) VISAR1, (b) VISAR2, and (c) SOP data for shot 101060. The two fringe events at the spatial center of the target, co-timed with the eight-comb, indicate shock breakout into quartz and methane. The self-emission of the quartz standard is clearly seen as the dark rectangular region on the SOP, and the methane self-emission occurs afterward on the image.

sion is necessary to lower the temperature of the shock state and bring it closer to the pressure–temperature conditions believed to exist inside planets. Therefore, these results constitute a significant enhancement of the data set on precompressed methane. Figure 23 shows a representative VISAR and SOP datum from one of the shots.

To summarize, while it was impossible to follow through with the original plan, the team demonstrated significant improvements with the DAC platform and obtained important data on methane, a closely related material, which will give new insight into planetary interiors.

X-Ray Phase-Contrast Imaging of Imploding Strong Shock Waves

Principal Investigators: W. Theobald, J. J. Ruby, and D. Cao, (LLE); L. Antonelli, M. Khan and N. Woolsey (York Plasma Institute, Department of Physics, University of York, UK); F. Barbato, V. Bouffetier, L. Ceurvorst, and A. Casner (CELIA, University of Bordeaux, France); and R. H. H. Scott (Central Laser Facility, STFC Rutherford Appleton Laboratory, UK)

The goal of this LBS joint shot day campaign was to demonstrate 2-D x-ray phase-contrast imaging (XPCI) of a converging strong shock wave in a spherical solid CH target using a short-pulse laser-driven backlighter source. The application of XPCI to diagnose laser-induced shock waves proved to be powerful in determining the shock-front position in both the high- and low-density regions of the target.⁴³ Due to the high sensitivity to density variations, XPCI is the ideal tool to detect the position of a shock front, especially in the case when it is propagating in a low-density region, in the presence of multiple shocks, detecting asymmetries in the shock front, and studying hydrodynamic instabilities such as the Rayleigh–Taylor and the Richtmyer–Meshkov instabilities. In a previous experiment, the XPCI technique was successfully demonstrated in planar target geometry on OMEGA EP by applying a short-pulse backlighter source to measure the density profile of a strong shock wave in a cylindrical CH target.⁴⁴ High-quality radiographs were obtained that clearly showed the phase-contrast enhancement at the shock front using a wire source target, providing a spatial resolution of $14 \pm 2 \mu\text{m}$ in the horizontal direction and $18 \pm 2 \mu\text{m}$ in the vertical direction. The next step was to apply the developed XPCI platform to spherical implosions on OMEGA and to provide 2-D snapshot XPCI radiographs of a converging shock wave in a solid CH sphere with a short-pulse laser-driven backlighter source.

The experimental setup is shown in Fig. 24(a). The 60 OMEGA UV ($\lambda = 351 \text{ nm}$) laser beams were focused on a CH sphere with a diameter of 1.05 mm using SG5-650 distributed phase plates, distributed polarization rotators, smoothing by spectral dispersion modulation, and a 1-ns square pulse. One of the two IR short-pulse beams from the OMEGA EP laser was focused onto a backlighter target that consisted of a Cu wire with a diameter of $10 \mu\text{m}$ glued onto a $10\text{-}\mu\text{m}$ -thick CH substrate with an area

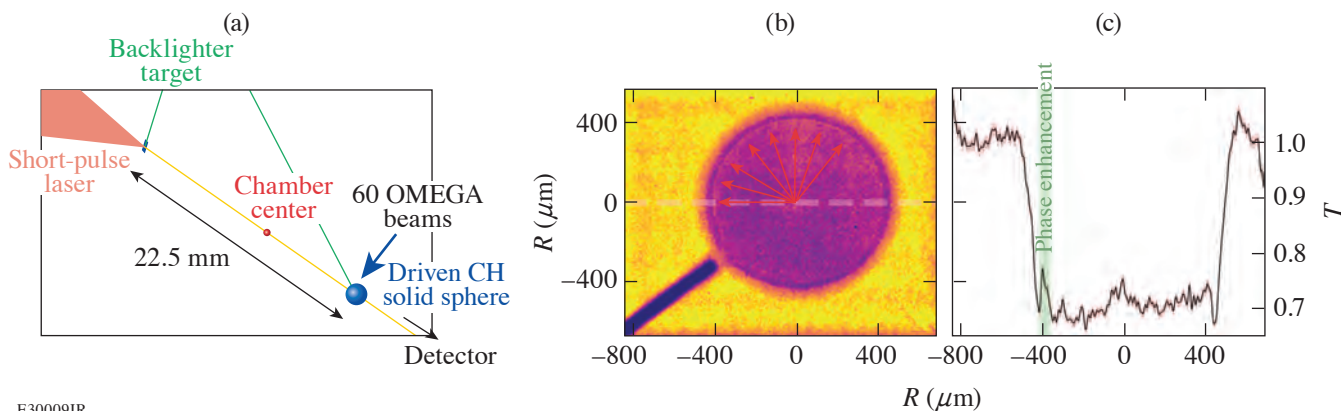


Figure 24

(a) Experimental setup and (b) sample measured radiograph of shot 99189 that was taken at a probing time of 6.5 ns after the start of the 1-ns drive pulse showing phase-contrast enhancement at the shock front. The CH sphere was imploded by the 60 OMEGA beams with a total energy of 640 J and an intensity of $2 \times 10^{13} \text{ W/cm}^2$. The dark diagonal strip at the lower left is the shadow of the target stalk. The red arrows in the sphere indicate the parts of the shock front that present phase enhancement. (c) Transmission lineout along the dashed horizontal line. The pink area indicates the experimental error. The signal excursion at the transmission minimum is caused by phase-contrast enhancement.

of $300 \times 300 \mu\text{m}^2$. The IR beam with 100-ps pulse duration was focused with an intensity in the range of $2 \times 10^{16} \text{ W/cm}^2$ to $1 \times 10^{17} \text{ W/cm}^2$ with normal incidence onto the target with the wire aligned along the radiography axis pointing to a passive imaging plate (IP) detector plate placed in a heavy metal shielded box. The backlighter produced a strong emission between 8 and 9 keV, predominately from the He_α and Ly_α resonance lines. The distance from the backlighter to the CH sphere was 2.2 cm and the distance from the CH sphere to the IP detector was 1.3 m, providing a spatial magnification of $60\times$. A $23\text{-}\mu\text{m}$ -thick Cu foil and a $254\text{-}\mu\text{m}$ -thick polyethylene terephthalate (PET) blast shield were placed in front of the detector, which provided a transmission of $\sim 40\%$ for the 8-keV backlighter radiation and strongly attenuated the x-ray emission for photon energies below 5 keV from the corona of the driven target.

We obtained radiographs of an imploding shock wave at different probing times by shifting the timing between the drive and the backlighter beams. Significant hard x-ray emission in the backlighter emission produced a strong background, which reduced the image contrast. In addition, the x-ray emission from the plasma of the driven target contributed to the background especially at high drive laser energies. Reducing the backlighter energy and the drive laser energy improved the image contrast, which made it possible to record radiographs of the imploding spherical shock wave at various times. The radiographs are of poorer image quality than the ones obtained in the previous experiment on OMEGA EP under similar experimental conditions. Phase-contrast enhancement was observed in the radiographs although with reduced quality. An example image is shown in Fig. 24 together with an inferred transmission lineout. The phase enhancement is not uniform and visible in some parts of the spherical implosion. This could be due to the nonperfect alignment of the source or an azimuthal variation in the shock strength. A backlighter-only shot with a static Au grid provided an *in-situ* measurement of the spatial resolution, which provided $22 \pm 3 \mu\text{m}$, worse than in the OMEGA EP planar target experiment. This could explain the lower amount of observed phase enhancement in the spherical target experiment.

The image-plate detector usage is restricted to low drive energies ($<1 \text{ kJ}$) because of the background x-ray emission from the plasma of the driven CH sphere. Higher drive energies require a time-gated detector. An attempt was made to use a time-resolved detector (two-strip time-gated x-ray imager) instead of the IP. This was partially successful. A time-gated radiography of the shock wave driven by a shaped laser pulse and 15 kJ of drive laser energy was obtained; however, the detector was not well aligned and significant hard x-ray emission from the backlighter produced a strong inhomogeneous background. Part of the imploding shock wave was observed on the bottom strip and the shadow of the target stalk on the upper strip. Lowering the short-pulse laser intensity helps to reduce this background, but it also diminishes the amount of useful Cu He_α emission at $\sim 8.4 \text{ keV}$ that radiographs the object. Further optimization of the spherical target platform is required by optimizing the signal-to-background ratio and the detector.

This material is based upon work supported by the Department of Energy National Nuclear Security Administration under Award Number DE-NA0003856, the University of Rochester, and the New York State Energy Research and Development Authority. The shots were provided under the umbrella of the LBS program.

Retrieving Density Profiles of Ion Species with Talbot–Lau Interferometry

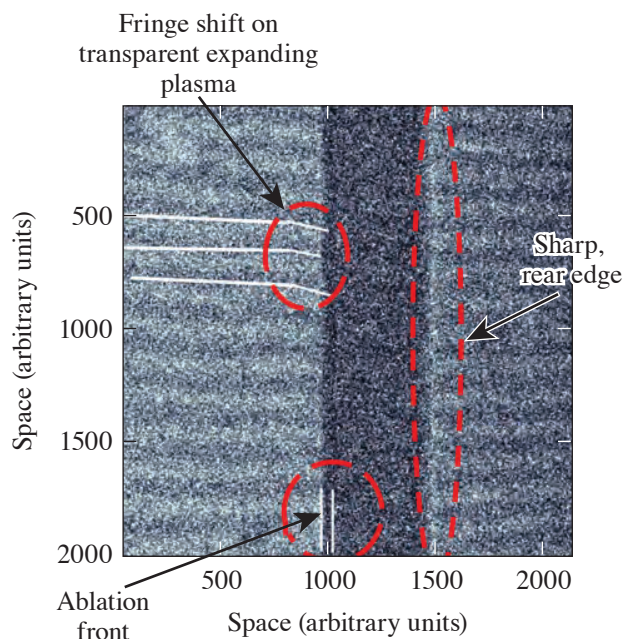
Principal Investigators: T. E. Weber (LANL); M. P. Valdivia (Johns Hopkins University); V. Bouffetier, G. Perez-Callejo, L. Cervoust and A. Casner (CELIA); and G. Kagan (Imperial College London)

In recent years, multispecies physics has been attracting an increasing amount of attention in the high-energy-density physics context. For example, a number of experiments indicate that in laser-driven spherical implosions of DT and D^3He plasmas, the relative concentration of the D and T ions can change, thereby degrading the yield. Another area where the multispecies effects can be of paramount importance is the physics of hohlraums. As the high-power lasers irradiate the inner surface of a hohlraum, the Au ions are ablated to create a high-Z plasma jet. This jet can then collide with another such jet or with a jet of different ions, resulting from the ablation of the outer surface of the fuel capsule.

Ideally, to understand the basic physics behind and implications of these effects, spatially resolved measurements of each species' densities would be needed. One could then validate directly the newly developed theoretical models for species separation and

interpenetration. One complication is that the relevant densities are often too high for standard diagnostics such as optical Thomson scattering. This project has attempted to understand spatial profiling of the relevant densities with a very novel diagnostic (the x-ray Talbot–Lau interferometer), which is currently being developed on OMEGA EP. The present version operates with 8-keV photon energy, which makes accessible electron densities of about 10^{23} cm^{-3} , therefore allowing one to study the conduction zone of the ablation layer.

The experiment parameters were as follows: A long-pulse laser (~ 150 to 900 J , 1 ns , $\sim 10^{13} \text{ W/cm}^2$) was used to drive a thin $5\text{-}\mu\text{m}$ foil, resulting in plasma jets emerging from the front and rear surfaces. A short-pulse laser (90 to 150 J , 10 ps , $\sim 10^{16} \text{ W/cm}^2$) was then used to drive a copper foil to produce an 8-keV probe beam for Talbot–Lau x-ray interferometry. Three basic types of driven foils were employed: plastic (CH), copper (Cu), and bronze (94% Cu/6% Sn). In principle, Talbot–Lau interferometry allows inference of an average atomic number that is directly related to the relative species concentration in a plasma with two ion species. Therefore, bronze targets were chosen based on attenuation and refraction signatures, which were expected to be the most pronounced for rather disparate species with the high-Z element being a minority.



U2805JR

Figure 25

The raw data with enhanced contrast from CH shot 35242 showing promising features. The image dimensions are equivalent to 675 to $675 \mu\text{m}$. Driving beam: 150 J , 1 ns , $700\text{-}\mu\text{m}$ spot size; backlighter: 150 J , 10 ps , $120\text{-}\mu\text{m}$ spot size, 0.5-ns delay with respect to the driving beam.

In the experiment, however, bronze (and pure copper) targets produced too much of the self-emission that overshadowed the 8-keV signal from the backlighter, dramatically reducing diagnostic signal-to-noise ratio, which was also observed when probing the plasma jets at later times. Therefore, CH targets were driven, and self-emission was then found to be much lower with the plasma densities extending all the way from solid to those transparent for 8-keV photons. Promising features were observed, as shown in Fig. 25. Talbot–Lau moiré fringe contrast is high enough to distinguish fringe shifts, indicating electron density gradients near the foil surface and making evident a strong high-density ablation front unresolvable by 8-keV illumination. While we are unlikely to be able to infer the individual species (i.e., the C and H) densities, inferring the total ion density profile may be possible. This alone would provide data to validate existing ablation models.

Extreme Deformation and Failure of High-Entropy Alloys by Laser Shock-Induced Compression and Tension

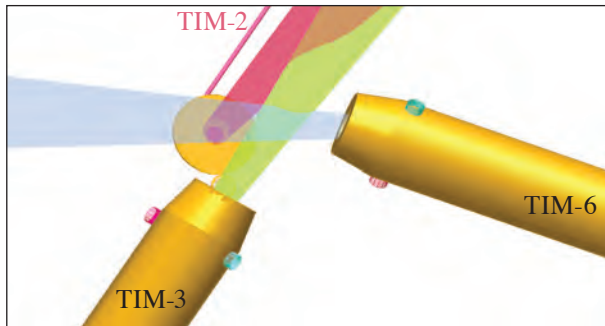
Principal Investigators: S. Zhao (LBNL)

Co-investigators: Q. Yu and C. Stan (LLNL)

High-entropy alloys (HEA's) are a class of metallic alloys containing three or more elements in significant atomic proportion. They exhibit generally high yield strength and fracture toughness and are good candidates for engineering applications such as

the aerospace industry. This project was initially interested in (1) the spall strength behavior of these materials, and (2) the 2-D velocity anisotropy through the HEA grain structure. Due to catastrophic failure of the OMEGA high-resolution velocimeter (OHRV) system, we were able to focus only on the first part of the LBS request.

We studied the spall strength of several HEA's and steels to several tens of GPa. The experimental setup (Fig. 26) consists of three individual targets that are independently shot, one of which was a spall velocimetry target and two of which were recovery tube spall targets.



U2806JR

Figure 26

Schematic diagram of the experimental setup. Two recovery tubes are mounted in TIM-3 and TIM-6. A VISAR target is mounted from TIM-2 and positioned such that the back of the target points toward TIM-5, where the ASBO is located. Each target is driven with a square laser pulse shape and one to two drive beams, depending on the desired shock strength, and the beams were defocused to ~3 mm in order to cover the entire sample surface. Since the materials do not have established shock behavior, energy was scaled between 100 and 500 J in order to cover a range of possible pressure.

During our one shot day, we were able to execute a total of nine shots. On the first half-day, we found that the VISAR targets had been mounted backward, causing a severe lack of reflectivity in the VISAR instrument. On the second half-day, we were target limited, due to the last-minute redesign of the experiment as a result of the OHRV failure. We collected three good VISAR data points and one data point where one VISAR leg malfunctioned. The recovery targets from both days remain to be analyzed as a result of a reduction in personnel at LBNL. Electron microscopy will be used to determine the grain behavior at the spall surface.

REFERENCES

1. M. Millot *et al.*, *Nat. Phys.* **14**, 297 (2018).
2. M. Millot *et al.*, *Nature* **569**, 251 (2019).
3. J. R. Rygg *et al.*, *Rev. Sci. Instrum.* **83**, 113904 (2012).
4. Y.-J. Kim *et al.*, *Sci. Rep.* **11**, 5610 (2021).
5. C. Wang *et al.*, *Phys. Plasmas* **22**, 102702 (2015).
6. C. H. Allen *et al.*, *Appl. Opt.* **61**, 1987 (2022).
7. *Report of the Workshop on High Energy Density Laboratory Physics Research Needs*, Office of Science, U.S. Department of Energy, Washington, DC (15–18 November 2009).
8. T. R. Boehly *et al.*, *Opt. Commun.* **133**, 495 (1997).
9. L. D. Landau, *Zh. Eksp. Teor. Fiz.* **14**, 240 (1944).
10. P. Clavin and L. Masse, *Phys. Plasmas* **11**, 690 (2004).

11. L. Willingale *et al.*, Phys. Rev. Lett. **96**, 245002 (2006).
12. N. Lemos *et al.*, J. Plasma Phys. **78**, 327 (2012).
13. J. L. Shaw *et al.*, Sci. Rep. **11**, 7498 (2021).
14. J. A. Akins *et al.*, Geophys. Res. Lett. **31** (2004).
15. D. E. Fratanduono *et al.*, Phys. Rev. B **97**, 214105 (2018).
16. B. Militzer, High Energy Density Phys. **9**, 152 (2013).
17. H. S. Bosch and G. M. Hale, Nucl. Fusion **32**, 611 (1992); **33**, 1919(E) (1993).
18. A. B. Zylstra *et al.*, Phys. Rev. C **101**, 042802(R) (2020).
19. Y. Kim *et al.*, Phys. Rev. C **85**, 061601 (2012).
20. R. S. Canon *et al.*, Phys. Rev. C **65**, 044008 (2002).
21. S. M. Vinko *et al.*, Nat. Commun. **6**, 6397 (2015).
22. D. J. Hoarty *et al.*, Phys. Rev. Lett. **110**, 265003 (2013).
23. D. Kraus *et al.*, Phys. Rev. E **94**, 011202(R) (2016).
24. J. Chihara, J. Phys.: Condens. Matter **12**, 231 (2000).
25. M. F. Kasim *et al.*, Phys. Plasmas **26**, 112706 (2019).
26. J. A. Frenje *et al.*, Phys. Rev. Lett. **107**, 122502 (2011).
27. D. T. Casey *et al.*, Phys. Rev. Lett. **109**, 025003 (2012).
28. C. J. Forrest *et al.*, Nucl. Instrum. Methods Phys. Res. A **888**, 169 (2018).
29. J. M. Kootsey, Nucl. Phys. A **113**, 65 (1968).
30. R. A. Simpson *et al.*, Phys. Plasmas **28**, 013108 (2021).
31. F. Wagner *et al.*, Phys. Rev. Lett. **116**, 205002 (2016).
32. S.-H. Guan and Z.-P. Liu, Phys. Chem. Chem. Phys. **18**, 4527 (2016).
33. K. Kadau *et al.*, Phys. Rev. Lett. **98**, 135701 (2007).
34. B. Dupé *et al.*, Phys. Rev. B **87**, 024103 (2013).
35. D. Zahn and S. Leoni, Phys. Rev. Lett. **92**, 250201 (2004).

36. F. Coppari *et al.*, *Nat. Geosci.* **14**, 121 (2021).
37. J. A. Cobble *et al.*, *Rev. Sci. Instrum.* **82**, 113504 (2011).
38. C. Stoeckl *et al.*, *Nucl. Instrum. Methods Phys. Res. B* **453**, 41 (2019).
39. E. L. Clark *et al.*, *Phys. Rev. Lett.* **85**, 1654 (2000).
40. P. Huang *et al.*, *Proc. Nat. Acad. Sci.* **117**, 5638 (2020).
41. W. L. Vos *et al.*, *Phys. Rev. Lett.* **71**, 3150 (1993).
42. B. L. Sherman *et al.*, *Phys. Rev. B* **86**, 224113 (2012).
43. L. Antonelli *et al.*, *Europhys. Lett.* **125**, 35002 (2019).
44. L. Antonelli *et al.*, “X-Ray Phase-Contrast Imaging of Strong Shocks on OMEGA EP,” to be submitted to *Review Scientific Instruments*.

FY21 LaserNetUS Program

M. S. Wei

Laboratory for Laser Energetics, University of Rochester

UR/LLE is part of the LaserNetUS Collaborative Network established in 2018 and funded by the Department of Energy (DOE) Fusion Energy Sciences (FES) within the Office of Science. Its mission is to advance and promote intense laser science and applications by providing scientists and students with broad access to unique facilities and enabling technologies, advancing the frontiers of laser-science research, and fostering collaboration among researchers and networks from around the world. During FY21, LaserNetUS consisted of ten institutions including Colorado State University, Lawrence Berkeley National Laboratory, Lawrence Livermore National Laboratory (LLNL), SLAC, The Ohio State University, the University of Michigan, University of Nebraska-Lincoln, Institut National de la Recherche Scientifique, the University of Rochester, and the University of Texas at Austin. Through a coordinated annual call for proposals and an independent proposal review panel (PRP) process, the LaserNetUS network makes available a variety of ultrafast, high-peak-power and high-energy, petawatt-class lasers including LLE's four-beam, high-energy and high-intensity OMEGA EP laser to users who do not have regular access to ultrahigh-intensity lasers.

UR/LLE provides an average of four shot days each year on OMEGA EP to LaserNetUS users. Since 2019, 13 projects have been awarded a total of 15 shot days on OMEGA EP, including seven projects from the first two solicitations for shots in Cycle-1 (2019–2020) and Cycle-2 (2020–2021) and six projects from the third solicitation completed during FY21 for experiments in Cycle-3 (2021–2022). During FY21, a total of 29 target shots were successfully conducted over four shot days for three LaserNetUS projects led by scientists from LLNL, University of California, San Diego (UCSD), and General Atomics (see Table I below). These experiments involved four graduate students and five postdoctoral researchers. FY21 LaserNetUS user experiments are summarized below.

Table I: One LaserNetUS Cycle-2 project and six LaserNetUS Cycle-3 projects were awarded beam time on OMEGA EP for experiments in FY21–FY22. Three projects (shaded cells) were successfully conducted over four shot days during FY21 and the remaining four Cycle-3 experiments with five approved shot days are scheduled for FY22.

Principal Investigator	Institution	Title	LaserNetUS beam-time cycle
Y.-J. Kim*	LLNL	Extreme Chemistry of Synthetic Uranus	2
K. Matsuo*	UCSD	Laser Ablation and Shock Generation as a Function of Laser Pulse Length at an Intensity of 10^{15} W/cm ²	3
M. J.-E. Manuel	General Atomics	Laboratory Study of Quasi-Parallel Magnetized Collisionless Shocks	3
M. Edwards*	LLNL	Reaching an Electron–Positron Plasma with OMEGA EP	3
G. Righi**	UCSD	Understanding Temperature Dependence of Iron Strength at High Pressure with Ramped Compression on OMEGA EP	3

Table I: One LaserNetUS Cycle-2 project and six LaserNetUS Cycle-3 projects were awarded beam time on OMEGA EP for experiments in FY21–FY22. Three projects (shaded cells) were successfully conducted over four shot days during FY21 and the remaining four Cycle-3 experiments with five approved shot days are scheduled for FY22 (continued).

Principal Investigator	Institution	Title	LaserNetUS beam-time cycle
D. Riley	Queen’s University, Belfast, Ireland	Recreating Accretion-Powered X-Ray Astrophysical Sources in the Laboratory	3
S. Zhang*	Princeton University	Study of Particle Acceleration in Magnetic Reconnection Using Laser-Powered Coils	3

*Postdoctoral researcher

**Graduate student

Extreme Chemistry in H:C:N:O Mixtures at the Interior Conditions of Icy Planets

Principal Investigator: Y.-J. Kim (LLNL)

Co-investigators: M. Bethkenhagen (École Normale Supérieure de Lyon, Université Lyon); and F. Coppari, S. Hamel, and M. Millot (LLNL)

Synthetic Uranus is a H:C:N:O mixture having a composition similar to the interior of icy planets such as Uranus and Neptune. The IcyPlanetsDAC-EP-21 Campaign on OMEGA EP under the support of the LaserNetUS Program aims at measuring the microstructure of the H:C:N:O ices with *in-situ* nanosecond x-ray diffraction¹ during dynamic compressions. This work expands on our recent discovery of superionic water ice^{1–3} and provides new insights into the chemistry (e.g., new bonding, mixing/demixing, polymerization, and precipitation) at the interior pressure–temperature conditions of the icy planets.

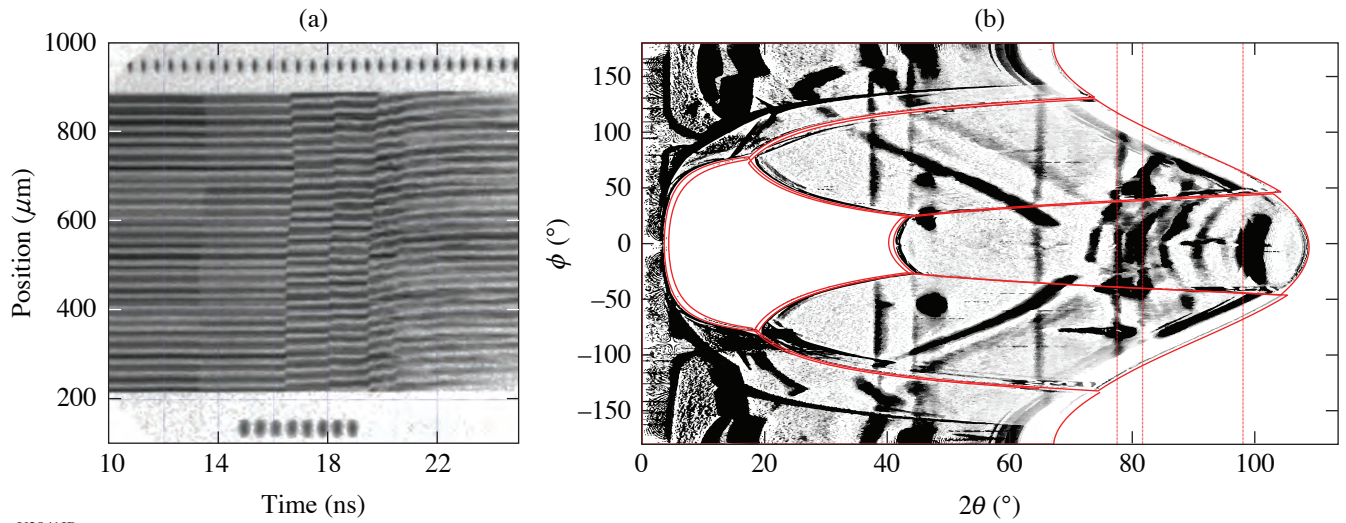
We prepared a liquid H:C:N:O mixture with water, ammonia, and isopropanol and documented its optical property at the ambient condition.⁴ For laser-driven dynamic compressions, this mixture was loaded into thin sample chambers fabricated with a chemical-resistive polymer and sealed by ablator and window materials. With excellent laser performance and support, we collected 13 system shots in the two-day allocations. Two OMEGA EP beams were stacked to produce a 20-ns drive, and another two beams were focused on a Cu backlighter for generating a 1-ns x-ray emission. At a steady shock state during a shock-wave reverberation, the x-ray diffraction (XRD) pattern of the mixture was recorded using the powder x-ray diffraction image-plate diagnostic. Doppler velocimetry [velocity interferometer for any reflector (VISAR)] was used to track the free surface velocity of the window, which was compared with hydrodynamic simulations for determining pressure–density–temperature conditions of the samples (see Fig. 1).

The ongoing data analysis on the diffraction patterns, surface velocities, and simulations will be used to improve our understanding of the interior structure of the icy planets.

Successful Platform Development Day for MagCShockPar

Principal Investigators: M. J.-E. Manuel (General Atomics); S. Bolaños, A. Bogale, and F. N. Beg (UCSD); and D. Michta and P. Tzeferacos (University of Rochester)

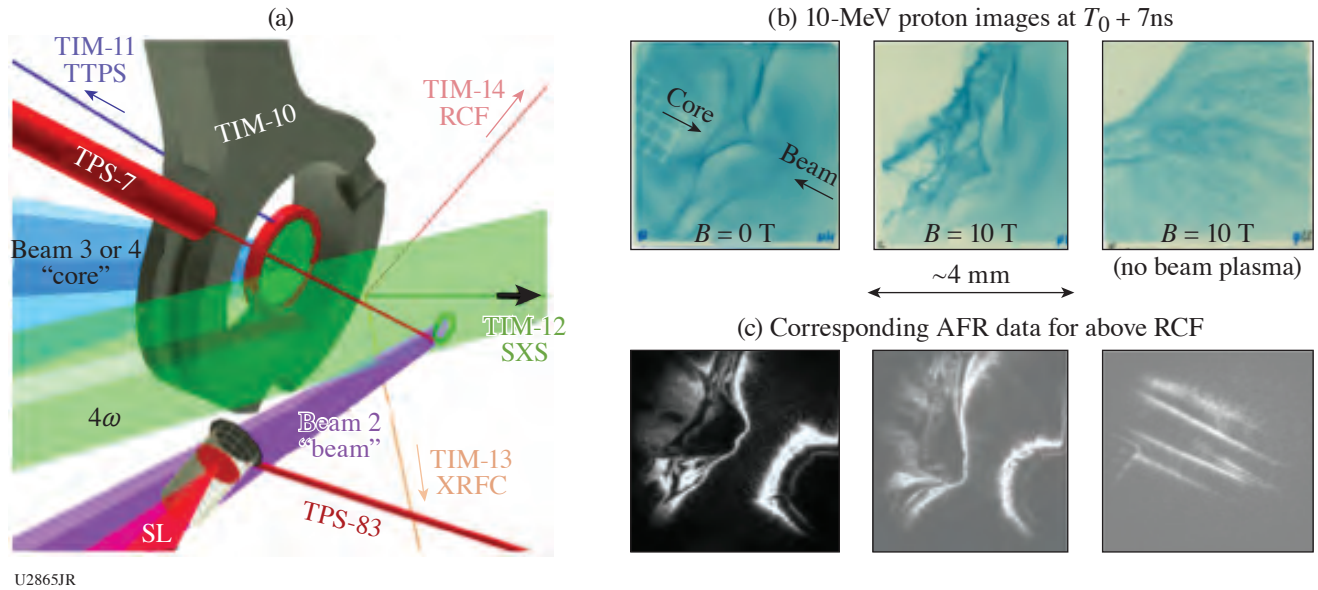
The formation of unmagnetized collisionless shocks has been extensively studied computationally and through laboratory experiments over the last decade^{5,6} to study the microphysics of formation and particle acceleration within these structures. However, many collisionless shocks observed in the universe exist within a background magnetic field, which can affect shock formation and particle acceleration. This LaserNetUS Campaign is the first experiment aimed at extending the previous platform into the magnetized regime in a quasi-parallel configuration on the OMEGA EP laser. In contrast to previous unmagnetized experiments, this campaign implemented a thin laser-driven titanium foil within a magneto-inertial fusion electrical system (MIFEDS) coil to create a cold, dense, magnetized “core” plasma. Then, a fast “beam” plasma using laser-ablated titanium impinges on the core in an asymmetric, collisionless interaction where the B field is parallel to the primary flow direction [see Fig. 2(a)]. The interaction was successfully diagnosed using short-pulse proton imaging on radiochromic film (RCF) and angular filter refractometry (AFR).



U2841JR

Figure 1
Example of VISAR and XRD data obtained from 50- μm -thick synthetic Uranus mixture at ~ 280 GPa and ~ 2300 K on OMEGA EP.

Initial results clearly show the formation of field structures due to the presence of both plasmas and the necessity of the parallel background magnetic field to produce the high-frequency filaments observed in the middle image shown in Fig. 2(b). Analysis of both RCF and AFR data is ongoing, and post-shot simulations are presently being done. A follow-up experiment will be proposed to study the temporal evolution of the observed high-frequency filaments and further characterize the plasma conditions in the interaction to compare with simulations and theory.



U2865JR

Figure 2
(a) VisRad schematic of the experiment showing beam and diagnostic configurations; (b) 10-MeV proton images from “proof-of-existence” experiments. The $B = 0$ -T image shows that large-scale field structures have formed at the center of the field of view 7 ns after the initial asymmetric interaction (T_0). With the B field on, similar bulk features are apparent (shifted down and to the left due to the field), but now high-frequency filaments are clearly visible on the core side of the asymmetric interaction. When only the core plasma is present in the B field, both bulk and high-frequency field structures are gone. (c) The AFR data correspond to the same shots as in (b) with the same spatial scale. TIM: ten-inch manipulator; TPS: Target Positioning System; SXS: streaked x-ray spectrometer; SL: sidlighter.

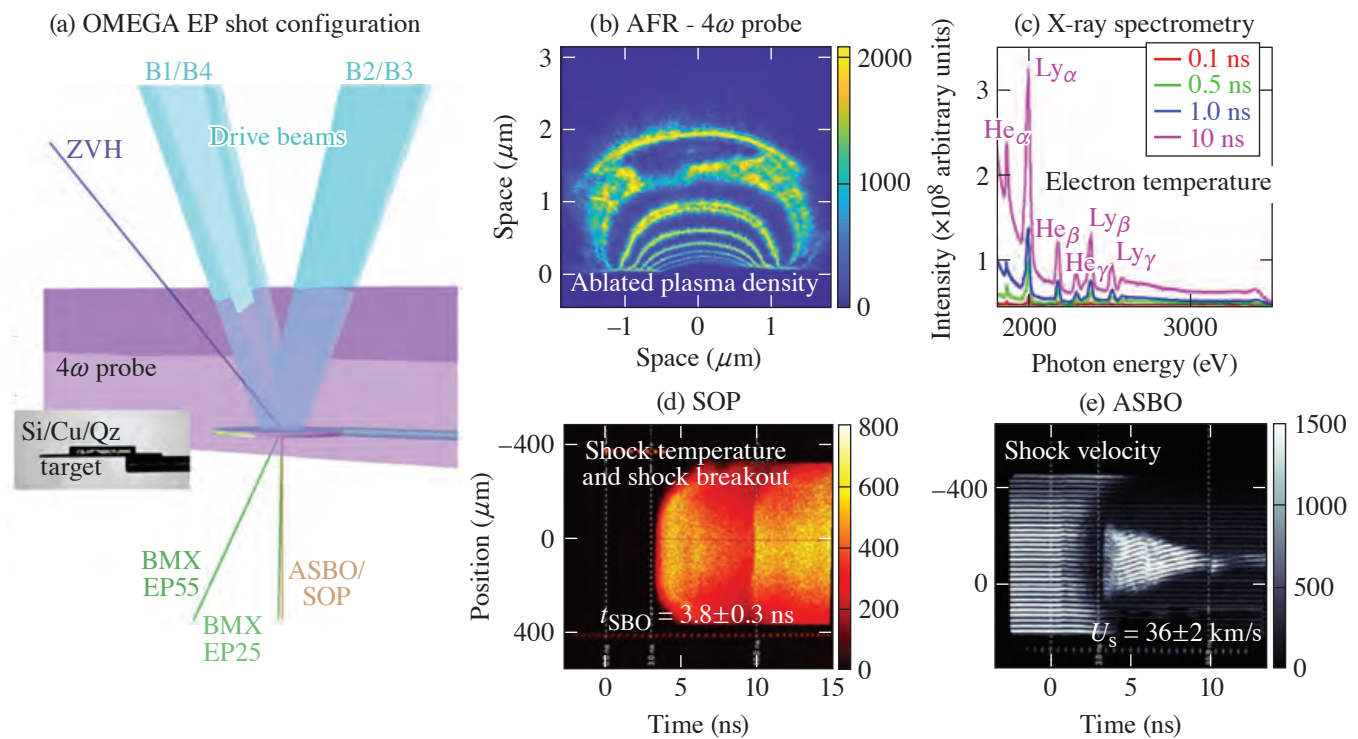
This material is based upon work supported by the Department of Energy (DOE), National Nuclear Security Administration under Award Number DE-NA0003842 and by the DOE Office of Science, Fusion Energy Sciences under Contract No. DE-SC0021061: the LaserNetUS initiative at the Omega Laser Facility.

Plasma Ablation and Shock Generation Using the Omega Laser Facility

Principal Investigators: K. Matsuo, E. Hahn, T. Cordova, M. Bailly-Grandvaux, R. E. Turner, J. E. Garay, and F. N. Beg (UCSD); and T. Joshi and R. B. Spielman (LLE)

X-ray-induced thermomechanical shock (TMS) is a major risk for electronics operating outside the Earth's atmosphere. Therefore, direct measurements using x rays to drive TMS are of significant interest; however, experimental platforms with high-enough x-ray flux are presently limited. Alternatively, careful implementation of high laser flux and fluence can be substituted to drive target ablation and the production of TMS at the relevant multi-Mbar levels. The major factors influencing the efficient coupling of the laser energy to the target are presently being investigated to reveal key aspects of the underlying physics of plasma blowoff as a function of the laser pulse length. We carried out extensive radiation-hydrodynamic modeling to facilitate an experimental design utilizing the OMEGA EP laser.

A schematic of the experiment and representative data from the critical diagnostics are shown in Fig. 3. Importantly, each experimental configuration maintained a constant laser intensity of $6 \times 10^{14} \text{ W/cm}^2$. From analytical scaling, the ablation



U2866JR

Figure 3

(a) Defense Threat Reduction Agency (DTRA) OMEGA EP experimental configuration. There was a systematic investigation of ablation physics and thermo-mechanical shock propagation at an intensity of $\sim 10^{15} \text{ W/cm}^2$ as a function of the laser pulse length. The targets consisted of three layers: (Si/Cu/Qz). (b) An angular filter refractometry (AFR) diagnostic used the 4ω probe to measure the density of the ablated plasma. (c) Time-integrated x-ray spectrometry can provide an inferred electron temperature using the K-shell line ratio of $\text{Ly}\gamma$ to $\text{He}\gamma$. (d) Streaked optical pyrometry (SOP) can measure shock-breakout times and the internal temperature of the quartz. (e) The active shock break-out (ASBO) diagnostic measures the timing and, therefore, the velocity of the decaying shock wave. ZVH: zinc Von Hamas; BMX: bremsstrahlung MeV x-ray spectrometer.

pressure is proportional to the instantaneous intensity to the power $\sim 2/3$ and independent of the pulse length.⁷ However, radiation-hydrodynamic modeling suggests a complex interplay between the pulse length and the ablation pressure as it translates to a TMS wave traveling through the multilayer target, further motivating a study of laser pulse length (100 ps, 500 ps, 1 ns, 10 ns) on the physics of plasma blowoff and strong shock generation. We performed ten shots in total, including two shots at 10-ns pulse duration, four shots at 1-ns pulse duration, two shots at 0.5-ns pulse duration, and two shots at 0.1-ns pulse duration. As shown in Fig. 3, the targets, fabricated at UCSD, consisted of three layers: single crystalline nominally undoped silicon, polycrystalline copper, and crystalline SiO₂ quartz (Si/Cu/Qz).

In these experiments, the measured ablation-front temperature is ~ 500 eV [Fig. 3(b), analyzing relative line intensities], independent of the pulse duration. Yet, the investigation of ablation temperature from the sole effect of pulse duration requires an experiment at constant laser fluence (planned next year) to complement the present study at constant intensity. Ablation density is indirectly inferred from the AFR diagnostic through a comparison with synthetic AFR images post-processed from the radiation-hydrodynamic simulations. The resulting TMS propagation into the dense target is measured in the quartz witness layer using ASBO (shock velocity) and SOP (shock temperature) diagnostics. For the longest pulse length (10 ns), the measured shock velocity is ~ 35 km/s (~ 22 Mbar), in agreement with the analytical scaling laws after considering the shock impedance matching of the Si/Cu/SiO₂ layers. Interestingly, the measured shock velocity for the shortest pulse (0.1 ns) is ~ 3 km/s (< 1 Mbar), marking a significant decrease in the shock pressure for subnanosecond pulses. This trend is also observed in the 0.5-ns and 1-ns pulse lengths, signaling that the supported shock pressure is proportional to the pulse duration and that shock-decay effects (rarefaction, dispersion, reflection/transmission) are not insignificant. Evidence of such multiwave features can be distinctly identified in the 10-ns pulse data [Figs. 3(d) and 3(e)], marking recognizable shock and release waves as they traverse the sample and enabling a direct measurement of the contribution thereof. These results clearly demonstrate that the laser pulse length plays a pivotal role in plasma ablation and strong-shock generation. Next, new scaling laws will be established using the experimental data for the ablation pressure's dependence on pulse length. The physics of laser coupling is different between the shortest pulse duration (0.1 ns) and the longest pulse duration (10 ns), which is likely the cause of discrepancy between the *FLASH* simulations and the experimental data observed in these cases. We will include a modified laser absorption model in *FLASH* that has been designed for short pulses and that we believe will better reproduce the experimental results for 0.1-ns pulse duration. A similar investigation is being sought for the 10-ns pulse, where the laser interaction with the longer ablated plasma in front of the ablator may also sensibly affect the laser coupling computed by *FLASH*. This endeavor will certainly benefit the community, maturing the models used in radiation-hydrodynamic simulations for subnanosecond or multianosecond laser interactions with a solid target.

This work is supported by DTRA under award number HDTRA1-20-2-0001.

1. M. Millot *et al.*, *Nature* **569**, 251 (2019).
2. M. Millot *et al.*, *Nat. Phys.* **14**, 297 (2018).
3. B. Cheng *et al.*, *Nat. Phys.* **17**, 1228 (2021).
4. Y.-J. Kim *et al.*, *Sci. Rep.* **11**, 5610 (2021).
5. H.-S. Park *et al.*, *High Energy Density Phys.* **8**, 38 (2012).
6. F. Fiuza *et al.*, *Nat. Phys.* **16**, 916 (2020).
7. D. Batani *et al.*, *Phys. Rev. E* **68**, 067403 (2003).

FY21 Lawrence Livermore National Laboratory Experimental Programs at the Omega Laser Facility

P. L. Poole,¹ R. F. Heeter,¹ F. Albert,¹ N. Candeias-Lemos,¹ S. Clarke,¹ A. L. Coleman,¹ F. Coppari,¹ T. Döppner,¹ M. Hohenberger,¹ A. Lazicki,¹ S. Jiang,¹ S. F. Khan,¹ Y.-J. Kim,¹ A. Krygier,¹ M. J. MacDonald,¹ E. V. Marley,¹ D. Martinez,¹ M. Millot,¹ B. B. Pollock,¹ D. Rusby,¹ A. M. Saunders,¹ R. Smith,¹ C. Stan,¹ G. F. Swadling,¹ E. Tubman,¹ S. Zhao,² and A. B. Zylstra¹

¹Lawrence Livermore National Laboratory

²Lawrence Berkeley National Laboratory

In fiscal year 2021 (FY21), Lawrence Livermore National Laboratory's (LLNL's) High-Energy-Density Physics (HED) and Indirect-Drive Inertial Confinement Fusion (ICF-ID) Programs conducted numerous campaigns on the OMEGA and OMEGA EP Laser Systems. This was the 23rd year of national laboratory collaborative experiments at Omega since the Nova Laser at LLNL shut down in 1999 (Ref. 1), building upon prior collaborations. In FY21 overall, these LLNL programs led 459 target shots, with 234 shots using only OMEGA and 214 shots using only OMEGA EP. Approximately 30% of the total number of shots (57 OMEGA shots and 43 OMEGA EP shots) supported the ICF-ID Campaign, with the remaining shots dedicated to experiments for HED physics grouped as hydrodynamics and plasma properties campaigns (35 OMEGA-only shots and 21 OMEGA EP-only shots), materials (68 OMEGA and 78 OMEGA EP), and outputs and survivability (23 OMEGA). Highlights of the various HED and ICF-ID campaigns are summarized in the following reports.

In addition to these experiments, LLNL principal investigators (PI's) led a variety of Laboratory Basic Science Campaigns using OMEGA and OMEGA EP, including 39 target shots using OMEGA and 52 shots using OMEGA EP.

Overall, LLNL PI's led a total of 459 shots at LLE in FY21. In addition, LLNL PI's supported 123 basic science shots in collaboration with the academic community, including 18 National Laser Users' Facility shots or Academic/Industrial Basic Science shots, and 14 LaserNetUS shots led by university collaborators.

This work was performed under the auspices of the U.S. Department of Energy by Lawrence Livermore National Laboratory under Contract Number DE-AC52-07NA27344.

Thermonuclear Burn and High-Yield Campaigns

Investigating the Behavior of Diamond Under Shock Compression to Its Melting Line with Pyrometry

Principal Investigator: M. Millot

Co-investigators: Y.-J. Kim, R. Briggs, and P. M. Celliers

High-density carbon (HDC)—diamond—ablaters are used in many ICF designs at the National Ignition Facility (NIF). Understanding the microphysics behavior of this material along the multishock compression path typical for ICF implosions is fundamental. Here we focus on elucidating the behavior of diamond under shock compression to its melting transition, near 10 Mbar. The specific goal for this study is to provide more-accurate data than the previous study by Eggert *et al.*² more than a decade ago and inform the possibility of lowering the adiabat in HDC implosions on the NIF by tightly benchmarking equation-of-state (EOS) models near the first shock state.

To document the melting temperature of diamond near 10 Mbar, we launched strong unsupported shocks in a planar package containing a diamond plate [Fig. 1(a)]. Using line-imaging Doppler velocimetry [VISAR (velocity interferometer for any reflector)] and streaked optical pyrometry (SOP), we were able to record high-quality data in the 6- to 20-Mbar range. Analysis is ongoing for the 13 data sets we collected. In addition, using quartz as an impedance-matching standard allowed us to collect high-precision shock pressure–density data along the Hugoniot to complement our previous work reported in Ref. 3.

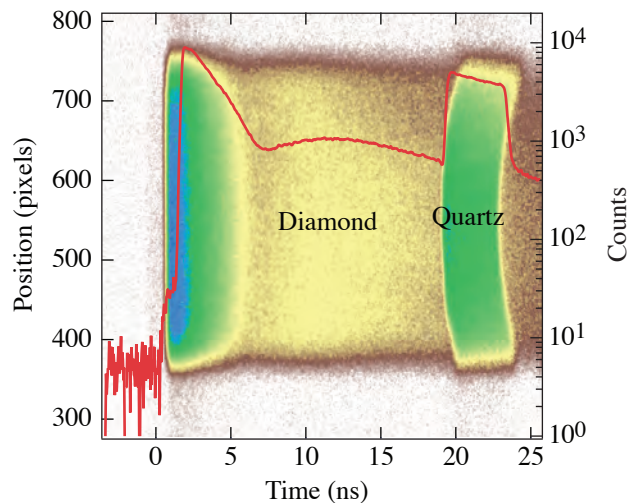


Figure 1

Example of a high-quality SOP image exhibiting sharp temporal and spatial resolution and a corresponding temporal lineout revealing a structured pyrometry signal indicative of a complex behavior under shock compression near 10 Mbar.

U2807JR

X-Ray Diffraction of Diamond Under Shock Compression and Shock-and-Release Near the Melting Line

Principal Investigator: M. Millot

Co-investigators: F. Coppari, D. Braun, A. Lazicki, Y.-J. Kim, P. M. Celliers, and J. H. Eggert

Using HDC—diamond—ablaters in ICF implosions on the NIF has enabled important advances thanks to its efficiency as an ablator and the possibility to use shorter laser pulses.^{4,5} However, the unique thermodynamic properties of carbon do present multiple challenges toward reaching higher fusion yield on the NIF. Among these challenges is whether rapid resolidification could occur after the first shock is transmitted to the hydrogen fuel and a release wave propagates backward toward the ablation front. Such a phenomenon would likely be a large source of implosion-quality degradation since the second shock would be launched into a slurry of nano-/microcrystalline diamond with a metallic fluid carbon.

Here we focus on elucidating the behavior of diamond under shock compression to completion of the melting line, near 12 Mbar, as well as under shock and subsequent decompression by an impedance-mismatch–generated release wave. The specific goal of this study is to characterize the atomic structure with *in-situ* nanosecond x-ray diffraction.

We launched strong steady shocks in a planar package containing a diamond plate mounted on the powder x-ray diffraction image-plate (PXRDI) diagnostic box and collected high-quality x-ray diffraction data (Fig. 2) at unprecedented conditions in the 6- to 12-Mbar range. Ongoing analysis will allow us to reveal the atomic structure of carbon at those conditions and document the transition from the compressed solid to the metallic warm dense fluid.

Investigating Gold-Wall/Gas-Fill Interactions in an Open Geometry

Principal Investigator: G. F. Swadling

Co-investigators: E. Marley and W. A. Farmer

The AuGasJet-20 Campaign aimed to develop a new experimental platform to study the interaction of ablated gold plasma with a He gas fill. The overall purpose of this work is to benchmark simulations and therefore drive progress toward a predictive hohlraum performance model. The experiments use an open geometry, which provides excellent diagnostic access to the gold

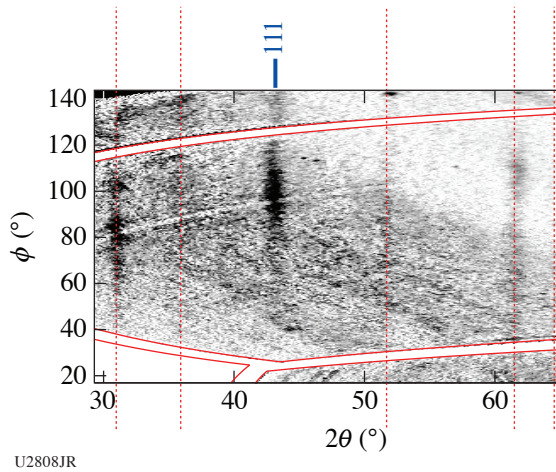


Figure 2
 Example of a high-quality x-ray diffraction image exhibiting a strong line for shock-compressed diamond (indicated by the solid blue line) together with reference lines (dotted red vertical lines).

plasma, allowing detailed measurements of the plasma parameters of the gold and helium as they interact using the OMEGA 4ω Thomson-Scattering System (TSS). To achieve these goals, the experiments use a supersonic gas nozzle to inject a 0.3-mg/cm^3 plume of gas over the surface of a gold foil (see Fig. 3). The surface of the foil is then heated with the OMEGA 3ω heater beams, and the cloud of plasma that results is probed with Thomson scattering $300\ \mu\text{m}$ from the foil surface. By using a gas jet, we aimed to remove the need for a “gas bag;” previous experiments using gas bags have shown that the shocks launched by the explosion bag wall significantly perturbs the experimental measurements. Using a gas jet also allows us to achieve ICF-relevant gas densities without resorting to a surrogate gas species or a cryogenic target design.

Two campaign days were scheduled in FY20 but the second day was delayed into FY21 when LLE shut down due to COVID. Thomson-scattering (TS) data collected in AuGasJet-20B was generally of a low quality. No signal was seen on a number of shots. We believe that the Thomson-scattering probe laser is struggling to penetrate the gold plasma plume produced in this experiment. This may be due to a more aggressive density gradient at the edge of this plume, compared to that produced in our previous experiments that have focused on probing plasmas ablated from spheres.

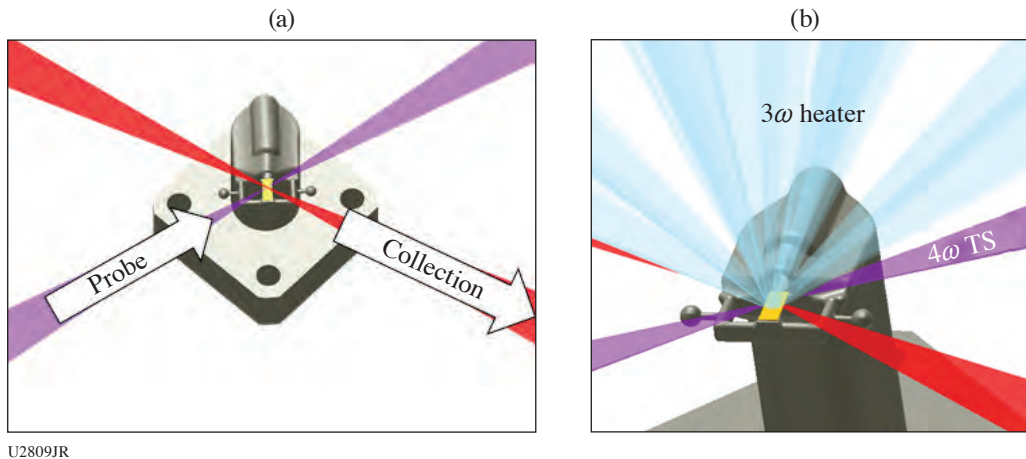


Figure 3
 Experimental setup. A gas jet is used to produce a “gas fill” over the surface of a gold foil.

Assessing Heat Transport in the Transition Between Local and Nonlocal Regimes

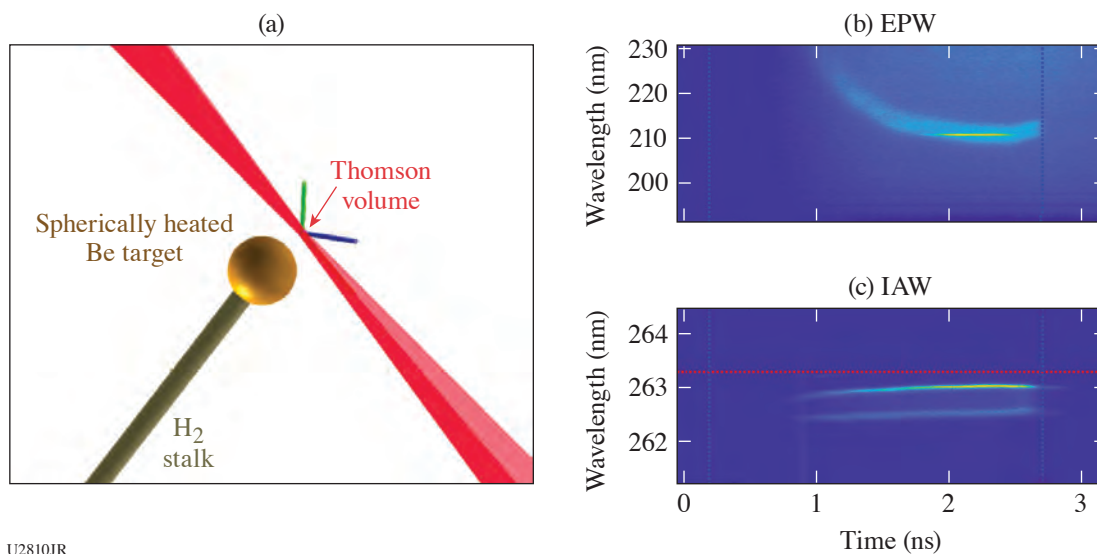
Principal investigator: G. F. Swadling

Co-investigators: E. Marley and W. A. Farmer

In the BeSphere-21A Campaign, we performed experiments heating beryllium-coated spheres in a direct-drive geometry. The experiments were diagnosed using the OMEGA TSS, scatter calorimeters, and the Dante x-ray spectrometer. The aim of these experiments was to make quantitative measurements of the parameters of the blow-off plasma produced from these spherical targets. A total of 14 target shots were completed.

A previous campaign of experiments investigating beryllium spheres used comparatively low intensities of 1 to 2.5×10^{14} W/cm²; at these intensities, coupling of the laser to the target was shown to be better than 90% (Ref. 6). On this most-recent shot day, heating intensity was increased from 5×10^{14} W/cm² to 1×10^{15} W/cm², comparable to the intensities at which we typically shoot ICF hohlraums.

The Thomson-scattering diagnostic measured the time-resolved spectrum of light scattered by fluctuations in n_e with wave vectors \vec{k} tangential to the surface of the sphere. The size of the scattering volume, defined by the overlap of the probe beam and collection cone, was $\sim 50 \mu\text{m}^3$. Measurements were made at locations 200, 300 and 400 μm from the sphere surface. The diagnostic recorded scattering from both high-frequency electron plasma wave fluctuations (EPW, T_e, n_e) and low-frequency ion-acoustic wave fluctuations (IAW, $T_e, T_i, v_{\text{flow}}$). Examples of the data recorded are shown in Fig. 4. Fitting these measured spectra results in quantitative measurements of the plasma parameters, which may be compared with the results of numerical modeling.



U2810JR

Figure 4

(a) Experimental setup and (b) example experimental data from BeSphere-21A.

Measurement of High-Z M-Shell Emission Using a Buried-Layer Platform

Principal Investigator: E. V. Marley

Co-investigators: R. F. Heeter, M. B. Schneider, G. E. Kemp, M. E. Foord, D. A. Liedahl, and J. Emig

This campaign was designed to measure the emitted M-shell spectra from well-characterized and uniform dysprosium and uranium plasmas to benchmark atomic kinetic models above and below the closed Ni-like subshell. The buried-layer target

geometry used for this experiment is capable of generating plasmas with an electron temperature of ~ 2 keV at electron densities of 1021 electrons per cubic centimeter. Similar plasmas are also found inside hohlraums during ICF experiments on the NIF, providing a stable platform to create uniform plasmas for radiation transport and atomic kinetic studies at relevant conditions.

Planar buried-layer targets were illuminated equally on both sides [Fig. 5(a)] to heat the sample. Two sample types were used during the campaign. The first was a 1400-Å-thick Dy/Cr mixture (0.27/0.73 by atom), and the second was a 1400-Å-thick U/Cr mixture. Both were designed to burn through completely before the end of the laser pulse, providing uniform plasma conditions to measure the M-shell emission of the high-Z component. The samples were buried between two 8- μm -thick layers of CH that acted as an inertial tamp that slowed the expansion of the sample.

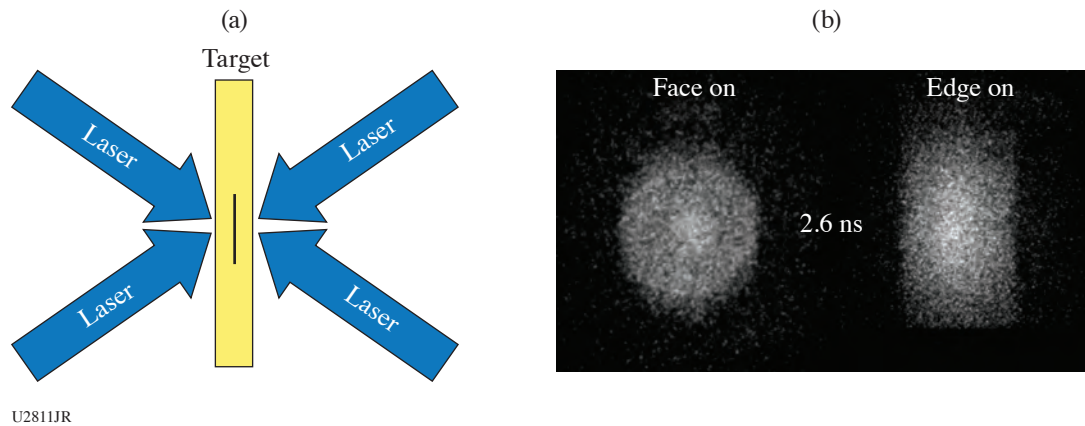


Figure 5
(a) Experimental configuration and (b) pinhole images of the emission area of shot 101947 at 2.6 ns.

Time-resolved 2-D images of the target's x-ray emission, viewed both face-on and side-on, were recorded using pinhole cameras coupled to framing cameras [see Fig. 5(b)]. The K-shell spectra from the Cr was used to determine the electron temperature of the plasma. The time-resolved spectra were recorded using crystal spectrometers coupled to framing cameras. Two crystal spectrometers were needed to record the 4 to 3 M-shell emission for both the Dy and the U, also time resolved. All of the framing cameras used, those for imaging as well as those for spectroscopy, were co-timed so the plasma conditions could be determined for the measured high-Z M-shell emission. A streak camera was also to be used to record a continuous record of the Dy M-shell emission, but it was not operational on the shot day.

The laser pulse shape used was a 3.0-ns square pulse with a 100-ps picket arriving 1 ns before the main pulse. A complete (five diagnostics, correctly timed and bias set) set of data was recorded for both target types, using both pulse shapes during the campaign at temperatures ~ 2 keV.

Plasma Growth on Nearby Targets During High-Intensity Laser–Plasma Interactions

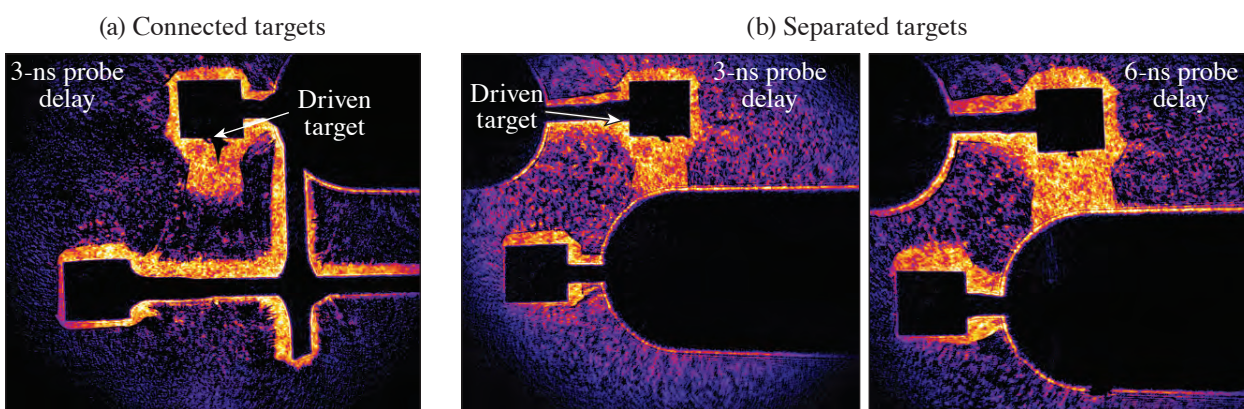
Principal Investigator: D. Rusby

Co-investigators: N. Lemos and A. J. Mackinnon

High-intensity laser–plasma interactions are capable of creating high-energy particles/radiation including MeV x rays that can be used to perform nondestructive radiography of high-areal-density objects. Many laser-generated x-ray radiography scenarios use multiple interactions separated in time to either accumulate more x-ray dose or create several temporal snapshots. In such scenarios, the importance of understanding the effects of multiple interactions on one another is of utmost importance. The earliest interaction will produce high-energy x rays and electrons that can pre-ionize nearby targets, producing a pre-plasma that can greatly affect any subsequent interactions. Additionally, this interaction generates a large return current that can ionize the target stalk.

The OMEGA EP laser with 900 J and a 10-ps pulse duration was focused onto a 1×1 -mm Ta cylinder used to generate x rays through bremsstrahlung. An additional identical target was placed ~ 1.5 mm away from the interaction. The additional target was held in place by either carbon stalks that are connected to the driven target or on its own separate target stalk. The 4ω probe was used to qualify the growth of the plasma on each of the targets. Two shots were taken using a separate target setup with the 4ω probe timed at 3 ns and 6 ns after the main interaction. One shot was performed on the connected targets with the probe timed at 3 ns. Composite images of the reference and on-shot data are shown in Fig. 6 to highlight the areas of plasma produced.

The plasma growth on the connected target is much greater than that of the separated targets. This is likely due to the return current that runs through the connected target stalks. The plasma that is generated on separated targets is directional. The side of the target that is facing the interaction of the driven target has much more plasma growth than the side that faces away. With the two scenarios investigated here, the preferable one for multiple laser interactions would be the separated targets. This investigation of plasma growth on targets has shown that with sequential high-intensity laser interactions, the choice of the target geometry will play a huge role. Simulations are being conducted to validate the results shown here, and further geometries, including shields, are being proposed and simulated.



U2812JR

Figure 6

Composite 4ω optical probe images of the reference and on-shot data showing the growth of the plasma on (a) connected targets and (b) separated targets.

Shock-Propagation Measurements in Gas-Tube Targets with MIFEDS-Based Magnetic Fields

Principal Investigator: B. B. Pollock (LLNL)

Co-investigators: H. Sio, E. Marley, and J. D. Moody (LLNL); and J. R. Davies, P. V. Heuer, J. L. Peebles, and D. H. Barnak (LLE)

The goal of the BLoopEOS Campaign is to measure changes in shock-propagation speed and plasma preheat in the presence of preimposed magnetic fields. For the FY21 experiments, the imposed B field is provided by dual magneto-inertial fusion electrical discharge system (MIFEDS) coils supplying 20- to 25-T B fields in a gas-filled tube target, similar to the shock-tube target used in previous ProtonShockEP Campaigns. One end of the tube is sealed with a $50\text{-}\mu\text{m}$ CH ablator, which is driven by three overlapping long-pulse beams from OMEGA EP, as shown in Fig. 7. This launches a shock into the gas-filled tube (mixtures of He and Ne) with the B field perpendicular to the shock-propagation direction. The shock-propagation speed is expected to increase with increasing applied B field. In addition, the B field in the shocked region is calculated to increase due to compression by the same amount because the compression of the plasma density provided by the field is frozen into the plasma just ahead of the shock. The system is probed perpendicular to both the shock propagation and the B field by target normal sheath acceleration (TNSA)-driven proton radiography. The MIFEDS is designed to allow the direction of the magnetic field to alternate between “up” and “down” in the side-on view, changing the net direction of proton deflection from the Lorentz force. This results in changing the proton deflection direction to being predominantly away from the shock front or toward it, respectively, which changes the structure of

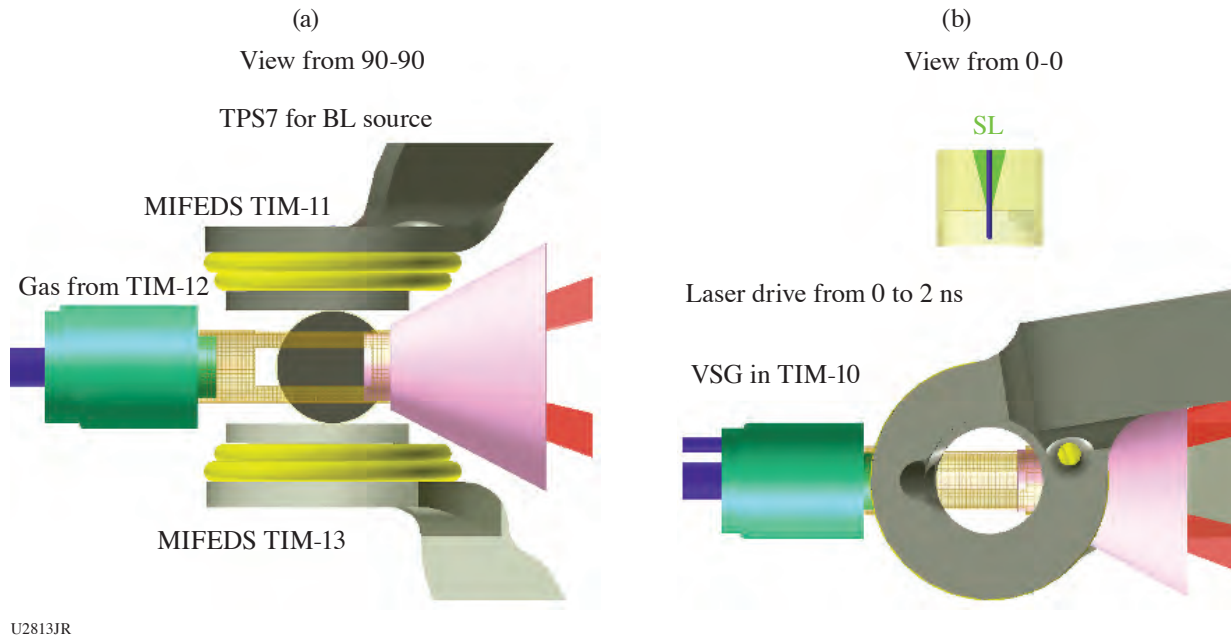


Figure 7

Experimental configuration showing the gas tube, the MIFEDS, the laser drive direction (here right to left), and the proton source. TIM: ten-inch manipulator; TPS: Target Positioning System.

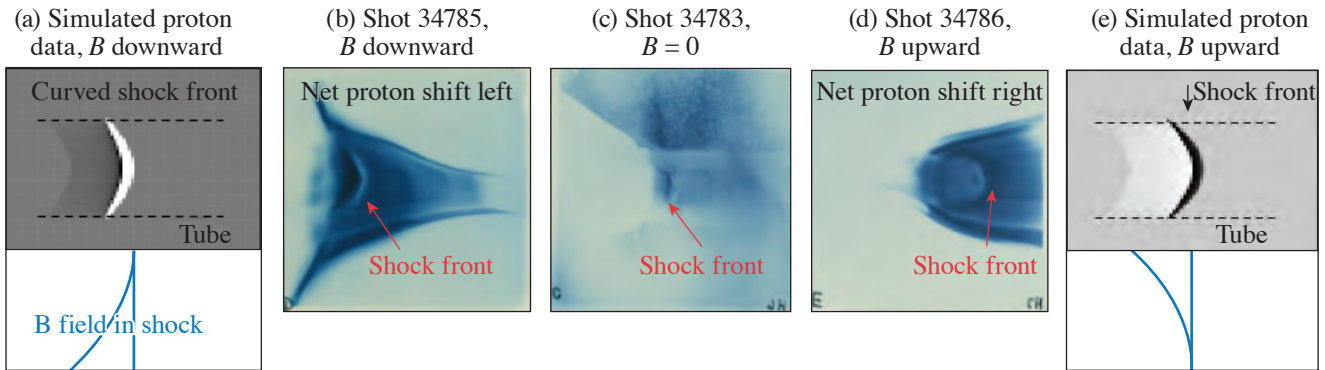


Figure 8

Proton radiography from two magnetized experiments with B fields applied in opposite directions and from one unmagnetized shot for reference. The magnetized shots are accompanied by calculated proton deflection images showing qualitative agreement to the data with respect to the brightness and curvature near the shock front. Here the laser is propagating from left to right.

the radiograph near the shock front. This can be seen in Fig. 8, where for shot 34785, the protons are shifted toward the ablator, resulting in a proton void at the shock front, while for shot 34786 the opposite is true. The proton data can be approximately reproduced in simulated proton images by assuming the shock amplifies the background field about a factor of 3 (from 20 T to 60 T). The shock is curved because of the small 400- μm laser spot size, and the B -field amplification is lower toward the shock edges. Spectroscopic measurements from the Ne emission along the length of the tube [recorded by the virtual synchronous generator (VSG) system] may show a shock-speed increase from 160 $\mu\text{m}/\text{ns}$ to 220 $\mu\text{m}/\text{ns}$ with the application of the B field as shown in Fig. 9. The speed increase is approximately the same for a B field “up” or “down,” which is the expected result. These results are encouraging, and further analysis of both measurements is in process.

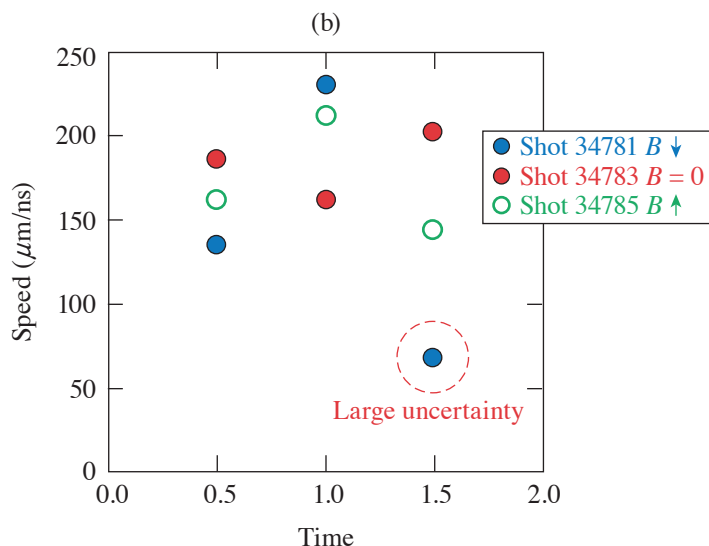
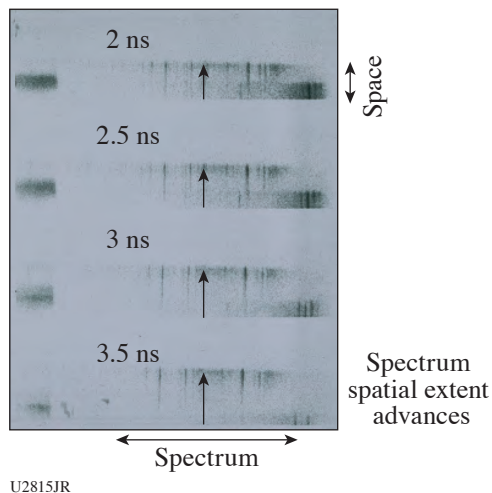
(a) Shot 34785, B downward, $M = 9$ 

Figure 9

X-ray framing camera measurements of the spectral emission from the Ne recorded by VSG and the extracted propagation velocities for three shots with $B = 0$, B upward, and B downward.

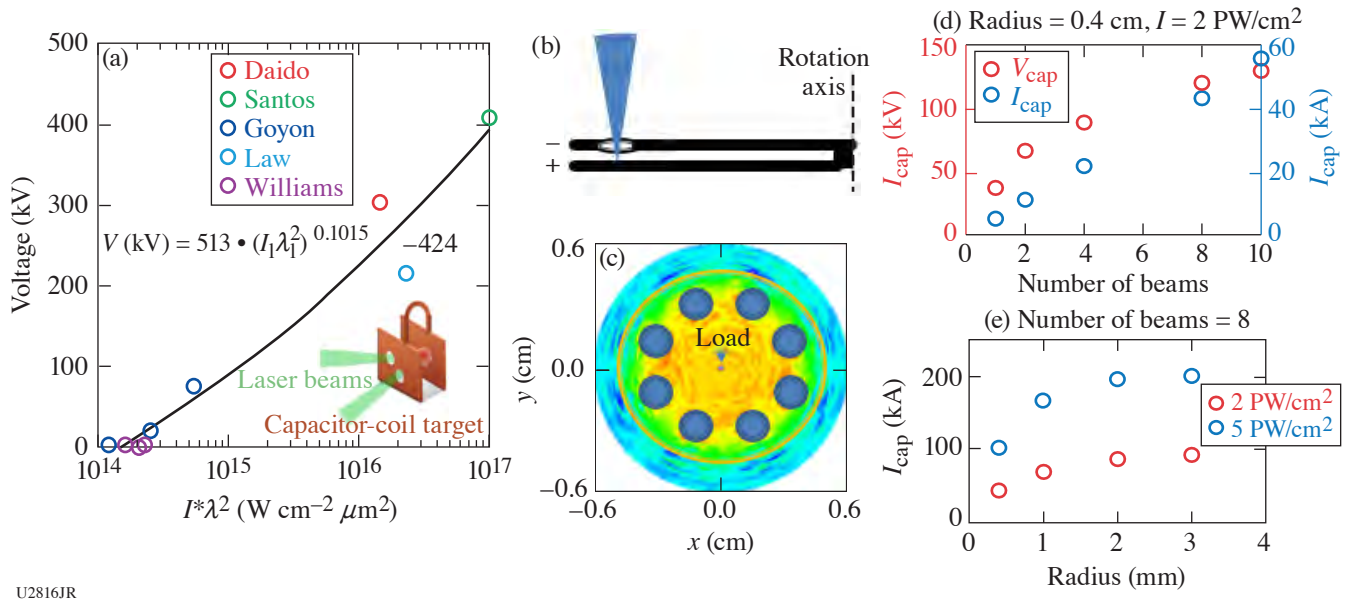
High Current Generation Based on Capacitor-Coil, Laser-Driven B-Field-Generation Techniques for a Magnetically Insulated Transmission Line

Principal Investigator: B. B. Pollock (LLNL)

Co-investigators: D. Welch (Voss Scientific), P. V. Heuer (LLE), and K. LeChien (LLNL)

The use of high-power laser drivers to produce large (~ 100 's T) magnetic fields in capacitor-coil-style targets has been studied and reported by several groups.^{7–11} The fields are the result of high current flows that are sourced by voltage differences between electrically connected parallel plates when one plate is irradiated by a high-power laser and hot electrons leaving the driven surface leave behind a positively charged region; an example is shown as an inset in Fig. 10(a). The MiniMITL Campaign takes advantage of this voltage-generation scheme, with a goal of maximizing the current density through a return post between the parallel plates of the system. Many prior works have generally used either a single laser driver or several beams focused close together to generate the initial voltage difference across the capacitor-coil target. The survey of Refs. 7–11 in Fig. 10(a) indicates that the voltage difference scales somewhat weakly with the intensity of the laser driver, reducing the efficacy of overlapping laser spots for increasing voltage (and current). Simulations using the geometry of Figs. 10(b) and 10(c) have recently demonstrated that for multiple laser spots uniformly distributed azimuthally at a fixed radius on the driven plate, it is possible to increase voltage and current nearly linearly with a number of drivers for appropriate spot-to-spot spacing. Figure 10(d) shows the effect of increasing the number of laser beams at 4-mm radius, with each beam intensity at 2 PW/cm². Up to about four beams, the voltage increases approximately linearly, then more slowly with additional beams. This is due to the separation between the spots becoming smaller with more beams at fixed radius and spot size. This behavior is also seen in Fig. 10(e), where the current for eight beams is shown to increase quickly up to ~ 2 -mm radius and then saturates.

The OMEGA EP Laser System is ideal for studying the current generation scaling from this scheme. MiniMITL21A uses up to all four of the OMEGA EP long-pulse beams to drive the rear plate of the target, with the beams pointed 90° apart from one another at a radius of 4.5 mm. The OMEGA EP pulse-shaping capability allows the laser intensity to be varied during the shot day, as well as the number of beams used in a single experiment. The primary diagnostic of the current through the return post is VISAR, viewing the exterior of the rear (driven) target plate, where the $J \times B$ forces of the current in the post and the induced azimuthal B field around it launch a shock in the plate. Ultimately four shots were successfully completed, but all in compromised targets due to damage from the shipping process. Despite that, some conclusions can still be drawn about the target design to



U2816JR

Figure 10

(a) Voltage as a function of laser intensity (and wavelength) for several published laser-driven B-field experiments. (b) Side-on profile of the MiniMITL target design, where the lower plane is laser driven to produce the initial voltage difference across the target. (c) Face-on profile of the target design, showing multiple laser spots uniformly azimuthally distributed around the driven plate at fixed radius from a return current post connecting it to the undriven side of the target [the rotation axis of part (b)]. (d) The driven voltage and current as functions of the number of drive beams at a fixed radius and beam intensity. (e) The driven current as a function of beam radius at two laser intensities.

make improvements for future shot days, both in terms of target survivability and diagnostic return. Additional shots have been requested for FY22 and will be again for FY23.

Modifications to Laser Scattering in Magnetized Plasmas

Principal Investigator: B. B. Pollock

Co-investigators: Y. Shi, E. Tubman, and J. Moody

Classical laser scattering in a plasma follows a dipole radiation pattern that is maximized perpendicular to the laser polarization and zero parallel to it. In the presence of strong magnetic fields (~ 100 's of T), however, the orbits of oscillating electrons can be sufficiently perturbed to result in appreciable scattering in the initial laser polarization direction. The MagLoopLPI Campaign seeks to study this modified scattering using a laser-driven magnetic-field source¹² to provide a strong background magnetic field in a foil blow-off plasma. To produce the magnetic field, a loop target similar to that described in Ref. 12 is driven by one long-pulse beam of the OMEGA EP Laser System as shown in Fig. 11(a). The target has been modified from Ref. 12 by removing material from the center of the B-field loop to be able to position a foil target within the highly magnetized region. Additionally, this target is being driven on an external surface to limit the x-ray and plasma expansion to the vicinity of the foil; an additional "awning" is also placed in the line of sight from the B-field drive laser spot to the foil to further prevent preheating and plasma filling of the loop region. A CH foil is then positioned such that it can be irradiated by a second long-pulse beam, and the expanding plasma plume will have the laser-driven B field pre-embedded as it moves along the B-field lines (quasi-parallel to the foil normal).

To probe the foil plasma, the short-pulse beams of OMEGA EP are focused 200- to 300- μm from the foil surface using the backlighter parabola (where in "co-prop" mode, both short-pulse beams are available). The probe pulse is ~ 100 ps and ~ 1 J so that the probe will be minimally perturbative to the plasma conditions of interest. New diode systems, designed for use in this configuration, will be positioned along the vectors shown in Fig. 11(b). There is one diode along the laser polarization direction

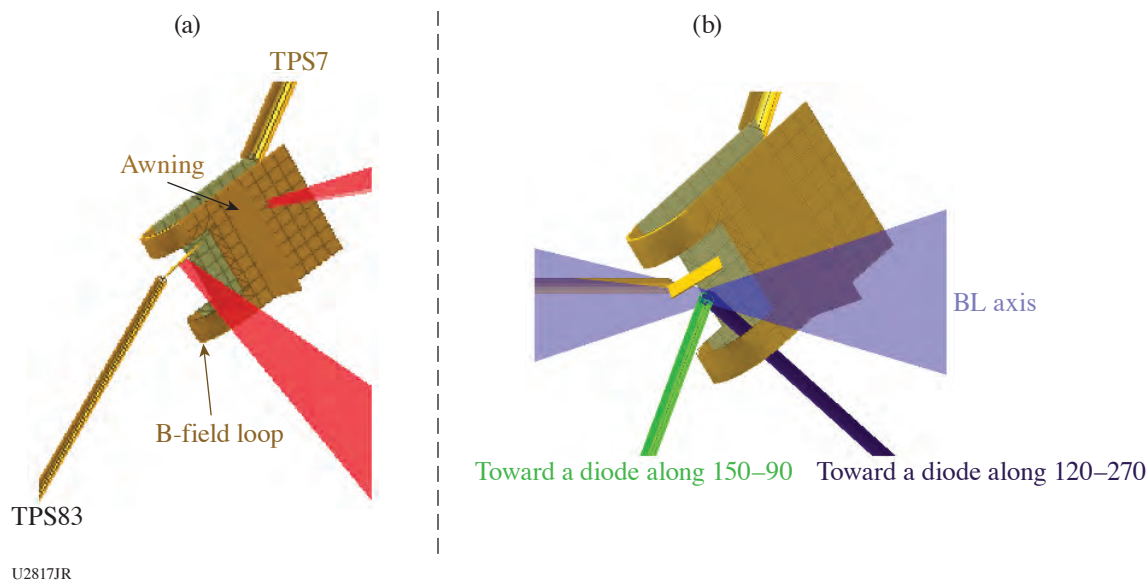


Figure 11
 (a) The B-field loop target is shown with the CH foil, along with their respective drive beams. (b) The drive beams have been suppressed to show the optical probing geometry for the short-pulse beams on the backlighter axis. The rods toward chamber coordinates of 150–90 and 120–270 indicate the directions to the new diode diagnostics.

and one perpendicular to make simultaneous scattering measurements in these directions; in the co-prop mode where both short-pulse beams are available, the polarization can effectively be rotated 90° between shots (since the two beams in this geometry are cross polarized). This configuration also allows switching to a B-field characterization setup with minimal beam modifications (the short-pulse beam is refocused and the power increased) to enable proton probing of the magnetic-field structures at the target. Due to qualification issues, the diodes were not fielded on MagLoopLPI21A, but the proton-probing setup was successfully used for six target shots. Figure 12 shows representative proton radiography from three separate conditions: (1) where only the foil was

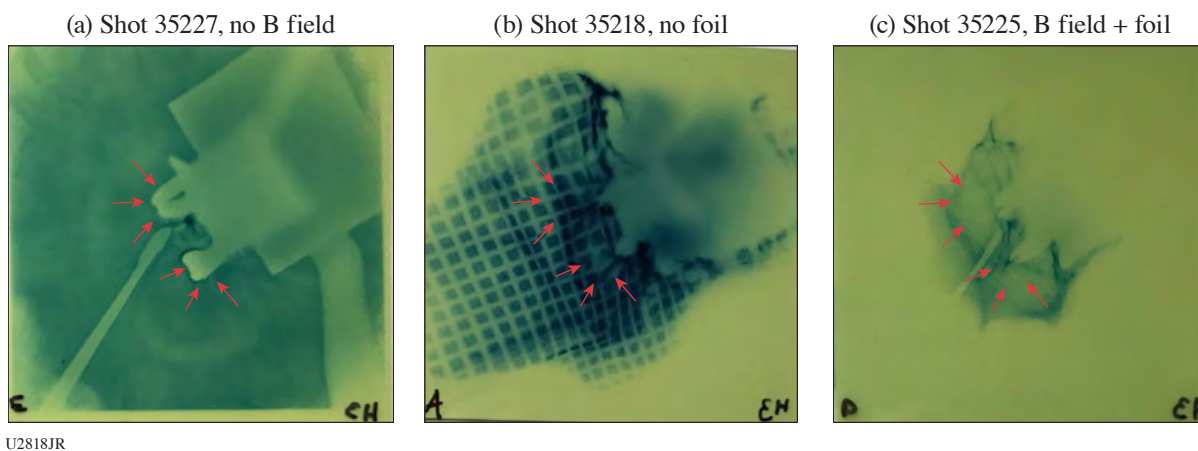


Figure 12
 Proton radiography data from three separate shots. (a) Shot 35227 had no B field, but did drive the foil between the loops. The red arrows indicate the shadows from the current loops in the B-field target it is undriven. (b) Shot 35218 produced a B field (estimated ~100 to 200 T based on previous experiments with similar drive). The Lorentz force on the protons is such that they are pulled inward toward the loops, where grid-line distortion near the arrows shows protons moving inward. The grid and foil could not be fielded simultaneously. (c) Shot 35225 corresponds to the foil being driven with a B field applied. Detailed analysis is underway for all shots.

driven, (2) only the B field was driven (allowing for a grid to be inserted), and (3) where both targets are irradiated. Additional shots have been allocated for FY22 to make the scattering measurements (allowing time to clear the diode qualification issues), and these radiographs have also led to several modifications to the targets for the follow-on day. First, the shadows of the current loops are clearly visible in the radiograph from shot 35227, as highlighted by the red arrows. When the magnetic field is applied, the Lorentz force on the protons pulls them toward the loops, complicating the analysis. In comparison, in previous experiments (cf. Ref. 12), the field direction was reversed and protons were pushed outward from the target; the size of the void region was then directly related to the strength of the B field. For FY22, the driven portion of the target will be modified to maintain the x ray and plasma blocking for the foil but to recover the previous B-field direction for proton probing. Additionally, while analysis is still ongoing for the proton data, there is evidence in the radiographs from shots 35218 and 35225 that the field structure is very complex in the region of the foil. At the expense of total field, the FY22 targets will return to the solid-loop target geometry and position the foil just outside this region. The primary measurement will be the scattering, but these changes should improve future radiography measurements as well.

Scaling of Multipicosecond Deuteron Acceleration for the Development of a Laser-Driven Neutron Source

Principal Investigator: G. G. Scott (LLNL)

Co-investigators: D. A. Mariscal, E. Folsom, R. F. Heeter, R. J. Wallace, E. S. Grace, R. A. Simpson, and T. Ma (LLNL); and D. Canning, S. T. Ivancic, and M. Krieger (LLE)

The well-known $d(^7\text{Li},n)^8\text{Be}$ has been subject to a number of laser-driven neutron-production investigations since it is a mechanism that produces a highly directional and energetic neutron beam, owing to the extremely exothermic nature of the reaction, and a pulsed neutron source with such properties might find use for a myriad of applications. To efficiently drive such a neutron beam, efficient acceleration of a deuteron flux above the $\sim 4\text{-MeV}$ activation energy of reaction is crucial. To this end, our experiment aims to investigate the first detailed scaling of deuteron acceleration from a CD foil as a function of laser energy, intensity, and pulse duration while simultaneously using a portion of the deuterons to drive neutron generation via a pitcher/catcher configuration. This study is inspired by recent results on the scaling of laser-driven proton acceleration in the multipicosecond regime,¹³ where $\sim 10\text{-ps}$ pulses were found to offer an optimum between drive time and laser pulse energy for optimal proton acceleration.

With deuterons being accelerated via TNSA, in the target normal direction, and with the $D(^7\text{Li},n)$ reaction known to have a strong directionality, a plasma mirror platform¹⁴ was utilized such that sidelighter and backlighter-only shots could be directed to a target with a fixed diagnostic orientation with respect to the target, and ion acceleration was diagnosed by the TIM-based Thomson parabola ion energy (TPIE) diagnostic fielded in the target normal direction.

Preliminary experimental data analysis presented in Fig. 13(a) shows that the maximum deuteron energy is primarily dependent on the laser energy driving the acceleration, with laser intensity being less important. As the driving pulse duration increases, the energy partition in deuteron beam compared to that of the simultaneously accelerated proton beam also increases. Higher-energy, longer-duration laser pulses, therefore, appear to be beneficial for increasing the efficiency of deuteron acceleration, and numerical modeling will be conducted to understand the acceleration dynamics, and data obtained from the OU-ESM (Osaka University electron spectrometer) and neutron times of flight will further inform us on this study.

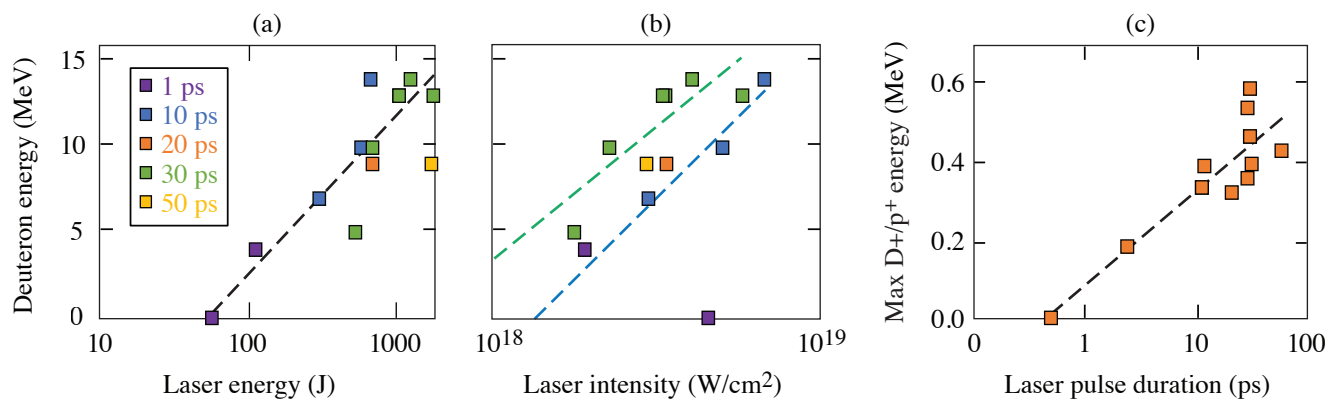
Hydrodynamics and Plasma Properties Campaigns

Mix-Width Measurements of Metallic Foams

Principal Investigator: D. A. Martinez (LLNL)

Co-investigators: S. F. Khan, T. Dittrich, S. G. Glendinning, R. J. Wallace, and T. Baumann (LLNL); and T. Woods, W. Man, and M. Arend (LLE)

This experiment series was designed to determine if the Ta_2O_5 foams at 0.85 g/cm^3 produce a smaller mix width compared to the previous mix-width data obtained with 0.9-g/cm^3 Cu foams due to the smaller cell size. For Ta_2O_5 , the cell size is estimated



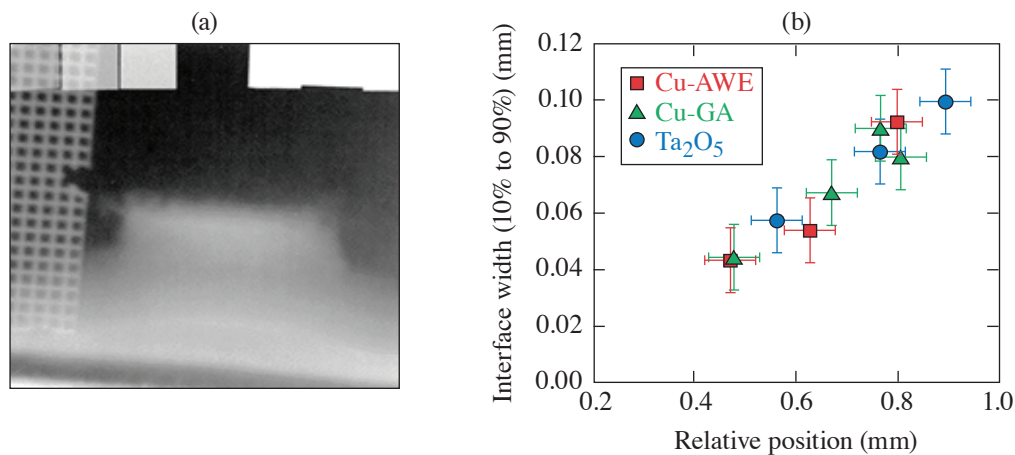
U2819JR

Figure 13

The maximum deuteron energy recorded on TPIE as a function of pulse duration and (a) laser energy and (b) laser intensity. (c) The ratio of maximum deuteron energy to proton energy as a function of pulse duration.

between 10 and 100 nm, while the Cu foams have a 1- μm cell size using a slip casting method. It is assumed that the cell size is the main seed for mix instabilities for foams.

The FmGrow-21A experiment used a half-hohlraum connected to a shock tube. The shock tube consisted of a polyethylene ablator and a metallic foam sample of Ta_2O_5 at 0.85 g/cm^3 , followed by a 50-mg/cm^3 carbon resorcinol formaldehyde (CRF) foam reservoir. The hohlraum was driven using 12 beams with a 1-ns square pulse to produce a peak radiation temperature of 200 eV. The resulting blast wave caused the metallic foam/reservoir interface to become unstable, resulting in Rayleigh–Taylor (RT) instability growth. The shock tube was imaged using a point-projection backlighter technique with a $10\text{-}\mu\text{m}$ -diam Ag wire on a polystyrene substrate and illuminated with an OMEGA EP short-pulse beam. The interface mix was characterized by 90%–10% transmission contour between the CRF/sample interface. Figure 14(a) shows a typical radiograph obtained during the experiment. The interface position was estimated using the Au washer around the shock tube [seen as the dark band on the bottom of Fig. 14(a)] and the position of the steepest gradient at the interface. Due to complications on the shot day, only two data points were obtained with data at 18 ns and 21 ns from the start of the OMEGA laser drive. The data were combined with the previous



U2820JR

Figure 14

(a) Background subtracted radiography of Ta_2O_5 foam (shot 99129) at 21 ns; (b) measured mix width as a function of interface position extracted from the radiographs. AWE: Atomic Weapons Establishment; GA: General Atomics.

Ta₂O₅ data on FoamGrw 19A at 23.5 ns and agree with the suggested trend [Fig. 14(b)]. Additionally, the Ta₂O₅ mix width from Ta₂O₅ also agrees with the Cu-foam data, suggesting there is no significant difference between the two foams with regard to the mix width. Further studies are looking at the role of decompression, which can mask the role of internal structure on mix width.

Interaction Between a Strong Laser Ablation Shock and a Shock Wave from the Supersonic-to-Subsonic Transition of Radiation

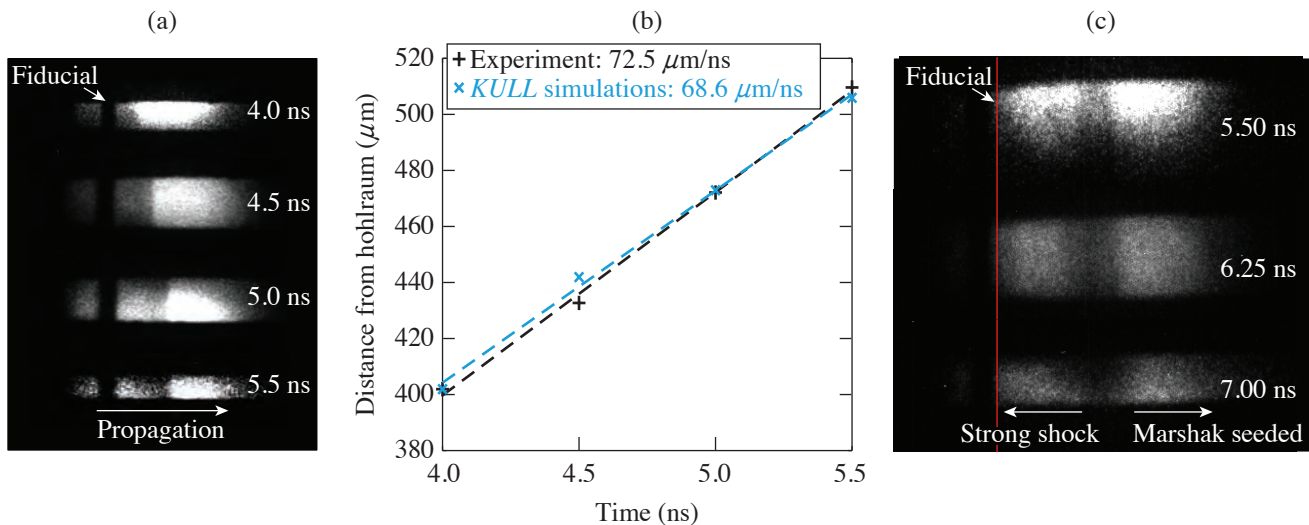
Principal Investigator: D. Rusby (LLNL)

Co-investigators: F. Albert, K. Widmann, C. Harris, A. Toreja, S. Murray, and S. Prisbrey (LLNL); and H. G. Rinderknecht (LLE)

Radiation transport plays an important role in many areas, such as ICF experiments, energy transport in the sun, or the penetration of the radiation field from a hot star or supernova interacting with an interstellar cloud. The ESPADA platform was designed to observe the shock front induced by the supersonic-to-subsonic transition of a Marshak wave (a radiation flow propagating into a medium) in silica aerogel and compare the results with the radiation-hydrodynamic code *KULL*. Supersonic-to-subsonic radiation transition induces a diagnosable shock wave that can be observed with x-ray radiography but has seldom been investigated in experiments.¹⁵ We successfully observed and measured this transition during our ESPADA-20A shot day. In 2021, we did two additional shot days (ESPADA-20B and ESPADA-21A) to observe the collision of the Marshak-induced shock wave with a strong (few-Mbar) laser ablation shock. Within this context, the strong shock is an effective and reliable probe of the Marshak-induced shock wave behavior, and the shock interactions provide a test of our ability to model the behavior of materials in a complex physical regime.

During the ESPADA-20B/21A shot days, a halfraum was driven to temperatures of ~ 100 eV by 21 OMEGA beams (3-ns flattop pulse shape with 273 J/beam). This x-ray drive launched a Marshak wave through a 2-mm-diam, 2-mm-long, 30- μm -thick gold tube filled with SiO₂ foam (33 mg/cm³) and attached on the other side of the halfraum. On the other side of the foam tube, a strong laser ablation shock was driven with six beams (same pulse shape and energy, 2.5 to 3 ns earlier) incident onto either a 10- μm CH or 2- μm Al ablator. A 12- μm -thick Ti foil was driven with 23 additional beams to provide a near-monochromatic 4.7-keV x-ray backlighter source oriented quasi-perpendicular to the gold tube's axis. A 200- μm -wide slit on each side of the tube allowed the x rays to pass through the foam, and the x-ray images of the target were recorded on a four-strip x-ray framing camera, at different times (Fig. 15).

Our initial results show reasonable agreement between the experiment and 2-D *KULL* simulations.¹⁶ Detailed simulations are underway for a post-shot comparison. Our next experiments (ESPADA 22) will use Ni-doped foams and Fresnel zone plates for increased spatial resolution.



U2821JR

Figure 15

Experimental data showing the (a) Marshak wave-induced shock and (c) its propagation after collision with a strong laser-ablation shock. (b) The experimental shock velocity is well reproduced by 2-D *KULL* simulations.

X-Ray Sources from Laser Wakefield Acceleration on OMEGA EP

Principal Investigator: F. Albert (LLNL)

Co-investigators: I. Pagano (LLNL and the University of Texas, Austin); N. Lemos, J. Williams, and H. Chen (LLNL); J. L. Shaw and D. H. Froula (LLE); A. Aghedo (Florida A&M University); and M. Sinclair and C. Joshi (University of California, Los Angeles)

X-ray backlighting is one of the most commonly used methods to look into the extreme temperatures, pressures, and densities created during laser-driven HED science experiments. Over the years, much effort has gone into developing backlighting techniques to look into these states of matter using new sources and diagnostics. The properties of an x-ray backlighter (flux, source size, spectrum, duration) required for an experiment depend on the application being studied and on the quantity being measured. The goal of the Wakefield-EP shot series is to develop a new type of x-ray backlighter, which could be advantageous for applications requiring broadband spectra, small source sizes (sub-50 μm), short-duration (less than 10 ps), and x rays extending beyond 100 keV. Our proposed x-ray sources are based on laser wakefield acceleration (LWFA) of electrons in the self-modulated regime (SMLWFA). Specifically, we aim to develop three different x-ray sources based on betatron radiation, Compton scattering, and bremsstrahlung emission.

The Wakefield-EP-21A and Wakefield-EP-LBS-21A shot days were a continuation of our previous work, aimed at producing and detecting betatron radiation produced by SMLWFA using a modified version of the electron–positron–proton spectrometer (EPPS) diagnostic. We enlarged apertures to 5 mm (instead of 1 mm) and included a hole at the back of the magnet box, as well as a stack of nine image plates at the back of the ten-inch manipulator (TIM) boat to detect betatron radiation. With the help of Monte Carlo simulations, we implemented diagnostic shielding enhancements for our 2021 shot days. As a result, we were able, for the first time, to simultaneously detect electrons and betatron x rays in our OMEGA EP experiments (Fig. 16).

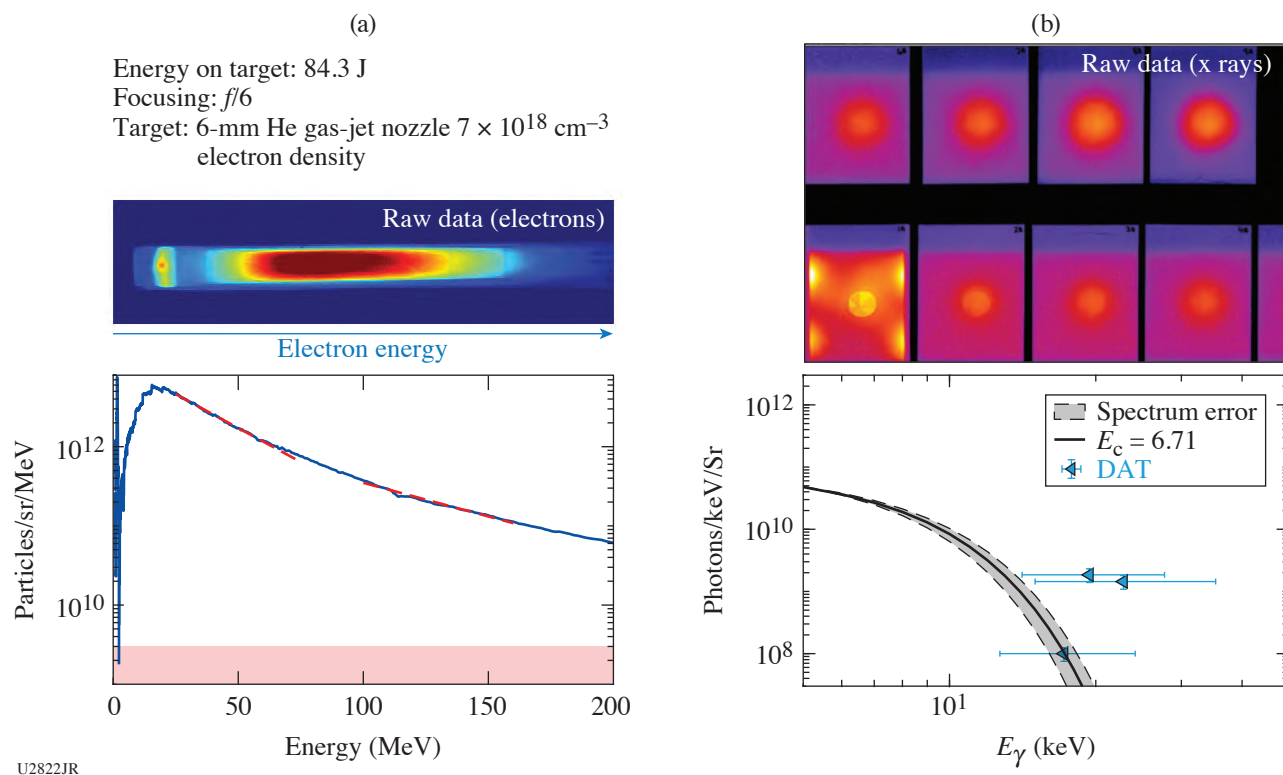


Figure 16

Results obtained during the WakefieldLBS-EP-21A shot day using the modified EPPS diagnostic. (a) Electron data; (b) betatron x-ray signal measured on the rear image plate stack of EPPS with reconstructed spectrum.

The wakefield platform produced robust electron beam data, recording >100-nC charge electron beam at each shot, as well as two temperature spectra extending up to about 200 MeV [Fig. 16(a)]. We also measured betatron x rays with critical energies between 5 to 10 keV and 10^{10} photons/keV/sr [Fig. 16(b)].

The Measure of X-Ray Emission from Laser-Compressed Spheres

Principal Investigator: E. V. Marley

Co-investigators: M. Tabak, K. Widmann, and J. Emig

This campaign, conducted to measure the x-ray emission from laser-compressed spheres, was the first campaign in the development of a new experimental platform. The target was a gas-filled, 800- μ m-diam plastic sphere illuminated by 60 beams with a 1-ns square pulse. Five framing cameras and one streak camera were used to record the x-ray emission. Two of the framing cameras were coupled to pinhole cameras to measure the size of the emitting volume. The remaining three framing cameras were coupled to spectrometers to record various bands of the x-ray emission of the compressed sphere (Fig. 17). The time-resolved emission was also recorded with Dante. The Henway spectrometer was also fielded to record the absolute, time-integrated emission of the compressed spheres. Eleven shots were completed successfully with data being collected on all eight diagnostics.

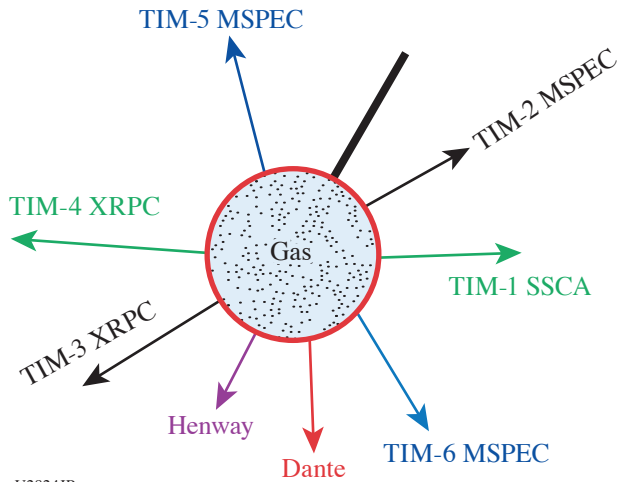


Figure 17
 Experimental configuration of the XELCS. MSPEC: multipurpose x-ray spectrometer; XRPC: x-ray pinhole camera; SSCA: static spherical cavity approximation.

U2824JR

Probing Buried-Layer Nuclear-Heated Samples

Principal Investigator: A. B. Zylstra

Co-investigator: J. Burggraf

There is significant interest in conducting nuclear physics experiments with target nuclei in a HED plasma environment. This is because under conditions typical for our experimental facilities, some nuclei can have excited states populated by interaction with the plasma. These processes are intrinsically interesting in themselves, and the subsequent impact of the excited states on nuclear physics is unknown. For example, in the r process of heavy-element nucleosynthesis, sequential neutron capture occurs on heavy elements under extreme conditions and such physics is often incorporated into “stellar enhancement factors” on the cross sections, which are purely theoretical.

To study this physics in the lab, we require a mechanism to heat samples to relevant conditions and then probe nuclear reactions with a source of particles. This campaign is designed to study the heating, starting with the buried-layer heating mechanism. Unlike previous applications of this heating technique, studying nuclear physics will require substantially larger sample masses for measurable signals. To this end, we began by performing a scaling experiment on OMEGA EP at the end of FY21 using buried Cu layers and x-ray spectroscopy.

The experimental configuration is shown in Fig. 18. Several spectrometers were used to measure Cu emission on each shot, with variables including laser energy, pulse duration, and buried Cu layer thickness scanned over the data. Data analysis is in progress.

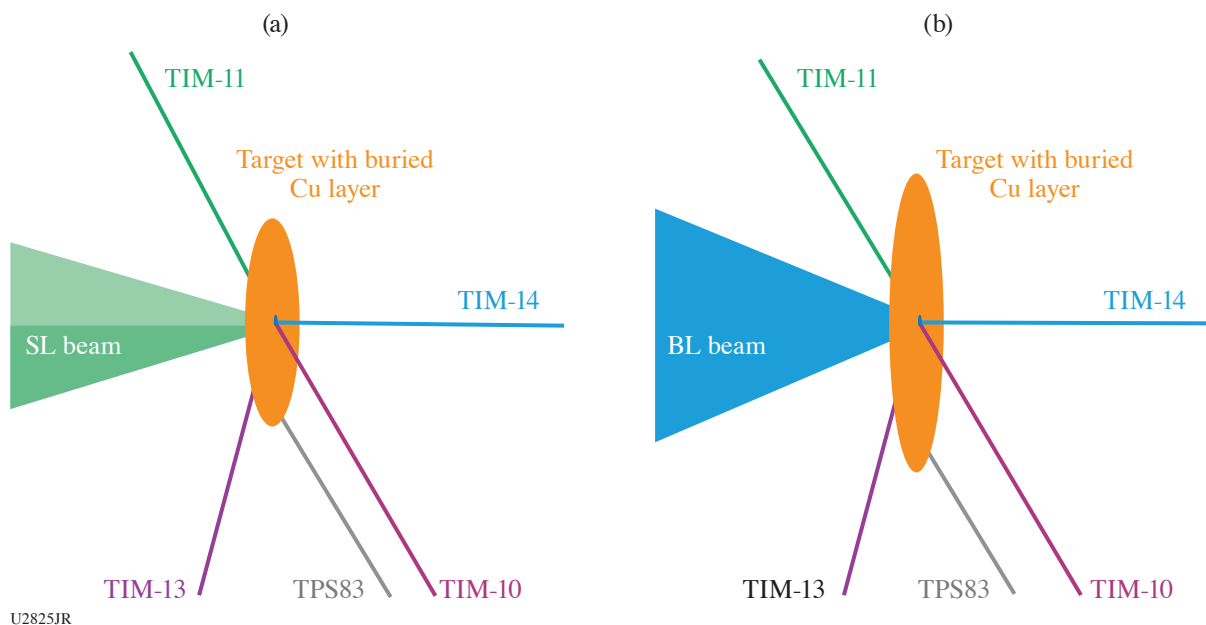


Figure 18
VisRad drawings of the experimental configuration for NucHeat-21A, which used alternating sidelighter (SL) and backlighter (BL) shots to increase data return.

Materials Campaigns

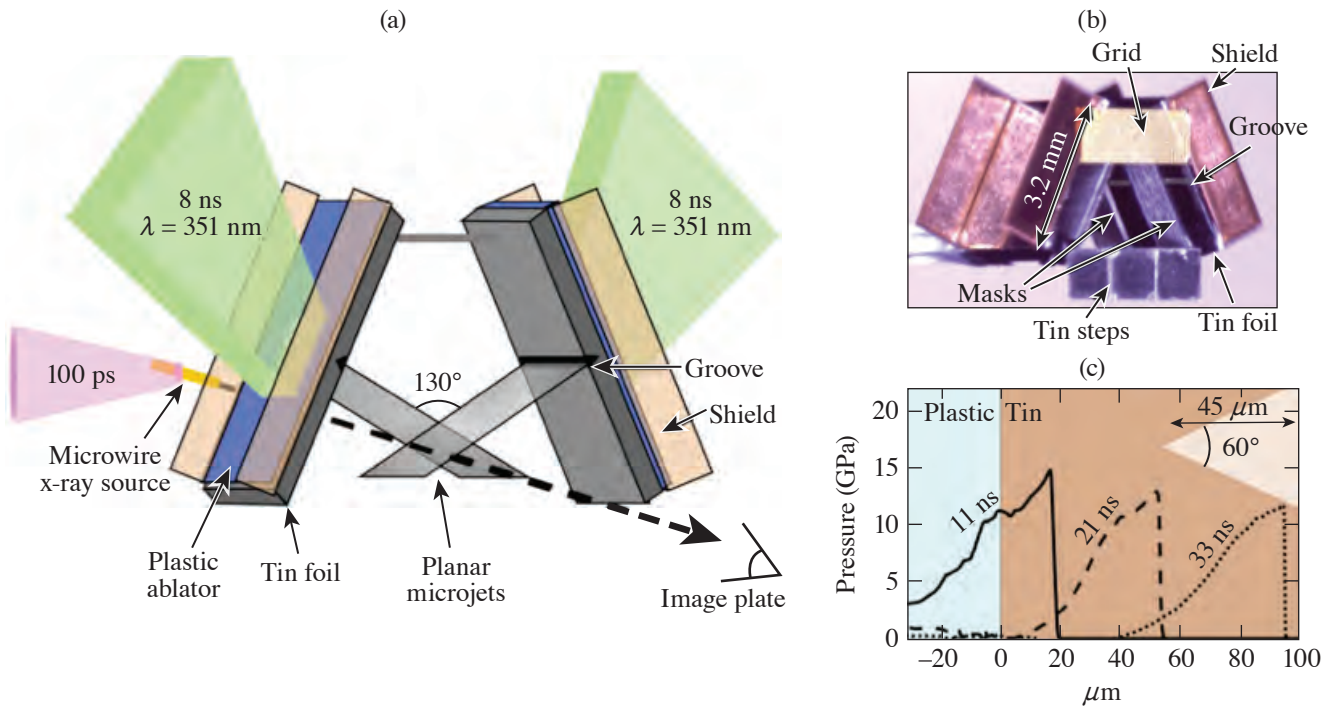
OMEGA-60 and OMEGA EP Experiments on Laser-Driven Tin Ejecta Microjet Interactions

Principal Investigator: A. M. Saunders (LLNL)

Co-investigators: C. V. Stan, K. K. Mackay, B. Morgan, J. Horwitz, S. J. Ali, T. Haxhimali, Y. Ping, F. Najjar, J. H. Eggert, and H.-S. Park (LLNL); and H. G. Rinderknecht (LLE)

The ejecta campaign on OMEGA 60 and OMEGA EP seek to understand the effects of ejecta microjet interactions from laser-driven tin targets through x-ray radiography measurements. An ejecta microjet forms when a shock breaks out from a free surface and interacts with a surface feature, such as a groove carved across the sample. The interaction of the shock with the free surface causes the surface feature to invert as a limiting case of the Richtmyer–Meshkov instability, and the groove turns into a planar jet of material propagating at velocities in excess of several kilometers per second. Micron-scale particles comprise ejecta microjets, and as such, the interaction of two ejecta microjets offers an experimental methodology for anyone interested in the collisions of high-velocity particle-laden flows.

Figure 19(a) shows a schematic of the radiography platform on OMEGA EP. Two long-pulse lasers drive shock waves into tin samples oriented toward each other. The inside surfaces of the tin foils have grooves carved across them. The shock waves generate planar microjets traveling toward each other, eventually to interact at the center of the two foils. At a later time, a short-pulse laser is incident on a titanium microwire, generating x rays to be used for radiography and captured by an image plate held in the shielded image-plate diagnostic. Figure 19(b) shows a picture of the target, and Fig. 19(c) shows the dimensions of the target and the groove, as well as radiation-hydrodynamic simulations of one shock wave propagating through a tin sample. The platform on OMEGA-60 is similarly built, with the geometry designed such that the jets interact with a 170° angle between them; a long-pulse laser on a pinhole backlighter is used to generate the x rays for the radiography measurement.



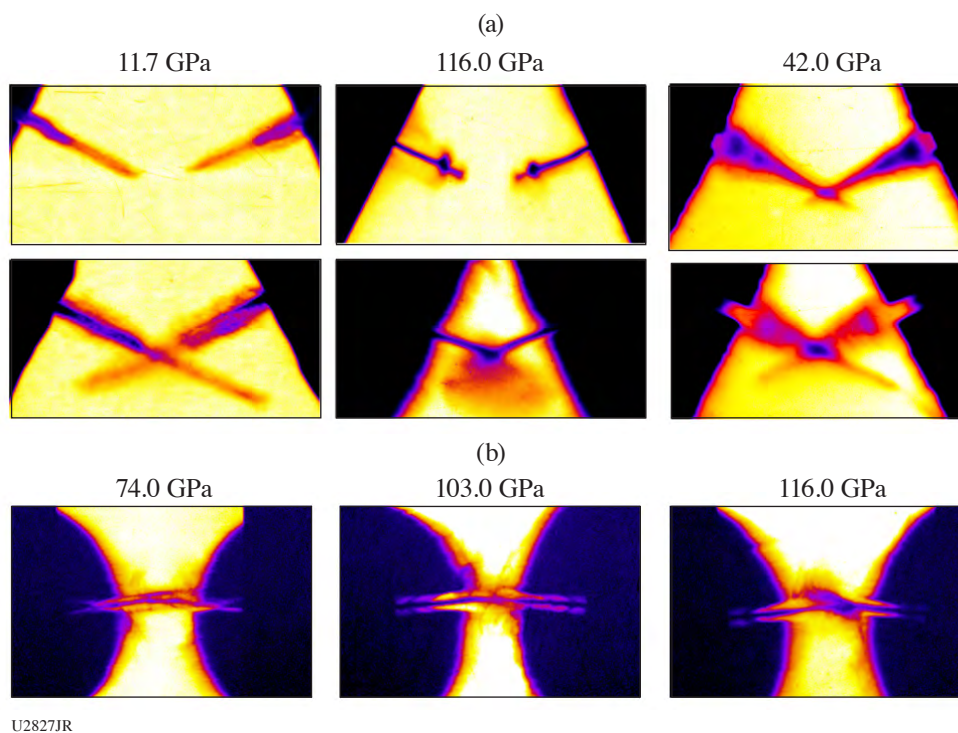
U2826JR

Figure 19

(a) A schematic of the platform on the OMEGA EP laser. Two long-pulse lasers drive shock waves into tin foil targets with grooves imprinted on their inner surfaces. The interactions of the shock waves with the grooves generate planar ejecta microjets that interact. A short-pulse laser incident on a microwire generates x rays for the radiography measurement. (b) A photo of the target. (c) Target thicknesses and groove dimensions with radiation-hydrodynamic simulations of a shock wave propagating through a tin sample.

Both the OMEGA-60 and OMEGA EP platforms were very successful in collecting radiography data on interacting ejecta microjets. Figure 20 shows examples of data collected from (a) the OMEGA EP and (b) the OMEGA-60 platforms. For experiments on OMEGA EP, we varied the laser drive energy such that we interacted jets at drive pressures ranging from 11.7 GPa to 116.0 GPa. The first two columns of Fig. 20(a) show images of jets at those high and low pressures before interaction (top row) and after interaction (bottom row). We observe that at the lower pressures, the jets appear not to interact, while at higher pressures, the jets interact strongly and form a corona of material around the center point. We also took data of interacting jets at an intermediate pressure, as seen in the right column of Fig. 20(a). These data occurred with a differently shaped groove, which resulted in the altered jet shape. No interactions were observed at this intermediate pressure. The results from the OMEGA EP platform were featured in a recently accepted article in *Physical Review Letters*.¹⁷

We wanted to understand the drive pressure at which interaction onset behavior changed, so we used the platform on OMEGA-60 to perform a finer pressure scan of head-on interacting jets. The data from this campaign can be seen in Fig. 20(b), where interaction images were taken at 74, 103, and 116 GPa. It appears like interaction behavior does not become apparent until pressures exceeding 103 GPa are reached. This is significant because tin is a material known to melt upon shock release at pressures exceeding approximately 50 GPa. If the interaction behavior changed as a function of tin material phase, we would expect to see a change at shock pressures around 50 GPa. However, because we see a change at higher pressures, this suggests that interaction behavior is driven by other jet characteristic, such as jet density, particle-size distribution, or jet velocity. Understanding the physics driving microjet collisions will be the study of future campaigns.



U2827JR

Figure 20

X-ray radiography images of laser-driven tin ejecta microjets and their interaction behavior observed in (a) OMEGA EP experiments and (b) OMEGA-60 experiments at various driver pressures.

Measuring the Hugoniot of Shocked LLM-105

Principal Investigator: S. M. Clarke (LLNL)

Co-investigators: M. C. Marshall (LLE); and J. H. Eggert, R. Smith, L. Leininger, and L. Fried (LLNL)

Generating high-quality experimental EOS data of insensitive high explosives (HE's) such as TATB and LLM-105 is essential to improving predictive modeling of the behavior of these materials. Previous work demonstrated the feasibility of using OMEGA EP to obtain EOS data on TATB.¹⁸ This research led to a better understanding of the overdriven state [pressures exceeding the Chapman–Jouguet (CJ) pressure] that would not have been achievable using standard gas-gun or explosive-driven techniques.

This campaign measured the shock Hugoniot of an LLM-105 formulation using the impedance-matching technique relative to an aluminum standard (Fig. 21). HE samples were created by pressing parts and polishing them down to the thinnest-possible dimension. They were attached to an Al pusher, which was driven by a CH ablator [Fig. 21(b)]. A LiF witness was used to infer the time dependence of the shock velocity in the adjacent opaque HE sample to obtain a more-accurate Hugoniot measurement than that using the average shock velocity determined from the shock transit time. Since the HE samples were relatively thick ($\sim 200 \mu\text{m}$), all four OMEGA EP beams were stitched together to obtain an ~ 40 -ns pulse [Fig. 21(c)] to support a nearly steady shock. For pressures under ~ 55 GPa, excellent reflectivity was observed at the Al/LiF witness interface [Fig. 21(d)], enabling us to extract particle velocity as a function of time using VISAR [Fig. 21(e)].

Preliminary analysis of the data using the average shock velocity in the HE sample suggests we are achieving higher densities than what was predicted by the unreacted Hugoniot [Fig. 21(f)]. Future analysis will focus on using the nonsteady waves approximation to get a better pressure determination in the HE samples based on our knowledge of the shock velocity history in

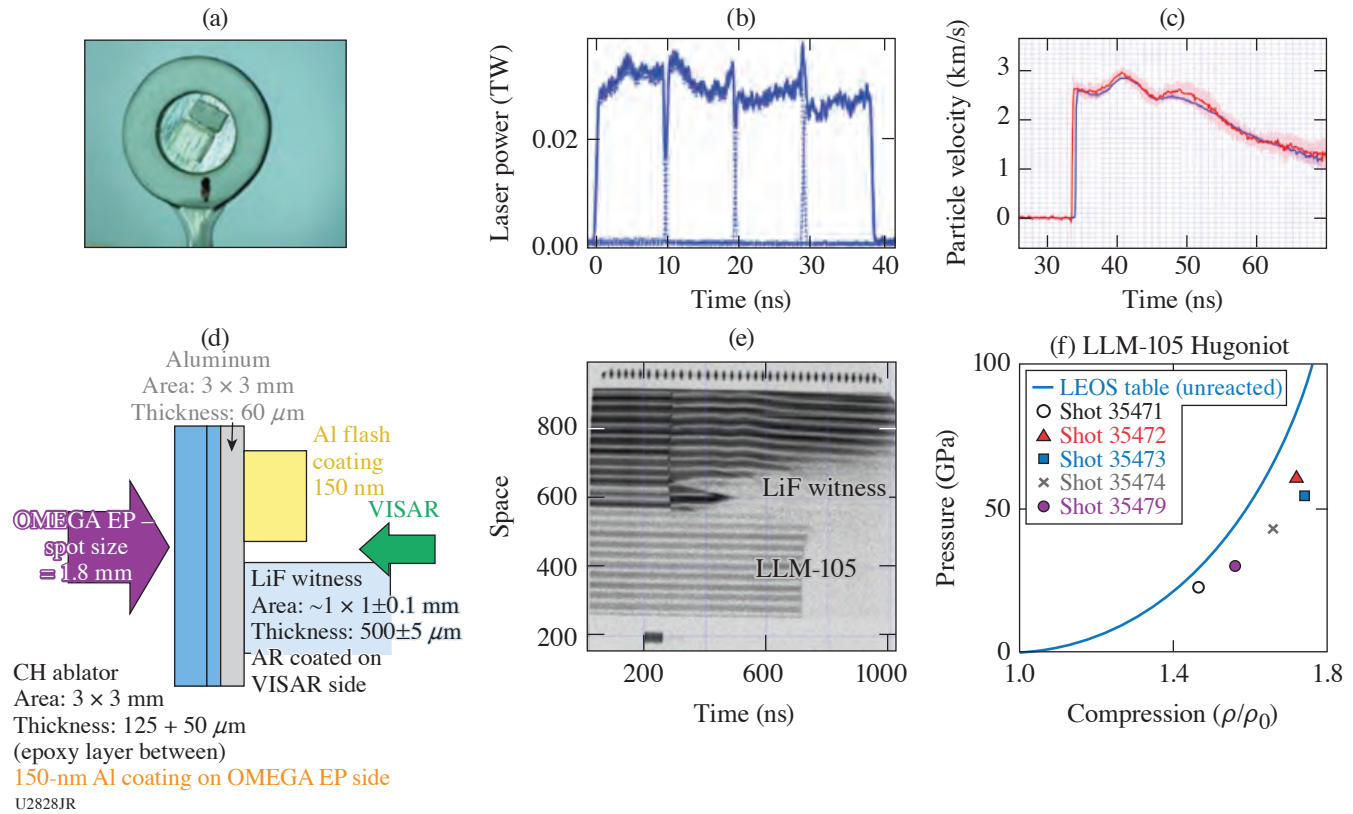


Figure 21

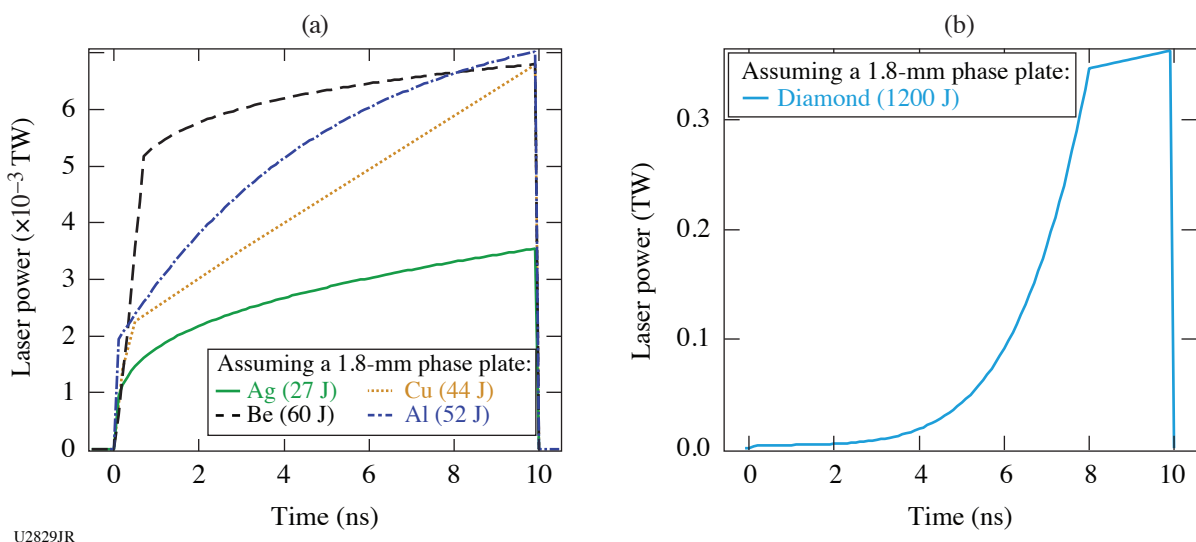
(a) Optical image of the as-shot target package. (b) Schematic of the target package detailing the position of the HE sample relative to the LiF witness. (c) Typical delivered pulse shape consisting of all four beams of OMEGA EP stitched together to create an ~ 40 -ns drive. (d) Typical active shock breakout (ASBO) data achieved during the shot showing excellent reflectivity at the Al/LiF witness interface and the shock breakouts of the aluminum baseplate and the LLM-105 formulated sample. (e) Al/LiF interface velocity versus time. (f) Preliminary plot of the data obtained during this campaign compared to the LEOS table for unreacted LLM-105.

the LiF witness. The next campaign will focus on extending the range of data from 15 GPa to 80 GPa and filling in more data points around the CJ pressure.

Generating Very Low-Pressure Shocks Using Alternative Ablator Materials

Principal Investigator: R. Smith

The purpose of this campaign is to evaluate alternative ablator materials for use in future low-pressure (1) shock-compression experiments (Be, Cu, Al, Ag) and (2) ramp-compression experiments (diamond). While Kapton[®] (polyimide) has been a widely used ablator material in laser-compression experiments, the use of this material is complicated by a proposed phase transformation at ~ 20 to 50 GPa, which can result in an unstable compression wave being formed (multiwave structure). Therefore, there is a need for alternative ablator materials that can transmit shock waves without additional compression-wave pulse shaping due to the deformation processes in the ablator material itself. In this study each target consisted of a $25\text{-}\mu\text{m}$ -thick ablator (for shock experiments) or a $100\text{-}\mu\text{m}$ -thick diamond ablator (for ramp experiments). These ablator materials were glued onto to a $0.2\text{-}\mu\text{m}$ Al-coated LiF window. The phase plate used in these experiments produced a 1.8-mm-diam laser spot on target, and the laser pulse shaping requested for each ablator material is shown in Fig. 22. The primary diagnostic was the EP-ASBO system (VISAR) that recorded the ablator-LiF particle velocity as a function of time. For all ten shots, the laser pulse shaping was excellent and high-quality data were obtained.



U2829JR

Figure 22

Laser pulse shape for (a) temporally steady-shock experiments through different ablator materials and (b) ramp-compression experiments.

Improving Reflection Diffraction Signal for the Forward-Backward X-Ray Diffraction Diagnostic

Principal Investigator: A. Krygier (LLNL)

Co-investigators: D. N. Polsin, M. K. Ginanne, and J. R. Rygg (LLE); and C. E. Wehrenberg and J. H. Eggert (LLNL)

We are developing a new platform to simultaneously measure transmission and reflection x-ray diffraction from a dynamically compressed sample. The goal of this platform is to determine the strain anisotropy induced in a sample due to material and flow strength. This platform is related to the PXRDIIP diagnostic but has unique challenges due to the need for multiple simultaneous backlighters.

In the XRDAFS-20A experiment, we were attempting to improve the reflection diffraction signal by improving backlighter alignment and reduce background sources. In preparing the instrument, we were able to identify a systematic alignment issue during the build that we corrected with a careful procedure. We also fielded metallic glass (diffractionless) shields on the pinhole to mitigate non-sample diffraction, which was found to work well. Three of the shots fielded undriven samples to test iterations in the configuration; the remaining two shots were driven, one of which was reflection backlighter only and the second of which attempted simultaneous reflection and transmission diffraction. The driven reflection measurement (Fig. 23) showed clear driven diffraction from iron—the first recorded reflection diffraction from a high-pressure sample on this platform. The second driven shot showed transmission diffraction, but not reflection, indicating continuing alignment issues to be addressed in experiments to come.

Transmission and Reflection Diffraction of Fe Using the FBXRD Diagnostic

Principal Investigator: A. Krygier (LLNL)

Co-investigators: D. N. Polsin, M. K. Ginanne, and J. R. Rygg (LLE); and C. E. Wehrenberg and J. H. Eggert (LLNL)

We are developing a new platform to simultaneously measure transmission and reflection x-ray diffraction from a dynamically compressed sample. The goal of this platform is to determine the strain anisotropy induced in a sample due to material and flow strength. This platform is related to the PXRDIIP diagnostic but has unique challenges due to the need for multiple simultaneous backlighters.

In the FBDiff-21A experiment, we were using the advances made on previous experiments to attempt to collect simultaneous transmission and reflection diffraction from shock-compressed iron. We varied the pinhole size and collimator diameter to scan

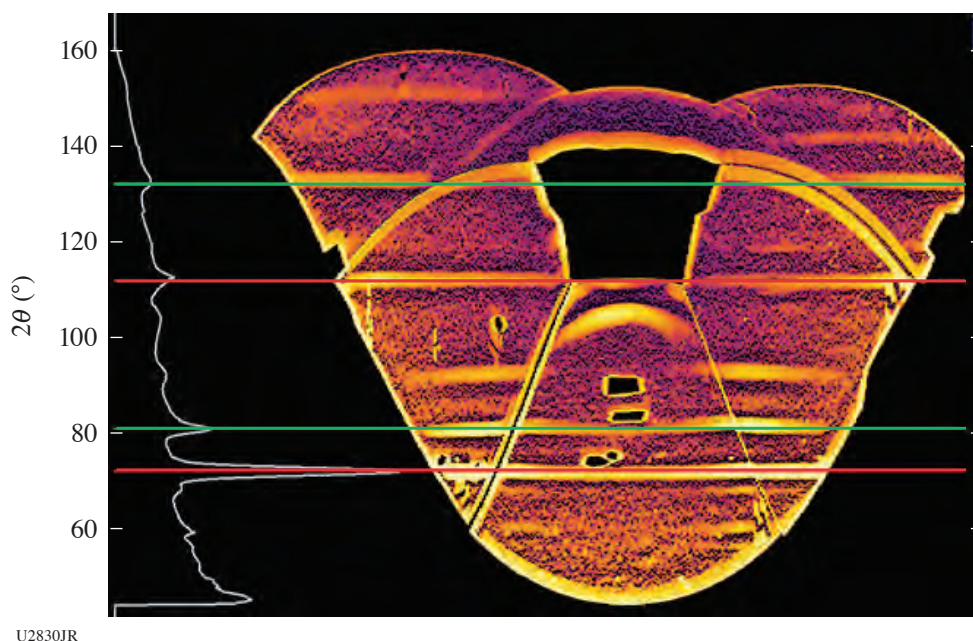


Figure 23
Background subtracted forward-backward x-ray diffraction (FBXRD) data in a reflection-only configuration, projected in polar-azimuthal coordinates. The red and green lines identify the expected location of diffraction from the W pinhole (red) and the Fe sample (green). Driven features are present at $2\theta \sim 90^\circ$.

different balances of expected diffraction quality (higher with smaller pinhole and collimator) and expected signal (higher with larger pinhole and collimator). We successfully observed simultaneously driven transmission diffraction and ambient reflection diffraction on more than one shot. There is still a significant amount of unwanted signal and apparent backlighter/collimator/sample alignment issues that will be the subject of future experiments (Fig. 24).

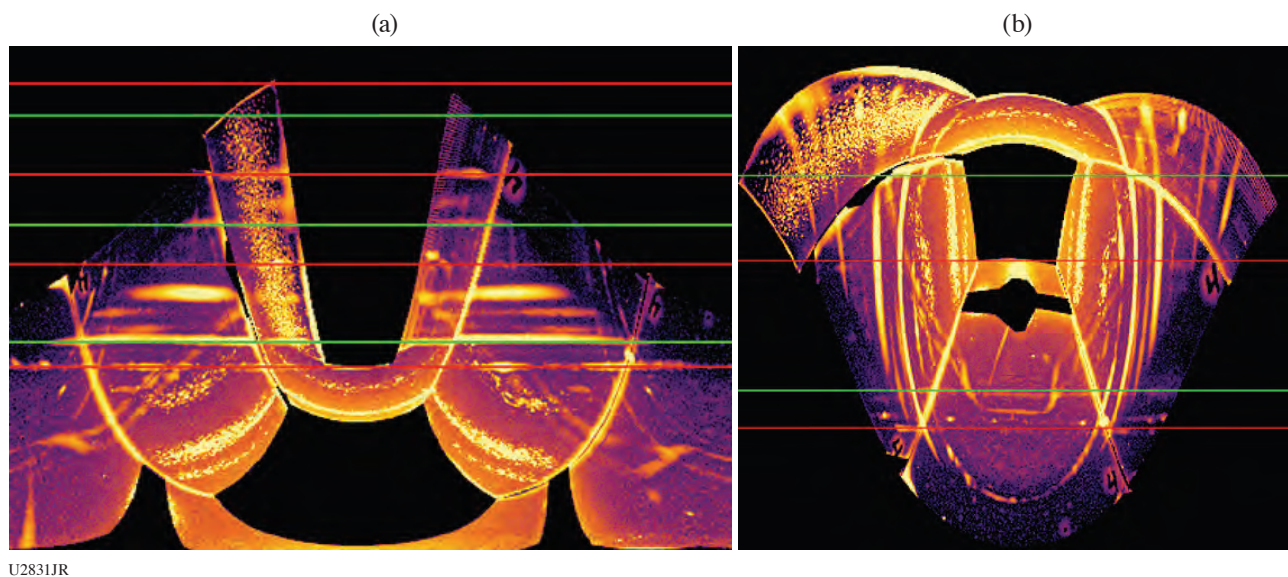


Figure 24
Background subtracted FBXRD data in transmission and reflection. The data are shown projected in polar-azimuthal coordinates with respect to each backlighter; (a) transmission geometry and (b) reflection. The red and green lines identify the expected location of diffraction from the W pinhole (red) and the Fe sample (green). Unmarked lines in the transmission data correspond to the high-pressure hcp phase of iron.

Off-Hugoniot Study of the Phase Behavior of Shock-Ramp-Compressed Au

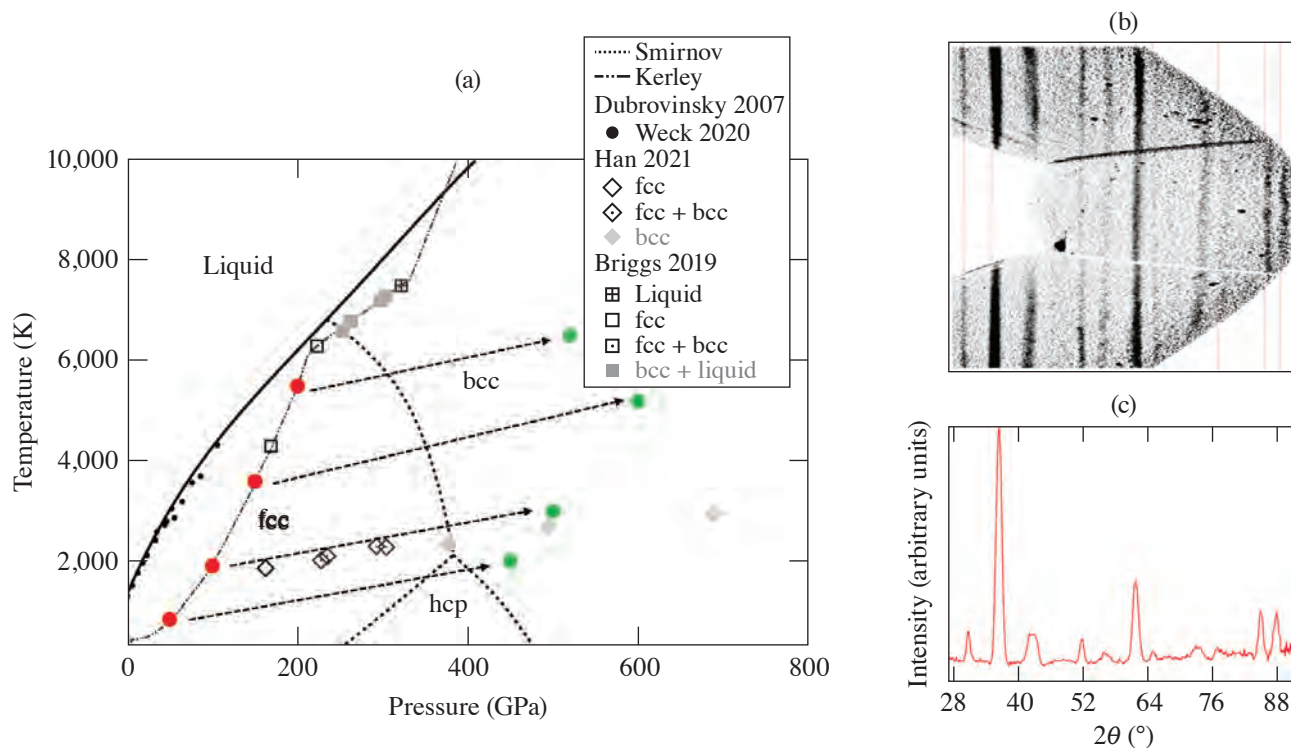
Principal Investigator: A. L. Coleman

Co-investigators: R. F. Smith, T. E. Lockard, D. C. Swift, and J. McNaney

Gold is widely used throughout the high-pressure community; in static compression, it is a commonly used pressure standard for diamond-anvil cell experiments¹⁹ as well as being used as a heat shield in dynamic compression target packages on the NIF and OMEGA.²⁰ While there has been much study of the structural behavior of Au at room temperature,^{21,22} its behavior at high pressures *and* high temperatures is not well constrained. When Au is used as a component in shock- and ramp-compression target packages, it is important that its structural behavior is well understood so that any contribution it makes to a diffraction data set may be confidently identified.

We have designed a series of shock-/ramp-compression shots to explore Au across a series of different temperature states. This was achieved by initially shocking the sample to an on-Hugoniot state and then ramp compressing to a final pressure state, where the sample was probed by x-ray diffraction to determine the crystallographic state. Figure 25(a) shows the designed initial shock (red) and final ramp (green) compressions, with initial shock states at 50, 100, 150, and 200 GPa. Also shown on this plot are predicted phase boundaries from Smirnov,²³ as well as previously obtained Au data from shock²⁴ and ramp²⁵ compression.

By using a multilayered target package and a series of individually designed laser drives, we were able to obtain high-quality diffraction data between 350 and 650 GPa; example raw and integrated data are shown in Figs. 25(b) and 25(c), respectively. VISAR was employed as a secondary diagnostic in the campaign to allow pressure determination. Over two shot days, we took 16 shots and successfully characterized the structural behavior of Au at several different pressure and temperature states.



U2832JR

Figure 25

(a) The phase diagram of Au with theoretically predicted phase boundaries and data from previous studies is shown. The shock- and ramp-compression states are shown by red and green points, respectively. (b) Raw and (c) integrated data from the Au target package are shown.

EXAFS Measurements of Shock Compressed Fe Using the IXTS Spectrometer for Temperature Determination

Principal Investigator: A. L. Coleman

Co-investigators: F. Coppari, Y. Ping, and J. McNaney

Temperature determination is a significant challenge in modern laser-driven, dynamic compression experiments. The nano-second time scales and extreme pressure and temperature conditions at which these experiments are conducted mean that the successful implementation of a temperature diagnostic is challenging and frequently not possible. A potential means of obtaining temperature information about a shock- or ramp-compressed sample lies in the analysis of EXAFS (extended x-ray absorption fine structure) data. As a material becomes hotter, thermal motion of the atoms becomes important and reduces the amplitude of the EXAFS oscillations in a manner that is proportional to the temperature increase.

The purpose of this campaign was to optimize the imaging x-ray Thomson spectrometer (IXTS)²⁶ [Fig. 26(a)] in order to obtain high-quality EXAFS data from Fe at a series of shock-compressed states with the intention of determining the sample's temperature through the analysis of the EXAFS spectra. In addition to running the IXTS as the primary diagnostic, VISAR data were also obtained to establish the pressure in the Fe sample. Over the course of the two half-day campaigns, 12 shots were taken. Shock-compressed and ambient data sets were obtained along with a flat-field shot (taken once every campaign), which was used to correct the effects of the IXTS crystal defects on the EXAFS data. This experimental configuration made use of a Ti foil backlighter x-ray source, driven by 8 kJ in a 1-ns laser pulse.²⁷ The main target, consisting of a Kapton[®] ablator, an iron foil, a Cu temper layer, and a LiF window (Cu being closely impedance matched to Fe allowed us to hold a steady shock-pressure state in the Fe layer for the entire 1-ns duration of the backlighter x-ray source).

During these campaigns we successfully determined that heating the sample from the backlighter source is of the order of ~ 300 K [Fig. 26(b)] by comparing data from an undriven target with FEFF calculations for Fe at different temperatures. We also established that the resolution of this experimental setup is ~ 8 eV. We collected EXAFS data from the Fe shock compressed up until melting and observed a reduction in the amplitude of EXAFS oscillation in targets that were shock compressed to higher temperatures [Fig. 26(c)]. Analysis is ongoing to implement flat-field correction and determine temperature from the measured EXAFS data.

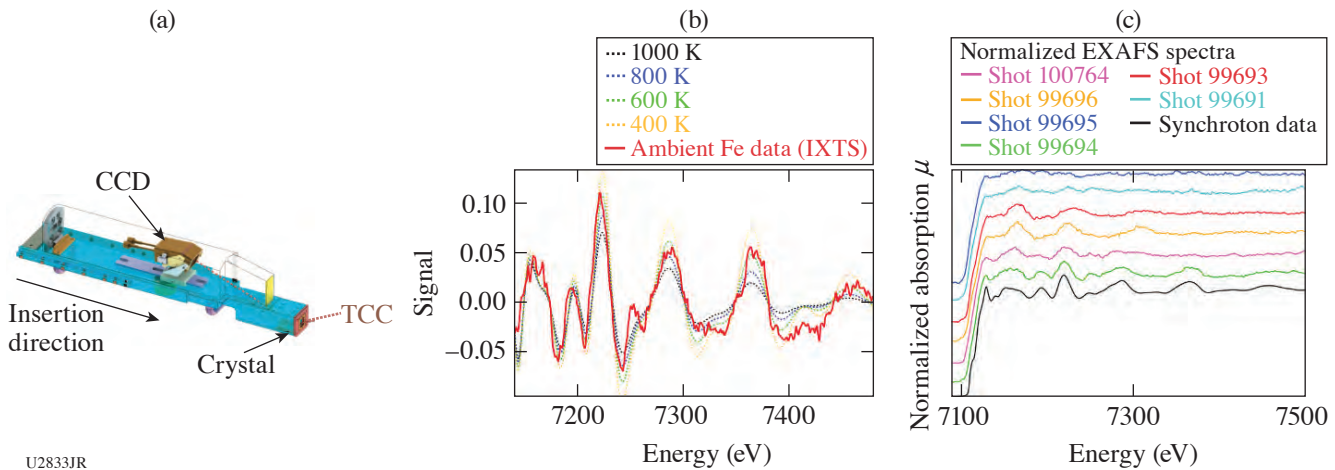


Figure 26

(a) The IXTS spectrometer schematic.²⁶ For our experiments, a curved Ge(220) crystal was used to disperse x rays in the energy range around the Fe absorption edge (7.1 keV). (b) EXAFS signal from an undriven Fe target is shown in red, along with simulated data from FEFF for different temperatures at ambient pressure (c) Ambient synchrotron data (black), ambient IXTS data (green), and shock-compressed data at increasing pressure and temperature are shown. As the temperature increases, the EXAFS oscillations decrease in amplitude due to Fe thermal motion. CCD: Charge-coupled device; TCC target chamber center.

Tin and Epoxy Strength Exploration Using the Rayleigh–Taylor Instability

Principal Investigator: C. V. Stan (LLNL)

Co-investigators: H.-S. Park, T. Lockard, D. Swift, and J. McNaney (LLNL); M. P. Hill (AWE); and G. Righi (University of California, San Diego)

We measure plastic deformation in tin using directly driven targets with machined sinusoidal perturbations, taking advantage of the RT instability. The targets consist of a Be ablator ($20\ \mu\text{m}$), a brominated plastic layer ($20\ \mu\text{m}$), epoxy (5 to $7\ \mu\text{m}$), rippled tin ($40\ \mu\text{m}$), a LiF window ($500\ \mu\text{m}$), and calibration features. Radiography data were collected at varying time points (20 to 50 ns from laser start time) using a microwire or microflag backlighter and a short-pulse beam to determine ripple growth. Prior work has shown that the growth of tin under these conditions ($\sim 1\ \text{Mbar}$, $\sim \text{K}$) was unusually and systematically low, pointing to possible extremely high strength in this material, which we were unable to match with conventional models.

One hypothesis is that the growth in tin may be suppressed by the possible strength in other target components, namely the brominated plastic or epoxy layers. To test this, we compressed tin targets to similar pressure conditions ($\sim 1\ \text{Mbar}$), but higher temperature ($\sim 7000\ \text{K}$), in order to induce melting. Deviations from the predicted ripple growth may then point to the effect of strength in plastic components on the RT growth within the system.

One VISAR and three radiography measurements were collected. The VISAR shows one strong initial shock to $\sim 3\ \text{km/s}$, followed by two more, smaller shocks, at ~ 10 and $\sim 20\ \text{ns}$ (Fig. 27). These correspond to the beam stitching times and may indicate that our individual beam pulse shapes or overlap times need adjustment going forward. The three radiographs show slightly low RT growth when compared to the models, although still just within the experimental error; further data analysis is needed. One interesting observation was that when a wire backlighter was used (30-ns data point), the data from different ripple amplitudes appeared more self-consistent, with a flatter background overall, than when a microflag backlighter was used (25- and 27.5-ns data points). A long-pulse backlighter will be implemented on future shots to investigate systematics associated with the choice of x-ray source.

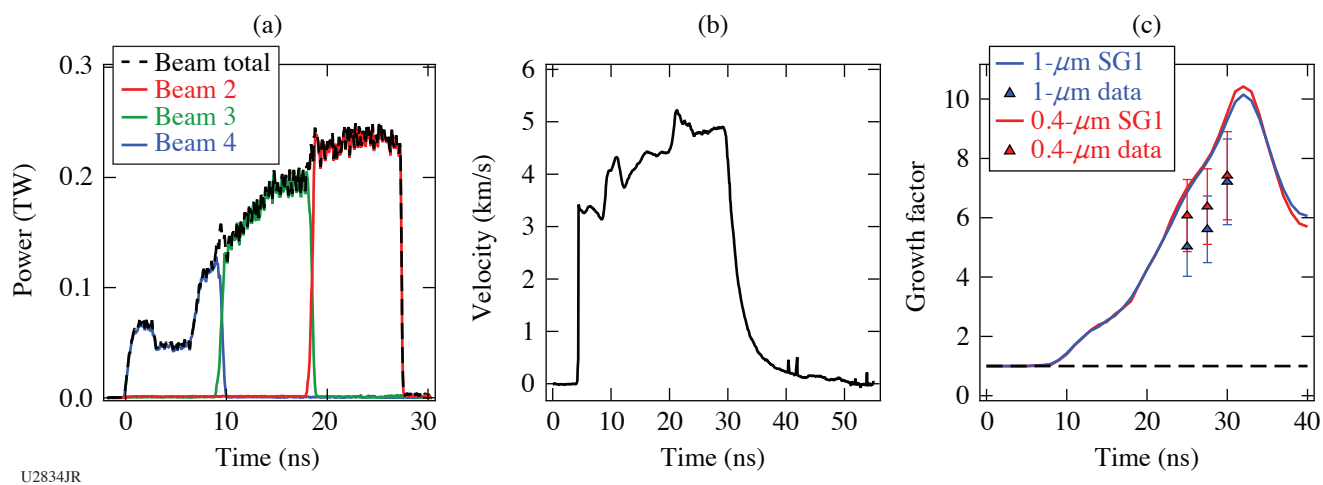


Figure 27

(a) Power delivery from three UV beams for one of the data shots. The total beam power is depicted by the dotted line. Power delivery closely matches the requested level. (b) VISAR Leg A data, showing shocks corresponding to power blips at beam stitching times. (c) RT growth calculated at three different data-collection times. The growth appears somewhat lower (but perhaps within error) of the predicted values.

Rayleigh–Taylor Strength Measurements of Copper Versus Epoxy

Principal Investigator: C. V. Stan (LLNL)

Co-investigators: H.-S. Park, T. Lockard, D. Swift, and J. McNaney (LLNL); M. P. Hill (AWE); and G. Righi (University of California, San Diego)

The effects of epoxy or other plastics on the RT growth of instabilities at temperatures relevant to solid metals (≤ 8000 K) and pressures around 1 to 2 Mbar have not been previously quantified. We have taken several measurements of directly driven tin targets with sinusoidal perturbations, where the perturbation growth was lower than can be explained by reasonable strength models. In this project we replaced tin with copper in order to provide additional benchmarking of the behavior of plastic-containing targets. The targets consisted of a Be ablator ($20\ \mu\text{m}$), a brominated plastic layer ($20\ \mu\text{m}$), epoxy (5 to $7\ \mu\text{m}$), rippled Cu ($40\ \mu\text{m}$), a LiF window ($500\ \mu\text{m}$), and fiducials. Ripple growth as a function of pressure/temperature variation was determined by face-on radiography, collected at 25 and 30 ns from laser start time using a microflag backlighter irradiated by a short-pulse beam (Fig. 28). The RT unstable interface was driven to two different temperature conditions using ramped drives with higher or lower initial shocks.

One VISAR and four radiography measurements were collected. Only the low-temperature drive was collected in VISAR due to instrumentation failure during the shot day; the results confirm that a smooth ramp with no stitching errors was produced. The four radiographs show somewhat poor contrast, which may be due to the choice of backlighter material (Cu) or the hard x-ray background from the high-intensity, short-pulse interaction with the foil. In the future, a long-pulse backlighter will be used to reduce this bremsstrahlung contribution. Preliminary analysis using only the fiducial ripples indicates that the growth is comparable to the models, suggesting that the epoxy layer may not be the cause of previously observed low growth rates in tin. The error bars are large enough at this early stage, however, to warrant caution in drawing firm conclusions. Future shots will focus on (1) determining the repeatability of the stitched drive via additional VISAR measurements and (2) comparing additional

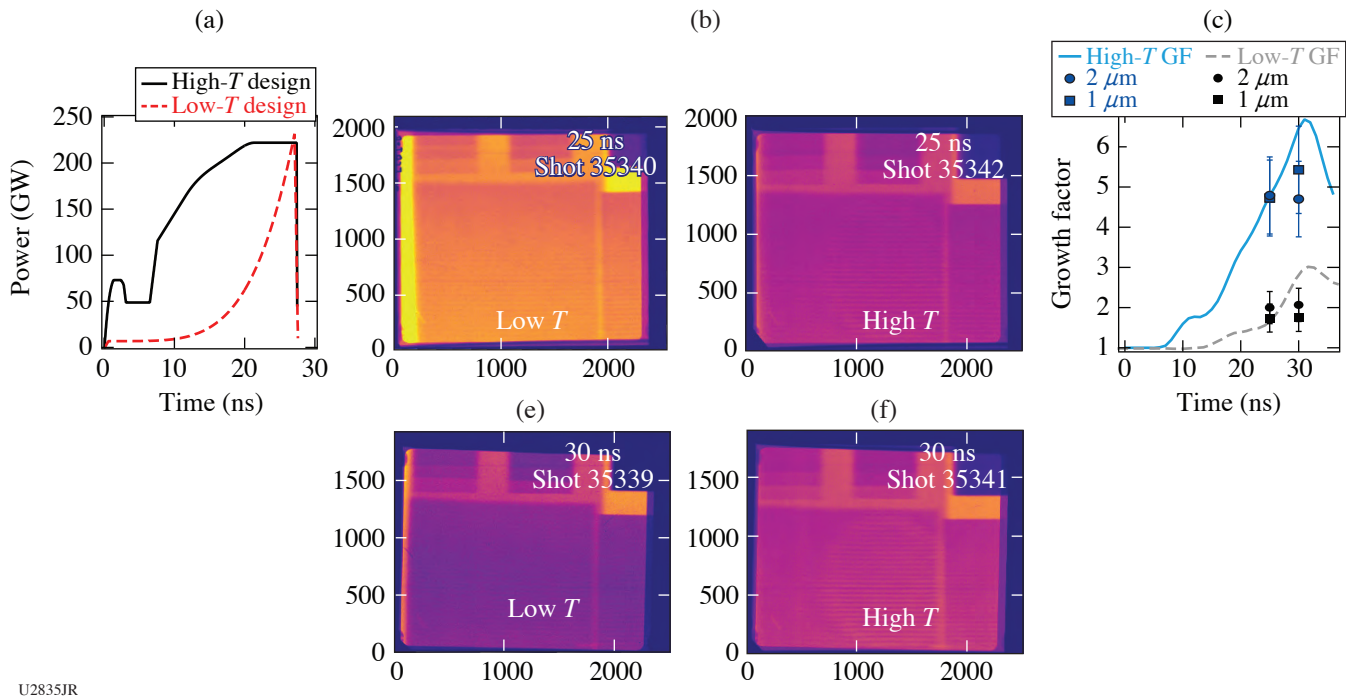


Figure 28

(a) Designed power delivery from three UV beams for high and low temperatures. The high-temperature path uses a leading shock to increase temperature rapidly, while bringing the total power and pressure peak to conditions comparable to that of the low-temperature path. (b) Radiography data collected during the shot day. (c) Preliminary calculated growth factors versus pre-shot modeling. Error bars are set to 20% of the measured value.

pusher/sample pairs. The second experiment type is platform development aimed at assessing how other pusher materials behave under similar conditions, which will inform future experiment design and model development choices.

Measuring Off-Hugoniot Equation of State by Shocking Porous Metals

Principal Investigator: A. Lazicki (LLNL)

Co-investigators: S. Jiang, F. Coppari, D. Erskine, R. London, J. Nilsen, M. MacDonald, and R. Heeter (LLNL); and M. C. Marshall (LLE)

This campaign was designed to use the crushing of pores in an initially porous sample to achieve a hot, approximately solid-density shock state. Data off of the principal Hugoniot have the potential to provide a more-discriminating test of theoretical models.

The campaign was allocated three half-days of shots in FY21. The last shot day was given some additional shots because of issues that arose with the campaign sharing the day, so we were able to collect a total of 21 shots over the year. On the first and second half-days, we measured the principal and off-Hugoniot states of gold by shocking samples of full-density and ~70% porous material (made from an Au–Ag alloy with the Ag removed), over a range of pressures. Targets with diamond ablaters, an Au heat shield, and quartz impedance-matching standard were mounted on a halfraum that was driven with 21 beams along the H7–H14 axis, and shock velocity and/or transit time in adjacent samples of quartz and porous metal were measured using the VISAR and SOP diagnostics (Fig. 29). On some of the shots, a second quartz window was glued to the rear surface of the Au sample to measure the off-Hugoniot release state. On the last shot day, we measured principal and off-Hugoniot states in Cu by shocking full-density and ~50% porous Cu samples (made by powder compaction). We attempted to constrain shock temperatures by pumping x-ray fluorescence from the Cu sample surface using a Ge backlighter and measuring the spectrum using the Z-Spec spectrometer with a cylindrical crystal. The spectroscopy data suggested that multiple x-ray sources were contributing to the signal, and the VISAR and SOP data indicated that the x-ray backlighter was itself providing a significant source of heating.

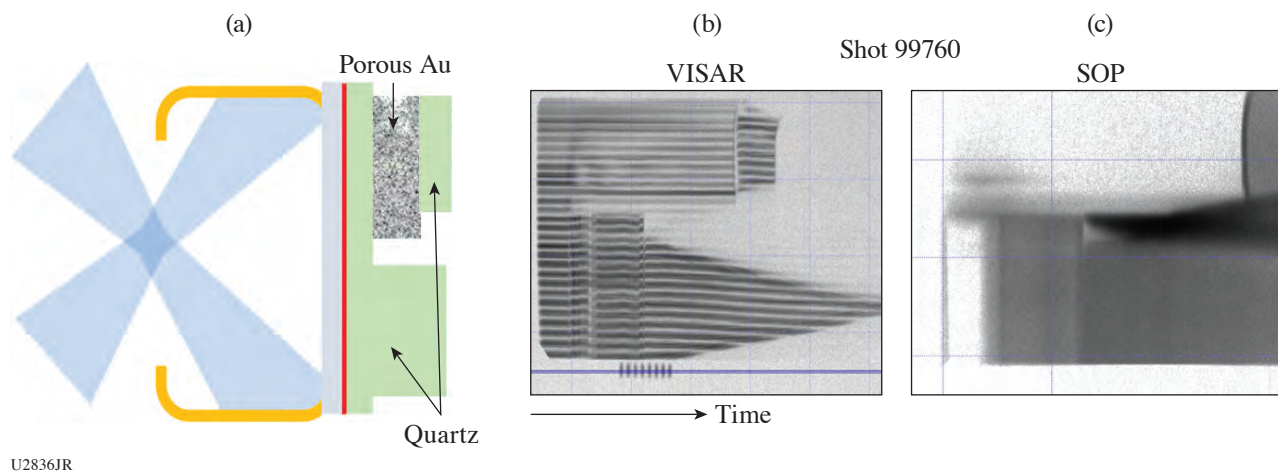


Figure 29

(a) Target configuration with VISAR and SOP data from one shot in the PorousEOS-21B Campaign, designed to measure principal- and off-Hugoniot states of Au. The VISAR diagnostic registers the *in-situ* velocity in the quartz impedance-matching standard and (b) VISAR and (c) SOP record the shock-transit time through the Au sample.

Developing X-Ray Fluorescence Spectroscopy as a Probe for High-Energy-Density Physics Experiments

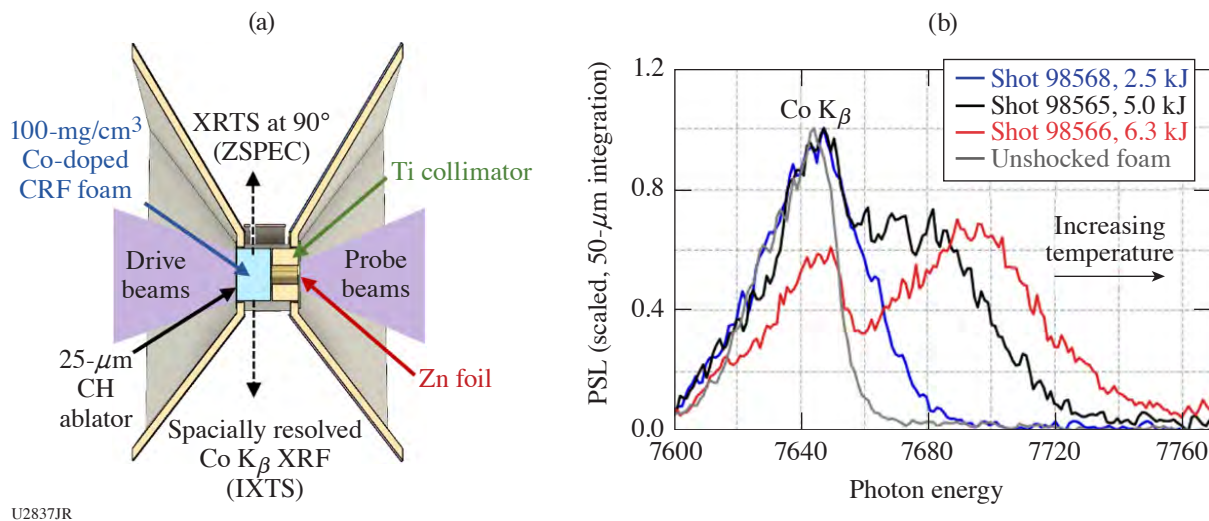
Principal Investigator: M. J. MacDonald (LLNL)

Co-investigators: T. Döppner, H. A. Scott, A. M. Saunders, P. A. Sterne, K. B. Fournier, and T. Baumann (LLNL); S. R. Klein, M. P. Springstead, K. H. Ma, and C. C. Kuranz (University of Michigan); and R. W. Falcone (University of California, Berkeley)

The goal of the FoamXRFTS-20B shot day was to continue the development of a platform using simultaneous x-ray fluorescence (XRF) spectroscopy and x-ray Thomson scattering (XRTS) to measure the EOS of shocked foams. The FoamXRFTS platform

measures XRF spectra from shock-heated foams with the goal of independently measuring the plasma temperature using XRTS to benchmark atomic models for future XRF diagnostics.

In these experiments, a planar shock wave heats a cylinder of foam doped with a mid-Z element, similar to previous results published from the Trident Laser Facility,²⁸ with the addition of an XRTS diagnostic. A laser-driven Zn He α backlighter both induced K-shell fluorescence from the Co-doped foam and served as the x-ray source for XRTS. A schematic of the experimental setup is shown in Fig. 30(a). The IXTS spectrometer recorded spatially resolved Co K β XRF, providing a measurement of the density profile of the shock wave in the foam in addition to resolving XRF spectra from the shocked and unshocked regions of the foam. This campaign has successfully demonstrated the ability to measure Co K β spectra from the shock-heated layer at a range of drive conditions with good sensitivity to the range of conditions produced, as shown in Fig. 30(b). Although the XRTS data collected in these experiments will be difficult to interpret due to noise in the data, the results will be helpful in improving the experimental setup for future campaigns. Additionally, a new conical crystal for the ZSPEC spectrometer was tested on this shot day, providing improved focusing over the 7- to 11-keV photon energy range with high collection efficiency. The conical ZSPEC will be a useful diagnostic for future x-ray spectroscopy experiments.



U2837JR

Figure 30

(a) Experimental configuration for the FoamXRFTS-20B shot day. (b) Co K β emission spectra for the unheated foam (gray) and three drive energies, showing a strong dependence of the emission energy of the Co K β emission with increasing drive energy and, therefore, plasma temperature.

Measurements of Release Isentropes of Proton Heated Warm Dense Matter with Streaked X-Ray Radiography

Principal Investigator: S. Jiang (LLNL)

Co-investigators: Y. Ping, A. Lazicki, A. Saunders, A. Do, D. Swift, J. Nilsen, P. A. Sterne, H. Whitley, and J. H. Eggert (LLNL); and M. P. Hill (AWE)

This campaign comprised two days on OMEGA EP during FY21. In FY20 we demonstrated that the platform can measure the release isentrope of warm dense matter that was heated isochorically with proton heating. The pressure–density isentrope was extracted from the streaked x-ray radiograph. The initial bulk temperature could be measured using SOP with a specially designed target. The spectrum and angular distribution of the proton source was recorded with a Thomson parabola and radiochromic films (RCF's). In FY21, we have successfully performed EOS measurement for Al at an ~ 2 -eV temperature with this platform. We have also demonstrated that the heating proton beam can be focused using a hemispherical target with proximal target structures. This enables us to perform higher-temperature measurement in the future.

The experiment used the OMEGA EP short pulse to generate a beam of protons that heated a 500- μm \times 50- μm \times 50- μm Al ribbon offset from the proton source. Three long-pulse beams were used to heat a V backlighter to provide an x-ray source

for streaked x-ray radiography. A raw radiograph image from the PJX camera is shown in Fig. 31(a). An on-shot SOP image was also displayed that suggested heating was almost completely from the proton beam and the x-ray preheat was negligible. The measured proton spectrum suggested an energy deposition density of about $9.3 \times 10^4 \text{ J/cm}^3$ in the Al sample or an initial temperature of $\sim 2 \text{ eV}$. This temperature also agreed with the measured bulk temperature from SOP. The derived release isentrope shown in Fig. 31(a) agreed with both the LEOS (red) and the *SESAME* 3720 (blue) EOS tables but did not agree with the XEOS 130 table (green).

We have also designed a hemispherical proton target with a Cu guiding structure to focus the heating proton beams generated by the short pulse. The RCF images from both a regular flat foil and this hemispherical target are shown in Fig. 31(b). The hemispherical target has generated a significantly more protons and can potentially heat the sample to a much higher temperature. We will perform a temperature scan with different proton targets in future experiments.

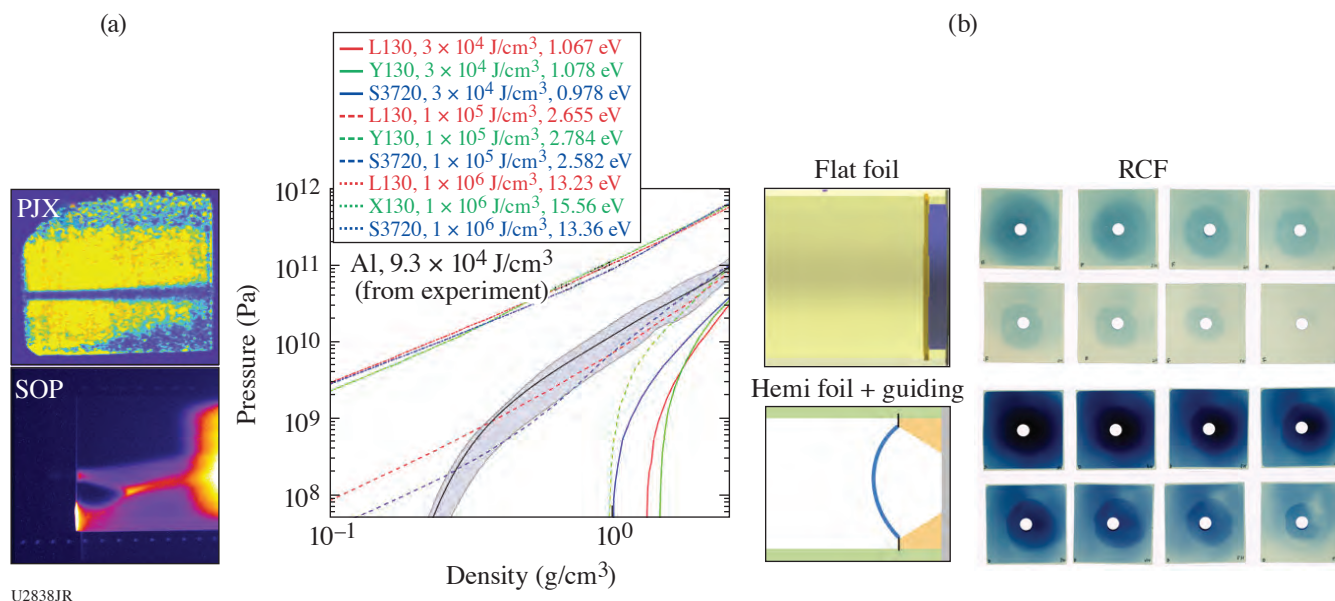


Figure 31

(a) Streaked radiograph, SOP data, and the extracted pressure–density isentrope curve. Isentrope curves from various EOS models at different energy densities/initial temperatures were also plotted for comparison. (b) RCF images of the proton beams generated by two different proton targets with the same laser pulse.

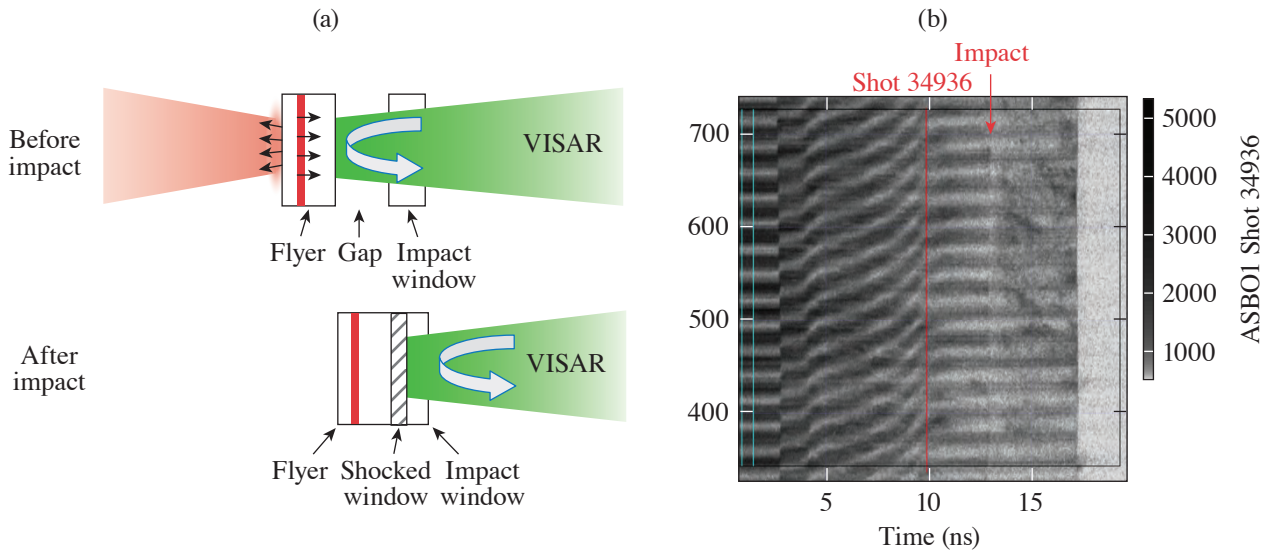
Laser-Driven Accelerated Diamond Flyer Plates for Absolute Equation-of-State Measurements

Principal Investigator: F. Coppari

Co-investigators: A. Lazicki, M. Millot, R. London, R. Heeter, and D. Braun

In order to characterize material EOS at HED conditions, there is a need for developing appropriate pressure standards. The goal here is to develop a platform for performing reference-free EOS measurements of materials in the multi-Mbar regime to be used as an absolutely calibrated pressure standard in future EOS measurements.

We were allocated one day on the OMEGA EP laser and conducted seven experiments, where we accelerated a diamond flyer plate to an increasingly high velocity across a vacuum gap of known thickness. We used the VISAR diagnostic to observe the impact of the flyer onto a diamond window. VISAR provided a measure of the flyer velocity before the impact. From that, considering the impact is symmetric, the particle velocity can be obtained. After the impact, the VISAR recorded the shock velocity [Fig. 32(a)]. From these two observables the pressure–density relation of diamond can be obtained by solving the Rankine–Hugoniot equations.²⁹



U2839JR

Figure 32

(a) Schematic showing the experimental concept and measurement. Lasers accelerate a diamond flyer across a vacuum gap, and VISAR is used to measure the flyer velocity before the impact and the shock velocity after the impact. (b) Representative VISAR data where a diamond flyer was accelerated to high velocity near 30 km/s. After the impact (red arrow), the fringe pattern is not so clear, preventing determination of the shock velocity.

A tailored-ramped pulse shape was used to slowly accelerate the flyer up to peak velocity, avoiding melting and keeping its density close to ambient density. Depending on the flyer velocity, the impact might generate a reflecting shock in the diamond window when the propagated shock is strong enough to melt the window.

During this campaign we varied the laser energy to span pressures across the diamond-melting transition. As pressure was increased, the VISAR record showed increased loss of reflectivity and nonuniformities pointing to the possibility that the diamond flyer may break up before the impact, providing an unreliable velocity measurement [Fig. 32(b)].

These issues are currently under evaluation, and they will have to be addressed before we can establish diamond as an absolute standard for equations of state measurements.

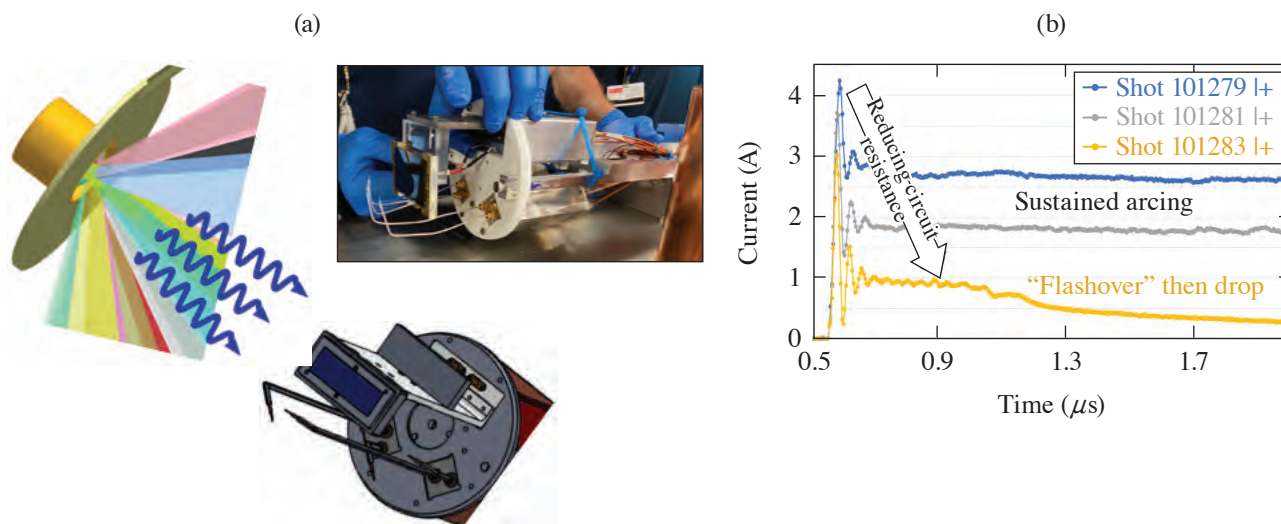
Outputs and Survivability Campaigns

Studying Electrostatic Discharge in Solar Cell Arrays Under Extreme X-Ray Irradiation

Principal Investigator: K. Widmann (LLNL)

Co-investigators: P. L. Poole, J. Emig, and B. E. Blue (LLNL); S. Seiler (Defense Threat Reduction Agency); S. Burnham (Air Force Research Academy); and J. Lorentzen, D. Scheiman, and P. Adamson (Naval Research Laboratory)

The SolarCellESD campaign seeks to determine experimentally whether prompt x rays can induce failure modes in solar arrays that are not accounted for by simply testing the individual solar cells alone because the voltage difference between neighboring cells can be hundreds of volts, depending on the overall layout of the array. These experiments on OMEGA have been fielding the smallest-possible array; i.e., 2×1 cells with electronic controls that allow the user to dial in a voltage difference (bias voltage) between the two cells and, therefore, to study the failure modes as a function of incident x-ray flux and bias voltage (Fig. 33). Previous campaigns have studied various shielding techniques, the addition of magnets to deflect charged-particle winds, and adjustments to the laser-driven x-ray source.



U2840JR

Figure 33

(a) A solar cell array (2×1) is held within the x-ray Langmuir probe diagnostic at variable standoff distances from a laser-driven hohlraum x-ray source. A variable bias voltage is placed between the cells to simulate working conditions. (b) Voltage characteristics indicative of sustained arcing were observed on this shot day to be controllable by resistance changes within the solar cell circuitry.

The FY21 shot day fielded solar cells in two TIM's with similar viewing angles on either side of a hohlraum x-ray source such that one could be used as a control while parameters such as the bias voltage, standoff, or circuit resistance were varied on the other. A hot hohlraum target was also used on this day to increase the x-ray fluence on the cells. The threshold fluence for sustained arcing was observed, while subsequent shots charting the arcing behavior as resistors were removed from the circuitry behind the solar cells. These data provide critical benchmarks that will build up on the utility this campaign has provided to in-use solar cell arrays on satellites.

Investigating Bremsstrahlung X-Ray Source via Magnetic Fields

Principal Investigator: P. L. Poole

Co-investigators: R. K. Kirkwood, S. C. Wilks, M. May, K. Widmann, and B. E. Blue

High-fluence x-ray sources can be used to test for extreme radiation environment effects³⁰ including nuclear survivability. Facilities like the NIF and Z can readily produce high fluences of x rays under 10 to 20 keV, but high-photon-energy versions of those line-emission-dominated sources are considerably weaker. The SRSxray Campaign on OMEGA investigates a different x-ray-generation mechanism that produces a bremsstrahlung spectrum using the hot electrons accelerated from strong plasma waves within the target.

In this campaign, two MIFEDS coils were utilized to generate an axial magnetic field within gold hohlraums; these fields serve to confine plasma flow and prolong the temperature and density conditions conducive to laser-plasma interactions (LPI's) that drive this x-ray source. Here, multiple wall thicknesses were used to assess the effects of B-field penetration to the plasma as well as variations in the low-density CH foam fills that have been developed on past days to enhance desired LPI. Figure 34(a) shows thicker targets enhancing the x-ray output in the desired >50 -keV range when the magnetic fields are off but with an output enhancement for thinner walls when the B field is present. These results help scale the trade-off between the B-field penetration and the greater attenuation of exiting x-ray radiation from the source.

Additionally, Fig. 34(b) shows backscattered light from two target configurations where this signal is strongly suppressed when the magnetic fields are present. This is in line with simulations³¹ and also suggests the plasma flow is constrained but still produces

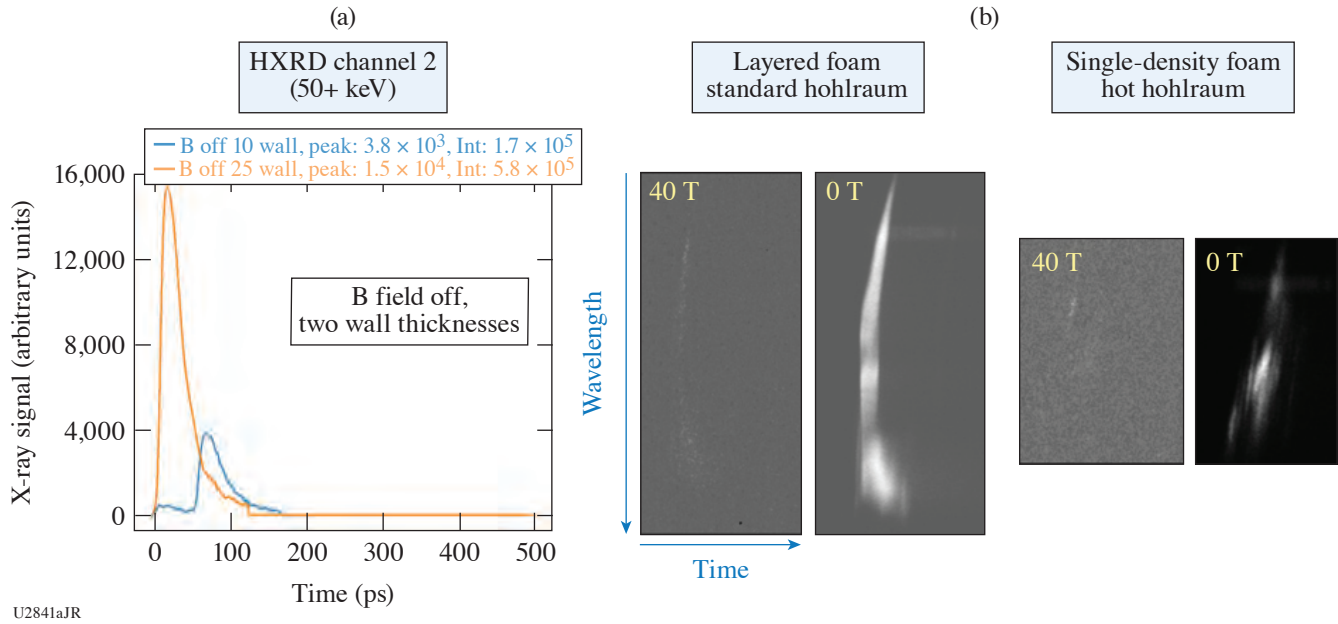


Figure 34

(a) X-ray signal from channel 2 (≥ 50 -keV photons) for two different hohlraum wall thicknesses, showing a strong increase for the thicker option (B field off here). (b) Streak camera data for SRS wavelengths show a reduction in backscattered light when strong B fields are present.

hot electrons relevant to increased x-ray bremsstrahlung output. These findings are instrumental to the design of upcoming NIF shots with magnetic fields intended to enhance this x-ray source.

Comparing CH and HDC Exploding-Pusher Performance

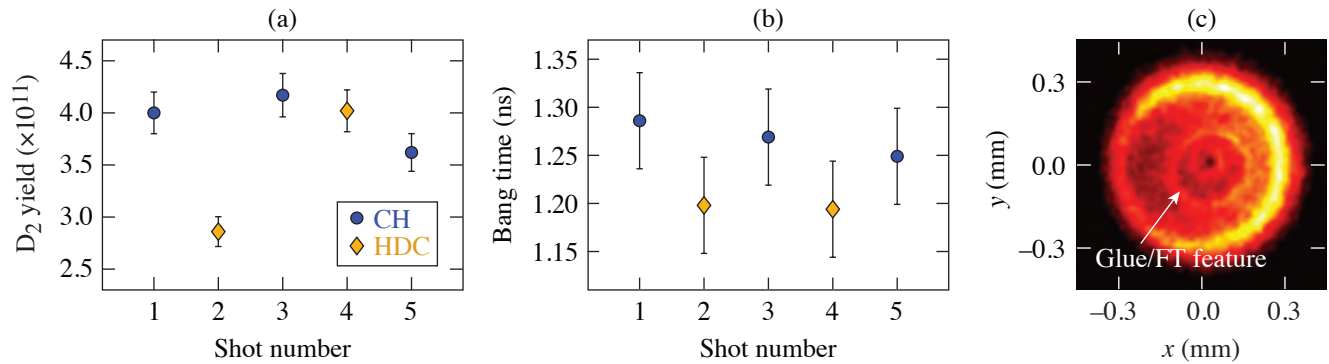
Principal Investigator: M. Hohenberger (LLNL)

Co-investigators: P. W. McKenty and M. J. Rosenberg (LLE); and L. Divol, C. B. Yeaman, B. E. Blue, and W. W. Hsing (LLNL)

Experiments were conducted to directly compare nuclear yield and performance of exploding-pusher (XP) targets with CH and HDC ablaters. The nuclear yield in XP's primarily stems from shock heating of the fusionable fill gas, and these implosions exhibit low convergence, low areal densities, and high ion temperatures. By virtue of their shock-driven nature, XP's are insensitive to degradation mechanisms that affect high-convergence implosions, such as electron preheat or RT instabilities. While yield amplification or a propagating burn is not accessible at these conditions, significant neutron yields $>10^{16}$ have been demonstrated on the NIF, making XP's robust sources for, e.g., nuclear effects studies or backlighters.³² Many of these applications greatly benefit from increased nuclear fluence, and increasing XP performance is a key programmatic goal. XP's fielded on the NIF are typically CH capsules, but HDC has been identified as a potentially interesting ablator material with simulations predicting increased absorption efficiency and therefore higher nuclear yields.

To test this experimentally, 860- μm -diam HDC and CH targets filled with room-temperature D_2 gas at 8 atm were symmetrically imploded with 60 OMEGA beams (~ 400 J/beam, 1-ns square). The targets were mass-matched featuring 4- μm - and 12- μm -thick walls, respectively. CH capsules were diffusion filled and mounted via an 18- μm stalk, while the nonpermeable HDC capsules required a 70- μm fill tube. Experimental data for the CH (circle) and HDC (diamond) are shown in Fig. 35. Notably, the CH yield is comparably robust varying between 3.6 and 4.2×10^{11} , while HDC exhibits significant variation for the two shots, either below (2.9×10^{11}) or matching (4.0×10^{11}) the CH. In contrast, the bang time is consistent for both HDC experiments and ~ 50 ps earlier than for the CH. A possible explanation for these data is the perturbation imposed by the fill tube and glue spot unique to the HDC design. Self-emission x-ray images of the HDC implosions exhibit a noticeable "ring" feature, which lines up with the expected position of the fill tube. No such feature is visible in the CH data. It is likely this caused detrimental mix

and capsule breakup for the HDC, thus limiting performance. The fact that one HDC implosion matched the CH performance despite this issue is a promising result, and future experiments will test a “fill-and-plug” design, with HDC capsules prefilled through a small hole. This is then plugged prior to fielding the capsule, thus sealing in the gas fill and causing a much smaller perturbation to the implosion.



U2872JR

Figure 35

(a) Experiments comparing HDC (diamond) and CH (circle) ablator performance in exploding-pusher implosions saw no yield improvement for the HDC. (b) HDC implosions exhibited a consistently earlier bang time. (c) Self-emission data of HDC implosion at 0.6 ns show a perturbation attributed to the fill tube and glue spot unique to the HDC design. No such feature can be seen in CH data.

Collisionless Shocks Produced in Magnetized Plasmas

Principal Investigator: E. Tubman (LLNL)

Co-investigators: B. Pollock, G. Swadling, D. Higginson, D. Larson, B. E. Blue, and H.-S. Park (LLNL); M. Manuel (GA); and P. Tzeferacos and K. Moczulski (University of Rochester)

This campaign sets out to investigate high-altitude nuclear explosions (HANE's) using the Omega Laser facility. HANE's conducted by both the USA and USSR between 1958 and 1962 sent out shock waves that created long-lasting radiation belts of high-energy, charged particles.³³ Satellites close to these events experienced substantial radiation damage, and the effects were even observed at the Earth's surface, such as in Hawaii where street lighting was affected. Computer simulations are not entirely accurate in modeling certain aspects of the HANE's, in particular the mechanism via which the radiation belts are formed. The Omega Laser Facility provides an ideal environment in which to produce collisionless shocks within magnetized, low-density plasma environments and assist in our understanding of the early-time evolution of HANE's and better inform our codes.³⁴

To field this experiment at the Omega Facility requires several different target components. First, a low-density, magnetized plasma “background” region is created using a hydrogen gas jet, within a MIFEDS Helmholtz coil setup. The gas jet produces a density of $\sim 10^{18}$ cm⁻³ and the MIFEDS themselves provide an ~ 10 -T field. The central region of the MIFEDS, where the gas is present, is irradiated with five laser beams producing an ionized, magnetized plasma. Then, after 6 ns to allow the background plasma to reduce in temperature, a second group of laser beams with $I \sim 5 \times 10^{14}$ W/cm² impact on a “piston” drive target composed of beryllium. This drives a high $M_A > 5$ shock from the front side of the target. The aim is to generate a collisionless shock coupled to the magnetized background ions. The shock, as it propagates outward, is expected to sweep up field, and a diamagnetic cavity may form at its front due to the large debris ion gyroradius and the low ambient plasma density.³⁵ Proton imaging, driven using the OMEGA EP beam, allows one to measure the magnetic-field structures, and a 2ω probe beam is used for Thomson scattering, enabling the plasma T_e , T_i , n_e , and flow velocity to be calculated. The setup for this experiment is shown in Fig. 36(a).

Figures 36(b) and 36(c) show radiograph images produced by the protons passing through the magnetic fields 4 ns after the drive beams have started ablating material from the Be target. Figure 36(b) shows a potential shock structure appearing (darker line) between two bubble-like voids. For this shot, the RCF contains many features and needs further analysis to confirm the

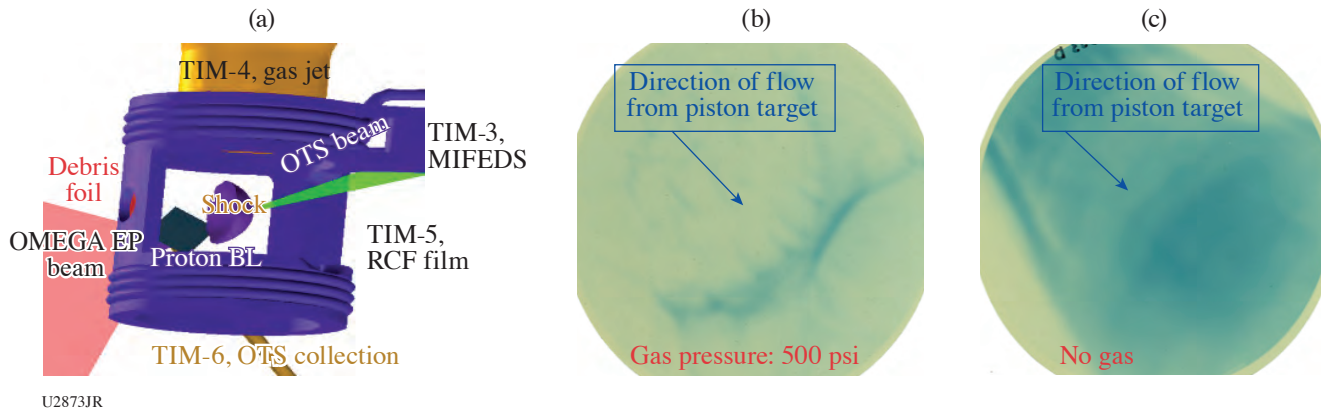


Figure 36 (a) A schematic of the setup for the experiment. The shock propagates from the front side of the target into the region of pre-ionized, premagnetized gas. (b) An RCF image of the shock driven from the piston target located in the top left (out of view) and propagates to bottom right, through a background plasma. (c) An RCF slice with no gas jet present where plasma is driven from the piston target through the magnetic fields produced by the MIFEDS.

structures observed. Figure 36(c) shows the field structure of the MIFEDS when no gas is present. Plasma will have been ablated from the piston target in the top left of the image and expanded outward; however, without the background gas, a shock feature is not observed.

In addition to the proton mapping of the fields, Thomson-scattering data were also collected for shots with and without a background gas. The results are shown in Fig. 37. The IAW scatter allows one to measure the flow velocities as well as temperatures and densities. The latter of these parameters will be further corroborated using the results from the electron plasma wave. The Thomson-scattering volume is located at the center of the MIFEDS coils and can be used to measure when the shock wave passes across this region. Figure 37(b) shows that no scatter is observed from this central region at earlier time (<2.5 ns after the beams are incident on the piston target) and the only signal at this time comes from stray light at the probe-laser wavelength. After 2.5 ns, we do see IAW scatter, and preliminary analysis of the features suggest that without the presence of a magnetized background plasma, the piston material propagates out with velocities of $v \sim 1500$ km/s. When a backing gas-jet pressure of ~ 100 psi is used, the piston material is slowed to ~ 1100 km/s [Fig. 37(a)]. Material behind the front of the plasma flow then decreases in both cases, as shown by the gradient in the scattered wavelength, tending back to the original probe wavelength. These measurements can be compared to the hydrodynamic simulations run using *HYDRA*. For the no-gas case, they match well with predictions. Further analysis will be completed on this data and will help to inform future shot days where we will also investigate the effects of driving shocks from diamond targets.

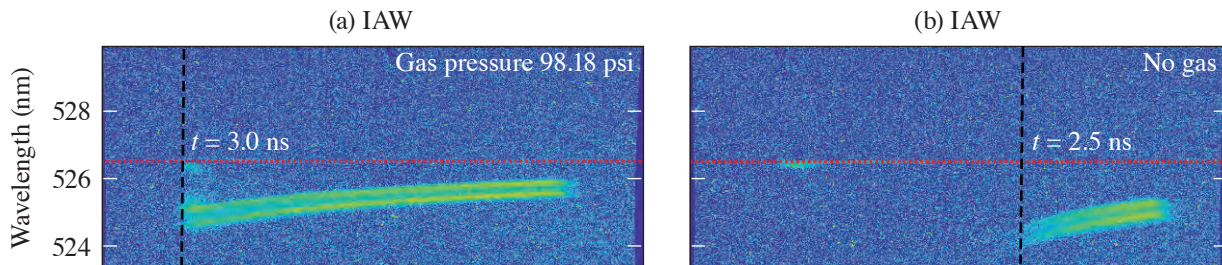


Figure 37 (a) The ion-acoustic feature from Thomson scattering shows material present in the central region of interest 3 ns after the lasers are incident on the piston target. The gas-jet backing pressure was ~ 100 psi. (b) The ion-acoustic feature shows faster propagation velocities when the piston target material propagates out into vacuum (no gas jet present).

1. *LLE 1999 Annual Report, October 1998–September 1999*, 222, Rochester, NY, LLE Document No. DOE/SF/19460-332 (2000).
2. J. H. Eggert *et al.*, *Nat. Phys.* **6**, 40 (2010).
3. M. Millot *et al.*, *Phys. Plasmas* **27**, 102711 (2020).
4. S. Le Pape *et al.*, *Phys. Rev. Lett.* **120**, 245003 (2018).
5. M. Millot *et al.*, *Phys. Rev. B* **97**, 144108 (2018).
6. W. A. Farmer *et al.*, *Phys. Plasmas* **27**, 082701 (2020).
7. C. Goyon *et al.*, *Phys. Rev. E* **95**, 033208 (2017).
8. J. J. Santos *et al.*, *New J. Phys.* **17**, 083051 (2015).
9. H. Daido *et al.*, *Phys. Rev. Lett.* **56**, 846 (1986).
10. K. F. F. Law *et al.*, *Appl. Phys. Lett.* **108**, 091104 (2016).
11. G. J. Williams *et al.*, *J. Appl. Phys.* **127**, 083302 (2020).
12. C. Goyon *et al.*, *Phys. Rev. E* **95**, 033208 (2017).
13. R. A. Simpson *et al.*, *Phys. Plasmas* **28**, 013108 (2021).
14. G. G. Scott *et al.*, *Rev. Sci. Instrum.* **93**, 043006. (2022).
15. C. Courtois *et al.*, *Phys. Plasmas* **28**, 073301 (2021).
16. D. R. Rusby *et al.*, *Bull. Am. Phys. Soc.* **66** (2021).
17. A. M. Saunders *et al.*, *Phys. Rev. Lett.* **127**, 155002 (2021).
18. M. C. Marshall *et al.*, *J. Appl. Phys.* **127**, 185901 (2020).
19. D. E. Fratanduono *et al.*, *Science* **372**, 1063 (2021).
20. J. R. Rygg *et al.*, *Rev. Sci. Instrum.* **91**, 043902 (2020).
21. N. Dubrovinskaia *et al.*, *Sci. Adv.* **2**, e1600341 (2016).
22. A. Dewaele *et al.*, *Nat. Commun.* **9**, 2913 (2018).
23. N. A. Smirnov, *J. Phys.: Condens. Matter* **29**, 105402 (2017).
24. R. Briggs *et al.*, *Phys. Rev. Lett.* **123**, 045701 (2019).

25. S. K. Han *et al.*, Phys. Rev. B **103**, 184109 (2021).
26. E. J. Gamboa *et al.*, Rev. Sci. Instrum. **83**, 10E108 (2012).
27. A. Do *et al.*, Rev. Sci. Instrum. **91**, 086101 (2020).
28. M. J. MacDonald *et al.*, J. Appl. Phys. **120**, 125901 (2016).
29. Ya. B. Zel'dovich and Yu. P. Raizer, *Physics of Shock Waves and High-Temperature Hydrodynamic Phenomena*, edited by W. D. Hayes and R. F. Probstein (Dover, Mineola, NY, 2002).
30. M. J. May *et al.*, Phys. Plasmas **25**, 056302 (2018).
31. B. J. Winjum *et al.*, Phys. Rev. E **98**, 043208 (2018).
32. C. B. Yeamans *et al.*, Nucl. Fusion **61**, 046031 (2021).
33. C. E. McIlwain, Science **142**, 355 (1963).
34. D. B. Schaeffer *et al.*, Phys. Rev. Lett. **119**, 025001 (2017).
35. D. S. Clark *et al.*, Phys. Plasmas **20**, 056318 (2013).

FY21 Los Alamos National Laboratory Experimental Campaigns at the Omega Laser Facility

Mshock 2021: Effects of Heating on Instability Growth

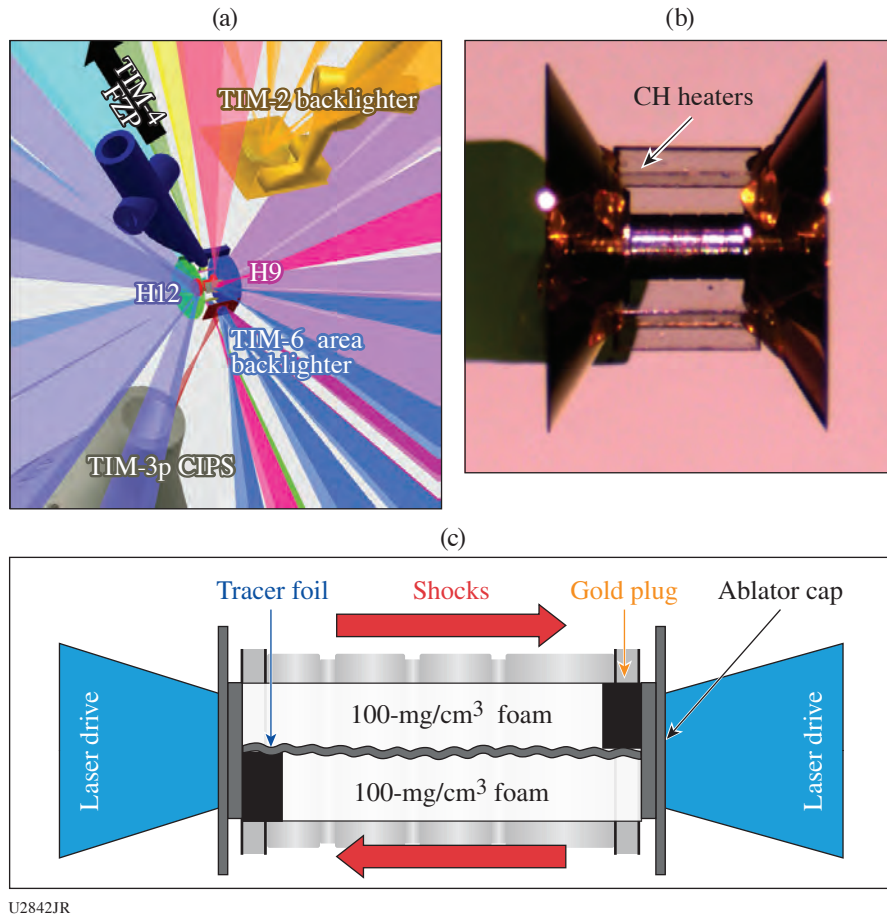
Principal Investigators: K. A. Flippo, F. W. Doss, A. Rasmus, C. Di Stefano, B. Tobias, and E. C. Merritt

The LANL High-Energy-Density Hydro team has adapted our OMEGA Shear instability platform to study the effects of heating on a mixing interface similar to what might occur in the inner shell of a double-shell-type inertial confinement fusion (ICF) design. The platform is motivated by simulations presented in Haines *et al.*¹ that suggested the timing of heating can have a significant impact on instability development. These experiments are an extension of previous work in 2020, where we had adapted a similar Richtmyer–Meshkov (RM)/Rayleigh–Taylor (RT) platform for studying the effects of heating on instability growth under shock–reshock conditions. In both platforms the mixing interface can be heated before, after, or during shock arrival and instability onset using hot-electron and x-ray emission from driven CH foils surrounding the main target at a distance. The current design allows for heating of a high-density interface surrounded by low-density foam. The mixing layer material can be chosen with any density and/or composition, but we typically chose solid-density plastic or metal foils, which can be heated from several eV up to around 100 eV depending on layer material and thickness and heater drive laser power. Strong shocks (from the drive beams) can then interact with these layers from either end of the shock tube. These experiments are intended as platform development for heated instability platform for OMEGA and as proof of principle for adaption to larger facilities such as the National Ignition Facility (NIF) as well.

In this experiment we use several variations of the LANL Shear Platform to test the effects of heat deposition on the mixing layer (heat flux out of the layer) and across the mixing layer (heat flux into the layer), but changing the materials (absorption properties) of various target components. The shear target (Fig. 1) is composed of a Be shock tube containing two hemi-cylindrical foams separated by a solid-density foil. At either end of the tube is a gold plug that blocks the shock on that side of the foil, creating a system of two counter-propagating shocks on either side of a mixing layer. In these experiments the tracer foil and foam are either Fe (high absorption) and 100 mg/cm³ CH (low absorption) to test heat flux out of the layer, or Be (low absorption) and 100 mg/cm³ Cu-doped CH (high absorption) to test heat flux into the layer. The shock tube is surrounded by several 10- μ m-thick CH foils driven by eight to nine beams that offer about 4 kJ of laser energy of which about 50% to 25% can be converted into hot electrons and x rays for heating the target. The main target also has an attached ten-inch manipulator TIM-6 backlighter (BL) that can be used to test a Fresnel zone plate array, and the setup has a TIM-2–inserted BL for use with the primary x-ray framing camera (XRFC) on TIM-3.

Experiments showed we were able to heat the target with no significant heating asymmetry as observed in the RM/RT platform (Fig. 2). This is consistent with our expectation that the Shear Platform would show more-uniform heating due to the mixing plane being orthogonal to the heating sources. We do see significant new structure in the radiographs of the heated mixing layer for both target material variations. However, the images also show more background shock structure, indicating that we may be driving radially inward shocks from heating the tube. Future experiments will help us determine how much of the new structure in the mixing layer is an effect of extra transient shocks, and how much is due to heating; they will also help us develop potential mitigation strategies for tube heating.

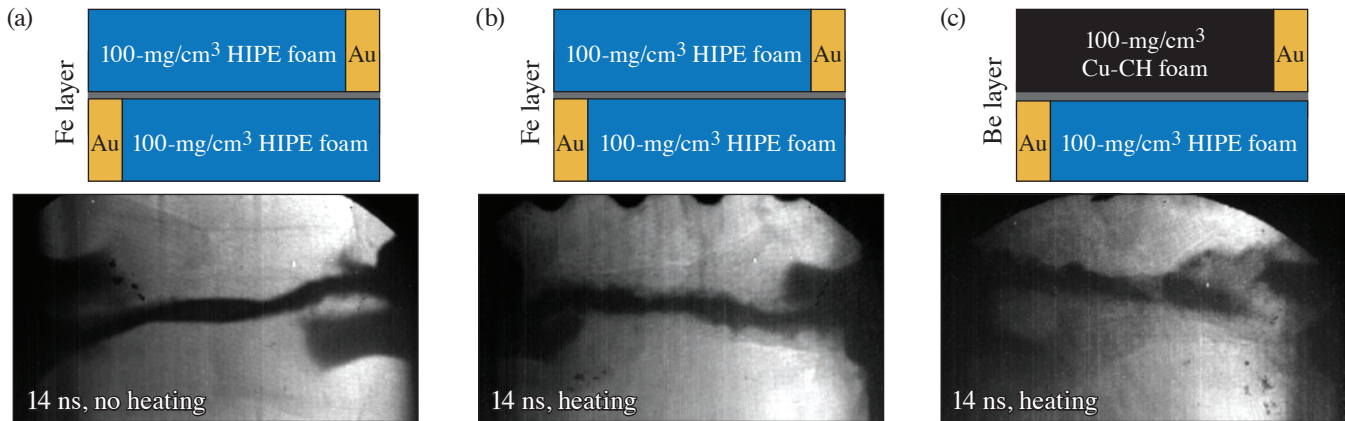
This work was supported by Los Alamos National Laboratory under Contract No. 89233218CNA000001 with Triad National Security, LLC.



U2842JR

Figure 1

(a) VisRad model of the shock-tube target, associated shock drive and heater drive beams, BL target, and diagnostic lines of sight. (b) Pre-shot target photograph with CH heater foils. (c) Schematic of the Shear physics package.



U2843JR

Figure 2

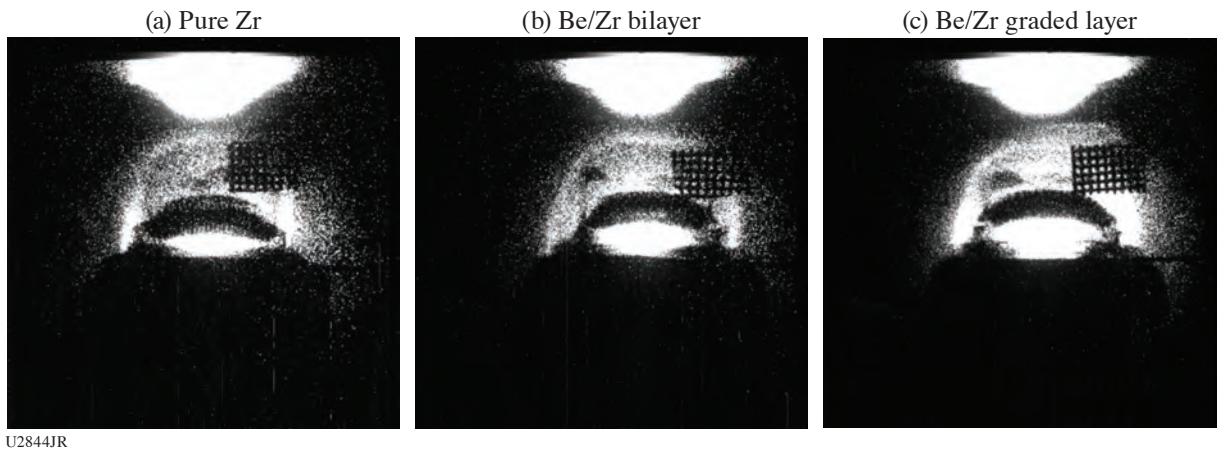
Radiography data of two target types with and without heating, at late times in the shear layer development.

DSPlanar

Principal Investigators: A. Rasmus, S. Palaniyappan, E. Loomis, D. Stark, N. Christensen, and A. Strickland

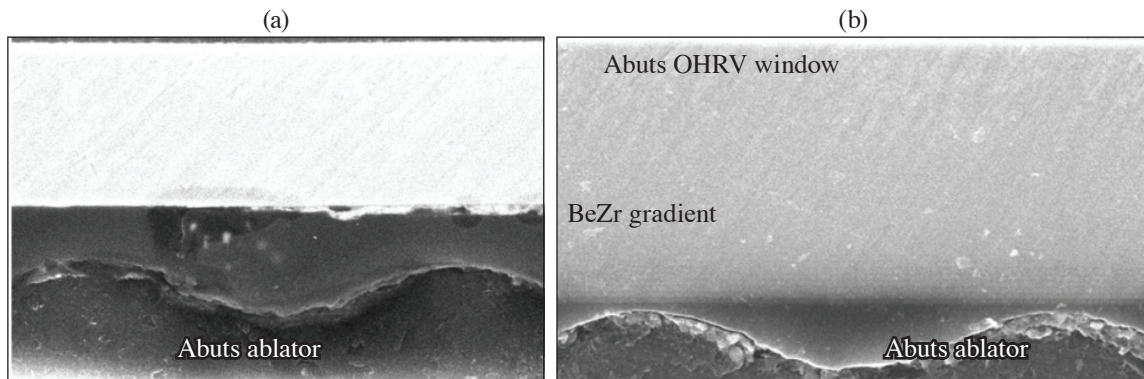
The Double-Shell Campaign uses a two-shell ICF target. Between the outer and inner shells, a foam cushion is used to assist in the transfer of momentum between the two shells. The inner shell is typically a high-Z metal. The large-density jump between the foam and inner shell presents an interface that is highly unstable to fluid instabilities due to the large Atwood number. A lower-density “tamper” (e.g., beryllium) is typically used to step the density transition between inner shell and foam pusher. A density gradient can be used to further damp instability growth. DSPlanar-21A and B aimed to test the damping of instability growth by a density gradient by measuring the impact of a density gradient on interface perturbation growth using radiography (21A) and on shock ripples using the OMEGA high-resolution velocimeter (OHRV), 2-D VISAR (velocity interferometer system for any reflector) diagnostic (21B).

DSPlanar-21A used radiography to compare hydrodynamic instability growth in pure-Zr layers, Be/Zr bilayers, and Be/Zr graded layers (see Figs. 3 and 4). The measured instability growth shows reduced growth in both the bilayer and graded-layer targets compared to the pure-Zr layer; however, among the bilayer and the graded layer, the difference in growth is not significant.



U2844JR

Figure 3
Radiographs of hydrodynamic instability growth in a (a) pure-Zr layer, (b) Be/Zr bilayer, and (c) Be/Zr graded layer.



U2845JR

Figure 4
SEM images of (a) a Be/Zr bilayer and (b) a graded layer. A sinusoidal perturbation is machined onto the Be face of each layer to seed a shock ripple.

DSPlanar-21B attempted to measure a difference between instability growth in the graded and bilayers by using the OHRV diagnostic and measuring a different aspect of instability growth, i.e., shock ripples instead of interface perturbations. DSPlanar-21B targets consisted of a stacked set of materials designed to produce a shock, imprint a ripple on it, damp the ripple by propagating it through a graded or steep material transition, and finally image the rippled shock inside a PMMA window (see Fig. 5). Be/Zr graded layers and bilayers (see Fig. 4), as well as Be/W graded layers, were shot. DSPlanar-21B achieved a limited set of physics goals due to the unavailability of the OHRV. As such, we shot our joint active shock breakout (ASBO)/OHRV targets using only the ASBO diagnostic. This reduced data set allowed us to troubleshoot blanking issues with our target stack and gain insight into shock timings and strengths in our targets.

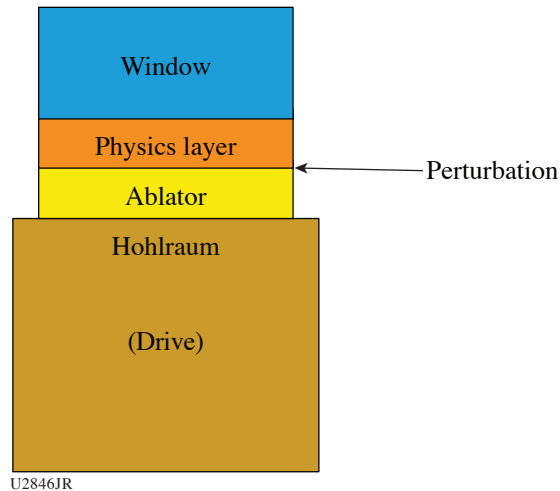


Figure 5
A schematic of DSPlanar-21B targets.

Gas-Filled Cylindrical Implosion at the Omega Laser Facility

Principal Investigators: S. Palaniyappan, J. P. Sauppe, L. Kot, K. A. Flippo, A. Strickland, T. Day, R. Roycroft, K. L. Stalsberg, and J. L. Kline

The CylDRT21A shot day was designed to study the nonlinear growth of the deceleration-phase RT growth in gas-filled and foam-filled scale-1 cylindrical implosion. The aluminum marker in the scale-1 cylinder has the nominal $m = 20$ sine wave perturbation with $4\text{-}\mu\text{m}$ amplitude on the inner side of the marker layer. We had two main goals for this shot day: (1) to study hydro-scaling between a NIF scale-3 cylinder implosion and an OMEGA scale-1 implosion with low foam-fill density at a convergence ratio of ~ 5 ; and (2) to test a propane gas-filled (10 mg/cm^3 , i.e., $\sim 5\text{-atm}$ pressure) scale-1 cylinder implosion in preparation for the FY22 NIF gas-filled cylindrical implosion.

Figure 6 shows the VisRad model of the foam-filled cylindrical implosion experiment. The main cylinder target is inserted via TIM-5 (also used as the gas fill line) and aligned along the P6–P7 axis. The TIM-4 axial backlighter (Fe) is attached to the main cylinder target. We use x-ray framing camera 3 (XRFC3) in TIM-6 to capture the on-axis radiograph of the cylinder and will use a nose tip with $12\times$ magnification with a $10\text{-}\mu\text{m}$ pinhole for the axial radiography. We also have $20\text{-}\mu\text{m}$ pinholes for backup. For the side view along the TIM-2/TIM-3 axis, we use $6\times$ magnification, a $15\text{-}\mu\text{m}$ single pinhole, and XRFC4 with a single strip. The sidelighter (V) is inserted via TIM-2.

Figure 7 shows the synthetic x-ray radiograph of the 10-mg/cm^3 gas-filled cylindrical implosion from the *xRAGE* simulation. The corresponding experimental figure is shown in Fig. 8 along with the side-on radiograph. The measured radiograph differs from the pre-shot calculation in the radial extent of the aluminum marker on the outer side. We are performing post-shot simulations to better understand the measured growth in comparison to the pre-shot simulation.

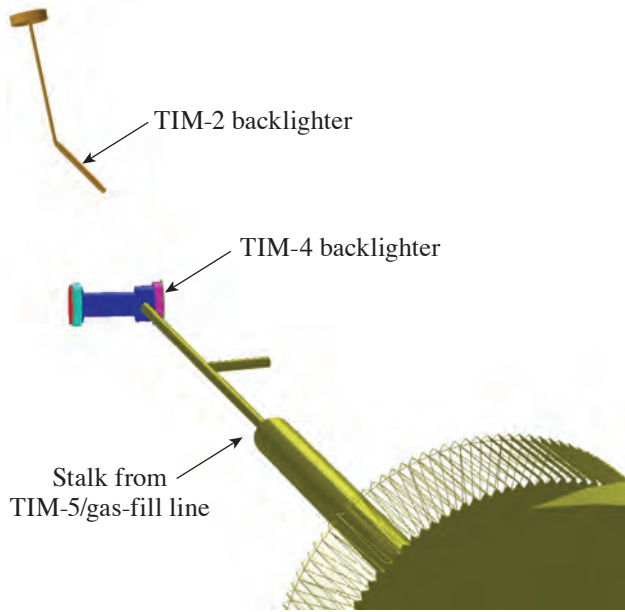
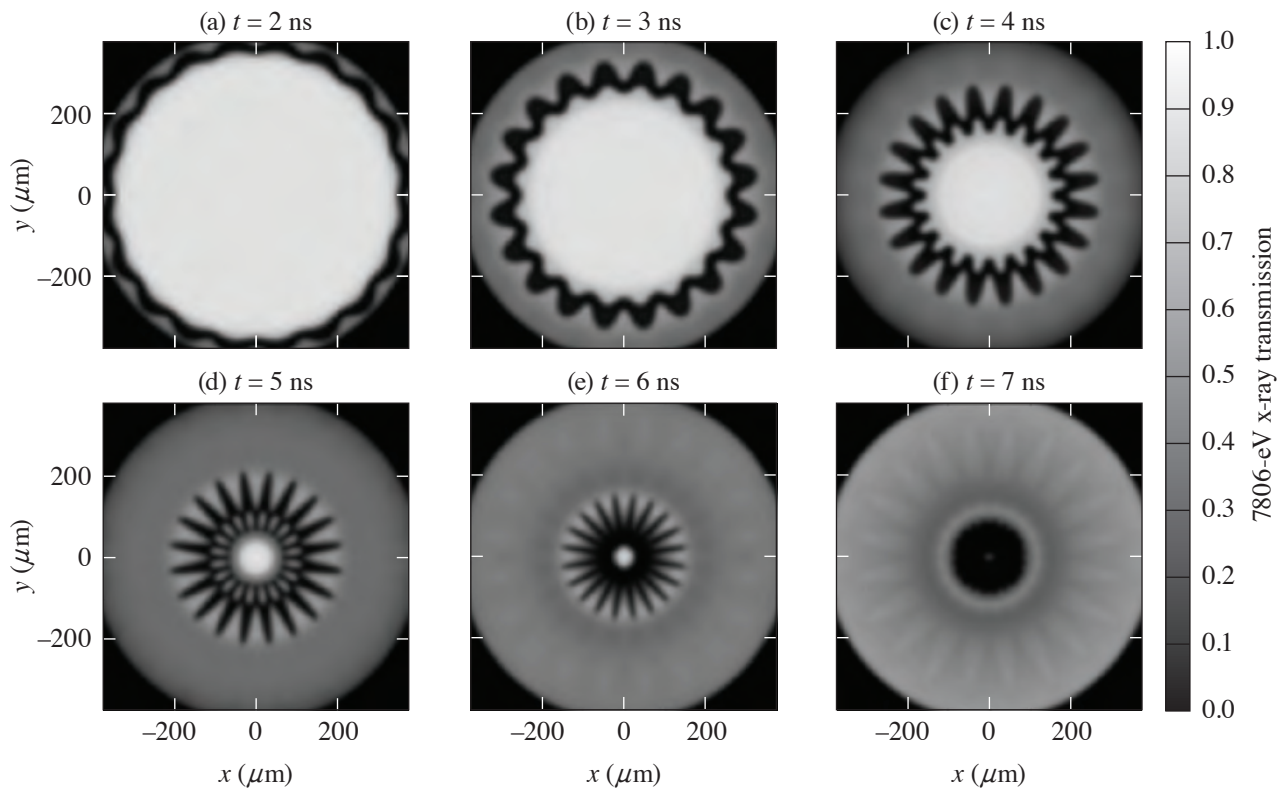


Figure 6
Experimental setup on OMEGA EP for proton beam generation.

U2847JR



U2848JR

Figure 7
Synthetic radiograph of the 10-mg/cm³ gas-filled cylindrical implosion with mode-20 sine wave initial perturbation from *xRAGE* calculation.

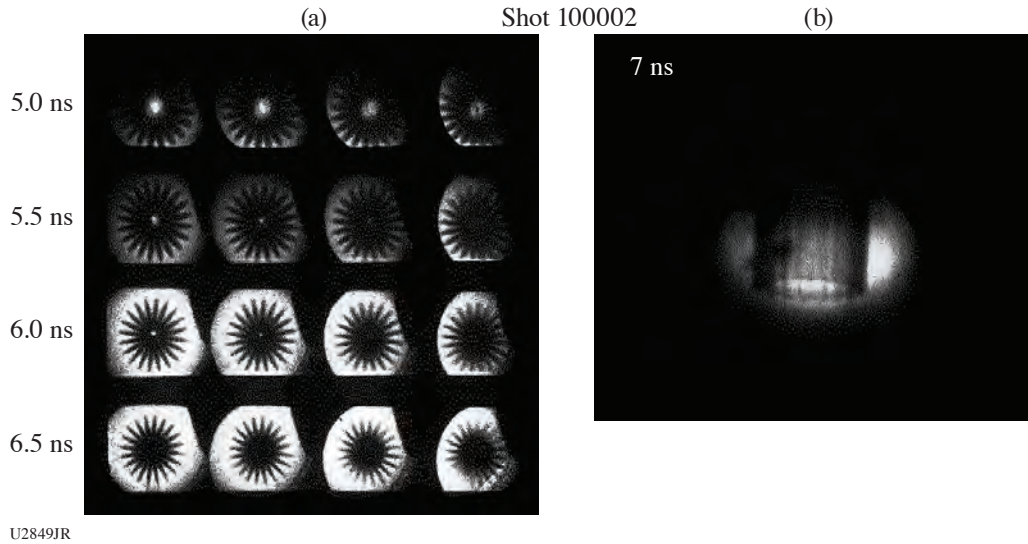


Figure 8
Experimental radiograph of the 10-mg/cm³ gas-filled cylindrical implosion. (a) Axial radiograph and (b) side-on radiograph.

Laser-Driven Proton Radiography of Shocked Plastic Foil

Principal Investigators: S. Palaniyappan, C. Huang, A. Favalli, D. Broughton, and R. Reinovsky (LANL); and S. Klein (University of Michigan)

1. Multi-Probe 21A

The goal for the FY21 Multi-Probe Project was to generate short-pulse laser-driven protons and radiograph the shocked plastic foil with those protons. During the Multi-Probe 21A shot day we characterized the protons generated from a short-pulse-driven thin plastic foil. Later, during the Multi-Probe 21B shot day, we used those protons to image a shocked plastic foil.

We generated a proton beam on OMEGA EP by driving a thin plastic foil with the sidelighter beam. The sidelighter beam delivered a maximum of 500 J with a 0.7-ps pulse duration. The foil thickness was 600 nm. The protons were detected using a radiochromic film (RCF) film pack held by the near-target arm (NTA) (see Fig. 9). Some plastic targets had a CPC (compound parabolic concentrator) in front of them to help better focus the laser beam.

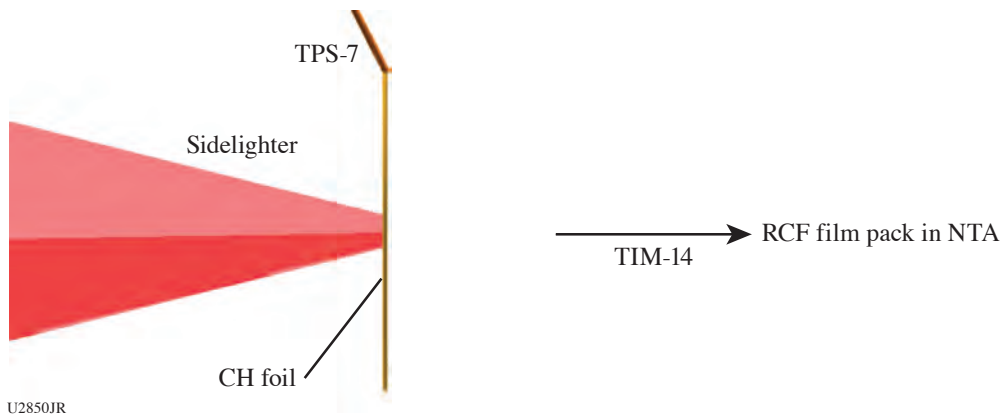
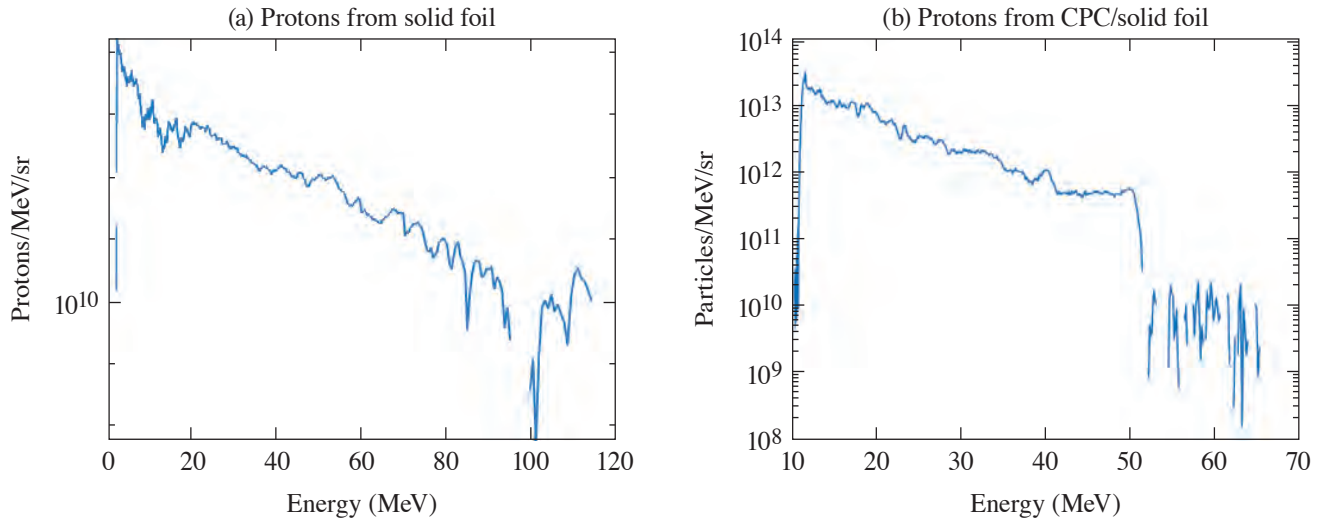


Figure 9
Experimental setup on OMEGA EP for proton-beam generation. TPS: Target Positioning System.

Figure 10 shows the measured proton spectra from both the thin plastic foil and the same foil with a CPC cone in the front. Compared to the targets with the CPC cones, the foils alone performed much better and generated protons up to ~100 MeV in energy. In comparison, the targets with the CPC cone generated protons up to 50 MeV in energy. This is contrary to what we had expected originally. Therefore, we decided to use only the thin plastic foils without the CPC cone for our future proton-generation experiments.

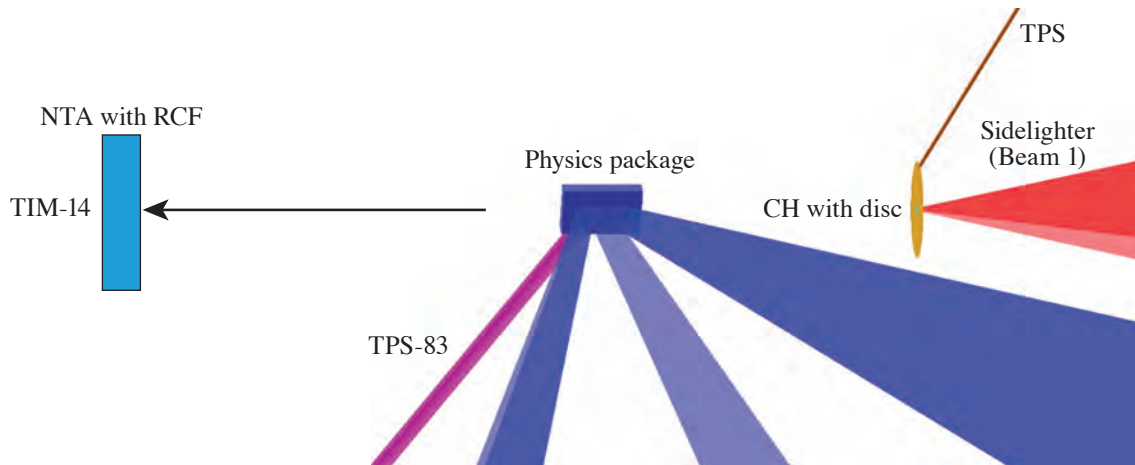


U2851JR

Figure 10
Measured proton spectra from (a) thin plastic foil and (b) thin plastic foil with CPC in the front.

2. Multi-Probe 21B

Figure 11 shows the experimental setup on OMEGA EP for proton radiography. The proton beams are generated from a short-pulse-driven thin plastic foil. Three long-pulse UV beams arranged in a line drive the physics package. The protons are detected using an RCF pack in TIM-14 held by the NTA.



U2852JR

Figure 11
Experimental setup on OMEGA EP for proton radiography.

Figure 12 shows the proton radiograph of the shock-driven thin plastic foil. We are currently working on understanding the proton radiograph.

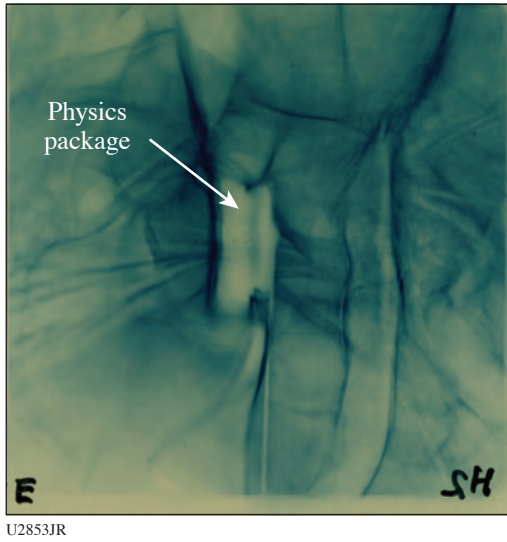


Figure 12
Proton radiograph of a shocked thin plastic foil.

Evaluation of Two-Photon Polymerization Printed Structures as Low-Density Supports in Multishell Targets

Principal Investigators: B. S. Scheiner, M. J. Schmitt, D. W. Schmidt, and L. Goodwin (LANL); and F. J. Marshall, P. M. Nilson, and R. S. Craxton (LLE)

The *Revolver 20 B/C* (delayed to FY21) Campaigns evaluated the fabrication and use of low-density (5- to 20-mg/cm³), two-photon polymerization (2PP) printed structures as a support for the inner shell of a direct-drive double-shell target.² The 2PP hemispherical structures, an example of which is shown in Fig. 13(a), were printed in a stochastic Voronoi lattice geometry³ and were composed of CH_{1.72}N_{0.086}O_{0.37}. From 1-D and 2-D simulations, it is expected that the lattices will begin to disassemble by absorbing the radiation from the ablator’s hot corona that penetrates the ablator shell. The extent to which

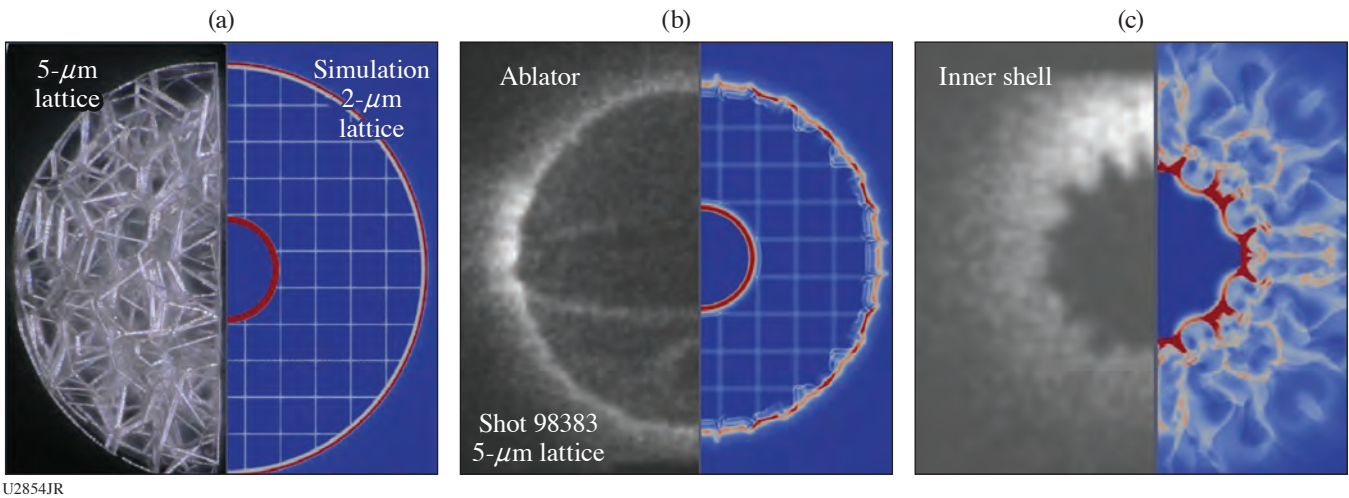


Figure 13
(a) An image of the 2PP inner-shell support is compared to the initial lattice of the cylindrical simulations. (b) Perturbations on the ablator surface due to the lattice are observed in both experiments and simulations. (c) Simulations are able to predict significant perturbations on the outer surface of the inner shell when the 2PP lattice disassembly is insufficient.

it can do so before bulk motion of the ablator depends on the lattice strut size and potentially on the lattice's ability to absorb x-ray radiation. In experiments, the extent of the lattice disassembly is determined by measuring the perturbations imparted to the ablator, measured by self-emission radiography as shown in Fig. 13(b), and to the inner metal shell, measured via 6.7-keV backlit radiography⁴ as shown in Fig. 13(c). Cylindrical simulations of surrogate lattice structures in the r - θ plane qualitatively exhibit many of the features shown in the radiographs. On the ablator, the pressure of the lattice struts against the imploding ablator shell results in bumps on the ablator surface seen in Fig. 13(b). On the inner shell, a nonuniform shock formed by the interaction of the perturbed, preheated metal shell with the residual lattice results in significant growth of spatial nonuniformity. This is seen qualitatively in the simulations and inner-shell radiograph of Fig. 13(c). Follow-on experiments at near full scale on the NIF, where implosion time scales will be greater by a factor of 5, will assess the perturbation reduction owing to more-complete lattice disassembly.

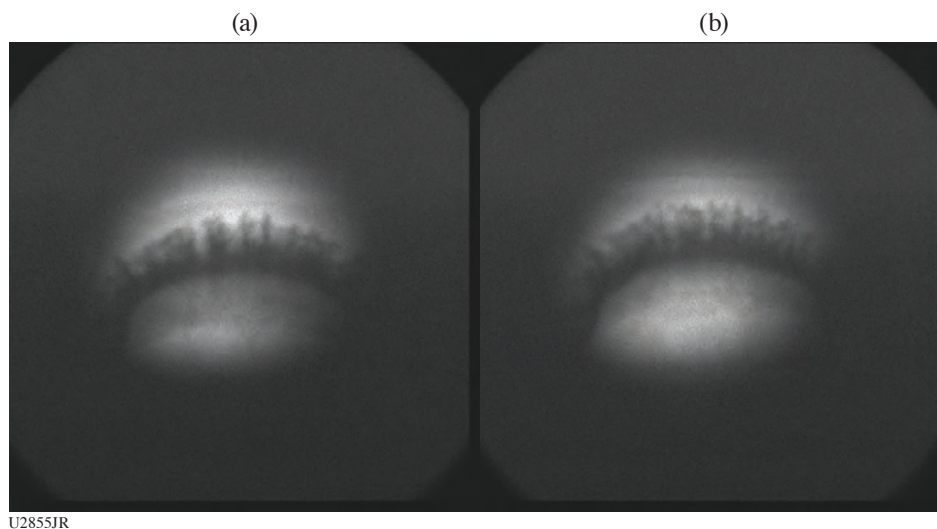
This research was supported by the Laboratory Directed Research and Development Program of Los Alamos National Laboratory under Project Number 20180051DR.

FY21 ModCons Experiments

Principal Investigators: A. Rasmus, J. Levesque, C. Di Stefano, K. A. Flippo, E. Merritt, F. Doss, K. Love, N. Christiansen, A. Strickland, and D. Schmidt

In FY21, the ModCons EP Campaign did a combination of data collection and diagnostic development. ModCons experiments utilize a shared experimental platform to study different aspects of hydrodynamic-instability growth on interfaces. Three long-pulse beams are used to create a semi-sustained shock, which drives instability growth. These campaigns utilize a Mn He $_{\alpha}$ (6.2-keV) backlighter, which is used in conjunction with the spherical crystal imager (SCI) or Fresnel zone plate (FZP) to create x-ray radiographs of interface evolution.

ModCons 21A measured the evolution of RM, with delayed-onset RT, for a broadband perturbation. This experiment finished a data set that examined how initial conditions alter multimode instability growth. In particular, we kept the wavelengths in the perturbation the same but weighted the amplitudes so that either short or wavelength modes dominated (see Fig. 14). These data will inform the initialization of sub-grid models of turbulence.



U2855JR

Figure 14

SCI images of multimode RM+ RT growth comparing how instability growth for initial perturbations biased toward (a) long- or (b) short-wavelength modes.

ModCons EP 21B was the first ModCons shot day that adapted the ModCons EP Platform to conditions relevant to the NIF MShock Campaigns studying successive shocks on a perturbed tracer layer. The goal of this campaign is to use scaled OMEGA EP experiments to supplement the NIF data by allowing us to observe interface growth at early times during the direct-drive-only portion of the NIF experiments. These experiments use the same shock tube and foam materials as the Mn SCI x-ray imaging setup from prior ModCons experiments. Changes to the platform include an additional ablator stack of CH and Au that is present on the NIF platform; also the laser drive will use three simultaneous beams at maximum power over a 1-ns pulse to reach intensities $\sim 600 \text{ TW/cm}^2$, roughly equivalent to the direct-drive energy used on the NIF MShock experiments prior to August 2021. For the first shot day, we used two single-mode sinusoidal perturbation types that had previously been used on the NIF experiments— $275\text{-}\mu\text{m}$ wavelength at $28\text{-}\mu\text{m}$ amplitude and $150\text{-}\mu\text{m}$ wavelength at $5\text{-}\mu\text{m}$ amplitude (see Fig. 15). We imaged the systems at 20, 23, 26, and 29 ns, from which we can compare the interface position to NIF results and simulations.

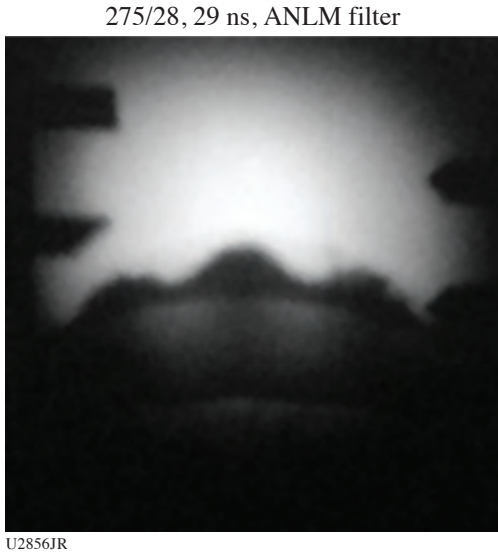


Figure 15
Filtered x-ray image of a $\lambda = 275\text{-}\mu\text{m}$ wavelength, amplitude = $28\text{-}\mu\text{m}$ perturbation at 29 ns after laser drive. The shapes around the edges are a spatial fiducial.

The measured interface positions from the ModCons-21B experiments suggest the system is consistently slower than the NIF results from experiments before August 2021. The modified NIF MShock Platform from August 2021 onward uses a reduced direct-drive intensity, and the trajectory of the new platform matches the OMEGA EP trajectory well. The continuation of this series will use the perturbation profile of the more-recent NIF MShock experiments and will attempt to improve analysis of mix parameters by averaging over multiple images at the same time over different shots (see Fig. 16).

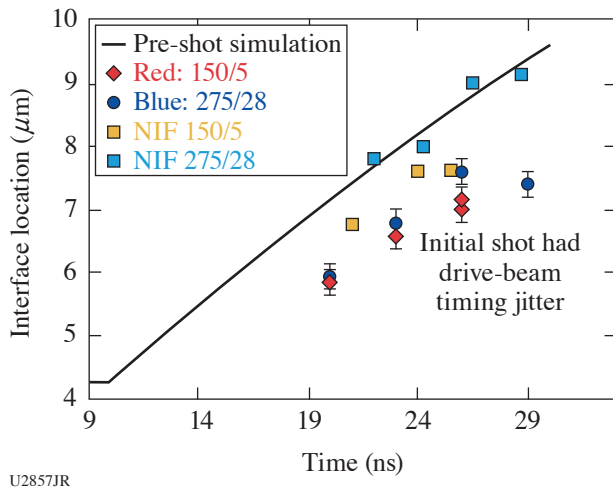


Figure 16
Comparison of the interface position over time for the OMEGA EP and NIF MShock experiments.

ModCons-21C fielded the LANL FZP diagnostic. These experiments established the survivability of the FZP's at small standoffs but did not obtain high-resolution images. We will be working on testing our FZP design on the benchtop moving forward and will then look at fielding them in experiments again once we understand how to field them better in a controlled environment.

OUTI Experimental Campaign Annual Report

Principal Investigators: H. M. Johns, P. M. Kozlowski, H. F. Robey, C. Fryer, S. Wood, T. Byvank, S. Coffing, T. S. Perry, C. J. Fontes, T. Urbatsch, and M. Douglas

The OUTI Experimental Campaign builds upon previous COAX⁵ and Radishock⁶ experimental campaigns. The stated goal of the campaign was to experimentally measure transmission (including bound-free) and temperature for transport across a density boundary that is handled differently by Sn/IMC numerical radiation transport. The goals of FY21 were to collect initial data required to develop a true-transmission analysis method in contrast to the previous bound-bound transmission-only method,⁵ to collect proof-of-concept data for collecting spectra from the outer foam in a COAX-like target, and to make improvements to the radiography side of the platform to reduce experimental uncertainties with respect to the COAX and Radishock Campaigns. OUTI21A collected 11 shots on 24 February 2021, while OUTI21B collected 7 shots on 5 August 2021 (Fig. 17).

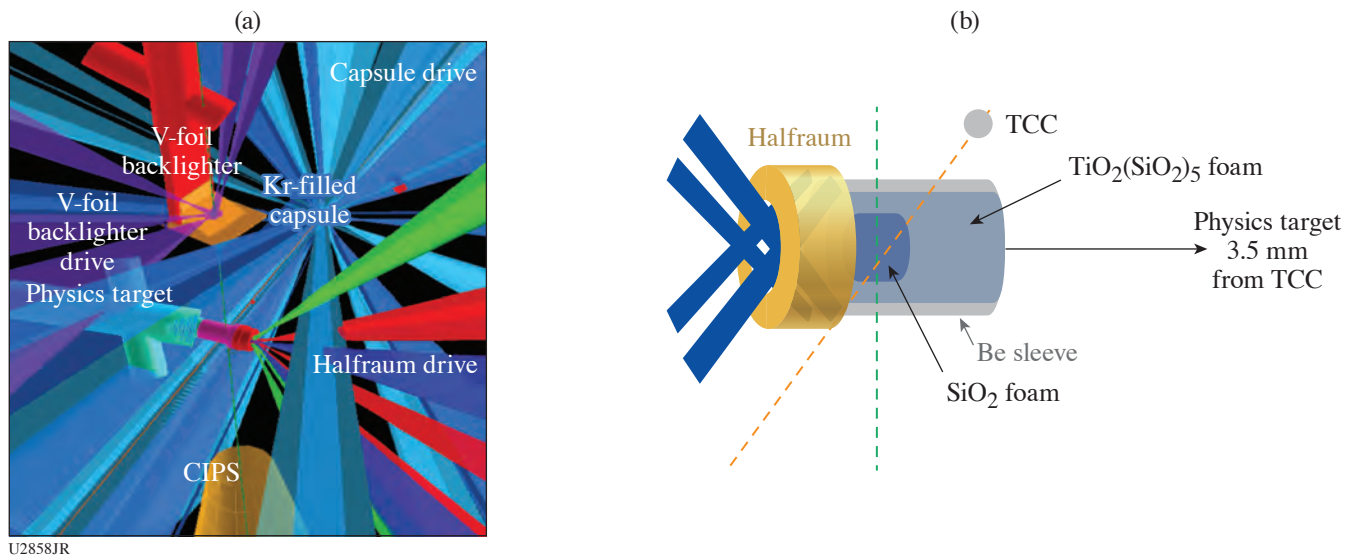
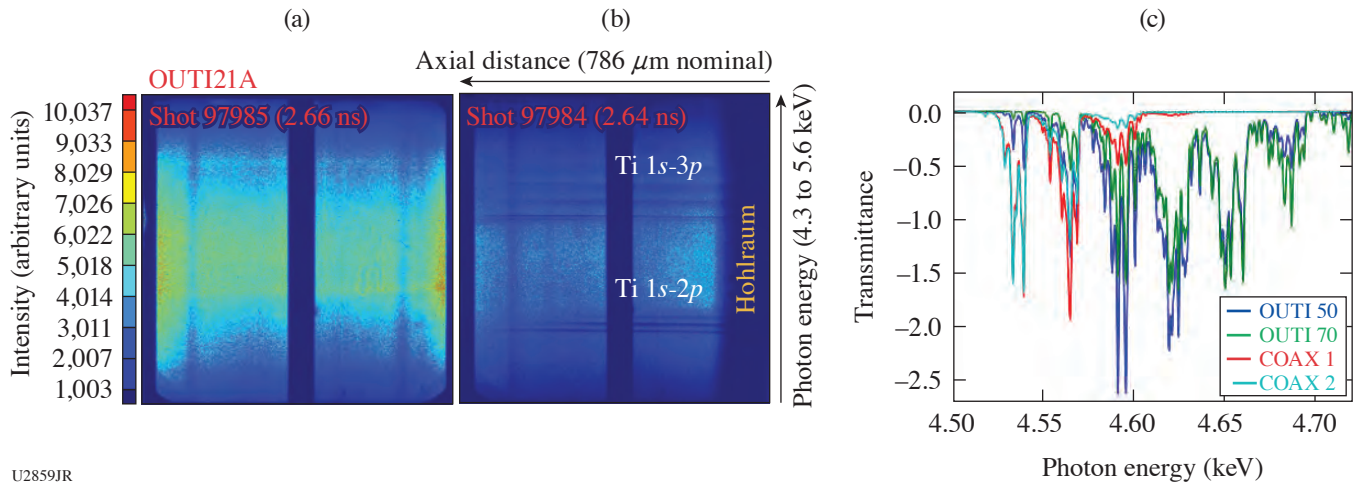


Figure 17

(a) VisRad display of the OUTI experimental campaign with close-up of OUTI physics target. (b) The OUTI physics target is a COAX-like⁵ target in reverse, with the outer foam containing Ti-laden foam and the inner foam containing only SiO₂. The platform itself draws heavily from the prior Radishock Campaign,⁶ using the same capsule and capsule drive, the same hohlraum and hohlraum drive, and the same V-foil backlighter. Due to differences in the physics target design, the final radiography design used three beams, while Radishock used five beams. TCC: target chamber center.

Prior to OUTI21A, no attempt had been made to capture absorption spectra from a region of the foam that was not driven by the halfraum. Because the size of the REH is limited to the radius of the inner foam, heat transport across the radius of the target, and therefore across any density boundary, must occur in order for absorption spectra to be obtained from dopant in the outer foam. Calculated COAX and OUTI spectra are shown in Fig. 18(c) for the same 20% TiO₂ and 80% SiO₂ molar ratio as was fielded in COAX.⁵ OUTI21A collected proof-of-concept data for this approach, also shown in Fig. 18(c). An examination of the flat-field data in comparison to continuum from the physics target shot 97984 shows that the intensity of even-continuum regions is much lower after passing through the physics target, as expected due to absorption from the SiO₂ foam and Ti bound-free absorption. In OUTI21B we intended to qualify a duplicate spectrometer to enable collection of a flat-field for every physics target shot; however, significant facility maintenance issues meant that while we were able to verify the efficacy of the new spectrometer, we were not able to collect the desired spectra and must do so on a later shot day in FY22. To verify that the new spectrometer works as intended, we collected a three-filter (Sc, Ti, V) dispersion measurement with both spectrometers.



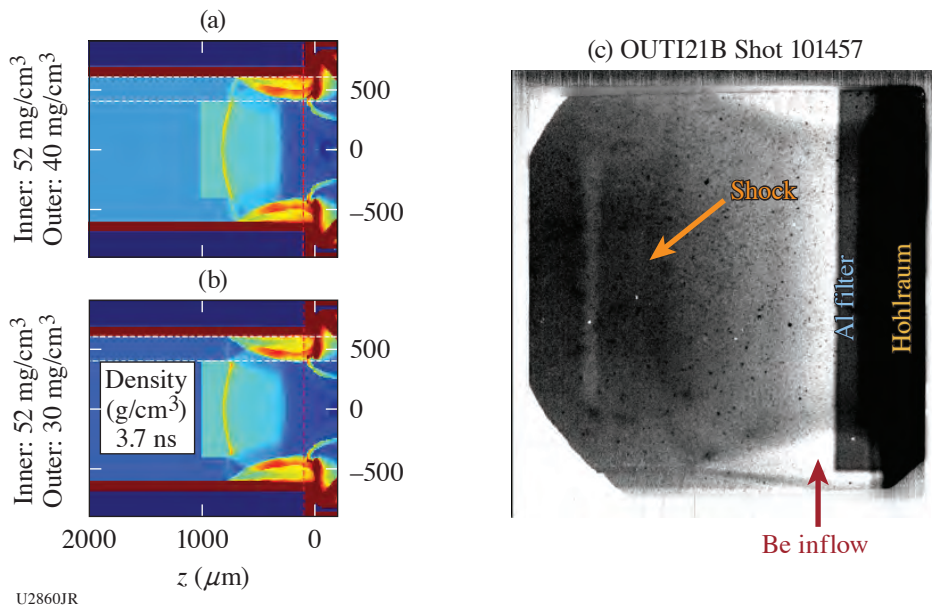
U2859JR

Figure 18

Wedge corrected data for (a) a flat-field shot 97985 and (b) a physics target shot 97984 are shown with a common intensity scale. (c) Calculated Ti K-shell spectra are shown for COAX with 50- and 70-mg/cm³ foams as well as for OUTI targets, in which the dopant is placed in the outer foam instead of the inner foam, for 50- and 70-mg/cm³ foams.

The OUTI Campaign also optimized radiography for this target design relative to the prior campaigns. We moved to a 200-ps pfm from a 500-ps pfm and reduced our down-sampling rate from an 18 × 18-pixel size to a 9 × 9-pixel size. We also optimized our backlighter illumination for this target type, resulting in radiographs such as that shown in Fig. 19. This radiograph includes both the lowest foam density we have ever shot (33 mg/cm³) as well as the largest-ever difference between inner- and outer-foam densities.

This work was performed under the auspices of the U.S. Department of Energy at Los Alamos National Laboratory under Contract No. 8923318CNA000001.



U2860JR

Figure 19

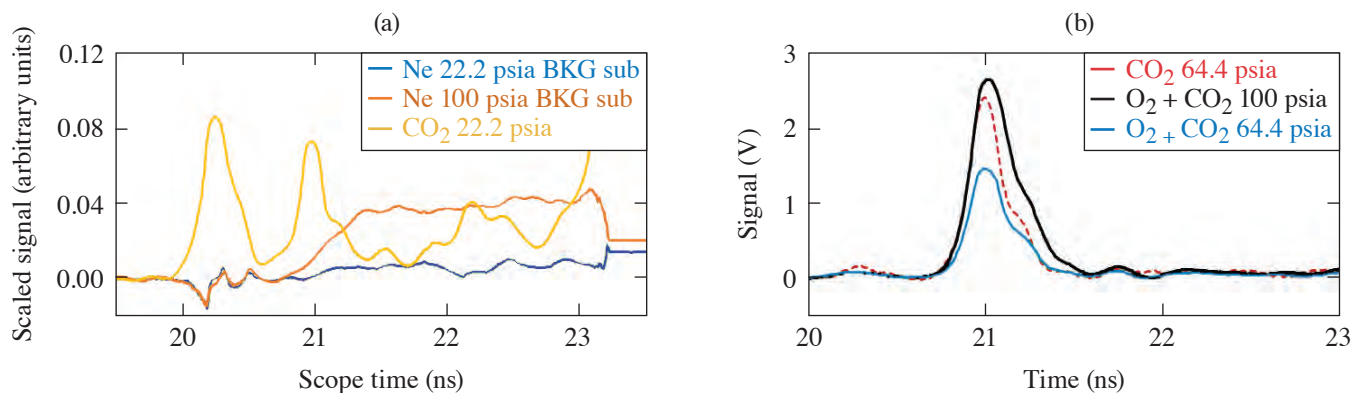
[(a),(b)] Two simulations show the density evolution of an OUTI target with (a) a nominal inner/outer foam density as well as (b) low inner/outer foam density shot 101457. (c) A flat-fielded radiograph (shots 101458 and 101457) shows qualitatively similar behavior to the simulation with low target-foam density in which the shock in the lower-density outer foam runs ahead of the higher-density inner foam. The as-shot foams were 33-mg/cm³ outer and 51-mg/cm³ inner.

GCD Diagdev-21A Investigating Gas Fluorescence in Gas Cherenkov Detectors

Principal Investigators: H. Geppert-Kleinrath, Y. Kim, and K. D. Meaney (LANL); and A. Leatherland (AWE)

The LANL-driven development of the new pulse dilation photomultiplier tube fielded on the gas Cherenkov detector (GCD)⁷ on the NIF allows for unprecedented temporal resolution in gamma reaction history (GRH) measurements of 10 ps (Ref. 8). First measurements of the DT fusion GRH revealed a tail feature not seen before.⁹ Further investigation made clear that gas fluorescence is the cause of the tail seen on GRH. To better understand and be able to mitigate the tail issue, different gases were tested on GCD-1 and GCD-3 on OMEGA (Fig. 20). The gases tested were CO₂ for benchmarking against N₂, Ne, and a mixture of 20% O and 80% CO₂. The targets shot were 1100- μ m-diam Hoppe glass spheres with 4.1- μ m-thick shells, filled to 10 atm of 50/50 DT. The targets were driven with a 60-beam 1-ns square laser drive. The shot day was successful in indicating that both neon gas fill and oxygen are viable paths forward in mitigating the tail issue (see Fig. 20). The neon tail can be subtracted from shot data resulting in cleaner D–T fusion reaction history measurements but reduced signal-to-noise ratio. Oxygen produces less tail than the CO₂ gas currently used in GCD's, but gas cells will need upgrades to accommodate oxygen. Neon was subsequently used to measure the burn width of record-setting shots on the NIF (N210808).

This material is based upon work supported by the Department of Energy National Nuclear Security Administration, Los Alamos National Laboratory Campaign 10 (J. Kline, C-10 Program Manager).



U2861JR

Figure 20

Example data for (a) neon gas fill and (b) an oxygen 20% and CO₂ 80% mixture. The neon tail can be subtracted from shot data for a cleaner signal. Oxygen produces less tail than CO₂ currently used in GCD's.

Thin Separated Fusion Reactants to Study Variation of Observed Complex Kinetic Mix

Principal Investigators: K. D. Meaney, Y. Kim, H. Geppert-Kleinrath, N. Hoffman (LANL); and J. W. Morton and C. R. D. Brown (AWE)

LANL investigates complex, dynamic mix experiments in high-energy-density conditions at the Omega Laser Facility. Los Alamos leverages its gamma-ray diagnostic expertise to make novel, constraining mix experiments. Specifically, the separated reactant technique places deuterium in part of the carbon shell of ICF capsules with hydrogen–tritium in the fuel. The amount of deuterium–tritium fusion is a measure of the amount of mix from that location of the shell into the fuel, with gamma-ray diagnostics allowing potential measurement of the fuel's hydrogen–tritium fusion (releasing 20-MeV gamma ray) as well as the relative timing between the two.

In 2017, a campaign of ultrathin (~150-nm) placed deuterated layers was started to obtain a data set of superhigh spatial resolution shell mix to challenge hydrodynamic codes and quantify kinetic effects. Although the campaign was successful by observing a kinetic, diffusion-dominated mix mechanism in capsule conditions that were previously understood with a turbulent mix layer,¹⁰

the data set also showed a complex, unexpected trend—the amount of mix decreased from the shell that was farther away from the fuel (as expected); however, at around 0.6- μm recession depth, the amount of mix increased again, implying that material in the shell far away from the fuel was mixing in more than the shell that was closer. This unintuitive data, termed the “mix dip,” was investigated in 2019. Testing hypothesized that the fill tube or P1 asymmetries were jetting material from a specific farther location; however, the 2019 data showed that these effects did not cause the mix dip. During this time, simulation and theoretical work continued with calculations showing no clear explanation for the data.

In 2021, we continued to investigate the mix dip, this time doing a direct repeat of the 2017 data of interest with higher spatial resolution and better capsule characterization. The data showed a large amount of variation at the same conditions with no clear observation of the mix dip, suggesting that in 2017, slight variation in the exact placement of the deuterated layer and its thickness could have been responsible for the confusing observed trend. The collected data will be used as part of sensitivity and uncertainty quantification from simulation for historic and future data sets. Likewise, the collected data contributes to a larger body of work of thin separated reactants that have the power to differentiate kinetic mix effects.

This material is based upon work supported by the Department of Energy National Nuclear Security Administration, Los Alamos National Laboratory Campaign 10 (J. Kline, C-10 Program Manager).

Development of the MixIT Diagnostic

Principal Investigators: V. Geppert-Kleinrath, C. Danly, C. Wilde, N. Birge, B. M. Haines, J. Jorgenson, E. Mendoza, L. Tafoya, and P. Volegov (LANL); and S. T. Ivancic, A. Sorce, and T. Burgett (LLE)

A mix of ablator, fill tube, or other high-Z contaminants into the fuel assembly of an ICF implosion is a known performance-limiting process. One of the leading uncertainties in contaminant mass estimates stems from the uncertainty in contaminant mass temperature, which is assumed to be in thermal equilibrium with the fuel. It has recently been shown that portions of contaminant mass do not necessarily thermally equilibrate with the neighboring fuel.¹¹ Therefore, a direct, spatially resolved temperature measurement of the hot spot could provide key contaminant mass temperature constraints crucial to accurate contaminant mass estimates. By combining the principles of a neutron time-of-flight (nTOF) diagnostic and a neutron-imaging system, the MixIT diagnostic is the first of its kind: a temperature imager for ICF.

A sketch of the core components of the MixIT diagnostic is shown in Fig. 21. The tungsten coded aperture projects an image of the neutron source (ICF plasma) onto a 1-D stack of scintillator tiles (EJ 262). One-millimeter optical fibers carry the light from each scintillator tile to the input of the streak camera. In collaboration with the OMEGA Diagnostics Group, OMEGA’s

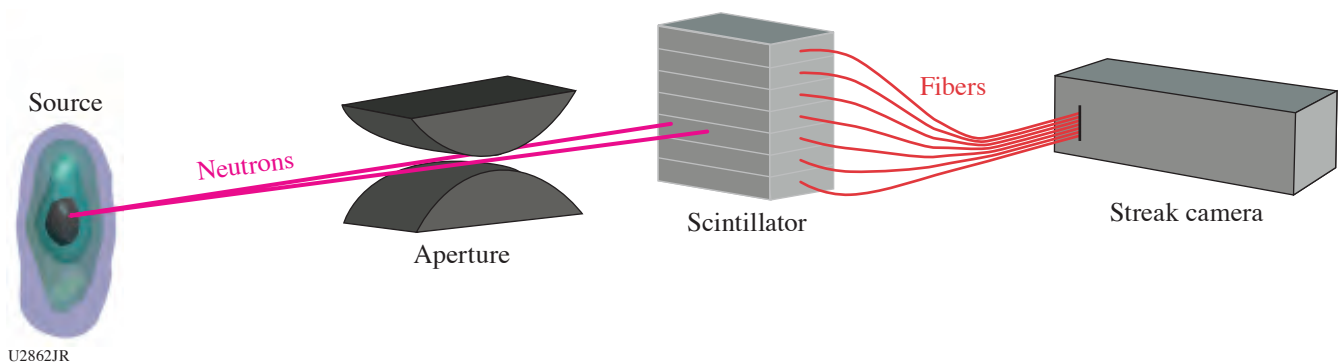


Figure 21

The fundamental components of the MixIT diagnostic. The aperture casts a neutron image of the source onto the 1-D scintillator array, fiber coupled to a streak camera. The recorded image essentially results in a nTOF (or energy) spectrum for each scintillator tile. From the spectra, temperatures can be determined and mapped back to the source.

“System 68” streak camera was fielded for this campaign. The streak camera records the fiber input over a 20-ns window with a resolution of roughly 40 ps. Therefore, a neutron energy spectrum and the plasma temperature are measured by each scintillator tile. This distribution can then be mapped back to the ICF plasma with sufficient knowledge of the aperture point spread function.

The team first captured data on 13 May 2021 during a ride-along on the EnergeticNeutron-21A shot day. A single scintillator pixel was coupled to System 68 to verify the light production and collection indicated by simulation. The shot day was highly successful. The team achieved the primary goal in capturing a streak image for the pixel, thereby validating our simulation efforts. Additionally, the team captured dark-field and charge-coupled device noise data, which have been incorporated into the MixIT diagnostic noise model. The scintillator pixel, along with the corresponding streak data, can be seen in Fig. 22.

The dedicated shot day, MixIT-21A, took place 9 September 2021. The team accomplished the goal of recording the first-ever spatially resolved temperature data [see Fig. 23(d)]. Calibration, flat-field [Figs. 23(a) and 23(b)], and dark-field data were also recorded. Analysis of the data is ongoing, and preliminary results are anticipated this year.

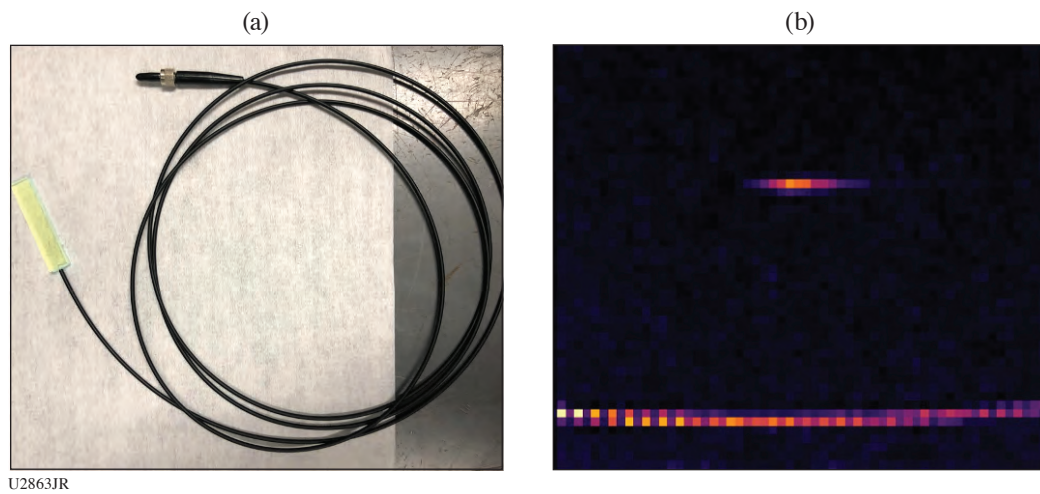


Figure 22
 (a) The scintillator tile fielded during the EnergeticNeutron-21A ride-along. (b) The signal captured by the streak camera. The bottom dotted line corresponds to a frequency comb used to calibrate the time domain of the recorded image. The streak in the middle of the image corresponds to the light from the single pixel.

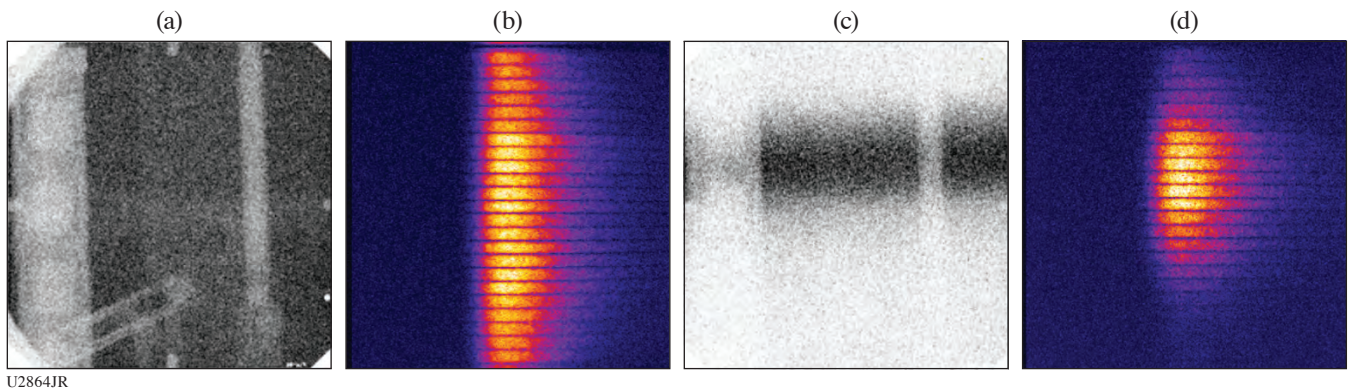


Figure 23
 (a) Image plate and (b) streak camera data captured for calibration shot 101818 without the neutron aperture inserted. (c) Image plate and (d) streak camera data for a production data shot.

1. B. M. Haines *et al.*, *Phys. Plasmas* **20**, 022309 (2013).
2. B. Scheiner *et al.*, *Phys. Plasmas* **27**, 122702 (2020).
3. L. A. Goodwin *et al.*, *Fusion Sci. Technol.* **78**, 66 (2022).
4. F. J. Marshall *et al.*, *Rev. Sci. Instrum.* **92**, 033701 (2021).
5. H. M. Johns *et al.*, *High Energy Density Phys.* **39** (2021).
6. H. M. Johns *et al.*, *LLE 2020 Annual Report*, 338–343, University of Rochester, DOE/NA/3856-1601 (2020).
7. H. W. Herrmann *et al.*, *Rev. Sci. Instrum.* **85**, 11E124 (2014).
8. V. Geppert-Kleinrath *et al.*, *Rev. Sci. Instrum.* **89**, 10I142 (2018).
9. H. Geppert-Kleinrath *et al.*, *High Energy Density Phys.* **37**, 100862 (2020).
10. A. B. Zylstra *et al.*, *Phys. Rev. E* **97**, 061201(R) (2018).
11. B. M. Haines *et al.*, *Nat. Commun.* **11**, 544 (2020).

FY21 Sandia National Laboratories Progress Report on Omega Laser Facility Experiments

B. A. Aguirre

Sandia National Laboratories

The Energetic Neutrons Campaign led by Sandia National Laboratories (SNL) had a successful year testing electronic devices and printed circuit boards (PCB's) under 14-MeV neutron irradiation at the Omega Laser Facility. During FY21 Sandia's neutron effects diagnostics (NED's) and data acquisition systems were upgraded to test novel commercial off-the-shelf and Sandia-fabricated electronic components that support SNL's National Security mission. The upgrades to the Sandia platform consisted of new cable chains, sample mount fixtures, and a new fiber optics platform for testing optoelectronic devices.

The new cable chains improved data quality and reduced the time required by LLE and Sandia to identify and solve issues with the electronic circuits under test. A variety of sample fixtures were designed and fabricated to mount new shapes and sizes of PCB's closer to the neutron source without interfering with other components fielded simultaneously. PCB's fielded in FY21

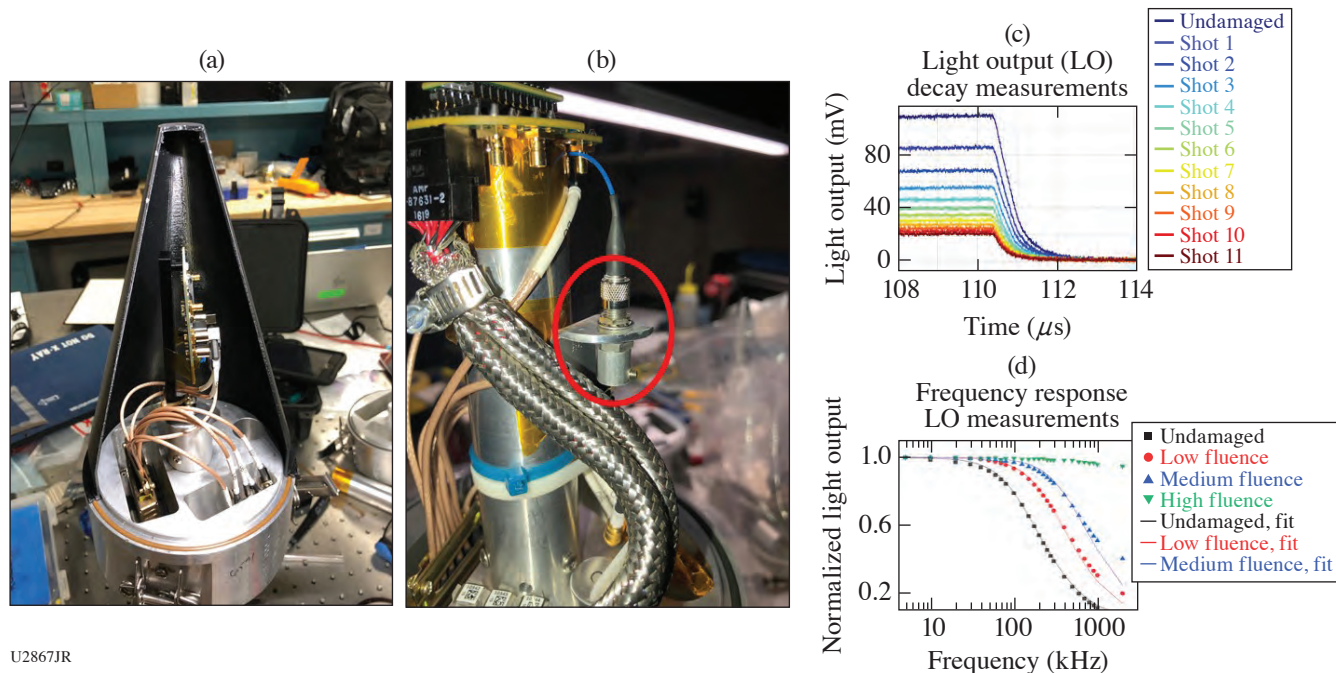


Figure 1
(a) A PCB mounted in one of the Sandia NED's used to study single-event effects; (b) an example of the setup used to test optoelectronic devices in the Sandia NED's; and (c) an example of the light output data measured after each shot during one of the Energetic Neutrons Campaigns.

contained a variety of components ranging from low to high voltage and from discrete devices to small integrated circuits as shown in Figs. 1(a) and 1(b).

The new fiber optics platform consisted of fiber optic cables, sample mount fixtures, and data acquisition systems that allowed Sandia to measure high-quality optical signals for the first time on OMEGA. Optical data will be used to calculate carrier lifetime degradation in semiconductor devices exposed to 14-MeV neutron irradiation using light output decay and frequency response measurements as shown in Fig. 1(c).

A SNL graduate student intern participated for the first time in one of the experiments on OMEGA performing *in-situ* testing of optoelectronic devices. The student developed software, connected hardware, acquired data, and performed data analysis during one of the energetic neutrons campaign in FY21; he will be participating again in FY22.

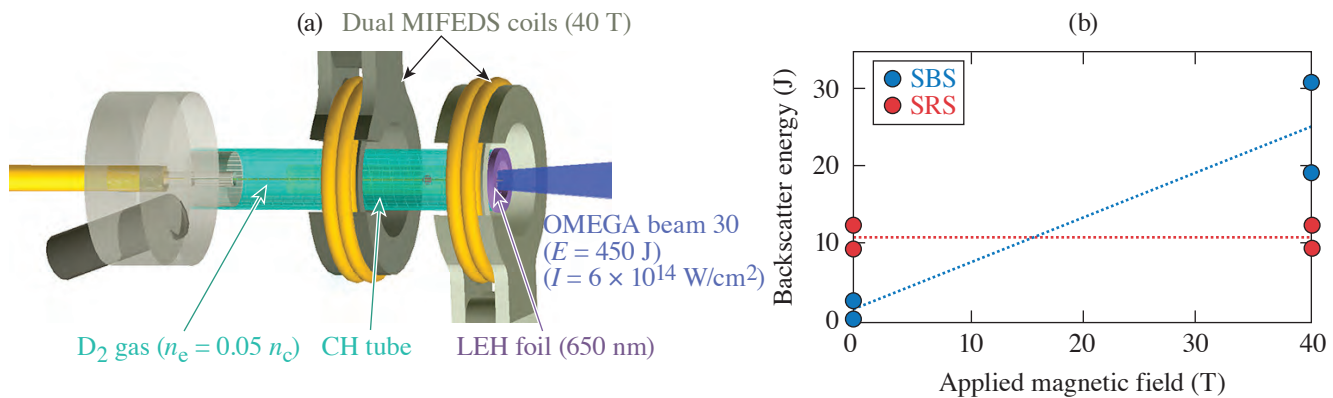
This work was performed at Sandia National Laboratories, a multimission laboratory managed and operated by National Technology and Engineering Solutions of Sandia LLC, a wholly owned subsidiary of Honeywell International Inc. for the U.S. Department of Energy’s National Nuclear Security Administration under contract DE-NA0003525. The views expressed in the article do not necessarily represent the views of the U.S. Department of Energy or the United States Government. SAND2021-14522 R.

Investigating the Effects of Magnetization on Laser–Plasma Instability Backscatter in MagLIF Preheat

Principal Investigators: J. R. Fein and A. J. Harvey-Thompson

The magnetized liner inertial fusion¹ (MagLIF) concept requires coupling energy from a multikilojoule laser to preheat magnetized D₂ before compression with a pulsed-power generator. The laser preheat process is sensitive to laser–plasma instabilities (LPI’s) and filamentation, which affect energy coupling and can lead to beam spray that introduces mix into the target. The LPI processes are affected by magnetic fields that affect plasma temperatures by suppressing thermal conduction but can exacerbate thermal self-focusing and filamentation and breakup of the beam. These effects have not been studied at conditions relevant to MagLIF.

To address the effect of magnetic fields on LPI in MagLIF preheat, magnetized D₂-filled gas tube experiments were conducted on OMEGA as part of the MiniMagLIF-21a shot day. Figure 2(a) shows the target geometry, wherein a single OMEGA beam (B30) heated a 650-nm polyimide window and D₂ gas inside a polyimide tube. The heating beam delivered a total of ~450 J in a 1-ns



U2868JR

Figure 2

(a) Target geometry of magnetized preheat experiments on OMEGA, showing a polyimide gas tube filled with D₂ and sealed with a 650-nm LEH window. The dual MIFEDS coils magnetized the target to peak fields ~40 T. (b) SBS and SRS direct backscatter energies as a function of applied magnetic field.

pulse with 300- μm spot, resulting in intensities $\sim 6 \times 10^{14}$ W/cm². Dual MIFEDS (magneto-inertial fusion electrical discharge system) coils imposed an ~ 40 -T magnetic field oriented along the tube axis. Five shots were conducted in total, including one calibration shot for the full-aperture backscatter system (FABS) and four target shots: two with and two without a magnetic field.

FABS systems monitored direct backscattered and sidescattered light from stimulated Raman (SRS) and stimulated Brillouin scattering (SBS), and an x-ray framing camera diagnosed time-gated emission to evaluate beam propagation. Preliminary data collected by the FABS calorimeters are shown in Fig. 2(b). SBS levels increased nearly 5 \times when the magnetic field was increased from 0 to 40 T, whereas virtually no change in the amount of SRS was observed. SBS streaked spectra from magnetized targets showed an additional feature at the laser wavelength not present in the spectra from the unmagnetized targets. Hard x rays, as recorded by the HERIE, decreased by a factor of ~ 2 in the magnetized targets compared to unmagnetized targets. While the increased SBS levels and decreased hard x rays in magnetized targets may have resulted from magnetization effects in the pre-heated gas and laser entrance hole (LEH) window, additional experiments are needed to rule out other causes. The preliminary data set from these experiments is helping to inform target modifications and diagnostic configurations for similar experiments set for January 2022.

Sandia National Laboratories is a multimission laboratory managed and operated by National Technology & Engineering Solutions of Sandia, LLC, a wholly owned subsidiary of Honeywell International Inc., for the U.S. Department of Energy's National Nuclear Security Administration under contract DE-NA0003525.

1. S. A. Slutz *et al.*, *Physics of Plasmas* **17**, 056303 (2010).

FY21 Naval Research Laboratory Report on Omega Laser Facility Experiments

NRL Transmission Grating Spectrometer Obtains X-Ray Spectra from High-Z Coatings Used for Imprint Mitigation on OMEGA EP

Principle Investigators: M. Karasik and J. Weaver (NRL), and D. Mastrosimone and D. N. Polsin (LLE)

During FY21, NRL in collaboration with LLE completed a shot day on OMEGA EP to further study the spectra of soft x rays emitted by high-Z (Au and Pd) coatings that are highly effective for imprint mitigation.^{1,2} Soft x-ray spectra of the indirect–direct hybrid drive with high-Z coatings were obtained using the NRL transmission grating spectrometer³ (NRL TGS) installed on OMEGA EP (see Fig. 1). A new higher-dispersion grating allowed us to measure the spectra to shorter wavelengths. The measurements show that the spectra are dominated by soft x-ray emission as expected and can be used to put a bound on target preheat. Additionally, excellent VISAR (velocity interferometer for any reflector), streaked optical pyrometry, and 4ω probe data were acquired to aid in the understanding of high-Z coating dynamics.

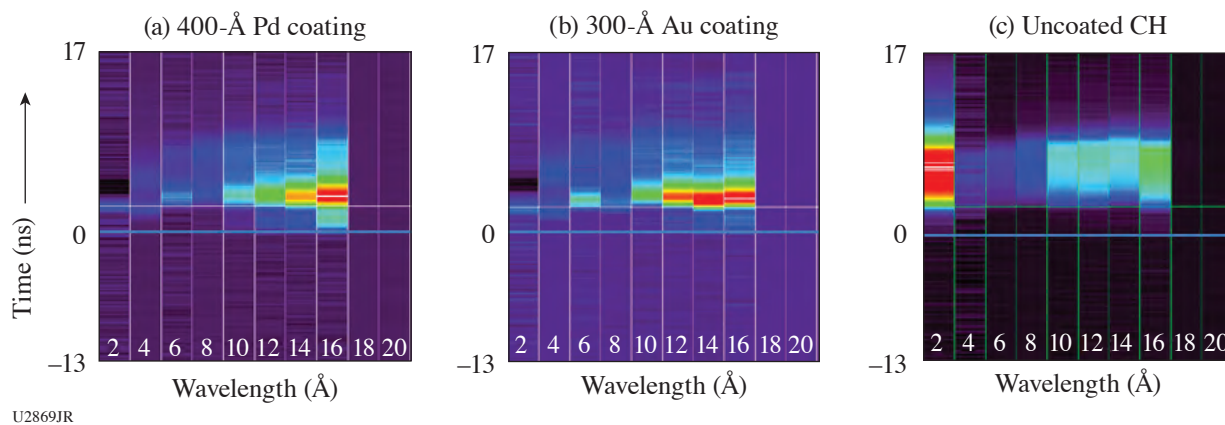


Figure 1

Examples of x-ray spectra obtained using the NRL TGS. Individual time-resolved spectral bins from diodes are combined to form spectra “streaked” in time. For coated targets, strong emission was seen early in the pulse consistent with initial x-ray drive. The measurements show that the spectra are dominated by soft x-ray emission, as expected. The data can be used to put a bound on x-ray preheat of a given ablator thickness. Note that the signal in the uncoated CH 2-Å bin is contaminated due to zero-order bleed.

This work is supported by U.S. DOE/NNSA.

1. M. Karasik *et al.*, Phys. Plasmas **28**, 032710 (2021).
2. S. P. Obenschain *et al.*, Phys. Plasmas **9**, 2234 (2002).
3. J. L. Weaver *et al.*, Rev. Sci. Instrum. **72**, 108 (2001).

Publications and Conference Presentations

Publications

- P. J. Adrian, J. Frenje, B. Aguirre, B. Bachmann, A. Birkel, M. Gatu Johnson, N. V. Kabadi, B. Lahmann, C. K. Li, O. M. Mannion, W. Martin, Z. L. Mohamed, S. P. Regan, H. G. Rinderknecht, B. Scheiner, M. J. Schmitt, F. H. Séguin, R. C. Shah, H. Sio, C. Sorce, G. D. Sutcliffe, and R. D. Petrasso, “An X-Ray Penumbral Imager for Measurements of Electron–Temperature Profiles in Inertial Confinement Fusion Implosions at OMEGA,” *Rev. Sci. Instrum.* **92**, 043548 (2021).
- K. S. Anderson, C. J. Forrest, O. M. Mannion, F. J. Marshall, R. C. Shah, D. T. Michel, J. A. Marozas, P. B. Radha, D. Edgell, R. Epstein, V. N. Goncharov, J. P. Knauer, M. Gatu Johnson, and S. Laffite, “Effect of Cross-Beam Energy Transfer on Target-Offset Asymmetry in Direct-Drive Inertial Confinement Fusion Implosions,” *Phys. Plasmas* **27**, 112713 (2020).
- C. D. Arrowsmith, N. Shukla, N. Charitonidis, R. Boni, H. Chen, T. Davenne, A. Dyson, D. H. Froula, J. T. Gudmundsson, B. T. Huffman, Y. Kadi, B. Reville, S. Richardson, S. Sarkar, J. L. Shaw, L. O. Silva, P. Simon, R. M. G. M Trines, R. Bingham, and G. Gregori, “Generating Ultradense Pair Beams Using 400 GeV/c Protons,” *Phys. Rev. Res.* **3**, 023103 (2021).
- D. H. Barnak, M. J. Bonino, P.-Y. Chang, J. R. Davies, E. C. Hansen, D. R. Harding, J. L. Peebles, and R. Betti, “Characterizing Laser Preheat for Laser-Driven Magnetized Liner Inertial Fusion Using Soft X-Ray Emission,” *Phys. Plasmas* **27**, 112709 (2020).
- I. A. Begishev, S.-W. Bahk, C. Dorrer, C. Feng, M. J. Guardalben, C. Jeon, R. G. Roides, M. Spilatro, B. Webb, D. Weiner, J. D. Zuegel, and J. Bromage, “A Highly Efficient, 10-J Output Signal Amplifier for Ultra-Intense All-OPCPA Systems,” *Proc. SPIE* **11666**, 1166607 (2021).
- I. A. Begishev, G. Brent, S. Carey, R. Chapman, I. A. Kulagin, M. H. Romanofsky, M. J. Shoup III, J. D. Zuegel, and J. Bromage, “High-Efficiency, Fifth-Harmonic Generation of a Joule-Level Neodymium Laser in a Large-Aperture Ammonium Dihydrogen Phosphate Crystal,” *Opt. Express* **29**, 1879 (2021).
- X. Bian, J. K. Shang, E. G. Blackman, G. W. Collins, and H. Aluie, “Scaling of Turbulent Viscosity and Resistivity: Extracting a Scale-Dependent Turbulent Magnetic Prandtl Number,” *Astrophys. J. Lett.* **917**, L3 (2021).
- A. F. A. Bott, P. Tzeferacos, L. Chen, C. A. J. Palmer, A. Rigby, A. R. Bell, R. Bingham, A. Birkel, C. Graziani, D. H. Froula, J. Katz, M. Koenig, M. W. Kunz, C. K. Li, J. Meinecke, F. Miniati, R. Petrasso, H.-S. Park, B. A. Remington, B. Reville, J. S. Ross, D. Ryu, D. Ryutov, F. H. Séguin, T. G. White, A. A. Schekochihin, D. Q. Lamb, and G. Gregori, “Time-Resolved Fast Turbulent Dynamo in a Laser Plasma,” *Proc. Natl. Acad. Sci.* **118**, e2015729118 (2021).
- S. Brygoo, P. Loubeyre, M. Millot, J. R. Rygg, P. M. Celliers, J. H. Eggert, R. Jeanloz, and G. W. Collins, “Evidence of Hydrogen–Helium Immiscibility at Jupiter-Interior Conditions,” *Nature* **593**, 517 (2021).
- E. M. Campbell, T. C. Sangster, V. N. Goncharov, J. D. Zuegel, S. F. B. Morse, C. Sorce, G. W. Collins, M. S. Wei, R. Betti, S. P. Regan, D. H. Froula, C. Dorrer, D. R. Harding, V. Gopalaswamy, J. P. Knauer, R. Shah, O. M. Mannion, J. A. Marozas, P. B. Radha, M. J. Rosenberg, T. J. B. Collins, A. R. Christopherson, A. A. Solodov, D. Cao, J. P. Palastro, R. K. Follett, and M. Farrell, “Direct-Drive Laser Fusion: Status, Plans and Future,” *Phil. Trans. R. Soc. A* **379**, 2020011 (2020).
- A. R. Christopherson, R. Betti, C. J. Forrest, J. Howard, W. Theobald, J. A. Delettrez, M. J. Rosenberg, A. A. Solodov, C. Stoeckl, D. Patel, V. Gopalaswamy, D. Cao, J. L. Peebles, D. H. Edgell, W. Seka, R. Epstein, M. S. Wei, M. Gatu Johnson, R. Simpson, S. P. Regan, and E. M. Campbell, “Direct Measurements of DT Fuel Preheat from Hot Electrons in Direct-Drive Inertial Confinement Fusion,” *Phys. Rev. Lett.* **127**, 055001 (2021).

- F. Coppari, R. F. Smith, J. Wang, M. Millot, D. Kim, J. R. Rygg, S. Hamel, J. H. Eggert, and T. S. Duffy, “Implications of Iron Oxide Phase Transition on the Interiors of Rocky Exoplanets,” *Nat. Geosci.* **14**, 121 (2021).
- L. E. Crandall, J. R. Rygg, D. K. Spaulding, T. R. Boehly, S. Brygoo, P. M. Celliers, J. H. Eggert, D. E. Fratanduono, B. J. Henderson, M. F. Huff, R. Jeanloz, A. Lazicki, M. C. Marshall, D. N. Polsin, M. Zaghoo, M. Millot, and G. W. Collins, “Equation of State of CO₂ Shock Compressed to 1 TPa,” *Phys. Rev. Lett.* **125**, 165701 (2020).
- L. E. Crandall, J. R. Rygg, D. K. Spaulding, M. F. Huff, M. C. Marshall, D. N. Polsin, R. Jeanloz, T. R. Boehly, M. Zaghoo, B. J. Henderson, S. Brygoo, P. M. Celliers, J. H. Eggert, D. E. Fratanduono, A. Lazicki, M. Millot, and G. W. Collins, “Equation-of-State, Sound Speed, and Reshock of Shock-Compressed Fluid Carbon Dioxide,” *Phys. Plasmas* **28**, 022708 (2021).
- J. R. Davies, H. Wen, J.-Y. Ji, and E. D. Held, “Transport Coefficients for Magnetic-Field Evolution in Inviscid Magneto-hydrodynamics,” *Phys. Plasmas* **28**, 012305 (2021).
- C. Dorrer, “Optical Parametric Amplification of Spectrally Incoherent Pulses,” *J. Opt. Soc. Am. B* **38**, 792 (2021).
- C. Dorrer, I. A. Begishev, S.-W. Bahk, and J. Bromage, “Characterization of Partially Deuterated KDP Crystals Using Two-Wavelength Phase-Matching Angles,” *Opt. Mater. Express* **11**, 774 (2021).
- C. Dorrer, M. Spilatro, S. Herman, T. Borger, and E. M. Hill, “Broadband Sum-Frequency Generation of Spectrally Incoherent Pulses,” *Opt. Express* **29**, 16,135 (2021).
- D. H. Edgell, A. M. Hansen, J. Katz, D. Turnbull, and D. H. Froula, “Unabsorbed Light Beamlets for Diagnosing Coronal Density Profiles and Absorption Nonuniformity in Direct-Drive Implosions on OMEGA,” *Rev. Sci. Instrum.* **92**, 043525 (2021).
- D. H. Edgell, P. B. Radha, J. Katz, A. Shvydky, D. Turnbull, and D. H. Froula, “Nonuniform Absorption and Scattered Light in Direct-Drive Implosions Driven by Polarization Smoothing,” *Phys. Rev. Lett.* **127**, 075001 (2021).
- R. Epstein, R. C. Mancini, D. T. Cliche, R. C. Shah, T. J. B. Collins, C. Stoeckl, P. W. McKenty, P. B. Radha, S. P. Regan, and V. N. Goncharov, “Self-Radiography of Imploded Shells on OMEGA Based on Additive-Free Multi-Monochromatic Continuum Spectral Analysis,” *Phys. Plasmas* **27**, 122709 (2020).
- W. A. Farmer, M. D. Rosen, G. F. Swadling, C. Bruulsema, C. D. Harris, W. Rozmus, M. B. Schneider, M. W. Sherlock, D. H. Edgell, J. Katz, and J. S. Ross, “Investigation of Heat Transport Using Directly Driven Gold Spheres,” *Phys. Plasmas* **28**, 032707 (2021).
- G. Fiksel, W. Fox, M. J. Rosenberg, D. B. Schaeffer, J. Matteucci, and A. Bhattacharjee, “Electron Energization During Merging of Self-Magnetized, High-Beta, Laser-Produced Plasmas,” *J. Plasma Phys.* **87**, 905870411 (2021).
- R. K. Follett, J. G. Shaw, J. F. Myatt, H. Wen, D. H. Froula, and J. P. Palastro, “Thresholds of Absolute Two-Plasmon-Decay and Stimulated Raman Scattering Instabilities Driven by Multiple Broadband Lasers,” *Phys. Plasmas* **28**, 032103 (2021).
- F. García-Rubio, R. Betti, J. Sanz, and H. Aluie, “Magnetic-Field Generation and Its Effect on Ablative Rayleigh–Taylor Instability in Diffusive Ablation Fronts,” *Phys. Plasmas* **28**, 012103 (2021).
- F. García-Rubio, R. Betti, J. Sanz, and H. Aluie, “Self-Consistent Theory of the Darrieus–Landau and Rayleigh–Taylor Instabilities with Self-Generated Magnetic Fields,” *Phys. Plasmas* **27**, 112715 (2020).
- M. Gatu Johnson, B. Aguirre, J. Armstrong, J. A. Fooks, C. Forrest, J. A. Frenje, V. Yu. Glebov, M. Hoppe, J. Katz, J. P. Knauer, W. Martin, C. E. Parker, H. G. Reynolds, M. E. Schoff, F. H. Séguin, C. Sorce, B. Sperry, C. Stoeckl, and R. D. Petrasso, “Using Millimeter-Sized Carbon–Deuterium Foils for High-Precision Deuterium–Tritium Neutron Spectrum Measurements in Direct-Drive Inertial Confinement Fusion at the OMEGA Laser Facility,” *Rev. Sci. Instrum.* **92**, 023503 (2021).
- V. Yu. Glebov, C. Stoeckl, C. J. Forrest, J. P. Knauer, O. M. Mannion, M. H. Romanofsky, T. C. Sangster, and S. P. Regan, “A Novel Photomultiplier Tube Neutron Time-of-Flight Detector,” *Rev. Sci. Instrum.* **92**, 013509 (2021).
- C. Goyon, M. R. Edwards, T. Chapman, L. Divol, N. Lemos, G. J. Williams, D. A. Mariscal, D. Turnbull, A. M. Hansen, and P. Michel, “Slow and Fast Light in Plasma Using Optical Wave Mixing,” *Phys. Rev. Lett.* **126**, 205001 (2021).

- P. E. Grabowski, S. B. Hansen, M. S. Murillo, L. G. Stanton, F. R. Graziani, A. B. Zylstra, S. D. Baalrud, P. Arnault, A. D. Baczewski, L. X. Benedict, C. Blancard, O. Čertík, J. Cléroutin, L. A. Collins, S. Copeland, A. A. Correa, J. Dai, J. Daligault, M. P. Desjarlais, M. W. C. Dharma-wardana, G. Faussurier, J. Haack, T. Haxhimali, A. Hayes-Sterbenz, Y. Hou, S. X. Hu, D. Jensen, G. Jungman, G. Kagan, D. Kang, J. D. Kress, Q. Ma, M. Marciante, E. Meyer, R. E. Rudd, D. Saumon, L. Shulenburg, R. L. Singleton Jr., T. Sjostrom, L. J. Stanek, C. E. Starrett, C. Ticknor, S. Valaitis, J. Venzke, and A. White, “Review of the First Charged-Particle Transport Coefficient Comparison Workshop,” *High Energy Density Phys.* **37**, 100905 (2020).
- D. Haberberger, A. Davies, J. L. Shaw, R. K. Follett, J. P. Palastro, and D. H. Froula, “Hot Raman Amplification,” *Phys. Plasmas* **28**, 062311 (2021).
- B. M. Haines, R. C. Shah, J. M. Smidt, B. J. Albright, T. Cardenas, M. R. Douglas, C. Forrest, V. Yu. Glebov, M. A. Gunderson, C. Hamilton, K. Henderson, Y. Kim, M. N. Lee, T. J. Murphy, J. A. Oertel, R. E. Olson, B. M. Patterson, R. B. Randolph, and D. Schmidt, “The Rate of Development of Atomic Mixing and Temperature Equilibration in Inertial Confinement Fusion Implosions,” *Phys. Plasmas* **27**, 102701 (2020).
- S. K. Han, R. F. Smith, D. Kim, J. K. Wicks, J. R. Rygg, A. Lazicki, J. H. Eggert, and T. S. Duffy, “Polymorphism of Gold Under Laser-Based Ramp Compression to 690 GPa,” *Phys. Rev. B* **103**, 184109 (2021).
- A. M. Hansen, K. L. Nguyen, D. Turnbull, B. J. Albright, R. K. Follett, R. Huff, J. Katz, D. Mastrosimone, A. L. Milder, L. Yin, J. P. Palastro, and D. H. Froula, “Cross-Beam Energy Transfer Saturation by Ion Heating,” *Phys. Rev. Lett.* **126**, 075002 (2021).
- L. E. Hansen, D. E. Fratanduono, S. Zhang, D. G. Hicks, T. Suer, Z. K. Sprowal, M. F. Huff, X. Gong, B. J. Henderson, D. N. Polsin, M. Zaghou, S. X. Hu, G. W. Collins, and J. R. Rygg, “Melting of Magnesium Oxide up to Two Terapascals Using Double-Shock Compression,” *Phys. Rev. B* **104**, 014106 (2021).
- D. R. Harding, M. D. Wittman, N. P. Redden, D. H. Edgell, and J. Ulreich, “Comparison of Shadowgraphy and X-Ray Phase-Contrast Methods for Characterizing a DT Ice Layer in an Inertial Confinement Fusion Target,” *Fusion Sci. Technol.* **76**, 814 (2020).
- A. J. Harvey-Thompson, M. R. Weis, D. E. Ruiz, M. S. Wei, A. B. Sefkow, T. Nagayama, E. M. Campbell, J. A. Fooks, M. E. Glines, and K. J. Peterson, “The Effect of Laser Entrance Hold Foil Thickness on MagLIF-Relevant Laser Preheat,” *Phys. Plasmas* **27**, 113301 (2020).
- B. J. Henderson, M. C. Marshall, T. R. Boehly, R. Paul, C. A. McCoy, S. X. Hu, D. N. Polsin, L. E. Crandall, M. F. Huff, D. A. Chin, J. J. Ruby, X. Gong, D. E. Fratanduono, J. H. Eggert, J. R. Rygg, and G. W. Collins, “Shock-Compressed Silicon: Hugoniot and Sound Speed to 2100 GPa,” *Phys. Rev. B* **103**, 094115 (2021).
- K. P. Hilleke, T. Ogitsu, S. Zhang, and E. Zurek, “Structural Motifs and Bonding in Two Families of Boron Structures Predicted at Megabar Pressures,” *Phys. Rev. Mater.* **5**, 053605 (2021).
- C. J. Horsfield, M. S. Rubery, J. M. Mack, H. W. Herrmann, Y. Kim, C. S. Young, S. E. Caldwell, S. C. Evans, T. S. Sedillo, A. M. McEvoy, N. M. Hoffman, M. A. Huff, J. R. Langenbrunner, G. M. Hale, D. C. Wilson, W. Stoeffl, J. A. Church, E. M. Grafil, E. K. Miller, and V. Yu. Glebov, “First Spectral Measurement of Deuterium-Tritium Fusion γ Rays in Inertial Fusion Experiments,” *Phys. Rev. C* **104**, 024610 (2021).
- H. Huang, K. R. P. Kafka, and S. G. Demos, “Electric-Field Enhancement Caused by Subwavelength-Sized Particles Located on the Surface of Multilayer Dielectric Mirrors,” *Opt. Express* **29**, 27,031 (2021).
- A. E. Hussein, A. V. Arefiev, T. Batson, H. Chen, R. S. Craxton, A. S. Davies, D. H. Froula, Z. Gong, D. Haberberger, Y. Ma, P. M. Nilson, W. Theobald, T. Wang, K. Weichman, G. J. Williams, and L. Willingale, “Towards the Optimisation of Direct Laser Acceleration,” *New J. Phys.* **23**, 023031 (2021).
- V. V. Ivanov, A. V. Maximov, R. Betti, L. S. Leal, J. D. Moody, K. J. Swanson, and N. A. Huerta, “Generation of Strong Magnetic Fields for Magnetized Plasma Experiments at the 1-MA Pulsed Power Machine,” *Matter Radiat. Extremes* **6**, 046901 (2021).
- G. W. Jenkins, C. Feng, and J. Bromage, “Overcoming Gas Ionization Limitations with Divided-Pulse Nonlinear Compression,” *Opt. Express* **28**, 31,943 (2020).
- S. Jiang, A. Link, D. Canning, J. A. Fooks, P. A. Kempler, S. Kerr, J. Kim, M. Krieger, N. S. Lewis, R. Wallace, G. J. Williams, S. Yalamanchili, and H. Chen, “Enhancing Positron Production Using Front Surface Target Structures,” *Appl. Phys. Lett.* **118**, 094101 (2021).

- T. M. Johnson, A. Birkel, H. E. Ramirez, G. D. Sutcliffe, P. J. Adrian, V. Yu. Glebov, H. Sio, M. Gatu Johnson, J. A. Frenje, R. D. Petrasso, and C. K. Li, "Yield Degradation Due to Laser Drive Asymmetry in D³He Backlit Proton Radiography Experiments at OMEGA," *Rev. Sci. Instrum.* **92**, 043551 (2021).
- N. V. Kabadi, P. J. Adrian, A. Bose, D. T. Casey, J. A. Frenje, M. Gatu Johnson, B. Lahmann, O. M. Mannion, R. D. Petrasso, H. G. Rinderknecht, F. H. Séguin, H. W. Sio, G. D. Sutcliffe, and A. B. Zylstra, "A Second Order Yield-Temperature Relation for Accurate Inference of Burn-Averaged Quantities in Multi-Species Plasmas," *Phys. Plasmas* **28**, 022701 (2021).
- N. V. Kabadi, R. Simpson, P. J. Adrian, A. Bose, J. A. Frenje, M. Gatu Johnson, B. Lahmann, C. K. Li, C. E. Parker, F. E. Séguin, G. D. Sutcliffe, R. D. Petrasso, S. Atzeni, J. Eriksson, C. Forrest, S. Fess, V. Yu. Glebov, R. Janezic, O. M. Mannion, H. G. Rinderknecht, M. J. Rosenberg, C. Stoeckl, G. Kagan, M. Hoppe, R. Luo, M. Schoff, C. Schuldberg, H. W. Sio, J. Sanchez, L. Berzak Hopkins, D. Schlossberg, K. Hahn, and C. Yeaman, "Thermal Decoupling of Deuterium and Tritium During the Inertial Confinement Fusion Shock-Convergence Phase," *Phys. Rev. E* **104**, L013201 (2021).
- N. Kabadi, A. Sorce, C. Stoeckl, H. W. Sio, P. Adrian, M. Bedzyk, J. Frenje, J. Katz, J. Knauer, J. Percy, D. Weiner, B. A. Aguirre, R. Betti, A. Birkel, D. Cao, M. Gatu Johnson, D. Patel, R. D. Petrasso, and S. P. Regan, "A Multi-Channel X-Ray Temporal Diagnostic for Measurement of Time-Resolved Electron Temperature in Cryogenic Deuterium-Tritium Implosions at OMEGA," *Rev. Sci. Instrum.* **92**, 023507 (2021).
- K. R. P. Kafka, B. N. Hoffman, H. Huang, and S. G. Demos, "Mechanisms of Picosecond Laser-Induced Damage from Interaction with Model Contamination Particles on a High Reflector," *Opt. Eng.* **60**, 031009 (2021).
- K. R. P. Kafka, B. N. Hoffman, A. A. Kozlov, and S. G. Demos, "Dynamics of Electronic Excitations Involved in Laser-Induced Damage in HfO₂ and SiO₂ Films," *Opt. Lett.* **46**, 1684 (2021).
- M. Kaloyan, S. Ghazaryan, C. G. Constantin, R. S. Dorst, P. V. Heuer, J. J. Pilgram, D. B. Schaeffer, and C. Niemann, "Raster Thomson Scattering in Large-Scale Laser Plasmas Produced at High Repetition Rate," *Rev. Sci. Instrum.* **92**, 093102 (2021).
- V. V. Karasiev and S. X. Hu, "Unraveling the Intrinsic Atomic Physics Behind X-Ray Absorption Line Shifts in Warm Dense Silicon Plasmas," *Phys. Rev. E* **103**, 033202 (2021).
- M. Karasik, J. Oh, S. P. Obenshain, A. J. Schmitt, Y. Aglitskiy, and C. Stoeckl, "Order-of-Magnitude Laser Imprint Reduction Using Pre-Expanded High-Z Coatings on Targets Driven by a Third Harmonic Nd:Glass Laser," *Phys. Plasmas* **28**, 032710 (2021).
- J. Katz, D. Turnbull, B. E. Kruschwitz, A. L. Rigatti, R. Rinefierd, and D. H. Froula, "A Transmitted-Beam Diagnostic for the Wavelength-Tunable UV Drive Beam on OMEGA," *Rev. Sci. Instrum.* **92**, 033526 (2021).
- C. F. Kawaguchi, K. A. Flippo, A. M. Rasmus, B. Tobias, T. Byvank, C. A. Di Stefano, E. C. Merritt, F. W. Doss, K. V. Kelso, N. N. Vazirani, C. Stoeckl, M. Bedzyk, R. Jungquist, and C. Mileham, "Improved Imaging Using Mn He- α X Rays at OMEGA EP," *Rev. Sci. Instrum.* **92**, 093508 (2021).
- D. Kawahito, M. Bailly-Grandvaux, M. Dozieres, C. McGuffey, P. Forestier-Colleoni, J. Peebles, J. J. Honrubia, B. Khair, S. Hansen, P. Tzeferacos, M. S. Wei, C. M. Krauland, P. Gourdain, J. R. Davies, K. Matsuo, S. Fujioka, E. M. Campbell, J. J. Santos, D. Batani, K. Bhutwala, S. Zhang, and F. N. Beg, "Fast Electron Transport Dynamics and Energy Deposition in Magnetized, Imploded Cylindrical Plasma," *Phil. Trans. R. Soc. A* **379**, 20200052 (2020).
- J. Kim, A. Link, D. Canning, P. Fitzsimmons, J. A. Fooks, S. Kerr, T. Ma, M. J. E. Manuel, D. Mariscal, R. Wallace, G. J. Williams, L. Willingale, F. N. Beg, and H. Chen, "Dynamic Focusing of Laser Driven Positron Jets by Self-Generated Fields," *New J. Phys.* **22**, 123020 (2020).
- Y. Kim, H. W. Herrmann, N. M. Hoffman, M. J. Schmitt, G. Kagan, A. M. McEvoy, A. B. Zylstra, J. M. Smidt, S. Gales, A. Leatherland, M. Rubery, M. Gatu Johnson, J. A. Frenje, V. Yu. Glebov, and C. Forrest, "First Observation of Increased DT Yield over Prediction due to Addition of Hydrogen," *Phys. Plasmas* **28**, 012707 (2021).
- P. M. King, K. Miller, N. Lemos, J. L. Shaw, B. F. Kraus, M. Thibodeau, B. M. Hegelich, J. Hinojosa, P. Michel, C. Joshi, K. A. Marsh, W. Mori, A. Pak, A. G. R. Thomas, and F. Albert, "Predominant Contribution of Direct Laser Acceleration to High-Energy Electron Spectra in a Low-Density Self-Modulated Laser Wakefield Accelerator," *Phys. Rev. Accel. Beams* **24**, 011302 (2021).
- P. Koester, F. Baffigi, G. Cristoforetti, L. Labate, L. A. Gizzi, S. Baton, M. Koenig, A. Colaitis, D. Batani, A. Casner, D. Raffestin, A. Tentori, J. Trela, C. Rousseaux, G. Boutoux, S. Brygoo,

- L. Jacquet, C. Reverdin, E. Le Bel, L. LeDeroff, W. Theobald, and K. Shigemori, “Bremsstrahlung Cannon Design for Shock Ignition Relevant Regime,” *Rev. Sci. Instrum.* **92**, 013501 (2021).
- T. Z. Kosci, H. Huang, T. J. Kessler, R. A. Negres, and S. G. Demos, “Determination of the Raman Polarizability Tensor in the Optically Anisotropic Crystal Potassium Dihydrogen Phosphate and Its Deuterated Analog,” *Sci. Rep.* **10**, 16283 (2020).
- A. A. Kozlov, S. G. Demos, D. Canning, B. N. Hoffman, B. E. Kruschwitz, A. L. Rigatti, and N. Savidis, and L. J. Waxer, “Long-Term Monitoring the Damage Performance of Multilayer Dielectric Grating Samples Residing Inside the Compressor Chamber of the OMEGA EP Laser,” *Opt. Eng.* **60**, 031008 (2021).
- R. G. Kraus, F. Coppari, D. E. Fratanduono, R. F. Smith, A. Lazicki, C. Wehrenberg, J. H. Eggert, J. R. Rygg, and G. W. Collins, “Melting of Tantalum at Multimegabar Pressures on the Nanosecond Timescale,” *Phys. Rev. Lett.* **126**, 255701 (2021).
- A. Kryjevski, T. Luu, and V. Karasiev, “Electronic Structure of Semiconductor Nanoparticles from Stochastic Evaluation of Imaginary-Time Path Integral,” *Phys. Rev. Res.* **3**, 023173 (2021).
- L. Lamainère, A. Ollé, M. Chores, N. Roquin, A. A. Kozlov, B. N. Hoffman, J. B. Oliver, S. G. Demos, L. Gallais, R. A. Negres, and A. Melnikaitis, “Round-Robin Measurements of the Laser-Induced Damage Threshold with Sub-Picosecond Pulses on Optical Single Layers,” *Opt. Eng.* **60**, 031005 (2021).
- O. L. Landen, J. D. Lindl, S. W. Haan, D. T. Casey, P. M. Celliers, D. N. Fittinghoff, N. Gharibyan, V. N. Goncharov, G. P. Grim, E. P. Hartouni, O. A. Hurricane, B. J. MacGowan, S. A. MacLaren, K. D. Meaney, M. Millot, J. L. Milovich, P. K. Patel, H. S. Robey, P. T. Springer, P. L. Volegov, and M. J. Edwards, “Fuel Convergence Sensitivity in Indirect Drive Implosions,” *Phys. Plasmas* **28**, 042705 (2021).
- A. Lazicki, D. McGonegle, J. R. Rygg, D. G. Braun, D. C. Swift, M. G. Gorman, R. F. Smith, P. G. Heighway, A. Higginbotham, M. J. Suggit, D. E. Fratanduono, F. Coppari, C. E. Wehrenberg, R. G. Kraus, D. Erskine, J. V. Bernier, J. M. McNaney, R. E. Rudd, G. W. Collins, J. H. Eggert, and J. S. Wark, “Metastability of Diamond Ramp-Compressed to 2 Terapascals,” *Nature* **589**, 532 (2021).
- A. Lees, R. Betti, J. P. Knauer, V. Gopalaswamy, D. Patel, K. M. Woo, K. S. Anderson, E. M. Campbell, D. Cao, J. Carroll-Nellenback, R. Epstein, C. Forrest, V. N. Goncharov, D. R. Harding, S. X. Hu, I. V. Igumenshchev, R. T. Janezic, O. M. Mannion, P. B. Radha, S. P. Regan, A. Shvydky, R. C. Shah, W. T. Shmayda, C. Stoeckl, W. Theobald, and C. Thomas, “Experimentally Inferred Fusion Yield Dependencies of OMEGA Inertial Confinement Fusion Implosions,” *Phys. Rev. Lett.* **127**, 105001 (2021).
- R. H. Lehmberg, M. F. Wolford, J. L. Weaver, D. Kehne, S. P. Obenschain, D. Eimerl, and J. P. Palastro, “Stimulated Rotational Raman Scattering of Arbitrarily Polarized Broadband Light,” *Phys. Rev. A* **102**, 063530 (2020).
- B. J. MacGowan, O. J. Landen, D. T. Casey, C. V. Young, D. A. Callahan, E. P. Hartouni, R. Hatarik, M. Hohenberger, T. Ma, D. Mariscal, A. Moore, R. Nora, H. G. Rinderknecht, D. Schlossberg, and B. M. Van Wousterghem, “Trending Low Mode Asymmetries in NIF Capsule Drive Using a Simple Viewfactor Metric,” *High Energy Density Phys.* **40**, 100944 (2021).
- O. M. Mannion, I. V. Igumenshchev, K. S. Anderson, R. Betti, E. M. Campbell, D. Cao, C. J. Forrest, M. Gatu Johnson, V. Yu. Glebov, V. N. Goncharov, V. Gopalaswamy, S. T. Ivancic, D. W. Jacobs-Perkins, A. Kalb, J. P. Knauer, J. Kwiatkowski, A. Lees, F. J. Marshall, M. Michalko, Z. L. Mohamed, D. Patel, H. G. Rinderknecht, R. C. Shah, C. Stoeckl, W. Theobald, K. M. Woo, and S. P. Regan, “Mitigation of Mode-One Asymmetry in Laser-Direct-Drive Inertial Confinement Fusion Implosions,” *Phys. Plasmas* **28**, 042701 (2021) (invited).
- O. M. Mannion, K. M. Woo, A. J. Crilly, C. J. Forrest, J. A. Frenje, M. Gatu Johnson, V. Yu. Glebov, J. P. Knauer, Z. L. Mohamed, M. H. Romanofsky, C. Stoeckl, W. Theobald, and S. P. Regan, “Reconstructing 3D Asymmetries in Laser-Direct-Drive Implosions on OMEGA,” *Rev. Sci. Instrum.* **92**, 033529 (2021).
- F. J. Marshall, S. T. Ivancic, C. Mileham, P. M. Nilson, J. J. Ruby, C. Stoeckl, B. S. Scheiner, and M. J. Schmitt, “High-Resolution X-Ray Radiography with Fresnel Zone Plates on the University of Rochester’s OMEGA Laser Systems,” *Rev. Sci. Instrum.* **92**, 033701 (2021) (invited).
- M. C. Marshall, M. Millot, D. E. Fratanduono, D. M. Sterbentz, P. C. Myint, J. L. Belof, Y.-J. Kim, F. Coppari, S. J. Ali, J. H. Eggert, R. F. Smith, and J. M. McNaney, “Metastability of Liquid Water Freezing into Ice VII Under Dynamic Compression,” *Phys. Rev. Lett.* **127**, 135701 (2021).

- C. A. McCoy, S. X. Hu, M. C. Marshall, D. N. Polsin, D. E. Fratanduono, Y. H. Ding, P. M. Celliers, T. R. Boehly, and D. D. Meyerhofer, “Measurement of the Sound Velocity and Grüneisen Parameter of Polystyrene at Inertial Confinement Fusion Conditions,” *Phys. Rev. B* **102**, 184102 (2020).
- A. L. Milder, J. Katz, R. Boni, J. P. Palastro, M. Sherlock, W. Rozmus, and D. H. Froula, “Measurements of Non-Maxwellian Electron Distribution Functions and Their Effect on Laser Heating,” *Phys. Rev. Lett.* **127**, 015001 (2021).
- A. L. Milder, J. Katz, R. Boni, J. P. Palastro, M. Sherlock, W. Rozmus, and D. H. Froula, “Statistical Analysis of Non-Maxwellian Electron Distribution Functions Measured with Angularly Resolved Thomson Scattering,” *Phys. Plasmas* **28**, 082102 (2021) (invited).
- B. Militzer, F. González-Cataldo, S. Zhang, K. P. Driver, and F. Soubiran, “First-Principles Equation of State Database for Warm Dense Matter Computation,” *Phys. Rev. E* **103**, 013203 (2021).
- B. Militzer, F. González-Cataldo, S. Zhang, H. D. Whitley, D. C. Swift, and M. Millot, “Nonideal Mixing Effects in Warm Dense Matter Studied with First-Principles Computer Simulations,” *J. Chem. Phys.* **153**, 184101 (2020).
- Z. L. Mohamed, O. M. Mannion, E. P. Hartouni, J. P. Knauer, and C. J. Forrest, “A Generalized Forward Fit for Neutron Detectors with Energy-Dependent Response Functions,” *J. Appl. Phys.* **128**, 214501 (2020).
- Z. L. Mohamed, O. M. Mannion, J. P. Knauer, C. J. Forrest, V. Yu. Glebov, C. Stoeckl, and M. H. Romanofsky, “Application of an Energy-Dependent Instrument Response Function to Analysis of nTOF Data from Cryogenic DT Experiments,” *Rev. Sci. Instrum.* **92**, 043546 (2021).
- K. L. Nguyen, L. Yin, B. J. Albright, A. M. Hansen, D. H. Froula, D. Turnbull, R. K. Follett, and J. P. Palastro, “Cross-Beam Energy Transfer Saturation by Ion Trapping-Induced Detuning,” *Phys. Plasmas* **28**, 082705 (2021).
- J. Nilsen, D. Åberg, H. D. Whitley, B. G. Wilson, L. H. Yang, P. A. Sterne, M. W. Daene, M. E. Martin, S. Zhang, and W. R. Johnson, “Role of Opacity at the 9 keV Back Lighter Energy Used in Measuring the Equation of State of Boron at Pressures up to a Gbar,” *High Energy Density Phys.* **37**, 100880 (2020).
- J. P. Palastro, B. Malaca, J. Vieira, D. Ramsey, T. T. Simpson, P. Franke, J. L. Shaw, and D. H. Froula, “Laser-Plasma Acceleration Beyond Wave Breaking,” *Phys. Plasmas* **28**, 013109 (2021).
- J. L. Peebles, G. Fiksel, M. R. Edwards, J. von der Linden, L. Willingale, D. Mastrosimone, and H. Chen, “Magnetically Collimated Relativistic Charge-Neutral Electron-Positron Beams from High-Power Lasers,” *Phys. Plasmas* **28**, 074501 (2021).
- G. Pien, B. E. Kruschwitz, S. F. B. Morse, and T. J. Kessler, “Experimental Operations at the Omega Laser Facility Amid COVID-19,” *ICUIL News* **11**, 10 (2020).
- A. Pineau, B. Chimier, S. X. Hu, and G. Duchateau, “Improved Modeling of the Solid-to-Plasma Transition of Polystyrene Ablator for Laser Direct-Drive Inertial Confinement Fusion Hydrocodes,” *Phys. Rev. E* **104**, 015210 (2021).
- S. Rai, M. Hecht, M. Maltrud, and H. Aluie, “Scale of Oceanic Eddy Killing by Wind from Global Satellite Observations,” *Sci. Adv.* **7**, eabf4920 (2021).
- D. Ramsey, P. Franke, T. T. Simpson, D. H. Froula, and J. P. Palastro, “Vacuum Acceleration of Electrons in a Dynamic Laser Pulse,” *Phys. Rev. E* **102**, 043207 (2020).
- S. P. Regan and E. M. Campbell, “Inertial Confinement Fusion—Experimental Physics: Laser Drive,” in *Encyclopedia of Nuclear Energy*, edited by E. Greenspan (Elsevier, Oxford, 2021), pp. 713–723.
- H. G. Rinderknecht, T. Wang, A. Laso Garcia, G. Bruhaug, M. S. Wei, H. J. Quevedo, T. Ditmire, J. Williams, A. Haid, D. Doria, K. M. Spohr, T. Toncian, and A. Arefiev, “Relativistically Transparent Magnetic Filaments: Scaling Laws, Initial Results and Prospects for Strong-Field QED Studies,” *New J. Phys.* **23**, 095009 (2021).
- M. J. Rosenberg, J. E. Hernandez, N. Butler, T. Filkins, R. E. Bahr, R. K. Jungquist, M. Bedzyk, G. Swadling, J. S. Ross, P. Michel, N. Lemos, J. Eichmiller, R. Sommers, P. Nyholm, R. Boni, J. A. Marozas, R. S. Craxton, P. W. McKenty, A. Sharma, P. B. Radha, D. H. Froula, P. Datte, M. Gorman, J. D. Moody, J. M. Heinmiller, J. Fornes, P. Hillyard, and S. P. Regan, “The Scattered Light Time-History Diagnostic Suite at the National Ignition Facility,” *Rev. Sci. Instrum.* **92**, 033511 (2021).
- J. J. Ruby, J. A. Gaffney, J. R. Rygg, Y. Ping, and G. W. Collins, “High-Energy-Density-Physics Measurements in Implosions Using Bayesian Inference,” *Phys. Plasmas* **28**, 032703 (2021).

- J. J. Ruby, J. R. Rygg, D. A. Chin, J. A. Gaffney, P. J. Adrian, D. Bishel, C. J. Forrest, V. Yu. Glebov, N. V. Kabadi, P. M. Nilson, Y. Ping, C. Stoeckl, and G. W. Collins, "Constraining Physical Models at Gigabar Pressures," *Phys. Rev. E* **102**, 053210 (2020).
- J. J. Ruby, J. R. Rygg, D. A. Chin, J. A. Gaffney, P. J. Adrian, C. J. Forrest, V. Yu. Glebov, N. V. Kabadi, P. M. Nilson, Y. Ping, C. Stoeckl, and G. W. Collins, "Energy Flow in Thin Shell Implosions and Explosions," *Phys. Rev. Lett.* **125**, 215001 (2020).
- D. B. Schaeffer, W. Fox, M. J. Rosenberg, H.-S. Park, G. Fiksel, and D. Kalantar, "Measurements of Electron Temperature in High-Energy-Density Plasmas Using Gated X-Ray Pinhole Imaging," *Rev. Sci. Instrum.* **92**, 043524 (2021).
- B. Scheiner, M. J. Schmitt, D. Schmidt, L. Goodwin, and F. J. Marshall, "Two-Photon Polymerization Printed Lattices as Support Structures in Multi-Shell ICF Targets: Platform Development and Initial Assessment," *Phys. Plasmas* **27**, 122702 (2020).
- R. H. H. Scott, K. Glize, L. Antonelli, M. Khan, W. Theobald, M. Wei, R. Betti, C. Stoeckl, A. G. Seaton, T. D. Arber, D. Barlow, T. Goffrey, K. Bennett, W. Garbett, S. Atzeni, A. Casner, D. Batani, C. Li, and N. Woolsey, "Shock Ignition Laser-Plasma Interactions in Ignition-Scale Plasmas," *Phys. Rev. Lett.* **127**, 065001 (2021).
- R. C. Shah, S. X. Hu, I. V. Igumenshchev, J. Baltazar, D. Cao, C. J. Forrest, V. N. Goncharov, V. Gopalaswamy, D. Patel, F. Philippe, W. Theobald, and S. P. Regan, "Observations of Anomalous X-Ray Emission at Early Stages of Hot-Spot Formation in Deuterium-Tritium Cryogenic Implosions," *Phys. Rev. E* **103**, 023201 (2021).
- J. L. Shaw, M. A. Romo-Gonzalez, N. Lemos, P. M. King, G. Bruhaug, K. G. Miller, C. Dorrer, B. Kruschwitz, L. Waxer, G. J. Williams, M. V. Ambat, M. M. McKie, M. D. Sinclair, W. B. Mori, C. Joshi, H. Chen, J. P. Palastro, F. Albert, and D. H. Froula, "Microcoulomb ($0.7 \pm 0.4/0.2 \mu\text{C}$) Laser Plasma Accelerator on OMEGA EP," *Sci. Rep.* **11**, 7498 (2021).
- A. Shvydky, D. Haberberger, A. V. Maximov, R. Boni, D. Cao, J. Carroll-Nellenback, D. H. Froula, V. N. Goncharov, S. X. Hu, I. V. Igumenshchev, S. T. Ivancic, V. V. Karasiev, J. P. Knauer, P. M. Nilson, P. B. Radha, S. P. Regan, J. R. Rygg, T. C. Sangster, M. D. Rosen, and V. A. Smalyuk, "Density Evolution After Shock Release from Laser-Driven Polystyrene (CH) Targets in Inertial Confinement Fusion," *Phys. Plasmas* **28**, 092703 (2021).
- T. T. Simpson, D. Ramsey, P. Franke, N. Vafaei-Najafabadi, D. Turnbull, D. H. Froula, and J. P. Palastro, "Nonlinear Spatiotemporal Control of Laser Intensity," *Opt. Lett.* **28**, 38,516 (2020).
- C. Stoeckl, M. J. Bonino, C. Mileham, S. P. Regan, W. Theobald, T. Ebert, and S. Sander, "Optimization of a Short-Pulse-Driven Si He $_{\alpha}$ Soft X-Ray Backlighter," *High Energy Density Phys.* **41**, 100973 (2021).
- G. Sutcliffe, P. Adrian, J. Percy, T. Johnson, N. Kabadi, S. Haque, C. Parker, B. Lahmann, J. Frenje, M. Gatu-Johnson, H. Sio, F. Séguin, B. Pollock, J. Moody, V. Glebov, R. Janezic, M. Koch, R. Petrasso, and C. Li, "A New Tri-Particle Backlighter for High-Energy-Density Plasmas," *Rev. Sci. Instrum.* **92**, 063524 (2021) (invited).
- C. A. Thomas, E. M. Campbell, K. L. Baker, D. T. Casey, M. Hohenberger, A. L. Kritcher, B. K. Spears, S. F. Khan, R. Nora, D. T. Woods, J. L. Milovich, R. L. Berger, D. Strozzi, D. D. Ho, D. Clark, B. Bachmann, L. R. Benedetti, R. Bionta, P. M. Celliers, D. N. Fittinghoff, G. Grim, R. Hatarik, N. Izumi, G. Kyrala, T. Ma, M. Millot, S. R. Nagel, P. K. Patel, C. Yeamans, A. Nikroo, M. Tabak, M. Gatu Johnson, P. L. Volegov, and S. M. Finnegan, "Deficiencies in Compression and Yield in X-Ray Driven Implosions," *Phys. Plasmas* **27**, 112705 (2020).
- C. A. Thomas, E. M. Campbell, K. L. Baker, D. T. Casey, M. Hohenberger, A. L. Kritcher, B. K. Spears, S. F. Khan, R. Nora, D. T. Woods, J. L. Milovich, R. L. Berger, D. Strozzi, D. D. Ho, D. Clark, B. Bachmann, L. R. Benedetti, R. Bionta, P. M. Celliers, D. N. Fittinghoff, G. Grim, R. Hatarik, N. Izumi, G. Kyrala, T. Ma, M. Millot, S. R. Nagel, P. K. Patel, C. Yeamans, A. Nikroo, M. Tabak, M. Gatu Johnson, P. Volegov, and S. M. Finnegan, "Experiments to Explore the Influence of Pulse Shaping at the National Ignition Facility," *Phys. Plasmas* **27**, 112708 (2020).
- C. A. Thomas, E. M. Campbell, K. L. Baker, D. T. Casey, M. Hohenberger, A. L. Kritcher, B. K. Spears, S. F. Khan, R. Nora, D. T. Woods, J. L. Milovich, R. L. Berger, D. Strozzi, D. D. Ho, D. Clark, B. Bachmann, L. R. Benedetti, R. Bionta, P. M. Celliers, D. N. Fittinghoff, G. Grim, R. Hatarik, N. Izumi, G. Kyrala, T. Ma, M. Millot, S. R. Nagel, P. K.

- Patel, C. Yeamans, A. Nikroo, M. Tabak, M. Gatu Johnson, P. L. Volegov, and S. M. Finnegan, "Principal Factors in Performance of Indirect-Drive Laser Fusion Experiments," *Phys. Plasmas* **27**, 112712 (2020).
- D. Turnbull, A. V. Maximov, D. Cao, A. R. Christopherson, D. H. Edgell, R. K. Follett, V. Gopalaswamy, J. P. Knauer, J. P. Palastro, A. Shvydky, C. Stoeckl, H. Wen, and D. H. Froula, "Impact of Spatiotemporal Smoothing on the Two-Plasmon-Decay Instability," *Phys. Plasmas* **27**, 102710 (2020).
- M. P. Valdivia, D. Stutman, C. Stoeckl, W. Theobald, G. W. Collins IV, V. Bouffetier, M. Vescovi, C. Mileham, I. A. Begishev, S. R. Klein, R. Melean, S. Muller, J. Zou, F. Veloso, A. Casner, F. N. Beg, and S. P. Regan, "Talbot-Lau X-Ray Deflectometer: Refraction-Based HEDP Imaging Diagnostic," *Rev. Sci. Instrum.* **92**, 065110 (2021).
- J. von der Linden, G. Fiksel, J. Peebles, M. R. Edwards, L. Willingale, A. Link, D. Mastrosimone, and H. Chen, "Confinement of Relativistic Electrons in a Magnetic Mirror en Route to a Magnetized Relativistic Pair Plasma," *Phys. Plasmas* **28**, 092508 (2021).
- J. von der Linden, J. Ramos-Méndez, B. Faddegon, D. Massin, G. Fiksel, J. P. Holder, L. Willingale, J. Peebles, M. R. Edwards, and H. Chen, "Dispersion Calibration for the National Ignition Facility Electron-Positron-Proton Spectrometers for Intense Laser Matter Interactions," *Rev. Sci. Instrum.* **92**, 033516 (2021).
- J. U. Wallace, K. L. Marshall, D. J. Batesky, T. Z. Kosc, B. N. Hoffman, S. Papernov, L. Garrett, J. Shojaie, and S. G. Demos, "Highly Saturated Glassy Liquid Crystal Films Having Nano- and Microscale Thicknesses for High-Power Laser Applications," *ACS Appl. Nano Mater.* **4**, 13 (2021).
- W. Y. Wang and R. S. Craxton, "Pentagonal Prism Spherical Hohlraums for OMEGA," *Phys. Plasmas* **28**, 062703 (2021).
- H. Wen, R. K. Follett, A. V. Maximov, D. H. Froula, F. S. Tsung, and J. P. Palastro, "Suppressing the Enhancement of Stimulated Raman Scattering in Inhomogeneous Plasmas by Tuning the Modulation Frequency of a Broadband Laser," *Phys. Plasmas* **28**, 042109 (2021).
- H. D. Whitley, G. E. Kemp, C. B. Yeamans, Z. B. Walters, B. E. Blue, W. J. Garbett, M. B. Schneider, R. S. Craxton, E. M. Garcia, P. W. McKenty, M. Gatu Johnson, K. Caspersen, J. I. Castor, M. Däne, C. L. Ellison, J. A. Gaffney, F. R. Graziani, J. E. Klepeis, N. B. Kostinski, A. L. Kritcher, B. Lahmann, A. E. Lazicki, H. P. Le, R. A. London, B. Maddox, M. C. Marshall, M. E. Martin, B. Militzer, A. Nikroo, J. Nilsen, T. Ogitsu, J. E. Pask, J. E. Pino, M. S. Rubery, R. Shepherd, P. A. Sterne, D. C. Swift, L. Yang, and S. Zhang, "Comparison of Ablators for the Polar Direct Drive Exploding Pusher Platform," *High Energy Density Phys.* **38**, 100928 (2021).
- K. M. Woo and R. Betti, "Impact of Areal-Density Asymmetries on the Loss of Confinement and Ignition Threshold in Inertial Confinement Fusion Capsules," *Phys. Plasmas* **28**, 054503 (2021).
- C. B. Yeamans, G. E. Kemp, Z. B. Walters, H. D. Whitley, P. W. McKenty, E. M. Garcia, Y. Yang, R. S. Craxton, and B. E. Blue, "High Yield Polar Direct Drive Fusion Neutron Sources at the National Ignition Facility," *Nucl. Fusion* **61**, 046031 (2021).
- H. Zhang, R. Betti, R. Yan, and H. Aluie, "Nonlinear Bubble Competition of the Multimode Ablative Rayleigh-Taylor Instability and Its Applications to Inertial Confinement Fusion," *Phys. Plasmas* **27**, 122701 (2020).
- J. Zhang, W. R. Donaldson, and G. P. Agrawal, "Impact of the Boundary's Sharpness on Temporal Reflection in Dispersive Media," *Opt. Lett.* **46**, 4053 (2021).
- J. Zhang, W. R. Donaldson, and G. P. Agrawal, "Temporal Reflection and Refraction of Optical Pulses Inside a Dispersive Medium: An Analytic Approach," *J. Opt. Soc. Am. B* **38**, 997 (2021).
- J. Zhang, W. R. Donaldson, and G. P. Agrawal, "Time-Domain Fabry-Perot Resonators Formed Inside a Dispersive Medium," *J. Opt. Soc. Am. B* **38**, 2376 (2021).
- S. Zhang, J. Li, C. M. Krauland, F. N. Beg, S. Muller, W. Theobald, J. Palastro, T. Filkins, D. Turnbull, D. Haberberger, C. Ren, R. Betti, C. Stoeckl, E. M. Campbell, J. Trela, D. Batani, R. H. H. Scott, and M. S. Wei, "Pump-Depletion Dynamics and Saturation of Stimulated Brillouin Scattering in Shock Ignition Relevant Experiments," *Phys. Rev. E* **103**, 063208 (2021).
- S. Zhang, M. C. Marshall, L. H. Yang, P. A. Sterne, B. Militzer, M. Däne, J. A. Gaffney, A. Shamp, T. Ogitsu, K. Caspersen, A. E. Lazicki, D. Erskine, R. A. London, P. M. Celliers, J. Nilsen, and H. D. Whitley, "Benchmarking Boron Carbide

Equation of State Using Computation and Experiment,” *Phys. Rev. E* **102**, 053203 (2020).

S. Zhang and M. A. Morales, “First-Principles Equations of State and Structures of Liquid Metals in Multi-Megabar Conditions,” *AIP Conf. Proc.* **2272**, 090004 (2020).

S. Zhang, H. D. Whitley, and T. Ogitsu, “Phase Transformation in Boron Under Shock Compression,” *Solid State Sci.* **108**, 106376 (2020).

Y. Zhang, J. R. Davies, P. V. Heuer, and C. Ren, “Kinetic Simulation Study of Magnetized Collisionless Shock Formation on a Terawatt Laser System,” *Phys. Plasmas* **28**, 072111 (2021).

A. B. Zylstra, C. Yeaman, S. Le Pape, A. MacKinnon, M. Hohenberger, D. N. Fittinghoff, H. Herrmann, Y. Kim, P. B. Radha, P. W. McKenty, R. S. Craxton, and M. Hoppe, “Enhanced Direct-Drive Implosion Performance on NIF with Wavelength Separation,” *Phys. Plasmas* **27**, 124501 (2020).

Conference Presentations

B. E. Ugur, “Computational Modeling and Design of Liquid Crystal Materials for Applications in the Terahertz Regime,” presented at the 2020 American Institute of Chemical Engineers Eckhardt Northeast Region Conference, virtual, 3–4 October 2020.

S. G. Demos, K. R. P. Kafka, B. N. Hoffman, A. A. Kozlov, H. Huang, J. B. Oliver, A. L. Rigatti, T. J. Kessler, T. Z. Kosc, N. Liu, R. Dent, A. A. Shestopalov, and J. C. Lambropoulos, “The Fundamental Mechanism of Laser-Induced Damage in Optical Components for Ultrashort-Pulse Laser Systems,” presented at OSA Laser Congress, virtual, 12–16 October 2020.

N. D. Urban, J. U. Wallace, K. L. Marshall, and S. G. Demos, “Photoswitchable Liquid Crystal Beam Shapers for High-Power Laser Applications,” presented at the Clarkson University Seminar, virtual, 13 October 2020.

C. J. Forrest, J. P. Knauer, W. U. Schröder, V. Yu. Glebov, O. M. Mannion, K. L. Marshall, Z. L. Mohamed, P. B. Radha, S. P. Regan, M. Romanofsky, T. C. Sangster, A. Schwemlein, M. Sickles, C. Sorce, C. Stoeckl, and J. Szczepanski, “Nuclear Science at the University of Rochester’s Omega Laser Facility,” presented at Ohio University, virtual, 20 October 2020.

B. Webb, “Next Generation Petawatt Laser Technology,” presented at the 8th Texas STEM Conference, virtual, 24 October 2020.

The following presentations were made at the 4th Asia-Pacific Conference on Plasma Physics, virtual, 26–31 October 2020:

R. K. Follett, J. G. Shaw, C. Dorrer, D. H. Edgell, D. H. Froula, H. Wen, J. Bromage, E. M. Hill, T. J. Kessler, A. V. Maximov, A. A. Solodov, E. M. Campbell, J. P. Palastro, J. F. Myatt, J. W. Bates, and J. L. Weaver, “Broadband Mitigation of the Multibeam Two-Plasmon Decay and Stimulated Raman Scattering Instabilities.”

A. A. Solodov, M. J. Rosenberg, M. Stoeckl, A. R. Christopherson, R. Betti, W. Seka, R. Epstein, C. Stoeckl, R. K. Follett, P. B. Radha, S. P. Regan, D. H. Froula, J. P. Palastro, V. N. Goncharov, J. F. Myatt, M. Hohenberger, B. Bachmann, and P. Michel, “Scaling and Mitigation of Hot-Electron Preheat Polar-Direct-Drive Experiments at the National Ignition Facility.”

H. Wen, R. K. Follett, A. V. Maximov, D. H. Froula, J. P. Palastro, and F. S. Tsung, “Kinetic Inflation of Stimulated Raman Scattering Driven by a Broadband Frequency-Modulated Laser Pulse.”

O. M. Mannion, K. S. Anderson, R. Betti, E. M. Campbell, D. Cao, C. J. Forrest, V. Yu. Glebov, V. N. Goncharov, V. Gopalaswamy, I. V. Igumenshchev, S. T. Ivancic, D. W. Jacobs-

Perkins, J. P. Knauer, A. Lees, F. J. Marshall, Z. L. Mohamed, D. Patel, S. P. Regan, H. G. Rinderknecht, R. C. Shah, C. Stoeckl, W. Theobald, K. M. Woo, B. D. Appelbe, J. P. Chittenden, A. J. Crilly, W. Taitano, P. Adrian, J. A. Frenje, N. V. Kabadi, and M. Gatu Johnson, “Applications of Neutron Spectroscopy in High-Energy-Density Science,” presented at the High Energy Density Science Association, virtual, 8 November 2020.

The following presentations were made at the the 45th International Conference on Infrared, Millimeter, and Terahertz Waves, virtual, 8–13 November 2020:

G. Chen, R. Adam, D. Bürgler, D. Cao, A. Pericolo, J. Cheng, I. Komissarov, S. Heidtfeld, L. Gladczuk, P. Przyslupski, H. Hardtdegen, M. Mikulics, C. M. Schneider, and R. Sobolewski, “Onset-Time Control of THz Transients Generated by Spintronic Emitters.”

G. Chen, D. Chakraborty, J. Cheng, C. Chimera, I. Komissarov, M. Mikulics, R. Adam, D. E. Bürgler, C. M. Schneider, H. Hardtdegen, and R. Sobolewski, “Magnetic-Field Enhancement of THz Surface Emission in Highly Resistive GaAs.”

G. Chen, M. Mikulics, R. Adam, A. Pericolo, J. Serafini, S. Preble, J. Cheng, C. Chimera, J. Komissarov, H. H. Hardtdegen, and R. Sobolewski, “Photomixing THz Generation from Nitrogen-Ion-Implanted GaAs Metal-Semiconductor-Metal Diodes Enhanced by a Bragg Mirror.”

J. Bromage, S.-W. Bahk, I. A. Begishev, S. Bucht, C. Dorrer, C. Feng, B. N. Hoffman, C. Jeon, C. Mileham, J. B. Oliver, R. G. Roides, M. J. Shoup III, M. Spilatro, B. Webb, and J. D. Zuegel, “MTW-OPAL: A Technology Development Platform for Ultra-Intense OPCPA Systems,” presented at ELI-NP Autumn School (ELIAS 2020), virtual, 9 November 2020.

The following presentations were made at the 62nd Annual Meeting of the American Physical Society Division of Plasmas Physics, virtual, 9–13 November 2020:

K. S. Anderson, W. Theobald, M. J. Rosenberg, J. A. Marozas, R. H. H. Scott, and K. Glize, “Cross-Beam Energy Transfer in Simulations of NIF-Scale Strong Spherical Shock Experiments.”

J. Baltazar, R. C. Shah, S. X. Hu, K. Churnetski, R. Epstein, V. N. Goncharov, I. V. Igumenshchev, T. Joshi, W. Theobald, and S. P. Regan, “Feasibility Study of Measuring In-Flight Shell Thickness for a Laser-Direct-Drive DT Cryogenic Implosion.”

Z. Barfield, D. H. Froula, J. P. Palastro, J. L. Peebles, D. Mastrosimone, A. M. Hansen, J. Katz, and P. Tzeferacos, “Thermal Transport in Low-Beta Laser-Produced Plasmas.”

D. H. Barnak, M. J. Bonino, J. R. Davies, E. C. Hansen, D. R. Harding, L. S. Leal, J. L. Peebles, P.-Y. Chang, R. Betti, J. D. Moody, and B. B. Pollock, “Achieving an Azimuthal Uniform Cylindrical Implosion on OMEGA.”

R. Betti, V. Gopalaswamy, J. P. Knauer, A. Lees, D. Patel, C. A. Thomas, and W. Theobald, “Exploring Pathways to Hydro-Equivalent Ignition on the OMEGA Laser.”

D. T. Bishel, E. V. Marley, M. B. Schneider, D. A. Liedahl, R. F. Heeter, M. E. Foord, G. E. Kemp, Y. Frank, J. A. Emig, G. Perez-Callejo, J. R. Rygg, G. W. Collins, and P. M. Nilson, “Open L-Shell Spectroscopy of Non-Local-Thermodynamic-Equilibrium Plasmas.”

G. Bruhaug, H. G. Rinderknecht, M. S. Wei, G. W. Collins, J. R. Rygg, Y. E. K. Garriga, and X. C. Zhang, “High-Power THz Sources for High-Energy-Density–Physics Applications.”

D. Cao, R. C. Shah, R. Epstein, A. R. Christopherson, V. Gopalaswamy, S. P. Regan, W. Theobald, and V. N. Goncharov, “Analysis of Techniques to Infer Hot-Spot Mixing Using Absolute X-Ray Emission for OMEGA Direct-Drive Layered Implosions.”

L. Ceurvorst, R. Betti, A. Bose, S. X. Hu, E. M. Campbell, S. P. Regan, J. L. Peebles, W. Theobald, A. Casner, C. A. McCoy, M. Karasik, and M. Tabak, “Imprint Mitigation with Hybrid Targets.”

D. A. Chin, P. M. Nilson, J. J. Ruby, X. Gong, M. K. Ginnane, B. J. Henderson, L. Crandall, D. N. Polsin, T. R. Boehly, J. R. Rygg, G. W. Collins, D. Trail, A. Amouretti, M. Harmand, R. Torchio, F. Coppari, A. Coleman, and Y. Ping, “Using X-Ray Absorption Spectroscopy to Study Iron Oxides at Extreme Compressions.”

K. Churnetski, W. Theobald, K. A. Woo, R. Ejaz, I. V. Igumenshchev, S. T. Ivancic, A. Kish, M. Michalko, R. C. Shah, R. Spielman, S. P. Regan, A. Raymond, P. Bell, A. Carpenter, A. McPhee, C. Trosseille, D. K. Bradley, J. D. Hares, A. K. L. Dymoke-Bradshaw, G. Rochau, L. Claus, M. Sanchez,

and D. Garand “The Third Line-of-Sight Time-Gated X-Ray Imager for OMEGA DT Cryogenic Implosions.”

T. J. B. Collins, M. Hohenberger, L. Divol, W. W. Hsing, J. A. Marozas, K. A. Bauer, R. S. Craxton, P. W. McKenty, P. B. Radha, S. P. Regan, M. J. Rosenberg, and E. M. Campbell, “Optimization of OMEGA Exploding-Pusher Performance Using Shaped Pulses.”

L. E. Crandall, J. R. Rygg, T. R. Boehly, B. J. Henderson, M. F. Huff, D. N. Polsin, M. Zaghoo, G. W. Collins, D. K. Spaulding, S. Brygoo, P. M. Celliers, J. H. Eggert, D. E. Fratanduono, A. Lazicki, M. C. Marshall, M. Millot, and R. Jeanloz, “Equation of State and Transport of CO₂ Shock Compressed to 1 TPa” (invited).

R. S. Craxton, W. Y. Wang, and E. M. Campbell, “A New Beam Configuration to Support Both Spherical Hohlräume and Symmetric Direct Drive.”

J. R. Davies, H. Wen, E. D. Held, and J.-Y. Ji, “Transport Coefficients for Magnetic-Field Evolution in Inviscid Magnetohydrodynamics.”

D. H. Edgell, R. K. Follett, J. Katz, J. A. Marozas, D. Turnbull, and D. H. Froula, “Low-Mode Asymmetry due to Polarization Smoothing in OMEGA Implosions.”

R. Epstein, A. Shvydky, I. E. Golovkin, and W.-F. Fong, “Non-equilibrium Thermodynamics of Plasma Under Collisional-Radiative Equilibrium.”

R. K. Follett, J. G. Shaw, C. Dorrer, D. H. Edgell, D. H. Froula, H. Wen, J. Bromage, E. M. Hill, T. J. Kessler, A. V. Maximov, A. A. Solodov, E. M. Campbell, J. P. Palastro, J. F. Myatt, J. W. Bates, and J. L. Weaver, “Broadband Mitigation of the Multibeam Two-Plasmon Decay and Stimulated Raman Scattering Instabilities.”

C. J. Forrest, V. Yu. Glebov, V. N. Goncharov, J. P. Knauer, O. M. Mannion, Z. L. Mohamed, P. B. Radha, S. P. Regan, R. C. Shah, C. Stoeckl, and K. M. Woo, “Evaluating the Residual Kinetic Energy in Direct-Drive Cryogenic Implosions on OMEGA.”

P. Franke, J. P. Palastro, D. Ramsey, T. T. Simpson, D. Turnbull, and D. H. Froula, “Dynamically Guided Self-Photon Acceleration.”

F. Garcia-Rubio, R. Betti, H. Aluie, and J. Sanz Recio, “Magnetic-Field Effect on Rayleigh-Taylor and Darrieus–Landau Instabilities.”

M. K. Ginnane, D. N. Polsin, X. Gong, T. R. Boehly, J. R. Rygg, G. W. Collins, A. Lazicki, R. Kraus, J. H. Eggert, M. C. Marshall, D. E. Fratanduono, J.-P. Davis, C. A. McCoy, C. Seagle, and S. Root, “X-Ray Diffraction Measurements of Dynamically Compressed Platinum.”

V. N. Goncharov, I. V. Igumenshchev, D. R. Harding, S. F. B. Morse, S. X. Hu, P. B. Radha, D. H. Froula, S. P. Regan, T. C. Sangster, and E. M. Campbell, “Novel Hot-Spot-Ignition Designs for Inertial Confinement Fusion with Liquid Deuterium–Tritium Spheres.”

V. Gopalaswamy, R. Betti, J. P. Knauer, A. Lees, D. Patel, A. R. Christopherson, K. M. Woo, D. Cao, C. A. Thomas, I. V. Igumenshchev, S. P. Regan, W. Theobald, R. C. Shah, P. B. Radha, and K. S. Anderson, “Inferring Degradation Mechanisms in OMEGA Cryogenic Implosions Through Statistical Modeling.”

A. M. Hansen, K. L. Nguyen, D. Turnbull, R. K. Follett, R. Huff, J. Katz, D. Mastro Simone, A. L. Milder, J. P. Palastro, D. H. Froula, B. Albright, and L. Yin, “Cross-Beam Energy Transfer Saturation.”

B. J. Henderson, T. R. Boehly, M. Zaghoo, J. R. Rygg, D. N. Polsin, X. Gong, L. Crandall, M. Huff, M. K. Ginnane, G. W. Collins, S. Ali, and P. M. Celliers, “Optical Spectroscopy Measurements of Decaying Shocks in Transparent Crystals.”

J. Hinz, V. V. Karasiev, and S. X. Hu, “A Machine-Learned, Orbital-Free, Force-Correction Model: Extending the Thermodynamic Range of Affordable Kohn–Sham Level Accuracy.”

S. X. Hu, P. M. Nilson, V. V. Karasiev, S. B. Hansen, T. Walton, and I. E. Golovkin, “Extreme Atomic Physics at 5- to 100-Gbar Pressures.”

M. Huff, J. R. Rygg, G. W. Collins, T. R. Boehly, M. Zaghoo, D. N. Polsin, M. Nakajima, B. J. Henderson, L. E. Crandall, M. C. Marshall, D. E. Fratanduono, M. Millot, R. F. Smith, J. H. Eggert, P. M. Celliers, and C. A. McCoy, “Measurements of Sound Speed in Iron Shock-Compressed to ~4000 GPa.”

I. V. Igumenshchev, O. M. Mannion, J. P. Knauer, R. Betti, E. M. Campbell, D. Cao, V. N. Goncharov, V. Gopalaswamy, D. Patel, S. P. Regan, R. C. Shah, A. Shvydky, W. Theobald, D. S. Clark, M. M. Marinak, and B. M. Haines, “Modeling Effects of Ion Viscosity on Dynamics of OMEGA Direct-Drive Cryogenic Implosions.”

V. V. Karasiev, D. I. Mihaylov, S. X. Hu, and S. B. Trickey, “Accurate Density Functional Theory Simulations Across Warm-Dense-Matter Regime: Thermal meta-GGA Exchange-Correlation and Nuclear-Quantum Effects.”

J. P. Knauer, R. Betti, V. Gopalaswamy, D. Cao, D. Patel, A. Lees, A. Shvydky, M. J. Bonino, E. M. Campbell, T. J. B. Collins, C. J. Forrest, V. Yu. Glebov, V. N. Goncharov, D. R. Harding, J. A. Marozas, F. J. Marshall, P. W. McKenty, J. L. Peebles, P. B. Radha, S. P. Regan, T. C. Sangster, C. Stoeckl, M. Gatu Johnson, J. A. Frenje, and R. D. Petrasso, “A Systematic Study of Laser Imprint for Direct Drive—From Seeds to Integrated Implosions.”

L. S. Leal, A. V. Maximov, E. C. Hansen, J. R. Davies, D. H. Barnak, J. L. Peebles, A. B. Sefkow, and R. Betti, “Simulations of Laser Preheat Effects on Yield in Mini-MagLIF Implosions on OMEGA.”

A. Lees, R. Betti, J. P. Knauer, V. Gopalaswamy, D. Patel, R. Epstein, J. Carroll-Nellenback, A. R. Christopherson, K. M. Woo, O. M. Mannion, Z. L. Mohamed, F. J. Marshall, C. Stoeckl, V. Yu. Glebov, S. P. Regan, R. C. Shah, D. H. Edgell, D. Cao, V. N. Goncharov, I. V. Igumenshchev, P. B. Radha, T. J. B. Collins, T. C. Sangster, E. M. Campbell, M. Gatu Johnson, R. D. Petrasso, C. K. Li, and J. A. Frenje, “Understanding the Fusion Yield and All of Its Dependencies Using Statistical Modeling of Experimental Data” (invited).

O. M. Mannion, K. S. Anderson, R. Betti, E. M. Campbell, D. Cao, C. J. Forrest, V. Yu. Glebov, V. N. Goncharov, V. Gopalaswamy, I. V. Igumenshchev, S. T. Ivancic, D. W. Jacobs-Perkins, J. P. Knauer, A. Lees, F. J. Marshall, Z. L. Mohamed, D. Patel, S. P. Regan, H. G. Rinderknecht, R. C. Shah, C. Stoeckl, W. Theobald, K. M. Woo, and M. Gatu Johnson, “Mode One Asymmetry in Laser-Direct-Drive Inertial Confinement Fusion Implosions” (invited).

O. M. Mannion, C. J. Forrest, V. Yu. Glebov, J. P. Knauer, P. W. McKenty, Z. L. Mohamed, S. P. Regan, C. Stoeckl, B. D. Appelbe, A. J. Crilly, W. Taitano, P. J. Adrian, J. A. Frenje, N. V. Kabadi, and M. Gatu Johnson, “Measurements of the DT and DD Neutron Energy Spectrum in High Temperature Fusing Plasmas.”

J. A. Marozas, K. S. Anderson, R. Betti, T. R. Boehly, R. Boni, M. J. Bonino, E. M. Campbell, D. Canning, D. Cao, T. J. B. Collins, R. S. Craxton, A. K. Davis, J. A. Delettrez, W. R. Donaldson, D. H. Edgell, R. Epstein, C. J. Forrest, D. H.

Froula, V. Yu. Glebov, V. N. Goncharov, D. R. Harding, S. X. Hu, H. Huang, I. V. Igumenshchev, R. T. Janezic, D. W. Jacobs-Perkins, J. Katz, R. L. Keck, J. H. Kelly, T. J. Kessler, B. E. Kruschwitz, J. P. Knauer, T. Z. Kosci, S. J. Loucks, F. J. Marshall, A. V. Maximov, P. W. McKenty, S. F. B. Morse, P. M. Nilson, J. C. Puth, P. B. Radha, S. P. Regan, H. G. Rinderknecht, M. J. Rosenberg, T. C. Sangster, R. Shah, W. T. Shmayda, R. W. Short, A. Shvydky, M. J. Shoup III, S. Skupsky, A. A. Solodov, C. Sorce, S. Stagnitto, C. Stoeckl, W. Theobald, D. Turnbull, J. Ulreich, M. D. Wittman, V. Gopalaswamy, J. D. Zuegel, J. A. Frenje, M. Gatu Johnson, R. D. Petrasso, H. Sio, B. Lahmann, P. Bell, B. E. Blue, S. Bhandarkar, D. K. Bradley, D. A. Callahan, A. Carpenter, D. T. Casey, J. Celeste, M. Dayton, C. S. Goyon, M. Hohenberger, O. A. Hurricane, G. E. Kemp, S. Le Pape, L. Masse, P. Michel, J. D. Moody, S. R. Nagel, A. Nikroo, R. Nora, L. Pickworth, J. E. Ralph, R. P. J. Town, R. J. Wallace, Z. B. Walters, P. Wegner, H. D. Whitley, C. B. Yeamans, M. Farrell, P. Fitzsimmons, C. Gibson, A. Greenwood, L. Carlson, T. Hilsabeck, H. Huang, J. D. Kilkenny, R. W. Luo, N. Rice, M. Schoff, W. Sweet, A. Tambazidis, T. Bernat, N. Petta, J. Hund, S. P. Obenschain, J. W. Bates, M. Karasik, A. J. Schmitt, J. Weaver, J. Hares, T. Dymoke-Bradshaw, R. E. Olson, M. J. Schmitt, S. Hsu, G. Rochau, L. Claus, Q. Looker, J. Porter, G. Robertson, M. Sanchez, and W. J. Garbett, “Laser-Direct-Drive Inertial Confinement Fusion—A Pathway to Ignition” (invited).

M. C. Marshall, M. Millot, D. E. Fratanduono, P. C. Myint, J. L. Belof, Y.-J. Kim, F. Coppari, J. H. Eggert, R. F. Smith, J. M. McNaney, D. M. Sterbentz, J. R. Rygg, and G. W. Collins, “Probing the Metastability Limit of Liquid Water Under Dynamic Compression.”

A. V. Maximov, D. Turnbull, D. H. Edgell, J. G. Shaw, R. K. Follett, H. Wen, D. H. Froula, and J. P. Palastro, “Nonlinear Absorption of Multiple Laser Beams due to the Two-Plasmon–Decay Instability.”

P. W. McKenty, M. J. Rosenberg, F. J. Marshall, D. R. Harding, R. S. Craxton, J. A. Marozas, T. J. B. Collins, R. Epstein, E. M. Campbell, S. Schiaffino, B. E. Blue, C. B. Yeamans, W. W. Hsing, C. Shulderberg, and M. Farrell, “Evaluation of Polar-Direct-Drive, Contoured-Shell Experiments at the National Ignition Facility.”

B. McLellan and S. Zhang, “Kinetic Transition Pathway of Pressure Driven Structural Transformations: The Case of Magnesium Oxide.”

- D. I. Mihaylov, V. V. Karasiev, and S. X. Hu, "Progress in Development of Thermal Hybrid Exchange-Correlation Density Functionals for Improving the Description of Warm Dense Matter."
- A. Milder, J. Katz, R. Boni, D. Nelson, D. Turnbull, J. P. Palastro, K. Daub, R. K. Follett, D. H. Froula, M. Sherlock, T. Chapman, and W. Rozmus, "Measurements of Electron Distribution Functions in Laser-Produced Plasmas Using Angularly Resolved Thomson Scattering" (invited).
- S. C. Miller, V. N. Goncharov, T. J. B. Collins, and J. Carroll-Nellenback, "A Study of 2D Internal Perturbation Evolution in Inertial Confinement Fusion Implosions."
- Z. L. Mohamed, O. M. Mannion, C. J. Forrest, J. P. Knauer, and E. P. Hartouni, "Construction and Implementation of an Energy-Dependent Instrument Response Function for Accurate Analysis of Neutron Time-of-Flight Data."
- K. L. Nguyen, A. M. Hansen, D. Turnbull, R. K. Follett, D. H. Froula, J. P. Palastro, L. Yin, and B. J. Albright, "Nonlinear Saturation of Cross-Beam Energy Transfer."
- P. M. Nilson, F. J. Marshall, J. Kendrick, J. J. Ruby, D. A. Chin, D. Bishel, D. Guy, S. T. Ivancic, C. Stoeckl, R. F. Earley, D. R. Harding, M. Bedzyk, G. Gates, D. W. Jacobs-Perkins, V. N. Goncharov, T. J. B. Collins, and R. Epstein, "Imaging of Hydrodynamic Perturbation Evolution Using a Fresnel Phase Zone Plate."
- J. P. Palastro, D. H. Froula, M. V. Ambat, R. Boni, E. M. Campbell, R. K. Follett, P. Franke, V. N. Goncharov, J. B. Oliver, D. Ramsey, J. L. Shaw, T. T. Simpson, D. Turnbull, H. Wen, S. Jolly, F. Quere, C. Benedetti, E. Esarey, G. Geddes, C. Schroeder, R. Bingham, S. Stoller, N. Vafaei-Najafabadi, G. Gregori, B. Malaca, A. Helm, J. Vieira, A. DiPiazza, A. Howard, K. Weichman, A. Arefiev, T. M. Antonsen, Jr., and Z. Li, "Laser-Plasma Interactions Driven by Spatiotemporally Structured Light Pulses" (invited).
- D. Patel, R. Betti, K. M. Woo, V. Gopalaswamy, J. C. Carrol, and A. Bose, "Hydrodynamic Scaling Relations for OMEGA Cryogenic Implosions."
- J. L. Peebles, J. R. Davies, D. H. Barnak, M. J. Bonino, T. Cracium, R. Betti, and P.-Y. Chang, "Axial Proton Radiography of Electric and Magnetic Fields Inside Laser-Driven Coils."
- H. Poole, D. Cao, J. R. Rygg, S. X. Hu, I. E. Golovkin, T. Walton, R. Epstein, M. Kasim, S. Vinko, G. Gregori, and S. P. Regan, "A Feasibility Study of Using X-Ray Thomson Scattering to Diagnose the Plasma Conditions of Laser-Direct-Drive, DT Cryogenic Implosions."
- P. B. Radha, W. Theobald, R. Betti, D. Cao, R. S. Craxton, C. J. Forrest, V. Yu. Glebov, V. N. Goncharov, V. Gopalaswamy, I. V. Igumenshchev, S. T. Ivancic, T. Joshi, J. P. Knauer, O. M. Mannion, F. J. Marshall, S. Miller, Z. L. Mohamed, D. Patel, S. P. Regan, H. G. Rinderknecht, T. C. Sangster, R. C. Shah, C. Stoeckl, C. A. Thomas, E. M. Campbell, M. Gatu Johnson, J. A. Frenje, and R. D. Petrasso, "Understanding the Performance of Polar-Drive Cryogenic Implosions on OMEGA."
- D. Ramsey, P. Franke, T. T. Simpson, M. V. Ambat, D. H. Froula, and J. P. Palastro, "Vacuum Acceleration of Electrons in a Dynamic Laser Pulse."
- S. P. Regan, W. Theobald, P. B. Radha, R. Betti, M. J. Rosenberg, R. S. Craxton, A. A. Solodov, A. Shvydky, K. S. Anderson, J. A. Marozas, T. J. B. Collins, V. N. Goncharov, D. Turnbull, E. M. Campbell, C. M. Shulberg, R. W. Luo, R. Heredia, B. Bachmann, T. Döppner, M. Hohenberger, R. Scott, K. Glize, A. Colaitis, and A. Casner, "Laser-Direct-Drive Energy-Coupling Experiments Using Spherical Solid-Plastic Targets at the National Ignition Facility."
- H. G. Rinderknecht, J. P. Knauer, W. Theobald, R. Fairbanks, B. Brannon, V. Kobilansky, R. Peck, J. Armstrong, M. Weisbeck, J. Brown, P. B. Radha, S. P. Regan, J. Kunimune, P. J. Adrian, M. Gatu Johnson, J. A. Frenje, F. H. Séguin, and B. Bachmann, "Knock-on Deuteron Imaging of the Hot Spot and Compressed Fuel in Direct-Drive Cryogenic ICF Implosions."
- M. J. Rosenberg, A. A. Solodov, A. R. Christopherson, R. Betti, P. B. Radha, C. Stoeckl, C. J. Forrest, V. Yu. Glebov, F. J. Marshall, S. P. Regan, T. J. B. Collins, D. H. Froula, J. P. Palastro, V. N. Goncharov, M. Hohenberger, B. Bachmann, G. N. Hall, P. Michel, and C. Kauland, "Hot-Electron Preheat in Hydrodynamically Scaled Direct-Drive Implosions at the National Ignition Facility and OMEGA."
- J. J. Ruby, J. R. Rygg, D. A. Chin, C. J. Forrest, V. Yu. Glebov, C. Stoeckl, G. W. Collins, B. Bachmann, J. A. Gaffney, Y. Ping, N. V. Kabadi, and P. J. Adrian, "Bayesian Inference of Energy Transfer in Gigabar Convergent Experiments" (invited).
- A. K. Schwemlein, C. Stoeckl, W. T. Shmayda, C. J. Forrest, J. P. Knauer, S. P. Regan, and W. U. Schröder, "Controllable

Target-Normal Sheath Acceleration Deuteron Beams Using Titanium Targets Toward Generating a Tritium Beam.”

A. B. Sefkow, B. G. Logan, and J. H. Nuckolls, “Directly Driven Magnetized Targets with Steep Density Gradients for Inertial Fusion Energy.”

R. C. Shah, S. X. Hu, I. V. Igumenshchev, J. Baltazar, D. Cao, C. J. Forrest, V. N. Goncharov, V. Gopalaswamy, D. Patel, W. Theobald, S. P. Regan, and F. Philippe, “In-Flight Shell Breakup in Direct-Drive DT Cryogenic Implosion.”

J. L. Shaw, M. A. Romo-Gonzalez, G. Bruhaug, C. Dorrer, B. E. Kruschwitz, L. J. Waxer, M. V. Ambat, M. M. McKie, J. P. Palastro, D. H. Froula, N. Lemos, P. M. King, G. J. Williams, H. Chen, F. Albert, M. D. Sinclair, and C. Joshi, “Microcoulomb-Class Laser-Plasma Accelerator on OMEGA EP.”

A. Shvydky, D. Haberberger, J. P. Knauer, S. X. Hu, S. T. Ivancic, J. Carroll-Nellenback, D. Cao, I. V. Igumenshchev, V. V. Karasiev, P. B. Radha, A. V. Maximov, S. P. Regan, T. C. Sangster, R. Boni, P. M. Nilson, V. N. Goncharov, D. H. Froula, M. D. Rosen, and V. A. Smalyuk, “Shock-Release Experiments on OMEGA EP.”

T. T. Simpson, D. Ramsey, P. Franke, M. V. Ambat, D. Turnbull, D. H. Froula, J. P. Palastro, and N. Vafaei-Najafabadi, “Non-linear Spatiotemporal Control of Laser Intensity.”

A. A. Solodov, M. J. Rosenberg, M. Stoeckl, A. R. Christopherson, R. Betti, W. Seka, R. Epstein, C. Stoeckl, R. K. Follett, P. B. Radha, S. P. Regan, D. H. Froula, J. P. Palastro, V. N. Goncharov, J. F. Myatt, M. Hohenberger, B. Bachmann, and P. Michel, “Scaling and Mitigation of Hot-Electron Preheat in Polar-Direct-Drive Experiments at the National Ignition Facility.”

Z. K. Sprowal, L. E. Crandall, J. R. Rygg, T. R. Boehly, D. N. Polsin, G. W. Collins, D. G. Hicks, and P. M. Celliers, “Double Shock Compression in Polystyrene to ~8 Mbar.”

C. Stoeckl, M. J. Bonino, C. Mileham, S. P. Regan, W. Theobald, T. Ebert, and S. Sander, “Optimization of a Short-Pulse-Driven Si He $_{\alpha}$ Soft X-Ray Backlighter.”

W. Theobald, P. B. Radha, S. P. Regan, K. S. Anderson, R. Betti, E. M. Campbell, D. Cao, R. S. Craxton, C. J. Forrest, V. Yu. Glebov, V. N. Goncharov, V. Gopalaswamy, I. V. Igumenshchev, T. Joshi, S. T. Ivancic, J. P. Knauer, A. Lees, O. M. Mannion, F. J. Marshall, M. Michalko, Z. L. Mohamed, D. Patel, R. C.

Shah, C. Stoeckl, C. A. Thomas, and M. Gatu Johnson, “OMEGA Subscale Cryogenic Implosions in Symmetric and Polar-Direct-Drive Beam Geometry.”

C. A. Thomas, D. Cao, W. Theobald, R. Betti, K. S. Anderson, K. A. Bauer, E. M. Campbell, A. R. Christopherson, T. J. B. Collins, R. S. Craxton, D. H. Edgell, R. Epstein, C. J. Forrest, V. Yu. Glebov, V. Gopalaswamy, I. V. Igumenshchev, S. T. Ivancic, D. W. Jacobs-Perkins, R. T. Janezic, T. Joshi, J. P. Knauer, J. Kwiatkowski, A. Lees, O. M. Mannion, F. J. Marshall, M. Michalko, Z. L. Mohamed, D. Patel, J. L. Peebles, P. B. Radha, S. P. Regan, H. G. Rinderknecht, M. J. Rosenberg, S. Sampat, T. C. Sangster, R. C. Shah, C. Stoeckl, and V. N. Goncharov, “Quantifying the Effects of Scale and Illumination Geometry in Laser Direct Drive.”

D. Turnbull, A. V. Maximov, D. Cao, A. R. Christopherson, D. H. Edgell, R. K. Follett, V. Gopalaswamy, J. P. Knauer, J. P. Palastro, A. Shvydky, C. Stoeckl, H. Wen, and D. H. Froula, “Impact of Spatiotemporal Smoothing on the Two-Plasmon-Decay Instability.”

P. Tzeferacos, R. Betti, J. R. Davies, F. Garcia-Rubio, E. C. Hansen, D. Michta, C. Ren, A. C. Reyes, W. Scullin, A. B. Sefkow, J. G. Shaw, H. Wen, and K. M. Woo, “A Simulation Resource Team for Innovative Fusion Concepts in the BETHE Program.”

W. Y. Wang and R. S. Craxton, “A Proposal for Spherical Hohlraum Experiments on OMEGA Using Seven Laser Entrance Holes.”

H. Wen, R. K. Follett, A. V. Maximov, D. H. Froula, J. P. Palastro, and F. S. Tsung, “Kinetic Inflation of Stimulated Raman Scattering Driven by a Broadband Frequency-Modulated Laser Pulse.”

K. M. Woo and R. Betti, “Impact of Low-Mode Areal Density Asymmetry on Loss of Confinement for Igniting Capsules.”

S. Zhang and S. X. Hu, “Large-Scale Molecular-Dynamics Studies on the Release of Shocked Polystyrene Under Inertial Confinement Fusion Conditions.”

Y. Zhang, C. Ren, J. R. Davies, and P. Heuer, “Kinetic Simulation Study of Magnetized Collisionless Shock Formation Using OMEGA EP.”

M. Sharpe, W. T. Shmayda, J. Wermer, and C. A. Bond, “Permeation of Isotopes through FeCrAl Alloys,” presented at Technology of Fusion Energy (TOFE) 2020, virtual, 15–19 November 2020.

D. H. Froula, “Progress in Flying Focus,” presented at High-Intensity Lasers and High-Field Phenomena, virtual, 16–20 November 2020 (invited).

B. E. Ugur and K. L. Marshall, “Computational Modeling and Design of Liquid Crystal Materials for Applications in the Terahertz Regime,” presented at the 2020 American Institute of Chemical Engineers Annual Meeting, virtual, 16–20 November 2020.

M. S. Wei, “OMEGA EP Laser Facility,” presented at the LaserNetUS Town Hall, virtual, 19 November 2020.

The following presentations were made at the Office of Experimental Science, FY2021 Annual Program Review, virtual, 1–3 December 2020:

E. M. Campbell, “ICF Facility Operations—LLE 10.7.”

S. P. Regan, “ICF Diagnostics and Instrumentation: LLE.”

T. C. Sangster, “LLE MTE 10.8.”

The following presentations were made at the Advanced Accelerator Concepts Seminar Series, virtual, 2 December 2020:

P. Franke, J. P. Palastro, J. L. Shaw, D. Ramsey, T. T. Simpson, M. V. Ambat, K. Daub, J. B. Oliver, R. Boni, C. Dorrer, J. Katz, and D. H. Froula, “Dephasingless Laser Wakefield Acceleration.”

J. L. Shaw, M. A. Romo-Gonzalez, G. Bruhaug, C. Dorrer, B. E. Kruschwitz, L. J. Waxer, M. V. Ambat, M. M. McKie, J. P. Palastro, D. H. Froula, N. Lemos, P. M. King, G. J. Williams,

H. Chen, F. Albert, M. D. Sinclair, and C. Joshi, “Microcoulomb-Class Laser-Plasma Accelerator on OMEGA EP.”

G. W. Collins, M. Zaghoo, M. Hiuff, L. Crandall, G. Tabak, B. J. Henderson, X. Gong, D. A. Chin, Z. K. Sprowal, J. J. Ruby, M. K. Ginnane, P. M. Nilson, D. N. Polsin, M. Marshall, J. R. Rygg, and R. Jeanloz, “Exploring Extrasolar Planets in the Laboratory,” presented at the American Geophysical Union Fall Meeting, virtual, 7–11 December 2020.

E. M. Campbell, “Direct-Drive Laser Fusion: Status, Plans, and the Future,” presented at the Freeman Dyson Seminar, virtual, 10 December 2020.

The following presentations were made at the 23rd Topical Conference on High-Temperature Plasma Diagnostics, virtual, 13–17 December 2020:

D. H. Barnak, J. R. Davies, J. P. Knauer, and P. M. Kozlowski, “Soft X-Ray Spectrum Unfold of K-Edge-Filtered X-Ray Diode Arrays Using Cubic Splines.”

D. T. Bishel, E. V. Marley, M. B. Schneider, D. A. Liedahl, R. F. Heeter, M. E. Foord, G. E. Kemp, Y. Frank, J. A. Emig, G. Perez-Callejo, J. R. Rygg, G. W. Collins, and P. M. Nilson, “Open L-Shell Spectroscopy of Nonlocal Thermodynamic Equilibrium Plasmas.”

D. H. Edgell, A. Hansen, J. Katz, D. Turnbull, and D. H. Froula, “Unabsorbed Light Beamlets for Diagnosing Coronal Density Profiles and Absorption Nonuniformity in Direct-Drive Implosions on OMEGA.”

S. T. Ivancic, W. Theobald, C. Sorce, M. Bedzyk, F. J. Marshall, C. Stoeckl, R. C. Shah, M. Lawrie, S. P. Regan, T. C. Sangster, E. M. Campbell, T. J. Hilsabeck, K. Englehorn, J. D. Kilkenny, T. M. Chung, J. D. Hares, A. K. L. Dymoke-Bradshaw, P. Bell, J. Celeste, A. C. Carpenter, M. Dayton, D. K. Bradley, M. C. Jackson, E. Hurd, L. Pickworth, S. R. Nagel, G. Rochau, J. Porter, M. Sanchez, L. Claus, G. Robertson, and Q. Looker, “Improving Time-Resolved X-Ray Hot-Spot Image Fidelity with Composite Imaging Using a Multiple Pinhole Imager.”

J. Katz, D. Turnbull, B. E. Kruschwitz, A. Rigatti, R. Rinefield, and D. H. Froula, "A Transmitted Beam Diagnostic for the Wavelength Tunable UV Drive Beam on OMEGA."

O. M. Mannion, C. J. Forrest, V. Yu. Glebov, I. V. Igumenshchev, S. T. Ivancic, D. W. Jacobs-Perkins, J. P. Knauer, Z. L. Mohamed, S. P. Regan, H. G. Rinderknecht, R. C. Shah, C. Stoeckl, W. Theobald, K. M. Woo, J. A. Frenje, M. Gatu Johnson, and A. J. Crilly, "Diagnosing 3-D Asymmetries in Laser-Direct-Drive Implosions on OMEGA" (invited).

F. J. Marshall, S. T. Ivancic, C. Mileham, P. M. Nilson, J. J. Ruby, C. Trejan, J. Kendrick, B. S. Schiener, and M. J. Schmitt, "High-Resolution X-Ray Radiography with Fresnel Zone Plates at the University of Rochester's OMEGA Laser Systems" (invited).

Z. L. Mohamed, O. M. Mannion, J. P. Knauer, C. J. Forrest, V. Yu. Glebov, and C. Stoeckl, "Application of an Energy-Dependent Instrument Response Function of nTOF Data from DT Cryogenic DT Experiments."

M. J. Rosenberg, T. Filkins, R. E. Bahr, R. Jungquist, M. Bedzyk, S. P. Regan, J. Hernandez, N. Butler, G. Swadling, J. Eichmiller, R. Sommers, P. Nyholm, P. Datte, and J. S. Ross, "SLTD: A Time-Resolved Scattered-Light Diagnostic Array at the National Ignition Facility."

S. Zhang, R. Paul, and M. A. Morales, "Benchmarking Phase Transitions in Periclase Under Multi-Megabar Pressures," presented at the American Geophysical Union Fall Meeting, virtual, 16 December 2020.

E. M. Campbell, "Laboratory for Laser Energetics Update," presented at the Fusion Power Associates 41st Annual Meeting and Symposium, virtual, 16–17 December 2020.

J. L. Shaw, M. V. Ambat, S.-W. Bahk, I. A. Begishev, R. Boni, J. Bromage, G. Bruhaug, S. Bucht, E. M. Campbell, A. Davies, C. Dorrer, P. Franke, R. K. Follett, V. N. Goncharov, D. Haberberger, A. Howard, G. W. Jenkins, J. Katz, T. J. Kessler, B. Kruschwitz, M. M. McKie, L. Nguyen, J. B. Oliver,

J. P. Palastro, D. Ramsey, M. A. Romo-Gonzalez, T. T. Simpson, D. Turnbull, L. J. Waxer, H. Wen, D. H. Froula, P. M. King, N. Lemos, G. J. Williams, H. Chen, F. Albert, M. D. Sinclair, C. Joshi, F. A. Hegmann, D. Purschke, S. Stoller, N. Vafaei-Najafabadi, B. Malaca, J. L. Martins, J. Vieira, S. Jolly, F. Quéré, A. Di Piazza, G. Gregori, Z. Li, T. M. Antonsen Jr., A. Arefiev, K. Weichman, and R. Bingham, "New Developments in Laser Wakefield Acceleration at the Laboratory for Laser Energetics," presented at the Oxford Hilary Series Seminar, virtual, 25 January 2021.

J. L. Peebles, J. R. Davies, D. H. Barnak, M. J. Bonino, T. Cracium, R. Betti, and P.-Y. Chang, "Probing Strong Electric and Magnetic Fields using Axial Proton Radiography of Laser-Driven Coils," presented at Charged Particle Radiography in High-Energy-Density Laboratory Plasmas, virtual, 25–28 January 2021.

J. P. Palastro, D. H. Froula, M. Ambat, R. Boni, E. M. Campbell, R. K. Follett, P. Franke, V. N. Goncharov, J. B. Oliver, D. Ramsey, J. L. Shaw, T. T. Simpson, D. Turnbull, H. Wen, S. Jolly, F. Quéré, C. Benedetti, E. Esarey, C. Geddes, C. Schroeder, R. Bingham, S. Stoller, N. Vafaei-Najafabadi, G. Gregori, B. Malaca, A. Helm, J. Vieira, A. DiPiazza, A. Howard, K. Weichman, A. Arefiev, T. M. Antonsen Jr., and Z. Li, "Laser-Plasma Interactions Driven by Spatiotemporally Structured Light Pulses," presented at the SOCAL Plasma Seminar, virtual, 9 February 2021.

S. Zhang, S. X. Hu, D. Haberberger, A. Shvydky, V. N. Goncharov, and D. E. Fratanduono, "Species Separation and Hydrogen Streaming: The Physics of CH Shock Release Revealed by Molecular Dynamics Simulations," presented at the NIF and JLF User Group Meeting 2021, virtual, 9–10 February 2021.

O. M. Mannion, K. S. Anderson, R. Betti, E. M. Campbell, D. Cao, C. J. Forrest, V. Yu. Glebov, V. N. Goncharov, V. Gopalaswamy, I. V. Igumenshchev, S. T. Ivancic, D. W. Jacobs-Perkins, J. P. Knauer, A. Lees, F. J. Marshall, Z. L. Mohamed, D. Patel, S. P. Regan, H. G. Rinderknecht, R. C. Shah, C. Stoeckl, W. Theobald, K. M. Woo, B. D. Appelbe, A. J. Crilly,

J. Chittenden, W. Taitano, P. Adrian, J. A. Frenje, N. Kabadi, and M. Gatu Johnson, “Neutron Spectroscopy in Laser-Direct-Drive Inertial Confinement Fusion Implosions,” presented at the Imperial College Seminar, virtual, 10 February 2021.

D. H. Froula, S. Jolly, F. Quéré, C. Benedetti, E. Esarey, C. Geddes, C. Schroeder, R. Bingham, S. Stoller, N. Vafaei-Najafabadi, G. Gregori, B. Malaca, A. Helm, J. Vieira, A. Di Piazza, A. Howard, A. Arefiev, T. M. Antonsen Jr., and Z. Li, “Spatiotemporal Pulse Shaping for Plasma Base Applications,” presented at the Imperial College Seminar, virtual, 17 February 2021.

R. B. Spielman, K. M. Woo, P. Tzeferacos, A. Reyes, C. R. Stillman, I. A. Begishev, C. Mileham, and J. Bromage, “Experiments and Modeling of SPL Absorption and Ablation with Picosecond Pulses,” presented at the Pulsed-Laser Workshop, virtual, 18 February 2021.

J. D. Zuegel, “Ultra-Short Pulse Laser (USPL) Science and Technology at LLE,” presented at the High Energy Laser Joint Technology Office Ultrashort Pulse Laser Workshop, virtual, 18 February 2021.

D. H. Froula, S. Jolly, F. Quéré, C. Benedetti, E. Esarey, C. Geddes, C. Schroeder, R. Bingham, S. Stoller, N. Vafaei-Najafabadi, G. Gregori, B. Malaca, A. Helm, J. Vieira, A. Di Piazza, A. Howard, A. Arafiev, T. M. Antonsen Jr., and Z. Li, “Spatiotemporal Pulse Shaping for Plasma Base Applications,” presented at the University of California-Irvine Seminar, virtual, 25 February 2021.

The following presentations were made at Photonics West 2021, virtual, 6–11 March 2021:

I. A. Begishev, S.-W. Bahk, C. Dorrer, C. Feng, M. J. Guardalben, C. Jeon, R. G. Roides, M. Spilatro, B. Webb, D. Weiner, J. D. Zuegel, and J. Bromage, “A Highly Efficient, 10-J Output Signal Amplifier for Ultra-Intense All-OPCPA Systems.”

T. Z. Kosc, T. J. Kessler, H. Huang, and S. G. Demos, “Minimizing Risk of Laser Damage due to Transverse Stimulated Raman Scattering in Large-Aperture KDP/DKDP Plates.”

O. M. Mannion, K. S. Anderson, R. Betti, E. M. Campbell, D. Cao, C. J. Forrest, V. Yu. Glebov, V. N. Goncharov, V. Gopalaswamy, I. V. Igumenshchev, S. T. Ivancic, D. W. Jacobs-Perkins, J. P. Knauer, A. Lees, F. J. Marshall, Z. L. Mohamed, D. Patel, S. P. Regan, H. G. Rinderknecht, R. C. Shah, C. Stoeckl, W. Theobald, K. M. Woo, B. D. Appelbe, A. J. Crilly, J. Chittenden, W. Taitano, P. Adrian, J. A. Frenje, N. Kabadi, and M. Gatu Johnson, “Neutron Spectroscopy in Laser-Direct-Drive Inertial Confinement Fusion Implosions,” presented at the UR Mechanical Engineering Seminar, virtual, 12 March 2021.

The following presentations were made at the APS March Meeting, virtual, 15–19 March 2021:

S. X. Hu, P. M. Nilson, V. V. Karasiev, R. Paul, M. Ghosh, J. Hinz, S. Zhang, D. Mihaylov, V. Recoules, N. Brouwer, M. Torrent, I. E. Golovkin, and T. Walton, “Understanding Matter at Superdense and Warm Conditions.”

D. I. Mihaylov, V. V. Karasiev, and S. X. Hu, “Progress in Development of Thermal Hybrid Exchange-Correlation Density Functionals for Improving the Description of Warm Dense Matter.”

R. Paul, S. X. Hu, V. V. Karasiev, R. Dias, “Phase Diagram of Ternary Carbon-Sulfur-Hydrogen System up to 300 GPa.”

D. N. Polsin, X. Gong, M. F. Huff, L. E. Crandall, B. J. Henderson, R. Paul, S. Burns, G. W. Collins, J. R. Rygg, A. Lazicki, F. Coppari, R. Smith, M. Millot, J. H. Eggert, M. I. McMahon, X. Wang, K. Hilleke, and E. Zurek, “High-Pressure Structural and Electronic Properties of Ramp-Compressed Sodium.”

S. Zhang, R. Paul, S. X. Hu, M. A. Morales, and F. D. Malone, “Benchmarking a Multi-Megabar Phase Diagram of MgO.”

D. H. Froula, J. P. Palastro, R. Boni, M. Ambat, P. Franke, J. Oliver, D. Ramsey, J. L. Shaw, T. T. Simpson, D. Turnbull,

S. Jolly, F. Quéré, C. Benedetti, E. Esarey, C. Geddes, C. Schroeder, R. Bingham, S. Stoller, N. Vafaei-Najafabadi, G. Gregori, B. Malaca, A. Helm, J. Vieira, A. DiPiazza, A. Howard, A. Arefiev, T. M. Antonsen Jr., and Z. Li, “Spatiotemporal Pulse Shaping for Plasma-Based Applications,” presented at the Industrial Associates Bi-Annual Meeting, virtual, 17–19 March 2021.

E. M. Campbell, “Nuclear Energy, Today and Tomorrow,” presented at Oklahoma University, virtual, 19 March 2021.

The following presentations were made at the 16th Direct-Drive and Fast-Ignition Workshop, virtual, 22–24 March 2021:

V. N. Goncharov, I. V. Igumenshchev, T. J. B. Collins, P. B. Radha, S. X. Hu, S. P. Regan, D. H. Froula, D. Harding, W. Theobald, M. J. Rosenberg, A. Shvydky, S. F. B. Morse, J. D. Zuegel, C. Dorrer, T. C. Sangster, and E. M. Campbell, “Expanding Ignition Parameter Space with the Dynamic Shell Formation Concept.”

S. X. Hu, V. V. Karasiev, P. M. Nilson, S. Zhang, M. Zaghoo, D. Mihaylov, J. Hinz, R. Paul, M. Ghosh, J. R. Rygg, V. N. Goncharov, G. W. Collins, E. M. Campbell, L. A. Collins, A. J. White, J. D. Kress, J. P. Colgan, O. Certik, V. Recoules, N. Brouwer, M. Torrent, I. E. Golovkin, M. Gu, T. Walton, and S. B. Hansen, “Overview of High-Energy-Density–Physics Research for the Direct-Drive Inertial Confinement Fusion Program at the Laboratory for Laser Energetics.”

K. L. Nguyen, A. M. Hansen, D. Turnbull, R. K. Follett, D. H. Froula, J. P. Palastro, L. Yin, and B. J. Albright, “Cross-Beam Energy Transfer Saturation by Ion Trapping-Induced Detuning.”

J. L. Peebles, S. X. Hu, W. Theobald, V. N. Goncharov, D. R. Harding, M. J. Bonino, P. M. Celliers, S. J. Ali, G. Duchateau, E. M. Campbell, T. R. Boehly, and S. P. Regan, “Experimental Measurements of Laser Imprint and Target-Based Mitigation Techniques on OMEGA and OMEGA EP.”

P. B. Radha, D. Cao, R. S. Craxton, D. H. Edgell, J. P. Knauer, J. A. Marozas, F. J. Marshall, M. J. Rosenberg, W. Seka, A. Shvydky, A. A. Solodov, C. Stoeckl, W. Theobald, C. A. Thomas, D. Turnbull, K. S. Anderson, R. Betti, E. M. Campbell, D. H. Froula, V. N. Goncharov, S. X. Hu, S. P. Regan,

M. Hohenberger, and J. D. Moody, “Laser-Coupling Studies on OMEGA and the National Ignition Facility.”

A. Shvydky, D. Haberberger, J. P. Knauer, S. X. Hu, S. T. Ivancic, J. Carroll-Nellenback, D. Cao, I. V. Igumenshchev, V. V. Karasiev, P. B. Radha, A. V. Maximov, S. P. Regan, T. C. Sangster, R. Boni, P. M. Nilson, V. N. Goncharov, D. H. Froula, M. D. Rosen, and V. A. Smalyuk, “Shock-Release Experiments on OMEGA EP.”

A. A. Solodov, M. J. Rosenberg, M. Stoeckl, A. R. Christopherson, R. Betti, P. B. Radha, C. Stoeckl, R. Epstein, R. K. Follett, W. Seka, S. P. Regan, J. P. Palastro, D. H. Froula, V. N. Goncharov, J. F. Myatt, M. Hohenberger, B. Bachmann, and P. Michel, “Hot-Electron Preheat and Mitigation in Polar-Direct-Drive Experiments at the National Ignition Facility.”

W. Theobald, S. P. Regan, J. Baltazar, K. A. Bauer, R. Betti, D. Bredesen, E. M. Campbell, D. Cao, K. Churnetski, D. H. Edgell, R. Epstein, C. J. Forrest, V. Yu. Glebov, V. N. Goncharov, V. Gopalaswamy, S. X. Hu, I. V. Igumenshchev, T. Joshi, S. T. Ivancic, D. W. Jacobs-Perkins, R. T. Janezic, T. J. Kessler, J. P. Knauer, J. Kwiatkowski, A. Lees, O. M. Mannon, F. J. Marshall, M. Michalko, Z. Mohamed, P. M. Nilson, D. Patel, J. L. Peebles, P. B. Radha, H. G. Rinderknecht, M. J. Rosenberg, S. Sampat, T. C. Sangster, R. C. Shah, A. Shvydky, A. A. Solodov, C. Sorce, C. Stoeckl, C. A. Thomas, L. J. Waxer, K. M. Woo, J. D. Zuegel, A. C. Carpenter, J. A. Frenje, M. Gatu Johnson, J. D. Hares, and J. D. Kilkenny, “Subscale Cryogenic Implosions and Diagnostic Development for Laser-Direct-Drive Research on OMEGA.”

D. H. Froula, S. Jolly, F. Quéré, C. Benedetti, E. Esarey, C. Geddes, C. Schroeder, R. Bingham, S. Stoller, N. Vafaei-Najafabadi, G. Gregori, B. Malaca, A. Helm, J. Vieira, A. DiPiazza, A. Howard, A. Arefiev, T. M. Antonsen Jr., and Z. Li, “Controlling Laser Beams for Grand Challenge Applications,” presented at UR ECE Seminar, virtual, 24 March 2021.

The following presentations were made at the High Energy Density Plasma Diagnostics Course, virtual, 30 March–3 June 2021:

K. Churnetski, M. Michalko, and S. T. Ivancic, “The Single Line-of-Sight Time-Resolved X-Ray Imager.”

S. T. Ivancic, “Omega Overview.”

S. T. Ivancic, “Test Project.”

S. T. Ivancic, “TRXI Install.”

H. McCLOW, O. M. Mannion, and Z. Mohamed, “Neutron Time-of-Flight Diagnostics.”

J. L. Peebles, J. R. Davies, D. H. Barnak, M. J. Bonino, G. Brent, T. Cracium, and R. Betti, “Laser-Drive Coils, How Well Do They Work?” presented at the HEDS Seminar, virtual, 1 April 2021.

E. M. Campbell, “LLE: Today and Tomorrow,” presented at the Institute of Optics Colloquium, virtual, 5 April 2021.

J. L. Shaw, G. Bruhaug, M. Freeman, F. Merrill, V. Geppert-Kleinrath, C. Wilde, and D. H. Froula, “Electron Radiography Based on Electron Beams from Self-Modulated Laser Wake-field Acceleration,” presented at LANSCE Futures Spring 2021 Workshop Series, virtual, 6 April 2021.

The following presentations were made at the 4th International Symposium on High Power Laser Science and Engineering, virtual, 11–16 April 2021:

J. Bromage, S.-W. Bahk, M. Bedzyk, I. A. Begishev, S. Bucht, C. Dorrer, C. Feng, C. Jeon, C. Mileham, R. G. Roides, K. Shaughnessy, M. J. Shoup III, M. Spilatro, B. Webb, D. Weiner, and J. D. Zuegel, “MTW-OPAL: A Technology Development Platform for Ultra-Intense OPCPA Systems.”

E. M. Campbell, “A Vision of the Future for High-Power Laser Research and Its Applications.”

E. M. Campbell, “Laser Fusion: Present Status and the Path to Fusion Energy,” presented at Cornell Energy Seminar, Cornell, NY, 15 April 2021.

S. P. Regan, “JASON Briefing,” presented at JASON, virtual, 15 April 2021.

A. K. Schwemmlin, C. Stoeckl, W. T. Shmayda, C. J. Forrest, J. P. Knauer, S. P. Regan, and W. U. Schröder, “Generating a TNSA Tritium Beam on OMEGA,” presented at the APS April Meeting, virtual, 17–20 April 2021.

J. P. Palastro, D. H. Froula, M. Ambat, E. M. Campbell, R. K. Follett, P. Franke, V. N. Goncharov, D. Ramsey, J. L. Shaw, T. T. Simpson, D. Turnbull, K. Weichman, H. Wen, S. Jolly, F. Quéré, C. Benedetti, E. Esarey, C. Geddes, C. Schroeder, R. Bingham, S. Stoller, N. Vafaei-Najafabadi, G. Gregori, B. Malaca, A. Helm, J. Vieira, A. Di Piazza, A. Howard, A. Arefiev, T. M. Antonsen, Jr., and Z. Li, “Laser–Plasma Interactions Driven by Spatiotemporally Structured Light Pulses,” presented at the Bothe Colloquium, virtual, 21 April 2021.

The following presentations were made at the Omega Laser Facility Users Group 2021 Workshop, virtual, 27–30 April 2021:

J. Bromage, S.-W. Bahk, M. Bedzyk, I. A. Begishev, S. Bucht, C. Dorrer, C. Feng, B. N. Hoffman, C. Jeon, C. Mileham, J. B. Oliver, R. G. Roides, E. M. Schiesser, K. Shaughnessy, M. J. Shoup III, M. Spilatro, B. Webb, D. Weiner, J. D. Zuegel, D. H. Froula, J. L. Shaw, P. M. Nilson, H. G. Rinderknecht, L. J. Waxer, J. C. Puth, and E. M. Hill, “Commissioned MTW-OPAL Laser and Proposed 2×25 PW EP-OPAL Laser.”

G. W. Collins, “Extreme Matters: Pressure to Explore New Worlds and Exotic Solids.”

E. C. Hansen, A. C. Reyes, M. B. P. Adams, J. Carroll-Nellenback, J. R. Davies, K. Weide, D. Q. Lamb, and P. Tzeferacos, “Implicit Anisotropic Magnetic Resistivity in the *FLASH* Code.”

P. V. Heuer, D. Stanczak, E. T. Everson, N. A. Murphy, and J. R. Davies, “Open Source High-Energy-Density–Physics Diagnostic Tools in PlasmaPy.”

T. R. Joshi, R. C. Shah, W. Theobald, I. V. Igumenshchev, D. Cao, and S. P. Regan, “Observations of the Modulations

Associated with the 60-Beam Overlap in X-Ray Self-Emission Images of Directly Driven Implosions.”

Y. Lu, H. Li, K. Flippo, K. Kelso, A. Liao, S. Li, E. Liang, and P. Tzeferacos, “Monte Carlo Simulations for Proton Radiography in High-Energy-Density Plasma Experiments.”

S. F. B. Morse, “Omega Facility OLUG 2021 Update: Progress on Recommendations and Items of General Interest.”

S. P. Regan, “2020 Review of Inertial Confinement Fusion Approaches: The Research Path to Ignition.”

A. Reyes and P. Tzeferacos, “High-Order Implicit-Explicit ADER-RK Methods for Hyperbolic Systems with Stiff Source Terms in the *FLASH* Code.”

P. Tzeferacos, A. Reyes, E. C. Hansen, Y. Lu, D. Michta, M. P. A. Adams, C. J. Armstrong, K. Moczulski, and D. Q. Lamb, “The *FLASH* Code for Computational High-Energy-Density Physics—Recent Additions and Improvements.”

M. S. Wei, “Omega Basic Science User Programs Update.”

E. M. Campbell, “Laser Fusion: Present Status and the Path to Fusion Energy,” presented at Cornell University, virtual, 5 May 2021.

P. Tzeferacos, “Extended MHD with *FLASH*: A Numerical Toolset for Magnetized Plasma Experiments,” presented at the Center for Matter Under Extreme Conditions Seminar, virtual, 5 May 2021.

The following presentations were made at CLEO 2021, virtual, 9–14 May 2021:

S.-W. Bahk, I. A. Begishev, B. Webb, C. Jeon, R. G. Roides, C. Feng, M. Spilatro, R. Cuffney, C. Dorrer, C. Mileham, S. Bucht, and J. Bromage, “Effect of Pump Beam on the Amplified Signal Wavefront in DKDP Optical Parametric Amplification.”

J. Bromage, S.-W. Bahk, M. Bedzyk, I. A. Begishev, S. Bucht, C. Dorrer, C. Feng, B. N. Hoffman, C. Jeon, C. Mileham, J. B.

Oliver, R. G. Roides, E. M. Schiesser, K. Shaughnessy, M. J. Shoup III, M. Spilatro, B. Webb, D. Weiner, and J. D. Zuegel, “MTW-OPAL: A Technology Development Platform for Ultra-Intense All-OPCPA Systems.”

C. Dorrer, I. A. Begishev, S.-W. Bahk, and J. Bromage, “Spatially Resolved Characterization of Partially Deuterated KDP Crystals for Parametric Amplification.”

C. Dorrer, M. Spilatro, T. Borger, S. Herman, and E. M. Hill, “Broadband Sum-Frequency Generation in a Novel Angularly Dispersed Noncollinear Geometry.”

C. Feng, C. Dorrer, C. Jeon, R. Roides, B. Webb, and J. Bromage, “Analysis of Pump-to-Signal Noise Transfer in Multi-Stage Optical Parametric Chirped-Pulse Amplification.”

The following presentations were made at the ARPA-E Summit, virtual, 24–27 May 2021:

J. R. Davies, C. J. Forrest, V. Yu. Glebov, J. P. Knauer, and H. McClow, “The LLE Diagnostic Resource Team for Innovative Fusion Concepts.”

P. Tzeferacos, R. Betti, J. R. Davies, F. Garcia-Rubio, E. C. Hansen, D. Michta, C. Ren, A. C. Reyes, W. Scullin, A. B. Sefkow, J. G. Shaw, H. Wen, and K. M. Woo, “A Simulation Source for Innovative Fusion Concepts in the BETHE Program.”

P. Tzeferacos, A. Reyes, E. C. Hansen, Y. Lu, D. Michta, M. P. A. Adams, C. J. Armstrong, K. Moczulski, and D. Q. Lamb, “*FLASH*: A Simulation Code for HEDP and Innovative Fusion Concepts.”

H. G. Rinderknecht, M. S. Wei, G. Bruhaug, K. Weichmann, J. P. Palastro, J. D. Zuegel, A. Arefiev, T. Wang, T. Toncian, A. Laso Garcia, D. Doria, K. Spohr, H. J. Quevedo, T. Ditmire, J. Williams, A. Haid, and D. Stutman, “Relativistically Transparent Magnetic Filaments as a Gamma-Ray Source for All-Optical Nuclear Photonics,” presented at Nuclear Photonics 2021, virtual, 7–9 June 2021.

W. T. Shmayda, “Fundamentals of Tritium Handling,” presented at TRANSAT Second Tritium School, virtual, 14–16 June 2021.

P. Heuer, “Charged-Particle Radiography with PlasmaPy,” presented at the Summer Undergraduate Laboratory Internship Summer School, virtual, 14–25 June 2021.

E. M. Campbell, “Laboratory for Laser Energetics (LLE): Supporting OES Strategic Goals,” presented at the OES Executive Meeting, virtual, 15–16 June 2021.

J. Bromage, S.-W. Bahk, M. Bedzyk, I. A. Begishev, S. Bucht, C. Dorrer, C. Feng, B. N. Hoffman, C. Jeon, C. Mileham, J. B. Oliver, R. G. Roides, E. M. Schiesser, K. Shaughnessy, M. J. Shoup III, M. Spilatro, B. Webb, D. Weiner, and J. D. Zuegel, “MTW-OPAL—A Technology Development Platform for Ultra-Intense OPCPA Systems,” presented at EQEC, virtual, 20–24 June 2021.

The following presentations were made at the 47th European Physical Society Conference on Plasma Physics, virtual, 21–25 June 2021:

P. Franke, J. P. Palastro, D. Turnbull, D. Ramsey, T. T. Simpson, J. L. Shaw, M. V. Ambat, J. Katz, I. A. Begishev, R. Boni, J. Bromage, K. Daub, J. B. Oliver, C. Dorrer, D. H. Froula, S. Jolly, F. Quéré, C. Benedetti, E. Esarey, C. Geddes, C. Schroeder, R. Bingham, S. Stoller, N. Vafaei-Najafabadi, G. Gregori, B. Malaca, A. Helm, J. Vieira, A. Di Piazza, A. Howard, A. Arefiev, T. M. Antonsen, Jr., and Z. Li, “Spatiotemporal Control of Laser Pulses for Broadband Extreme Ultraviolet Generation.”

A. M. Hansen, K. L. Nguyen, D. Turnbull, R. K. Follett, R. Huff, J. Katz, D. Mastro Simone, A. L. Milder, J. P. Palastro, D. H. Froula, B. Albright, and L. Yin, “Cross-Beam Energy Transfer Saturation.”

E. M. Campbell, “Laboratory for Laser Energetics (LLE): Today and Tomorrow,” presented at the Pulsed-Power Sciences Center, virtual, 23 June 2021.

P. Heuer, “Charged-Particle Radiography with PlasmaPy,” presented at Plasma Hack Week, virtual, 28 June–2 July 2021.

E. M. Campbell, “A Vision of the Future for High-Power Laser Research and Its Applications,” presented at Frontiers in Lasers and Applications, virtual, 5–29 July 2021.

E. M. Campbell, “Inertial Confinement Fusion: Present State of Research for Energy Demonstration and Potential Spin-Offs,” presented at Curso de Verano de la Universidad Complutense de Madrid (UCM) El Escorial, virtual, 12–13 July 2021.

W. T. Shmayda, “Overview of Tritium Handling,” presented at the Nevada National Security Site, virtual, 14 July 2021.

K. L. Marshall, B. E. Ugur, and W. Scullin, “Toward High-Performance Terahertz-Region Liquid Crystals: Computational Modeling of Fused-Ring Nematic and Discotic Mesogens,” presented at Liquid Crystals XXV, virtual, 1–5 August 2021 (invited).

K. Churnetski, K. M. Woo, W. Theobald, P. B. Radha, R. Betti, V. Gopalaswamy, I. V. Igumenshchev, S. T. Ivancic, M. Michalko, R. C. Shah, C. A. Thomas, and S. P. Regan, “Three-Dimensional Hot-Spot Reconstruction from Cryogenic Deuterium–Tritium Polar-Direct-Drive Implosions on OMEGA,” presented at High-Energy-Density Science Summer School, virtual, 2–6 August 2021.

D. Mihaylov, V. V. Karasiev, S. X. Hu, J. R. Rygg, V. N. Goncharov, and G. W. Collins, “Improved First-Principles

Equation-of-State Table of Deuterium,” presented at the American Physical Society Topical Group on Shock Compression of Condensed Matter Early Career Symposium, virtual, 3–4 August 2021.

—————
C. Dorrer, “Parametric Amplification of Spectrally Incoherent Signals,” presented at the Nonlinear Optics Topical Meeting, virtual, 9–13 August 2021.

—————
The following presentations were made at the 2021 LaserNetUS User Meeting, virtual, 17–19 August 2021:

S.-W. Bahk, I. A. Begishev, S. Bucht, C. Dorrer, C. Feng, B. N. Hoffman, C. Jeon, C. Mileham, J. B. Oliver, R. G. Roides, M. J. Shoup III, M. Spilatro, B. Webb, J. D. Zuegel, and J. Bromage, “‘First Light’ Results from MTW-OPAL: An All-OPCPA Platform for Laser Development and Petawatt Science.”

E. M. Campbell, “Inertial Fusion Energy (IFE): Opportunities and Challenges.”

—————
E. M. Campbell, “NAS Study on High Energy Density Science,” presented at the National Academy of Sciences Site Visit, virtual, 26 August 2021.

—————
D. H. Froula, “Taming Plasmas and Controlling Laser Beams for Grand Challenge Applications,” presented at the Fusion Energy Sciences Advisory Committee Meeting, virtual, 30 August 2021.

—————
E. M. Campbell, “Laboratory for Laser Energetics (LLE) Comments on HIBEF Dedication,” presented at the HIBEF Inauguration, virtual, 31 August 2021.

—————
R. B. Spielman, “Pulsed-Power Innovations Needed for Next-Generation, High-Current Drivers,” presented at the 48th

IEEE International Conference on Plasma Science, virtual, 12–16 September 2021.

—————
L. Savino, S. Atzeni, V. N. Goncharov, and I. V. Igumenshev, “Studies on Dynamical Shell Formation for Direct-Drive Laser Fusion,” presented at the 107th Italian Physical Society Conference, virtual, 13–17 September 2021.

—————
J. D. Zuegel, “2021 Multi-Petawatt Physics Prioritization (MP3) Workshop,” presented at the 4th Extremely High Intensity Laser Physics Conference, virtual, 13–17 September 2021.

—————
E. M. Campbell, “Inertial Fusion Energy (IFE): Opportunities and Challenges,” Fusion Energy Council of Canada Annual General Meeting, virtual, 15 September 2021.

—————
S. Zhang, R. Paul, M. Ghosh, S. X. Hu, L. E. Hansen, J. R. Rygg, G. W. Collins, M. Morales, F. Malone, and D. E. Fratanduono, “Multi-Megabar Phase Transitions from First-Principles Examples in MgO and Fe,” presented at the Center for Matter at Atomic Pressures Seminar, virtual, 17 September 2021.

—————
C. Dorrer, J. Bromage, S.-W. Bahk, M. Bedzyk, I. A. Begishev, S. Bucht, C. Feng, B. N. Hoffman, C. Jeon, C. Mileham, J. B. Oliver, R. G. Roides, E. M. Schiesser, K. Shaughnessy, M. J. Shoup III, M. Spilatro, B. Webb, D. Weiner, and J. D. Zuegel, “MTW-OPAL: A Technology Development Platform for Ultra-Intense OPCPA Systems,” presented at Topical Problems of Nonlinear Wave Physics, virtual, 19–22 September 2021.

—————
S. Zhang, “Molecular to Atomic Transition in Liquid Silica at Extreme Conditions,” presented at the Emerging Leader Celebration, virtual, 20–21 September 2021.

The following presentations were made at the 5th Asia Pacific Conference on Plasma Physics, virtual, 26 September–1 October 2021:

S. X. Hu, P. M. Nilson, V. V. Karasiev, D. Bishel, V. Recoules, N. Brouwer, M. Torrent, I. E. Golovkin, M. Gu, T. Walton, and S. B. Hansen, “Probing Extreme Atomic Physics of Warm and Superdense Plasmas” (invited).

P. Tzeferacos, “TDYNO: Laser-Driven Laboratory Plasma Astrophysics Experiments of Magnetized Turbulence and Fluctuation Dynamo.”

K. Weichman, A. V. Arefiev, H. Mao, F. N. Beg, J. P. Palastro, A. P. L. Robinson, M. Murakami, S. Fujioka, J. J. Santos,

T. Toncian, Y. Shi, T. Ditmire, H. Quevedo, and V. V. Ivanov, “Effects of KiloTesla-Level Magnetic Fields on Relativistic Laser–Plasma Interactions” (invited).

C. J. Forrest, A. Crilly, B. Applebe, V. Yu. Glebov, J. P. Knauer, O. M. Mannion, Z. L. Mohamed, P. B. Radha, S. P. Regan, A. K. Schwemmlin, and C. Stoeckl, “Inferring Absolute Neutron Energy Spectra from Time-of-Flight Spectrometers Operating in Current Mode,” presented at the Neutron Detector Workshop, Knoxville, TN, 30 September–2 October 2021.

Appendix A: Executive Summary Tables

Table I: LLE-funded University of Rochester Frank Horton Fellowship Program supported 63 graduate students in FY21.

Student Name	Dept.	Faculty Advisor	LLE Advisor	Research Area	Notes
M. V. Ambat	ME	D. H. Froula		Dephasing laser wakefield accelerator	
A. Armstrong	PA	P. Tzeferacos		Relative, HED magnetized turbulence: Charting the uncharted plasma regimes of fluctuation dynamo	
V. Anand	PA	J. Carroll-Nellenback		The role of exoplanetary magnetic fields in atmospheric evolution and habitability	
J. Baltazar	ME	S. P. Regan	R. C. Shah	ICF implosion physics	
Z. Barfield	PA	D. H. Froula		Lateral transport with and without magnetic fields	
D. T. Bishel	PA	G. W. Collins	P. M. Nilson	Mapping the atomic physics of complex ions with detailed nonlocal thermodynamic equilibrium spectroscopy	
G. Bruhaug	ME	G. W. Collins	J. R. Rygg/ H. G. Rinderknecht/ M. S. Wei	Advanced x-ray particle sources for HED and ICF diagnostic applications	
S. Cao	ME	C. Ren		Large-scale fluid and kinetic simulation study of laser-plasma instabilities and hot-electron generation in shock ignition	
K. Churnetski	ME	S. P. Regan	W. Theobald	Three-dimensional analysis of the time-gated x-ray emission from the hot spot of DT cryogenic implosions in the polar-direct-drive configuration on OMEGA	New
A. Debrecht	PA	A. Frank		Radiation magnetohydrodynamics of exoplanet winds and evaporation	
R. Dent	CH	A. Shestopalov	S. G. Demos	Optimization of coating properties and processing steps in optical grating manufacturing for high-intensity laser applications	
R. Ejaz	ME	R. Betti		Understanding the physics of areal-density degradation in direct-drive OMEGA implosions through dedicated experiments and statistical modeling	New
M. Evans	PA	P.-A. Gourdain		The study of warm dense matter generated by pulsed-power generators	

Table I: LLE-funded University of Rochester Frank Horton Fellowship Program supported 63 graduate students in FY21 (continued).

Student Name	Dept.	Faculty Advisor	LLE Advisor	Research Area	Notes
C. Fagan	CH	W. U. Schröder	W. T. Shmayda	The role of surface chemistry and microstructure on the retention of tritium in structural metals	Graduated in 2021
P. Farmakis	ME	R. Betti	R. Betti/ P. Tzeferacos	Three-dimensional reconstruction of the compressed core in OMEGA direct-drive implosions	New
P. Franke	PAS	D. H. Froula		Measuring the dynamics of electron plasma waves with Thomson scattering	
M. Ghosh	CH	P. Huo	S. Zhang	High pressure chemistry: How are diamonds formed from hydrocarbons?	
M. K. Ginnane	ME	G. W. Collins	J. R. Rygg	Characterization and melting of platinum at high pressures	
X. Gong	ME	G. W. Collins	J. R. Rygg	Structure and electronic properties of sodium and potassium at high pressure	
V. Gopalaswamy	ME	R. Betti		Statistical analysis of OMEGA direct-drive cryogenic DT implosions	Graduated in 2021
S. Gupta	OPT	P. S. Carney	M. D. Wittman	Quantitative confocal phase imaging for the inspection of target capsules	
A. M. Hansen	PA	D. H. Froula		Electron plasma wave dynamics	Graduated in 2021
L. E. Hansen	PA	G. W. Collins	J. R. Rygg	Equation of state of planetary fluids	Graduated in 2021
B. J. Henderson	PA	G. W. Collins	J. R. Rygg	Broadband reflectivity of shock-compressed materials	
J. Hinz	PA	S. G. Rajeev	V. V. Karasiev	Developing accurate free-energy density functionals via machine learning for warm-dense-matter simulations	
R. Holcomb	OPT	J. Bromage		Machine-learning control of high-average-power lasers for ultrafast applications	
M. Huff	PA	G. W. Collins	J. R. Rygg	Sound-speed measurements on shocked material	
G. W. Jenkins	OPT	J. Bromage		Divided-pulse coherent combination for scaling high-power nonlinear processes	
M. Jeske	CH	M. Anthamatten	D. R. Harding	Direct laser writing of high-resolution shape memory networks for mechanical interlocking	
R. Jia	CH	A. Shestopalov	S. G. Demos	Effects of organic monolayer coatings on optical substrates	
A. Kish	PA	A. B. Sefkow		Development and implementation of energy-conserving particle pushing algorithms for hybrid fluid-kinetic simulations	
M. Lavell	ME	A. B. Sefkow		Hybrid fluid-kinetic models for plasma simulations	

Table I: LLE-funded University of Rochester Frank Horton Fellowship Program supported 63 graduate students in FY21 (continued).

Student Name	Dept.	Faculty Advisor	LLE Advisor	Research Area	Notes
L. S. Leal	PA	R. Betti	A. V. Maximov	Simulations and studies of ICF relevant laser-generated plasma in external magnetic fields	
A. Lees	PA	H. Aluie	R. Betti	Understanding the fusion yield dependencies in OMEGA implosions using statistical modeling	
O. M. Mannion	PA	S. P. Regan	C. J. Forrest	Measurements of the bulk fluid motion in direct-drive experiments	Graduated in 2021
M. McKie	PA	D. H. Froula		Wave breaking of electron plasma waves as it applies to hot-electron generation and laser-plasma amplifiers	
K. R. McMillen	PA	D. H. Froula	J. L. Shaw	Investigate the effects of the far-field laser profile on laser-wakefield acceleration	New
B. McLellan	PA	P. Tzeferacos	S. Zhang/ S. X. Hu	Theoretical study of structural transformation, transition pathways, and optical properties of crystals and amorphous solids under pressure	
A. L. Milder	PA	D. H. Froula		Measurement of electron distribution function using collective Thomson scattering	Graduated in 2021
S. C. Miller	ME	V. N. Goncharov	P. B. Radha	Hydrodynamic instabilities in ICF implosions	
K. Moczulski	ME	P. Tzeferacos		Characterization of magnetized turbulence and fluctuation dynamo through <i>FLASH</i> simulations and OMEGA experiments	New
Z. L. Mohamed	PA	D. H. Froula	J. P. Knauer	Gamma emission from fusion reactions	Graduated in 2021
K. L. Nguyen	PA	D. H. Froula	J. P. Palastro	Nonlinear saturation of cross-beam energy transfer	
K. Nichols	PA	S. X. Hu	S. X. Hu	<i>Ab initio</i> investigations into material properties under planetary mantle/core boundary and ICF conditions	New
S. F. Nwabunwanne	ECE	W. R. Donaldson	W. R. Donaldson	Design, fabrication, and characterization of AlGaIn-based ultrafast metal–semiconductor–metal photodiodes	
H. Pantell	PA	G. W. Collins	M. Zaghoo	Thermodynamic and mass transport properties of silicate at extreme conditions	
H. Pasan	PA	R. Dias	G. W. Collins	Novel hydrogen rich materials at HED conditions: Route to “hot” superconductivity	
D. Patel	ME	R. Betti		High and mid-mode number stability of OMEGA cryogenic implosions	
R. Paul	ME	S. X. Hu		High pressure phase diagram of ramp-compressed materials	

Table I: LLE-funded University of Rochester Frank Horton Fellowship Program supported 63 graduate students in FY21 (continued).

Student Name	Dept.	Faculty Advisor	LLE Advisor	Research Area	Notes
D. Ramsey	PA	D. H. Froula	J. P. Palastro	Nonlinear Thomson scattering from spatiotemporally shaped laser pulses	
J. Ruby	CH	W. U. Schröder	W. T. Shmayda	Asymmetric permeation	New
J. J. Ruby	PA	G. W. Collins	J. R. Rygg	Understanding the thermodynamics of spherically imploding shocks	Graduated in 2021
A. Schwemlein	PA	W. U. Schröder	J. P. Knauer/ W. T. Shmayda	Thermonuclear fusion and breakup reaction between light nuclei	Graduated in 2021
T. T. Simpson	PA	D. H. Froula	J. P. Palastro	A flying focus driven by self-focusing	
E. Smith	PA	G. W. Collin/ J. R. Rygg		Understanding materials assembled to extreme states via laser-driven implosions using Bayesian inference	New
Z. K. Sprowal	PA	G. W. Collins		Off-Hugoniot studies in hydrogen and hydrocarbons	
G. Tabak	PA	G. W. Collins/ J. R. Rygg	M. Zaghoo	Experimental investigation of warm dense matter	
M. Vandusen-Gross	PA	D. H. Froula	H. G. Rinderknecht	Electron and gamma diagnostics for relativistically transparent magnetic filament experiments	New
M. Wang	CHE	D. R. Harding		Use of two-photon polymerization to “write” millimeter-size structures with micron resolution	
C. A. Williams	PA	J. R. Davies	R. Betti	High-fusion-yield target designs for direct-drive ICF on OMEGA and the NIF	
J. Young	PA	P.-A. Gourdain		Laser-triggered X pinches on MTW	
Y. Zhang	ME	J. R. Davies		Kinetic simulation study of magnetized collisionless shock formation and reformation	New
Y. Zou	PA	A. Frank		Common envelope evolution: HEDP studies of gravitational wave merger properties: The role of EOS and radiation transport	

ME: Mechanical Engineering; PA: Physics and Astronomy; CH: Chemistry; CHE: Chemical Engineering; OPT: Institute of Optics; ECE: Electrical and Computer Engineering

Table II: Fifteen students completed their Ph.D. theses in calendar year 2021.

Name	Ph.D. Institution	Current position employer
Zaarah L. Mohamed	University of Rochester	Postdoc, LANL
Varchas Gopaldaswamy	University of Rochester	Assistant Scientist, LLE
Linda E. Hansen	University of Rochester	Postdoc, SNL
Owen M. Mannion	University of Rochester	Postdoc, SNL
Aaron M. Hansen	University of Rochester	Postdoc, SNL
Avram L. Milder	University of Rochester	Postdoc, University of Alberta
Arnold Schwemmlin	University of Rochester	Postdoc, UR CMAP
Cody E. Fagan	University of Rochester	Lead Engineer, SHINE Medical Technologies
John J. Ruby	University of Rochester	Lawrence Fellow, LLNL
Yunus Akbas	University of Rochester	Seismic Imaging Analyst, CGG
Neel V. Kabadi	MIT	Assistant Scientist, UR-CMAP
Victorien Bouffetier	University of Bordeaux	Postdoc, Eu-XFEL
Abraham Chien	Princeton University	Private Industry
Heath LeFevre	University of Michigan	NSF Postdoc Fellow, University of Michigan
Brandon Lahmann	MIT	Postdoc, LLNL



UNIVERSITY *of*
ROCHESTER